SPACE-TIME CHANNEL MODELING, SIMULATION, AND CODING

A Thesis
Presented to
The Academic Faculty

by

Alenka G. Zajić

In Partial Fulfillment
of the Requirements for the Degree
Doctor of Philosophy in the
Electrical and Computer Engineering

Georgia Institute of Technology
December 2008

SPACE-TIME CHANNEL MODELING, SIMULATION, AND CODING

Approved by:

Professor Gordon L. Stüber, Advisor
School of Electrical and Computer Engineering
Georgia Institute of Technology

Professor Steven W. McLaughlin
School of Electrical and Computer Engineering
Georgia Institute of Technology

Professor Ye (Geoffrey) Li
School of Electrical and Computer Engineering
Georgia Institute of Technology

Professor George F. Riley
School of Electrical and Computer Engineering
Georgia Institute of Technology

Professor Gregory D. Durgin
School of Electrical and Computer Engineering
Georgia Institute of Technology

Professor Hyesoon Kim
School of Computer Science
Georgia Institute of Technology

Date Approved: July 18th 2008

To

my parents Branka Mršulja-Zajić & Gradimir Zajić,

my brother Vojin Zajić,

and

my husband Miloš Prvulović.

ACKNOWLEDGEMENTS

It has been an honor to have Prof. Gordon L. Stüber as my thesis advisor. He has taught me most of what I know about the way to conduct, publish, and present research. He has also been very supportive and has stood as a good example of a great advisor. I especially value the freedom he gave me in conducting the research. It made these four years at Georgia Tech enjoyable and fun.

I would like to thank my thesis committee members, which I deeply respect and hope to become like in my own academic career, for their efforts to improve this thesis.

This thesis would not have been possible without the unwavering support of my husband, Miloš Prvulović, who has shown infinite love and patience over the years while I worked on the research. I was also helped and encouraged by my parents and my brother. Without their support and love this thesis would not have been completed.

Finally, I have had great lab-mates at the Wireless Systems Lab. It has been a pleasure to share ideas and coffee-breaks with Galib, Sami, Nauman, Baris, Michael, Joon Beom, Qing, Kihong, Hyung-Seok, Chirag, Heewon, and Apurva.

TABLE OF CONTENTS

LIST OF TABLES

LIST OF FIGURES

SUMMARY

Several emerging wireless applications require direct transmission between mobile terminals. Examples of these applications are mobile ad-hoc wireless networks, intelligent transportation systems, relay-based cellular networks, and future combat systems. Development of these mobile-to-mobile (M-to-M) systems depends on a good characterization of channel propagation. Another important consideration in modern communication systems is the use of multipath propagation to improve reliability and capacity of wireless systems. This is achieved by employing multiple antennas in multiple-input multiple-output (MIMO) systems and using techniques such as transmit and receive diversity. Considering the demand for high-speed wireless services, MIMO M-to-M systems are the leading candidates for future communication systems.

To enable the successful design of MIMO M-to-M systems, our research focuses on modeling of MIMO M-to-M multipath fading channels and on diversity techniques for MIMO systems. Specifically, we propose two-dimensional (2-D) and three-dimensional (3-D) MIMO M-to-M statistical channel models that encompass narrowband and wideband MIMO channel scenarios for macro- and micro-cell environments. Furthermore, we validate the new models against measured data and find very close agreement between them. Using our 3-D models, we also investigate different antenna array configurations and their effect on the capacity of MIMO M-to-M systems. Contrary to common assumptions, we have found that there is no significant loss of capacity if the antenna array is tilted from the horizontal plane. Finally, we propose the design criteria for space-time coded continuous phase modulated systems.

Our work would provide other researchers the tools needed to design and test future MIMO M-to-M communication systems.

CHAPTER I

INTRODUCTION

1.1 Motivation

Mobile communications is a rapidly growing area of the telecommunications industry because of its ability to connect people "on the move." All present-day mobile radio systems offer mobility only on one (the user's) end, while the service provider's end is immobile. This is in contrast to several emerging wireless communication systems where mobile users can directly communicate with each other. Such systems are referred to as mobile-to-mobile (M-to-M) communication systems [1]. The driving force behind M-to-M communications is the consumer demand for better quality of service, new applications, and increased mobility support. The M-to-M systems find applications in mobile ad-hoc wireless networks, intelligent transportation systems, and future cellular systems employing cooperative diversity techniques [2].

To successfully design M-to-M systems, a detailed knowledge of radio propagation channels for M-to-M links is necessary. M-to-M channels differ from fixed-to-mobile (F-to-M) cellular radio channels, where the base station is stationary, elevated, and relatively free of local scattering. In M-to-M communication channels, both the transmitter and receiver are in motion and equipped with low elevation antennas. To enable successful design of M-to-M systems, our research focuses on the study and characterization of M-to-M multipath fading channels. The first objective of this thesis is to develop new simulation models for single-input single-output (SISO) F-to-M and M-to-M channels and compare them with existing simulation models.

In the past, multipath propagation in the wireless medium was viewed as an obstacle in designing reliable communication links. However, decades of research have changed this paradigm. Modern communication systems try to leverage this multipath property to improve reliability and capacity of the system. This is achieved by employing multiple antennas in multiple-input multiple-output (MIMO) systems and using techniques such as transmit and receive diversity. Information theory has shown that the wireless channel can support enormous theoretical capacities if the multipath propagation is properly exploited using MIMO techniques [3]. Considering the demand for high-speed wireless services, MIMO systems seem to be the future of communication systems. The second objective of this theses is to develop two- and three-dimensional theoretical and simulation models for MIMO M-to-M multipath fading channels.

Transmit and receive diversity are well-known techniques to exploit the increased capacity of MIMO channels. Space-time (ST) coding is a transmit diversity technique that exploits a dense scattering environment by using multiple transmit antennas [4]. One of the design criteria for space-time codes is to attain full spatial diversity so that all channels in the MIMO system contribute an independent spatial diversity gain. Coding gain optimization is another design objective for space-time codes. Many different ST codes have been developed for quasi-static Rayleigh fading channels and linear modulations [4]–[14].

Continuous phase modulation (CPM) is a nonlinear modulation scheme with high bandwidth efficiency [15]. Space-time code design for CPM is more difficult than for linear modulations because of the nonlinearity of the modulation and its more complex performance matrices. To the best of our knowledge, a general framework for ST-CPM in terms of diversity order and coding gain is not available in the open literature. The final objective of this thesis is to determine the conditions under which CPM space-time codes will attain both full spatial diversity and optimal coding gain.

1.2 Simulation Models for SISO F-to-M and M-to-M Fading Channels

Simulation of fading channels is commonly used as opposed to field trials, because it allows for less expensive and more reproducible system tests and evaluations. There are several different methods for simulating F-to-M cellular and M-to-M fading channels. The most widely accepted methods are filtered noise models [16] - [19] and sum-of-sinusoids (SoS) models [20] - [34]. The filtered noise models filter Gaussian noise through appropriately designed filters to generate the channel waveform with the desired channel power spectral density (the Doppler spectrum). The main limitation of this approach is that only rational forms of the Doppler spectrum can be produced, whereas the Doppler spectrum is typically non-rational [35]. In contrast to filtered noise models, SoS models have low complexity and produce channel waveforms that have high accuracy and a perfectly band-limited Doppler spectrum. Owing to these advantages, our research focuses on SoS models.

1.2.1 SoS Simulation Models for SISO F-to-M Fading Channels

Many approaches have been suggested for SoS modeling of SISO F-to-M Rayleigh fading channels. Clarke [20] was among the first to propose a mathematical reference model for Rayleigh fading channels. A simplified version of Clarke's model, proposed by Jakes [21], has been widely used for about three decades. However, Jakes' model fails to meet most statistical properties required by the reference model [22] and is not wide-sense stationary [23]. Consequently, various modifications of Jakes' model have been reported [23] - [26]. Each new model improves some statistical properties, but none of them obtains all the desired statistical properties of Clarke's reference model.

To improve on previously reported models, Zheng and Xiao proposed several new statistical models [27] - [29]. By leaving all three parameter sets (amplitudes, phases, and Doppler frequencies) as random variables, Zheng and Xiao's models obtain statistical properties similar to those of the reference model. However, their models are no longer ergodic; their statistical properties vary for each simulation trial, but converge to the desired properties when averaged over 50 to 100 simulation trials.

By analyzing previously reported models, it can be observed that most of the models have difficulty in creating uncorrelated in-phase and quadrature components of the complex faded envelope and in creating multiple uncorrelated faded envelopes. To address these problems, we propose new SoS simulation models for F-to-M Rayleigh fading channels. The new models obtain correct statistical properties and overcome the difficulty of creating uncorrelated in-phase and quadrature components and of creating multiple uncorrelated faded envelopes.

1.2.2 SoS Simulation Models for SISO M-to-M Fading Channels

Several methods for simulating SISO M-to-M channels have been proposed in the literature. Wang and Cox [1] described a model that approximates the continuous Doppler spectrum by a discrete line spectrum. However, the correlation functions are periodic functions of the time delay, and the method requires numerical integration of the Doppler spectrum [34]. Patel *et al.* [34] proposed two SoS models for SISO M-to-M channels. First, they modified the Method of Exact Doppler Spread (MEDS) proposed by Patzold *et al.* for F-to-M channels [36]. However, the statistical correlation functions of the simulated faded envelope match those of the reference model only for a small range of normalized time delays. To improve the properties of the proposed model, Patel *et al.* [34] also modified a statistical SoS model proposed by Zheng *et al.* for F-to-M channels [28]. However, the model requires a large number of simulation trials (at least 50) to obtain adequate ensemble averaged statistical properties.

Existing models have notable difficulties producing time averaged auto- and cross-correlation functions that match those of the reference model. To address these difficulties, we propose a new statistical SoS model for SISO M-to-M Rayleigh fading channels.

1.3 2-D and 3-D Theoretical and Simulation Models for MIMO M-to-M Multipath Fading Channels

The demand for high-speed wireless services makes MIMO M-to-M systems the leading candidates for future communication systems. To enable the successful design of these systems, our research focuses on development of 2-D and 3-D theoretical and simulation models for MIMO M-to-M multipath fading channels.

1.3.1 2-D Models for MIMO M-to-M Multipath Fading Channels

Pätzold *et al.* were the first to propose a 2-D reference model for MIMO M-to-M channels [37]. Based on this reference model, they also proposed a 2-D deterministic SoS model called the Modified Method of Exact Doppler Spreads (MMEDS) [38]. Previously reported models for both, SISO M-to-M channels [1], [31] - [34] and MIMO M-to-M channels [37], [38] consider radio propagation in outdoor macro-cells, assuming that all rays are only double-bounced. However, the channel measurements for narrowband and wideband M-to-M communications [39], [40] show that this assumption is not always correct.

To address this problem, we propose a new 2-D parametric reference model that constructs the received complex faded envelope as a superposition of the line-of-sight, single-bounced, and double-bounced rays. The parametric nature of the model makes it adaptable to a variety of propagation environments, i.e., outdoor micro- and macro-cells. For example, our reference model will describe the radio propagation in outdoor macro-cells as a combination of single- and double-bounced rays, taking into account that the double-bounced rays bear more energy than single-bounced rays.

The reference model in [37] as well as our 2-D parametric reference model assume an infinite number of scatterers, which prevents practical implementation. Therefore, we also propose new SoS simulation models for 2-D isotropic scattering environments and compare them with the simulator in [38].

1.3.2 3-D Models for MIMO M-to-M Multipath Fading Channels

All previously reported models for SISO M-to-M channels [1], [31], [32], [34] and MIMO M-to-M channels [37], [38] assume that the fields incident on the transmitter or the receiver antennas are composed of a number of waves travelling only in the *horizontal* plane. This assumption is valid only for certain environments, e.g., rural areas. However, this seems inappropriate for urban environments where the transmitter and receiver antenna arrays are often located in close proximity to and lower than the surrounding buildings. Scattered waves may propagate by diffraction from the edges of buildings down to the street and, thus, not necessarily travel horizontally.

To more appropriately model radio propagation in an urban M-to-M environment, we propose the *narrowband* and *wideband* 3-D reference models for MIMO M-to-M multipath fading channels. From the 3-D reference models, we derive the first- and second-order channel statistics. Also, deterministic and statistical SoS simulation models for narrowband and wideband 3-D non-isotropic scattering environments are developed. Furthermore, our simulation models are used to evaluate the effect of space-time correlation on the outage capacity of uniform linear antenna arrays. Finally, we compare the first- and second-order channel statistics with those obtained from measured data. The close agreement between the analytical and empirical curves confirms the utility of the proposed 3-D models.

1.4 A Space-time Code Design for CPM

Space-time (ST) coding transmits coded waveforms from multiple antennas to maximize link performance. *Full spatial diversity* is one design objective for ST codes, being upper bounded by the product $L_t \times L_r$, where L_t and L_r are the number of transmit and receive antennas, respectively. *Coding gain* optimization is another design objective for space-time codes. Many different ST codes have been developed for quasi-static Rayleigh fading channels [4]–[14]. Tarokh *et al.* [4] devised the rank and determinant criteria for spatial diversity that optimizes the worst case pair-wise error probability (PWEP) and presented some simple design rules that guarantee full spatial diversity for linear modulation schemes. Several ST code designs based on the rank and determinant criteria are proposed in [5]–[7]. In [8], the determinant criterion is strengthened by showing that the Euclidean distance must be optimized in order to optimize the product distance. Finally, in [9], it is shown that different design criteria apply depending on the diversity order. For sufficient degrees of freedom ($L_t \times L_r \geq 4$), the code performance is governed by the minimum squared Euclidean distance of the code. For small $L_t \times L_r$, the rank and determinant criteria will govern the code performance.

One of the main difficulties encountered when deriving general design rules for ST codes is that the diversity and coding design criteria apply to the complex domain of baseband-modulated wavemforms, whereas block code designs are usually conducted over finite fields. Hammons and Gamal [10] proposed rank criteria that ensure full diversity for space-time codes with binary phase–shift keying (BPSK) and quaternary phase–shift keying (QPSK). Liu *et al.* [11] generalized these rank criteria for higher-order quadrature amplitude modulation (QAM) constellations. Space-time coding can also be applied to continuous phase modulated signals. Zhang and Fitz [41], [42] derived design criteria for space-time coded CPM (ST-CPM) on quasi-static fading channels and identified a rank criterion, but only for some particular CPM schemes.

Some attempts to optimize the coding gain of ST-CPM have been made in [43]–[45]. In [43], [44], an orthogonal ST-CPM system is proposed with $L_t = 2$, where different CPM schemes are used on the two transmit antennas. This method attains full diversity and good coding gain, but it requires bandwidth expansion because of a large CPM modulation index. In [45], a ST-CPM scheme is proposed with $L_t = 2$ that uses different mapping rules on the two antennas to achieve full diversity and optimal coding gain. However, the extension to $L_t > 2$ has not been considered.

In conclusion, a general framework for ST-CPM is lacking both in terms of diversity order and coding gain. Hence, we derive conditions under which M-ary partial- and full-response CPM space-time codes will attain both full spatial diversity and optimal coding gain.

1.5 Research Contributions

This section summarizes the contributions of this thesis.

- Development of novel SoS simulation models for SISO F-to-M Rayleigh fading channels and comparison with existing simulation models [46].

- Development of a novel statistical SoS simulation model for SISO M-to-M Rayleigh fading channels [47].

- Development of novel 2-D reference and simulation models for MIMO M-to-M Ricean fading channels [48].

- Development of novel 3-D reference and simulation models for narrowband MIMO M-to-M multipath fading channels [50].

- Development of novel 3-D reference and simulation models for wideband MIMO M-to-M multipath fading channels [50].

- Derivation of the envelope level crossing rate and average envelope fade duration for M-to-M multipath fading channels [51].

- Experimental validation of our 3-D models for wideband MIMO M-to-M multipath fading channels [52].

- Derivation of the conditions under which CPM space-time codes attain both full spatial diversity and optimal coding gain [53].

1.6 Thesis Outline

The remainder of this thesis is organized as follows. Chapter 2 reviews the important concepts of propagation modeling, describes F-to-M and M-to-M channels, reviews existing techniques for modeling and simulation of F-to-M and M-to-M channels, and reviews a linear decomposition of CPM signals. Chapter 3 describes our SoS simulation models for SISO F-to-M Rayleigh fading channels. Chapter 4 describes our SoS statistical simulation model for SISO M-to-M Rayleigh fading channels. Chapter 5 presents our 2-D parametric reference and simulation models for MIMO M-to-M Ricean fading channels. Chapter 6 describes our 3-D "two-cylinder" geometrical propagation model and presents our 3-D reference and simulation models for narrowband MIMO M-to-M multipath fading channels. Chapter 7 describes our 3-D "concentric-cylinders" geometrical propagation model and presents our 3-D reference and simulation models for wideband MIMO M-to-M multipath fading channels. Chapter 8 derives the envelope level crossing rate and average envelope fade duration for M-to-M multipath fading channels. Chapter 9 describes our MIMO M-to-M channel-sounding experimental campaign and presents the experimental validation of our theoretical and simulation models presented in Chapters 6 - 8. Chapter 10 details the conditions under which CPM space-time codes attain both full spatial diversity and optimal coding gain. Finally, Chapter 11 concludes the thesis by summarizing our research contributions and by addressing open areas of research in wireless channel modeling, simulation, and coding.

CHAPTER II

BACKGROUND

The design of spectrally efficient wireless communication systems requires a detailed understanding of the multipath propagation environment. Furthermore, the design of highly reliable and high-speed wireless communication systems requires the use of multiple antennas as well as transmit and receive diversity techniques. With this in mind, this chapter briefly reviews important concepts of propagation modeling, describes F-to-M and M-to-M channels, reviews existing techniques for modeling and simulation of F-to-M and M-to-M channels, and reviews ST-CPM systems.

2.1 Propagation Modeling

Fading, in general, refers to the time variation of the received signal power caused by changes in the transmission medium or path. Fading is usually classified as large-scale fading or small-scale fading. Path loss and shadow fading are called large-scale fading because they are dominant when the receiver moves over distances greater than several tens of the carrier wavelength. Large-scale fading plays an important role in determining the cell coverage area, outage, and handoffs. On the other hand, small-scale fading is caused by multipath propagation. This effect plays an important role in determining link level performance in terms of bit error rates, average fade durations, etc.

2.1.1 Path Loss and Shadow Fading

Path loss is the attenuation in the transmitted signal as it propagates from the transmitter ($\mathrm{T_x}$) to the receiver ($\mathrm{R_x}$). This attenuation may be caused by effects such as free-space loss, refraction, diffraction, reflection, and absorption. Path loss is also influenced by terrain contours, environment (e.g., a city or a muddy path in the woods), propagation medium (e.g., dry or moist air), the distance between the $\mathrm{T_x}$ and $\mathrm{R_x}$, and the height and location of antennas.

The simplest path loss model assumes a line-of-sight (LoS) link between the $\mathrm{T_x}$ and $\mathrm{R_x}$ and propagation in free space. Under these assumptions, the received signal power is given as [35]

$$P_R = P_T G_T G_R \frac{\lambda^2}{4\pi d^2}, \tag{1}$$

where P_T is the transmitted power, G_T and G_R are the transmit and receive antenna gains, respectively, λ is the carrier wavelength, and d is the distance between the $\mathrm{T_x}$ and $\mathrm{R_x}$. Note that the path loss exponents (the power of the distance dependence) in this equation are 2 for free-space propagation.

The signals in wireless communications, however, do not experience free space propagation. Therefore, several different models such as the Okumura-Hata, Lee, Walfish-Ikegami, etc., [35] have been proposed to model path loss in different propagation environments such as urban, rural, and indoor areas. Experiments indicate that the actual path loss exponents are between 3 - 8. A detailed description of different path loss models can be found in [35].

The path loss models described above assume that the path loss is constant at a given distance. However, the presence of obstacles such as buildings and trees results in random variations of the received power at a given distance. This effect is called shadow fading.

Experimental results show that shadow fading can be modeled as a log-normal random variable. The shadow fading distribution is given by [35]

$$f_{\Omega_p}(x) = \frac{10}{x\sigma_\Omega \sqrt{2\pi}\ln 10} \exp\left[-\frac{(10\log_{10} x - \mu_{\Omega_p(\mathrm{dBm})})^2}{2\sigma_\Omega^2}\right], \tag{2}$$

where Ω_p denotes the mean squared envelope level, μ_{Ω_p} is the area mean expressed in dBm and σ_Ω is the standard deviation of the shadow fading. Typical σ_Ω values range from 5 - 10 dB.

2.1.2 Multipath Propagation and Fading

Multipath propagation is the propagation mechanism manifested when the transmitted signal reaches the receive antenna by two or more paths. The presence of local scattering objects, such as mountains and buildings, often obstructs a direct wave path between the $\mathrm{T_x}$ and $\mathrm{R_x}$. Then, a non-line-of-sight (NLoS) propagation path will exist between the $\mathrm{T_x}$ and $\mathrm{R_x}$. As a consequence, the waves must propagate via reflection, diffraction, and scattering. At the receiver, waves arrive from many different directions and with different delays. The multiple waves combine vectorially at the receiver antenna (a phenomenon called multipath fading) to produce a composite received signal.

Diffuse wave components arise under NLoS propagation due to the presence of scatterers in the environment. In the presence of such diffuse components, the fading is described by a Rayleigh distribution. However, when a specular component, i.e., LoS or a strong reflected path, also arrives at the receiver, the fading is described by a Rician distribution. The interested reader is referred to [54] for a detailed discussion of fading and the physics behind it.

The channel can be modeled by a linear time-variant filter that has the complex low-pass impulse response [35]

$$h(t,\tau) = \sum_{l=1}^{L} g_l(t)\delta(\tau - \tau_l), \tag{3}$$

where L is the total number of resolvable multipath components, $g_l(t)$ is the time-varying complex faded envelope associated with the l^{th} resolvable multipath component arriving with an average time delay τ_l. Each time-varying complex faded envelope $g_l(t)$ is either Rayleigh or Rician faded.

Time selectivity and frequency selectivity are two important properties of the channel impulse response. Time selectivity refers to the property that the channel impulse response changes with time. This is caused by the motion of the $\mathrm{T_x}$, the $\mathrm{R_x}$, and/or the scatterers. When viewed in the frequency domain, time selectivity appears as Doppler shifts in the transmitted signal, causing a broadening of the transmitted signal spectrum. This effect is also called frequency dispersion. Based on the rate with which the channel impulse response changes relative to the signal transmission rate, channels may be classified as fast fading or slow fading. Fast fading implies that the channel changes within the transmitted symbol duration, while slow fading implies that the channel is approximately constant within a symbol duration. A good measure of channel selectivity is given by the channel coherence time, or equivalently, the Doppler spread, i.e., the time duration for which the channel can be considered as approximately time-invariant.

Frequency selectivity refers to the property that the channel impulse response changes with frequency. Multipath components that arrive with different time delays cause this frequency selectivity. Based on their degree of frequency selectivity, channels may be classified as frequency-flat or frequency-selective channels. If all the transmitted frequencies undergo approximately identical amplitude and phase changes, the channel is called frequency-flat. On the other hand, if all transmitted frequencies experience different amplitude and phase changes, the channel is termed frequency-selective. Frequency selectivity is measured in terms of the coherence bandwidth, i.e., the bandwidth over which the channel's frequency response remains constant. The channel can be considered frequency-flat only if the transmission is *narrowband* compared to the channel's coherence bandwidth. Otherwise, the channel is frequency-selective.

2.2 F-to-M Channels

A fixed-to-mobile (F-to-M) cellular channel is a channel between a base station (BS), which is stationary, elevated, and relatively free of local scattering, and a mobile station (MS) that is mobile, low elevated, and surrounded by local scatterers, as shown in Fig. 1. In the past four decades, several modeling and simulation approaches for F-to-M channels have been proposed. The pioneering work done by Clarke provides a theoretical reference model for SISO F-to-M channels [20].

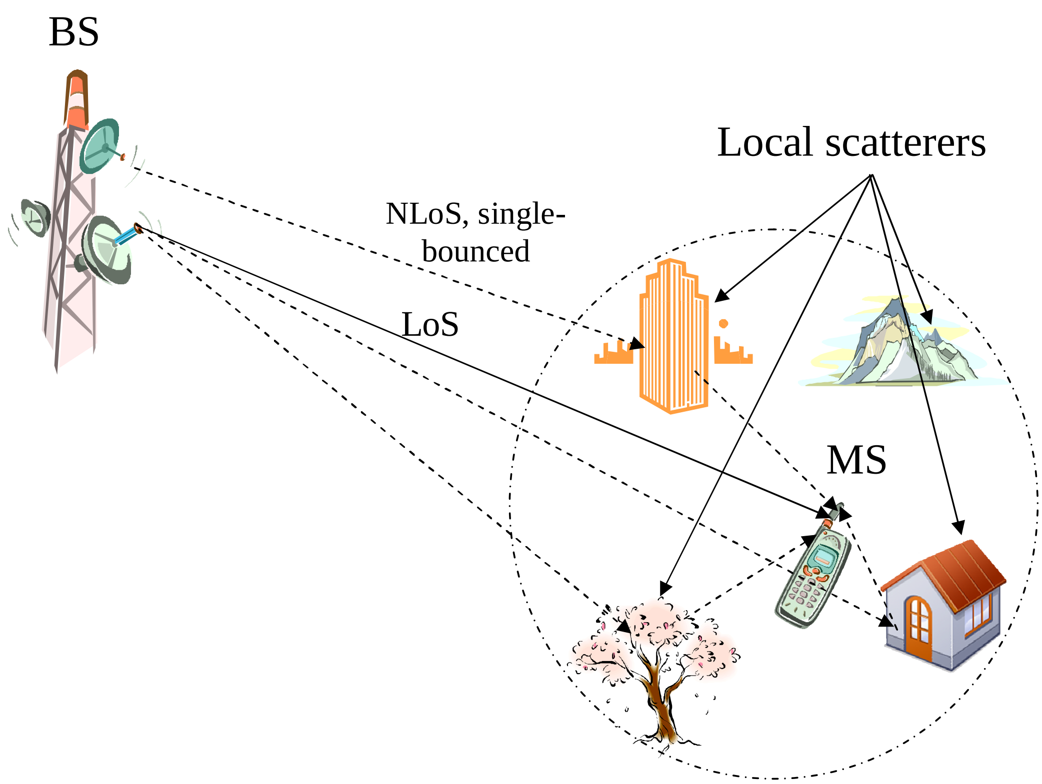

Figure 1: Typical F-to-M propagation environment.

Clarke's reference model defines the complex faded envelope under narrowband, frequency flat fading, and NLoS propagation assumptions as [20]

$$g(t) \quad = \quad \lim_{N\to\infty} \sum_{n=1}^{N} C_n \exp\{j(\omega_d t \cos\alpha_n + \phi_n)\}, \tag{4}$$

where N is the number of propagation paths and ϕ_n is the random phase of the n^{th} multipath component, uniformly distributed on the interval $[-\pi, \pi)$. The maximum angular Doppler frequency, ω_d, is defined as $\omega_d = 2\pi f_d = (2\pi v)/\lambda$, where f_d is the maximum Doppler frequency in Hertz, λ is the carrier wavelength, and v is the speed of the MS. The angle of arrival, α_n, depends on the scattering environment and the antenna radiation pattern. It is assumed that C_n, α_n, and ϕ_n are mutually independent and that α_n is uniformly distributed on the interval $[-\pi, \pi)$. Invoking the Central Limit Theorem [35], the real part, $g_i(t) = \Re\{g(t)\}$, and the imaginary part, $g_q(t) = \Im\{g(t)\}$, of the complex faded envelope are Gaussian random processes as $N \to \infty$. Therefore, the envelope $|g(t)|$ is Rayleigh distributed and the phase $\Theta_g(t)$ is uniformly distributed. The auto- and cross-correlation functions of the reference model, assuming a 2-D scattering environment, are summarized below [35]

$$
\begin{aligned}
R_{g_{i/q}g_{i/q}}(\tau) &= \mathrm{E}\left[g_{i/q}(t+\tau)g_{i/q}(t)\right] = J_0(\omega_d\tau), && (5)\\
R_{g_ig_q}(\tau) &= R_{g_qg_i}(\tau) = \mathrm{E}\left[g_{i/q}(t+\tau)g_{q/i}(t)\right] = 0, && (6)\\
R_{g_kg_l}(\tau) &= \frac{1}{2}\mathrm{E}\left[g_k(t+\tau)g_l(t)^*\right] = \begin{cases} J_0(\omega_d\tau) & l = k \\ 0 & l \neq k \end{cases}, && (7)\\
R_{|g_k|^2|g_k|^2}(\tau) &= \mathrm{E}\left[|g_k(t+\tau)|^2\,|g_k(t)|^2\right] = 4 + 4J_0(\omega_d\tau), && (8)
\end{aligned}
$$

where $E[\cdot]$ is the statistical expectation operator, $(\cdot)^*$ denotes the complex conjugate operator, and $J_0(\cdot)$ is the zeroth-order Bessel function of the first kind.

These statistical properties enable the system designer to make informed decisions when choosing modulation, interleaving, and coding schemes at the transmitting end and the type of channel estimator and decoder at the receiving end.

2.3 M-to-M Channels

Mobile-to-mobile (M-to-M) channels have characteristics that are widely different from F-to-M cellular channels. In M-to-M channels, both the $\mathrm{T_x}$ and $\mathrm{R_x}$ are in motion, equipped with low elevation antennas, and surrounded by local scatterers, as shown in Fig. 2. Akki and Haber [31], [32] showed the received signal envelope of M-to-M channels is Rayleigh faded under NLoS conditions, but the statistical properties differ from F-to-M channels. They were the first to propose a theoretical reference model for SISO M-to-M channels [31].

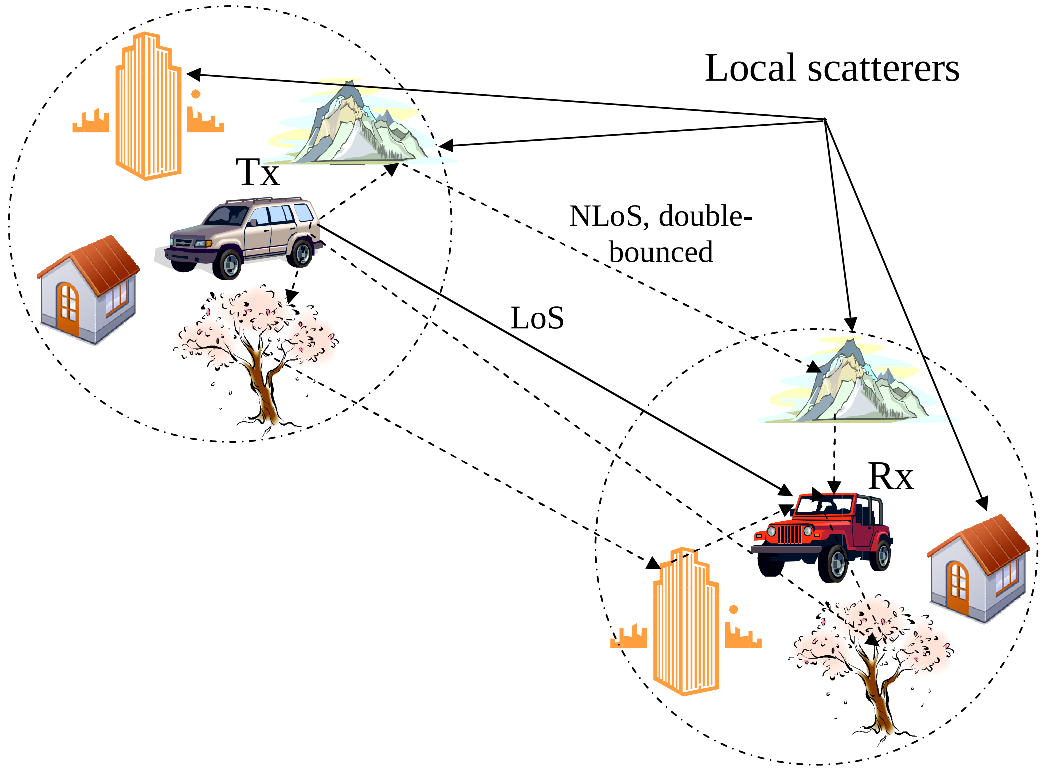

Figure 2: Typical M-to-M propagation environment.

2.3.1 The Reference Model for SISO M-to-M Fading Channels

Akki and Haber's SISO M-to-M reference model defines the complex faded envelope under narrowband, frequency flat fading, and NLoS propagation assumptions as [31]

$$g(t) \;=\; \lim_{N\to\infty}\sqrt{\frac{2}{N}}\sum_{n=1}^{N}\exp\left\{j[\omega_1 t\cos(\alpha_n)+\omega_2 t\cos(\beta_n)+\phi_n]\right\}, \tag{9}$$

where N is the number of propagation paths, ω_1 and ω_2 are the maximum angular Doppler frequencies, α_n and β_n are the angle of departure and the angle of arrival of the n^{th} propagation path measured with respect to the $\mathrm{T_x}$ and $\mathrm{R_x}$ velocity vectors, respectively, and ϕ_n is the phase associated with the n^{th} propagation path. It is assumed that α_n, β_n, and ϕ_n are mutually independent random variables and that ϕ_n is uniformly distributed on the interval $[-\pi, \pi)$. Invoking the Central Limit Theorem, the I component, $g_i(t) = \Re\{g(t)\}$, and the Q component, $g_q(t) = \Im\{g(t)\}$, of the complex faded envelope are Gaussian random processes as $N \to \infty$. Therefore, the envelope $|g(t)|$ is Rayleigh distributed and the phase $\Theta_g(t)$ is uniformly distributed. The auto- and cross-correlation functions of the reference model, assuming omnidirectional antennas and a 2-D isotropic scattering environment, are in the limit $N \to \infty$ [31], [32]

$$\begin{aligned}
R_{g_i g_i}(\tau) &= \mathrm{E}[g_i(t+\tau)g_i(t)] = J_0(\omega_1\tau)J_0(\omega_2\tau), && (10)\\
R_{g_q g_q}(\tau) &= \mathrm{E}[g_q(t+\tau)g_q(t)] = J_0(\omega_1\tau)J_0(\omega_2\tau), && (11)\\
R_{g_i g_q}(\tau) &= R_{g_q g_i}(\tau) = \mathrm{E}[g_i(t+\tau)g_q(t)] = 0, && (12)\\
R_{gg}(\tau) &= \frac{1}{2}\mathrm{E}[g(t+\tau)g(t)^*] = J_0(\omega_1\tau)J_0(\omega_2\tau). && (13)
\end{aligned}$$

Note that auto-correlation functions of M-to-M channels are a product of two Bessel functions in contrast to F-to-M channel, where the corresponding functions involve single Bessel functions [35].

2.3.2 The Reference Model for MIMO M-to-M Fading Channels

Pätzold *et al.* were the first to propose a two-dimensional (2-D) reference model for MIMO M-to-M channels [37], [38]. They used the "two-ring" model, proposed in [55], to derive their reference model.

Figure 3 shows the "two-ring" model for MIMO M-to-M channels with $L_t = L_r = 2$ antenna elements. This model defines two rings of fixed scatterers, one around the $\mathrm{T_x}$ and another around the $\mathrm{R_x}$. Around the transmitter, M omnidirectional scatterers lie on a ring of radius R_t, and the m^{th} transmit scatterer is denoted by $S_T^{(m)}$. Similarly, around the receiver, N omnidirectional scatterers lie on a ring of radius R_r and the n^{th} receive scatterer is denoted by $S_R^{(n)}$. The distance between the transmitter and the receiver is D. The spacing between two antenna elements at the $\mathrm{T_x}$ and $\mathrm{R_x}$ is denoted by δ_T and δ_R, respectively. Angles θ_T and θ_R describe the orientation of the $\mathrm{T_x}$'s antenna array and the $\mathrm{R_x}$'s antenna array, respectively, relative to the x-axis.

Similarly, the T_x and R_x are moving with speeds v_T and v_R in directions described by angles γ_T and γ_R, respectively. The symbols $\alpha_T^{(m)}$ and $\alpha_R^{(n)}$ denote the angles of departures (AoD) and the angles of arrival (AoA), respectively. Finally, the symbols ϵ_{pm}, ϵ_{mn}, and ϵ_{nq} denote distances $A_T^{(p)}$ - $S_T^{(m)}$, $S_T^{(m)}$ - $S_R^{(n)}$, and $S_R^{(n)}$ - $A_R^{(q)}$, respectively, as shown in Fig 3.

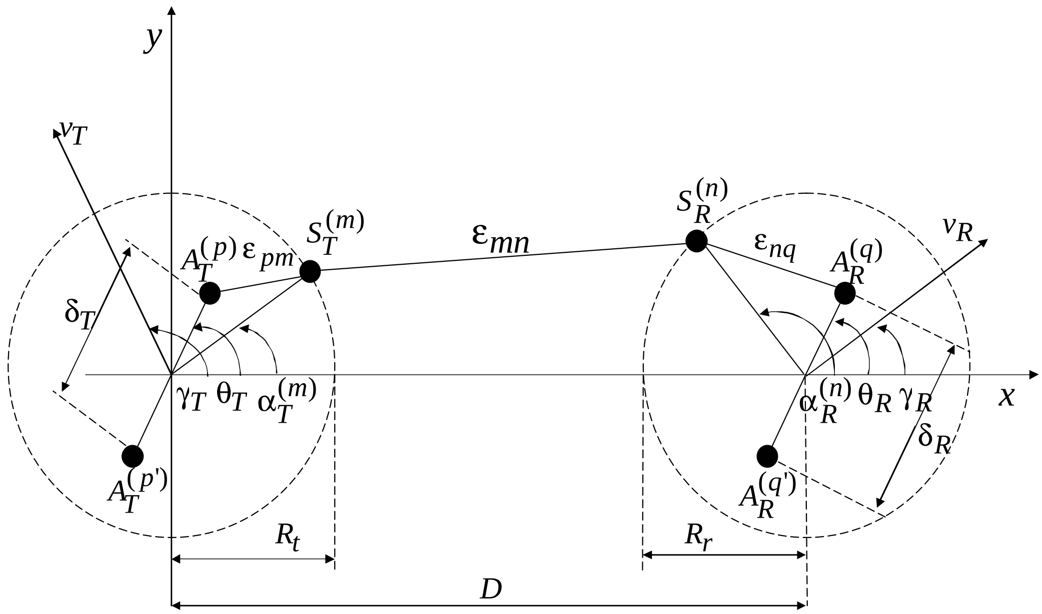

Figure 3: Geometrical "two-ring" model for MIMO M-to-M channels with $L_t = L_r = 2$ antenna elements.

Using the "two-ring" model, the reference model [37], [38] defines the complex faded envelope of the link $A_T^{(p)}$ - $A_R^{(q)}$ under narrowband, frequency flat fading, and NLoS propagation assumptions as

$$h_{pq}(t) = \lim_{M,N\to\infty} \frac{1}{\sqrt{MN}} \sum_{m,n=1}^{M,N} a_{p,m}\ c_{m,n}\ b_{n,q} \exp\left\{j\left[2\pi\left(f_T^{(m)} + f_R^{(n)}\right)t + \phi_{mn} + \phi_0\right]\right\}, \tag{14}$$

where $\phi_0 = -(R_t + D + R_r)\,2\pi/\lambda$, parameters $a_{p,m}$, $c_{m,n}$, and $b_{n,q}$ are defined as

$$a_{p,m} = \exp\left[j\frac{2\pi}{\lambda}(0.5L_t + 0.5 - p)\,\delta_T \cos\left(\alpha_T^{(m)} - \theta_T\right)\right], \tag{15}$$

$$c_{m,n} = \exp\left[j\frac{2\pi}{\lambda}\left(R_t \cos\alpha_T^{(m)} - R_r \cos\alpha_R^{(n)}\right)\right], \tag{16}$$

$$b_{n,q} = \exp\left[j\frac{2\pi}{\lambda}(0.5L_r + 0.5 - q)\,\delta_R \cos\left(\alpha_R^{(n)} - \theta_R\right)\right], \tag{17}$$

and parameters p and q take values from the sets $p \in \{1, \ldots, L_t\}$ and $q \in \{1, \ldots, L_r\}$, respectively. Additionally, it is assumed that AoDs $\alpha_T^{(m)}$, AoAs $\alpha_R^{(n)}$, and phases ϕ_{mn} are mutually independent random variables and that ϕ_{mn} is uniformly distributed on the interval $[0, 2\pi)$. Frequencies $f_T^{(m)}$ and $f_R^{(n)}$ are equal to $f_{T\max} \cos(\alpha_T^{(m)} - \gamma_T)$ and $f_{R\max} \cos(\alpha_R^{(n)} - \gamma_R)$, respectively, where $f_{T\max} = v_T/\lambda$ and $f_{R\max} = v_R/\lambda$ are the maximum Doppler frequencies of the $\mathrm{T_x}$ and $\mathrm{R_x}$, respectively, and λ is the carrier wavelength.

The cross-correlation function of the MIMO M-to-M reference model, assuming omni-directional antennas and a 2-D isotropic scattering environment, are in the limit $N \to \infty$ [38]

$$\begin{aligned} R_{pq,\tilde{p}\tilde{q}}(\delta_T, \delta_R, \tau) &= \mathrm{E}\left[h_{pq}(t) h^*_{\tilde{p}\tilde{q}}(t+\tau)\right] \\ &= J_0\left(2\pi\sqrt{\frac{(\tilde{p}-p)\delta_T}{\lambda} + (f_{T\max}\tau)^2 - 2\frac{(\tilde{p}-p)\delta_T}{\lambda}\tau\cos\left(\alpha_T - \gamma_T\right)}\right) \\ &\times\ J_0\left(2\pi\sqrt{\frac{(\tilde{q}-q)\delta_R}{\lambda} + (f_{R\max}\tau)^2 - 2\frac{(\tilde{q}-q)\delta_R}{\lambda}\tau\cos\left(\alpha_R - \gamma_R\right)}\right), \end{aligned} \tag{18}$$

where $p, \tilde{p} \in \{1, \ldots, L_t\}$ and $q, \tilde{q} \in \{1, \ldots, L_r\}$.

2.4 Simulation Models for Fading Channels

As mentioned in Chapter 1, there are several different methods for simulating fading channels. The most accepted of these methods are filtered noise models [16] - [19] and sum-of-sinusoids-based (SoS) models [24] - [30]. The filtered noise models filter Gaussian noise through appropriately designed filters to generate the channel waveform with the desired channel power spectral density (the Doppler spectrum). The main limitation with this approach is that only rational forms of the Doppler spectrum can be produced, whereas the Doppler spectrum is typically non-rational [35]. To approximate the non-rational Doppler spectrum, a high-order filter is required. Unfortunately, a high-order filter has a long impulse response which significantly increases the run times for software simulation. Furthermore, the Doppler spectrum obtained using this method is not band-limited because filters with sharp stop-bands are difficult to implement in practice. On the other hand, the SoS models generate the channel waveform by superimposing a finite number of properly selected sinusoids. In contrast to filtered noise models, SoS models have low complexity and produce channel waveforms that have high accuracy and a perfectly band-limited Doppler spectrum. In addition, SoS models can be easily extended to develop space-time correlated channel models for MIMO antenna systems. Owing to these advantages, our research focuses on SoS models.

Generally, SoS models can be classified as either deterministic or statistical. Deterministic SoS models have fixed phases, amplitudes, and Doppler frequencies for all simulation trials. In contrast, statistical SoS models leave at least one of the parameter sets (amplitudes, phases, or Doppler frequencies) as random variables that vary with each simulation trial. The statistical properties of statistical SoS models also vary for each simulation trial, but converge to the desired properties when averaged over a large number of simulation trials. An ergodic statistical model is one that converges to the desired properties in a single simulation trial.

2.4.1 SoS Simulation Models for SISO F-to-M Channels

Clarke's reference model described in Section 2.2 assumes an infinite number of scatterers, which makes this model impractical for use in simulators. Hence, it is desirable to design simulation models with a finite number of scatterers, while still matching the statistical properties of the reference model.

Many approaches have been suggested for SoS simulation of SISO F-to-M Rayleigh fading channels. Several different approaches are described below.

2.4.1.1 Jakes' Model - Model I

Jakes derived his well-known deterministic simulation model for F-to-M Rayleigh fading channels [21] starting from (4) and selecting $C_n = 1/\sqrt{N}$, $\theta_n = 2\pi n/N$, and $\phi_n = 0$

for $n = 0, \ldots, N$. Using the symmetry of the 2-D isotropic scattering environment, Jakes reduced the number of sinusoidal components necessary for simulation from N to $M = (N-2)/4$. The complex faded envelope is defined as $g(t) = g_i(t) + jg_q(t)$, where

$$g_i(t) = \sqrt{\frac{4}{N}} \cos(\beta_0) \cos(\omega_d t) + \sqrt{\frac{8}{N}} \sum_{n=1}^{M} \cos(\beta_n) \cos\left[\omega_d t \cos\left(\frac{2\pi n}{N}\right)\right], \quad (19)$$

$$g_q(t) = \sqrt{\frac{4}{N}} \sin(\beta_0) \cos(\omega_d t) + \sqrt{\frac{8}{N}} \sum_{n=1}^{M} \sin(\beta_n) \cos\left[\omega_d t \cos\left(\frac{2\pi n}{N}\right)\right], \quad (20)$$

and where ω_d is the maximum angular Doppler frequency. The parameter β_n is defined as $\beta_n = \pi n/M$ for $n = 0, \ldots, M$.

It is often desirable to generate multiple uncorrelated faded envelopes, something that Model I cannot do. Dent *et al.* [24] modified Model I by using orthogonal Walsh-Hadamard codewords to de-correlate the multiple faded envelopes. The k^{th} complex faded envelope is defined as $g_k(t) = g_{ik}(t) + jg_{qk}(t)$, where

$$g_{ik}(t) = \sum_{n=1}^{M} A_k(n) \cos\left(\frac{\pi n}{M+1}\right) \cos\left\{\omega_d t \cos\left(\frac{2\pi n}{N}\right) + \frac{\pi n}{M+1} + \frac{2\pi n(k-1)}{M+1}\right\}, (21)$$

$$g_{qk}(t) = \sum_{n=1}^{M} A_k(n) \sin\left(\frac{\pi n}{M+1}\right) \cos\left\{\omega_d t \cos\left(\frac{2\pi n}{N}\right) + \frac{\pi n}{M+1} + \frac{2\pi n(k-1)}{M+1}\right\}, (22)$$

$M = (N-2)/4$, $k = 1, \ldots, M$, and $A_k(n)$ is the n^{th} element of the k^{th} row of a Hadamard matrix $\mathbf{H}_M$ of dimension $M \times M$.

By reducing the number of sinusoidal components, Jakes simplified simulation of SISO F-to-M Rayleigh fading channels. However, his model does not satisfy most of the statistical properties of the reference model [22] and it is not wide-sense stationary (WSS) [23]. Model I satisfies only the following properties: the I and Q components of the complex faded envelope are Gaussian random processes for $N \to \infty$ and the auto-correlation function of the complex faded envelope is equal to $J_0(\omega_d \tau)$. Also, the model of Dent *et al.* [24] yields a cross-correlation between different faded envelopes that is strictly zero only for time lag $\tau = 0$. As a result, various modifications of Model I have been proposed in the literature [23], [25], [26].

2.4.1.2 *Pop and Beaulieu's Model - Model II*

Pop and Beaulieu [23] showed that Model I is not WSS and modified Model I to fix this problem. This was done by removing the constraint $\phi_n = 0$ from Model I and allowing the phases ϕ_n to be independent random variables uniformly distributed on the interval $[0, 2\pi)$. The procedure yields an ergodic statistical (deterministic) simulator, since the random phases are generated only once for all simulation trials. The k^{th} complex faded envelope is defined as $g_k(t) = g_{ik}(t) + jg_{qk}(t)$, where

$$g_{ik}(t) = \sqrt{\frac{4}{N}}\cos(\beta_0)\cos(\omega_d t + \phi_{0k}) + \sqrt{\frac{8}{N}}\sum_{n=1}^{M}\cos(\beta_n)\cos\left[\omega_d t\cos\left(\frac{2\pi n}{N}\right) + \phi_{nk}\right] \tag{23}$$

$$g_{qk}(t) = \sqrt{\frac{4}{N}}\sin(\beta_0)\cos(\omega_d t + \phi_{0k}) + \sqrt{\frac{8}{N}}\sum_{n=1}^{M}\sin(\beta_n)\cos\left[\omega_d t\cos\left(\frac{2\pi n}{N}\right) + \phi_{nk}\right] \tag{24}$$

$M = (N-2)/4$, and $k = 0, \ldots, M-1$. The parameter β_n is defined as $\beta_n = \pi n/M$ for $n = 0, \ldots, M$. Although WSS, Model II inherits its statistical properties from Model I. Hence, this model does not satisfy most of the other statistical properties required by the reference model.

2.4.1.3 *Li and Huang's Model - Model III*

To improve Model II, Li and Huang [25] proposed a deterministic model that generates multiple uncorrelated faded envelopes $g_k(t)$. Model III assumes P independent complex faded envelopes, each with $M = N/4$ sinusoidal terms in the I and Q components. The k^{th} complex faded envelope is $g_k(t) = g_{ik}(t) + jg_{qk}(t)$, where

$$g_{ik}(t) = 2C\sum_{n=0}^{M-1}\cos\left(\omega_d t\cos\alpha_{nk} + \phi_{nk}^{i}\right), \tag{25}$$

$$g_{qk}(t) = 2C\sum_{n=0}^{M-1}\sin\left(\omega_d t\sin\alpha_{nk} + \phi_{nk}^{q}\right), \tag{26}$$

and where $k = 0, .., P-1$, ϕ_{nk}^{i} and ϕ_{nk}^{q} are independent random phases uniformly distributed on the interval $[0, 2\pi)$, α_{nk} is the n^{th} angle of arrival in the k^{th} complex faded envelope, and C is a constant gain. The angles of arrival are $\alpha_{nk} = (2\pi n)/N +$

$(2\pi k)/(PN) + \alpha_{00}$ for $n = 0, \ldots, M-1$, $k = 0, \ldots P-1$, where α_{00} is an initial angle of arrival, chosen to be $0 < \alpha_{00} < (2\pi)/(PN)$ and $\alpha_{00} \neq \pi/(PN)$.

Model III preserves the desirable statistical properties of Model II, while generating multiple uncorrelated faded envelopes. Compared to Model II, the I and Q components of the complex faded envelope in Model III are less correlated. However, Model III fails to satisfy equations (5) and (8) of the reference model.

2.4.1.4 MEDS Model - Model IV

To resolve the remaining disadvantages of Model II, Pätzold *et al.* [26] proposed a deterministic model called the Method of Exact Doppler Spreads (MEDS). The auto-correlation functions of the I and Q components of the complex faded envelope are designed to satisfy equation (5). The k^{th} complex faded envelope is defined as $g_k(t) = g_{ik}(t) + jg_{qk}(t)$, where

$$g_{(i/q)k}(t) = \sqrt{\frac{2}{N_{i/q}}} \sum_{n=1}^{Ni/q} \cos\left[\omega_d t \sin \alpha_n^{i/q} + \phi_{nk}^{i/q}\right] \tag{27}$$

for $k = 0, \ldots, P-1$, and where $\phi_{nk}^{i/q}$ are independent random phases uniformly distributed on the interval $[0, 2\pi)$, P is the number of desired faded envelopes, and $N_{i/q}$ is the number of sinusoidal terms in the I and Q components of $g_k(t)$, respectively. The n^{th} angle of arrival is given by $\alpha_n^{i/q} = \pi(n-0.5)/(2N_{i/q})$ for $n = 1, \ldots, N_{i/q}$.

Model IV preserves the desirable properties of Model II. In addition, the auto-correlation functions of the I and Q components in Model IV satisfy (5). Compared to Model II, the I and Q components of the complex faded envelope in Model IV are less correlated if $N_q = N_i + 1$. However, Model IV produces multiple faded envelopes that are correlated.

2.4.1.5 Zheng and Xiao's Models

To improve on previously reported models, Zheng and Xiao proposed several new statistical simulation models [27] - [29]. By allowing all three parameter sets (amplitudes, phases, and Doppler frequencies) to be random variables, Zheng and Xiao's models obtain statistical properties similar to ones required by the reference model. However, the models are no longer ergodic. The statistical properties of these models vary for each simulation trial, but they converge to desired properties when averaged over 50 to 100 simulation trials. A detailed comparison of the statistical properties for Zheng and Xiao's models is presented in [30]. It is shown that the model presented in [28] has the statistical properties closest to those of the reference model and requires the fewest simulation trials (50). We will refer to this model as Model V.

Model V: The k^{th} complex faded envelope is defined as $g_k(t) = g_{ik}(t) + jg_{qk}(t)$, where

$$
\begin{aligned}
g_{ik}(t) &= \sqrt{\frac{2}{M}} \sum_{n=1}^{M} \cos\left[\omega_d t \cos\alpha_{nk} + \phi_{nk}^{i}\right], & (28) \\
g_{qk}(t) &= \sqrt{\frac{2}{M}} \sum_{n=1}^{M} \cos\left[\omega_d t \sin\alpha_{nk} + \phi_{nk}^{q}\right], & (29)
\end{aligned}
$$

for $k = 0, \ldots, P-1$, and where ϕ_{nk}^{i} and ϕ_{nk}^{q} are independent random phases uniformly distributed on the interval $[-\pi, \pi)$. Model V assumes P independent complex envelopes, each with $M = N/4$ sinusoidal terms in the I and Q components. The n^{th} angle of arrival in the k^{th} complex envelope α_{nk} is $\alpha_{nk} = (2\pi n - \pi + \theta_k)/(4M)$ for $n = 1, \ldots, M$, where the θ_k are independent random variables uniformly distributed on the interval $[-\pi, \pi)$.

Since the motivation for our SISO F-to-M statistical simulation model described in Chapter 3 originates in [27], we will present this model as well.

Model VI: The k^{th} complex faded envelope is defined as $g_k(t) = g_{ik}(t) + jg_{qk}(t)$, where

$$g_{ik}(t) = \frac{2}{\sqrt{M}} \sum_{n=1}^{M} \cos(\psi_{nk}) \cos[\omega_d t \cos\alpha_{nk} + \phi_k], \tag{30}$$

$$g_{qk}(t) = \frac{2}{\sqrt{M}} \sum_{n=1}^{M} \sin(\psi_{nk}) \cos[\omega_d t \cos\alpha_{nk} + \phi_k], \tag{31}$$

$\alpha_{nk} = (2\pi n - \pi + \theta_k)/(4M)$, ψ_{nk}, θ_k, and ϕ_k are statistically independent random variables, uniformly distributed on the interval $[-\pi, \pi)$, and $n = 1, \ldots, M$, $k = 0, \ldots, P-1$.

Patel *et al.* [30] have shown that the I and Q components of the complex faded envelope in Model VI are not Gaussian random processes and that the auto-correlation of the squared envelope is non-stationary. These problems can be solved by replacing the random phase ϕ_k, which is the same for all sinusoidal terms in the k^{th} complex envelope, with mutually independent random phases ϕ_{nk}, uniformly distributed on the interval $[-\pi, \pi)$. We refer to this model as modified Model VI.

2.4.2 SoS Simulation Models for SISO and MIMO M-to-M Channels

The reference models described in Section 2.3 assume an infinite number of scatterers, making these models impractical for simulators. This section describes the simulation models with a finite number of scatterers that still match the statistical properties of the reference models.

2.4.2.1 SoS Simulation Models for SISO M-to-M Channels

Patel *et al.* [34] were the first to propose SoS simulation models for SISO M-to-M channels. They used the "two-ring" concept in [55] to derive their models. Using this model, the received complex faded envelope under narrowband, frequency flat fading, and NLoS propagation assumptions is defined as [34]

$$g(t) = \sqrt{\frac{2}{NM}} \sum_{n=1}^{N} \sum_{m=1}^{M} \exp\{j[\omega_1 t \cos(\alpha_n) + \omega_2 t \cos(\beta_m) + \phi_{nm}]\}, \tag{32}$$

where NM is the number of propagation paths, ω_1 and ω_2 are the maximum angular Doppler frequencies, ϕ_{mn} denotes the phase, and α_n and β_m denote the angle of departure and angle of arrival, respectively. Note that the single summation in (9) is replaced by a double summation, because each wave on its way from the $\mathrm{T_x}$ to the $\mathrm{R_x}$ is reflected twice. The channel characteristics remain the same as the reference model in (9), because each path will undergo a Doppler shift due to the motion of the $\mathrm{T_x}$ and $\mathrm{R_x}$.

The first model proposed by Patel *et al.* [34] is an ergodic statistical SoS model. By choosing only the phases to be random variables, the statistical properties of this model converge to the desired properties in a single simulation trial. We refer to this model as M-to-M Model I.

M-to-M Model I: The complex faded envelope is $g(t) = g_i(t) + jg_q(t)$, where

$$g_i(t) = \sqrt{\frac{2}{N_i M_i}} \sum_{m=1}^{M_i} \sum_{n=1}^{N_i} \cos\left(\omega_1 t \cos\left(\alpha_n^i\right) + \omega_2 t \cos(\beta_m^i) + \phi_{nm}^i\right), \tag{33}$$

$$g_q(t) = \sqrt{\frac{2}{N_q M_q}} \sum_{m=1}^{M_q} \sum_{n=1}^{N_q} \cos\left(\omega_1 t \cos\left(\alpha_n^q\right) + \omega_2 t \cos(\beta_m^q) + \phi_{nm}^q\right), \tag{34}$$

and where ϕ_{nm}^i and ϕ_{nm}^q are independent random phases uniformly distributed on the interval $[-\pi, \pi)$. The n^{th} angle of departure is equal to $\alpha_n^{i/q} = \pi(n - 0.5)/(2N_{i/q})$, for $n = 1, 2, \ldots, N_{i/q}$. The m^{th} angle of arrival is equal to $\beta_m^{i/q} = \pi(m - 0.5)/(M_{i/q})$, for $m = 1, 2, \ldots, M_{i/q}$.

This model has the disadvantage that the statistical properties match those of the reference model only for a small range of normalized time delays ($0 \leq f_1 T_s \leq 3$, where T_s denotes the sampling period). To improve these statistical properties, Patel *et al.* [34] also proposed a statistical SoS model. We call this M-to-M Model II.

M-to-M Model II: The complex faded envelope is defined as $g(t) = g_i(t) + jg_q(t)$, where

$$g_i(t) = \sqrt{\frac{2}{NM}} \sum_{n=1}^{N} \sum_{m=1}^{M} \cos\left(\omega_1 t \cos\left(\alpha_n\right) + \omega_2 t \cos(\beta_m) + \phi_{nm}^i\right), \tag{35}$$

$$g_q(t) = \sqrt{\frac{2}{NM}} \sum_{n=1}^{N} \sum_{m=1}^{M} \cos\left(\omega_1 t \sin\left(\alpha_n\right) + \omega_2 t \cos(\beta_m) + \phi_{nm}^q\right), \tag{36}$$

and where ϕ_{nm}^i and ϕ_{nm}^q are independent random phases uniformly distributed on the interval $[-\pi, \pi)$. Model II assumes N scatterers located on the $\mathrm{T_x}$ ring and M scatterers located on the $\mathrm{R_x}$. The n^{th} angle of departure is $\alpha_n = (2\pi n - \pi + \theta)/(4N)$, where θ is an independent random variable uniformly distributed in the interval $[-\pi, \pi)$. The m^{th} angle of arrival is equal to $\beta_m = (2\pi m - \pi + \psi)/(2M)$ where ψ is an independent random variable uniformly distributed in the interval $[-\pi, \pi)$.

M-to-M Model II obtains better statistical properties than M-to-M Model I. However, this model requires a large number of simulation trials (at least 50) to obtain adequate ensemble averaged statistical properties.

2.4.2.2 SoS Simulation Models for MIMO M-to-M Channels

M-to-M Models I and II were developed for SISO M-to-M channels. Recently, efforts have been made to develop the simulation models for MIMO M-to-M channels. Hogstad *et al.* [38] were the first to propose an ergodic statistical MIMO M-to-M SoS model called the Modified Method of Exact Doppler Spreads (MMEDS). By choosing only the phases to be random variables, the statistical properties of this model converge to those of the reference model in a single simulation trial. Using the reference model described in Section 2.3.2 and assuming 2-D scattering, they defined the received complex faded envelope as [38]

$$h_{pq}(t) = \sum_{m,n=1}^{M,N} \frac{a_{p,m} c_{m,n} b_{n,q}}{\sqrt{MN}} e^{j\left[2\pi f_{T\max} t \cos(\alpha_T^{(m)} - \gamma_T) + 2\pi f_{R\max} t \cos(\alpha_R^{(n)} - \gamma_R) + \phi_{mn}\right]}, \tag{37}$$

where $a_{p,m} = \exp\left(j\pi(L_t + 1 - 2p)\delta_T \cos(\alpha_T^{(m)} - \theta_T)/\lambda\right)$, $c_{m,n} = \exp(j2\pi(R_t \cos\alpha_T^{(m)} - R_r \cos\alpha_R^{(n)})/\lambda)$, $b_{n,q} = \exp\left(j\pi(L_r + 1 - 2q)\delta_R \cos(\alpha_R^{(n)} - \theta_R)/\lambda\right)$, and parameters p and q take values from the sets $p \in \{1, \ldots, L_t\}$ and $q \in \{1, \ldots, L_r\}$, respectively. Parameters θ_T, θ_R, γ_T, γ_R, $f_{T\max}$, and $f_{R\max}$ are defined as in Section 2.3.2. With the MMEDS model, the phases ϕ_{mn} are independent random variables uniformly distributed on the interval $[0, 2\pi)$, and the angles of departure $\alpha_T^{(m)}$ and the angles of arrival $\alpha_R^{(n)}$ are chosen as follows:

$$\alpha_T^{(m)} = \frac{2\pi}{M}(m - 0.5) + \gamma_T, \tag{38}$$

$$\alpha_R^{(n)} = \frac{2\pi}{N}(n - 0.5) + \gamma_R, \tag{39}$$

for $m = 1, \ldots, M$, $n = 1, \ldots, N$, respectively.

2.5 Linear Decomposition of CPM with Excess-Phase

The CPM excess-phase baseband complex envelope is [15]

$$s(t, \mathbf{x}) = \sqrt{2/T_c} e^{j\phi(t,\mathbf{x})}, \tag{40}$$

where $\phi(t, \mathbf{x}) = 2\pi h \sum_{k=0}^{N_c-1} x_{k+1}\beta(t - kT_c)$ is the excess-phase, h is the modulation index, $\mathbf{x} = (x_0, \cdots, x_{N_c-1})$ is the information sequence with elements chosen from the M-ary alphabet $\{\pm 1, \pm 3, \cdots, \pm(M - 1)\}$, and T_c is the symbol duration. The function $\beta(t)$ is the phase shaping pulse defined by $\beta(t) = \int_0^t q(\tau)d\tau$, and $q(t)$ is the frequency shaping pulse of length LT_c, such that $\beta(LT_c) = 1/2$. The CPM waveform has full-response when $L = 1$ and partial-response when $L > 1$.

Mengali and Morelli [56] showed that M-ary full-response CPM signals can be represented as

$$s(t; \mathbf{x}) = \sum_{k=0}^{R-1} \sum_{n=0}^{N_c-1} B_{k,n} g_k(t - nT_c), \tag{41}$$

where $R = M - 1 = 2^F - 1$. Functions $g_k(t)$ are equal to

$$g_k(t) = \prod_{l=0}^{F-1} s^{(l)}(t + e_{l,k}T_c), \tag{42}$$

where the $s^{(l)}(t)$ are defined as

$$s^{(l)}(t) = \begin{cases} \dfrac{\sin\left(2\pi h 2^l \beta(t)\right)}{\sin(\pi h 2^l)} & , \quad 0 \le t < T_c \\ s^{(l)}(2T_c - t) & , \quad T_c \le t \le 2T_c \\ 0 & , \quad \text{otherwise} \end{cases} . \tag{43}$$

Symbols $B_{k,n}$ are defined as

$$B_{k,n} = \exp\left(j2\pi h \sum_{l=0}^{F-1} 2^l A_{l,n-e_{l,k}} - j\pi h d_{k,n} \right), \tag{44}$$

where $A_{l,n-e_{l,k}} = \sum_{r=0}^{n-e_{l,k}} \gamma_{l,r}$, $d_{k,n} = \sum_{l=0}^{F-1} 2^l (n - e_{l,k} + 1)$, and $\gamma_{l,n} \in \{0, 1\}$. are coefficients in the binary representation of the code symbol $c_n = (x_n - M + 1)/2$. Integers $e_{l,k}$ used in (42) - (44), are chosen to satisfy $e_{l,k} \in \{0, 1\}$ and $\prod_{l=0}^{F-1} e_{l,k} = 0$.

2.6 ST-CPM with Excess-Phase - System Model

This section describes a space-time coded excess-phase CPM system with L_t transmit antennas and L_r receive antennas. As shown in Fig. 4, the ST encoder uses a block code $\mathcal{C}$ to encode blocks of K_b information symbols into length-$N = N_c L_t$ codeword vectors $\mathbf{c} \in \mathcal{C}$ that are mapped onto an $L_t \times N_c$ matrix $\mathbf{C}$ in the following manner: codeword

$$\mathbf{c} \;=\; \left(c_0^{(1)}, c_0^{(2)}, \ldots, c_0^{(L_t)}, c_1^{(1)}, c_1^{(2)}, \ldots, c_1^{(L_t)}, \ldots, c_{N_c-1}^{(1)}, c_{N_c-1}^{(2)}, \ldots, c_{N_c-1}^{(L_t)} \right) \tag{45}$$

is mapped to the $L_t \times N_c$ matrix

$$\mathbf{C} = \begin{bmatrix} c_0^{(1)} & c_1^{(1)} & \cdots & c_{N_c-1}^{(1)} \\ c_0^{(2)} & c_1^{(2)} & \cdots & c_{N_c-1}^{(2)} \\ \vdots & \vdots & \ddots & \vdots \\ c_0^{(L_t)} & c_1^{(L_t)} & \cdots & c_{N_c-1}^{(L_t)} \end{bmatrix}, \tag{46}$$

where $c_k^{(i)}$ is the code symbol assigned to i-th transmit antenna at time epoch k.

The outputs of the space-time encoder are L_t streams of symbols. Each stream of symbols after modulation mapping is input to a CPM modulator. The CPM modulated signals are simultaneously transmitted from L_t transmit antennas.

The signal at each receiver antenna is a noisy superposition of the L_t transmitted signals, each affected by quasi-static flat Rayleigh fading, and independent zero-mean

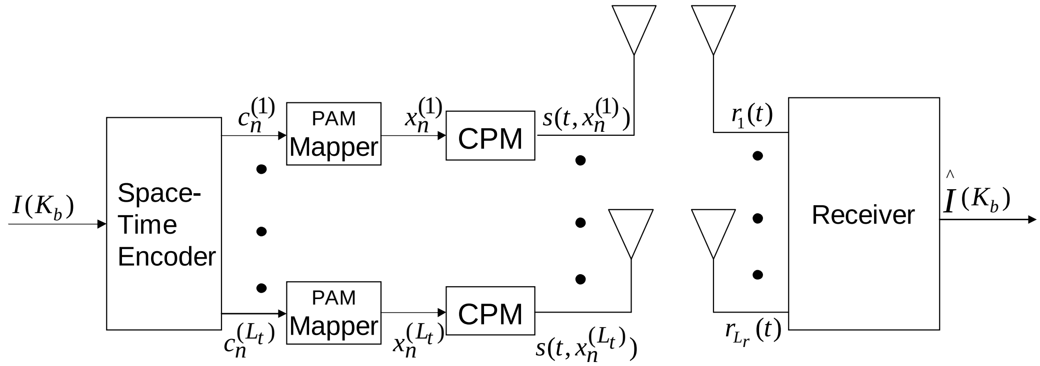

Figure 4: Space-time coded excess-phase CPM system.

complex additive white Gaussian noise (AWGN). The received signal can be represented in the convenient vector form

$$\mathbf{r}(t) = \mathbf{H}^{\top}\sqrt{E_s}\mathbf{s}(t, \mathbf{X}) + \mathbf{n}(t), \tag{47}$$

where $\mathbf{s}(t, \mathbf{X}) = \left[s_1\left(t, \mathbf{x}^{(1)}\right), \ldots, s_{L_t}\left(t, \mathbf{x}^{(L_t)}\right)\right]^{\top}$ is the vector of transmitted signals, $\mathbf{x}^{(i)} = \left[x_0^{(i)}, x_1^{(i)}, \ldots, x_{N_c-1}^{(i)}\right]$ is the vector of the ST coded CPM symbols assigned to i-th transmit antenna, $\mathbf{r}(t) = [r_1(t), \ldots, r_{L_r}(t)]^{\top}$ is the vector of received signals, $\mathbf{n}(t) = [n_1(t), \ldots, n_{L_r}(t)]^{\top}$ contains the noise samples that are independent zero-mean complex Gaussian random variables with variance $N_0/2$ per dimension, $\mathbf{H} = [h_{ij}]_{L_t \times L_r}$ is the matrix of complex channel fading gains, E_s is the symbol energy, and $(\ \cdot\ )^{\top}$ denotes the matrix transpose operation.

The optimum receiver for ST-CPM employs maximum-likelihood sequence detection (MLSD). The typical method for analyzing the performance with MLSD is to evaluate an upper bound on the pairwise error probability for any two space-time codewords $\mathbf{c}$ and $\hat{\mathbf{c}}$, presented in matrix form $\mathbf{C}$, and $\hat{\mathbf{C}}$, as defined in (46). Let $\mathbf{s}(t, \mathbf{X})$ and $\hat{\mathbf{s}}(t, \hat{\mathbf{X}})$ denote the CPM vectors corresponding to matrices $\mathbf{C}$ and $\hat{\mathbf{C}}$, respectively. The pairwise error probability is [10]

$$\begin{aligned} P_e(\mathbf{C}, \hat{\mathbf{C}}|\mathbf{H}) &= P(\mathbf{s}(t, \mathbf{X}) \rightarrow \hat{\mathbf{s}}(t, \hat{\mathbf{X}})|\mathbf{H}) \\ &= Q\left(\frac{\| \mathbf{H}^{\top}\Delta\mathbf{s}(t) \|}{\sqrt{2N_0}}\right) \leq \frac{1}{2}\exp\left(\frac{\| \mathbf{H}^{\top}\Delta\mathbf{s}(t) \|}{4N_0}\right), \end{aligned} \tag{48}$$

where $\Delta\mathbf{s}(t) = \mathbf{s}(t, \mathbf{X}) - \hat{\mathbf{s}}(t, \hat{\mathbf{X}})$. Let $\mathbf{C_s}$ be the matrix of correlation functions of the differential CPM signals received at the different antennas [41]

$$\mathbf{C_s} = \tag{49}$$
$$\begin{bmatrix} \int_0^{N_cT_c} |\Delta s_1(t)|^2 dt & \int_0^{N_cT_c} \Delta s_1(t)\Delta s_2^*(t) dt & \cdots & \int_0^{N_cT_c} \Delta s_1(t)\Delta s_{L_t}^*(t) dt \\ \int_0^{N_cT_c} \Delta s_2(t)\Delta s_1^*(t) dt & \int_0^{N_cT_c} |\Delta s_2(t)|^2 dt & \cdots & \int_0^{N_cT_c} \Delta s_2(t)\Delta s_{L_t}^*(t) dt \\ \vdots & \vdots & \ddots & \vdots \\ \int_0^{N_cT_c} \Delta s_{L_t}(t)\Delta s_1^*(t) dt & \int_0^{N_cT_c} \Delta s_{L_t}(t)\Delta s_2^*(t) dt & \cdots & \int_0^{N_cT_c} |\Delta s_{L_t}(t)|^2 dt \end{bmatrix},$$

where differential CPM signals are defined as $\Delta s_i(t) \stackrel{\triangle}{=} s_i(t, \mathbf{x}^{(i)}) - \hat{s}_i(t, \hat{\mathbf{x}}^{(i)})$ for $1 \leq i \leq L_t$ and T_c denotes the symbol duration. For a quasi-static flat Rayleigh fading channel, the pairwise error probability has the following, asymptotically tight, upper bound [4]:

$$P_e(\mathbf{C}, \hat{\mathbf{C}}|\mathbf{H}) \leq \left(\frac{1}{\prod_{i=1}^{r}(1 + \lambda_i E_s/4N_0)} \right)^{L_r} \leq \left(\frac{\eta E_s}{4N_0} \right)^{-rL_r}, \tag{50}$$

where r is the rank of matrix $\mathbf{C_s}$, $\{\lambda_1, \cdots, \lambda_r\}$ are the nonzero eigenvalues of $\mathbf{C_s}$, and $\eta = (\lambda_1\lambda_2 \cdots \lambda_r)^{1/r}$ is their geometric mean. From (50), we can conclude that ST-CPM has a direct analogy to ST-coded linear modulation. The rank criterion and the determinant criterion used for space-time linear modulation are directly applicable to ST-CPM, the only difference being that CPM has the "signal" matrix defined in (49).

CHAPTER III

EFFICIENT SIMULATION OF SISO F-TO-M RAYLEIGH FADING WITH ENHANCED DE-CORRELATION PROPERTIES

3.1 Overview

In Chapter 2, we have presented several different SoS models for SISO F-to-M cellular channels. In particular, we described the Clarke's mathematical reference model [20], the Jakes' simulation model [21], and the various modifications of Jakes' simulation model, reported in [23] - [29]. We have observed that these models have difficulty of creating uncorrelated I and Q components of the complex faded envelope and of creating multiple uncorrelated faded envelopes. To address these problems, we propose new SoS simulation models for SISO F-to-M Rayleigh fading channels.

First, an ergodic statistical (deterministic) model is proposed that overcomes the difficulty of creating uncorrelated I and Q components and of creating multiple uncorrelated faded envelopes. This is achieved by using orthogonal functions for the I and Q components and by introducing an asymmetrical arrangement of arrival angles into the model proposed in [23]. The statistical properties of our model are derived and verified by simulation. Compared to existing models, our new model yields a lower cross-correlation between different faded envelopes and between the I and Q components of each complex faded envelope. However, the auto-correlation functions of the I and Q components still do not exactly match the theoretical functions.

The proposed deterministic model can be modified by introducing additional randomness to yield a new non-ergodic statistical model having the correct statistical properties. The motivation for this model originates in [27]. The properties of the resulting statistical model are derived and verified by simulation. Compared to Zheng and Xiao's models [27] - [29], our new statistical model converges faster, has less correlated I and Q components, and yields less correlated multiple faded envelopes.

The remainder of this chapter is organized as follows. Section 3.2 describes our new SoS simulation models for SISO F-to-M Rayleigh fading channels and analyzes their statistical properties. Section 3.3 evaluates the new models and compares them to models presented in Section 2.4.1. Section 3.4 provides some concluding remarks.

3.2 New Simulation Models for SISO F-to-M Channels

Our evaluation of Models I - VI introduced in Section 2.4.1 has revealed that most have difficulty of creating uncorrelated I and Q components of each complex faded envelope and of generating multiple uncorrelated faded envelopes. Our goal is to solve these problems by using orthogonal functions for the I and Q components of the complex faded envelope.

The following function is considered as the k^{th} complex faded envelope

$$g_k(t) \;=\; \sum_{n=0}^{N-1} C_n e^{j(\omega_d t \cos\alpha_{nk} + \phi_{nk})}, \tag{51}$$

where $C_n = (2e^{j\beta_n})/\sqrt{N}$, α_{nk}, ϕ_{nk}, and ω_d are the random path gain, the angle of arrival, the phase associated with the n^{th} propagation path, and the maximum angular Doppler frequency, respectively. It is assumed that P independent complex faded envelopes are required ($k = 0, \ldots, P-1$) each consisting of N sinusoidal components.

To reduce the number of sinusoidal components needed for simulation, we use a method similar to the one described in [25]. By choosing $M = N/4$ to be an integer and by taking into account shifts of the angles α_{nk} and ϕ_{nk} in each quadrant of the circle, the sum in (51) can be split into four terms, viz.

$$g_k(t) = \frac{2}{\sqrt{N}} \sum_{n=1}^{M} e^{j\beta_n} e^{j[\omega_d t \cos\alpha_{nk} + \phi_{nk}]} + \frac{2}{\sqrt{N}} \sum_{n=1}^{M} e^{j\beta_n} e^{j[\omega_d t \cos(\alpha_{nk}+0.5\pi) + (\phi_{nk}+0.5\pi)]} \quad (52)$$

$$+ \frac{2}{\sqrt{N}} \sum_{n=1}^{M} e^{j\beta_n} e^{j[\omega_d t \cos(\alpha_{nk}+\pi) + (\phi_{nk}+\pi)]} + \frac{2}{\sqrt{N}} \sum_{n=1}^{M} e^{j\beta_n} e^{j[\omega_d t \cos(\alpha_{nk}+1.5\pi) + (\phi_{nk}+1.5\pi)]}.$$

Equation (52) can be further simplified to

$$\begin{aligned} g_k(t) &= \frac{2}{\sqrt{N}} \sum_{n=1}^{M} 2\cos(\beta_n)\cos(\omega_d t \cos\alpha_{nk} + \phi_{nk}) \\ &+ j\frac{2}{\sqrt{N}} \sum_{n=1}^{M} 2\sin(\beta_n)\sin(\omega_d t \sin\alpha_{nk} + \phi_{nk}). \end{aligned} \quad (53)$$

Based on $g_k(t)$, we define our new simulation models.

3.2.1 A New SISO F-to-M Deterministic Model

We first propose an ergodic statistical (deterministic) model, which needs only one simulation trial to obtain the desired statistical properties. The k^{th} complex faded envelope is defined as $g_k(t) = g_{ik}(t) + jg_{qk}(t)$, where

$$g_{ik}(t) = \frac{2}{\sqrt{N}} \left[\sum_{n=0}^{M} a_n \cos(\omega_d t \cos\alpha_{nk} + \phi_{nk}) \right], \quad (54)$$

$$g_{qk}(t) = \frac{2}{\sqrt{N}} \left[\sum_{n=0}^{M} b_n \sin(\omega_d t \sin\alpha_{nk} + \phi_{nk}) \right]. \quad (55)$$

The motivation for this model originates in Model II. As in Model II, the phases ϕ_{nk} are chosen to be independent random variables uniformly distributed on the interval $[0, 2\pi)$, and the path gains β_n are defined as $\beta_n = \pi n/M$ for $n = 0, \ldots, M$. By including $\beta_0 = 0$ in (53), the total number of propagation paths is increased slightly to $N = 4M + 2$. Parameters a_n and b_n are defined as follows:

$$a_n = \begin{cases} 2\cos(\beta_n), & n = 1, ..., M \\ \sqrt{2}\cos(\beta_n), & n = 0 \end{cases}, \quad (56)$$

$$b_n = \begin{cases} 2\sin(\beta_n), & n = 1, ..., M \\ \sqrt{2}\sin(\beta_n), & n = 0 \end{cases}. \quad (57)$$

The angles of arrival α_{nk} are defined as in Model III: $\alpha_{nk} = (2\pi n)/N + (2\pi k)/(PN) + \alpha_{00}$ for $n = 0, \ldots, M$, $k = 0, \ldots, P-1$. This ensures an asymmetrical arrangement of arrival angles, which minimizes the cross-correlation between different faded envelopes. In addition, we optimize the initial angle of arrival α_{00} (through an exhaustive search) to minimize the cross-correlation between the I and Q components of each complex faded envelope. As a result, we obtain $\alpha_{00} = (0.2\pi)/(PN)$.

Remark 1: Model II and the new deterministic model differ in the selection of the angles of arrival and the cosine and sine functions. Our choice makes $g_{ik}(t)$ and $g_{qk}(t)$ orthogonal and, therefore, uncorrelated functions.

Remark 2: Model III and the new model differ in the selection of path gains, cosine and sine functions, and the number of random phases. By choosing the path gains to be random variables instead of being constants, we obtain less correlation in the I and Q components of the complex faded envelope than in Model III. Also, the use of fewer random variables makes our model less complex than Model III.

The auto- and cross-correlation functions of the I and Q components, the auto- and cross-correlation functions of the multiple faded envelopes, and the squared envelope auto-correlation of our new model are, respectively,

$$\lim_{N\to\infty} R_{g_{ik}g_{ik}}(\tau) = \lim_{N\to\infty} \frac{4}{N}\sum_{n=0}^{M} \frac{a_n^2}{2}\cos(\omega_d \cos\alpha_{nk}\tau) = J_0(\omega_d\tau) + J_4(\omega_d\tau), \quad (58)$$

$$\lim_{N\to\infty} R_{g_{qk}g_{qk}}(\tau) = \lim_{N\to\infty} \frac{4}{N}\sum_{n=0}^{M} \frac{b_n^2}{2}\cos(\omega_d \sin\alpha_{nk}\tau) = J_0(\omega_d\tau) - J_4(\omega_d\tau), \quad (59)$$

$$R_{g_{ik}g_{qk}}(\tau) = R_{g_{qk}g_{ik}}(\tau) = R_{g_k g_{l\neq k}}(\tau) = 0, \quad (60)$$

$$\begin{aligned} \lim_{N\to\infty} R_{g_k g_k}(\tau) &= \lim_{N\to\infty} \frac{4}{N}\sum_{n=0}^{M} \frac{a_n^2}{2}\cos(\omega_d \cos\alpha_{nk}\tau) \\ &+ \lim_{N\to\infty} \frac{4}{N}\sum_{n=0}^{M} \frac{b_n^2}{2}\cos(\omega_d \sin\alpha_{nk}\tau) = J_0(\omega_d\tau), \end{aligned} \quad (61)$$

$$\begin{aligned} R_{|g_k|^2|g_k|^2}(\tau) &= \frac{8}{N^2}\sum_{n=0}^{M} a_n^4 + \frac{8}{N^2}\sum_{n=0}^{M} b_n^4 + 2R^2_{g_{i_k}g_{i_k}}(\tau) \\ &+ 2R^2_{g_{q_k}g_{q_k}}(\tau) + 4R^2_{g_{i_k}g_{q_k}}(\tau), \end{aligned} \quad (62)$$

where $J_0(\cdot)$ is the zeroth-order Bessel function of the first kind and $J_4(\cdot)$ is the forth-order Bessel function of the first kind. Derivations of these expressions are presented in Appendix A.

Figures 5 and 6 confirm that, for $M = P = 8$, the auto- and cross-correlations of the quadrature components and the auto- and cross-correlation of the multiple faded envelopes approach values given by (58) - (61), respectively.

Our new model satisfies (6) and (7) of the reference model. However, the auto-correlations of the quadrature components and the auto-correlation of the squared envelope do not satisfy (5) and (8), respectively.

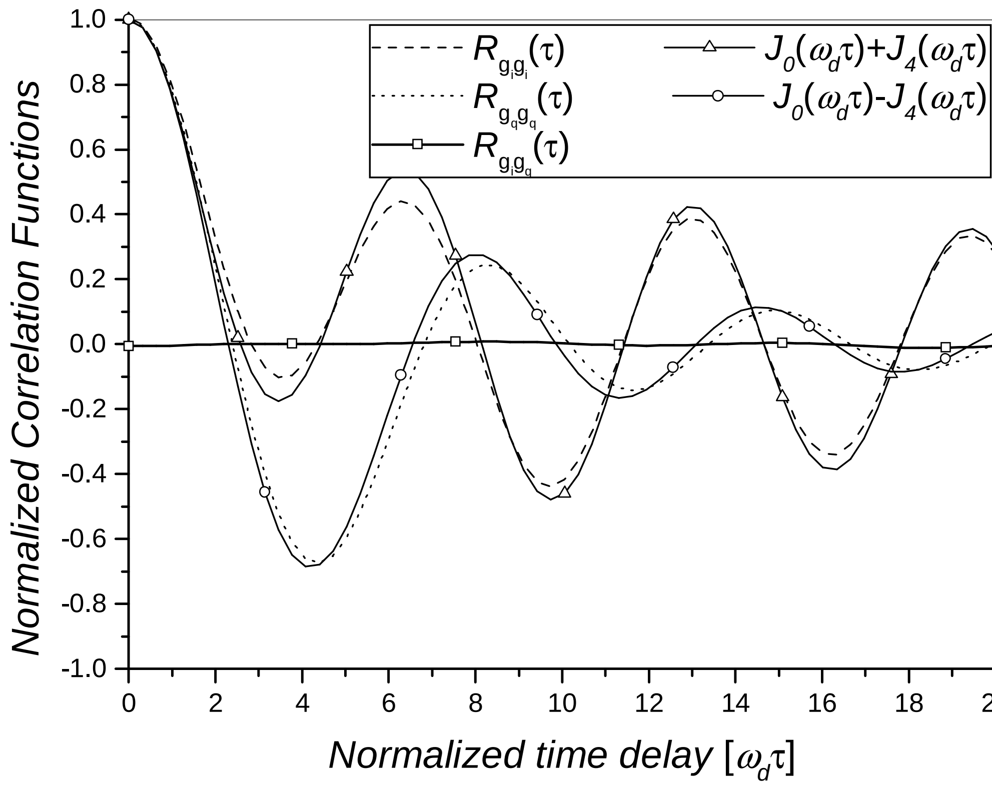

Figure 5: Theoretical and simulated auto-correlation functions and the cross-correlation function of the I and Q components of the new F-to-M deterministic model.

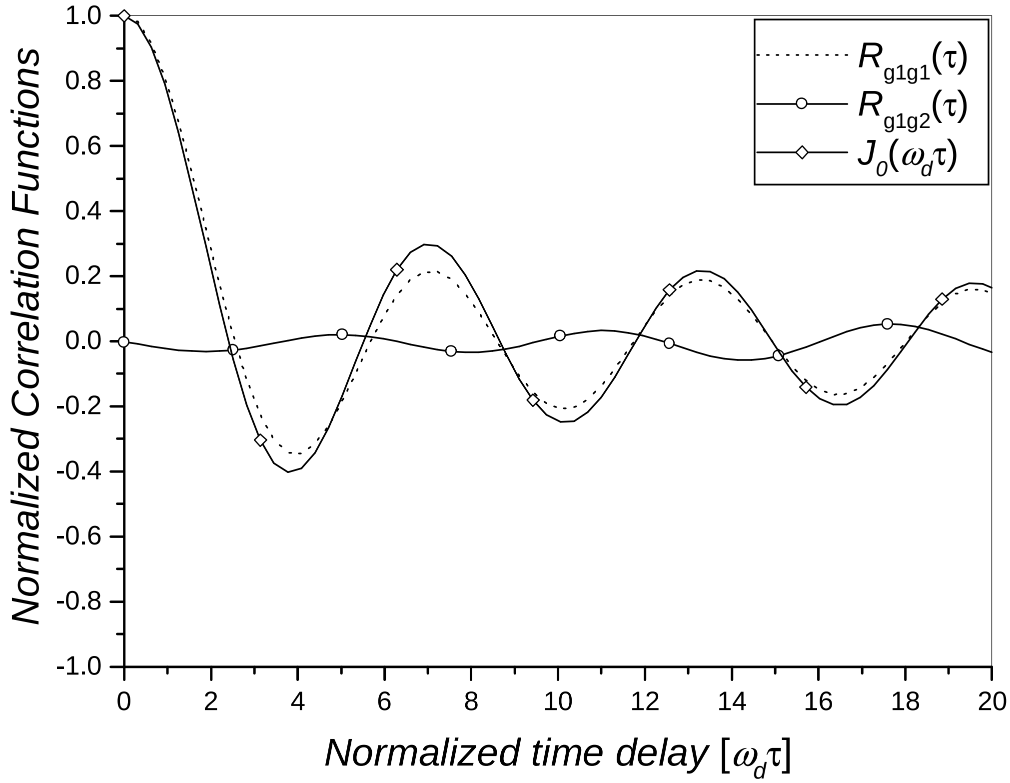

Figure 6: Theoretical and simulated auto-correlation functions and the cross-correlation function of the first and the second complex envelope of the new F-to-M deterministic model.

3.2.2 A New SISO F-to-M Statistical Model

Our new deterministic model can be modified to possess all statistical properties of the reference model, by letting all three parameters $C_{nk} = (2e^{j\beta_{nk}})/\sqrt{(N)}$, α_{nk}, and ϕ_{nk} to be random variables, similar to Model VI. The k^{th} complex faded envelope is defined as $g_k(t) = g_{ik}(t) + jg_{qk}(t)$, where

$$g_{ik}(t) = \frac{2}{\sqrt{N}}\sum_{n=1}^{M} 2\cos(\beta_{nk})\cos(\omega_d t\cos\alpha_{nk} + \phi_{nk}), \tag{63}$$

$$g_{qk}(t) = \frac{2}{\sqrt{N}}\sum_{n=1}^{M} 2\sin(\beta_{nk})\sin(\omega_d t\sin\alpha_{nk} + \phi_{nk}). \tag{64}$$

It is assumed that P independent complex envelopes are desired ($k = 0, \ldots, P-1$), each having $M = N/4$ sinusoidal terms in the I and Q components. The parameters ϕ_{nk}, β_{nk}, and θ are independent random variables uniformly distributed on the interval

$[-\pi, \pi)$. The angles of arrival are chosen as follows: $\alpha_{nk} = (2\pi n)/N + (2\pi k)/(PN) + (\theta - \pi)/N$, for $n = 1, \ldots, M$, $k = 0, \ldots, P-1$. The angles of arrival in the k^{th} complex faded envelope are obtained by rotating the angles of arrival in the $(k-1)^{th}$ complex envelope by $(2\pi)/(PN)$.

Remark 3: Model VI and the new statistical model differ in the selection of the angles of arrival for the multiple faded envelopes, and in the selection of the cosine and sine functions and random phases. Compared to Model VI, our choice of the cosine and sine functions makes the I and Q components of the complex faded envelope less correlated. Also, compared to Model VI, our choice of the angles of arrival for the multiple faded envelopes makes them less correlated.

Remark 4: The quadrature components of the complex faded envelope in Model VI are not Gaussian random processes [30]. Our choice of random phases solves this problem. In [30], it is also shown that the auto-correlation of the squared envelope in Model VI is non-stationary. In Appendix B, we prove that the auto-correlation of the squared envelope of our new model is stationary and satisfies (8) for $M \to \infty$.

Remark 5: The modified Model VI and the new statistical model differ only in the combination of cosine and sine functions for the first complex faded envelope $(k = 0)$. Zheng and Xiao [28] mentioned that different combinations of cosine and sine functions for the quadrature components leads to different statistical models with identical or similar statistical properties. However, the I and Q components of the complex faded envelope in our new statistical model are less correlated compared to modified Model VI. Furthermore, our new model needs fewer simulation trials to obtain the correct statistical properties. If different combinations of cosine and sine functions can improve statistical properties and/or reduce the number of simulation trials, then such combinations merit investigation.

It can be shown that our statistical model exhibits properties (5) - (8) of the reference model. The proofs are presented in Appendix B. Figures 7 and 8 show that, for $M = P = 8$ and $N_{\text{stat}} = 30$ trials, the auto- and cross-correlations of the I and Q components, and the auto- and cross-correlations of the complex faded envelopes approach those of the reference model. Note that different sets of 30 simulation trials yield slightly different simulation results. To quantify these differences, variances are computed averaging over 100 sets of 30 simulation trials. The variances of the auto- and cross-correlations of the I and Q components, and the auto- and cross-correlations of the complex faded envelopes are, respectively, $\text{Var}\left(R_{g_{i/qk}g_{i/qk}}\right) = 1.5 \cdot 10^{-3}$, $\text{Var}\left(R_{g_{ik}g_{qk}}\right) = 1.35 \cdot 10^{-4}$, $\text{Var}(R_{g_k g_k}) = 6.81 \cdot 10^{-4}$, $\text{Var}\left(R_{g_k g_{l \neq k}}\right) = 8.4 \cdot 10^{-4}$. The variances are extremely small.

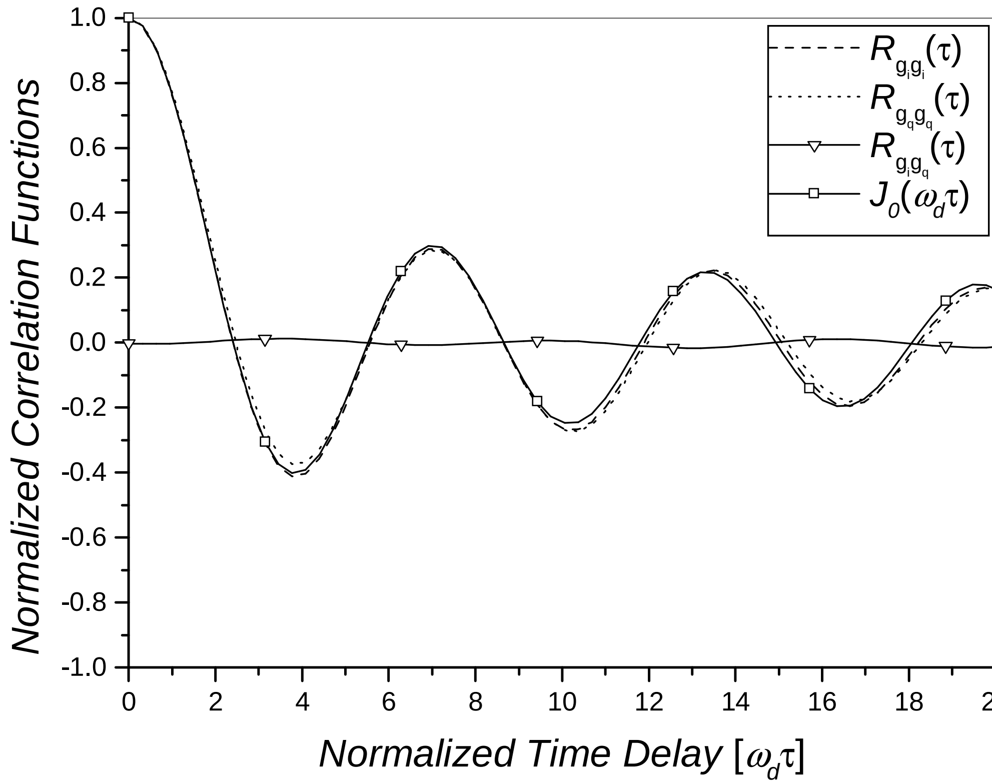

Figure 7: Theoretical and simulated ($N_{\text{stat}} = 30$) auto-correlation functions and the cross-correlation function of the I and Q components of the new F-to-M statistical model.

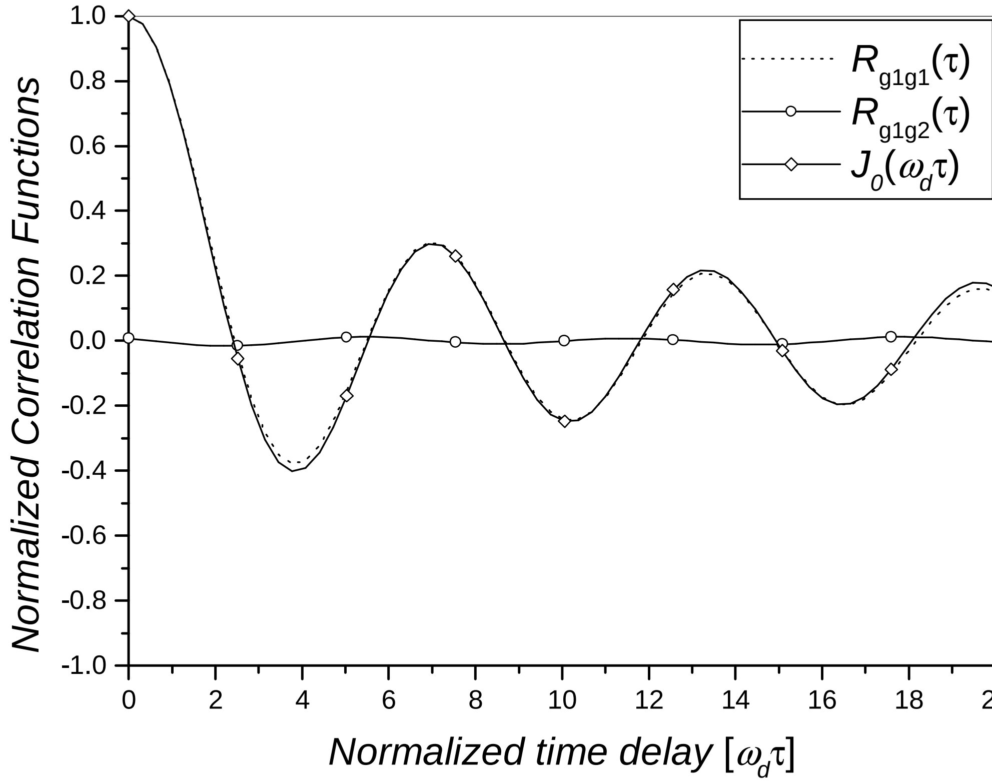

Figure 8: Theoretical and simulated ($N_{\text{stat}} = 30$) auto-correlation functions and the cross-correlation function of the first and the second fader in the new F-to-M statistical model.

3.3 Performance Evaluation of SISO F-to-M Models

This section compares the performance and complexity of our new models with Models I - VI. In all simulations, we use a normalized sampling period $f_dT_s = 0.05$ (f_d is the maximum Doppler frequency and T_s is the sampling period) and $M = P = 8$. However, for Model IV we use $N_i = 8$ and $N_q = 9$ to obtain uncorrelated quadrature components of the complex envelope. Note that in Models II - IV and in our new deterministic model, the random phases associated with the n^{th} propagation path are computed before the actual simulation starts, because an ergodic statistical (deterministic) simulator needs only one simulation trial. During the simulations, all parameters are kept constant to provide simulation results that are always the same, i.e., deterministic. In our new deterministic model and in Model II we use the following set of uniformly distributed random numbers (in radians): $\phi_{n,0}$ =[4.0387, 1.7624, 2.7844, 1.5590, 0.9523, 1.2972, 5.7420, 3.6592, 4.3548] and $\phi_{n,1}$ =[5.3798, 3.0556, 2.1528, 2.6296, 0.7457, 3.2572, 6.1027, 2.0670, 2.1304]. The same set of numbers is used in Model IV, for the Q component $g_q(t)$, while for the I component $g_i(t)$ we use $\phi^i_{n,0}$ =[2.2107, 5.3033, 2.4634, 1.0679, 2.2818, 4.6113, 0.7513, 0.7383] and $\phi^i_{n,1}$ =[3.2627, 4.7036, 0.5824, 2.1097, 4.6264, 5.4790, 0.9391, 0.2017]. Model III uses the same set of numbers as Model IV for the I component $g_i(t)$, while for the Q component $g_q(t)$ we use: $\phi^q_{n,0}$ =[2.6372, 4.7339, 4.9865, 5.7784, 5.3059, 2.3099, 3.8994, 4.5933], and $\phi^q_{n,1}$ =[4.1175, 2.4616, 3.9403, 4.3911, 2.4948, 2.5981, 4.115, 5.2610]. Using these parameters, we calculate the mean square error (MSE) and maximum deviations (MAX) from the theoretical value (zero) for the normalized cross-correlation of the I and Q components, and for the normalized cross-correlation of the first and the second faded envelopes. The results are shown in Table 1. Note that different

Table 1: Mean square error (MSE) and maximum deviation (MAX).

Simulators	MSE $R_{g_I g_Q}$	Max $R_{g_I g_Q}$	MSE Real($R_{g_1 g_2}$)	Max Real($R_{g_1 g_2}$)
Model I	$2.63 \cdot 10^{-2}$	$42.61 \cdot 10^{-2}$	$5.92 \cdot 10^{-2}$	$52.3 \cdot 10^{-2}$
Model II	$2.47 \cdot 10^{-2}$	$44.88 \cdot 10^{-2}$	$5.39 \cdot 10^{-2}$	$59.74 \cdot 10^{-2}$
Model III	$1.28 \cdot 10^{-2}$	$24.30 \cdot 10^{-2}$	$5.20 \cdot 10^{-3}$	$15.14 \cdot 10^{-2}$
Model IV	$8.80 \cdot 10^{-3}$	$17.46 \cdot 10^{-2}$	$4.90 \cdot 10^{-2}$	$61.01 \cdot 10^{-2}$
New Deterministic Model	$4.25 \cdot 10^{-5}$	$1.61 \cdot 10^{-2}$	$1.60 \cdot 10^{-3}$	$5.75 \cdot 10^{-2}$
Model V ($N_{stat} = 50$)	$9.80 \cdot 10^{-5}$	$2.27 \cdot 10^{-2}$	$6.26 \cdot 10^{-5}$	$2.30 \cdot 10^{-2}$
Model V ($N_{stat} = 100$)	$4.46 \cdot 10^{-5}$	$2.05 \cdot 10^{-2}$	$3.87 \cdot 10^{-5}$	$1.11 \cdot 10^{-2}$
Model VI ($N_{stat} = 50$)	$6.50 \cdot 10^{-4}$	$5.89 \cdot 10^{-2}$	$1.06 \cdot 10^{-4}$	$2.30 \cdot 10^{-2}$
Model VI ($N_{stat} = 100$)	$2.52 \cdot 10^{-4}$	$3.57 \cdot 10^{-2}$	$7.25 \cdot 10^{-5}$	$1.60 \cdot 10^{-2}$
Modified Model VI ($N_{stat} = 50$)	$3.75 \cdot 10^{-4}$	$3.83 \cdot 10^{-2}$	$6.51 \cdot 10^{-5}$	$1.56 \cdot 10^{-2}$
Modified Model VI ($N_{stat} = 100$)	$1.14 \cdot 10^{-4}$	$2.48 \cdot 10^{-2}$	$4.93 \cdot 10^{-5}$	$1.48 \cdot 10^{-2}$
New Statistical Model ($N_{stat} = 30$)	$5.08 \cdot 10^{-5}$	$1.44 \cdot 10^{-2}$	$3.31 \cdot 10^{-5}$	$1.17 \cdot 10^{-2}$
New Statistical Model ($N_{stat} = 50$)	$1.91 \cdot 10^{-5}$	$0.94 \cdot 10^{-2}$	$6.47 \cdot 10^{-6}$	$0.60 \cdot 10^{-2}$
New Statistical Model ($N_{stat} = 100$)	$1.62 \cdot 10^{-5}$	$0.69 \cdot 10^{-2}$	$2.38 \cdot 10^{-6}$	$0.35 \cdot 10^{-2}$

choices of phases yield different simulation results. To quantify these differences, we compute the mean and variance of the mean square error over 10^3 simulation trials each using a randomly selected phase vector. The mean MSE (μMSE) and variance of the MSE (VMSE) of the cross-correlation of the I and Q component are, respectively, $\mu\text{MSE}\big(R_{g_{ik}g_{qk}}\big) = 1.2 \cdot 10^{-5}$, $\text{VMSE}\big(R_{g_{ik}g_{qk}}\big) = 3.36 \cdot 10^{-5}$. Likewise, the mean and variance of the MSE of the cross-correlation of the complex faded envelopes are, respectively $\mu\text{MSE}\big(R_{g_k g_{l\neq k}}\big) = 1.4 \cdot 10^{-3}$, $\text{VMSE}\big(R_{g_k g_{l\neq k}}\big) = 1.22 \cdot 10^{-31}$. All quantities are very small. To further estimate the magnitude of differences between simulation results, we ran our deterministic simulator with different permutations of phases which were evenly distributed on the interval $[0, 2\pi)$ with zero as a starting point. The results are presented in Table 2.[1]

Table 2: Magnitude of deviations in the new F-to-M deterministic model.

	Value	Phase Vector
The Highest MSE ($R_{g_I g_Q}$)	$1.05 \cdot 10^{-4}$	ϕ_{n0} =[4.8869, 5.5851, 4.1888, 2.7925, 1.3963, 3.4907, 0.6981, 0, 2.0944]
The Lowest MSE ($R_{g_I g_Q}$)	$2.87 \cdot 10^{-6}$	ϕ_{n0} =[0.6981, 1.3963, 3.4907, 5.5851, 4.1888, 2.0944, 0, 4.8869, 2.7925]
The Highest Max Deviation ($R_{g_I g_Q}$)	$2.78 \cdot 10^{-2}$	ϕ_{n0} =[4.1888, 5.5851, 4.8869, 1.3963, 0.6981, 3.4907, 2.0944, 0, 2.7925]
The Lowest Max Deviation ($R_{g_I g_Q}$)	$3.78 \cdot 10^{-3}$	ϕ_{n0} =[4.8869, 0, 2.0944, 5.5851, 0.6981, 4.1888, 3.4907, 3.4907, 1.3963]
The Highest MSE (Real($R_{g_1 g_2}$))	$3.3 \cdot 10^{-3}$	ϕ_{n0} =[4.8869, 5.5851, 4.1888, 2.7925, 1.3963, 3.4907, 0.6981, 0, 2.0944] ϕ_{n1} =[2.0944, 2.7925, 5.5851, 0.6981 4.8869, 3.4907, 0 , 4.1888, 1.3963]
The Lowest MSE (Real($R_{g_1 g_2}$))	$1.8 \cdot 10^{-3}$	ϕ_{n0} =[0.6981, 1.3963, 3.4907, 5.5851, 4.1888, 2.0944, 0, 4.8869, 2.7925] ϕ_{n1} =[4.8869, 2.0944, 4.1888, 2.7925, 3.4907, 0, 0.6981, 1.3963, 5.5851]
The Highest Max Deviation (Real($R_{g_1 g_2}$))	$1.08 \cdot 10^{-1}$	ϕ_{n0} =[4.1888, 5.5851, 4.8869, 1.3963, 0.6981, 3.4907, 2.0944, 0, 2.7925] ϕ_{n1} =[0.6981, 1.3963, 3.4907, 0, 2.0944, 4.886, 5.5851, 4.1888, 2.7925]
The Lowest Max Deviation (Real($R_{g_1 g_2}$))	$1.03 \cdot 10^{-1}$	ϕ_{n0} =[4.8869, 0, 2.0944, 5.5851, 0.6981, 4.1888, 3.4907, 3.4907, 1.3963] ϕ_{n1} =[5.5851, 2.0944, 4.1888, 2.7925, 3.4907, 0.6981, 0, 1.3963, 4.8869]

[1] Results presented in Table II are representative of the magnitude of differences between simulations. Choosing some other set of uniformly distributed random numbers may exceed the presented range of variations.

To compare complexity of the new models and Models I - VI, Table 3 summarizes the number of simulation trials required to obtain desired statistical properties, the number of operations needed to generate one sample of the complex faded envelope and the relative simulation times needed to generate a sample of the complex faded envelope with desired statistical properties, in Matlab on a Pentium III laptop. Here, we count only the frequently executed operations and the number of random

Table 3: Complexity of different SISO F-to-M models.

Statistical models	Number of simulation trials	Relative sim. time to generate a sample of $g_k(t)$ w. desired stat. properties	Estimated number of computations needed to generate one sample of $g_k(t)$		
			cosine	addition/ multiplication	number of random variables
Model I	1	Tx	$4M$	$2M$ / $2M$	None
Model II	1	$1.03Tx$	$4M$	$3M$ / $2M$	$M+1$
Model III	1	$1.52Tx$	$4M$	$4M$ / 0	$2M$
Model IV	1	$1.52Tx$	$4M$	$4M$ / 0	$2M$
New Deterministic Model	1	$1.98Tx$	$6M$	$4M$ / $2M$	$M+1$
Model V	50	$4.85Tx$	$4M$	$4M$ / 0	$2M+1$
Model VI	100	$7.37Tx$	$4M$	$3M$ / $2M$	$M+2$
Modified Model VI	100	$7.45Tx$	$4M$	$3M$ / $2M$	$2M+1$
New Statistical Model	30	$3.15Tx$	$6M$	$4M$ / $2M$	$2M+1$

variables. Table 3 shows that our choice of the cosine functions, which makes the I and Q components of the complex faded envelope uncorrelated, slightly increases the complexity of our models.

Figure 9 compares the cross-correlation functions of the I and Q components obtained by our new deterministic model and Models I - V. For clarity, we only plot the results for Model V, being the best of Zheng and Xiao's models. Since Model V is statistical model, we plot the average of $N_{\text{stat}} = 50$ trials. Figure 9 and Table 1 show that our deterministic model yields a lower cross-correlation between the I and Q components of the complex faded envelope, and also a lower maximum deviation from the theoretical value. In Figure 10, we compare cross-correlation functions of two

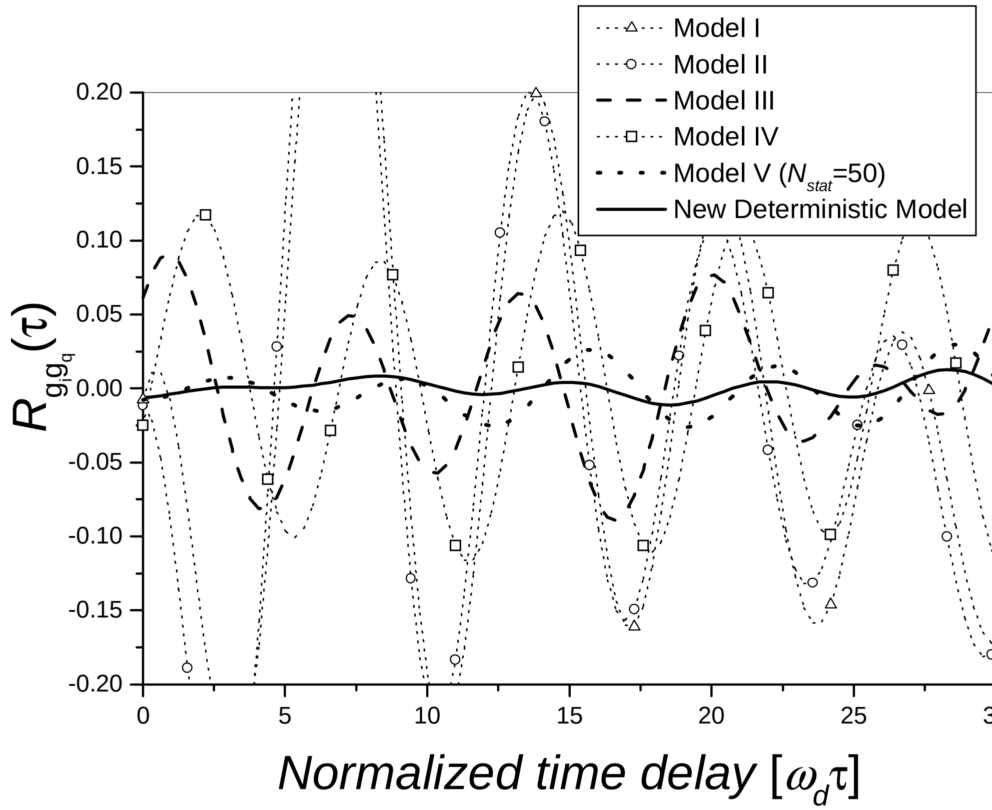

Figure 9: The normalized cross-correlation function of the I and Q components of the new F-to-M deterministic model and Models I - V.

faded envelopes for our new deterministic model and for Models I-V (for $N_{\text{stat}} = 50$ trials). The curve plotted for Model I is obtained from a simulation of Jakes' modified model presented in [24]. We conclude that our deterministic model yields a low cross-correlation between two different faded envelopes, as do Models III and V.

Figures 11 and 12 compare the cross-correlation functions of the I and Q components and the cross-correlation functions of two faded envelopes, respectively, for our new statistical model and Models V and modified VI. For Models V and modified VI, we average over $N_{\text{stat}} = 100$ trials, while for our new statistical model we average over $N_{\text{stat}} = 30$ and $N_{\text{stat}} = 50$ trials. From Fig. 11 and Table 1, we conclude that our new statistical model with $N_{\text{stat}} = 30$ has a similar performance as Models V and modified VI with $N_{\text{stat}} = 100$. An increase of the number of trials to $N_{\text{stat}} = 50$

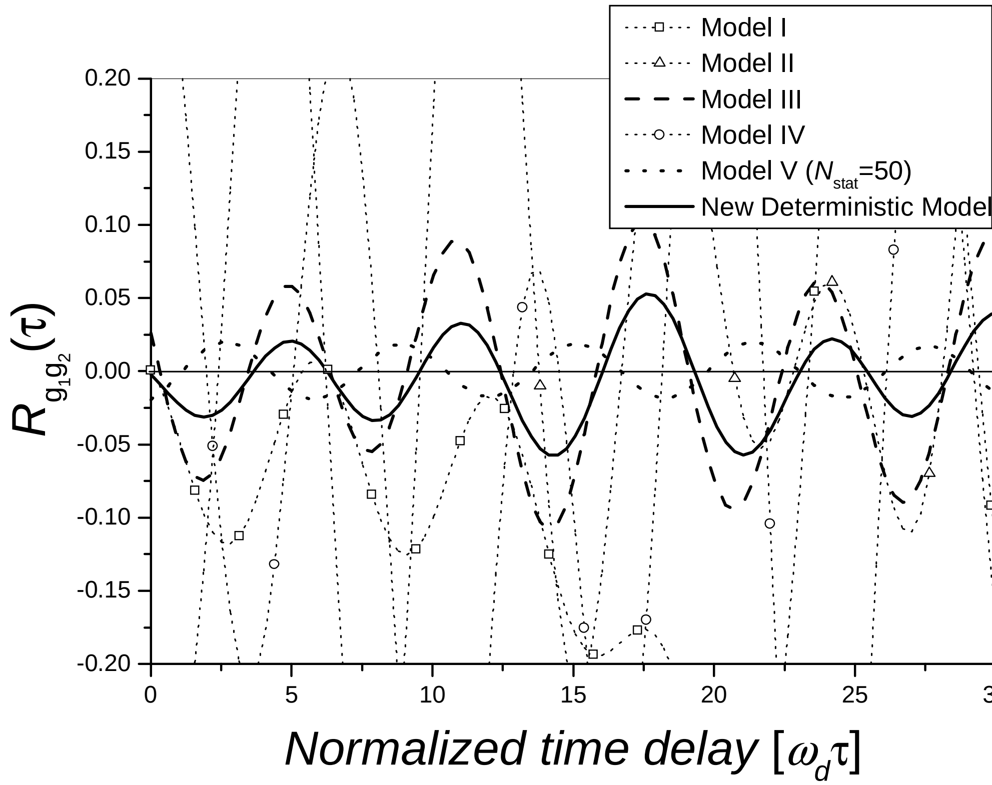

Figure 10: The normalized cross-correlation function of the first and the second complex envelope of the new F-to-M deterministic model and of Models I - V.

yields a significantly lower cross-correlation between the I and Q components of the complex faded envelope. An increase of the number of trials to $N_{\text{stat}} = 50$ yields a significantly lower cross-correlation between the I and Q components of the complex faded envelope. Furthermore, with $N_{\text{stat}} = 50$ trials, the new statistical model achieves a larger de-correlation between different complex envelopes than do Models V and modified Model VI with $N_{\text{stat}} = 100$ trials. Figures 11 - 13 show that our new statistical model converges faster than the other statistical models. Adequate statistics can be achieved with only 30 trials using our new statistical model.

3.4 Summary

This chapter proposed new SoS fading simulators for SISO F-to-M Rayleigh fading channels. We first presented a deterministic (ergodic statistical) simulator in Section 3.2.1 that overcomes the difficulty of creating uncorrelated I and Q components

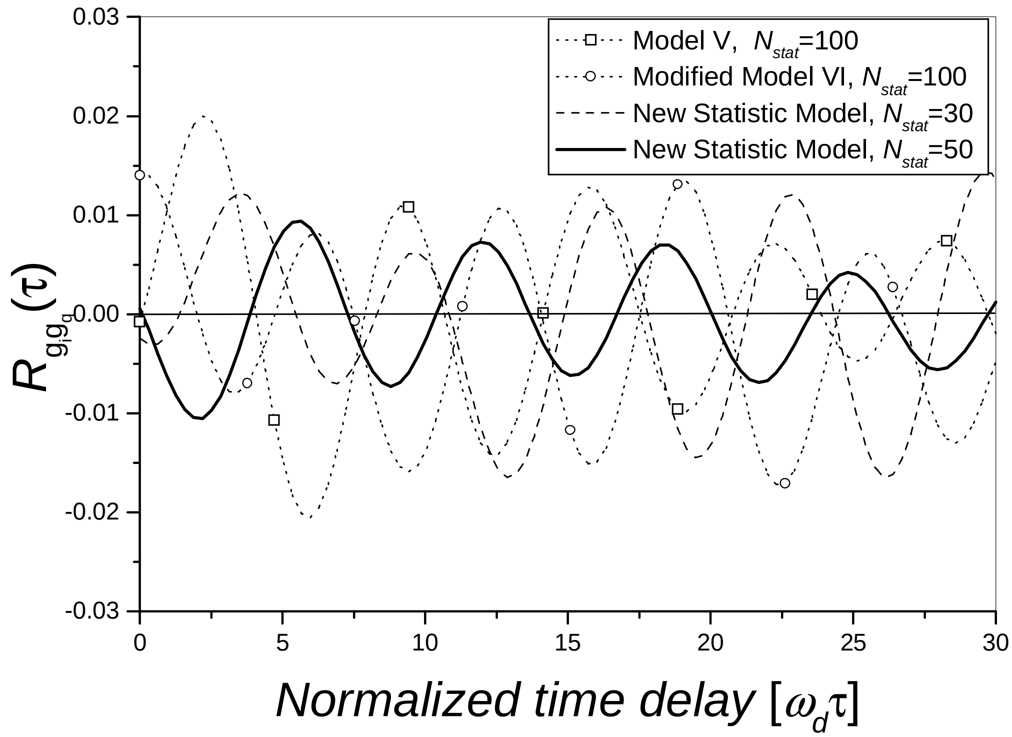

Figure 11: The normalized cross-correlation function of the I and Q components of the new F-to-M statistical model, of Model V, and of modified Model VI.

of each complex faded envelope and the difficulty of creating multiple uncorrelated faded envelopes. This is achieved by using orthogonal functions for the I and Q components of the complex faded envelope and by introducing an asymmetrical arrangement of arrival angles into the model proposed in [23]. The statistical properties of this new model are derived and verified using simulation. Compared to Models I - VI, our new deterministic model yields a lower cross-correlation between different faded envelopes, and between the I and Q components of each complex faded envelope. However, our deterministic model still has the disadvantage that the autocorrelation functions of the I and Q components do not match those of the reference model. To overcome this disadvantage, we introduce a new statistical model in Section 3.2.2. Properties of the resulting new statistical model are derived and verified using simulation. The new model matches the statistical properties of the reference model and, when compared to [27] - [29], converges faster and has a lower correlation

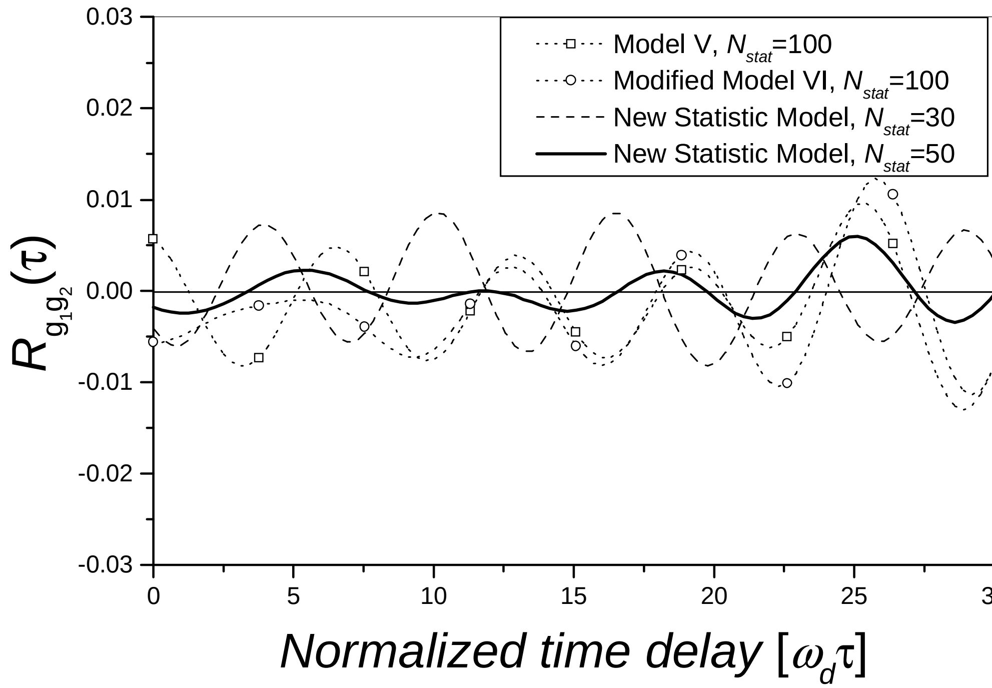

Figure 12: The normalized cross-correlation function of the first and the second fader of the new F-to-M statistical model, of F-to-M Model V, and of modified F-to-M Model VI.

between the I and Q components of the complex faded envelope and between different faded envelopes.

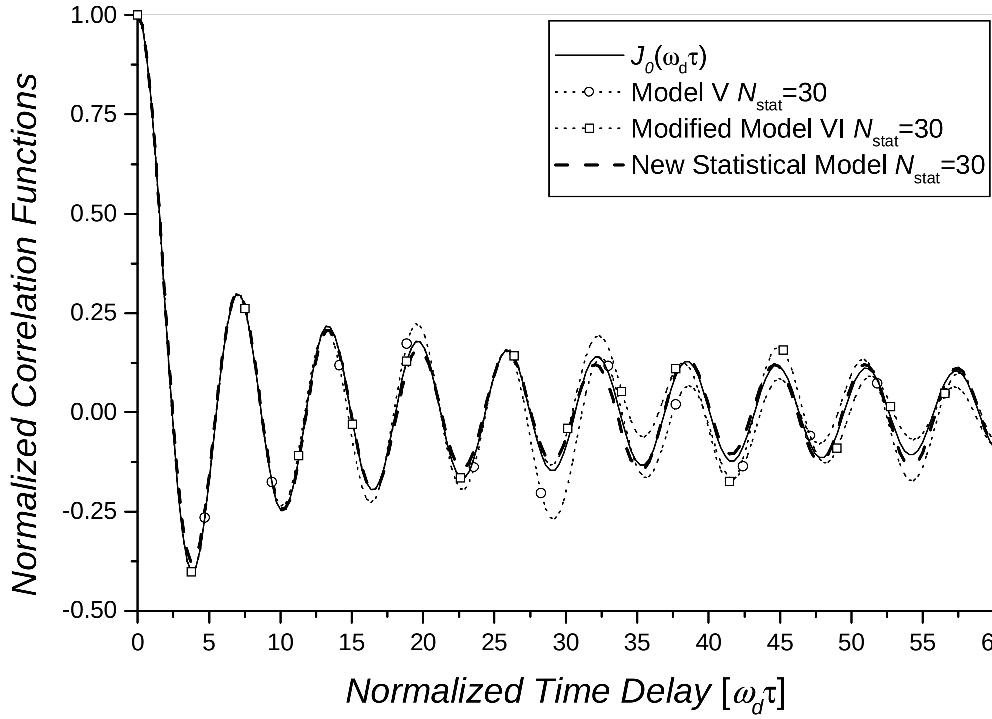

Figure 13: The theoretical and simulated normalized auto-correlation functions of the new F-to-M statistical model, of Model V, and of modified Model VI.

CHAPTER IV

A STATISTICAL SIMULATION MODEL FOR SISO M-TO-M CHANNELS

4.1 Overview

Chapter 2 described several methods for simulating M-to-M channels [34]. However, these simulation models have notable difficulties in producing time averaged auto- and cross-correlation functions that match those of the reference model [31]. Hence, this chapter proposes a new statistical SoS model for M-to-M Rayleigh fading channels. We employ "double ring" model, where orthogonal functions are chosen as the I and Q components of the complex faded envelope. Moreover, our new model is designed to directly generate *multiple* uncorrelated complex faded envelopes, a lacking feature in the existing models reported in [1] and [34]. The statistical properties of our model are derived and verified by simulation. Compared to existing models, this chapter shows our new model has more rapidly converging ensemble average statistics, has a lower variance of the auto-correlation functions, has less correlated I and Q components, and it produces uncorrelated multiple faded envelopes.

The remainder of this chapter is organized as follows. Section 4.2 describes our new statistical SoS simulation model and analyzes its statistical properties. Section 4.3 evaluates the new model and compares it to previously reported models in [34]. Finally, Section 4.4 provides some concluding remarks.

4.2 A New SISO M-to-M Statistical Simulation Model

Previously reported models in [1], [34] have a noted difficulty in producing time averaged auto- and cross-correlation functions that match those of the reference model.

We solve this problem by using a "double ring" concept and by choosing orthogonal functions for the I and Q components of the complex faded envelope. Also, this model is designed to directly generate multiple uncorrelated complex envelopes.

The following function is considered as the k^{th} complex faded envelope

$$g_k(t) = \sum_{n=1}^{N}\sum_{m=1}^{M} C\exp\{j[\omega_1 t\cos(\alpha_{nk}) + \omega_2 t\cos(\beta_{mk}) + \phi_{nmk}]\}, \tag{65}$$

where ω_1, ω_2, α_{nk}, β_{mk}, and ϕ_{nmk} are the maximum radian Doppler frequencies, the random angles of departure, the random angles of arrival, and the random phases, respectively, and $C = 2/\sqrt{MN}$. It is assumed that P independent complex faded envelopes are required ($k = 0, \ldots, P-1$) each consisting of NM sinusoidal components.

The number of sinusoidal components needed for simulation can be reduced by choosing $N_0 = N/4$ to be an integer, by taking into account shifts of the angles α_{nk} and ϕ_{nmk}, and by splitting the sum in (65) into four terms, *viz.*,

$$g_k(t) = C\sum_{m=1}^{M} e^{j\omega_2 t\cos(\beta_{mk})}\left[\sum_{n=1}^{N_0}\left\{e^{j(\omega_1 t\cos(\alpha_{nk})+\phi_{nmk})} + e^{j(\omega_1 t\cos(\alpha_{nk}+\pi/2)+\phi_{nmk}+\pi/2)}\right\}\right] \tag{66}$$

$$+ C\sum_{m=1}^{M} e^{j\omega_2 t\cos(\beta_{mk})}\left[\sum_{n=1}^{N_0}\left\{e^{j(\omega_1 t\cos(\alpha_{nk}+\pi)+\phi_{nmk}+\pi)} + e^{j(\omega_1 t\cos(\alpha_{nk}+3\pi/2)+\phi_{nmk}+3\pi/2)}\right\}\right].$$

Equation (66) simplifies to

$$\begin{aligned} g_k(t) &= \frac{2}{\sqrt{N_0 M}}\sum_{n=1}^{N_0}\sum_{m=1}^{M}\cos\left(\omega_2 t\cos\beta_{mk}\right)\cos\left(\omega_1 t\cos\alpha_{nk} + \phi_{nmk}\right) \\ &+ j\frac{2}{\sqrt{N_0 M}}\sum_{n=1}^{N_0}\sum_{m=1}^{M}\sin\left(\omega_2 t\cos\beta_{mk}\right)\sin\left(\omega_1 t\sin\alpha_{nk} + \phi_{nmk}\right). \end{aligned} \tag{67}$$

Based on $g_k(t)$, we define our new statistical simulation model.

Definition: The k^{th} complex faded envelope is $g_k(t) = g_{ik}(t) + jg_{qk}(t)$, where

$$g_{ik}(t) = \frac{2}{\sqrt{N_0 M}}\sum_{n=1}^{N_0}\sum_{m=1}^{M}\cos\left(\omega_2 t\cos\beta_{mk}\right)\cos\left(\omega_1 t\cos\alpha_{nk} + \phi_{nmk}\right), \tag{68}$$

$$g_{qk}(t) = \frac{2}{\sqrt{N_0 M}}\sum_{n=1}^{N_0}\sum_{m=1}^{M}\sin\left(\omega_2 t\cos\beta_{mk}\right)\sin\left(\omega_1 t\sin\alpha_{nk} + \phi_{nmk}\right). \tag{69}$$

It is assumed that P independent complex envelopes are desired ($k = 0, \ldots, P-1$), each having MN_0 sinusoidal terms in the I and Q components. The angles of departures and the angles of arrivals are chosen as follows:

$$\alpha_{nk} = \frac{2\pi n}{4N_0} + \frac{2\pi k}{4PN_0} + \frac{\theta - \pi}{4N_0}, \tag{70}$$

$$\beta_{mk} = 0.5\left(\frac{2\pi m}{M} + \frac{2\pi k}{PM} + \frac{\psi - \pi}{M}\right), \tag{71}$$

for $n = 1, \ldots, N_0$, $m = 1, \ldots, M$, $k = 0, \ldots, P-1$. The angles of departures and the angles of arrivals in the k^{th} complex faded envelope are obtained by rotating the angles od departures and the angles of arrivals in the $(k-1)^{th}$ complex envelope by $(2\pi)/(4PN_0)$ and $(2\pi)/(2PM)$, respectively. The parameters ϕ_{nmk}, θ, and ψ are independent random variables uniformly distributed on the interval $[-\pi, \pi)$.

Our statistical model can be shown to exhibit properties (10) - (13) of the reference model. The derivations of these expressions are presented in Appendix C. Figures 14 and 15 show that, for $N_0 = M = P = 8$ and $N_{\text{stat}} = 30$ trials, the auto- and cross-correlations of the I and Q components, and the auto- and cross-correlations of the complex faded envelopes approach those of the reference model.

4.3 Performance Evaluation of SISO M-to-M Models

This section compares the performance and complexity of our new model with M-to-M Models I and II described in Section 2.4.2.1. In all simulations, we use a normalized sampling period $f_1 T_s = 0.01$ ($f_1 = f_2$ are the maximum Doppler frequencies and T_s is the sampling period) and $M = N_0 = P = 8$. For M-to-M Model II, we use $N_i = M_i = 8$ and $N_q = M_q = 9$ to obtain a complex envelope with uncorrelated quadrature components. Using these parameters, we have calculated the mean square errors (MSE) and maximum deviations (MAX) from the theoretical value (zero) for the normalized cross-correlations of the I and Q components, and for the normalized cross-correlations of the first and the second faded envelopes. The results are shown

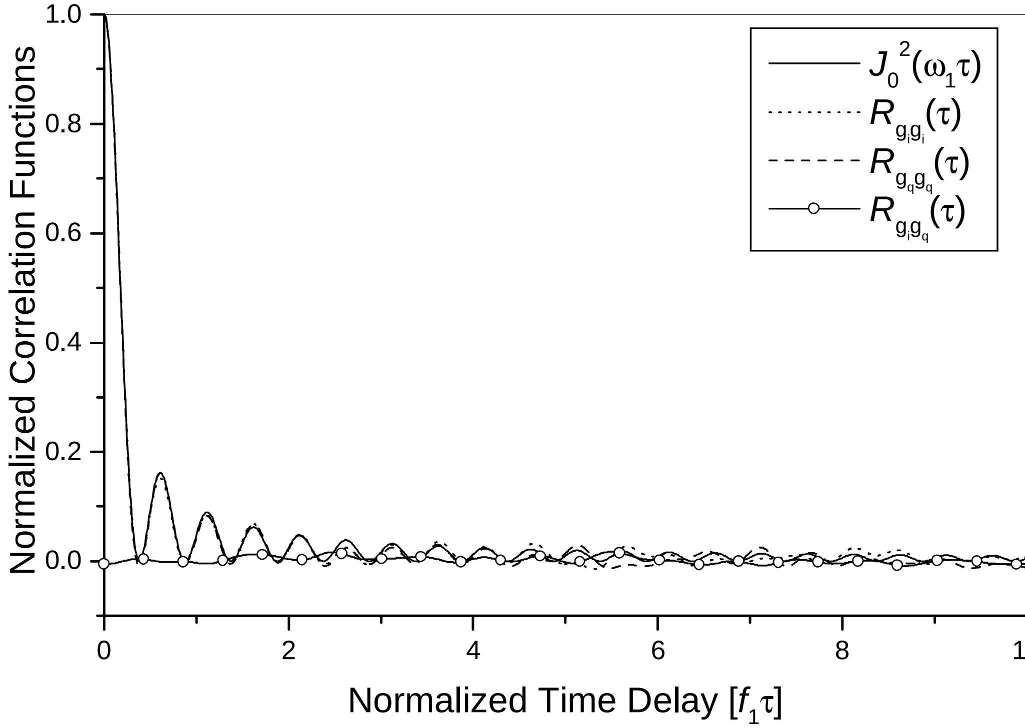

Figure 14: Theoretical and simulated ($N_{\mathrm{stat}} = 30$) auto-correlation functions and the cross-correlation function of the I and Q components of the new statistical M-to-M model.

in Table 4. Note that different simulation trials yield slightly different simulation results. To estimate these differences, the variances are computed by averaging over 10^3 simulation trials. The variances of the normalized cross-correlations of the I and Q components, and the variances of the normalized cross-correlations of the first and the second faded envelopes are also shown in Table 4. From Table 4, we conclude that our new statistical model with $N_{\mathrm{stat}} = 1$ has cross-correlations similar to M-to-M Model I and M-to-M Model II with $N_{\mathrm{stat}} = 1$. The new statistical model with $N_{\mathrm{stat}} = 30$ performs similar to M-to-M Model II with $N_{\mathrm{stat}} = 50$ and significantly better than M-to-M Model I. Increasing the number of simulation trials to $N_{\mathrm{stat}} = 50$ yields a lower cross-correlation between the I and Q components of the complex faded envelope.

To compare complexity of the new statistical model and M-to-M Models I and II, Table 5 summarizes the number of simulation trials required to obtain desired

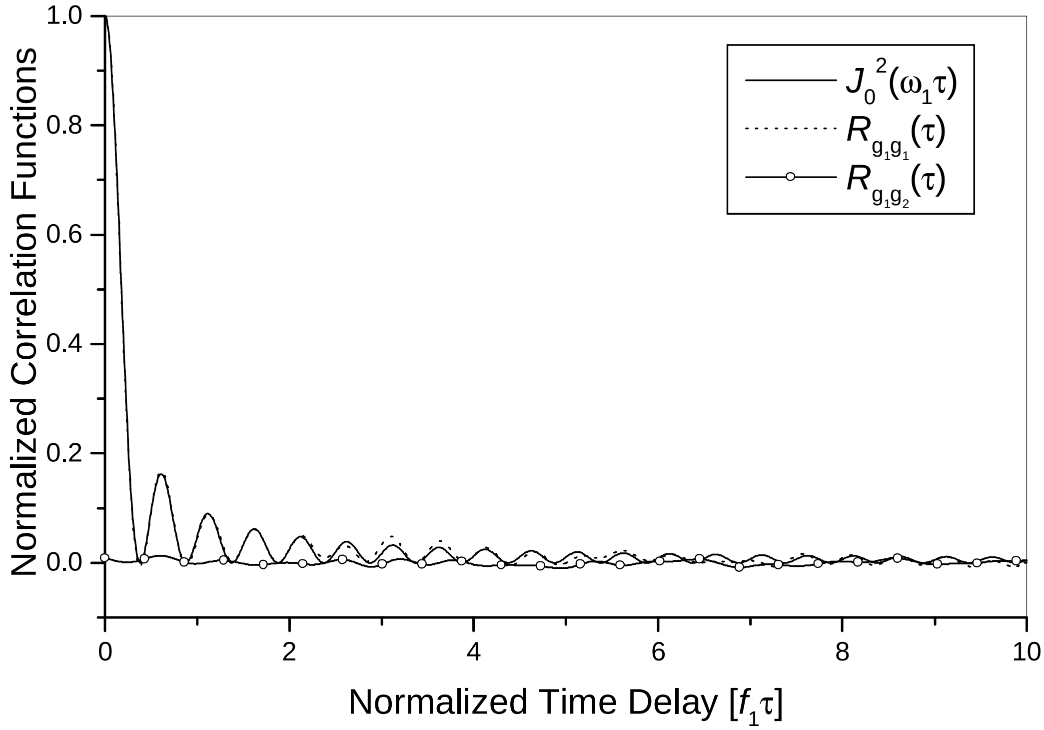

Figure 15: Theoretical and simulated ($N_{\text{stat}} = 30$) auto-correlation functions and the cross-correlation function of the first and the second faded envelopes in the new statistical M-to-M model.

statistical properties, the number of operations needed to generate one sample of the complex envelope, and the relative simulation times needed to generate a sample of the complex faded envelope with desired statistical properties, in Matlab on a Pentium III processor. Here, we count only the frequently executed operations and the number of random variables. Table 5 shows that our choice of the cosine functions, which makes statistical properties of the I and Q components similar to those of the reference model, slightly increases the complexity of our model.

Figures 16 and 17 compare the variance of the auto-correlation functions of the quadrature components averaged over 10^3 simulation trials, for the reference model, M-to-M Models I and II, and the new statistical model. For the statistical models, the variance can be defined as [57] $\text{Var}[R(\cdot)] = E[|\hat{R}(\cdot) - \lim_{N\to\infty} R(\cdot)|^2]$, where $\hat{R}(\cdot)$ denotes the time averaged correlations and $R(\cdot)$ denotes the statistical correlation function. For M-to-M Model I, the equivalent quantity is the squared error

Table 4: Mean square error, maximum deviation and variations.

Simulators	Model I	Model II $N_{stat}=1$	Model II $N_{stat}=50$	New Stat. Model $N_{stat}=1$	New Stat. Model $N_{stat}=30$	New Stat. Model $N_{stat}=50$
MSE($R_{g_i g_q}$)	$1.8\cdot10^{-3}$	$1.1\cdot10^{-3}$	$3.16\cdot10^{-5}$	$8.81\cdot10^{-4}$	$4.39\cdot10^{-5}$	$2.05\cdot10^{-5}$
Max($R_{g_i g_q}$)	$9.61\cdot10^{-2}$	$5.91\cdot10^{-2}$	$1.27\cdot10^{-2}$	$6.84\cdot10^{-2}$	$1.28\cdot10^{-2}$	$7.0\cdot10^{-3}$
Var$\left(R_{g_i g_q}\right)$	$2.74\cdot10^{-6}$	$4.59\cdot10^{-6}$	$6.67\cdot10^{-9}$	$3.11\cdot10^{-6}$	$5.69\cdot10^{-9}$	$2.51\cdot10^{-9}$
MSE($R_{g_1 g_2}$)	$5.8\cdot10^{-3}$	$1.1\cdot10^{-3}$	$1.31\cdot10^{-5}$	$7.02\cdot10^{-4}$	$3.59\cdot10^{-5}$	$1.26\cdot10^{-5}$
Max($R_{g_1 g_2}$)	$15.9\cdot10^{-2}$	$6.34\cdot10^{-2}$	$0.63\cdot10^{-2}$	$6.57\cdot10^{-2}$	$0.96\cdot10^{-2}$	$5.6\cdot10^{-3}$
Var$\left(R_{g_1 g_2}\right)$	$1.24\cdot10^{-4}$	$1.77\cdot10^{-6}$	$7.38\cdot10^{-10}$	$1.22\cdot10^{-6}$	$3.0\cdot10^{-9}$	$4.39\cdot10^{-10}$

Table 5: Complexity of different SISO M-to-M models.

Simulation models	Number of simulation trials	Estimated number of computations needed to generate one sample of $g_k(t)$			Relative simulation time for one simulation trial
		cosine	addition	random variable	
Model I	1	$6MN$	$4MN$	$2MN$	Tx
Model II	50	$6MN$	$4MN$	$2MN+2$	$1.25Tx$
New Statistical Model	30	$8MN$	$2MN$	$MN+2$	$1.65Tx$

$|\hat{R}(\cdot) - R(\cdot)|^2$. The variance for the reference model is obtained using $\mathrm{Var}[R_{g_i g_i}(\tau)] = \mathrm{Var}[R_{g_q g_q}(\tau)] = [1 + J_0(2\omega_1\tau)J_0(2\omega_2\tau) - 2J_0^2(\omega_1\tau)J_0^2(\omega_2\tau)]\,/(2N)$, as defined in [34]. The variance provides a measure of the usefulness of the model in simulating the desired channel with a finite N. A lower variance means that a smaller number of simulation trials are needed to achieve the desired statistical properties and, hence, the corresponding model is better. Since the reference model does not exploit the symmetry of the "double ring" model, as the new statistical model and M-to-M Models I and II do, for fair comparison, we use $N = 4N_0 \times 2M = 512$ sinusoids for simulation of the reference model. From Fig. 16, we conclude that our new statistical model with $N_{\mathrm{stat}} = 1$ has a similar variance as M-to-M Model I and a lower variance than M-to-M Model II with $N_{\mathrm{stat}} = 1$. However, Fig. 16 shows that all three models do not perform as well as the reference model. An increase in the number of simulation trials to $N_{\mathrm{stat}} = 30$ in the new statistical model yields a significantly lower variance of the auto-correlation function of the quadrature component. Fig. 17 shows that the new statistical model with $N_{\text{stat}} = 30$ outperforms M-to-M Models I and II and the reference model.

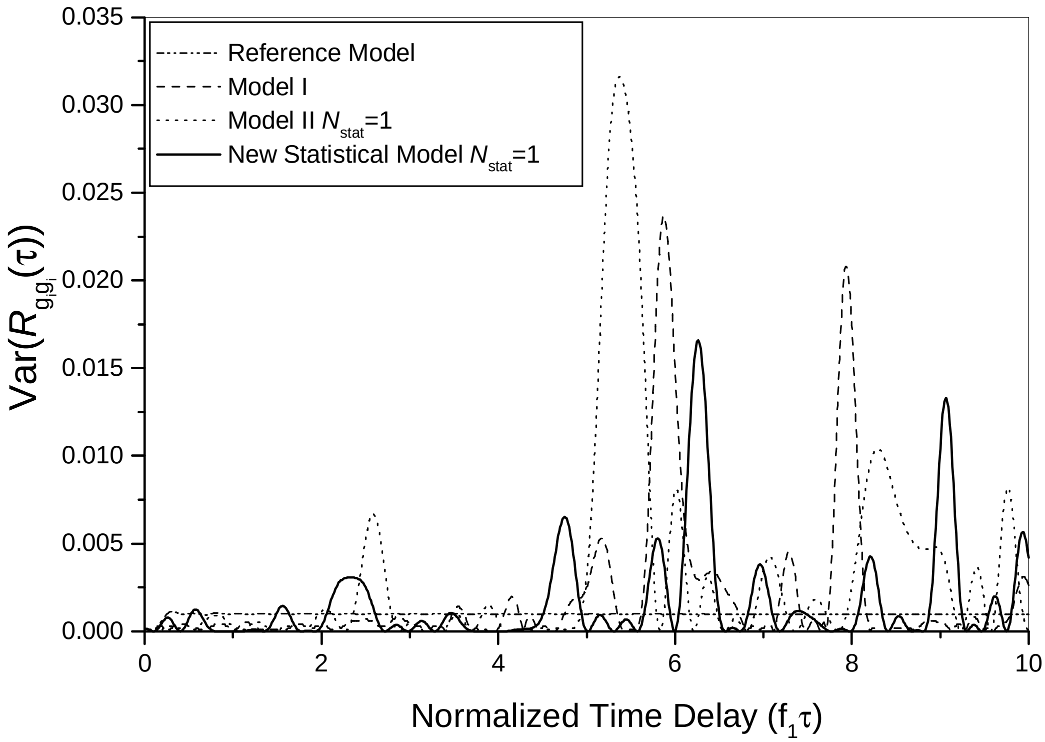

Figure 16: Variance of the auto-correlation function of the quadrature component with $N_{\text{stat}} = 1$.

Tables 4 and 5 and Figs. 16 - 17 show that our new statistical model converges faster than other statistical models, has a lower variance of the auto-correlation functions, and has a lower correlation between the I and Q components of the complex faded envelope than M-to-M Models I and II. Adequate statistics can be achieved with only 30 trials using our new statistical model.

4.4 Summary

This chapter presented a new statistical SoS model for M-to-M channels. The properties of the proposed model have been derived and verified using simulation. The statistics of the new model match those of the reference model for a large range of

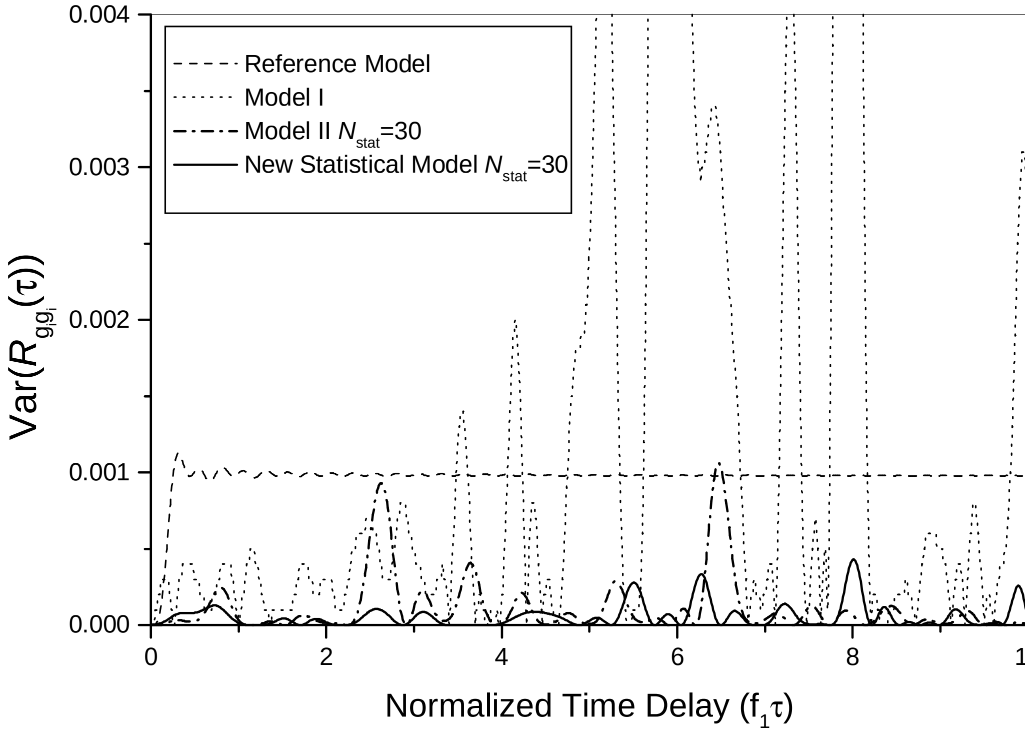

Figure 17: Variance of the auto-correlation function of the quadrature component with $N_{\text{stat}} = 30$.

normalized time delays ($0 \leq f_1 T_s \leq 8$). Our new statistical model converges faster, has a lower variance of the auto-correlation functions and has a lower correlation between the I and Q components of the complex faded envelope than other models discussed in this paper. Finally, unlike existing M-to-M models, our model generates multiple uncorrelated faded envelopes as well.

CHAPTER V

SPACE-TIME CORRELATED M-TO-M CHANNELS: MODELING AND SIMULATION

5.1 Overview

Chapter 2 reviewed the first reference model for narrowband MIMO M-to-M channels [37] and the deterministic SoS model called the Modified Method of Exact Doppler Spreads (MMEDS) [38]. These models consider radio propagation in outdoor macro-cells, assuming that all rays are only double-bounced. However, channel measurements for narrowband and wideband M-to-M communications [39], [40] show that this assumption is not always correct.

To address this problem, this chapter proposes a new 2-D parametric reference model that employs a "two-ring" model and constructs the received complex faded envelope as a superposition of the LoS, single-bounced, and double-bounced rays. The parametric nature of the model makes it adaptable to a variety of propagation environments, i.e., outdoor micro- and macro-cells. For example, our reference model describes the radio propagation in outdoor macro-cells as a combination of single- and double-bounced rays, taking into account that the double-bounced rays bear more energy than the single-bounced rays. In particular, if there are no single-bounced and LoS rays, our model simplifies to the model proposed in [37], [38]. From the new reference model, we derive a closed-form joint space-time correlation function for 2-D non-isotropic scattering environment. For 2-D isotropic scattering and no single-bounced and LoS rays, our space-time correlation function is shown to reduce to the one derived in [37]. Furthermore, we derive the space-time correlation functions of the I and Q components of the complex faded envelope for 2-D isotropic scattering environment. Finally, we derive the space-Doppler power spectrum of the complex faded envelope assuming 2-D non-isotropic scattering environment.

The reference models assume an infinite number of scatterers, which prevents practical implementation. Hence, we propose an ergodic statistical (deterministic) SoS simulation model for 2-D isotropic scattering environment. We employ a "two-ring" model that combines the LoS, single-bounced, and double-bounced rays and has orthogonal functions as the I and Q components of the complex faded envelope. The statistical properties of our model are verified by simulations. Furthermore, by allowing amplitudes, phases, and Doppler frequencies to be random variables, the deterministic model is modified to better match statistical properties of the reference model. This model is called the statistical simulation model. The statistical properties of the statistical model vary for each simulation trial, but will converge to desired ensemble averaged properties when averaged over a sufficient number of simulation trials. The statistical properties of this model are also verified by simulations. Finally, we compare the performance and complexity of our new models with the MMEDS model. For fair comparison, we remove the LoS and single-bounced components of the complex faded envelope from our models. Our deterministic model performs similar to the MMEDS model [38], but requires smaller number of scatterers and has shorter simulation time. Compared to the deterministic and the MMEDS model, the statistical properties of the statistical model match those of the reference model over a wider range of normalized time delays while using smaller number of scatterers.

The remainder of the chapter is organized as follows. Section 5.2 describes the communication system and presents the new parametric reference model for MIMO M-to-M channels. Section 5.3 presents the derivation of the closed-form joint space-time correlation function for 2-D non-isotropic scattering, the derivation of the space-time correlation functions of the I and Q components of the complex faded envelope for 2-D isotropic scattering, and the derivation of the space-Doppler power spectrum of the complex faded envelope for 2-D non-isotropic scattering. Section 5.4 details our deterministic and statistical simulation models. Section 5.5 presents simulation results for our new models and compares them to the MMEDS model in [38]. Section 5.6 provides some concluding remarks.

5.2 A New Reference Model for MIMO M-to-M Channels

This chapter considers a narrowband single-user MIMO communication system with L_t transmit and L_r receive omnidirectional antenna elements. It is assumed that both the $\mathrm{T_x}$ and $\mathrm{R_x}$ are in motion and equipped with low elevation antennas. Here, we consider the radio propagation in outdoor micro- and macro-cells, which is characterized by 2-D scattering with either LoS or NLoS conditions between the transmitter and receiver. The MIMO channel can be described by an $L_r \times L_t$ matrix $\mathbf{H}(t) = [h_{ij}(t)]_{L_r \times L_t}$ of complex faded envelopes.

The geometry of the proposed model is shown in Figs. 18 and 19. Figure 18 shows the "two-ring" model with single- and double-bounced rays for a MIMO M-to-M channel with $L_t = L_r = 2$ antenna elements. Figure 19 shows the LoS paths for the channel in Fig. 18. This elementary 2×2 antenna configuration will be used later to construct uniform linear antenna arrays with arbitrary number of antennas. The "two-ring" model defines two rings of fixed scatterers, one around the $\mathrm{T_x}$ and another around the $\mathrm{R_x}$, as shown in Fig. 18. Around the transmitter, M omnidirectional scatterers lie on a ring of radius R_t, and the m^{th} transmit scatterer is denoted by $S_T^{(m)}$. Similarly, around the receiver, N omnidirectional scatterers lie on a ring of radius R_r and the n^{th} receive scatterer is denoted by $S_R^{(n)}$. The distance between the $\mathrm{T_x}$ and $\mathrm{R_x}$ is D. It is assumed that the radii R_t and R_r are much smaller than the distance D between the $\mathrm{T_x}$ and $\mathrm{R_x}$, i.e., $\max\{R_t, R_r\} \ll D$ (local scattering condition). Furthermore, it is assumed that the distance D is smaller than $4R_tR_rL_r/(\lambda(L_t-1)(L_r-1))$ (channel does not experience keyhole behavior [58]), where λ denotes the carrier wavelength. The spacing between two adjacent antenna elements at the $\mathrm{T_x}$ and $\mathrm{R_x}$ is denoted by δ_T and δ_R, respectively. It is assumed that δ_T and δ_R are much smaller than the radii R_t and R_r, i.e., $\max\{\delta_T, \delta_R\} \ll \min\{R_t, R_r\}$. Angles θ_T and θ_R describe the orientation of the $\mathrm{T_x}$ and $\mathrm{R_x}$ antenna array, respectively, relative to the x-axis. Similarly, the $\mathrm{T_x}$ and $\mathrm{R_x}$ are moving with speeds v_T and v_R in directions described by angles γ_T and γ_R, respectively. In Fig. 18, the symbols $\alpha_T^{(m)}$ and $\alpha_T^{(n)}$ are the angles of departures (AoD) of the waves that impinge on the scatterers $S_T^{(m)}$ and $S_R^{(n)}$, whereas $\alpha_R^{(m)}$ and $\alpha_R^{(n)}$ are the angles of arrivals (AoA) of the waves scattered from $S_T^{(m)}$ and $S_R^{(n)}$, respectively. The symbols ϵ_{pm}, ϵ_{mq}, ϵ_{pn}, ϵ_{nq}, and ϵ_{mn} denote distances $A_T^{(p)} - S_T^{(m)}$, $S_T^{(m)} - A_R^{(q)}$, $A_T^{(p)} - S_R^{(n)}$, $S_R^{(n)} - A_R^{(q)}$, and $S_T^{(m)} - S_R^{(n)}$, respectively, as shown in Fig. 18. In Fig. 19, the symbols α_{Rq}^{LoS} and ϵ_{pq} denote the AoAs of the LoS paths and the distance $A_T^{(p)} - A_R^{(q)}$, respectively.

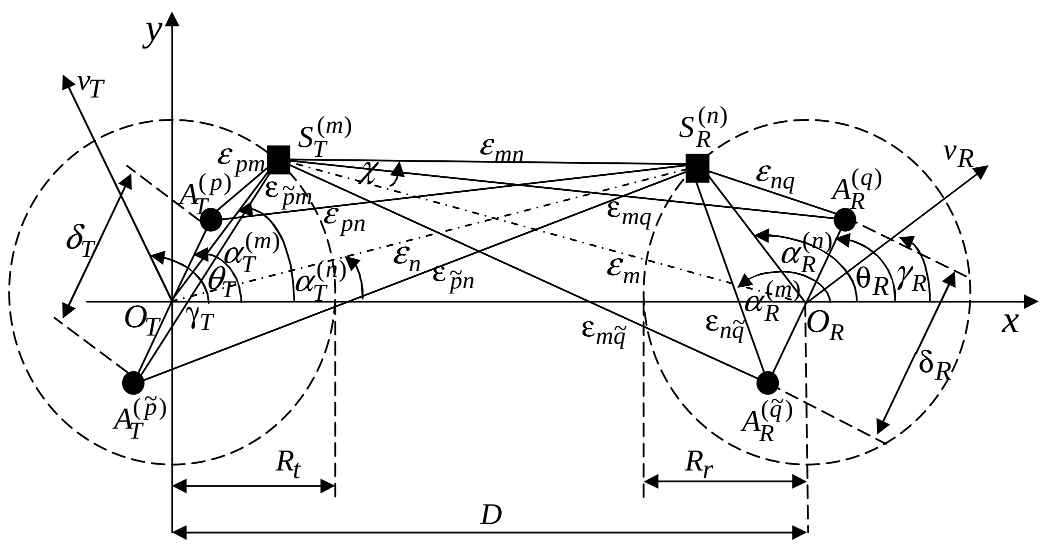

Figure 18: Single- and double-bounced "two-ring" model for MIMO M-to-M channel with $L_t = L_r = 2$ antenna elements.

From the geometrical model described above, the received complex faded envelope of the link $A_T^{(p)} - A_R^{(q)}$ is a superposition of the single-bounced transmit, single-bounced receive, the double-bounced rays, and the LoS and can be written as follows

$$h_{pq}(t) \quad = \quad h_{pq}^{SBT}(t) + h_{pq}^{SBR}(t) + h_{pq}^{DB}(t) + h_{pq}^{LoS}(t), \tag{72}$$

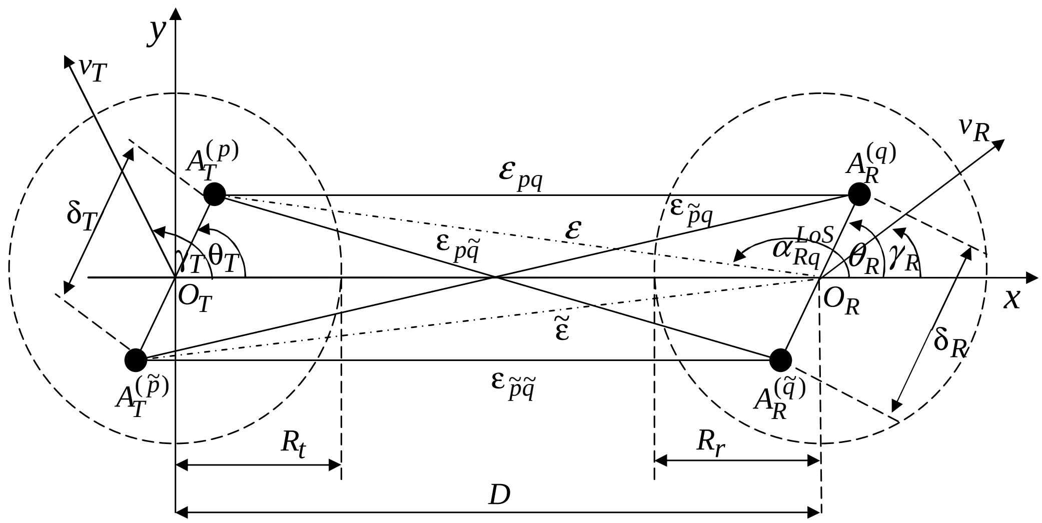

Figure 19: The LoS paths in the 2x2 channel of Fig. 18.

where the single-bounced components of the received complex faded envelope are, respectively,

$$h_{pq}^{SBT}(t) = \sqrt{\frac{\eta_T \Omega_{pq}}{K_{pq}+1}} \lim_{M\to\infty} \sum_{m=1}^{M} \frac{e^{j\phi_m - j\frac{2\pi}{\lambda}(\epsilon_{pm}+\epsilon_{mq}) + j2\pi t[f_{T\max}\cos(\alpha_T^{(m)}-\gamma_T)+f_{R\max}\cos(\alpha_R^{(m)}-\gamma_R)]}}{\sqrt{M}}, \tag{73}$$

$$h_{pq}^{SBR}(t) = \sqrt{\frac{\eta_R \Omega_{pq}}{K_{pq}+1}} \lim_{N\to\infty} \sum_{n=1}^{N} \frac{e^{j\phi_n - j\frac{2\pi}{\lambda}(\epsilon_{pn}+\epsilon_{nq}) + j2\pi t[f_{T\max}\cos(\alpha_T^{(n)}-\gamma_T)+f_{R\max}\cos(\alpha_R^{(n)}-\gamma_R)]}}{\sqrt{N}}, \tag{74}$$

the double-bounced component of the received complex faded envelope is

$$h_{pq}^{DB}(t) = \sqrt{\frac{\eta_{TR}\Omega_{pq}}{K_{pq}+1}} \lim_{M,N\to\infty} \sum_{m=1}^{M}\sum_{n=1}^{N} \frac{1}{\sqrt{MN}} \times e^{-j\frac{2\pi}{\lambda}(\epsilon_{pm}+\epsilon_{mn}+\epsilon_{nq}) + j2\pi t[f_{T\max}\cos(\alpha_T^{(m)}-\gamma_T)+f_{R\max}\cos(\alpha_R^{(n)}-\gamma_R)] + j\phi_{mn}}, \tag{75}$$

and the LoS component of the received complex faded envelope is

$$h_{pq}^{LoS}(t) = \sqrt{\frac{K_{pq}\Omega_{pq}}{K_{pq}+1}} e^{j2\pi t f_{T\max}\cos(\pi-\alpha_{Rq}^{LoS}-\gamma_T)} e^{j2\pi t f_{R\max}\cos(\alpha_{Rq}^{LoS}-\gamma_R) - j\frac{2\pi}{\lambda}\epsilon_{pq}}. \tag{76}$$

In (73) – (76), Ω_{pq} and K_{pq} denote the transmitted power and the Ricean factor of the subchannel $A_T^{(p)}$ – $A_R^{(q)}$, respectively. Parameters η_T, η_R, and η_{TR} specify how much the single- and double-bounced rays contribute in the total power Ω_{pq}, i.e., these parameters satisfy $\eta_T + \eta_R + \eta_{TR} = 1$. Frequencies $f_{T\max} = \upsilon_T/\lambda$ and $f_{R\max} = \upsilon_R/\lambda$ are the maximum Doppler frequencies associated with the $\mathrm{T_x}$ and $\mathrm{R_x}$, respectively. It is assumed that the AoDs ($\alpha_T^{(m)}$ and $\alpha_T^{(n)}$) and the AoAs ($\alpha_R^{(m)}$ and $\alpha_R^{(n)}$) are random variables. Note that double-bounced rays have the AoD, $\alpha_T^{(m)}$, independent from the AoA, $\alpha_R^{(n)}$, [58], whereas single-bounced rays have the AoA, $\alpha_R^{(m)}$, dependent on the AoD, $\alpha_T^{(m)}$, and the AoD, $\alpha_T^{(n)}$, dependent on the AoA $\alpha_R^{(n)}$ (see Appendix D). Finally, it is assumed that the phases ϕ_m, ϕ_n, and ϕ_{mn} are random variables uniformly distributed on the interval $[-\pi, \pi)$ and independent from the angles of departure and the angles of arrival.

As shown in Appendix D, the distances ϵ_{pm}, ϵ_{mq}, ϵ_{pn}, ϵ_{nq}, ϵ_{mn}, and ϵ_{pq} can be expressed as functions of the angles $\alpha_T^{(m)}$, $\alpha_R^{(n)}$, and α_{Rq}^{LoS} as follows:

$$
\begin{aligned}
\epsilon_{pm} &\approx R_t - (0.5L_t + 0.5 - p)\delta_T \cos\left(\theta_T - \alpha_T^{(m)}\right), && (77)\\
\epsilon_{mq} &\approx D - (0.5L_r + 0.5 - q)\delta_R \left[\Delta_T \sin\theta_R \sin\alpha_T^{(m)} - \cos\theta_R\right], && (78)\\
\epsilon_{pn} &\approx D - (0.5L_t + 0.5 - p)\delta_T \left[\Delta_R \sin\theta_T \sin\alpha_R^{(n)} + \cos\theta_T\right], && (79)\\
\epsilon_{nq} &\approx R_r - (0.5L_r + 0.5 - q)\delta_R \cos\left(\alpha_R^{(n)} - \theta_R\right), && (80)\\
\epsilon_{mn} &= \epsilon_m \frac{\sin\left(\alpha_R^{(m)} - \alpha_R^{(n)}\right)}{\sin\left(\chi + \left(\alpha_R^{(m)} - \alpha_R^{(n)}\right)\right)} \approx D, && (81)\\
\epsilon_{pq} &\approx D - (0.5L_t + 0.5 - p)\delta_T \cos\theta_T - (0.5L_r + 0.5 - q)\delta_R \cos\left(\alpha_{Rq}^{LoS} - \theta_R\right), && (82)
\end{aligned}
$$

where parameters p and q take values from the sets $p \in \{1, \ldots, L_t\}$ and $q \in \{1, \ldots, L_r\}$, respectively, $\Delta_T = R_t/D$, and $\Delta_R = R_r/D$.

Using (77) – (82), the single-bounced transmit, single-bounced receive, double-bounced, and LoS components of the complex faded envelope become, respectively,

$$
h_{pq}^{SBT}(t) = \sqrt{\frac{\eta_T \Omega_{pq}}{K_{pq}+1}} \lim_{M\to\infty} \sum_{m=1}^{M} \frac{e^{j\frac{\pi}{\lambda}(L_t+1-2p)\delta_T \cos(\theta_T - \alpha_T^{(m)})}}{\sqrt{M}} e^{j\phi_m - j\frac{2\pi}{\lambda}(D+R_t)} \tag{83}
$$

$$
\times\ e^{j\frac{\pi}{\lambda}(L_r+1-2q)\delta_R[\Delta_T \sin\theta_R \sin\alpha_T^{(m)} - \cos\theta_R]} e^{j2\pi t[f_{T\max}\cos(\alpha_T^{(m)} - \gamma_T) + f_{R\max}(\Delta_T \sin\gamma_R \sin\alpha_T^{(m)} - \cos\gamma_R)]},
$$

$$h_{pq}^{SBR}(t) = \sqrt{\frac{\eta_R \Omega_{pq}}{K_{pq}+1}} \lim_{N\to\infty} \sum_{n=1}^{N} \frac{e^{j\frac{\pi}{\lambda}(L_r+1-2q)\delta_R \cos(\alpha_R^{(n)}-\theta_R)}}{\sqrt{N}} e^{j\phi_n - j\frac{2\pi}{\lambda}(D+R_r)} \tag{84}$$
$$\times\ e^{j\frac{\pi}{\lambda}(L_t+1-2p)\delta_T[\Delta_R \sin\theta_T \sin\alpha_R^{(n)}+\cos\theta_T]} e^{j2\pi t[f_{R\max}\cos(\alpha_R^{(n)}-\gamma_R)+f_{T\max}(\Delta_R\sin\gamma_T\sin\alpha_R^{(n)}+\cos\gamma_T)]},$$
$$h_{pq}^{DB}(t) = \sqrt{\frac{\eta_{TR}\Omega_{pq}}{K_{pq}+1}} \lim_{M,N\to\infty} \sum_{m,n=1}^{M,N} \frac{e^{j\phi_{mn}-j\frac{2\pi}{\lambda}(D+R_r+R_t)}}{\sqrt{MN}} e^{j\frac{\pi}{\lambda}(L_t+1-2p)\delta_T\cos(\theta_T-\alpha_T^{(m)})} \tag{85}$$
$$\times\ e^{j\frac{\pi}{\lambda}(L_r+1-2q)\delta_R\cos(\alpha_R^{(n)}-\theta_R)} e^{j2\pi t[f_{T\max}\cos(\alpha_T^{(m)}-\gamma_T)+f_{R\max}\cos(\alpha_R^{(n)}-\gamma_R)]},$$
$$h_{pq}^{LoS}(t) = \sqrt{\frac{K_{pq}\Omega_{pq}}{1+K_{pq}}}\ e^{-j\frac{2\pi}{\lambda}D}\ e^{j2\pi t f_{T\max}\cos(\pi-\alpha_{Rq}^{LoS}-\gamma_T)+j2\pi t f_{R\max}\cos(\alpha_{Rq}^{LoS}-\gamma_R)} \tag{86}$$
$$\times\ e^{j\frac{\pi}{\lambda}[(L_t+1-2p)\delta_T\cos\theta_T+(L_r+1-2q)\delta_R\cos(\alpha_{Rq}^{LoS}-\theta_R)]}.$$

The complex faded envelope in (72) also can be written as $h_{pq}(t) = h_{pq}^{(I)}(t)+jh_{pq}^{(Q)}(t)$ where

$$h_{pq}^{(I)}(t) = \Re\{h_{pq}^{SBT}(t)\}+\Re\{h_{pq}^{SBR}(t)\}+\Re\{h_{pq}^{DB}(t)\}+\Re\{h_{pq}^{LoS}(t)\}, \tag{87}$$
$$h_{pq}^{(Q)}(t) = \Im\{h_{pq}^{SBT}(t)\}+\Im\{h_{pq}^{SBR}(t)\}+\Im\{h_{pq}^{DB}(t)\}+\Im\{h_{pq}^{LoS}(t)\}, \tag{88}$$

are the I and Q components of the complex faded envelope, and $\Re\{\ \cdot\ \}$ and $\Im\{\ \cdot\ \}$ denote the real and imaginary operation, respectively.

5.3 Space-time Correlation Functions and Space-Doppler Power Spectral Density

Assuming a 2-D non-isotropic scattering environment, we now derive the closed-form space-time correlation function of the complex faded envelope in (72). We also show that this space-time correlation function reduces to the one derived in [37] if there are no single-bounced and LoS rays and 2-D isotropic scattering is assumed. Furthermore, we derive the space-time correlation functions of the I and Q components of the complex faded envelope for a 2-D isotropic scattering environment. Finally, we derive the space-Doppler power spectral density of the complex faded envelope, assuming a 2-D non-isotropic scattering environment.

The normalized space-time correlation function between two complex faded envelopes $h_{pq}(t)$ and $h_{\tilde{p}\tilde{q}}(t)$ is defined as

$$\begin{aligned}
R_{pq,\tilde{p}\tilde{q}}(\delta_T, \delta_R, \tau) &= \frac{\mathrm{E}\left[h_{pq}(t)h_{\tilde{p}\tilde{q}}(t+\tau)^*\right]}{\sqrt{\mathrm{E}[|h_{pq}(t)|^2]\mathrm{E}[|h_{\tilde{p}\tilde{q}}(t)|^2]}} \qquad (89)\\
&= \frac{\mathrm{E}\left[h_{pq}^{SBT}(t)h_{\tilde{p}\tilde{q}}^{SBT}(t+\tau)^*\right]}{\sqrt{\mathrm{E}[|h_{pq}^{SBT}(t)|^2]\mathrm{E}[|h_{\tilde{p}\tilde{q}}^{SBT}(t)|^2]}} + \frac{\mathrm{E}\left[h_{pq}^{DB}(t)h_{\tilde{p}\tilde{q}}^{DB}(t+\tau)^*\right]}{\sqrt{\mathrm{E}[|h_{pq}^{DB}(t)|^2]\mathrm{E}[|h_{\tilde{p}\tilde{q}}^{DB}(t)|^2]}}\\
&+ \frac{\mathrm{E}\left[h_{pq}^{SBR}(t)h_{\tilde{p}\tilde{q}}^{SBR}(t+\tau)^*\right]}{\sqrt{\mathrm{E}[|h_{pq}^{SBR}(t)|^2]\mathrm{E}[|h_{\tilde{p}\tilde{q}}^{SBR}(t)|^2]}} + \frac{\mathrm{E}\left[h_{pq}^{LoS}(t)h_{\tilde{p}\tilde{q}}^{LoS}(t+\tau)^*\right]}{\sqrt{\mathrm{E}[|h_{pq}^{LoS}(t)|^2]\mathrm{E}[|h_{\tilde{p}\tilde{q}}^{LoS}(t)|^2]}},
\end{aligned}$$

where $(\ \cdot\ )^*$ denotes complex conjugate operation, $\mathrm{E}[\ \cdot\ ]$ is the statistical expectation operator, $p, \tilde{p} \in \{1, \ldots, L_t\}$, and $q, \tilde{q} \in \{1, \ldots, L_r\}$.

Using (83), (84), and (89), the space-time correlation functions of the single-bounced components can be written as

$$\begin{aligned}
R_{pq,\tilde{p}\tilde{q}}^{SBT}(\delta_T, \delta_R, \tau) &= \frac{\mathrm{E}\left[h_{pq}^{SBT}(t)h_{\tilde{p}\tilde{q}}^{SBT}(t+\tau)^*\right]}{\sqrt{\mathrm{E}[|h_{pq}^{SBT}(t)|^2]\mathrm{E}[|h_{\tilde{p}\tilde{q}}^{SBT}(t)|^2]}} = \lim_{M\to\infty} \frac{\eta_T}{M} \qquad (90)\\
&\times \sum_{m=1}^{M} \mathrm{E}\Bigg[e^{j\frac{2\pi}{\lambda}[(\tilde{p}-p)\delta_T \cos(\theta_T - \alpha_T^{(m)}) + (\tilde{q}-q)\delta_R(\Delta_T \sin\theta_R \sin\alpha_T^{(m)} - \cos\theta_R)]}\\
&\times e^{-j2\pi\tau[f_{T\max}\cos(\alpha_T^{(m)} - \gamma_T) + f_{R\max}(\Delta_T \sin\gamma_R \sin\alpha_T^{(m)} - \cos\gamma_R)]}\Bigg],
\end{aligned}$$

$$\begin{aligned}
R_{pq,\tilde{p}\tilde{q}}^{SBR}(\delta_T, \delta_R, \tau) &= \frac{\mathrm{E}\left[h_{pq}^{SBR}(t)h_{\tilde{p}\tilde{q}}^{SBR}(t+\tau)^*\right]}{\sqrt{\mathrm{E}[|h_{pq}^{SBR}(t)|^2]\mathrm{E}[|h_{\tilde{p}\tilde{q}}^{SBR}(t)|^2]}} = \lim_{N\to\infty} \frac{\eta_R}{N} \qquad (91)\\
&\times \sum_{n=1}^{N} \mathrm{E}\Bigg[e^{j\frac{2\pi}{\lambda}[(\tilde{q}-q)\delta_R \cos(\alpha_R^{(n)} - \theta_R) + (\tilde{p}-p)\delta_T(\Delta_R \sin\theta_T \sin\alpha_R^{(n)} + \cos\theta_T)]}\\
&\times e^{-j2\pi\tau[f_{T\max}(\Delta_R \sin\gamma_T \sin\alpha_R^{(n)} + \cos\gamma_T) + f_{R\max}\cos(\alpha_R^{(n)} - \gamma_R)]}\Bigg].
\end{aligned}$$

Using (85) and (89), the space-time correlation function of the double-bounced component becomes

$$R_{pq,\tilde{p}\tilde{q}}^{DB}(\delta_T,\delta_R,\tau) = \frac{\mathrm{E}\left[h_{pq}^{DB}(t)h_{\tilde{p}\tilde{q}}^{DB}(t+\tau)^*\right]}{\sqrt{\mathrm{E}[|h_{pq}^{DB}(t)|^2]\mathrm{E}[|h_{\tilde{p}\tilde{q}}^{DB}(t)|^2]}} \tag{92}$$
$$= \lim_{M,N\to\infty}\frac{\eta_{TR}}{MN}\sum_{m=1}^{M}\sum_{n=1}^{N}\mathrm{E}\Big[e^{-j2\pi\tau(f_{T\max}\cos(\alpha_T^{(m)}-\gamma_T)+f_{R\max}\cos(\alpha_R^{(n)}-\gamma_R))}$$
$$\times\ e^{j\frac{2\pi}{\lambda}[(\tilde{q}-q)\delta_R\cos(\alpha_R^{(n)}-\theta_R)+(\tilde{p}-p)\delta_T\cos(\theta_T-\alpha_T^{(m)})]}\Big].$$

Since the number of local scatterers in the reference models described in Section 5.2 is infinite, the discrete AoDs, $\alpha_T^{(m)}$, and AoAs, $\alpha_R^{(n)}$, can be replaced with continuous random variables α_T and α_R with probability density functions (pdf) $f(\alpha_T)$ and $f(\alpha_R)$, respectively. Hence, the space-time correlation functions of the single- and double-bounced components can be rewritten as

$$R_{pq,\tilde{p}\tilde{q}}^{SBT}(\delta_T,\delta_R,\tau) = \eta_T\int_{-\pi}^{\pi} e^{j\frac{2\pi}{\lambda}(\tilde{p}-p)\delta_T\cos(\theta_T-\alpha_T)}e^{j\frac{2\pi}{\lambda}(\tilde{q}-q)\delta_R(\Delta_T\sin\theta_R\sin\alpha_T-\cos\theta_R)} \tag{93}$$
$$\times\ e^{-j2\pi\tau f_{T\max}\cos(\alpha_T-\gamma_T)}e^{-j2\pi\tau f_{R\max}(\Delta_T\sin\gamma_R\sin\alpha_T-\cos\gamma_R)}f(\alpha_T)d\alpha_T,$$

$$R_{pq,\tilde{p}\tilde{q}}^{SBR}(\delta_T,\delta_R,\tau) = \eta_R\int_{-\pi}^{\pi} e^{j\frac{2\pi}{\lambda}(\tilde{q}-q)\delta_R\cos(\alpha_R-\theta_R)}e^{j\frac{2\pi}{\lambda}(\tilde{p}-p)\delta_T(\Delta_R\sin\theta_T\sin\alpha_R+\cos\theta_T)} \tag{94}$$
$$\times\ e^{-j2\pi\tau f_{R\max}\cos(\alpha_R-\gamma_R)}e^{-j2\pi\tau f_{T\max}(\Delta_R\sin\gamma_T\sin\alpha_R+\cos\gamma_T)}f(\alpha_R)d\alpha_R,$$

$$R_{pq,\tilde{p}\tilde{q}}^{DB}(\delta_T,\delta_R,\tau) = \eta_{TR}\int_{-\pi}^{\pi}\int_{-\pi}^{\pi} e^{-j2\pi\tau[f_{T\max}\cos(\alpha_T-\gamma_T)+f_{R\max}\cos(\alpha_R-\gamma_R)]} \tag{95}$$
$$\times\ e^{j\frac{2\pi}{\lambda}[(\tilde{p}-p)\delta_T\cos(\alpha_T-\theta_T)+(\tilde{q}-q)\delta_R\cos(\alpha_R-\theta_R)]}f(\alpha_T)f(\alpha_R)d\alpha_T d\alpha_R.$$

Prior work uses several different scatterer distributions, such as uniform [59], von Mises [60], Gaussian, and Laplacian [61]. In this section we use the von Mises pdf because it approximates many of the afore mentioned distributions (e.g., uniform and Gaussian), matches well measured results in [62], and in contrast to afore mentioned distributions, leads to closed-form solutions for many useful situations. The von Mises pdf is defined as [60]

$$f(\theta) \triangleq \frac{1}{2\pi I_0(k)}\exp\left[k\cos(\theta-\mu)\right], \tag{96}$$

where $\theta \in [-\pi, \pi)$, $I_0(\,\cdot\,)$ is the zeroth-order modified Bessel function of the first kind, $\mu \in [-\pi, \pi)$ is the mean angle at which the scatterers are distributed on the ring, and k controls the spread of scatterers around the mean. When $k = 0$, $f(\theta) = 1/(2\pi)$ is a uniform distribution yielding 2-D isotropic scattering. As k increases, the scatterers become more clustered around angle μ and the scattering becomes increasingly non-isotropic. By denoting the von Mises pdf for the $\mathrm{T_x}$ and $\mathrm{R_x}$ scatterers as $f(\alpha_T) = \exp[k_T \cos(\alpha_T - \mu_T)]/(2\pi I_0(k_T))$ and $f(\alpha_R) = \exp[k_R \cos(\alpha_R - \mu_R)]/(2\pi I_0(k_R))$, respectively, the space-time correlation functions of the single- and double-bounced components become, respectively,

$$\begin{aligned} R^{SBT}_{pq,\tilde{p}\tilde{q}}(\delta_T, \delta_R, \tau) &= \frac{\eta_T}{2\pi I_0(k_T)} \\ &\times \int_{-\pi}^{\pi} e^{j\frac{2\pi}{\lambda}(\tilde{p}-p)\delta_T \cos(\theta_T - \alpha_T)} e^{j\frac{2\pi}{\lambda}(\tilde{q}-q)\delta_R(\Delta_T \sin\theta_R \sin\alpha_T - \cos\theta_R)} \\ &\times e^{k_T \cos(\alpha_T - \mu_T)} e^{-j2\pi\tau[f_{T\max}\cos(\alpha_T - \gamma_T) + f_{R\max}(\Delta_T \sin\gamma_R \sin\alpha_T - \cos\gamma_R)]} d\alpha_T, \end{aligned} \tag{97}$$

$$\begin{aligned} R^{SBR}_{pq,\tilde{p}\tilde{q}}(\delta_T, \delta_R, \tau) &= \frac{\eta_R}{2\pi I_0(k_R)} \\ &\times \int_{-\pi}^{\pi} e^{j\frac{2\pi}{\lambda}(\tilde{q}-q)\delta_R \cos(\alpha_R - \theta_R)} e^{j\frac{2\pi}{\lambda}(\tilde{p}-p)\delta_T(\Delta_R \sin\theta_T \sin\alpha_R + \cos\theta_T)} \\ &\times e^{k_R \cos(\alpha_R - \mu_R)} e^{-j2\pi\tau[f_{T\max}(\Delta_R \sin\gamma_T \sin\alpha_R + \cos\gamma_T) + f_{R\max}\cos(\alpha_R - \gamma_R)]} d\alpha_R, \end{aligned} \tag{98}$$

$$\begin{aligned} R^{DB}_{pq,\tilde{p}\tilde{q}}(\delta_T, \delta_R, \tau) &= \frac{\eta_{TR}}{4\pi^2 I_0(k_T) I_0(k_R)} \\ &\times \int_{-\pi}^{\pi}\int_{-\pi}^{\pi} e^{k_T \cos(\alpha_T - \mu_T)} e^{k_R \cos(\alpha_R - \mu_R)} e^{j\frac{2\pi}{\lambda}(\tilde{p}-p)\delta_T \cos(\alpha_T - \theta_T)} \\ &\times e^{j\frac{2\pi}{\lambda}(\tilde{q}-q)\delta_R \cos(\alpha_R - \theta_R)} e^{-j2\pi\tau[f_{T\max}\cos(\alpha_T - \gamma_T) + f_{R\max}\cos(\alpha_R - \gamma_R)]} d\alpha_T d\alpha_R. \end{aligned} \tag{99}$$

Using trigonometric transformations, (97) and (98) become, respectively,

$$\begin{aligned} R^{SBT}_{pq,\tilde{p}\tilde{q}}(\delta_T, \delta_R, \tau) &= \frac{\eta_T e^{-j\frac{2\pi}{\lambda}(\tilde{q}-q)\delta_R \cos\theta_R + j2\pi\tau f_{R\max}\cos\gamma_R}}{2\pi I_0(k_T)} \\ &\times \int_{-\pi}^{\pi} e^{x_{SBT}\cos\alpha_T + y_{SBT}\sin\alpha_T} d\alpha_T, \end{aligned} \tag{100}$$

$$\begin{aligned} R^{SBR}_{pq,\tilde{p}\tilde{q}}(\delta_T, \delta_R, \tau) &= \frac{\eta_R e^{j\frac{2\pi}{\lambda}(\tilde{p}-p)\delta_T \cos\theta_T - j2\pi\tau f_{T\max}\cos\gamma_T}}{2\pi I_0(k_R)} \\ &\times \int_{-\pi}^{\pi} e^{x_{SBR}\cos\alpha_R + y_{SBR}\sin\alpha_R} d\alpha_R, \end{aligned} \tag{101}$$

where parameters x_{SBT}, y_{SBT}, x_{SBR}, and y_{SBR} are $x_{SBT} = j(2\pi/\lambda)(\tilde{p}-p)\delta_T \cos\theta_T - j2\pi\tau f_{T\max}\cos\gamma_T + k_T\cos\mu_T$, $y_{SBT} = j(2\pi/\lambda)((\tilde{p}-p)\delta_T\sin\theta_T + (\tilde{q}-q)\delta_R\Delta_T\sin\theta_R) - j2\pi\tau(f_{T\max}\sin\gamma_T + f_{R\max}\Delta_T\sin\gamma_R) + k_T\sin\mu_T$, $x_{SBR} = j(2\pi/\lambda)(\tilde{q}-q)\delta_R\cos\theta_R - j2\pi\tau f_{R\max}\cos\gamma_R + k_R\cos\mu_R$, and $y_{SBR} = j(2\pi/\lambda)((\tilde{p}-p)\delta_T\Delta_R\sin\theta_T + (\tilde{q}-q)\delta_R\sin\theta_R) - j2\pi\tau(f_{T\max}\Delta_R\sin\gamma_T + f_{R\max}\sin\gamma_R) + k_R\sin\mu_R$. Finally, using the equality $\int_{-\pi}^{\pi} e^{a\sin(c)+b\cos(c)}dc = 2\pi I_0\left(\sqrt{a^2+b^2}\right)$ [63, eq. 3.338-4], the space-time correlation functions of the single-bounced components become

$$R_{pq,\tilde{p}\tilde{q}}^{SBT}(\delta_T,\delta_R,\tau) = \eta_T e^{-j\frac{2\pi}{\lambda}(\tilde{q}-q)\delta_R\cos\theta_R + j2\pi\tau f_{R\max}\cos\gamma_R}\frac{I_0\left(\sqrt{x_{SBT}^2+y_{SBT}^2}\right)}{I_0(k_T)}, \quad (102)$$

$$R_{pq,\tilde{p}\tilde{q}}^{SBR}(\delta_T,\delta_R,\tau) = \eta_R e^{j\frac{2\pi}{\lambda}(\tilde{p}-p)\delta_T\cos\theta_T - j2\pi\tau f_{T\max}\cos\gamma_T}\frac{I_0\left(\sqrt{x_{SBR}^2+y_{SBR}^2}\right)}{I_0(k_R)}. \quad (103)$$

Since α_T and α_R are independent random variables, the double integral in (99) reduces to the product of two single integrals. By grouping the terms in (99) into those containing α_T and those containing α_R, and by using trigonometric transformations and the equality [63, eq. 3.338-4], the space-time correlation function of the double-bounced component becomes

$$R_{pq,\tilde{p}\tilde{q}}^{DB}(\delta_T,\delta_R,\tau) = \eta_{TR}\frac{I_0\left(\sqrt{x_{DB}^2+y_{DB}^2}\right)I_0\left(\sqrt{z_{DB}^2+w_{DB}^2}\right)}{I_0(k_T)I_0(k_R)}, \quad (104)$$

where parameters x_{DB}, y_{DB}, z_{DB}, and w_{DB} are $x_{DB} = j2\pi(\tilde{p}-p)\delta_T\cos\theta_T/\lambda - j2\pi\tau f_{T\max}\cos\gamma_T + k_T\cos\mu_T$, $y_{DB} = j2\pi(\tilde{p}-p)\delta_T\sin\theta_T/\lambda - j2\pi\tau f_{T\max}\sin\gamma_T + k_T\sin\mu_T$, $z_{DB} = j2\pi(\tilde{q}-q)\delta_R\cos\theta_R/\lambda - j2\pi\tau f_{R\max}\cos\gamma_R + k_R\cos\mu_R$, and $w_{DB} = j2\pi(\tilde{q}-q)\delta_R\sin\theta_R/\lambda - j2\pi\tau f_{R\max}\sin\gamma_R + k_R\sin\mu_R$, respectively.

Using (77) and (89), the space-time correlation function of the LoS component can be written as

$$R_{pq,\tilde{p}\tilde{q}}^{LoS}(\delta_T,\delta_R,\tau,t) = \sqrt{K_{pq}K_{\tilde{p}\tilde{q}}}e^{-j2\pi(\epsilon_{pq}-\epsilon_{\tilde{p}\tilde{q}})/\lambda}e^{-j2\pi\tau[f_{T\max}\cos(\pi-\alpha_{R\tilde{q}}^{LoS}-\gamma_T)+f_{R\max}\cos(\alpha_{R\tilde{q}}^{LoS}-\gamma_R)]}$$
$$\times e^{j2\pi t f_{T\max}[\cos(\pi-\alpha_{Rq}^{LoS}-\gamma_T)-\cos(\pi-\alpha_{R\tilde{q}}^{LoS}-\gamma_T)]}e^{j2\pi t f_{R\max}[\cos(\alpha_{Rq}^{LoS}-\gamma_R)-\cos(\alpha_{R\tilde{q}}^{LoS}-\gamma_R)]}. \quad (105)$$

Based on the assumption $\max\{R_t, R_r\} \ll D$, from Fig. 19 we obtain $\alpha_{Rq}^{LoS} = \alpha_{R\tilde{q}}^{LoS} \approx \pi$ which in turn simplifies (105) to

$$R_{pq,\tilde{p}\tilde{q}}^{LoS}(\delta_T, \delta_R, \tau) \approx \sqrt{K_{pq}K_{\tilde{p}\tilde{q}}} e^{j\frac{2\pi}{\lambda}\delta_T \cos\theta_T - j\frac{2\pi}{\lambda}\delta_R \cos\theta_R} e^{j2\pi\tau f_{T\max}\cos\gamma_T - j2\pi\tau f_{R\max}\cos\gamma_R}. \tag{106}$$

Finally, the normalized space-time correlation function $R_{pq,\tilde{p}\tilde{q}}(\delta_T, \delta_R, \tau)$ between two complex faded envelopes $h_{pq}(t)$ and $h_{\tilde{p}\tilde{q}}(t)$ becomes a summation of the normalized space-time correlation functions $R_{pq,\tilde{p}\tilde{q}}^{SBT}(\delta_T, \delta_R, \tau)$, $R_{pq,\tilde{p}\tilde{q}}^{SBR}(\delta_T, \delta_R, \tau)$, $R_{pq,\tilde{p}\tilde{q}}^{DB}(\delta_T, \delta_R, \tau)$, and $R_{pq,\tilde{p}\tilde{q}}^{LoS}(\delta_T, \delta_R, \tau)$, defined in (102) - (104) and (106), respectively.

Many existing correlation functions are special cases of the MIMO M-to-M space-time correlation function in (89). The simplest special case of (89) is Clarke's temporal correlation function $J_0(2\pi f_{R\max}\tau)$ [20], obtained for $K = 0$ (NLoS condition), $k_R = 0$ (2-D isotropic scattering around $\mathrm{R_x}$), $f_{T\max} = \delta_T = \delta_R = 0$ (stationary $\mathrm{T_x}$, single-antenna $\mathrm{T_x}$ and $\mathrm{R_x}$), and no scattering around $\mathrm{T_x}$ (set $\eta_T = \eta_{TR} = 0$ to cancel one of the Bessel functions), where $J_0(\;\cdot\;)$ is the first kind zeroth-order Bessel function. Expressions for other space-time correlation functions based on the "one-ring" model [64], [65] can be similarly obtained. The temporal correlation function for M-to-M channels, assuming 2-D isotropic scattering, $J_0(2\pi f_{T\max}\tau)J_0(2\pi f_{R\max}\tau)$ [31] is obtained for $K = 0$, $\eta_T = \eta_R = 0$, $k_T = k_R = 0$, and $\delta_T = \delta_R = 0$. Similarly, the spatial correlation function for M-to-M channel $J_0(2\pi(\tilde{p} - p)\delta_T/\lambda)J_0(2\pi(\tilde{q} - q)\delta_R/\lambda)$ [66] is obtained for $K = 0$, $\eta_T = \eta_R = 0$, $k_T = k_R = 0$, and $\tau = 0$. Finally, the space-time correlation function for M-to-M channels, assuming 2-D isotropic scattering, $J_0\left(\sqrt{x_{DB}^2 + y_{DB}^2}\right) J_0\left(\sqrt{z_{DB}^2 + w_{DB}^2}\right)$ [37] is obtained for $K = 0$, $\eta_T = \eta_R = 0$, and $k_T = k_R = 0$.

The space-time correlation functions of the I and Q components of the complex faded envelope can be obtained by substituting (87) and (88) into (89). For a large number of scatterers ($M, N \to \infty$) and 2-D isotropic scattering the space-time correlation functions of the I and Q components of the complex faded envelope are

$$
\begin{aligned}
& R^{(I/Q,I/Q)}_{pq,\tilde{p}\tilde{q}}(\delta_T,\delta_R,\tau) = \Re\left\{R_{pq,\tilde{p}\tilde{q}}(\delta_T,\delta_R,\tau)\right\} \\
= \;& \eta_T \cos\left(2\pi\tau f_{R\max}\cos\gamma_R - 2\pi(\tilde{q}-q)(\delta_R/\lambda)\cos\theta_R\right) J_0\left(\sqrt{x^2_{iSBT}+y^2_{iSBT}}\right) \\
+ \;& \eta_R \cos\left(2\pi(\tilde{p}-p)(\delta_T/\lambda)\cos\theta_T - 2\pi\tau f_{T\max}\cos\gamma_T\right) J_0\left(\sqrt{x^2_{iSBR}+y^2_{iSBR}}\right) \\
+ \;& \eta_{TR} J_0\left(\sqrt{x^2_{iDB}+y^2_{iDB}}\right) J_0\left(\sqrt{z^2_{iDB}+w^2_{iDB}}\right) \\
+ \;& \sqrt{K_{pq}K_{\tilde{p}\tilde{q}}}\cos\Big[2\pi(\delta_T/\lambda)\cos\theta_T - 2\pi(\delta_R/\lambda)\cos\theta_R + 2\pi\tau f_{T\max}\cos\gamma_T \\
- \;& 2\pi\tau f_{R\max}\cos\gamma_R\Big],
\end{aligned}
\tag{107}
$$

$$
\begin{aligned}
& R^{(I,Q)}_{pq,\tilde{p}\tilde{q}}(\delta_T,\delta_R,\tau) = \Im\left\{R_{pq,\tilde{p}\tilde{q}}(\delta_T,\delta_R,\tau)\right\} \\
= \;& \eta_T \sin\left(2\pi\tau f_{R\max}\cos\gamma_R - 2\pi(\tilde{q}-q)(\delta_R/\lambda)\cos\theta_R\right) J_0\left(\sqrt{x^2_{iSBT}+y^2_{iSBT}}\right) \\
+ \;& \eta_R \sin\left(2\pi(\tilde{p}-p)(\delta_T/\lambda)\cos\theta_T - 2\pi\tau f_{T\max}\cos\gamma_T\right) J_0\left(\sqrt{x^2_{iSBR}+y^2_{iSBR}}\right) \\
+ \;& \sqrt{K_{pq}K_{\tilde{p}\tilde{q}}}\sin\Big[2\pi(\delta_T/\lambda)\cos\theta_T - 2\pi(\delta_R/\lambda)\cos\theta_R 2\pi\tau f_{T\max}\cos\gamma_T \\
- \;& 2\pi\tau f_{R\max}\cos\gamma_R\Big],
\end{aligned}
\tag{108}
$$

where parameters y_{iSBT}, y_{iSBR}, x_{iSBT}, x_{iSBR}, x_{iDB}, y_{iDB}, z_{iDB}, and w_{iDB} are equal to $y_{iSBT} = 2\pi[(\tilde{p}-p)(\delta_T/\lambda)\sin\theta_T + (\tilde{q}-q)(\delta_R/\lambda)\Delta_T\sin\theta_R - \tau(f_{T\max}\sin\gamma_T + f_{R\max}\Delta_T \sin\gamma_R)]$, $y_{iSBR} = 2\pi[((\tilde{q}-q)(\delta_R/\lambda)\sin\theta_R + (\tilde{p}-p)(\delta_T/\lambda)\Delta_R\sin\theta_T) - \tau(f_{T\max}\Delta_R\sin\gamma_T + f_{R\max}\sin\gamma_R)]$, $x_{iSBT} = 2\pi[(\tilde{p}-p)(\delta_T/\lambda)\cos\theta_T - \tau f_{T\max}\cos\gamma_T]$, $x_{iSBR} = 2\pi[(\tilde{q}-q)(\delta_R/\lambda)\cos\theta_R - \tau f_{R\max}\cos\gamma_R]$, $x_{iDB} = 2\pi[(\tilde{p}-p)(\delta_T/\lambda)\cos\theta_T - \tau f_{T\max}\cos\gamma_T]$, $y_{iDB} = 2\pi[(\tilde{p}-p)(\delta_T/\lambda)\sin\theta_T - \tau f_{T\max}\sin\gamma_T]$, $z_{iDB} = 2\pi[(\tilde{q}-q)(\delta_R/\lambda)\cos\theta_R - \tau f_{R\max}\cos\gamma_R]$, $w_{iDB} = 2\pi[(\tilde{q}-q)(\delta_R/\lambda)\sin\theta_R - \tau f_{R\max}\sin\gamma_R]$. The derivations of these expressions are presented in Appendix E.

The space-Doppler power spectral density (sD-psd) of the complex faded envelope is the Fourier transformation of the space-time correlation function. We start the derivation for the sD-psds of the single-bounced components by noting that the functions $I_0\left(\sqrt{x_{SBT}^2+y_{SBT}^2}\right)$ and $I_0\left(\sqrt{x_{SBR}^2+y_{SBR}^2}\right)$ can be written as

$$I_0\left[j2\pi f_{T\max}\sqrt{(\tau-A_{SBT})^2+\left(\frac{p_{x_{SBT}}q_{y_{SBT}}}{f_{T\max}}-\frac{p_{y_{SBT}}q_{x_{SBT}}}{f_{T\max}}+\frac{w_{y_{SBT}}}{2\pi f_{T\max}}\right)^2}\right], \tag{109}$$

$$I_0\left[j2\pi f_{R\max}\sqrt{(\tau-A_{SBR})^2+\left(\frac{p_{x_{SBR}}q_{y_{SBR}}}{f_{R\max}}-\frac{p_{y_{SBR}}q_{x_{SBR}}}{f_{R\max}}+\frac{w_{y_{SBR}}}{2\pi f_{R\max}}\right)^2}\right], \tag{110}$$

where $p_{x_{SBT}}=(\tilde{p}-p)(\delta_T/\lambda)\cos\theta_T$, $q_{x_{SBT}}=\cos\gamma_T$, $A_{SBT}=(2\pi p_{x_{SBT}}q_{x_{SBT}}+2\pi p_{y_{SBT}} q_{y_{SBT}}+w_{x_{SBT}})/2\pi f_{T\max}$, $p_{y_{SBT}}=[(\tilde{p}-p)\delta_T\sin\theta_T+(\tilde{q}-q)\delta_R\Delta_T\sin\theta_R]/\lambda$, $q_{y_{SBT}}\approx\sin\gamma_T$, $A_{SBR}=(2\pi p_{x_{SBR}}q_{x_{SBR}}+2\pi p_{y_{SBR}}q_{y_{SBR}}+w_{x_{SBR}})/2\pi f_{R\max}$, $w_{x_{SBT}}=-jk_T\cos(\gamma_T-\mu_T)$, $w_{y_{SBT}}=-jk_T\sin(\gamma_T-\mu_T)$, $p_{x_{SBR}}=(\tilde{q}-q)(\delta_R/\lambda)\cos\theta_R$, $q_{x_{SBR}}=\cos\gamma_R$, $w_{x_{SBR}}=-jk_R\cos(\gamma_R-\mu_R)$, $p_{y_{SBR}}=[(\tilde{p}-p)\delta_T\Delta_R\sin\theta_T+(\tilde{q}-q)\delta_R\sin\theta_R]/\lambda$, $q_{y_{SBR}}\approx\sin\gamma_R$, and $w_{y_{SBR}}=-jk_R\sin(\gamma_R-\mu_R)$. Using (109), (110), and equality $\int_0^\infty I_0(\alpha\sqrt{t^2+u^2})\cos(\beta t)dt=\cosh(u\sqrt{\alpha^2-\beta^2})/\sqrt{\alpha^2-\beta^2}$ [63, eq. 6.677-3], the sD-psds of the single-bounced components become

$$\begin{aligned}\mathcal{F}\{R_{pq,\tilde{p}\tilde{q}}^{SBT}(\delta_T,\delta_R,\tau)\} &= \frac{\eta_T}{I_0(k_T)}\frac{\exp\{-j2\pi p_{x_{SBR}}-j2\pi(f-f_{R\max}\cos\gamma_R)A_{SBT}\}}{\pi f_{T\max}\sqrt{1-[(f-f_{R\max}\cos\gamma_R)/f_{T\max}]^2}}\\ &\times \cosh\Big[(k_T\sin(\mu_T-\gamma_T)+j2\pi p_{x_{SBT}}q_{y_{SBT}}-j2\pi p_{y_{SBT}}q_{x_{SBT}})\\ &\times \sqrt{1-[(f-f_{R\max}\cos\gamma_R)/f_{T\max}]^2}\Big],\end{aligned} \tag{111}$$

$$\begin{aligned}\mathcal{F}\{R_{pq,\tilde{p}\tilde{q}}^{SBR}(\delta_T,\delta_R,\tau)\} &= \frac{\eta_R}{I_0(k_R)}\frac{\exp\{j2\pi p_{x_{SBT}}-j2\pi(f+f_{T\max}\cos\gamma_T)A_{SBR}\}}{\pi f_{R\max}\sqrt{1-[(f+f_{T\max}\cos\gamma_T)/f_{R\max}]^2}}\\ &\times \cosh\Big[(k_R\sin(\mu_R-\gamma_R)+j2\pi p_{x_{SBR}}q_{y_{SBR}}-j2\pi p_{y_{SBR}}q_{x_{SBR}})\\ &\times \sqrt{1-[(f+f_{T\max}\cos\gamma_T)/f_{R\max}]^2}\Big],\end{aligned} \tag{112}$$

where $\cosh(\;\cdot\;)$ is the hyperbolic cosine, $|f-f_{R\max}\cos\gamma_R|\leq f_{T\max}$ and $|f+f_{T\max}\cos\gamma_T|\leq f_{R\max}$.

Note that existing power spectral densities derived assuming "one-ring" model, are special cases of (112). The simplest special case of (112) is Clarke's power spectrum

$1/(\pi\sqrt{f_{R\max}^2 - f^2})$, $|f| \leq f_{R\max}$ [20], obtained for $k_R = 0$, $f_{T\max} = 0$, $k_T = 0$, and $\delta_T = \delta_R = 0$. Similarly, the 2-D non-isotropic power spectral density in (3) of [60] is obtained for $f_{T\max} = 0$ and $\delta_T = \delta_R = 0$.

We start the derivation for the sD-psd of the double-bounced component by noting that

$$\begin{aligned}&\mathcal{F}\left\{I_0\left(\sqrt{x_{DB}^2 + y_{DB}^2}\right) I_0\left(\sqrt{z_{DB}^2 + w_{DB}^2}\right)\right\} \\ &= \ \mathcal{F}\left\{I_0\left(\sqrt{x_{DB}^2 + y_{DB}^2}\right)\right\} \odot \mathcal{F}\left\{I_0\left(\sqrt{z_{DB}^2 + w_{DB}^2}\right)\right\}, \end{aligned} \tag{113}$$

where $\odot$ denotes convolution. Using (113) and similar reasoning as above, the space-Doppler power spectral density of the double-bounced component becomes

$$\begin{aligned}&\mathcal{F}\{R_{pq,\tilde{p}\tilde{q}}^{DB}(\delta_T, \delta_R, \tau)\} = \frac{\eta_{TR}}{I_0(k_T)\pi f_{T\max}\sqrt{1-(f/f_{T\max})^2}} \\ &\times\ e^{-j(2\pi p_{x_{DB}} q_{x_{DB}} + 2\pi p_{y_{DB}} q_{y_{DB}} + j k_T \cos(\gamma_T - \mu_T))f/f_{T\max}} \\ &\times\ \cosh\left[(k_T \sin(\mu_T - \gamma_T) + j2\pi p_{x_{DB}} q_{y_{DB}} - j2\pi p_{y_{DB}} q_{x_{DB}})\sqrt{1-(f/f_{T\max})^2}\right] \\ &\odot\ \frac{e^{-j(2\pi p_{z_{DB}} q_{z_{DB}} + 2\pi p_{w_{DB}} q_{w_{DB}} + j k_R \cos(\gamma_R - \mu_R))f/f_{R\max}}}{I_0(k_R)\pi f_{R\max}\sqrt{1-(f/f_{R\max})^2}} \\ &\times\ \cosh\left[(k_R \sin(\mu_R - \gamma_R) + j2\pi p_{z_{DB}} q_{w_{DB}} - j2\pi p_{w_{DB}} q_{z_{DB}})\sqrt{1-(f/f_{R\max})^2}\right], \end{aligned} \tag{114}$$

where $p_{x_{DB}} = (\tilde{p} - p)(\delta_T/\lambda)\cos\theta_T$, $q_{x_{SBT}} = \cos\gamma_T$, $p_{y_{DB}} = (\tilde{p} - p)(\delta_T/\lambda)\sin\theta_T$, $q_{y_{SBT}} = \sin\gamma_T$, $p_{z_{DB}} = (\tilde{q} - q)(\delta_R/\lambda)\cos\theta_R$, $q_{z_{DB}} = \cos\gamma_R$, $p_{w_{DB}} = (\tilde{q} - q)(\delta_R/\lambda)\sin\theta_R$, $q_{w_{DB}} = \sin\gamma_R$, and $|f| \leq f_{T\max} + f_{R\max}$.

For 2-D isotropic scattering and $\delta_T = \delta_R = 0$ (SISO system), the sD-psd of the double-bounced component has the closed-form expression [31]:

$$\mathcal{F}\{R_{pq,\tilde{p}\tilde{q}}^{DB}(0, 0, \tau)\} = \frac{1}{\pi^2\sqrt{s} f_{T\max}} K\left[\frac{1+s}{2\sqrt{s}}\sqrt{1-\left(\frac{f}{(1+s)f_{T\max}}\right)^2}\right], \tag{115}$$

where $K[\ \cdot\ ]$ is the complete elliptic integral of the first kind and s is the ratio of the maximum Doppler frequencies $f_{R\max}$ and $f_{T\max}$, i.e., $s = f_{R\max}/f_{T\max}$. To validate the derived sD-psd in (114), we compare this expression for 2-D isotropic scattering and $\delta_T = \delta_R = \gamma_T = \gamma_R = 0$ with the sD-psd in (115). For different ratios $s = f_{R\max}/f_{T\max}$, Fig. 20 shows good agreement between the sD-psds in (114) and (115).

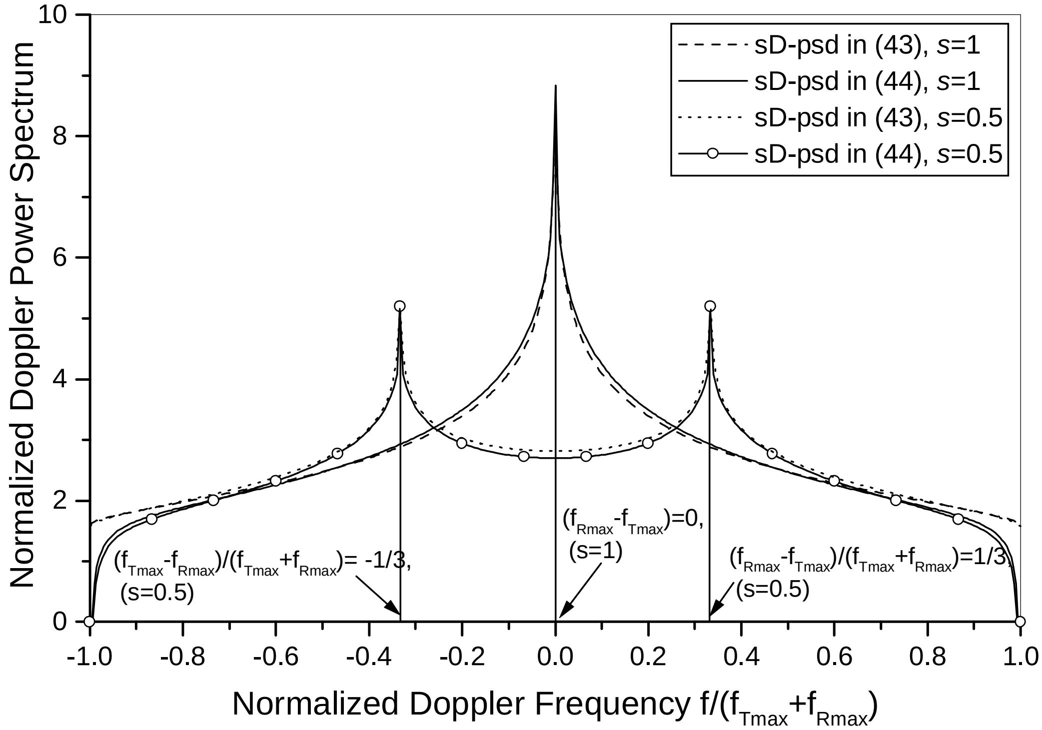

Figure 20: Comparison of the normalized Doppler power spectra in (114) and (115) for $\delta_T = \delta_R = 0$ and different rations $s = f_{R\max}/f_{T\max}$.

By calculating the Fourier transformation of the space-time correlation function in (106), we obtain the space-Doppler power spectral density of the LoS component:

$$\begin{aligned} \mathcal{F}\{R^{LoS}_{pq,\tilde{p}\tilde{q}}(\delta_T, \delta_R, \tau)\} &= \sqrt{K_{pq}K_{\tilde{p}\tilde{q}}} e^{j\frac{2\pi}{\lambda}[(\tilde{p}-p)\delta_T \cos\theta_T - (\tilde{q}-q)\delta_R \cos\theta_R]} \\ &\times \delta(f - f_{T\max}\cos\gamma_T + f_{R\max}\cos\gamma_R), \end{aligned} \tag{116}$$

where $\delta(\ \cdot\ )$ denotes the Dirac delta function.

Finally, the sD-psd $S_{pq,\tilde{p}\tilde{q}}(\delta_T, \delta_R, f)$ between two complex faded envelopes $h_{pq}(t)$ and $h_{\tilde{p}\tilde{q}}(t)$ becomes a summation of the sD-psds $S^{SBT}_{pq,\tilde{p}\tilde{q}}(\delta_T, \delta_R, f)$, $S^{SBR}_{pq,\tilde{p}\tilde{q}}(\delta_T, \delta_R, f)$, $S^{DB}_{pq,\tilde{p}\tilde{q}}(\delta_T, \delta_R, f)$, and $S^{LoS}_{pq,\tilde{p}\tilde{q}}(\delta_T, \delta_R, f)$, defined as in (111), (112), (114), and (116), respectively.

In Figs. 21 and 22, we plot the sD-psd, $S_{pq,\tilde{p}\tilde{q}}(\delta_T, \delta_R, f)$, for several MIMO systems with parameters $s = f_{R\max}/f_{T\max} = 1$, $\delta_T = \delta_R \in \{0.5\lambda,\ 1\lambda,\ 5\lambda,\ 10\lambda\}$, $\theta_T = \pi/3$, $\theta_R = \pi/4$, $\gamma_T = \gamma_R = \pi/2$, and $L_t = L_r = 2$. In these figures, we analyze the radio propagation in outdoor micro- and macro-cells, assuming 2-D isotropic scattering ($k_T = k_R = 0$) and line-of-sight ($K = 10$) conditions between the transmitter and receiver. In Fig. 21, we assume that the single-bounced rays bear more energy than the double-bounced rays, i.e., $\eta_T = \eta_R = 0.4$ and $\eta_{TR} = 0.2$, which is characteristic for the outdoor micro-cell propagation. We can observe that this spectrum is similar to the U-shaped spectrum of F-to-M cellular channels. In Fig. 22, we consider the macro-cell propagation, i.e. the double-bounced rays bear more energy than the single-bounced rays ($\eta_T = \eta_R = 0.1$ and $\eta_{TR} = 0.8$). In this case, the sD-psd differs from the U-shaped spectrum of cellular channels. Finally, compared to measured Doppler spectra in [39], [40], our theoretical Doppler spectra closely match.

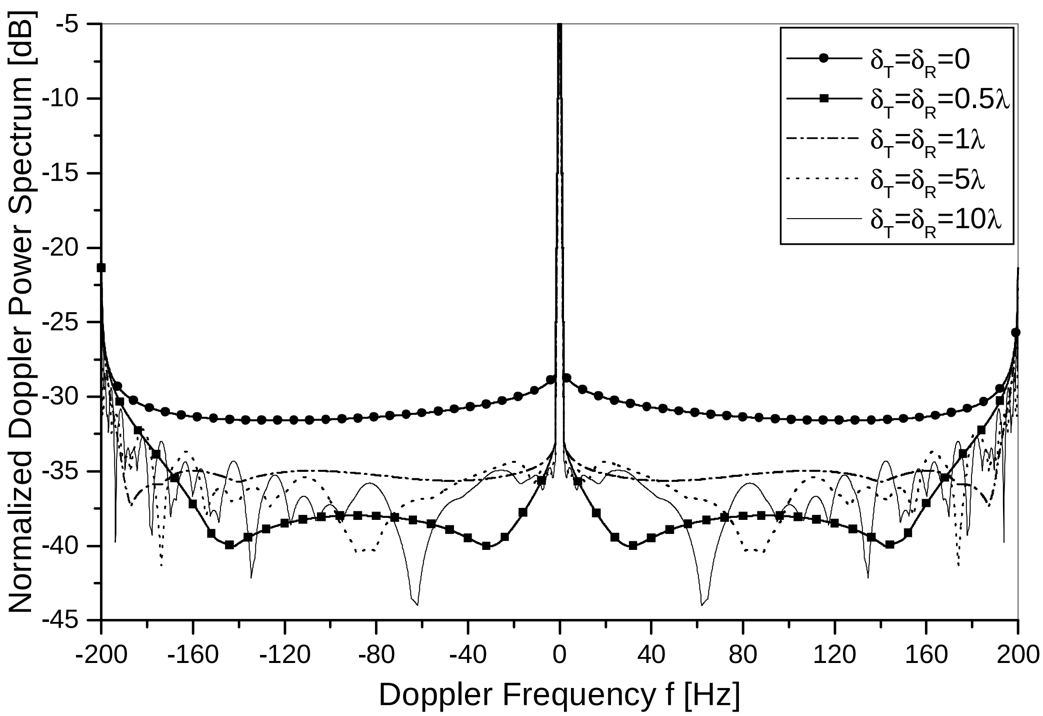

Figure 21: The normalized space-Doppler power spectra characteristic for the outdoor M-to-M micro-cells.

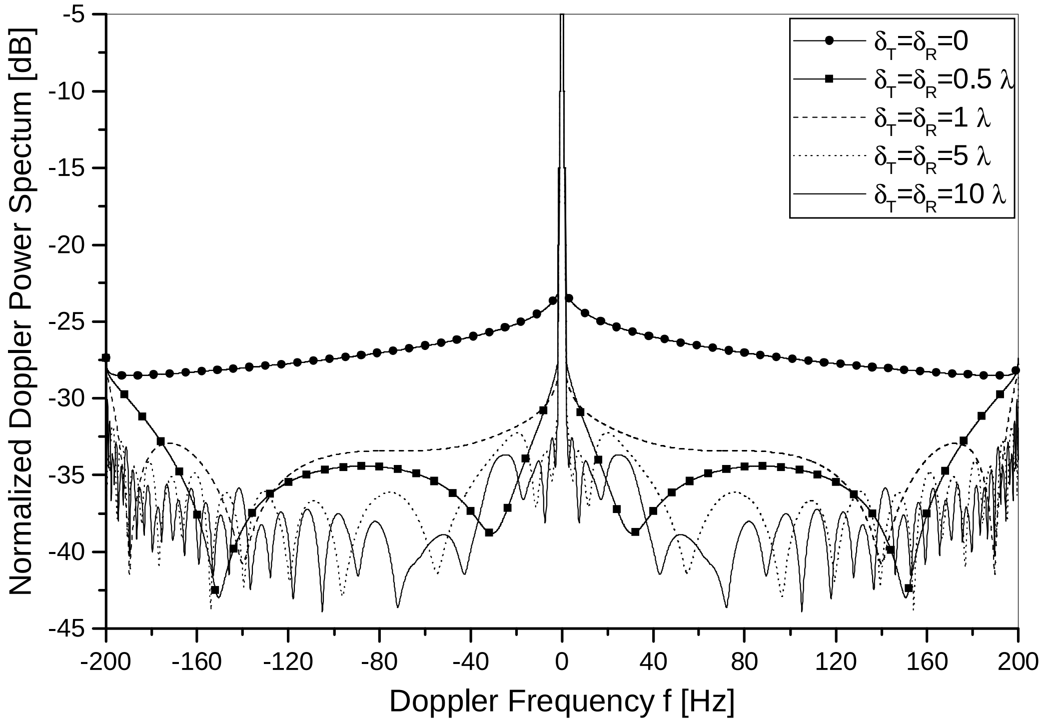

Figure 22: The normalized space-Doppler power spectra characteristic for the outdoor M-to-M macro-cells.

5.4 MIMO M-to-M Simulation Models

The reference model for MIMO M-to-M channels described in Section 5.2 assumes an infinite number of scatterers, which prevents practical implementation. It is desirable to design simulation models with a finite number of scatterers, while still matching the statistical properties of the reference model. Hence, we propose simulation models that describe propagation in outdoor micro- and macro-cells. In our models, the complex faded envelope is designed as a superposition of the LoS, the single-bounced, and the double-bounced rays. Assuming 2-D isotropic scattering and using the reference model described in Section 5.2, we propose the following function as a received complex faded envelope: $h_{pq}(t) = h_{pq}^{(I)}(t) + jh_{pq}^{(Q)}(t)$ where

$$h_{pq}^{(I)}(t) = \sum_{m=1}^{M} \frac{2P_T}{\sqrt{M}} \cos\Big[\beta_m - K_q \cos\theta_R - 2\pi t f_{R\max} \cos\gamma_R\Big] \cos\Big[K_p \cos\left(\theta_T - \alpha_T^{(m)}\right)$$
$$+ 2\pi t f_{T\max} \cos\left(\alpha_T^{(m)} - \gamma_T\right) + K_q \Delta_T \sin\theta_R \sin\alpha_T^{(m)} + 2\pi t f_{R\max} \Delta_T \sin\gamma_R \sin\alpha_T^{(m)} + \phi_m\Big]$$
$$+ \sum_{n=1}^{N} \frac{2P_R}{\sqrt{N}} \cos\left[\beta_n + K_p \cos\theta_T + 2\pi t f_{T\max} \cos\gamma_T\right] \cos\Big[K_q \cos\left(\alpha_R^{(n)} - \theta_R\right)$$
$$+ 2\pi t f_{R\max} \cos\left(\alpha_R^{(n)} - \gamma_R\right) + K_p \Delta_R \sin\theta_T \sin\alpha_R^{(n)} + 2\pi t f_{T\max} \Delta_R \sin\gamma_T \sin\alpha_R^{(n)} + \phi_n\Big]$$
$$+ \sum_{m,n=1}^{M,N} \frac{2P_{TR}}{\sqrt{MN}} \cos\Big[K_p \cos\left(\theta_T - \alpha_T^{(m)}\right) + 2\pi t f_{T\max} \cos\left(\alpha_T^{(m)} - \gamma_T\right)\Big] \cos\Big[K_q \cos\left(\alpha_R^{(n)} - \theta_R\right)$$
$$+ 2\pi t f_{R\max} \cos\left(\alpha_R^{(n)} - \gamma_R\right) + \phi_{mn}\Big] + P_{LoS} \cos\Big[K_p \cos\theta_T + K_q \cos(\alpha_{Rq}^{LoS} - \theta_R)$$
$$+ 2\pi t (f_T^{LoS} + f_R^{LoS})\Big], \tag{117}$$

$$h_{pq}^{(Q)}(t) = \sum_{m=1}^{M} \frac{2P_T}{\sqrt{M}} \sin\Big[\beta_m - K_q \cos\theta_R - 2\pi t f_{R\max} \cos\gamma_R\Big] \cos\Big[K_p \sin\left(\theta_T - \alpha_T^{(m)}\right)$$
$$+ 2\pi t f_{T\max} \sin\left(\alpha_T^{(m)} - \gamma_T\right) + K_q \Delta_T \sin\theta_R \cos\alpha_T^{(m)} + 2\pi t f_{R\max} \Delta_T \sin\gamma_R \cos\alpha_T^{(m)} + \phi_m\Big]$$
$$+ \sum_{n=1}^{N} \frac{2P_R}{\sqrt{N}} \sin\Big[\beta_n + K_p \cos\theta_T + 2\pi t f_{T\max} \cos\gamma_T\Big] \cos\Big[K_q \sin\left(\alpha_R^{(n)} - \theta_R\right)$$
$$+ 2\pi t f_{R\max} \sin\left(\alpha_R^{(n)} - \gamma_R\right) + K_p \Delta_R \sin\theta_T \cos\alpha_R^{(n)} + 2\pi t f_{T\max} \Delta_R \sin\gamma_T \cos\alpha_R^{(n)} + \phi_n\Big]$$
$$+ \sum_{m,n=1}^{M,N} \frac{2P_{TR}}{\sqrt{MN}} \sin\Big[K_p \cos\left(\theta_T - \alpha_T^{(m)}\right) + 2\pi t f_{T\max} \cos\left(\alpha_T^{(m)} - \gamma_T\right)\Big] \sin\Big[K_q \sin\left(\alpha_R^{(n)} - \theta_R\right)$$
$$+ 2\pi t f_{R\max} \sin\left(\alpha_R^{(n)} - \gamma_R\right) + \phi_{mn}\Big] + P_{LoS} \sin\Big[K_p \cos\theta_T + K_q \cos(\alpha_{Rq}^{LoS} - \theta_R)$$
$$+ 2\pi t (f_T^{LoS} + f_R^{LoS})\Big], \tag{118}$$

are the I and Q components of the complex faded envelope, β_m and β_n are the random path gains, $P_T = \sqrt{\eta_T \Omega_{pq}/(K_{pq}+1)}$, $P_R = \sqrt{\eta_R \Omega_{pq}/(K_{pq}+1)}$, $P_{TR} = \sqrt{\eta_{TR} \Omega_{pq}/(K_{pq}+1)}$, $K_q = 2\pi(0.5L_r + 0.5 - q)\delta_R/\lambda$, $P_{LoS} = \sqrt{K_{pq}\Omega_{pq}/(1+K_{pq})}$, $K_p = 2\pi(0.5L_t + 0.5 - p)\delta_T/\lambda$, $f_T^{LoS} = f_{T\max} \cos(\pi - \alpha_{Rq}^{LoS} - \gamma_T)$ and $f_R^{LoS} = f_{R\max}$ $\cos(\alpha_{Rq}^{LoS} - \gamma_R)$.

The I and Q components in (117) and (118) are constructed as follows: the single-bounced components of the complex faded envelope are constructed using a similar method to one described in Section 3.2 for the SISO F-to-M model, whereas the double-bounced components of the complex faded envelope are constructed using a similar method to one described in Section 4.2 for the SISO M-to-M model.

We first propose an ergodic statistical (deterministic) model, which needs only one simulation trial to obtain the desired statistical properties. The complex faded envelope is $h_{pq}(t) = h_{pq}^{(I)}(t) + jh_{pq}^{(Q)}(t)$, where functions $h_{pq}^{(I)}(t)$ and $h_{pq}^{(Q)}(t)$ are defined in (117) and (118). For this model, the phases ϕ_{mn} are generated as independent random variables uniformly distributed on the interval $[-\pi, \pi)$. The AoDs, AoAs and random path gains are chosen as follows:

$$\begin{aligned}
\alpha_T^{(m)} &= \frac{\pi}{M}(m - 0.5) + \gamma_T && (119)\\
\alpha_R^{(n)} &= \frac{2\pi}{N}(n - 0.5) + \gamma_R, && (120)\\
\beta_m &= \frac{\pi(m - 0.5)}{M}, && (121)\\
\beta_n &= \frac{2\pi(n - 0.5)}{N}, && (122)
\end{aligned}$$

for $m = 1, \ldots, M$, $n = 1, \ldots, N$, respectively.

By allowing amplitudes, phases, and Doppler frequencies to be random variables, our deterministic model can be modified to match statistical properties of the reference model over a wider range of normalized time delays, while at the same time requiring a smaller number of scatterers around the $\mathrm{T_x}$ and $\mathrm{R_x}$. The statistical properties of this model vary for each simulation trial, but will converge to desired ensemble averaged properties when averaged over a sufficient number of simulation trials.

The complex faded envelope is $h_{pq}(t) = h_{pq}^{(I)}(t) + jh_{pq}^{(Q)}(t)$, where functions $h_{pq}^{(I)}(t)$ and $h_{pq}^{(Q)}(t)$ are defined as in (117) and (118), respectively. The angles of departures and the angles of arrivals are chosen as follows:

$$\alpha_T^{(m)} = 0.5\left(\frac{2\pi m}{M} + \frac{\psi - \pi}{M}\right), \quad (123)$$

$$\alpha_R^{(n)} = \frac{2\pi n}{N} + \frac{\theta - \pi}{N}, \quad (124)$$

for $m = 1, \ldots, M$, $n = 1, \ldots, N$, respectively. The parameters ϕ_{mn}, β_m, β_n, θ, and ψ are independent random variables uniformly distributed on the interval $[-\pi, \pi)$.

5.5 Simulation Results

This section presents simulation results of our new models. In all simulations, we use a normalized sampling period $f_{T\max}T_s = 0.01$ ($f_{T\max} = f_{R\max}$ are the maximum Doppler frequencies and T_s is the sampling period). The orientations of the $\mathrm{T_x}$ and $\mathrm{R_x}$ antenna arrays are chosen to be $\theta_T = \theta_R = \pi/2$. The angles of motion for the $\mathrm{T_x}$ and $\mathrm{R_x}$ are chosen to be $\gamma_T = \pi/4$ and $\gamma_R = 0$, respectively. The Rice factor is $K = 0.2$ and the AoA of the specular component is $\alpha_{Rq}^{LoS} = \pi$.

Figures 23 and 24 present the space-time correlation functions ($\delta_T = \delta_R = 0.5\lambda$) of the I and Q components of the complex faded envelope, respectively, for the system with $L_t = L_r = 4$ antennas, using $M = 22$ and $N = 40$ scatterers in the deterministic model. In Fig. 23, we assume that the single-bounced rays bear more energy than the double-bounced rays, i.e., $\eta_T = 0.7$, $\eta_R = 0.2$, and $\eta_{TR} = 0.1$. In Fig. 24, we assume that the double-bounced rays bear more energy than the single-bounced rays, i.e., $\eta_T = \eta_R = 0.2$ and $\eta_{TR} = 0.6$. Results show that the space-time correlation functions of the deterministic model approach the theoretical ones in the range of normalized time delays, $0 \leq f_{T\max}T_s \leq 6$.

Figures 25 and 26 present the space-time correlation functions ($\delta_T = \delta_R = 0.5\lambda$) of the I and Q components of the complex faded envelope, respectively, for a system with $L_t = L_r = 4$ antennas, using $N = M = 16$ scatterers and $N_{\text{stat}} = 50$ simulation trials in the statistical model. In Fig. 25, we assume that $\eta_T = 0.5$, $\eta_R = 0.4$, and

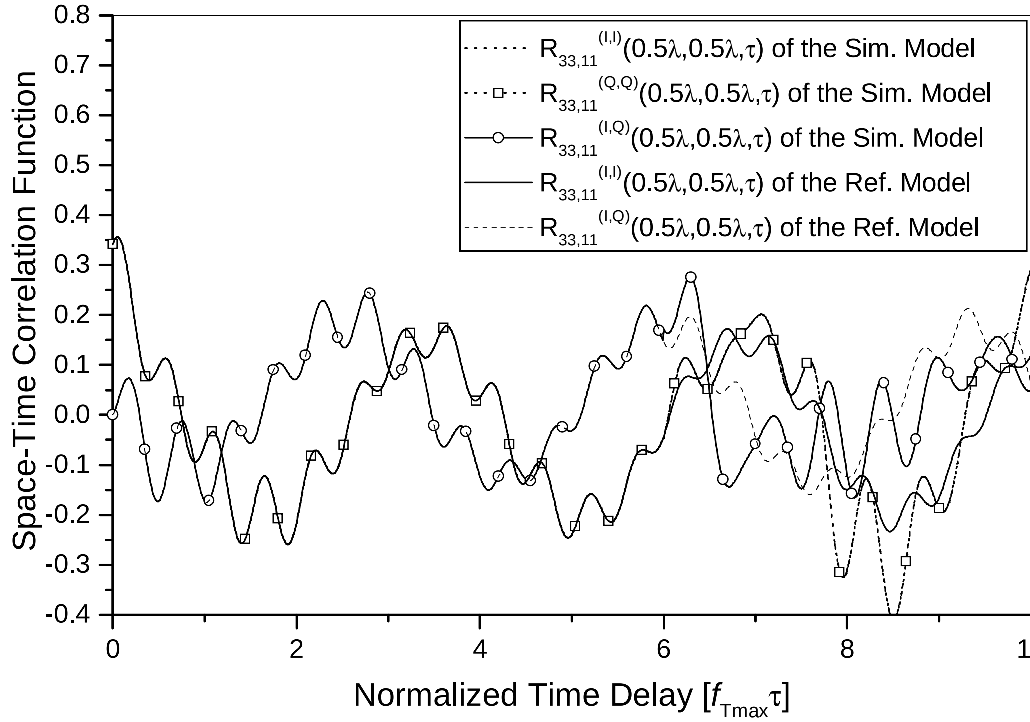

Figure 23: The theoretical and simulated normalized space-time correlation functions of the I and Q components of the 2-D MIMO M-to-M deterministic model for the radio propagation in outdoor micro-cells.

$\eta_{TR} = 0.1$, whereas in Fig. 26, we assume that $\eta_T = \eta_R = 0.05$ and $\eta_{TR} = 0.9$. Results show that the space-time correlation functions of the 2-D MIMO M-to-M statistical model approach the theoretical ones in the range of normalized time delays, i.e. $0 \leq f_{T\max}T_s \leq 10$.

Here we compare the performance and complexity of our new models with the MMEDS model described in Section 2.4.2.2. For fair comparison, we remove the LoS and single-bounced components of the complex faded envelope from our models. Figure 27 compares the temporal auto-correlation functions of the complex faded envelopes obtained by the deterministic, the statistical, and the MMEDS model. For the MMEDS model and the deterministic model, the temporal correlation functions are obtained using $M = 40$, $N = 38$ and $M = 22$, $N = 40$ scatterers, respectively. For the statistical model, the temporal correlation function is obtained using $N = M = 14$

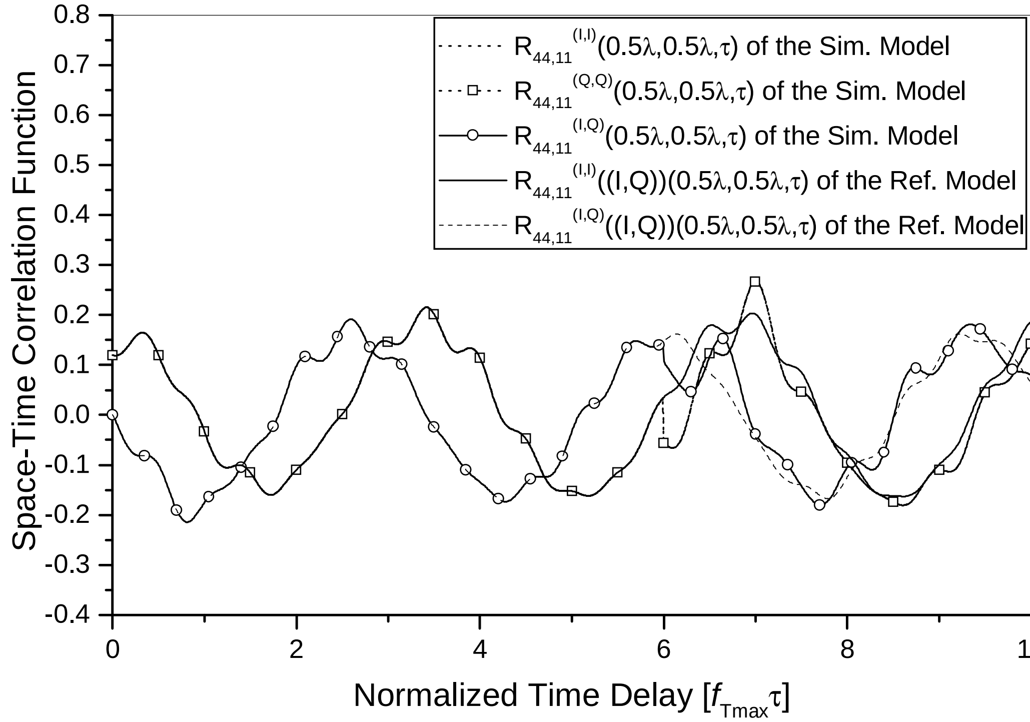

Figure 24: The theoretical and simulated normalized space-time correlation functions of the I and Q components of the 2-D MIMO M-to-M deterministic model for the radio propagation in outdoor macro-cells.

scatterers and $N_{\text{stat}} = 50$ trials. Figure 27 shows that the temporal correlation function of the MMEDS model approaches the theoretical one for normalized time delays in the range $0 \leq f_{T\max}T_s \leq 6$. The temporal correlation function of the deterministic model approaches the theoretical one in the same range of the normalized time delays as the MMEDS model, but requires a smaller number of scatterers. Finally, the temporal correlation function of the statistical model approaches the theoretical one in a wider range of normalized time delays (i.e., $0 \leq f_{T\max}T_s \leq 10$) than the deterministic and the MMEDS model.

Figure 28 compares the space-time correlation functions of the complex faded envelopes for system with $L_t = L_r = 2$ antennas, obtained by the deterministic, the statistical, and the MMEDS model. For the MMEDS model and the deterministic model, the space-time correlation functions are obtained using the same number of scatterers as in Fig. 27 and antenna distances $\delta_T = \delta_R = 1\ \lambda$. For the statistical

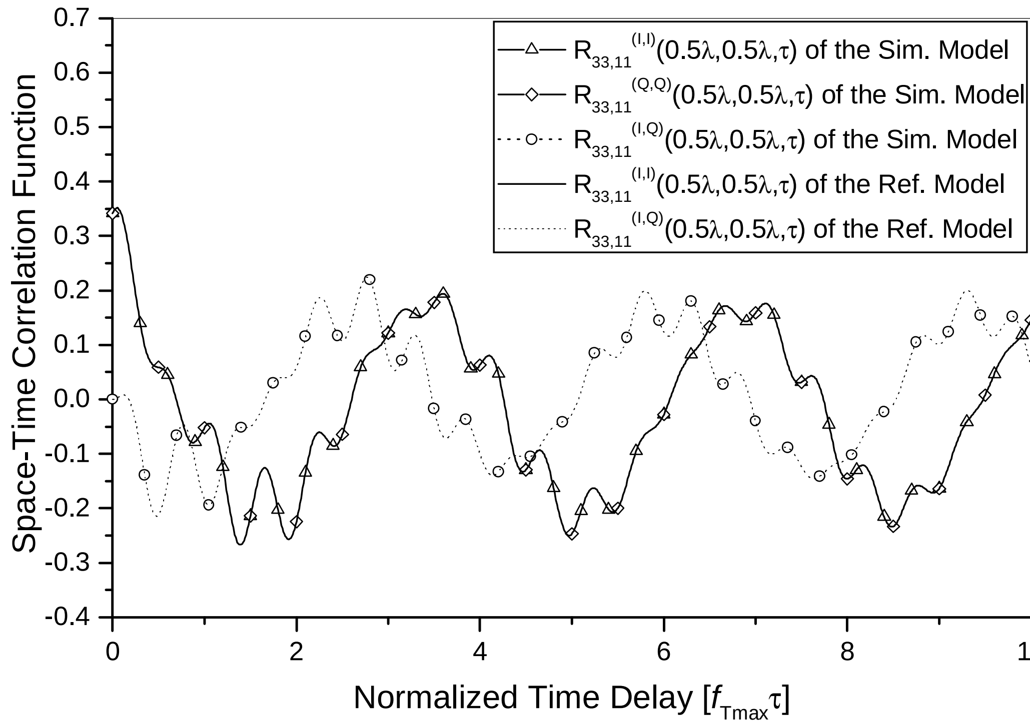

Figure 25: The theoretical and simulated normalized space-time correlation functions of the I and Q components of the 2-D MIMO M-to-M statistical model for the radio propagation in outdoor micro-cells.

model, the space-time correlation function is obtained using $N = M = 22$ scatterers, antenna distances $\delta_T = \delta_R = 1\ \lambda$, and $N_{\text{stat}} = 50$ trials. Figure 28 shows that the space-time correlation function of the MMEDS model approaches the theoretical one for normalized time delays in the range $0 \leq f_{T\max}T_s \leq 5$. The space-time correlation function of the deterministic model approaches the theoretical one in a somewhat wider range of normalized time delays (i.e., $0 \leq f_{T\max}T_s \leq 6$), while requiring a smaller number of scatterers than the MMEDS model. The space-time correlation function of the statistical model approaches the theoretical one in the widest range of normalized time delays (i.e., $0 \leq f_{T\max}T_s \leq 10$).

Simulation results presented in Fig. 28 indicate that larger distances between antenna elements require a larger number of scatterers to match theoretical statistics for the same normalized time delays as in Fig. 27. For the statistical model, instead of using many scatterers (e.g., 40) in all simulations, we propose to adaptively select

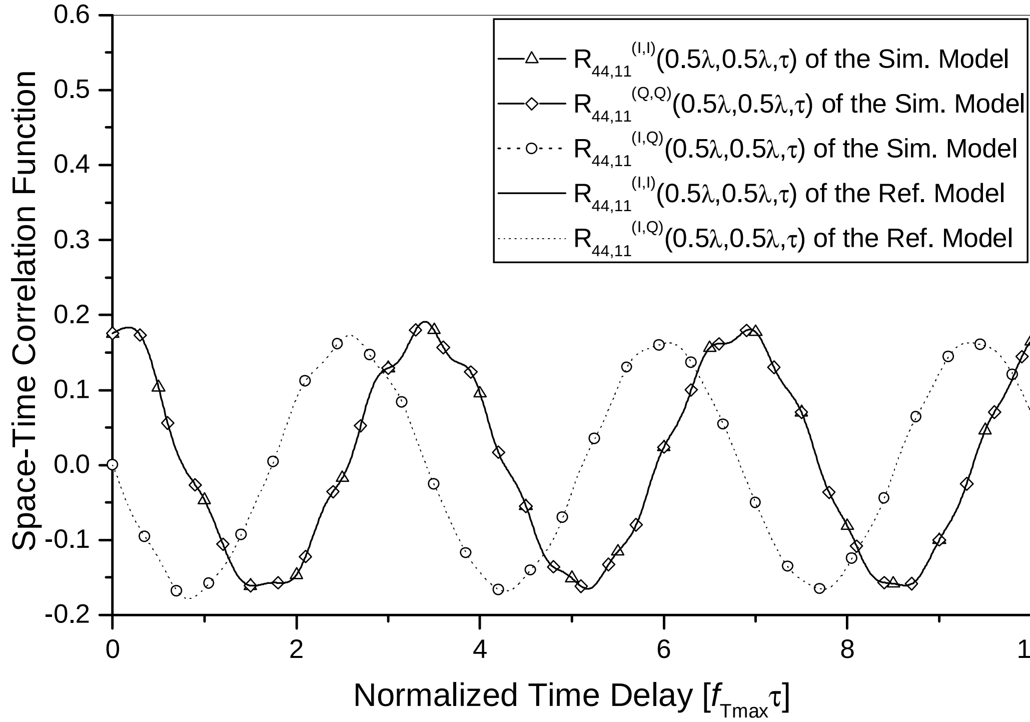

Figure 26: The theoretical and simulated normalized space-time correlation functions of the I and Q components of the 2-D MIMO M-to-M statistical model for the radio propagation in outdoor macro-cells.

the number of scatterers depending on the distances between antenna elements. If we assume that a mean square error (MSE) of $\leq 10^{-3}$ is required for the simulated space-time correlation function of the complex faded envelope (relative to the theoretical one), we need at least $M = 14+2\lceil\delta_T/0.3\lambda\rceil$ and $N = 14+2\lceil\delta_R/0.3\lambda\rceil$ scatterers[1]. This methodology can also be applied to the deterministic and MMEDS models. However, to obtain similar statistics as with the statistical model, the number of scatterers needs to be larger, i.e., $70 + 10\lceil\delta_{T/R}/0.3\lambda\rceil$.

To compare complexity of the various models, Table 6 summarizes the number of simulation trials and the number of scatterers required to obtain similar statistical properties, the number of operations in one simulation trial needed to generate the complex faded envelope and the relative simulation times (including averaging over

[1]Operation $\lceil\cdot\rceil$ denotes rounding up to the next integer.

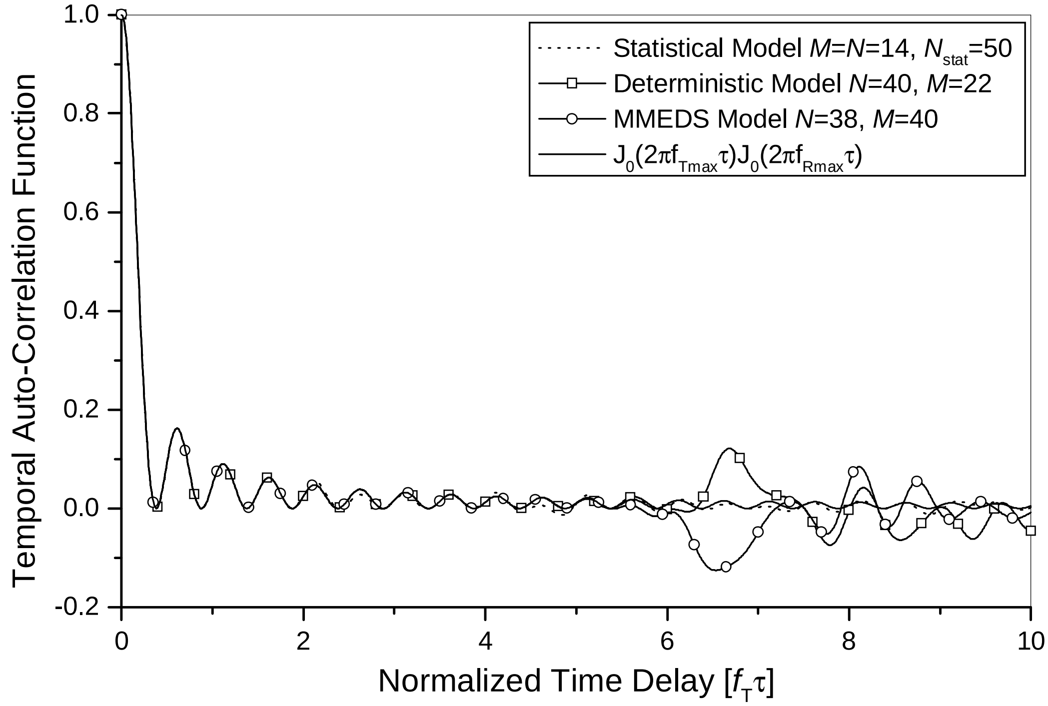

Figure 27: The normalized temporal auto-correlation function ($\delta_T = \delta_R = 0$) of the complex faded envelope of the 2-D MIMO M-to-M statistical, 2-D MIMO M-to-M deterministic, MMEDS, and 2-D MIMO M-to-M reference model.

N_{stat} simulation trials) needed to generate the complex faded envelopes, in Matlab on a Pentium III laptop. Here, we count only the frequently executed operations and the number of random variables. Table 6 shows that the deterministic model has a lower complexity then the MMEDS model, whereas the statistical model has the highest complexity. Both of our new models require a smaller number of scatterers than the MMEDS model, which leads to shorter simulation times.

From Table 6 and Figs. 26 - 28 we can conclude that, our deterministic model performs similar to the MMEDS model, but has lower complexity and shorter simulation time. On the other hand, our statistical model, with slight increase in complexity, outperforms the deterministic and the MMEDS models. Finally, our deterministic and statistical model are more general and can be used to model various outdoor micro- and macro-cell propagation environments.

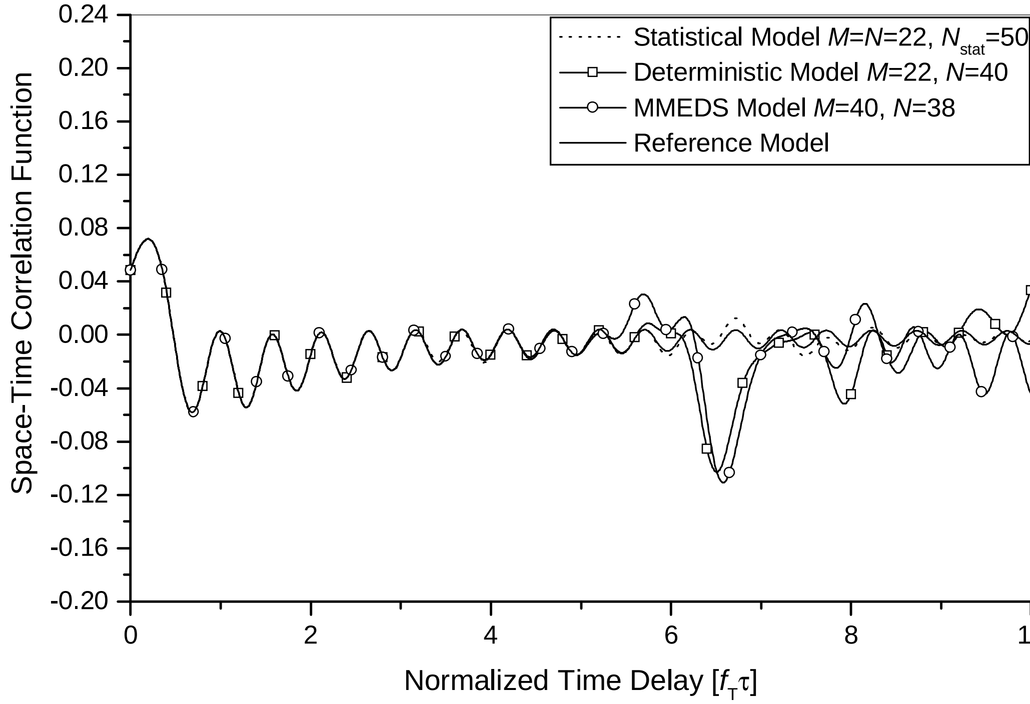

Figure 28: The normalized space-time correlation function ($\delta_T = \delta_R = 1\lambda$) of the complex faded envelope of the 2-D MIMO M-to-M statistical, 2-D MIMO M-to-M deterministic, MMEDS, and 2-D MIMO M-to-M reference model.

5.6 Summary

This chapter proposed the parametric reference model for MIMO M-to-M Ricean fading channels. From this model, the closed-form joint space-time correlation function and the space-Doppler power spectrum for 2-D non-isotropic scattering environment are derived. Furthermore, the space-time correlation functions of the in-phase and quadrature components of the complex faded envelope for 2-D isotropic scattering environment are derived. Finally, the deterministic and statistical SoS simulation models for MIMO M-to-M Ricean fading channels are proposed. The statistical properties of the simulation models are verified by simulations. The results show that the simulation models are a good approximation of the reference model and that they outperform existing simulation models.

Table 6: Complexity of different MIMO M-to-M models.

Simulation models	Number of simulation trials	Estimated number of computations needed to generate $h_{pq}(t)$ (one simulation trial)				Relative simulation time needed to generate $h_{pq}(t)$
		number of scatterers	cosine	addition	random variable	
MMEDS Model	1	MN	$7MN$	$10MN$	MN	T
New Deterministic Model	1	$M_d N_d = MN/2$	$12M_d N_d = 6MN$	$14M_d N_d = 7MN$	$M_d N_d = MN/2$	$0.24T$
New Statistical Model	50	$M_s N_s \approx MN/25$	$12M_s N_s = 0.48MN$	$14M_s N_s = 0.56MN$	$M_s N_s + 2 = MN/25+2$	$0.95T$ (including averaging over 50 trials)

CHAPTER VI

THREE-DIMENSIONAL MODELING, SIMULATION AND CAPACITY ANALYSIS OF SPACE-TIME CORRELATED M-TO-M CHANNELS

6.1 Overview

All previously reported models for SISO M-to-M channels [1], [31], [32], [34], [47] and MIMO M-to-M channels [37], [38], [48][1] assume that the fields incident on the $\mathrm{T_x}$ or $\mathrm{R_x}$ antennas are composed of a number of waves travelling only in the *horizontal* plane. This assumption is valid only for certain environments, e.g., rural areas. However, it seems inappropriate for urban environments where the $\mathrm{T_x}$ and $\mathrm{R_x}$ antenna arrays are often located in close proximity to and lower than the surrounding buildings. Scattered waves may propagate by diffraction from the edges of buildings down to the street and, thus, not necessarily travel horizontally.

In contrast, this chapter proposes a 3-D reference model for MIMO M-to-M multipath fading channels. First, we introduce a *"two-cylinder"* 3-D geometrical propagation model for MIMO M-to-M channels. This model can be considered as an extension of the "one-cylinder" model for F-to-M channels proposed in [67], [68]. By taking into account local scattering around both the $\mathrm{T_x}$ and $\mathrm{R_x}$, and by including mobility of both the $\mathrm{T_x}$ and $\mathrm{R_x}$, we obtain our "two-cylinder" model. Then, by using this model, we propose a new 3-D reference model. From the 3-D reference model, we derive a closed-form joint space-time correlation function for a 3-D non-isotropic scattering environment.

[1] These SISO and MIMO M-to-M models are detailed in Chapters 2, 4, and 5.

The reference model assumes an infinite number of scatterers, which prevents practical implementation. Hence, we propose deterministic and statistical SoS based simulation models for a 3-D non-isotropic scattering environment. The statistical properties of our models are verified by simulations. We use our statistical simulation model to evaluate the effect of the space-time correlation on the outage capacity of uniform linear antenna arrays (ULAs) and to compare the capacities of linear, circular, and spherical antenna arrays. First, we study the effect of antenna spacing on the outage capacity. Our results show that increasing the distances between ULA elements beyond 2λ has a negligible effect on the outage capacity. These results differ from the results obtained for F-to-M channels (with fixed, elevated base station antennas), where increasing $\mathrm{R_x}$ antenna element spacing beyond 5λ and $\mathrm{T_x}$ antenna element spacing beyond 2λ has a negligible effect on the capacity [55]. Second, we study the effect of antenna orientation angles on the outage capacity. When the radio propagation environment is characterized by 2-D *isotropic* scattering, the orientations of the $\mathrm{T_x}$ and $\mathrm{R_x}$ antenna arrays in the x - y plane are observed to have no influence on the capacity. This property of M-to-M channels is in contrast to F-to-M channels, where the $\mathrm{T_x}$ broadside antenna arrays (array elements placed on the y - axis) and $\mathrm{R_x}$ inline antenna arrays (array elements placed on the x - axis) provide higher capacity than the $\mathrm{T_x}$ and $\mathrm{R_x}$ broadside antenna arrays [64], [69]. When the radio propagation environment is characterized by 2-D *non-isotropic* scattering, the optimum capacity depends on the relative angle between the $\mathrm{T_x}$ ($\mathrm{R_x}$) antenna array and the orientation of local scatterers around the $\mathrm{T_x}$ ($\mathrm{R_x}$). Furthermore, our results show that if the available area in the x - y plane is insufficient for the antenna array realization, the antenna array can be vertically tilted without a significant capacity loss. The results also show that the 2-D models actually underestimate available capacity. Finally, we compare the capacities of linear, circular, and spherical antenna arrays. The results show that if volume available for antenna array realization is constrained, circular antenna arrays placed in the x - y plane will provide the highest capacity.

The remainder of this chapter is organized as follows. Section 6.2 describes the system geometry and presents the 3-D reference model for MIMO M-to-M channels. Section 6.3 presents the derivation of the closed-form joint space-time correlation function for 3-D non-isotropic scattering. Section 6.4 presents the 3-D SoS deterministic and statistical simulation models. Section 6.5 briefly reviews MIMO channel capacity, evaluates the effect of the space-time correlation on the outage capacity of ULAs, and compares the capacities of uniform linear, circular, and spherical antenna arrays. Finally, Section 6.6 provides some concluding remarks.

6.2 A 3-D Reference Model for MIMO M-to-M Channels

This chapter considers a narrowband MIMO communication system with L_T transmit and L_R receive omnidirectional antenna elements. Both the $\mathrm{T_x}$ and receiver $\mathrm{R_x}$ are in motion and are equipped with low elevation antennas. The radio propagation environment is characterized by 3-D scattering with NLoS propagation conditions between the $\mathrm{T_x}$ and $\mathrm{R_x}$. The MIMO channel is described by an $L_R \times L_T$ matrix $\mathbf{H}(t) = [h_{ij}(t)]_{L_R \times L_T}$ of complex low-pass faded envelopes.

Figure 29 shows our "two-cylinder" model for a MIMO M-to-M channel with $L_T = L_R = 2$ antenna elements. This elementary 2×2 antenna configuration will be used later to construct linear, circular, and spherical multielement antenna arrays. The "two-cylinder" model defines two cylinders, one around the $\mathrm{T_x}$ and another around the $\mathrm{R_x}$, as shown in Fig. 29. Around the transmitter, M fixed omnidirectional scatterers lie on the surface of a cylinder of radius R_t, and the m^{th} transmit scatterer is denoted by $S_T^{(m)}$. Similarly, around the receiver, N fixed omnidirectional scatterers lie on the surface of a cylinder with radius R_r, and the n^{th} receive scatterer is denoted by $S_R^{(n)}$. The parameters in Fig. 29 are defined in Table 7.

It is assumed that the radii R_t and R_r are much smaller than the distance D, i.e.,

$\max\{R_t, R_r\} \ll D$ (local scattering condition). Furthermore, it is assumed that the distance D is smaller than $4R_tR_rL_R/(\lambda(L_T-1)(L_R-1))$ (channel does not experience keyhole behavior [58]), where λ denotes the carrier wavelength. Finally, it is assumed that the spacing between two antenna elements at $\mathrm{T_x}$ and $\mathrm{R_x}$, $d_T(p,\tilde{p})$ and $d_R(q,\tilde{q})$, are much smaller than the radii R_t and R_r, i.e., $\max\{d_T(p,\tilde{p}), d_R(q,\tilde{q})\} \ll \min\{R_t, R_r\}$.

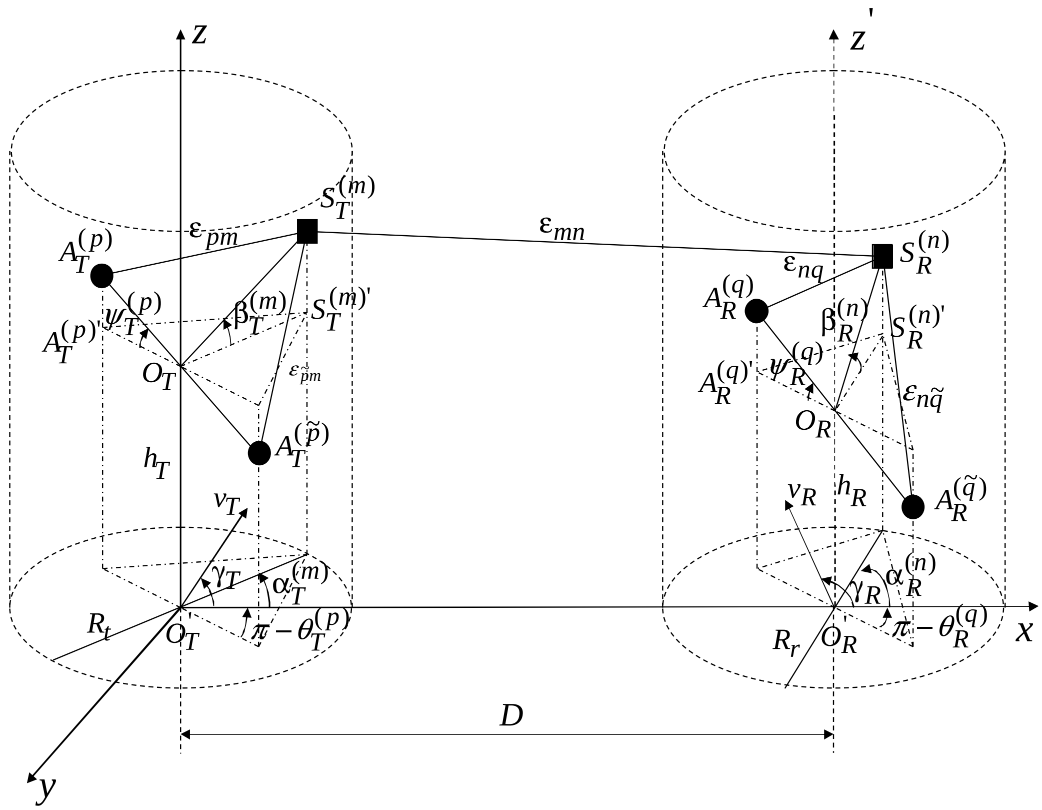

Figure 29: The 3-D geometrical model for MIMO M-to-M channels with $L_T = L_R = 2$ antenna elements.

As shown in Appendix F, the distances $\epsilon_{p,m}$, $\epsilon_{\tilde{p},m}$, $\epsilon_{n,q}$, $\epsilon_{n,\tilde{q}}$, and $\epsilon_{m,n}$ can be expressed as functions of the random angles $\alpha_T^{(m)}$, $\alpha_R^{(n)}$, $\beta_T^{(m)}$, and $\beta_R^{(n)}$ as follows:

$$\begin{aligned}\epsilon_{p,m} &\approx \frac{R_t}{\cos\beta_T^{(m)}} - d(A_T^{(p)}, O_T)\sin\psi_T^{(p)}\sin\beta_T^{(m)} - d(A_T^{(p)}, O_T)\cos\theta_T^{(p)}\cos\psi_T^{(p)} \\ &\times \cos\alpha_T^{(m)}\cos\beta_T^{(m)} - d(A_T^{(p)}, O_T)\sin\theta_T^{(p)}\cos\psi_T^{(p)}\sin\alpha_T^{(m)}\cos\beta_T^{(m)}, \end{aligned} \quad (125)$$

$$\begin{aligned}\epsilon_{\tilde{p},m} &\approx \frac{R_t}{\cos\beta_T^{(m)}} - d(A_T^{(\tilde{p})}, O_T)\sin\psi_T^{(\tilde{p})}\sin\beta_T^{(m)} - d(A_T^{(\tilde{p})}, O_T)\cos\theta_T^{(\tilde{p})}\cos\psi_T^{(\tilde{p})} \\ &\times \cos\alpha_T^{(m)}\cos\beta_T^{(m)} - d(A_T^{(\tilde{p})}, O_T)\sin\theta_T^{(\tilde{p})}\cos\psi_T^{(\tilde{p})}\sin\alpha_T^{(m)}\cos\beta_T^{(m)}, \end{aligned} \quad (126)$$

$$\epsilon_{n,q} \approx \frac{R_r}{\cos\beta_R^{(n)}} - d(A_R^{(q)}, O_R)\sin\psi_R^{(q)}\sin\beta_R^{(n)} - d(A_R^{(q)}, O_R)\cos\theta_R^{(q)}\cos\psi_R^{(q)} \times \cos\alpha_R^{(n)}\cos\beta_R^{(n)} - d(A_R^{(q)}, O_R)\sin\theta_R^{(q)}\cos\psi_R^{(q)}\sin\alpha_R^{(n)}\cos\beta_R^{(n)}, \tag{127}$$

$$\epsilon_{n,\tilde{q}} \approx \frac{R_r}{\cos\beta_R^{(n)}} - d(A_R^{(\tilde{q})}, O_R)\sin\psi_R^{(\tilde{q})}\sin\beta_R^{(n)} - d(A_R^{(\tilde{q})}, O_R)\cos\theta_R^{(\tilde{q})}\cos\psi_R^{(\tilde{q})} \times \cos\alpha_R^{(n)}\cos\beta_R^{(n)} - d(A_R^{(\tilde{q})}, O_R)\sin\theta_R^{(\tilde{q})}\cos\psi_R^{(\tilde{q})}\sin\alpha_R^{(n)}\cos\beta_R^{(n)}, \tag{128}$$

$$\epsilon_{m,n} \approx \sqrt{D^2 + (h_T - h_R)^2} \approx D, \tag{129}$$

where $p, \tilde{p} \in \{1, \ldots, L_T\}$, $q, \tilde{q} \in \{1, \ldots, L_R\}$, and parameters $d(A_T^{(p)}, O_T)$ and $d(A_R^{(q)}, O_R)$ denote distances (positive scalars) between the p^{th} transmit antenna element and the center of the T_x antenna array and the q^{th} receive antenna element and the center of the R_x antenna array, respectively.

Table 7: Definition of the parameters in Figure 29.

D	The distance between the centers of the Tx and Rx cylinders.
R_t, R_r	The radius of the Tx and Rx cylinder, respectively.
$d_T(p, \tilde{p})$	The spacing between p^{th} and $\tilde{p}^{th}$ antenna elements at the Tx.
$d_R(q, \tilde{q})$	The spacing between q^{th} and $\tilde{q}^{th}$ antenna elements at the Rx.
$\theta_T^{(p)}$, $\theta_R^{(q)}$	The azimuth angle of the p^{th} transmit and q^{th} receive antenna element (relative to the *x*-axis), respectively.
$\psi_T^{(p)}$, $\psi_R^{(q)}$	The elevation angle of the p^{th} transmit and q^{th} receive antenna element (relative to the *x*-*y* plane), respectively.
v_T, v_R	The velocities of the Tx and Rx, respectively.
γ_T, γ_R	The moving directions of the Tx and Rx, respectively.
$\alpha_T^{(m)}, \alpha_R^{(n)}$	The azimuth angles of departure (AAoD) and the azimuth angles of arrival (AAoA), respectively.
$\beta_T^{(m)}, \beta_R^{(n)}$	The elevation angles of departure (EAoD) and the elevation angles of arrival (EAoA), respectively.
ε_{pm}, $\varepsilon_{\tilde{p}m}$, ε_{mn}, ε_{nq}, and $\varepsilon_{n\tilde{q}}$	The distances $d\left(A_T^{(p)}, S_T^{(m)}\right)$, $d\left(A_T^{(\tilde{p})}, S_T^{(m)}\right)$, $d\left(S_T^{(m)}, S_R^{(n)}\right)$, $d\left(S_R^{(n)}, A_R^{(q)}\right)$, and $d\left(S_R^{(n)}, A_R^{(\tilde{q})}\right)$
h_T, h_R	The distances $d\left(O_T, O_T^{'}\right)$ and $d\left(O_R, O_R^{'}\right)$, respectively.

From the 3-D geometrical model, we observe that the waves from the T_x antenna elements impinge on the scatterers located on the T_x cylinder and scatter from the scatterers located on the $\mathrm{R_x}$ cylinder before they arrive at the $\mathrm{R_x}$ antenna elements. In contrast to NLoS F-to-M channels where single-bounced waves are prevalent, in NLoS urban M-to-M channels the double-bounced waves are dominant. In the 3-D reference model, the number of local scatterers around the $\mathrm{T_x}$ and $\mathrm{R_x}$ is infinite. Consequently, the received complex faded envelope of the link $A_T^{(p)}$ - $A_R^{(q)}$ is

$$\begin{aligned} h_{pq}(t) &= \lim_{M,N\to\infty} \sqrt{\frac{1}{MN}} \sum_{m=1}^{M}\sum_{n=1}^{N} G_p\left(\alpha_T^{(m)},\beta_T^{(m)}\right) G_q\left(\alpha_R^{(n)},\beta_R^{(n)}\right) e^{j\phi_{mn}} \\ &\times\ e^{-j\frac{2\pi}{\lambda}(\epsilon_{p,m}+\epsilon_{m,n}+\epsilon_{n,q})+j2\pi t[f_{T\max}\cos(\alpha_T^{(m)}-\gamma_T)\cos\beta_T^{(m)}+f_{R\max}\cos(\alpha_R^{(n)}-\gamma_R)\cos\beta_R^{(n)}]}, \end{aligned} \tag{130}$$

where $f_{T\max} = v_T/\lambda$ and $f_{R\max} = v_R/\lambda$ are the maximum Doppler frequencies associated with the $\mathrm{T_x}$ and $\mathrm{R_x}$, respectively, and $G_p(\alpha_T^{(m)},\beta_T^{(m)})$ and $G_q(\alpha_R^{(n)},\beta_R^{(n)})$ denote the antenna patterns of the p^{th} transmit and q^{th} receive antenna element, respectively. Since omnidirectional antenna elements are assumed (i.e., antenna patterns can be normalized to one), the antenna patterns are omitted in further analysis. It is assumed that the azimuth and elevation angles of departure (AAoDs and EAoDs) and the azimuth and elevation angles of arrival (AAoAs and EAoAs) are random variables. Since all rays are double-bounced, the angles of departure are independent from the angles of arrival [58]. Finally, it is assumed that the phases ϕ_{mn} are random variables uniformly distributed on the interval $[-\pi,\pi)$ and independent from the angles of departure and angles of arrival.

Using (125) - (129), the complex faded envelope in (130) can be rewritten as

$$\begin{aligned} h_{pq}(t) &= \lim_{M,N\to\infty} \frac{1}{\sqrt{MN}} \sum_{m=1}^{M}\sum_{n=1}^{N} a_{p,m}\ b_{n,q}\ e^{j\phi_{mn}} \\ &\times\ e^{j2\pi t[f_{T\max}\cos(\alpha_T^{(m)}-\gamma_T)\cos\beta_T^{(m)}+f_{R\max}\cos(\alpha_R^{(n)}-\gamma_R)\cos\beta_R^{(n)}]}, \end{aligned} \tag{131}$$

where

$$a_{p,m} = e^{-j\frac{\pi}{\lambda}D-j\frac{2\pi}{\lambda}\frac{R_t}{\cos\beta_T^{(m)}}+j\frac{2\pi}{\lambda}d_{T_x}^{(p)}\cos\alpha_T^{(m)}\cos\beta_T^{(m)}+j\frac{2\pi}{\lambda}d_{T_y}^{(p)}\sin\alpha_T^{(m)}\cos\beta_T^{(m)}+j\frac{2\pi}{\lambda}d_{T_z}^{(p)}\sin\beta_T^{(m)}}, \tag{132}$$

$$b_{n,q} = e^{-j\frac{\pi}{\lambda}D-j\frac{2\pi}{\lambda}\frac{R_r}{\cos\beta_R^{(n)}}+j\frac{2\pi}{\lambda}d_{R_x}^{(q)}\cos\alpha_R^{(n)}\cos\beta_R^{(q)}+j\frac{2\pi}{\lambda}d_{R_y}^{(q)}\sin\alpha_R^{(n)}\cos\beta_R^{(n)}+j\frac{2\pi}{\lambda}d_{R_z}^{(q)}\sin\beta_R^{(n)}}, \tag{133}$$

$$d_{T_x}^{(p)} = d(A_T^{(p)},O_T)\cos\theta_T^{(p)}\cos\psi_T^{(p)}, \tag{134}$$

$$d_{T_y}^{(p)} = d(A_T^{(p)}, O_T) \sin\theta_T^{(p)} \cos\psi_T^{(p)}, \quad (135)$$

$$d_{T_z}^{(p)} = d(A_T^{(p)}, O_T) \sin\psi_T^{(p)}, \quad (136)$$

$$d_{R_x}^{(q)} = d(A_R^{(q)}, O_R) \cos\theta_R^{(q)} \cos\psi_R^{(q)}, \quad (137)$$

$$d_{R_y}^{(q)} = d(A_R^{(q)}, O_R) \sin\theta_R^{(q)} \cos\psi_R^{(q)}, \quad (138)$$

$$d_{R_z}^{(q)} = d(A_R^{(q)}, O_R) \sin\psi_R^{(q)}. \quad (139)$$

Parameters $d_{T_x}^{(p)}$, $d_{T_y}^{(p)}$, and $d_{T_z}^{(p)}$ are coordinates of the p^{th} transmit antenna element relative to the center of $\mathrm{T_x}$ antenna array, whereas parameters $d_{R_x}^{(q)}$, $d_{R_y}^{(q)}$, and $d_{R_z}^{(q)}$ are coordinates of the q^{th} receive antenna element relative to the center of $\mathrm{R_x}$ antenna array. Note that these parameters depend on antenna array configuration and can be positive or negative numbers. In this chapter, we focus on the uniform linear antenna arrays(ULA), the uniform circular antenna arrays (UCA), and the spherical antenna arrays. For ULAs, the coordinates of antenna elements are defined as follows:

$$d_{T_x/R_x}^{(p/q)} = \frac{1}{2}(L_{T/R} + 1 - 2p(q)) d_{T/R} \cos\theta_{T/R} \cos\psi_{T/R}, \quad (140)$$

$$d_{T_y/R_y}^{(p/q)} = \frac{1}{2}(L_{T/R} + 1 - 2p(q)) d_{T/R} \sin\theta_{T/R} \cos\psi_{T/R}, \quad (141)$$

$$d_{T_z/R_z}^{(p/q)} = \frac{1}{2}(L_{T/R} + 1 - 2p(q)) d_{T/R} \sin\psi_{T/R}, \quad (142)$$

where $d_{T/R}$ denotes the spacing between two adjacent antenna elements at the transmitter/receiver, $\theta_{T/R}$ describes the orientation of all transmit/receive antenna elements in the x - y plane (relative to the x - axis), and $\psi_{T/R}$ describes the elevation angle of all transmit/receive antenna elements, relative to the x - y plane. For UCAs, the coordinates of antenna elements are defined as follows:

$$d_{T_x/R_x}^{(p/q)} = r_{T/R} \cos\left(\frac{2\pi p(q)}{L_{T/R}}\right) \cos\psi_{T/R}, \quad (143)$$

$$d_{T_y/R_y}^{(p/q)} = r_{T/R} \sin\left(\frac{2\pi p(q)}{L_{T/R}}\right) \cos\psi_{T/R}, \quad (144)$$

$$d_{T_z/R_z}^{(p/q)} = r_{T/R} \sin\psi_{T/R}, \quad (145)$$

where $r_{T/R}$ denotes the radius of the transmit/receive antenna array circle and $\psi_{T/R}$ describes the elevation angle of all transmit/receive antenna elements, relative to the

x - y plane. Finally, for spherical antenna arrays, the coordinates of antenna elements are defined as follows:

$$d_{T_x/R_x}^{(p/q)} = r_{T/R} \cos\theta_{T/R}^{(p/q)} \cos\psi_{T/R}^{(p/q)}, \tag{146}$$

$$d_{T_y/R_y}^{(p/q)} = r_{T/R} \sin\theta_{T/R}^{(p/q)} \cos\psi_{T/R}^{(p/q)}, \tag{147}$$

$$d_{T_z/R_z}^{(p/q)} = r_{T/R} \sin\psi_{T/R}^{(p/q)}, \tag{148}$$

where $r_{T/R}$ denotes the radius of the transmit/receive spherical antenna array, $\theta_{T/R}^{(p/q)}$ denotes the azimuth angle of the p^{th} transmit (q^{th} receive) antenna element relative to the x - axis, and $\psi_{T/R}^{(p/q)}$ denotes the elevation angle of the p^{th} transmit (q^{th} receive) antenna element relative to the x - y plane.

6.3 Space-time Correlation Function of the 3-D Reference Model

Assuming a 3-D non-isotropic scattering environment, we now derive the space-time correlation function of the complex faded envelope described in (131). The normalized space-time correlation function between two complex faded envelopes $h_{pq}(t)$ and $h_{\tilde{p}\tilde{q}}(t)$ is defined as

$$R_{pq,\tilde{p}\tilde{q}}[\tau] = \frac{\mathrm{E}\left[h_{pq}(t)h_{\tilde{p}\tilde{q}}^*(t+\tau)\right]}{\sqrt{\mathrm{E}[|h_{pq}(t)|^2]\mathrm{E}[|h_{\tilde{p}\tilde{q}}(t)|^2]}}, \tag{149}$$

where $(\;\cdot\;)^*$ denotes the complex conjugate operation, $\mathrm{E}[\;\cdot\;]$ is the statistical expectation operator, $p, \tilde{p} \in \{1, \ldots, L_T\}$, and $q, \tilde{q} \in \{1, \ldots, L_R\}$. Using (131) and (149), the space-time correlation function can be written as

$$\begin{aligned} R_{pq,\tilde{p}\tilde{q}}[\tau] = & \lim_{M,N\to\infty} \frac{1}{MN} \sum_{m=1}^{M}\sum_{n=1}^{N} \mathrm{E}\Big[a_{p,m}\; b_{n,q}\; a_{\tilde{p},m}^*\; b_{n,\tilde{q}}^* \\ & \times \; e^{-j2\pi\tau[f_{T\max}\cos(\alpha_T^{(m)}-\gamma_T)\cos\beta_T^{(m)}+f_{R\max}\cos(\alpha_R^{(n)}-\gamma_R)\cos\beta_R^{(n)}]}\Big]. \end{aligned} \tag{150}$$

Since the number of local scatterers in the reference model described in Section 6.2 is infinite, the discrete AAoDs, $\alpha_T^{(m)}$, EAoDs, $\beta_T^{(m)}$, AAoAs, $\alpha_R^{(n)}$, and EAoAs, $\beta_R^{(n)}$, can be replaced with continuous random variables α_T, β_T, α_R, and β_R with joint probability density functions (pdfs) $f(\alpha_T, \beta_T)$ and $f(\alpha_R, \beta_R)$, respectively. We assume that the azimuth and elevation angles are independent of each other, and thus, the joint pdfs $f(\alpha_T, \beta_T)$ and $f(\alpha_R, \beta_R)$ can be decomposed to $f(\alpha_T)f(\beta_T)$ and $f(\alpha_R)f(\beta_R)$, respectively. This assumption is based on experimental data in [70], [71]. Hence, (150) can be rewritten as

$$\begin{aligned} R_{pq,\tilde{p}\tilde{q}}[\tau] &= \int_{-\beta_{R_m}}^{\beta_{R_m}} \int_{-\beta_{T_m}}^{\beta_{T_m}} \int_{-\pi}^{\pi} \int_{-\pi}^{\pi} e^{-j2\pi\tau f_{T\max}\cos(\alpha_T-\gamma_T)\cos\beta_T} \\ &\times \; e^{-j2\pi\tau f_{R\max}\cos(\alpha_R-\gamma_R)\cos\beta_R + j\frac{2\pi}{\lambda}[d_{T_x}^{(p,\tilde{p})}\cos\alpha_T\cos\beta_T + d_{T_z}^{(p,\tilde{p})}\sin\beta_T]} \\ &\times \; e^{j\frac{2\pi}{\lambda}[d_{T_y}^{(p,\tilde{p})}\sin\alpha_T\cos\beta_T + d_{R_x}^{(q,\tilde{q})}\cos\alpha_R\cos\beta_R + d_{R_y}^{(q,\tilde{q})}\sin\alpha_R\cos\beta_R + d_{R_z}^{(q,\tilde{q})}\sin\beta_R]} \\ &\times \; f(\alpha_T)f(\beta_T)f(\alpha_R)f(\beta_R)d\alpha_T d\beta_T d\alpha_R d\beta_R, \end{aligned} \tag{151}$$

where $d_{T_x}^{(p,\tilde{p})} = d_{T_x}^{(p)} - d_{T_x}^{(\tilde{p})}$, $d_{T_y}^{(p,\tilde{p})} = d_{T_y}^{(p)} - d_{T_y}^{(\tilde{p})}$, $d_{T_z}^{(p,\tilde{p})} = d_{T_z}^{(p)} - d_{T_z}^{(\tilde{p})}$, $d_{R_x}^{(q,\tilde{q})} = d_{R_x}^{(q)} - d_{R_x}^{(\tilde{q})}$, $d_{R_y}^{(q,\tilde{q})} = d_{R_y}^{(q)} - d_{R_y}^{(\tilde{q})}$, $d_{R_z}^{(q,\tilde{q})} = d_{R_z}^{(q)} - d_{R_z}^{(\tilde{q})}$, and β_{T_m} and β_{R_m} are the non-negative maximum elevation angles of the scatterers around the $\mathrm{T_x}$ and $\mathrm{R_x}$, respectively.

To characterize the random azimuth angles α_T and α_R, we use the von Mises probability density function (pdf) given in (96). Prior work uses several different scatterer distributions, such as uniform [72], cosine [68], and Gaussian [73], to characterize the random elevation angles β_T and β_R. Here, we use the pdf [68]

$$f(\varphi) = \begin{cases} \frac{\pi}{4|\varphi_m|}\cos\left(\frac{\pi}{2}\frac{\varphi}{\varphi_m}\right) & , \quad |\varphi| \leq |\varphi_m| \leq \frac{\pi}{2} \\ 0 & , \quad \text{otherwise} \end{cases}, \tag{152}$$

because it matches well the experimental data in [71]. Parameter φ_m is the absolute value of the maximum elevation angle and lies in the range $0^\circ \leq |\varphi_m| \leq 20^\circ$ [71]. Such elevation angles are typical for the "street-canyon" type of propagation [74], which is prevalent in mobile-to-mobile communications where both the $\mathrm{T_x}$ and $\mathrm{R_x}$ are in motion and equipped with low elevation antennas (e.g., two cars driving through streets). Note that elevation angles between 20° and 80° have been observed for "over the roof" propagation [74], which is characteristic for fixed-to-mobile communications where the base-station is elevated above the roofs of the buildings.

By grouping the terms in (151) into those containing α_T and β_T and those containing α_R and β_R, the integrals in (151) reduce to the product of two double integrals, because the random angles α_T and β_T are independent from the random angles α_R and β_R. By denoting the von Mises pdf for the $\mathrm{T_x}$ and $\mathrm{R_x}$ azimuth angles as $f(\alpha_T) = \exp[k_T \cos(\alpha_T - \mu_T)]/(2\pi I_0(k_T))$ and $f(\alpha_R) = \exp[k_R \cos(\alpha_R - \mu_R)]/(2\pi I_0(k_R))$, respectively, and by denoting the pdf for the $\mathrm{T_x}$ and $\mathrm{R_x}$ elevation angles as $f(\beta_T) = \pi\cos(\pi\beta_T/(2\beta_{T_m}))/(4\beta_{T_m})$ and $f(\beta_R) = \pi\cos(\pi\beta_R/(2\beta_{R_m}))/(4\beta_{R_m})$, respectively, using trigonometric transformations, and the equality $\int_{-\pi}^{\pi}\exp\{a\sin(c) + b\cos(c)\}dc = 2\pi I_0(\sqrt{a^2+b^2})$ [63, eq. 3.338-4], the space-time correlation function becomes

$$\begin{aligned} R_{pq,\tilde{p}\tilde{q}}[\tau] &= \int_{-\beta_{T_m}}^{\beta_{T_m}} \cos\left(\frac{\pi}{2}\frac{\beta_T}{\beta_{T_m}}\right) \frac{\pi e^{j\frac{2\pi}{\lambda}d_{T_z}^{(p,\tilde{p})}\sin\beta_T}}{4\beta_{T_m}} \frac{I_0\left(\sqrt{x^2+y^2}\cos\beta_T\right)}{I_0(k_T)} d\beta_T \\ &\times \int_{-\beta_{R_m}}^{\beta_{R_m}} \cos\left(\frac{\pi}{2}\frac{\beta_R}{\beta_{R_m}}\right) \frac{\pi e^{j\frac{2\pi}{\lambda}d_{R_z}^{(q,\tilde{q})}\sin\beta_R}}{4\beta_{R_m}} \frac{I_0\left(\sqrt{z^2+w^2}\cos\beta_R\right)}{I_0(k_R)} d\beta_R, \end{aligned} \tag{153}$$

where parameters x, y, z, and w are defined as $x = j2\pi d_{T_x}^{(p,\tilde{p})}/\lambda - j2\pi\tau f_{T\max}\cos\gamma_T + k_T\cos\mu_T/\cos\beta_T$, $y = j2\pi d_{T_y}^{(p,\tilde{p})}/\lambda - j2\pi\tau f_{T\max}\sin\gamma_T + k_T\sin\mu_T/\cos\beta_T$, $z = j2\pi d_{R_x}^{(q,\tilde{q})}/\lambda - j2\pi\tau f_{R\max}\cos\gamma_R + k_R\cos\mu_R/\cos\beta_R$, $w = j2\pi d_{R_y}^{(q,\tilde{q})}/\lambda - j2\pi\tau f_{R\max}\sin\gamma_R + k_R\sin\mu_R/\cos\beta_R$. To obtain the space-time correlation function for 3-D MIMO M-to-M channels, the integrals in (153) must be evaluated numerically, because they lack closed-form solutions. However, since β_T and β_R are small angles, i.e., $\beta_T, \beta_R \leq 20°$, using the small angle approximations $\cos\beta_T, \cos\beta_R \approx 1$, $\sin\beta_T \approx \beta_T$, and $\sin\beta_R \approx \beta_R$, the space-time correlation function can be approximated as

$$\begin{aligned} R_{pq,\tilde{p}\tilde{q}}[\tau] &\approx \frac{I_0\left(\sqrt{x_1^2+y_1^2}\right)}{I_0(k_T)} \frac{I_0\left(\sqrt{z_1^2+w_1^2}\right)}{I_0(k_R)} \int_{-\beta_{T_m}}^{\beta_{T_m}} \frac{\pi}{4\beta_{T_m}} \cos\left(\frac{\pi}{2}\frac{\beta_T}{\beta_{T_m}}\right) e^{j\frac{2\pi}{\lambda}d_{T_z}^{(p,\tilde{p})}\beta_T} d\beta_T \\ &\times \int_{-\beta_{R_m}}^{\beta_{R_m}} \frac{\pi}{4\beta_{R_m}} \cos\left(\frac{\pi}{2}\frac{\beta_R}{\beta_{R_m}}\right) e^{j\frac{2\pi}{\lambda}d_{R_z}^{(q,\tilde{q})}\beta_R} d\beta_R, \end{aligned} \tag{154}$$

where parameters x_1, y_1, z_1, and w_1 are

$$x_1 = j2\pi d_{T_x}^{(p,\tilde{p})}/\lambda - j2\pi\tau f_{T\max}\cos\gamma_T + k_T\cos\mu_T, \tag{155}$$

$$y_1 = j2\pi d_{T_y}^{(p,\tilde{p})}/\lambda - j2\pi\tau f_{T\max}\sin\gamma_T + k_T\sin\mu_T, \tag{156}$$

$$z_1 = j2\pi d_{R_x}^{(q,\tilde{q})}/\lambda - j2\pi\tau f_{R\max}\cos\gamma_R + k_R\cos\mu_R, \tag{157}$$

$$w_1 = j2\pi d_{R_y}^{(q,\tilde{q})}/\lambda - j2\pi\tau f_{R\max}\sin\gamma_R + k_R\sin\mu_R. \tag{158}$$

Finally, solving the integrals in (154), the space-time correlation function becomes

$$\begin{aligned} R_{pq,\tilde{p}\tilde{q}}[\tau] &= R_{p,\tilde{p}}^{T}[\tau]R_{q,\tilde{q}}^{R}[\tau] \approx \\ &\frac{I_0\left(\sqrt{x_1^2+y_1^2}\right)}{I_0(k_T)}\frac{\cos\left(\frac{2\pi}{\lambda}\beta_{T_m}d_{T_z}^{(p,\tilde{p})}\right)}{\left[1-\left(\frac{4\beta_{T_m}d_{T_z}^{(p,\tilde{p})}}{\lambda}\right)^2\right]}\frac{I_0\left(\sqrt{w_1^2+z_1^2}\right)}{I_0(k_R)}\frac{\cos\left(\frac{2\pi}{\lambda}\beta_{R_m}d_{R_z}^{(q,\tilde{q})}\right)}{\left[1-\left(\frac{4\beta_{R_m}d_{R_z}^{(q,\tilde{q})}}{\lambda}\right)^2\right]}. \end{aligned} \tag{159}$$

To illustrate the validity of the approximate space-time correlation function in (159), we compare it with the numerically obtained space-time correlation function in (153). Figures 30 and 31 show the real and imaginary part of the space-time correlation functions in (153) and (159) obtained assuming a uniform linear array with $L_T = L_R = 2$ antenna elements and the parameters $d_T = d_R = 0.5\lambda$, $\theta_T = \theta_R = \pi/4$, $\psi_T = \psi_R = 2\pi/3$, $\gamma_T = 20°$, $\gamma_R = 40°$, $\mu_T = 70°$, $\mu_R = 20°$, and $k_T = k_R = 20$. Results show excellent agreement between the space-time correlation functions in (153) and (159) for the maximum elevation angles $\beta_{T_m} = \beta_{R_m} = 20°$. The similar results can be obtained for the maximum elevation angles smaller than 20°. Since such elevation angles are typical for M-to-M communications, the space-time correlation function of the M-to-M channel impulse response can be characterized using (159). If "over the roof" propagation occurs, which is characteristic of F-to-M communications, and the maximum elevation angles are larger than 20°, the approximations used to obtain (159) do not hold any more. To illustrate the discrepancy between the exact and approximate space-time correlation functions, Figs. 30 and 31 also show the real and imaginary part of the space-time correlation functions in (153) and (159)

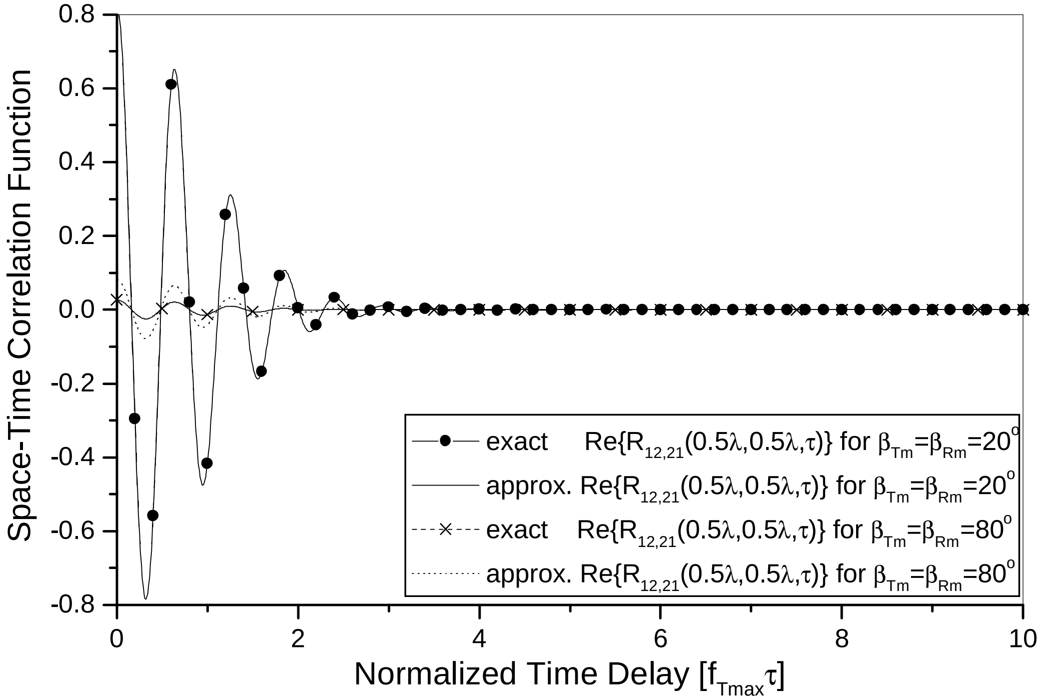

Figure 30: The real part of the normalized space-time correlation functions in (153) and (159).

obtained for the maximum elevation angles $\beta_{T_m} = \beta_{R_m} = 80°$ (the largest elevation angles found in the literature [74]). The results show that there is still a relatively small discrepancy between the space-time correlation functions in (153) and (159).

The 2-D space-time correlation function for M-to-M channels suggests that two vertically placed antennas are completely correlated and no diversity gain is available. However, the 3-D space-time correlation function shows that vertically placed antennas can have small correlations and provide considerable diversity gain. To illustrate this, Fig. 32 shows the spatial correlation functions of two uniformly and vertically spaced antennas at the $\mathrm{T_x}$ for several maximum elevation angles β_{T_m}. Other parameters used to obtain curves in Fig. 32 are $L_R = 1$, $\theta_T = \theta_R = 0$, $\psi_T = \pi/2$, $\psi_R = 0$, $\gamma_T = \gamma_R = 0$, and $k_T = k_R = 0$. As the maximum elevation angle β_{T_m} increases from $1°$ to $20°$, the correlation between the two antennas reduces dramatically.

Finally, Fig. 33 compares the Doppler power spectral density (D-psd) of the complex faded envelope in (131) with the measured SISO narrowband D-psd in [39]. The

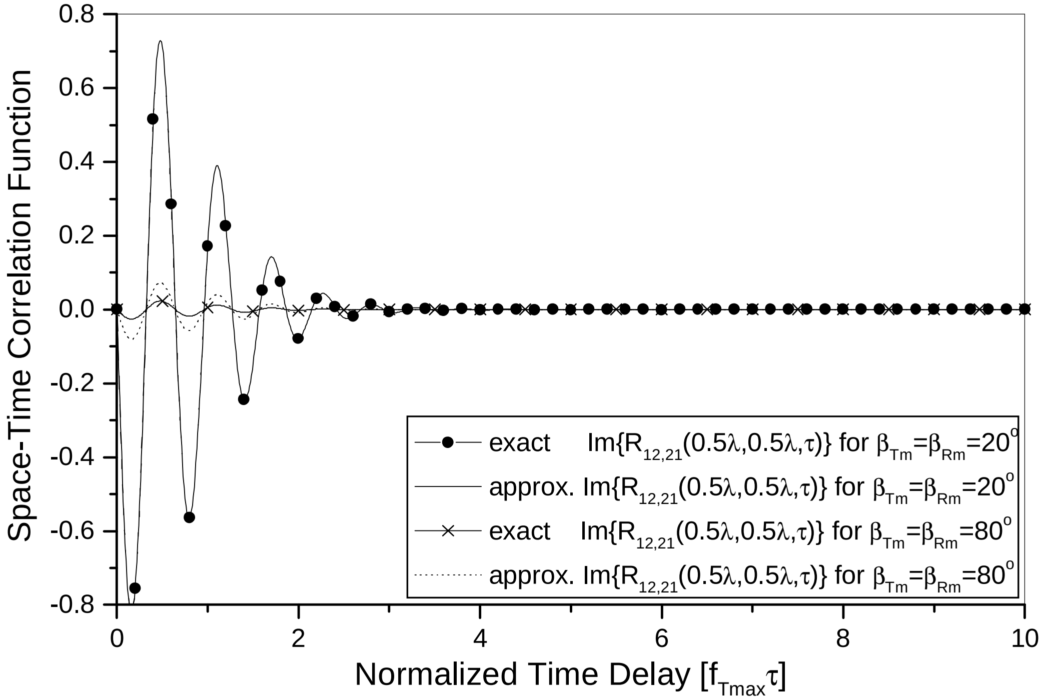

Figure 31: The imaginary part of the normalized space-time correlation functions in (153) and (159).

D-psd is defined as the Fourier transform of space-time correlation function and is calculated as $S_{pq,\tilde{p}\tilde{q}}[f] = \mathcal{F}\left\{R_{pq,\tilde{p}\tilde{q}}[\tau]\right\} = \mathcal{F}\left\{R^T_{p,\tilde{p}}[\tau]\right\} \odot \mathcal{F}\left\{R^R_{q,\tilde{q}}[\tau]\right\}$, where $\odot$ denotes convolution. Parameters used to obtain simulation results in Fig. 33 are $L_t = L_r = 1$, $\beta_{Tm} = \beta_{Rm} = 15°$, $\theta_T = \theta_R = \pi/4$, $\psi_T = \psi_R = \pi/3$, $\gamma_T = 0$, $\gamma_R = 10°$, $k_T = k_R = 3.3$, $\mu_T = 0$, $\mu_R = \pi$, and $f_{T\max} = f_{R\max} = 100$ Hz. The measured results are taken from Fig. 7(a) (urban environment) of [39]. The close agreement between the theoretical and empirical curves confirms the utility of the proposed narrowband model.

6.4 3-D Simulation Models for MIMO M-to-M Channels

The reference model described in Section 6.2 assumes an infinite number of scatterers, which prevents practical implementation. Here, we design simulation models with a finite number of scatterers, while still matching the statistical properties of the reference model.

Using the reference model in (131) with a finite number of scatterers and assuming

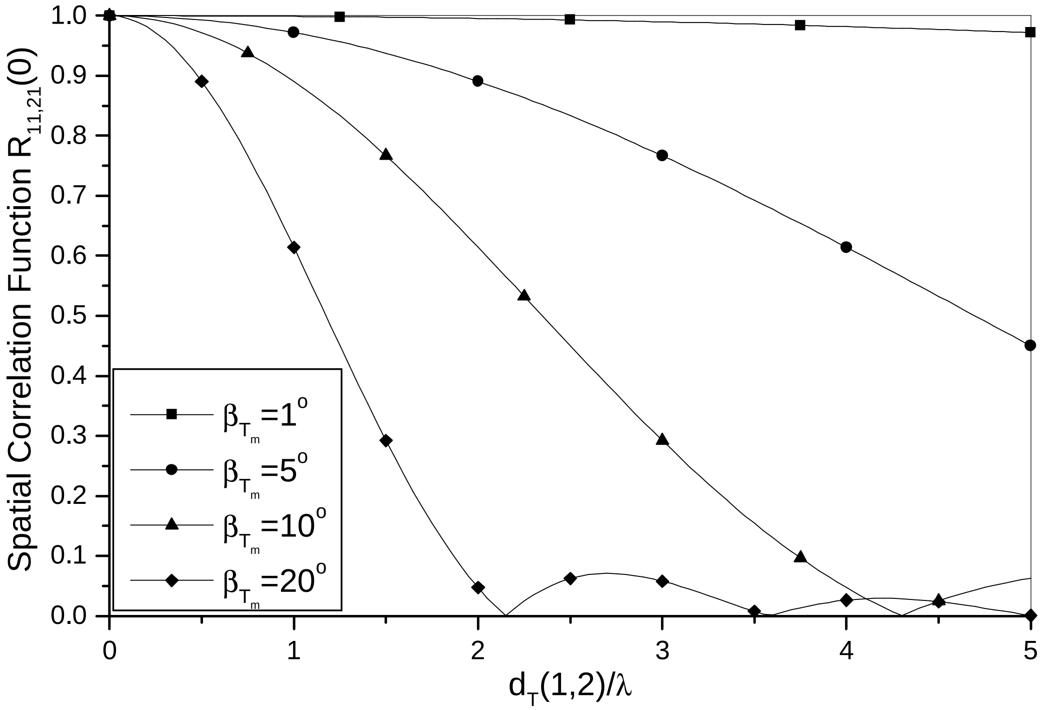

Figure 32: The normalized spatial correlation functions of two uniformly and vertically spaced antennas at the $\mathrm{T_x}$, for several maximum elevation angles β_{T_m}.

3-D non-isotropic scattering, the following function is considered for the received complex faded envelope

$$h_{pq}(t) = \frac{1}{\sqrt{MN}} \sum_{m=1}^{M} \sum_{n=1}^{N} a_{p,m} \; b_{n,q} \; e^{j\phi_{mn}} \times e^{j2\pi t [f_{T\max} \cos(\alpha_T^{(m)} - \gamma_T) \cos \beta_T^{(m)} + f_{R\max} \cos(\alpha_R^{(n)} - \gamma_R) \cos \beta_R^{(n)}]}, \tag{160}$$

where parameters $a_{p,m}$ and $b_{n,q}$ are defined in (132) and (133), respectively. The angles of departure, $\alpha_T^{(m)}$ and $\beta_T^{(m)}$, and the angles of arrival, $\alpha_R^{(n)}$ and $\beta_R^{(n)}$, are random variables and the angles of departure are independent from the angles of arrival. The phases ϕ_{mn} are also random variables uniformly distributed on the interval $[-\pi, \pi)$ and independent from the angles of departure and angles of arrival. The AAoDs, $\alpha_T^{(m)}$, and the AAoAs, $\alpha_R^{(n)}$, are modeled using the von Mises pdfs $f(\alpha_T) =$

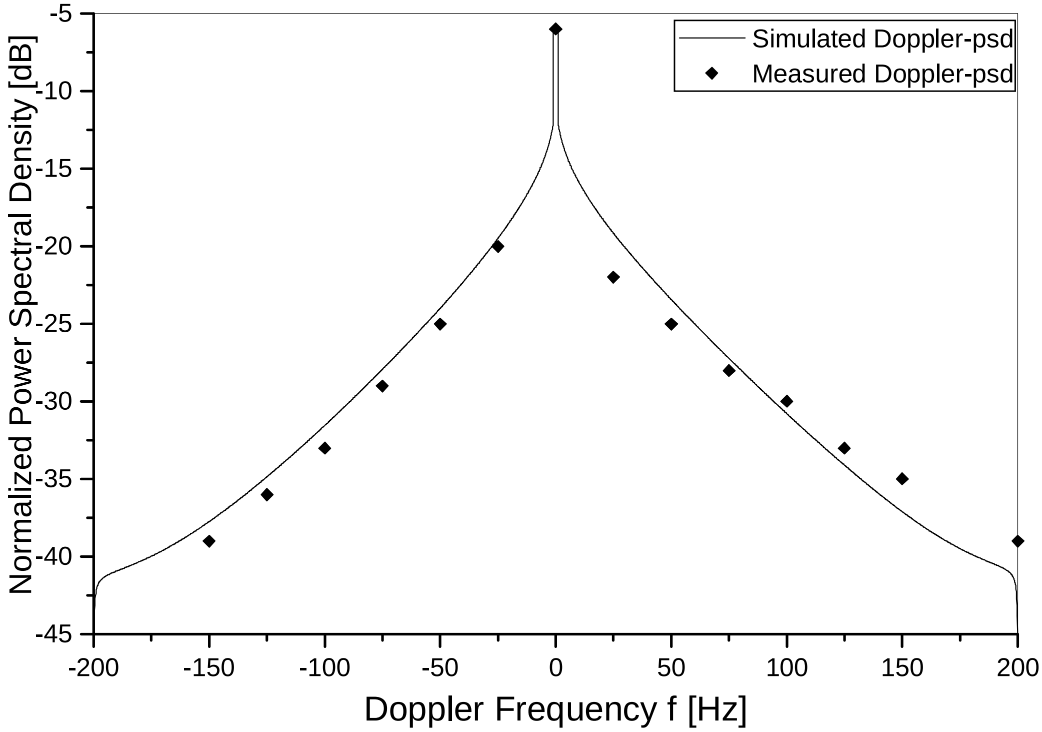

Figure 33: The normalized simulated and measured [39] Doppler power spectra.

$\exp[k_T \cos(\alpha_T - \mu_T)]/(2\pi I_0(k_T))$ and $f(\alpha_R) = \exp[k_R \cos(\alpha_R - \mu_R)]/(2\pi I_0(k_R))$, respectively. They are generated as follows:

$$\alpha_T^{(m)} = F_T^{-1}(\eta_m), \tag{161}$$

$$\alpha_R^{(n)} = F_R^{-1}(\delta_n), \tag{162}$$

for $m = 1, \ldots, M$, $n = 1, \ldots, N$. Function $F_{T/R}(\ \cdot\ )^{-1}$ denotes the inverse function of the von Mises cumulative distribution function (cdf) and can be evaluated using method in [75]. Parameters η_m and δ_n are independent random variables uniformly distributed on the interval $[0, 1)$. The EAoDs, $\beta_T^{(m)}$, and the EAoAs, $\beta_R^{(n)}$, are modeled using the pdfs $f(\beta_T) = \pi\cos(\pi\beta_T/(2\beta_{T_m}))/(4\beta_{T_m})$ and $f(\beta_R) = \pi\cos(\pi\beta_R/(2\beta_{R_m}))/(4\beta_{R_m})$, respectively, and are generated as follows:

$$\beta_T^{(m)} = \frac{2\beta_{T_m}}{\pi}\arcsin(2\nu_m - 1), \tag{163}$$

$$\beta_R^{(n)} = \frac{2\beta_{R_m}}{\pi}\arcsin(2\zeta_n - 1), \tag{164}$$

for $m = 1, \ldots, M$, $n = 1, \ldots, N$, where ν_m and ζ_n are independent random variables uniformly distributed on the interval $[0, 1)$.

For the maximum elevation angles β_{T_m} and β_{R_m} in the range $0^\circ \leq \beta_{T_m}, \beta_{R_m} \leq 20^\circ$ the elevation angles can be approximated using $\cos\beta_T^{(m)}, \cos\beta_R^{(n)} \approx 1$, $\sin\beta_T^{(m)} \approx \beta_T^{(m)}$, and $\sin\beta_R^{(n)} \approx \beta_R^{(n)}$. Then, the complex faded envelope in (160) can be approximated as

$$\begin{aligned} h_{pq}(t) &\approx \frac{1}{\sqrt{M_A M_E N_A N_E}} \sum_{m,i=1}^{M_A,M_E} \sum_{n,k=1}^{N_A,N_E} c_{p,m,i} d_{n,k,q} \\ &\times e^{j2\pi t[f_{T\max}\cos(\alpha_T^{(m)}-\gamma_T)+f_{R\max}\cos(\alpha_R^{(n)}-\gamma_R)+j\phi_{m,i,n,k}]}, \end{aligned} \tag{165}$$

where $M_A M_E = M$, $N_A N_E = N$, parameters $c_{p,m,i}$ and $d_{n,k,q}$ are defined as

$$c_{p,m,i} = e^{-j\frac{2\pi}{\lambda}[\frac{D}{2}+R_t-d_{T_x}^{(p)}\cos\alpha_T^{(m)}-d_{T_y}^{(p)}\sin\alpha_T^{(m)}-d_{T_z}^{(p)}\sin\beta_T^{(i)}]}, \tag{166}$$

$$d_{n,k,q} = e^{-j\frac{2\pi}{\lambda}[\frac{D}{2}+R_r-d_{R_x}^{(q)}\cos\alpha_R^{(n)}-d_{R_y}^{(q)}\sin\alpha_R^{(n)}-d_{R_z}^{(q)}\sin\beta_R^{(k)}]}, \tag{167}$$

and $d_{T_x/R_x}^{(p/q)}$, $d_{T_y/R_y}^{(p/q)}$, and $d_{T_z/R_z}^{(p/q)}$ are defined as in (134) - (139).

6.4.1 Deterministic and Statistical 3-D MIMO M-to-M Simulation Models

First, we propose an ergodic statistical (deterministic) model. This model has only the phases $\phi_{m,i,n,k}$ as random variables and needs only one simulation trial to obtain the desired statistical properties. We use the complex faded envelope in (165) and generate the AAoDs, AAoAs, EAoDs, and EAoAs as follows:

$$\alpha_T^{(m)} = F_T^{-1}\left(\frac{m-0.5}{M_A}\right), \tag{168}$$

$$\alpha_R^{(n)} = F_R^{-1}\left(\frac{n-0.5}{N_A}\right), \tag{169}$$

$$\beta_T^{(i)} = \frac{2\beta_{T_m}}{\pi} \arcsin\left(\frac{2i-1}{M_E} - 1\right), \tag{170}$$

$$\beta_R^{(k)} = \frac{2\beta_{R_m}}{\pi} \arcsin\left(\frac{2k-1}{N_E} - 1\right), \tag{171}$$

for $m = 1, \ldots, M_A$, $n = 1, \ldots, N_A$, $i = 1, \ldots, M_E$, $k = 1, \ldots, N_E$, respectively.

For $M, N \to \infty$, our deterministic model can be shown to exhibit properties of the reference model. The space-time correlation function of the complex faded envelope in (165) matches the approximate space-time correlation function in (159). The derivation of the space-time correlation function of the complex faded envelope in (165) is presented in Appendix G.

Figure 34 shows the real part of the space-time correlation function for the deterministic model with $M_A = 30$, $M_E = 5$, $N_A = 30$, and $N_E = 5$ scatterers and a uniform linear antenna array with $L_T = L_R = 2$ antennas. Other parameters used to obtain the curves in Fig. 34 are $d_T = d_R = 1\lambda$, $\theta_T = \theta_R = \pi/3$, $\psi_T = \psi_R = \pi/4$, $\gamma_T = \pi/6$, $\gamma_R = \pi/12$, $\beta_{T_m} = \beta_{R_m} = 15°$, and $k_T = k_R = 0$. Figure 34 does not show the imaginary part of the space-time correlation function because it is zero for $k_T = k_R = 0$. The results show that the space-time correlation function of the deterministic model closely matches the theoretical one in the range of normalized time delays, $0 \leq f_{T\max} T_s \leq 5$. The deterministic model can match the theoretical one over a wider range of normalized time delays if a larger number of scatterers is used in the simulation model.

Deterministic simulators are often used because they are easy to implement and have short simulation times. However, they do not reflect actual channel realizations because their scatterers are placed at specific sights for all simulation trials. By allowing both the phases and Doppler frequencies to be random variables, our deterministic model can be modified to better model the fading processes. Furthermore, this new (statistical) model matches statistical properties of the reference model over a wider range of normalized time delays, while at the same time requiring a smaller number of scatterers. The statistical properties of the statistical model vary for each simulation trial, but will converge to desired ensemble averaged properties when averaged over a sufficient number of simulation trials.

We use the complex faded envelope in (165) and generate the AAoDs, AAoAs,

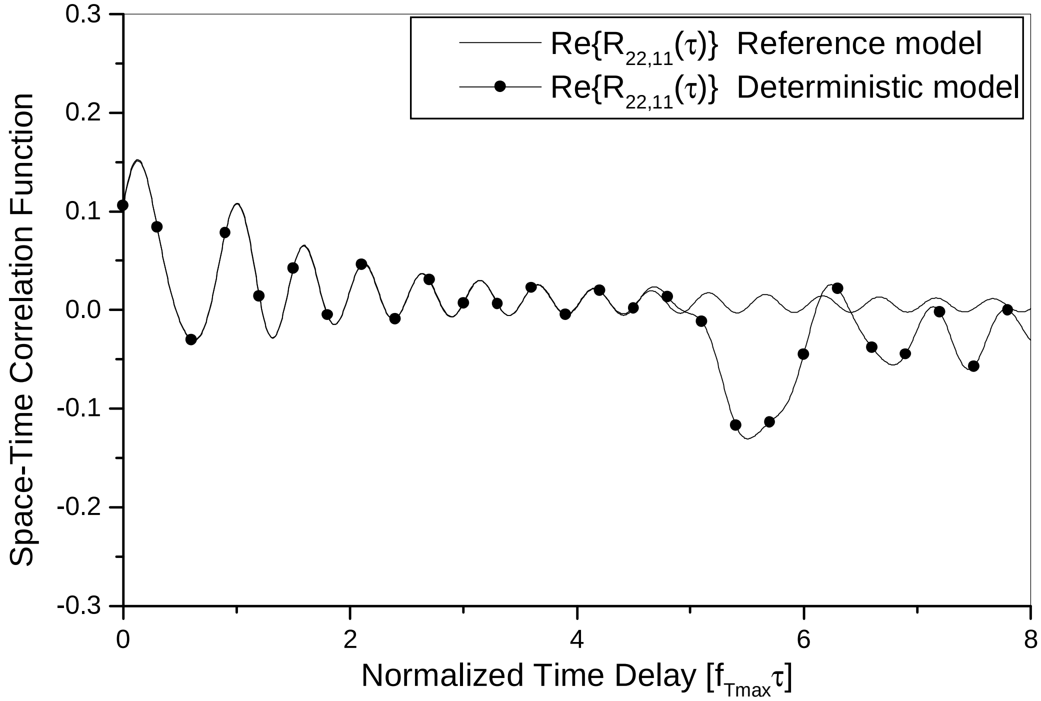

Figure 34: The real part of the space-time correlation function of the 3-D MIMO M-to-M deterministic and reference models.

EAoDs, and EAoAs as follows:

$$\alpha_T^{(m)} = F_T^{-1}\left(\frac{m+\theta_A-1}{M_A}\right), \tag{172}$$

$$\alpha_R^{(n)} = F_R^{-1}\left(\frac{n+\psi_A-1}{N_A}\right), \tag{173}$$

$$\beta_T^{(i)} = \frac{2\beta_{T_m}}{\pi}\arcsin\left(\frac{2(i+\theta_E-1)}{M_E}-1\right), \tag{174}$$

$$\beta_R^{(k)} = \frac{2\beta_{R_m}}{\pi}\arcsin\left(\frac{2(k+\psi_E-1)}{N_E}-1\right), \tag{175}$$

for $m = 1, \ldots, M_A$, $n = 1, \ldots, N_A$, $i = 1, \ldots, M_E$, $k = 1, \ldots, N_E$, respectively. The parameters θ_A, ψ_A, θ_E, and ψ_E are independent random variables uniformly distributed on the interval $[0, 1)$.

For arbitrary number of scatterers, i.e., any M, N, our statistical model can be shown to exhibit properties of the reference model. The derivation of the space-time correlation function of the complex faded envelope in (165) is presented in Appendix G.

Figure 35 shows the real part of the space-time correlation function for the statistical model with $M_A = 20$, $M_E = 3$, $N_A = 20$, and $N_E = 3$ scatterers, $N_{\text{stat}} = 50$ simulation trials and an uniform linear antenna array with $L_T = L_R = 2$ antennas. Other parameters are the same as in Fig. 34. The results in Figs. 34 and 35 show

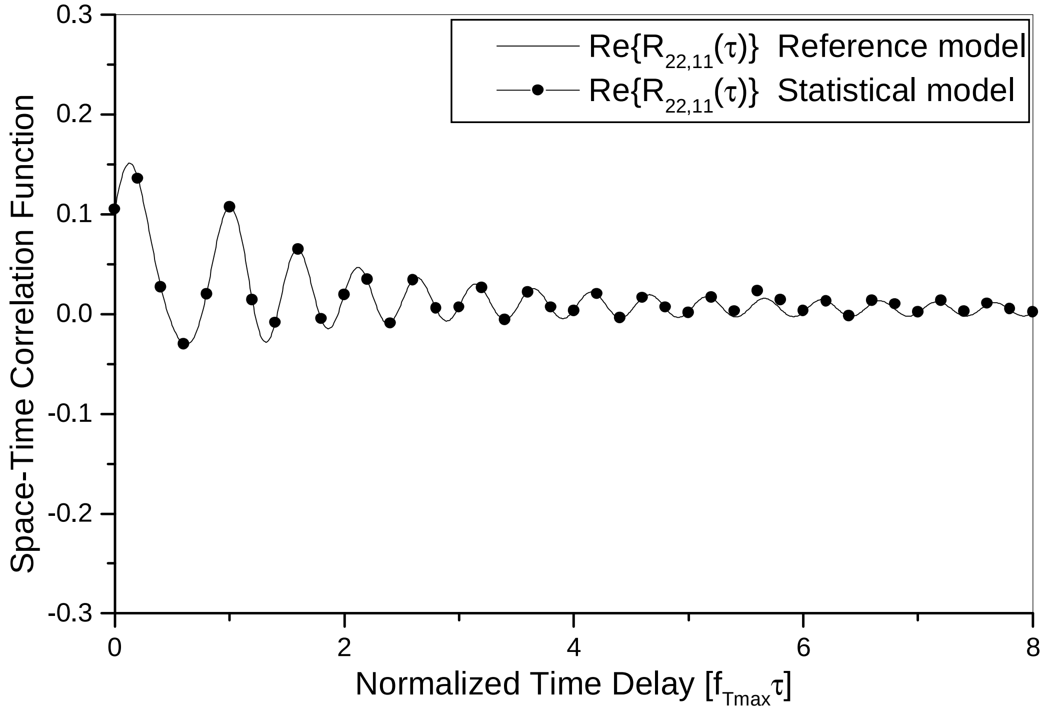

Figure 35: The real part of the space-time correlation function of the 3-D MIMO M-to-M statistical and reference models.

that the space-time correlation function of the statistical model matches that of the reference model over a wider range of normalized time delays, i.e., $0 \leq f_{T\max} T_s \leq 10$, compared to the space-time correlation function of the deterministic model.

6.5 Numerical Analysis of M-to-M Channel Capacity

In this section, we first briefly review the MIMO channel capacity and show that our simulation models can be used to evaluate M-to-M channel capacity. Then, we evaluate the effect of the space-time correlation on the outage capacity of uniform linear antenna arrays. Finally, we compare the capacities of uniform linear, uniform circular, and spherical antenna arrays to determine the best antenna configuration.

6.5.1 Review of MIMO Channel Capacity

The instantaneous channel capacity (in bit/s/Hz) of a stochastic MIMO channel, under an average transmit power constraint is [55], [38]

$$C(t) = \log_2 \det\left(\mathbf{I}_{L_R} + \frac{\rho}{L_T}\mathbf{H}(t)\mathbf{H}^H(t)\right), \tag{176}$$

where it is assumed that $L_T \geq L_R$, the transmitter has no channel knowledge, and the receiver has perfect channel knowledge. In (176), $\mathbf{H}(t) = [h_{ij}(t)]_{L_R \times L_T}$ is the $L_R \times L_T$ matrix of complex faded envelopes, $(\ \cdot\ )^H$ denotes the transpose conjugate operation, $\det(\ \cdot\ )$ denotes the matrix determinant, $\mathbf{I}_{L_R}$ is the $L_R \times L_R$ identity matrix, and ρ is the average signal-to-noise ratio (SNR). In this thesis, the ergodic capacity of a MIMO channel is defined as the expectation of the instantaneous capacity over time, i.e.,

$$\mathrm{E}[C(t)] = \mathrm{E}\left[\log_2 \det\left(\mathbf{I}_{L_R} + \frac{\rho}{L_T}\mathbf{H}(t)\mathbf{H}^H(t)\right)\right]. \tag{177}$$

In the practice, the outage capacity is often used to characterize the properties of the MIMO channel. Here, the outage capacity C_{out} is associated with an outage probability P_{out} which gives the probability that the instantaneous channel capacity, C, falls below C_{out}.

There are several ways to generate the channel matrix $\mathbf{H}$. One way is to use the simulation models proposed in Section 6.4. The elements of the channel matrix can be obtained directly, using (165). We will refer to these models as the deterministic and statistical physical models. The other way is to generate the channel matrix as a product of the white channel matrix and the square root of desired correlation matrix. We will refer to this model as the non-physical model. The non-physical model generates the M-to-M channel matrix as [58]

$$\mathbf{H} = (\mathbf{R}_R[0])^{1/2}\mathbf{G}(\mathbf{R}_T[0])^{T/2}, \tag{178}$$

where $\mathbf{G}$ is an $L_R \times L_T$ stochastic matrix with complex Gaussian i.i.d. entries, $(\,\cdot\,)^{1/2}$ denotes the matrix square root operation, $(\,\cdot\,)^T$ denotes the transpose operation, and $\mathbf{R}_R[0]$ and $\mathbf{R}_T[0]$ are the $L_R \times L_R$ receive and $L_T \times L_T$ transmit correlation matrices, respectively. The elements of matrices $\mathbf{R}_R[0]$ and $\mathbf{R}_T[0]$ are obtained using (159).

Here we compare the ergodic capacities obtained using the non-physical and physical models. Fig. 36 shows the ergodic capacity against SNR, ρ, for several uniform linear antenna arrays ($L_T = L_R = 2$, $L_T = L_R = 4$, and $L_T = L_R = 6$). The parameters used to obtain the curves in Fig. 36 are $\theta_T = \theta_R = \pi/4$, $\psi_T = \psi_R = \pi/6$, $\gamma_T = 0$, $\gamma_R = 20°$, $\beta_{T_m} = \beta_{R_m} = 15°$, $k_T = k_R = 5$, $\mu_T = \pi/2$, and $\mu_R = 3\pi/2$. The spacing between two adjacent antenna elements at the $\mathrm{T_x}$ and $\mathrm{R_x}$ is chosen to be 0.5λ. The deterministic simulation model uses $M_A = N_A = 60$, and $M_E = N_E = 5$ scatterers, whereas the statistical simulation model uses $M_A = N_A = 20$, and $M_E = N_E = 3$ scatterers and $N_{\mathrm{stat}} = 50$ simulation trials. Results show good agreement between the non-physical and physical models.

6.5.2 Effect of Space-time Correlation on Outage Capacity of Uniform Linear Antenna Arrays

In this section, the effect of the space-time correlation on the outage capacity of ULAs is investigated. In all simulations, the outage capacity C_{out} is calculated for a 1% outage probability and the statistical physical model is used to calculate the outage capacity. The coordinates of antenna elements at the $\mathrm{T_x}$ and $\mathrm{R_x}$ are calculated using equations (140) - (142). A normalized sampling period $f_{T\max}T_s = 0.01$ ($f_{T\max} = f_{R\max}$ are the maximum Doppler frequencies and T_s is the sampling period) is used in all simulations. Finally, the statistical physical model uses $M_A = N_A = 20$, and $M_E = N_E = 3$ scatterers and $N_{\mathrm{stat}} = 50$ simulation trials.

Figure 37 shows the outage capacity as a function of the spacing between the $\mathrm{T_x}$ and $\mathrm{R_x}$ antenna array elements. Parameters used to obtain the curves in Fig. 37 are $\gamma_T = \gamma_R = 20°$, $\theta_T = \theta_R = \pi/4$, $\psi_T = \psi_R = \pi/3$, $\beta_{T_m} = \beta_{R_m} = 15°$, $\rho = 15$ dB,

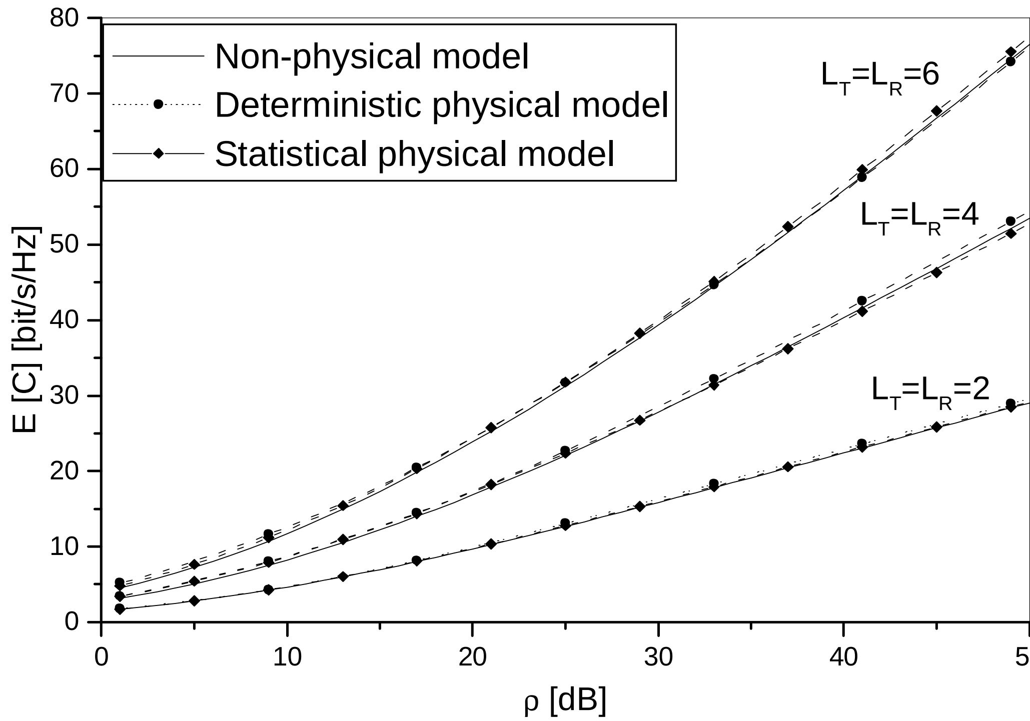

Figure 36: Comparison of the ergodic capacities obtained using the non-physical model and the 3-D MIMO M-to-M deterministic and statistical physical models.

$L_T = L_R = 3$, $\mu_T = 0°$, $\mu_R = 180°$, and $k_T = k_R = 10$ (non-isotropic scattering environment). We can observe that increasing antenna element spacings d_T and d_R from 0.1λ to 2λ increases the capacity from 6 bit/s/Hz to 12 bit/s/Hz. However, increasing antenna element spacings d_T and d_R beyond 2λ has a negligible effect on the capacity. These results differ from results obtained for F-to-M cellular channels (with fixed, elevated base station antennas), where increasing the R_x antenna element spacing d_R beyond 5λ and the T_x antenna element spacing d_T beyond 2λ has a negligible effect on the capacity [55].

Figure 38 shows the influence of the T_x and R_x antenna array orientations on the capacity when T_x and R_x antenna arrays are placed in the x - y plane. To analyze antenna array orientations only in the x - y plane, the elevation angles ψ_T and ψ_R are set to zero. The parameters used to obtain the curves in Fig. 38 are $\gamma_T = \gamma_R = 20°$, $\theta_T = \theta_R = \pi/4$, $d_T = d_R = 1\lambda$, $\rho = 15$ dB, $L_T = L_R = 3$,

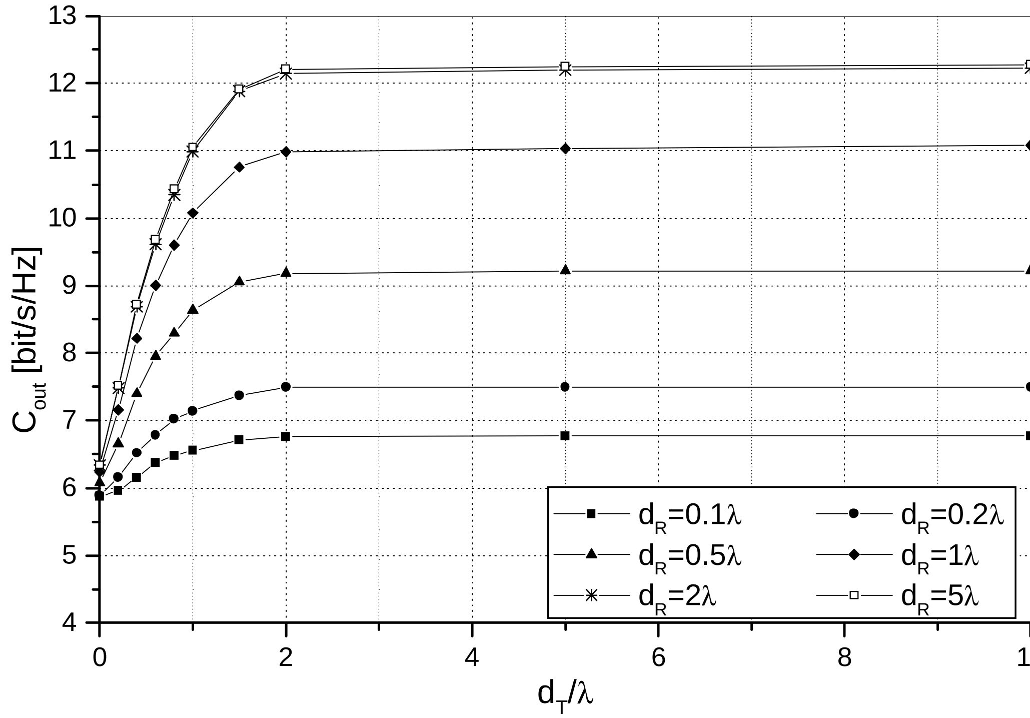

Figure 37: The outage capacity as a function of spacing between the T_x and R_x antenna array elements.

$\mu_T = 0°$ and $\mu_R = 180°$. From Fig. 38, we can observe that when 2-D isotropic scattering is assumed ($k_T = k_R = 0$), orientations of the T_x and R_x antenna arrays have no influence on the capacity. Note that this property of M-to-M channels is in contrast to F-to-M cellular channels (with elevated base station antennas), where T_x broadside antenna arrays ($\theta_T = 90°$) and R_x inline antenna arrays ($\theta_R = 0°$) provide higher capacity than T_x and R_x broadside antenna arrays [64, 69]. When 2-D non-isotropic scattering is assumed ($k_T = k_R = 10$), we can observe that the outage capacity is the lowest for inline antenna arrays and the highest for broadside antenna arrays. Increasing antenna angles θ_T and θ_R from 0° to 45° increases capacity by 4.1 bit/s/Hz. However, a further increase of antenna angles θ_T and θ_R from 45° to 90° increases the outage capacity by only 0.8 bit/s/Hz. On the other hand, if local scatterers are centered around the y - axis, (i.e., $\mu_T = 90°$ and $\mu_R = 270°$) the outage capacity will be the lowest for broadside antenna arrays and the highest

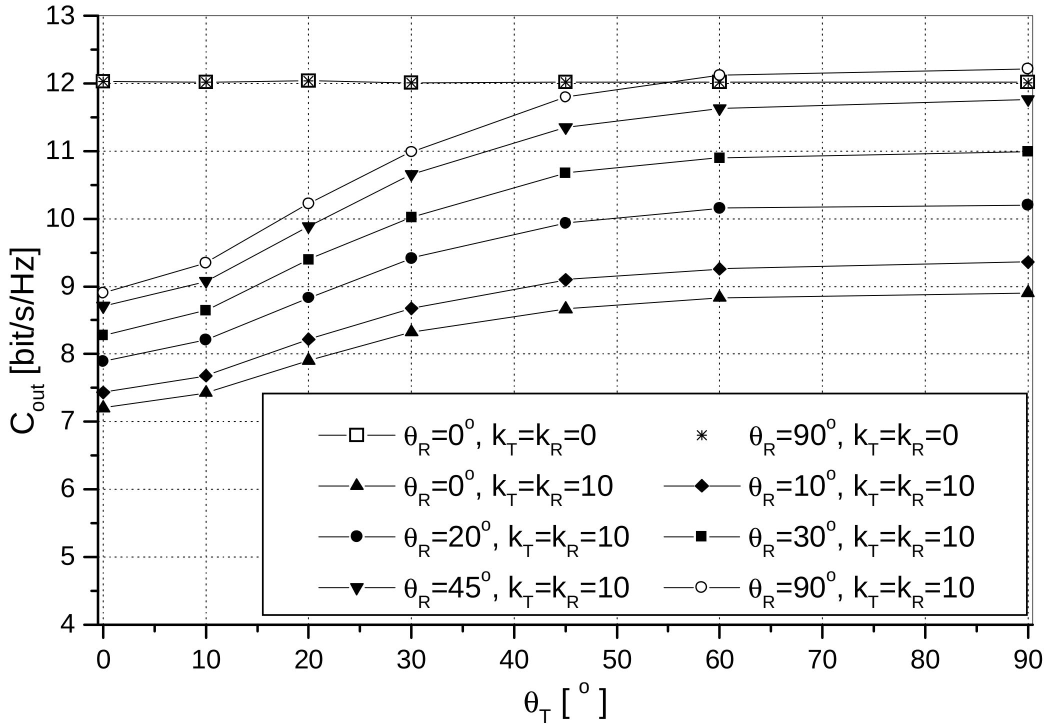

Figure 38: The outage capacity as a function of the $\mathrm{T_x}$ and $\mathrm{R_x}$ antenna array orientations, θ_T and θ_R.

for inline antenna arrays. This implies that the optimum capacity depends on the relative angle between the $\mathrm{T_x}$ antenna array and the local scatterers around the $\mathrm{T_x}$, i.e., $\mu_T - \theta_T$, and on the relative angle between the $\mathrm{R_x}$ antenna array and the local scatterers around the $\mathrm{R_x}$, i.e., $\mu_R - \theta_R$.

Figure 39 shows the influence of the $\mathrm{T_x}$ and $\mathrm{R_x}$ antenna elevation angles on the outage capacity. The parameters used to obtain the curves in Fig. 39 are $\gamma_T = \gamma_R = 20°$, $\theta_T = \theta_R = \pi/2$, $\beta_{T_m} = \beta_{R_m} = 15°$, $\rho = 15$ dB, $L_T = L_R = 3$, $\mu_T = 0°$ and $\mu_R = 180°$. From Fig. 39, observe that when isotropic scattering in the x - y plane is assumed ($k_T = k_R = 0$) and the distances between antenna array elements are $d_T = d_R = 0.2\lambda$, increasing antenna angles ψ_T and ψ_R from 0° to 45° has a small influence on the outage capacity. A further increase in the antenna elevation angles drastically decreases the capacity. When the distance between antenna array elements is increased to $d_T = d_R = 1\lambda$, increasing angles ψ_T and ψ_R from 0° to 70° has a small influence on the outage capacity. Furthermore, when non-isotropic scattering in the x - y plane is assumed ($k_T = k_R = 10$) and the distances between antenna array elements are $d_T = d_R = 1\lambda$, increasing antenna angles ψ_T and ψ_R from $0°$ to $45°$ decreases the outage capacity by only 0.4 bit/s/Hz. A further increase of antenna elevation angles drastically decreases the outage capacity. Figure 39 implies that if available area in the x - y plane is not sufficient for the antenna array realization, the antenna array can be moderately tilted without significant loss of outage capacity.

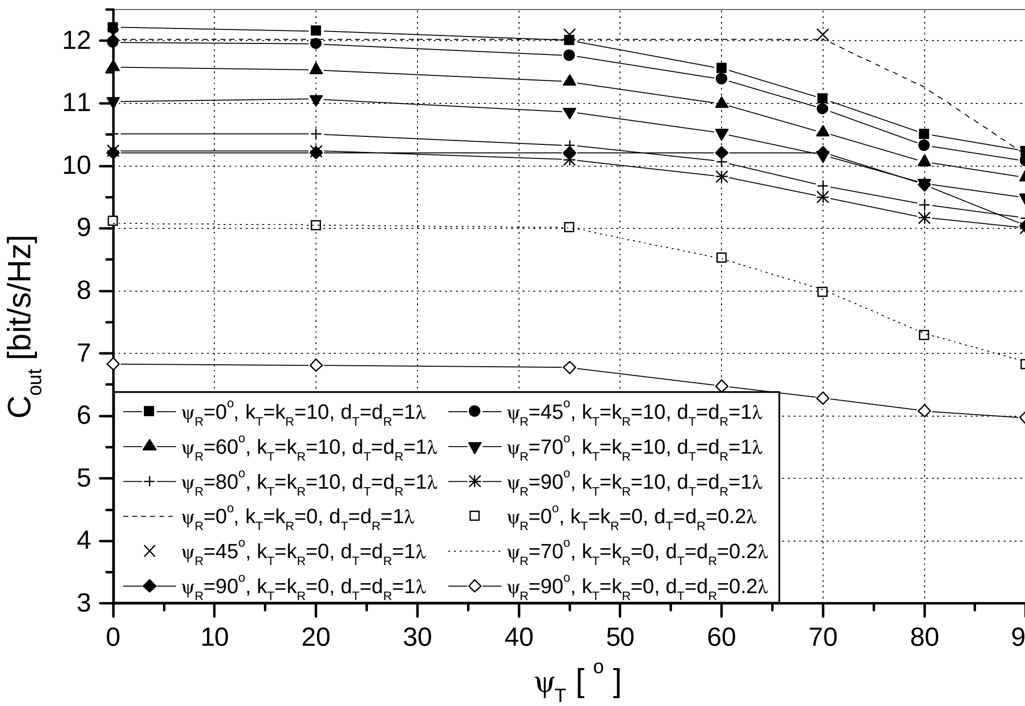

Figure 39: The outage capacity as a function of the T_x and R_x antenna array elevations, ψ_T and ψ_R.

Finally, Fig. 40 shows the capacity as a function of the maximum elevation angles β_{T_m} and β_{R_m}. The parameters used to obtain the curves in Fig. 40 are $\gamma_T = \gamma_R = 20°$, $\theta_T = \theta_R = \pi/4$, $\psi_T = \psi_R = \pi/3$, $d_T = d_R = 1\lambda$, $\rho = 15$ dB, $L_T = L_R = 3$, $\mu_T = 0°$, $\mu_R = 180°$, and $k_T = k_R = 10$. Observe that by increasing maximum elevation angles β_{T_m} and β_{R_m} from $1°$ to $20°$ the outage capacity increases by up to 1 bit/s/Hz. This result implies that the 2-D models actually underestimate available capacity.

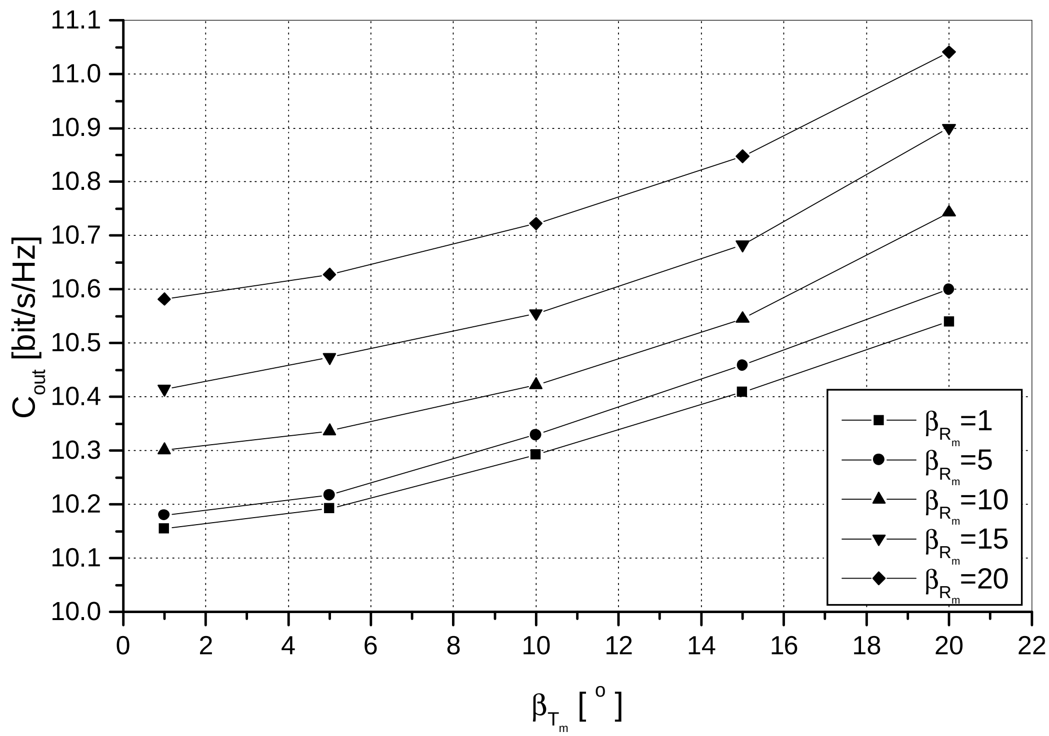

Figure 40: The outage capacity as a function of the maximum elevation angles β_{T_m} and β_{R_m}.

6.5.3 Comparison of Linear, Circular, and Spherical MIMO Antenna Configurations

In the previous section, the effect of the space-time correlation on the outage capacity of ULAs was investigated. Here, we compare the capacities of uniform linear, circular, and spherical antenna arrays. Again, the outage capacity C_{out} is calculated for a 1% outage probability and the physical model is used to calculate the outage capacity. In all simulations, a normalized sampling period $f_{T\max}T_s = 0.01$ is used and $M_A = N_A = 20$, and $M_E = N_E = 3$ scatterers and $N_{\text{stat}} = 50$ simulation trials are used in the statistical simulation model. The angles of motion for the $\mathrm{T_x}$ and $\mathrm{R_x}$ are chosen to be $\gamma_T = \gamma_R = 40°$. The maximum elevation angles are chosen to be $\beta_{T_m} = \beta_{R_m} = 15°$. The number of transmit and receive antennas is set to $L_T = L_R = 8$. Finally, isotropic scattering is assumed in the x - y plane, i.e., $k_T = k_R = 0$.

The coordinates of the ULA elements are calculated as in the previous section. The azimuth and elevation angles used for the ULA are $\theta_T = \theta_R = \pi/4$ and $\psi_T = \psi_R = \arcsin(1/\sqrt{3})$, respectively. The coordinates of the circular antenna array elements at the $\mathrm{T_x}$ and $\mathrm{R_x}$ are calculated using equations (143) - (145). The elevation angles used for the circular antenna arrays are $\psi_T = \psi_R = \arcsin(1/\sqrt{3})$. Finally, the coordinates of the spherical antenna array elements at the $\mathrm{T_x}$ and $\mathrm{R_x}$ are calculated using equations (146) - (148). The azimuth and elevation angles used for the spherical antenna arrays are $\theta_T^{(p)} = 2\pi p/L_T$, $\theta_T^{(\tilde{p})} = 2\pi\tilde{p}/L_T$, $\theta_R^{(q)} = 2\pi q/L_R$, $\theta_R^{(\tilde{q})} = 2\pi\tilde{q}/L_R$, and $\psi_T = \psi_R = \pm\arcsin(1/\sqrt{3})$.

There are two ways to compare antenna arrays. One maintains an equal spacing between two adjacent antenna elements in the uniform linear, circular, and spherical antenna arrays. The other designs uniform linear, circular, and spherical antenna arrays to occupy the same volume.

First, we assume that the spacings between two adjacent antenna elements of the uniform linear, circular, and spherical antenna arrays are equal, i.e., $d_T = d_R = 0.5\lambda$ and $r_T = r_R = 0.5\lambda/(2\sin(\pi/8))$. Figure 41 shows the outage capacity against SNR, ρ, for several uniform linear, circular, and spherical antenna arrays when isotropic scattering is assumed in the x - y plane ($k_T = k_R = 0$). As expected, non-tilted ($\psi_T = \psi_R = 0$) and tilted ($\psi_T = \psi_R = \arcsin(1/\sqrt{3})$) ULAs have a higher outage capacity than non-tilted and tilted circular and spherical antenna arrays because their non-adjacent antenna elements are placed further apart compared to circular and spherical antenna arrays. When isotropic scattering is assumed in the x - y plane, the orientations of ULAs have no influence on the capacity, and hence, ULAs will always provide higher capacity than circular and spherical antenna arrays. Note that when non-isotropic scattering is assumed in the x - y plane ($k_T, k_R > 0$), ULAs have higher capacity than circular and spherical antenna arrays only if the ULA orientation angles θ_T and θ_R are chosen to maximize the relative angles between the $\mathrm{T_x}$ and $\mathrm{R_x}$ antenna arrays and the local scatterers around the $\mathrm{T_x}$ and $\mathrm{R_x}$, i.e., $\mu_T - \theta_T$

and $\mu_R - \theta_R$, respectively. If the angles $\mu_T - \theta_T$ and $\mu_R - \theta_R$ are known to a reasonable accuracy, it is advantageous to deploy uniform linear antenna arrays with optimized angles θ_T and θ_R. Otherwise, circular antenna arrays may be a better choice because they will provide more a consistent outage capacity.

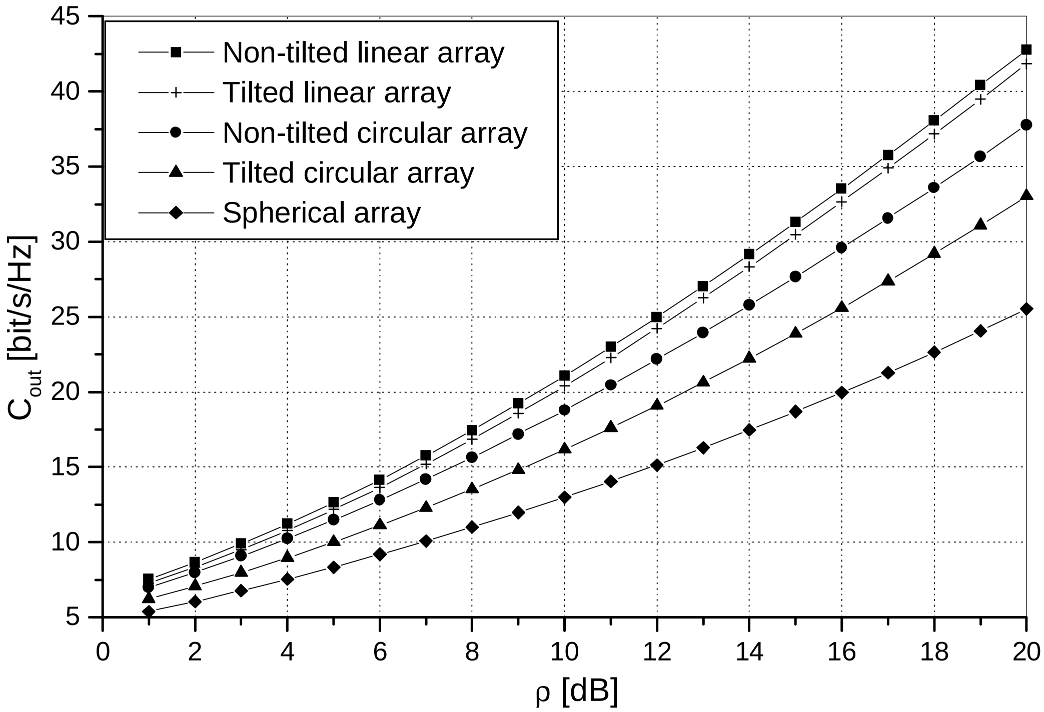

Figure 41: The outage capacity against SNR, ρ, for several uniform linear, circular, and spherical antenna arrays having equal spacing between two adjacent antenna elements.

In practice, the available volume for antenna array realization and packaging is often constrained. Suppose, for example, that the uniform linear, circular, and spherical antenna arrays are designed to fit in a sphere of radius $(\sqrt{3}/2)\lambda$. Then, the spacing between two adjacent antenna elements of the ULA is $d_T = d_R = (\sqrt{3}/8)\lambda$, whereas the radii of the circular and spherical antenna arrays are $r_T = r_R = (\sqrt{3}/2)\lambda$. It is assumed that omnidirectional antenna elements are realized as patch antennas. Figure 42 shows the outage capacity against SNR, ρ, for several uniform linear, circular and spherical antenna arrays occupying equal volume. As expected, the tilted ($\psi_T = \psi_R = \arcsin(1/\sqrt{3})$) uniform linear and circular antenna arrays have a smaller outage capacity compared to the non-tilted ($\psi_T = \psi_R = 0$) ones. An interesting result is that non-tilted circular antenna arrays have higher outage capacity than spherical antenna arrays by about 1 bit/s/Hz. Tilted circular and spherical antenna arrays have similar outage capacity, and a much higher outage capacity than non-tilted and tilted ULAs. From Fig. 42 we can conclude that if the available volume for antenna array realization is constrained, circular antenna arrays placed in the x - y plane will provide the highest outage capacity.

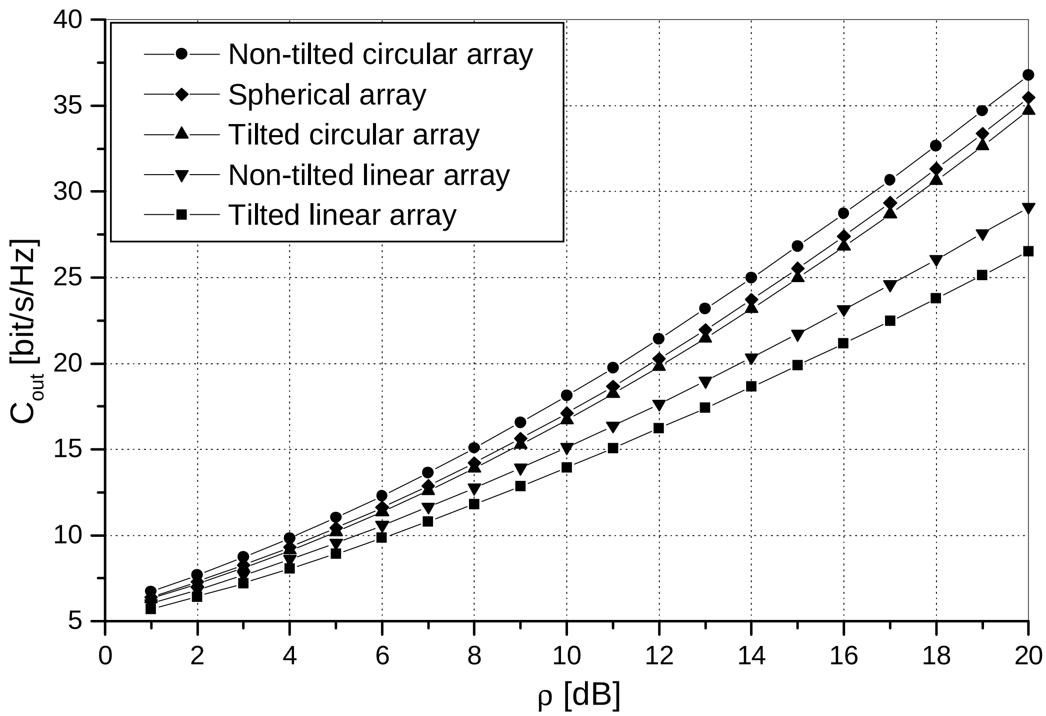

Figure 42: The outage capacity against SNR, ρ, for several uniform linear, circular and spherical antenna arrays occupying equal volume.

6.6 Summary

In this chapter, the “two-cylinder” geometrical propagation model is introduced. Based on this geometrical model, the 3-D reference model for MIMO M-to-M multipath fading channels is proposed. From the reference model, the closed-form joint space-time correlation function for a 3-D non-isotropic scattering environment is derived. Furthermore, the deterministic and statistical SoS simulation models for MIMO

M-to-M multipath-fading channels are proposed. The statistics of the simulation models are derived and verified by simulation. Finally, these simulation models are used to evaluate the effect of the space-time correlation on the outage capacity of uniform linear antenna arrays and to compare the capacities of linear, circular, and spherical antenna arrays.

CHAPTER VII

3-D MODELING AND SIMULATION OF WIDEBAND MIMO M-TO-M CHANNELS

7.1 Overview

In Chapter 6, we have proposed the narrowband 3-D models for MIMO M-to-M multipath fading channels. However, to completely characterize MIMO M-to-M multipath fading channels, it is necessary to develop 3-D models for *wideband* MIMO M-to-M channels.

The previously reported 2-D and 3-D models for M-to-M channels characterize outdoor NLoS radio propagation assuming that all rays are only double-bounced. Unfortunately, these models do not always match the measurements [40], [83], especially those when the vehicles are close to the large objects such as highway dividers or sound blockers on the edge of the highway. The possible reason for the mismatch is the presence of the single-bounced rays, which are ignored in the previously proposed models. Note that the single-bounced rays, if present, bear more energy than the double-bounced rays, and cannot be ignored. Hence, we propose a 3-D mathematical reference model for wideband MIMO M-to-M channels that combines the LoS, single-bounced, and double-bounced rays. To describe our 3-D reference model, we first introduce a 3-D geometrical model for wideband MIMO M-to-M channels, referred to as the "concentric-cylinders" model. This model is extension of the "two-cylinder" model for narrow-band M-to-M channels proposed in Chapter 6. Then, we propose the parametric reference model that employs a concentric-cylinders model and constructs the input delay-spread function as a superposition of LoS, single-bounced, and double-bounced rays. The parametric nature of the model makes it adaptable to a variety of propagation environments, i.e., urban and highway environments. From the new reference model, we derive a space-time-frequency correlation function (stf-cf) for a 3-D non-isotropic scattering environment. We present some simulation results to verify theoretical derivations and show that the time and frequency dispersion of a wide sense stationary uncorrelated scattering (WSSUS) channel cannot be treated independently. From the stf-cf, we derive the space-Doppler power spectral density (sD-psd) and the power space-delay spectrum (psds) for a 3-D non-isotropic scattering environment. Finally, we present some simulation results for the sD-psd and psds and compare them with SISO measured data to verify theoretical derivations. The close agreement between the theoretical and empirical curves confirms the utility of the proposed wideband model and implies that the input delay-spread function should be modeled as a superposition of LoS, single-bounced, and double-bounced rays.

The reference models assume an infinite number of scatterers, which prevents practical implementation. Hence, we propose an ergodic statistical (deterministic) SoS simulation model for a 3-D non-isotropic scattering environment. We employ a "concentric-cylinders" model that combines LoS, single-bounced, and double-bounced rays and has orthogonal functions as the I and Q components of the time-variant transfer function. The statistical properties of our model are verified by simulations. Furthermore, by allowing the phases, Doppler frequencies, and time delays to be random variables, the deterministic model can be modified to better match statistical properties of the reference model. This model is called the statistical simulation model. The statistical properties of this (statistical) model vary for each simulation trial, but will converge to desired ensemble averaged properties when averaged over a sufficient number of simulation trials. The statistical properties of this model are also verified by simulations. Compared to the deterministic model, the statistical properties of the statistical model match those of the reference model over a wider range of normalized time delays while using smaller number of scatterers.

The remainder of the chapter is organized as follows. Section 7.2 introduces the geometrical "concentric-cylinders" model and presents a 3-D reference model for wideband MIMO M-to-M channels. Section 7.3 derives the stf-cf, the sD-psd, and the psds for 3-D non-isotropic scattering. Section 7.4 details the deterministic and statistical SoS simulation models. Finally, Section 7.5 provides some concluding remarks.

7.2 A Reference Model for Wideband MIMO M-to-M Channels

This chapter considers a wideband MIMO communication system with L_t transmit and L_r receive omnidirectional antenna elements. It is assumed that both the $\mathrm{T_x}$ and $\mathrm{R_x}$ are in motion and equipped with low elevation antennas. The radio propagation occurs in outdoor metropolitan environments that are characterized by 3-D wide sense stationary uncorrelated scattering (WSSUS) with either LoS or NLoS conditions between the $\mathrm{T_x}$ and $\mathrm{R_x}$. The MIMO channel can be described by an $L_r \times L_t$ matrix $\mathbf{H}(t, \tau) = [h_{ij}(t, \tau)]_{L_r \times L_t}$ of the input delay-spread functions.

First, we introduce a 3-D geometrical model for wideband MIMO M-to-M channels, called a concentric-cylinders model. The vertical concentric cylinders are chosen because most of the scatterers in outdoor metropolitan environments (e.g., buildings, highway dividers, etc.) have straight vertical surfaces. Fig. 43 shows the concentric-cylinders model with LoS, single-, and double-bounced rays for a MIMO M-to-M channel with $L_t = L_r = 2$ antenna elements. This elementary 2×2 antenna configuration will be used later to construct uniform linear antenna arrays with an arbitrary number of omnidirectional antenna elements. The concentric-cylinders model defines four vertical cylinders, two around the $\mathrm{T_x}$ and another two around the $\mathrm{R_x}$, as shown in Fig. 43. Around the transmitter, M fixed omnidirectional scatterers occupy a volume between cylinders of radii R_{t1} and R_{t2}. It is assumed that the M scatterers lie on L cylindric surfaces of radii $R_{t1} \leq R_t^{(l)} \leq R_{t2}$, where $1 \leq l \leq L$. The

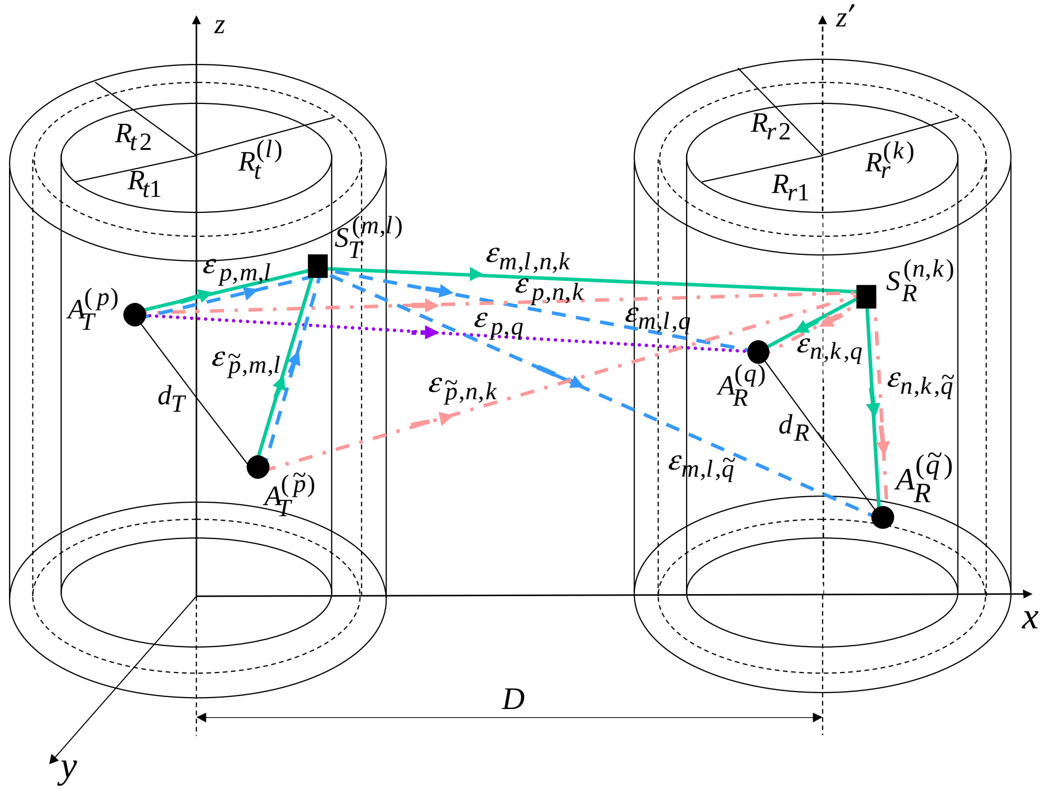

Figure 43: The concentric-cylinders model with LoS , single-bounced transmit, single-bounced receive, and double-bounced rays for a MIMO M-to-M channel with $L_t = L_r = 2$ antenna elements.

l^{th} cylindric surface contains $M^{(l)}$ fixed omnidirectional scatterers, and the $(m,l)^{th}$ transmit scatterer is denoted by $S_T^{(m,l)}$, where $1 \leq m \leq M^{(l)}$. Similarly, around the receiver, N fixed omnidirectional scatterers occupy a volume between cylinders of radii R_{r1} and R_{r2}. It is assumed that the N scatterers lie on F cylindric surfaces of radii $R_{r1} \leq R_r^{(k)} \leq R_{r2}$, where $1 \leq k \leq F$. The k^{th} cylindric surface contains $N^{(k)}$ fixed omnidirectional scatterers, and the $(n,k)^{th}$ receive scatterer is denoted by $S_R^{(n,k)}$, where $1 \leq n \leq N^{(k)}$. The distance between the centers of the $\mathrm{T_x}$ and $\mathrm{R_x}$ cylinders is D. It is assumed that the radii R_{t2} and R_{r2} are sufficiently smaller than the distance D (local scattering condition). Furthermore, it is assumed that the distance D is smaller than $4R_{t1}R_{r1}L_r/(\lambda(L_t-1)(L_r-1))$ (channel does not experience keyhole behavior [58]), where λ denotes the carrier wavelength. The spacing between antenna elements at the $\mathrm{T_x}$ and $\mathrm{R_x}$ is denoted by d_T and d_R, respectively. It is assumed that

d_T and d_R are much smaller than the radii R_{t1} and R_{r1}. The symbols $\epsilon_{p,m,l}$, $\epsilon_{m,l,q}$, $\epsilon_{p,n,k}$, $\epsilon_{n,k,q}$, $\epsilon_{m,l,n,k}$, and $\epsilon_{p,q}$ denote distances $A_T^{(p)}$ - $S_T^{(m,l)}$, $S_T^{(m,l)}$ - $A_R^{(q)}$, $A_T^{(p)}$ - $S_R^{(n,k)}$, $S_R^{(n,k)}$ - $A_R^{(q)}$, $S_T^{(m,l)}$ - $S_R^{(n,k)}$, and $A_T^{(p)}$ - $A_R^{(q)}$ respectively, as shown in Fig. 43. For ease of reference, Fig. 44 shows only one of the L cylindric surfaces around the $\mathrm{T_x}$ and one of F cylindric surfaces around the $\mathrm{R_x}$ and details the geometry of the LoS , single-bounced transmit, single-bounced receive, and double-bounced rays. Angles

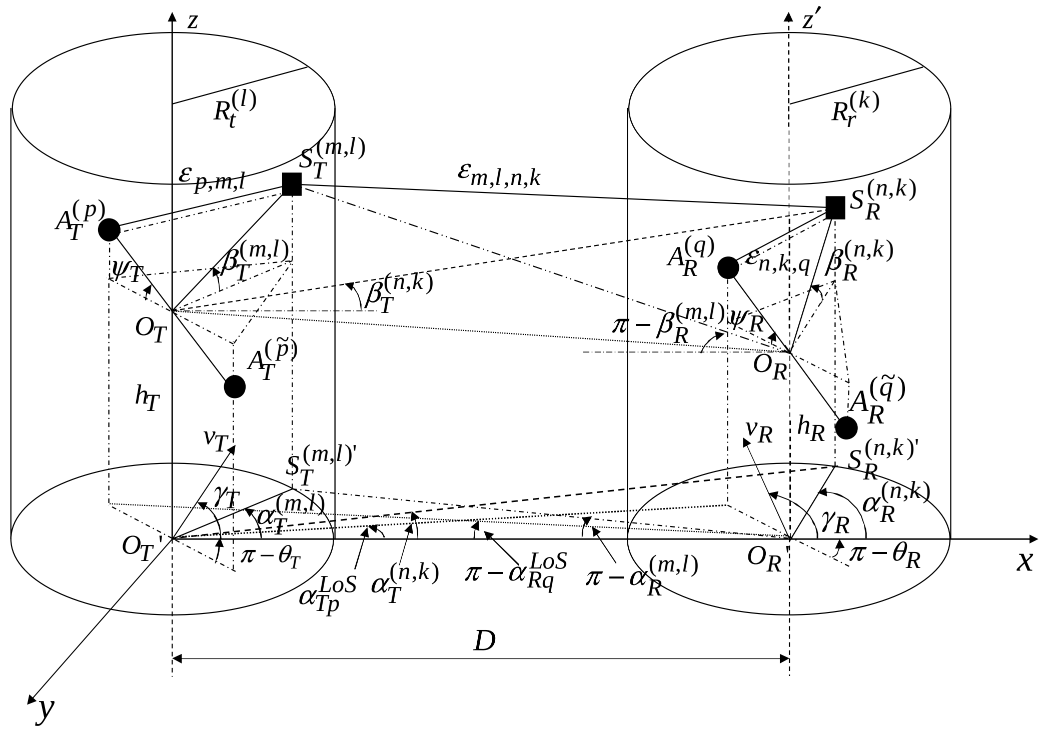

Figure 44: The l^{th} and k^{th} cylinders from Fig. 43 with the detailed geometry of the LoS , single-bounced transmit, single-bounced receive, and double-bounced rays.

θ_T and θ_R in Fig. 44 describe the orientation of the $\mathrm{T_x}$ and $\mathrm{R_x}$ antenna array in the x - y plane, respectively, relative to the x - axis. Similarly, angles ψ_T and ψ_R describe the elevation of the $\mathrm{T_x}$'s antenna array and the $\mathrm{R_x}$'s antenna array relative to the x - y plane, respectively. The $\mathrm{T_x}$ and $\mathrm{R_x}$ are moving with speeds v_T and v_R in directions described by angles γ_T and γ_R in the x - y plane (relative to the x - axis), respectively. The symbols $\alpha_T^{(m,l)}$ and $\alpha_T^{(n,k)}$ are the azimuth angles of departures (AAoD) of the waves that impinge on the scatterers $S_T^{(m,l)}$ and $S_R^{(n,k)}$, whereas $\alpha_R^{(m,l)}$ and $\alpha_R^{(n,k)}$ are the azimuth angles of arrivals (AAoA) of the waves scattered from $S_T^{(m,l)}$ and $S_R^{(n,k)}$, respectively. Similarly, the symbols $\beta_T^{(m,l)}$ and $\beta_R^{(n,k)}$ denote the elevation angle of departure (EAoD) and the elevation angle of arrival (EAoA), respectively. Finally, the symbols α_{Rq}^{LoS}, α_{Tp}^{LoS} denote the AAoDs and AAoAs of the LoS paths. For ease of reference, the parameters defined in Figs. 43 and 44 are summarized in Table 8.

Table 8: Definition of the parameters used in the concentric-cylinders geometrical model.

D	The distance between the centers of the Tx and Rx cylinders.
$R_t^{(l)}, R_r^{(k)}$	The radius of the l^{th} Tx and k^{th} Rx cylinder, respectively.
d_T , d_R	The spacing between two adjacent antenna elements at the Tx and Rx, respectively.
θ_T , θ_R	The orientation of the Tx and Rx antenna array in the x-y plane (relative to the *x*-axis), respectively.
ψ_T , ψ_R	The elevation of the Tx's and Rx's antenna array relative to the x-y plane, respectively.
v_T , v_R	The velocities of the Tx and Rx, respectively.
γ_T , γ_R	The moving directions of the Tx and Rx, in the x-y plane (relative to the *x*-axis), respectively.
h_T , h_R	The distances $d\left(O_T, O_T^{'}\right)$ and $d\left(O_R, O_R^{'}\right)$, respectively.
R_{t1}, R_{t2}, R_{r1}, R_{r2}	The min and max radii of the cylinders around the Tx and Rx, respectively.
$\alpha_T^{(m,l)}, \alpha_T^{(n,k)}$	The azimuth angles of departure (AAoD) of the waves that impinge on the scatterers $S_T^{(m,l)}$ and $S_R^{(n,k)}$, respectively.
$\alpha_R^{(m,l)}, \alpha_R^{(n,k)}$	The azimuth angles of arrival (AAoA) of the waves scattered from $S_T^{(m,l)}$ and $S_R^{(n,k)}$, respectively.
$\beta_T^{(m,l)}, \beta_T^{(n,k)}$	The elevation angles of departure (EAoD) of the waves that impinge on the scatterers $S_T^{(m,l)}$ and $S_R^{(n,k)}$, respectively.
$\beta_R^{(m,l)}, \beta_R^{(n,k)}$	The elevation angles of arrival (EAoA) of the waves scattered from $S_T^{(m,l)}$ and $S_R^{(n,k)}$, respectively.
α_{Rq}^{LoS} , α_{Tp}^{LoS}	The AAoA and the AAoD of the LoS paths, respectively.
$\varepsilon_{p,m,l}$, $\varepsilon_{m,l,q}$, $\varepsilon_{p,n,k}$, $\varepsilon_{n,k,q}$, $\varepsilon_{m,l,n,k}$ and ε_{pq}	The distances $d\left(A_T^{(p)}, S_T^{(m,l)}\right)$, $d\left(S_T^{(m,l)}, A_R^{(q)}\right)$, $d\left(A_T^{(p)}, S_R^{(n,k)}\right)$, $d\left(S_T^{(m)}, S_R^{(n)}\right)$, $d\left(S_R^{(n,k)}, A_R^{(q)}\right)$, $d\left(S_T^{(m,l)}, S_R^{(n,k)}\right)$, and $d\left(A_T^{(p)}, A_R^{(q)}\right)$, respectively.

Observe from the 3-D geometrical model in Fig. 43 that some waves from the T_x antenna elements may traverse directly to the R_x antenna elements (LoS rays) , while others are single-bounced at the T_x (i.e., the waves from the T_x antenna elements scatter from the scatterers located around the $\mathrm{T_x}$ before arriving at the $\mathrm{R_x}$ antenna elements), single-bounced at the $\mathrm{R_x}$ (i.e., the waves from the $\mathrm{T_x}$ antenna elements scatter from the scatterers located around the $\mathrm{R_x}$ before arriving at the $\mathrm{R_x}$ antenna elements), and/or double-bounced (i.e., the waves from the $\mathrm{T_x}$ antenna elements impinge on the scatterers located around the $\mathrm{T_x}$ and scatter from the scatterers located around the $\mathrm{R_x}$ before arriving at the $\mathrm{R_x}$ antenna elements). Hence, the input delay-spread function of the link $A_T^{(p)}$ - $A_R^{(q)}$ can be written as a superposition of the LoS, single-bounced transmit (SBT), single-bounced receive (SBR) and double-bounced (DB) rays

$$h_{pq}(t,\tau) \;=\; h_{pq}^{SBT}(t,\tau)+h_{pq}^{SBR}(t,\tau)+h_{pq}^{DB}(t,\tau)+h_{pq}^{LoS}(t,\tau). \tag{179}$$

The single-bounced components of the input delay-spread function are, respectively,

$$h_{pq}^{SBT}(t,\tau)=\sqrt{\frac{\eta_T}{K+1}}\lim_{M\to\infty}\frac{1}{\sqrt{M}}$$
$$\sum_{l=1}^{L}\sum_{m=1}^{M^{(l)}}\sqrt{G_p\left(\alpha_T^{(m,l)},\beta_T^{(m,l)}\right)G_q\left(\alpha_R^{(m,l)},\beta_R^{(m,l)}\right)}\xi_{m,l}g_{m,l}(t)\delta(\tau-\tau_{m,l}), \tag{180}$$

$$h_{pq}^{SBR}(t,\tau)=\sqrt{\frac{\eta_R}{K+1}}\lim_{N\to\infty}\frac{1}{\sqrt{N}}$$
$$\sum_{k=1}^{F}\sum_{n=1}^{N^{(k)}}\sqrt{G_p\left(\alpha_T^{(n,k)},\beta_T^{(n,k)}\right)G_q\left(\alpha_R^{(n,k)},\beta_R^{(n,k)}\right)}\xi_{n,k}g_{n,k}(t)\delta(\tau-\tau_{n,k}), \tag{181}$$

where $G_p(\cdot,\cdot)$ and $G_q(\cdot,\cdot)$ denote the antenna patterns of the p^{th} transmit and q^{th} receive antenna element, respectively. Furthermore, $\xi_{m,l}$, $\xi_{n,k}$, $\tau_{m,l}$, and $\tau_{n,k}$ denote the amplitudes and time delays of the multipath components, respectively. Finally, functions $g_{m,l}(t)$ and $g_{n,k}(t)$ are defined as

$$g_{m,l}(t)= \tag{182}$$
$$e^{-j\frac{2\pi}{\lambda}\left(\epsilon_{p,m,l}+\epsilon_{m,l,q}\right)+j2\pi t\left[f_{T\max}\cos\left(\alpha_T^{(m,l)}-\gamma_T\right)\cos\beta_T^{(m,l)}+f_{R\max}\cos\left(\alpha_R^{(m,l)}-\gamma_R\right)\cos\beta_R^{(m,l)}\right]+j\phi_{m,l}},$$

$$g_{n,k}(t)= \tag{183}$$
$$e^{-j\frac{2\pi}{\lambda}\left(\epsilon_{p,n,k}+\epsilon_{n,k,q}\right)+j2\pi t\left[f_{T\max}\cos\left(\alpha_T^{(n,k)}-\gamma_T\right)\cos\beta_T^{(n,k)}+f_{R\max}\cos\left(\alpha_R^{(n,k)}-\gamma_R\right)\cos\beta_R^{(n,k)}\right]+j\phi_{n,k}},$$

where $f_{T\max} = \upsilon_T/\lambda$ and $f_{R\max} = \upsilon_R/\lambda$ are the maximum Doppler frequencies associated with the $\mathrm{T_x}$ and $\mathrm{R_x}$, respectively. The amplitudes of the multipath components, $\xi_{m,l}$ and $\xi_{n,k}$, are defined as

$$\xi_{m,l} = \frac{\sqrt{P_{pq}}\lambda}{4\pi}\left[\left|d\left(O_T, S^{(m,l)}\right)\right| + \left|d\left(S^{(m,l)}, O_R\right)\right|\right]^{-\gamma/2} \approx \Omega_{pq}\left(1 - \frac{\gamma}{2}\frac{R_t^{(l)}}{D}\right), \quad (184)$$

$$\xi_{n,k} = \frac{\sqrt{P_{pq}}\lambda}{4\pi}\left[\left|d\left(O_T, S^{(n,k)}\right)\right| + \left|d\left(S^{(n,k)}, O_R\right)\right|\right]^{-\gamma/2} \approx \Omega_{pq}\left(1 - \frac{\gamma}{2}\frac{R_r^{(k)}}{D}\right), \quad (185)$$

respectively, where P_{pq} is the power transmitted through the subchannel $A_T^{(p)}$ - $A_R^{(q)}$, K is the Rice factor (ratio of LoS to scatter received power), γ is the path loss exponent, $d(\cdot,\cdot)$ denotes distance between two points, and $\Omega_{pq} = D^{-\gamma/2}\sqrt{P_{pq}}\lambda/4\pi$. Finally, the time delays $\tau_{m,l}$ and $\tau_{n,k}$ are defined as the travel times of the waves scattered from the scatterers $S_T^{(m,l)}$ and $S_R^{(n,k)}$, i.e.,

$$\tau_{m,l} = \frac{D + R_t^{(l)}(1 - \cos\alpha_T^{(m,l)})}{c_0 \cos\beta_T^{(m,l)}} \quad (186)$$

$$\tau_{n,k} = \frac{D + R_r^{(k)}(1 + \cos\alpha_R^{(n,k)})}{c_0 \cos\beta_R^{(n,k)}}, \quad (187)$$

where c_0 is the speed of light. The double-bounced component of the input delay-spread function is

$$h_{pq}(t,\tau) = \sqrt{\frac{\eta_{TR}}{K+1}} \lim_{M,N\to\infty} \frac{1}{\sqrt{MN}} \quad (188)$$
$$\sum_{l,m=1}^{L,M^{(l)}} \sum_{k,n=1}^{F,N^{(k)}} \sqrt{G_p\left(\alpha_T^{(m,l)}, \beta_T^{(m,l)}\right) G_q\left(\alpha_R^{(n,k)}, \beta_R^{(n,k)}\right)}\,\xi_{m,l,n,k}\, g_{m,l,n,k}(t)\,\delta(\tau - \tau_{m,l,n,k}),$$

where $G_p(\cdot,\cdot)$ and $G_q(\cdot,\cdot)$ denote the antenna patterns of the p^{th} transmit and q^{th} receive antenna element, respectively, and $\xi_{m,l,n,k}$ and $\tau_{m,l,n,k}$ are the amplitude and time delay of the multipath component, respectively. Function $g_{m,l,n,k}(t)$ is defined as

$$\begin{aligned} g_{m,l,n,k}(t) &= e^{-j\frac{2\pi}{\lambda}\left(\epsilon_{p,m,l}+\epsilon_{m,l,n,k}+\epsilon_{n,k,q}\right)+j\phi_{m,l,n,k}} \\ &\times\ e^{j2\pi t\left[f_{T\max}\cos\left(\alpha_T^{(m,l)}-\gamma_T\right)\cos\beta_T^{(m,l)}+f_{R\max}\cos\left(\alpha_R^{(n,k)}-\gamma_R\right)\cos\beta_R^{(n,k)}\right]}. \end{aligned} \quad (189)$$

The amplitude of the multipath component, $\xi_{m,l,n,k}$, is defined as

$$\begin{aligned} \xi_{m,l,n,k} &= \frac{\sqrt{P_{pq}}\lambda}{4\pi}\left[\left|d\left(O_T{}', S^{(m,l)}\right)\right| + \left|d\left(S^{(m,l)}, S^{(n,k)}\right)\right| + \left|d\left(S^{(n,k)}, O_R'\right)\right|\right]^{\gamma/2} \\ &\approx \Omega_{pq}\left(1 - \frac{\gamma}{2}\frac{R_t^{(l)} + R_r^{(k)}}{2D}\right). \end{aligned} \tag{190}$$

Finally, the time delay $\tau_{m,l,n,k}$ is defined as the travel time of the wave impinged on the scatterer $S_T^{(m,l)}$ and scattered from the scatterer $S_R^{(n,k)}$, i.e.,

$$\tau_{m,l,n,k} = \frac{D}{c_0} + \frac{R_t^{(l)}(1 - \cos\alpha_T^{(m,l)})}{c_0\cos\beta_T^{(m,l)}} + \frac{R_r^{(k)}(1 + \cos\alpha_R^{(n,k)})}{c_0\cos\beta_R^{(n,k)}}. \tag{191}$$

The parameters η_T, η_R, and η_{TR} in (180), (181), and (188), respectively, specify how much the single- and double-bounced rays contribute in the total power P_{pq}, i.e., these parameters satisfy $\eta_T + \eta_R + \eta_{TR} = 1$. It is assumed that the angles of departures ($\alpha_T^{(m,l)}$, $\alpha_T^{(n,k)}$, $\beta_T^{(m,l)}$, and $\beta_T^{(n,k)}$) and the angles of arrivals ($\alpha_R^{(n,k)}$, $\alpha_R^{(m,l)}$, $\beta_R^{(n,k)}$, and $\beta_R^{(m,l)}$) are random variables. Furthermore, it is assumed that the radii $R_t^{(l)}$ and $R_r^{(k)}$ are independent random variables. Finally, it is assumed that the phases $\phi_{m,l}$, $\phi_{n,k}$, and $\phi_{m,l,n,k}$ are random variables uniformly distributed on the interval $[-\pi, \pi)$ and independent from the angles of departure, the angles of arrival, and the radii of the cylinders. Using the assumptions introduced above and the Central Limit Theorem [76], we can conclude that $h_{pq}^{SBT}(t,\tau)$, $h_{pq}^{SBR}(t,\tau)$, and $h_{pq}^{DB}(t,\tau)$ are independent complex Gaussian random processes with zero means. Furthermore, note that double-bounced rays have the angles of departure ($\alpha_T^{(m,l)}$ and $\beta_T^{(m,l)}$) independent from the angles of arrival ($\alpha_R^{(n,k)}$ and $\beta_R^{(n,k)}$) [58]. On the other hand, single-bounced rays have angles of arrival ($\alpha_R^{(m,l)}$ and $\beta_R^{(m,l)}$) that are dependent on the angles of departure ($\alpha_T^{(m,l)}$ and $\beta_T^{(m,l)}$) and angles of departure ($\alpha_T^{(n,k)}$ and $\beta_T^{(n,k)}$) that are dependent on the angles of arrival ($\alpha_R^{(n,k)}$ and $\beta_R^{(n,k)}$). Appendix H shows that

$$\alpha_R^{(m,l)} \approx \pi - \Delta_T^{(l)}\sin\alpha_T^{(m,l)}, \tag{192}$$

$$\beta_R^{(m,l)} \approx \pi - \left(\Delta_T^{(l)}\beta_T^{(m,l)} + \Delta_H/D\right), \tag{193}$$

$$\alpha_T^{(n,k)} \approx \Delta_R^{(k)}\sin\alpha_R^{(n,k)}, \tag{194}$$

$$\beta_T^{(n,k)} \approx \Delta_R^{(k)} \beta_R^{(n,k)} - \Delta_H / D, \tag{195}$$

where $\Delta_T^{(l)} = R_t^{(l)}/D$ and $\Delta_R^{(k)} = R_r/D$.

The LoS component of the input delay-spread function is

$$\begin{aligned} h_{pq}^{LoS}(t,\tau) &= \sqrt{\frac{K}{K+1}}\sqrt{G_p\left(\alpha_{Tp}^{LoS},\beta_{Tp}^{LoS}\right)G_q\left(\alpha_{Rq}^{LoS},\beta_{Rq}^{LoS}\right)} \\ &\times \xi_{LoS} e^{j2\pi t f_{T\max}\cos(\alpha_{Tp}^{LoS}-\gamma_T)+j2\pi t f_{R\max}\cos(\alpha_{Rq}^{LoS}-\gamma_R)-j\frac{2\pi}{\lambda}\epsilon_{p,q}}\delta(\tau-\tau_{LoS}), \end{aligned} \tag{196}$$

where $G_p(\cdot,\cdot)$ and $G_q(\cdot,\cdot)$ denote the antenna patterns of the p^{th} transmit and q^{th} receive antenna element, respectively, the LoS amplitude is $\xi_{LoS} \approx \Omega_{pq}$, and the LoS time delay is $\tau_{LoS} = \sqrt{D^2+\Delta_H^2}/c_0$.

Appendix I shows tha the distances $\epsilon_{m,l,q}$, $\epsilon_{p,n,k}$, $\epsilon_{p,m,l}$, $\epsilon_{n,k,q}$, $\epsilon_{m,l,n,k}$, and $\epsilon_{p,q}$ can be expressed as functions of the random variables $\alpha_T^{(m,l)}$, $\beta_T^{(m,l)}$, $\alpha_R^{(n,k)}$, $\beta_R^{(n,k)}$, α_{Rq}^{LoS}, $R_t^{(l)}$, and $R_r^{(k)}$ as follows:

$$\epsilon_{m,l,q} \approx D - \frac{L_r+1-2q}{2} d_R \cos\psi_R \left[\Delta_T^{(l)} \sin\theta_R \sin\alpha_T^{(m,l)} - \cos\theta_R\right], \tag{197}$$

$$\epsilon_{p,n,k} \approx D - \frac{L_t+1-2p}{2} d_T \cos\psi_T \left[\Delta_R^{(k)} \sin\theta_T \sin\alpha_R^{(n,k)} + \cos\theta_T\right], \tag{198}$$

$$\begin{aligned} \epsilon_{p,m,l} &\approx R_t^{(l)} - \frac{L_t+1-2p}{2} \\ &\times \left[d_{Tx}\cos\alpha_T^{(m,l)}\cos\beta_T^{(m,l)} + d_{Ty}\sin\alpha_T^{(m,l)}\cos\beta_T^{(m,l)} + d_{Tz}\sin\beta_T^{(m,l)}\right], \end{aligned} \tag{199}$$

$$\begin{aligned} \epsilon_{n,k,q} &\approx R_r^{(k)} - \frac{L_r+1-2q}{2} \\ &\times \left[d_{Rx}\cos\alpha_R^{(n,k)}\cos\beta_R^{(n,k)} + d_{Ry}\sin\alpha_R^{(n,k)}\cos\beta_R^{(n,k)} + d_{Rz}\sin\beta_R^{(n,k)}\right], \end{aligned} \tag{200}$$

$$\epsilon_{m,l,n,k} \approx D, \tag{201}$$

$$\begin{aligned} \epsilon_{p,q} &\approx D \\ &- \frac{L_t+1-2p}{2} d_T \cos\psi_T \cos\theta_T - \frac{L_r+1-2q}{2} d_R \cos\psi_R \cos(\alpha_{Rq}^{LoS} - \theta_R), \end{aligned} \tag{202}$$

where parameters p and q take values from the sets $p \in \{1,\ldots,L_t\}$ and $q \in \{1,\ldots,L_r\}$, respectively, $d_{Tx} = d_T\cos\psi_T\cos\theta_T$, $d_{Ty} = d_T\cos\psi_T\sin\theta_T$, $d_{Tz} = d_T\sin\psi_T$, $d_{Rx} = d_R\cos\psi_R\cos\theta_R$, $d_{Ry} = d_R\cos\psi_R\sin\theta_R$, and $d_{Rz} = d_R\sin\psi_R$.

To simplify further analysis, we use the time-variant transfer function instead of the input delay-spread function. The time-variant transfer function is defined as the

Fourier transform of the input delay-spread function [35]. Using (179) - (202), the time-variant transfer function can be written as

$$T_{pq}(t,f) = \mathcal{F}_\tau\left\{h_{pq}(t,\tau)\right\} = T_{pq}^{SBT}(t,f) + T_{pq}^{SBR}(t,f) + T_{pq}^{DB}(t,f) + T_{pq}^{LoS}(t,f), \quad (203)$$

where the single-bounced transmit, single-bounced receive, double-bounced, and LoS components of the time-variant transfer function are, respectively,

$$\begin{aligned}
T_{pq}^{SBT}(t,f) &= \mathcal{F}_\tau\left\{h_{pq}^{SBT}(t,\tau)\right\} && (204)\\
&= \Omega_{pq}\sqrt{\frac{\eta_T}{K+1}}\lim_{M\to\infty}\sum_{l=1}^{L}\sum_{m=1}^{M^{(l)}}\frac{\left(1-\frac{\gamma}{2}\frac{R_t^{(l)}}{D}\right)}{\sqrt{M}}a_{p,m,l}^{SBT}b_{q,m,l}^{SBT}\\
&\times\ e^{j2\pi t f_{R\max}(\cos\gamma_R-\Delta_T^{(l)}\sin\gamma_R\sin\alpha_T^{(m,l)})\cos(\Delta_T^{(l)}\beta_T^{(m,l)}+\Delta_H/D)}\\
&\times\ e^{j2\pi t f_{T\max}\cos(\alpha_T^{(m,l)}-\gamma_T)\cos\beta_T^{(m,l)}}e^{-j\frac{2\pi}{c_0\cos\beta_T^{(m,l)}}f[D+R_t^{(l)}(1-\cos\alpha_T^{(m,l)})]+j\phi_{m,l}},\\
T_{pq}^{SBR}(t,f) &= \mathcal{F}_\tau\left\{h_{pq}^{SBR}(t,\tau)\right\} && (205)\\
&= \Omega_{pq}\sqrt{\frac{\eta_R}{K+1}}\lim_{N\to\infty}\sum_{k=1}^{K}\sum_{n=1}^{N^{(k)}}\frac{\left(1-\frac{\gamma}{2}\frac{R_r^{(k)}}{D}\right)}{\sqrt{N}}a_{p,n,k}^{SBR}b_{q,n,k}^{SBR}\\
&\times\ e^{j2\pi t f_{T\max}(\Delta_R^{(k)}\sin\gamma_T\sin\alpha_R^{(n,k)}+\cos\gamma_T)\cos(\Delta_R^{(k)}\beta_R^{(n,k)}+\Delta_H/D)}\\
&\times\ e^{j2\pi t f_{R\max}\cos(\alpha_R^{(n,k)}-\gamma_R)\beta_R^{(n,k)}}e^{-j\frac{2\pi}{c_0\cos\beta_R^{(n,k)}}f[D+R_r^{(k)}(1+\cos\alpha_R^{(n,k)})]+j\phi_{n,k}},\\
T_{pq}^{DB}(t,f) &= \mathcal{F}_\tau\left\{h_{pq}^{DB}(t,\tau)\right\} && (206)\\
&= \Omega_{pq}\sqrt{\frac{\eta_{TR}}{K+1}}\lim_{M,N\to\infty}\sum_{l,m=1}^{L,M^{(l)}}\sum_{k,n=1}^{K,N^{(k)}}\frac{\left(1-\frac{\gamma}{2}\frac{R_t^{(l)}+R_r^{(k)}}{2D}\right)}{\sqrt{MN}}a_{p,m,l}^{DB}b_{q,n,k}^{DB}\\
&\times\ e^{j2\pi t[f_{T\max}\cos(\alpha_T^{(m,l)}-\gamma_T)\cos\beta_T^{(m,l)}+f_{R\max}\cos(\alpha_R^{(n,k)}-\gamma_R)\cos\beta_R^{(n,k)}]}\\
&\times\ e^{-j\frac{2\pi}{c_0}f[D+\frac{R_t^{(l)}(1-\cos\alpha_T^{(m,l)})}{\cos\beta_T^{(m,l)}}+\frac{R_r^{(k)}(1+\cos\alpha_R^{(n,k)})}{\cos\beta_R^{(n,k)}}]+j\phi_{m,l,n,k}},\\
T_{pq}^{LoS}(t,f) &= \mathcal{F}_\tau\left\{h_{pq}^{LoS}(t,\tau)\right\} = \Omega_{pq}\sqrt{\frac{K}{1+K}} && (207)\\
&\times\ e^{j2\pi t[f_{T\max}\cos(\pi-\alpha_{Rq}^{LoS}-\gamma_T)+f_{R\max}\cos(\alpha_{Rq}^{LoS}-\gamma_R)]}e^{-j\frac{2\pi}{c_0}f\sqrt{D^2+\Delta H^2}-j\frac{2\pi}{\lambda}D}\\
&\times\ e^{j\frac{2\pi}{\lambda}[(0.5L_t+0.5-p)d_T\cos\theta_T\cos\psi_T+(0.5L_r+0.5-q)d_R\cos\psi_R\cos(\alpha_{Rq}^{LoS}-\theta_R)]},
\end{aligned}$$

where parameters $a^{SBT}_{p,m,l}$, $b^{SBT}_{q,m,l}$, $a^{SBR}_{p,n,k}$, $b^{SBR}_{q,n,k}$, $a^{DB}_{p,m,l}$, and $b^{DB}_{q,n,k}$ are, respectively,

$$
\begin{aligned}
a^{SBT}_{p,m,l} &= e^{j\frac{2\pi}{\lambda}(0.5L_t+0.5-p)[d_{Tx}\cos\alpha_T^{(m,l)}\cos\beta_T^{(m,l)}+d_{Ty}\sin\alpha_T^{(m,l)}\cos\beta_T^{(m,l)}+d_{Tz}\sin\beta_T^{(m,l)}]}, && (208)\\
b^{SBT}_{q,m,l} &= e^{j\frac{2\pi}{\lambda}(0.5L_r+0.5-q)d_R\cos\psi_R[\Delta_T^{(l)}\sin\theta_R\sin\alpha_T^{(m,l)}-\cos\theta_R]-j\frac{2\pi}{\lambda}(D+R_t^{(l)})}, && (209)\\
a^{SBR}_{p,n,k} &= e^{j\frac{2\pi}{\lambda}(0.5L_t+0.5-p)d_T\cos\psi_T[\Delta_R^{(k)}\sin\theta_T\sin\alpha_R^{(n,k)}+\cos\theta_T]-j\frac{2\pi}{\lambda}(D+R_r^{(k)})}, && (210)\\
b^{SBR}_{q,n,k} &= e^{j\frac{2\pi}{\lambda}(0.5L_r+0.5-q)[d_{Rx}\cos\alpha_R^{(n,k)}\cos\beta_R^{(n,k)}+d_{Ry}\sin\alpha_R^{(n,k)}\cos\beta_R^{(n,k)}+d_{Rz}\sin\beta_R^{(n,k)}]}, && (211)\\
a^{DB}_{p,m,l} &= e^{j\frac{2\pi}{\lambda}(0.5L_t+0.5-p)[d_{Tx}\cos\alpha_T^{(m,l)}\cos\beta_T^{(m,l)}+d_{Ty}\sin\alpha_T^{(m,l)}\cos\beta_T^{(m,l)}+d_{Tz}\sin\beta_T^{(m,l)}]}\\
&\times\ e^{-j\frac{2\pi}{\lambda}(D/2+R_t^{(l)})}, && (212)\\
b^{DB}_{q,n,k} &= e^{j\frac{2\pi}{\lambda}(0.5L_r+0.5-q)[d_{Rx}\cos\alpha_R^{(n,k)}\cos\beta_R^{(n,k)}+d_{Ry}\sin\alpha_R^{(n,k)}\cos\beta_R^{(n,k)}+d_{Rz}\sin\beta_R^{(n,k)}]}\\
&\times\ e^{-j\frac{2\pi}{\lambda}(D/2+R_r^{(k)})}. && (213)
\end{aligned}
$$

7.3 *Stf-cf, SD-psd, Psds of the 3-D Reference Model*

Assuming a 3-D non-isotropic scattering environment, we first derive the stf-cf of the 3-D reference model. Then, we present some simulation results to verify theoretical derivations and show that the time and frequency dispersion of WSSUS channel cannot be treated independently. Using the derived stf-cf, we derive the sD-psd and the psds for a 3-D non-isotropic scattering environment. Finally, we present some simulation results for the sD-psd and psds and compare them with measured data.

7.3.1 Space-time-frequency Correlation Function (stf-cf)

The normalized stf-cf between two time-variant transfer functions defined in (203), i.e., $T_{pq}(t,f)$ and $T_{\tilde{p}\tilde{q}}(t,f)$, is defined as

$$
R_{pq,\tilde{p}\tilde{q}}(\Delta t,\Delta f) = \frac{\mathrm{E}\left[T_{pq}(t,f)^{*}T_{\tilde{p}\tilde{q}}(t+\Delta t,f+\Delta f)\right]}{\sqrt{\mathrm{Var}[T_{pq}(t,f)]\mathrm{Var}[T_{\tilde{p}\tilde{q}}(t,f)]}}, \qquad (214)
$$

where $(\ \cdot\ )^{*}$ denotes complex conjugate operation, $\mathrm{E}[\ \cdot\ ]$ is the statistical expectation operator, $\mathrm{Var}[\ \cdot\ ]$ is the statistical variance operator, $p,\tilde{p}\in\{1,\ldots,L_t\}$, $q,\tilde{q}\in\{1,\ldots,L_r\}$. Since $T^{SBT}_{pq}(t,f)$, $T^{SBR}_{pq}(t,f)$, and $T^{DB}_{pq}(t,f)$ are independent complex

Gaussian random processes with zero means, (214) can be simplified to

$$\begin{aligned} R_{pq,\tilde{p}\tilde{q}}(\Delta t, \Delta f) &= R^{SBT}_{pq,\tilde{p}\tilde{q}}(\Delta t, \Delta f) + R^{SBR}_{pq,\tilde{p}\tilde{q}}(\Delta t, \Delta f) \\ &+ R^{DB}_{pq,\tilde{p}\tilde{q}}(\Delta t, \Delta f) + R^{LoS}_{pq,\tilde{p}\tilde{q}}(\Delta t, \Delta f), \end{aligned} \tag{215}$$

where $R^{SBT}_{pq,\tilde{p}\tilde{q}}(\Delta t, \Delta f)$, $R^{SBR}_{pq,\tilde{p}\tilde{q}}(\Delta t, \Delta f)$, $R^{DB}_{pq,\tilde{p}\tilde{q}}(\Delta t, \Delta f)$, and $R^{LoS}_{pq,\tilde{p}\tilde{q}}(\Delta t, \Delta f)$ denote the normalized stf-cfs of the single-bounced transmit, single-bounced receive, double-bounced, and LoS components, respectively, and are defined as

$$R^{SBT}_{pq,\tilde{p}\tilde{q}}(\Delta t, \Delta f) = \frac{\mathrm{E}\left[T^{SBT}_{pq}(t,f)^* T^{SBT}_{\tilde{p}\tilde{q}}(t+\Delta t, f+\Delta f)\right]}{\Omega_{pq}/(1+K)}, \tag{216}$$

$$R^{SBR}_{pq,\tilde{p}\tilde{q}}(\Delta t, \Delta f) = \frac{\mathrm{E}\left[T^{SBR}_{pq}(t,f)^* T^{SBR}_{\tilde{p}\tilde{q}}(t+\Delta t, f+\Delta f)\right]}{\Omega_{pq}/(1+K)}, \tag{217}$$

$$R^{DB}_{pq,\tilde{p}\tilde{q}}(\Delta t, \Delta f) = \frac{\mathrm{E}\left[T^{DB}_{pq}(t,f)^* T^{DB}_{\tilde{p}\tilde{q}}(t+\Delta t, f+\Delta f)\right]}{\Omega_{pq}/(1+K)}, \tag{218}$$

$$R^{LoS}_{pq,\tilde{p}\tilde{q}}(\Delta t, \Delta f) = \frac{\mathrm{E}\left[T^{LoS}_{pq}(t,f)^* T^{LoS}_{\tilde{p}\tilde{q}}(t+\Delta t, f+\Delta f)\right]}{\Omega_{pq}/(K+1)}. \tag{219}$$

Since the number of local scatterers in the reference model described in Section 7.2 is infinite, the discrete AAoDs, $\alpha_T^{(m,l)}$, EAoDs, $\beta_T^{(m,l)}$, AAoAs, $\alpha_R^{(n,k)}$, EAoAs, $\beta_R^{(n,k)}$, and radii $R_t^{(l)}$ and $R_r^{(k)}$ can be replaced with continuous random variables α_T, β_T, α_R, β_R, R_t, and R_r with joint probability density functions (pdfs) $f(\alpha_T, \beta_T, R_t)$ and $f(\alpha_R, \beta_R, R_r)$, respectively. We assume that the azimuth angles, elevation angles, and radii are independent of each other, and thus, the joint pdfs $f(\alpha_T, \beta_T, R_t)$ and $f(\alpha_R, \beta_R, R_r)$ can be decomposed to $f(\alpha_T)f(\beta_T)f(R_t)$ and $f(\alpha_R)f(\beta_R)f(R_r)$, respectively. This assumption is based on experimental data in [70], [71]. To characterize the random azimuth angles α_T and α_R, we use the von Mises pdf given in (96). To characterize the random elevation angles β_T and β_R, we use the pdf in (152). To characterize the radii R_t and R_r we use the pdfs $f(R_t) = 2R_t/(R_{t2}^2 - R_{t1}^2)$ and $f(R_r) = 2R_r/(R_{r2}^2 - R_{r1}^2)$, respectively. We denote the von Mises pdfs for the $\mathrm{T_x}$ and $\mathrm{R_x}$ azimuth angles and the pdfs for the $\mathrm{T_x}$ and $\mathrm{R_x}$ elevation angles as $f(\alpha_T) = \exp\left[k_T \cos(\alpha_T - \mu_T)\right]/2\pi I_0(k_T)$, $f(\alpha_R) = \exp\left[k_R \cos(\alpha_R - \mu_R)\right]/2\pi I_0(k_R)$, $f(\beta_T) =$

$\pi\cos(\pi\beta_T/(2\beta_{T_m}))/(4|\beta_{T_m}|)$, and $f(\beta_R) = \pi\cos(\pi\beta_R/(2\beta_{R_m}))/(4|\beta_{R_m}|)$, respectively. Using trigonometric transformations, the equality $\int_{-\pi}^{\pi}\exp\{a\sin(c)+b\cos(c)\}dc = 2\pi I_0\left(\sqrt{a^2+b^2}\right)$ [63, eq. 3.338-4], and the results in Chapter 6, the stf-cfs of the single-bounced transmit, single-bounced receive, and double-bounced components can be closely approximated as

$$
\begin{aligned}
R_{pq,\tilde{p}\tilde{q}}^{SBT}(\Delta t,\Delta f) &\approx \frac{\eta_T}{I_0(k_T)}\frac{\cos\left(\frac{2\pi}{\lambda}\beta_{Tm}(p-\tilde{p})d_{Tz}\right)}{1-\left(\frac{4\beta_{Tm}(p-\tilde{p})d_{Tz}}{\lambda}\right)^2}e^{-j\frac{2\pi}{\lambda}(q-\tilde{q})d_{Rx}-j2\pi\Delta t f_{R\max}\cos\gamma_R} && (220)\\
&\times \int_{R_{t1}}^{R_{t2}}\left(1-\gamma\frac{R_t}{D}\right)e^{-j\frac{2\pi}{c_0}\Delta f(D+R_t)}I_0\left(\sqrt{x_{SBT}^2+y_{SBT}^2}\right)\frac{2R_t}{R_{t2}^2-R_{t1}^2}dR_t,\\
R_{pq,\tilde{p}\tilde{q}}^{SBR}(\Delta t,\Delta f) &\approx \frac{\eta_R}{I_0(k_R)}\frac{\cos\left(\frac{2\pi}{\lambda}\beta_{Rm}(q-\tilde{q})d_{Rz}\right)}{1-\left(\frac{4\beta_{Rm}(q-\tilde{q})d_{Rz}}{\lambda}\right)^2}e^{j\frac{2\pi}{\lambda}(p-\tilde{p})d_{Tx}+j2\pi\Delta t f_{T\max}\cos\gamma_T} && (221)\\
&\times \int_{R_{r1}}^{R_{r2}}\left(1-\gamma\frac{R_r}{D}\right)e^{-j\frac{2\pi}{c_0}\Delta f(D+R_r)}I_0\left(\sqrt{x_{SBR}^2+y_{SBR}^2}\right)\frac{2R_r}{R_{r2}^2-R_{r1}^2}dR_r,\\
R_{pq,\tilde{p}\tilde{q}}^{DB}(\Delta t,\Delta f) &\approx A_{DB}\int_{R_{t1}}^{R_{t2}}2e^{-j\frac{2\pi}{c_0}\Delta f R_t}R_t I_0\left(\sqrt{x_{DB}^2+y_{DB}^2}\right)dR_t && (222)\\
&\times\int_{R_{r1}}^{R_{r2}}e^{-j\frac{2\pi}{c_0}\Delta f R_r}R_r I_0\left(\sqrt{w_{DB}^2+z_{DB}^2}\right)\left(1-\gamma\frac{R_r}{D}\right)dR_r\\
&+A_{DB}\int_{R_{r1}}^{R_{r2}}2e^{-j\frac{2\pi}{c_0}\Delta f R_r}R_r I_0\left(\sqrt{w_{DB}^2+z_{DB}^2}\right)dR_r\\
&\times\int_{R_{t1}}^{R_{t2}}e^{-j\frac{2\pi}{c_0}\Delta f R_t}R_t I_0\left(\sqrt{x_{DB}^2+y_{DB}^2}\right)\left(1-\gamma\frac{R_t}{D}\right)dR_t,
\end{aligned}
$$

where parameters x_{SBT}, y_{SBT}, x_{SBR}, y_{SBR}, x_{DB}, y_{DB}, z_{DB}, w_{DB}, and A_{DB} are

$$
\begin{aligned}
x_{SBT} &\approx j(2\pi/\lambda)(p-\tilde{p})d_{Tx}+j2\pi\Delta t f_{T\max}\cos\gamma_T+j2\pi\Delta f R_t/c_0+k_T\cos\mu_T, && (223)\\
y_{SBT} &\approx j2\pi\left[(p-\tilde{p})d_{Ty}/\lambda+(q-\tilde{q})d_{Ry}\Delta_T/\lambda+\Delta t\left(f_{T\max}\sin\gamma_T+f_{R\max}\Delta_T\sin\gamma_R\right)\right]\\
&+ k_T\sin\mu_T, && (224)\\
x_{SBR} &\approx j(2\pi/\lambda)(q-\tilde{q})d_{Rx}+j2\pi\Delta t f_{R\max}\cos\gamma_R-j2\pi\Delta f R_r/c_0+k_R\cos\mu_R, && (225)\\
y_{SBR} &\approx j2\pi\left[(q-\tilde{q})d_{Ry}/\lambda+(p-\tilde{p})d_{Ty}\Delta_R/\lambda+\Delta t\left(f_{R\max}\sin\gamma_R+f_{T\max}\Delta_R\sin\gamma_T\right)\right]\\
&+ k_R\sin\mu_R, && (226)\\
x_{DB} &\approx j(2\pi/\lambda)(p-\tilde{p})d_{Tx}+j2\pi\Delta t f_{T\max}\cos\gamma_T+j2\pi\Delta f R_t/c_0+k_T\cos\mu_T, && (227)
\end{aligned}
$$

$$y_{DB} \approx j(2\pi/\lambda)(p-\tilde{p})d_{Ty} + j2\pi\Delta t f_{T\max}\sin\gamma_T + k_T\sin\mu_T, \quad (228)$$

$$z_{DB} \approx j(2\pi/\lambda)(q-\tilde{q})d_{Rx} + j2\pi\Delta t f_{R\max}\cos\gamma_R - j2\pi\Delta f R_r/c_0 + k_R\cos\mu_R, \quad (229)$$

$$w_{DB} \approx j(2\pi/\lambda)(q-\tilde{q})d_{Ry} + j2\pi\Delta t f_{R\max}\sin\gamma_R + k_R\sin\mu_R, \quad (230)$$

$$A_{DB} = \frac{\eta_{TR}}{I_0(k_T)I_0(k_R)} \frac{\cos\left(\frac{2\pi}{\lambda}\beta_{Tm}(p-\tilde{p})d_{Tz}\right)}{1-\left(\frac{4\beta_{Tm}(p-\tilde{p})d_{Tz}}{\lambda}\right)^2} \frac{\cos\left(\frac{2\pi}{\lambda}\beta_{Rm}(q-\tilde{q})d_{Rz}\right)}{1-\left(\frac{4\beta_{Rm}(q-\tilde{q})d_{Rz}}{\lambda}\right)^2} \times \frac{e^{-j2\pi\Delta f D/c_0}}{(R_{t2}^2-R_{t1}^2)(R_{r2}^2-R_{r1}^2)}. \quad (231)$$

Using (207) and (219) and approximation $\alpha_{Rq}^{LoS} = \alpha_{R\tilde{q}}^{LoS} \approx \pi$, the stf-cf of the LoS component can be approximated as

$$R_{pq,\tilde{p}\tilde{q}}^{LoS}(\Delta t, \Delta f) \approx \sqrt{K_{pq}K_{\tilde{p}\tilde{q}}} \times e^{j\frac{2\pi}{\lambda}[(p-\tilde{p})d_{Tx}-(q-\tilde{q})d_{Rx}]+j2\pi\Delta t[f_{T\max}\cos\gamma_T - f_{R\max}\cos\gamma_R]-\frac{2\pi}{c_0}\Delta f\sqrt{D^2+\Delta H^2}}. \quad (232)$$

Note that the stf-cfs for the single-bounced transmit, single-bounced receive, and double-bounced components of the time-variant transfer function must be evaluated numerically because the integrals in (220) - (222) do not have closed-form solutions. However, if we assume that the time and frequency dispersion are statistically independent, the closed-form expressions for the stf-cfs of the single-bounced transmit, single-bounced receive, and double-bounced components can be obtained. In the literature, it is often assumed that the time dispersion (i.e., the time delays) and the frequency dispersion (i.e., the Doppler spreads) are statistically independent because the time delays depend on the relative locations of the random scatterers (i.e., the angles of arrival, the angles of departure, and the distances among the $\mathrm{T_x}$, $\mathrm{R_x}$, and scatterers), whereas the Doppler spreads depend on the motions of the $\mathrm{T_x}$ and $\mathrm{R_x}$ [77, 78]. However, note that the Doppler spread does not depend only on the speeds of the $\mathrm{T_x}$ and $\mathrm{R_x}$, but also is the function of the angles of departure and the angles of arrival. Hence, both the time delays and the Doppler spreads depend on the relative location of the random scatterers, which implies that they are not statistically independent. Since the angles of departure and the angels of arrival cannot be neglected in the Doppler spreads, the other way to obtain the independence between the time delays and the Doppler spreads is to assume that the waves scattered form the relatively close scatterers have equal time delays. Then, the influence of the angles of arrival and the angles of departure on the time delays can be neglected, making the time delays and the Doppler spreads statistically independent. The 2-D geometry-based statistical models often achieve the independence between the time delays and the Doppler spreads, assuming that all waves scattered from the scatterers lying on the same circle have equal time delays [35]. These time delays are equal to the average of all time delays obtained from the scatterers lying on the same circle. Similarly, in our 3-D geometry-based statistical model, we will assume that all waves scattered from the scatterers lying on the same cylindrical surface have equal (averaged) time delays. Then, the time delays in (186), (187), and (191) can be approximated as

$$\tau_{m,l} \approx \tau_l = \frac{D + R_t^{(l)}}{c_0} \tag{233}$$

$$\tau_{n,k} \approx \tau_k = \frac{D + R_r^{(k)}}{c_0}, \tag{234}$$

$$\tau_{m,l,n,k} \approx \tau_{l,k} = \frac{D + R_t^{(l)} + R_r^{(k)}}{c_0}. \tag{235}$$

Under these assumptions, the space-time-frequency correlation function in (215) can be factored as [78]

$$\begin{aligned} R_{pq,\tilde{p}\tilde{q}}(\Delta t, \Delta f) &= R_{pq,\tilde{p}\tilde{q}}(\Delta t) R_{pq,\tilde{p}\tilde{q}}(\Delta f) \\ &= R_{pq,\tilde{p}\tilde{q}}^{SBT}(\Delta t) R_{pq,\tilde{p}\tilde{q}}^{SBT}(\Delta f) + R_{pq,\tilde{p}\tilde{q}}^{SBR}(\Delta t) R_{pq,\tilde{p}\tilde{q}}^{SBR}(\Delta f) \\ &+ R_{pq,\tilde{p}\tilde{q}}^{DB}(\Delta t) R_{pq,\tilde{p}\tilde{q}}^{DB}(\Delta f) + R_{pq,\tilde{p}\tilde{q}}^{LoS}(\Delta t) R_{pq,\tilde{p}\tilde{q}}^{LoS}(\Delta f), \end{aligned} \tag{236}$$

where the closed-form expressions for $R_{pq,\tilde{p}\tilde{q}}^{SBT}(\Delta t)$, $R_{pq,\tilde{p}\tilde{q}}^{SBT}(\Delta f)$, $R_{pq,\tilde{p}\tilde{q}}^{SBR}(\Delta t)$, $R_{pq,\tilde{p}\tilde{q}}^{SBR}(\Delta f)$, $R_{pq,\tilde{p}\tilde{q}}^{DB}(\Delta t)$, and $R_{pq,\tilde{p}\tilde{q}}^{DB}(\Delta f)$ are derived in Appendix J, while the closed-form space-time-frequency correlation function of the LoS component, i.e., $R_{pq,\tilde{p}\tilde{q}}^{LoS}(\Delta t) R_{pq,\tilde{p}\tilde{q}}^{LoS}(\Delta f)$, remains the same as in (232).

To validate assumptions used to obtain the closed-form stf-cfs in (416) - (418), we compare these equations with the numerically obtained stf-cfs in (220) - (222). Figs. 45 - 47 compare the space-time correlation functions, the frequency correlation functions, and the space-time-frequency correlation functions in (220) - (222) and (416) - (418). The parameters used to obtain curves in Figs. 45 - 47 are summarized in the III - V columns of the Table 9. Fig. 45 shows excellent agreement between the space-time correlation functions. This is an expected result, because the ap-

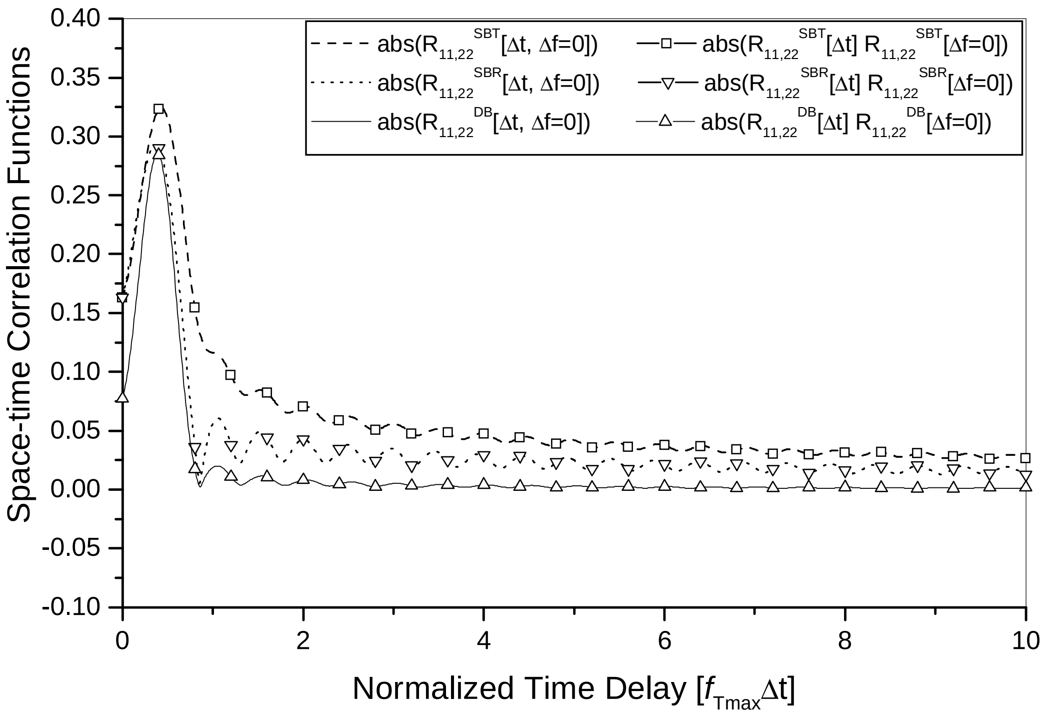

Figure 45: Comparison of the normalized space-time correlation functions in (220) - (222) and (416) - (418).

proximations in (233) - (235) affect only time delays, which are set to zero in both, the closed-form and numerically obtained space-time correlation functions. Fig. 46 shows relatively good agreement between the frequency correlation functions. Note that the frequency correlation functions are obtained from the space-time-frequency correlation functions by eliminating the space and time components (i.e., by setting $d_T = d_R = \tau = 0$). Hence, this result shows that the approximated and exact time

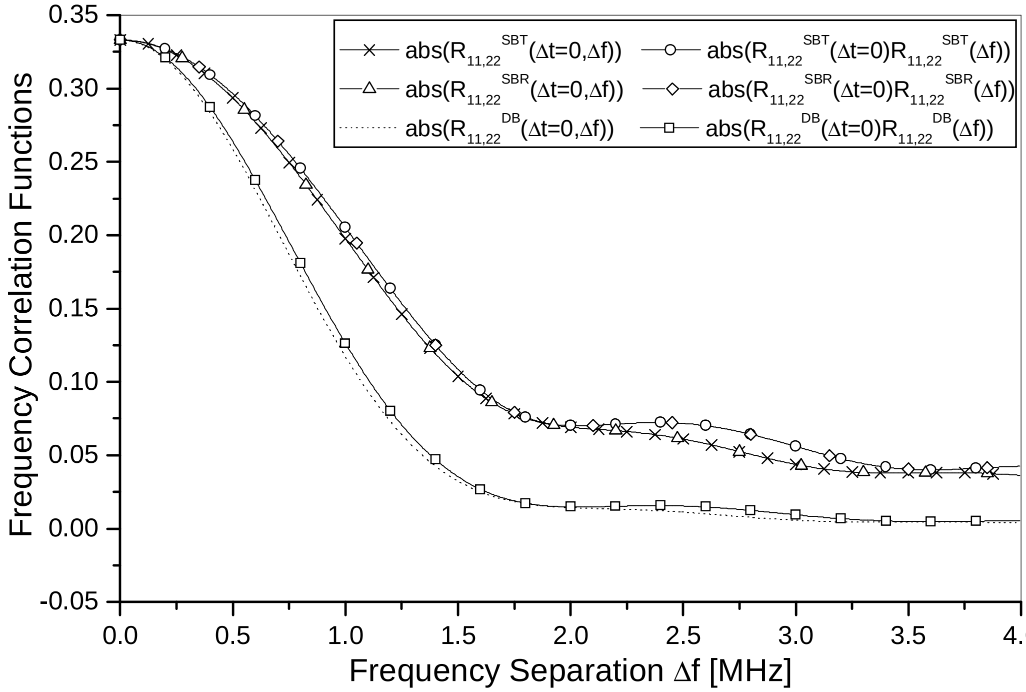

Figure 46: Comparison of the frequency correlation functions in (220) - (222) and (416) - (418).

delays have similar values, i.e., verifies the approximations in (233) - (235). However, Fig. 47 shows that equations (416) - (418) underestimate the space-time-frequency correlation functions. The reason for these discrepancy is the fact that the time delays in the closed-form expressions are not functions of the angles of departure or the angles of arrivals and do not affect the Bessel functions in (416) - (418). On the other hand, the time delays in the numerically obtained expressions are functions of the angles of departure and the angles of arrival and affect the Bessel functions in (220) - (222). Even small differences between the input values of the Bessel functions in (220) - (222) and (416) - (418), respectively, can significantly change the final results. Hence, the influence of the angles of arrival and the angles of departure on the time delays cannot be neglected and the numerically obtained space-time-frequency correlation functions in (220) - (222) should be used. Note that the similar results are obtained for the 2-D models (i.e., for $\beta_{Tm} = \beta_{Rm} = 0°$). These results are not surprising because in the practice, the time delays and the Doppler spreads are not independent [79].

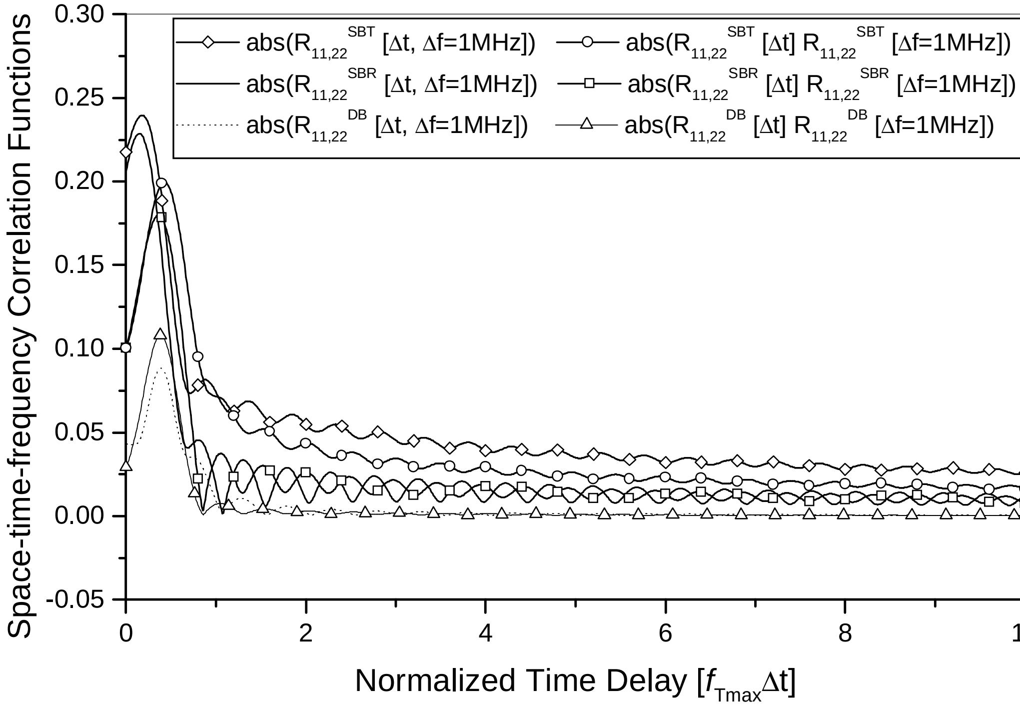

Figure 47: Comparison of the normalized space-time-frequency correlation functions in (220) - (222) and (416) - (418).

7.3.2 Space-Doppler Power Spectral Density (sD-psd)

The sD-psd of the time-variant transfer function is the Fourier transform of the space-time correlation function $R_{pq,\tilde{p}\tilde{q}}(\Delta t, \Delta f = 0)$. From (215) follows that the sD-psd is a summation of the sD-psd functions of the single-bounced transmit, single-bounced receive, double-bounced, and LoS components. Appendix K shows that the sD-psds of the single-bounced transmit, single-bounced receive, double-bounced, and

LoS components are, respectively,

$$S_{pq,\tilde{p}\tilde{q}}^{SBT}(\nu) = \mathcal{F}_{\Delta t}\{R_{pq,\tilde{p}\tilde{q}}^{SBT}(\Delta t, \Delta f = 0)\} = \frac{\eta_T}{I_0(k_T)} \frac{\cos\left(\frac{2\pi}{\lambda}\beta_{T_m}(p-\tilde{p})d_{Tz}\right)}{1-\left(\frac{4\beta_{T_m}(p-\tilde{p})d_{Tz}}{\lambda}\right)^2} \tag{237}$$
$$\times \frac{\exp\{j2\pi(\nu + f_{R\max}\cos\gamma_R)A_{SBT} - j2\pi p_{x_{SBR}}\}}{\pi f_{T\max}\sqrt{1-[(\nu+f_{R\max}\cos\gamma_R)/f_{T\max}]^2}} \left[\frac{(3-2\gamma R_{t2}/D)R_{t2}^2}{3(R_{t2}^2 - R_{t1}^2)}\right.$$
$$\left.-\frac{(3-2\gamma R_{t1}/D)R_{t1}^2}{3(R_{t2}^2-R_{t1}^2)}\right] \cosh\Big[(k_T\sin(\mu_T-\gamma_T) + j2\pi p_{x_{SBT}}\sin\gamma_T - j2\pi p_{y_{SBT}}\cos\gamma_T)$$
$$\times \sqrt{1-[(\nu+f_{R\max}\cos\gamma_R)/f_{T\max}]^2}\Big]$$

$$S_{pq,\tilde{p}\tilde{q}}^{SBR}(\nu) = \mathcal{F}_{\Delta t}\{R_{pq,\tilde{p}\tilde{q}}^{SBR}(\Delta t, \Delta f = 0)\} = \frac{\eta_R}{I_0(k_R)} \frac{\cos\left(\frac{2\pi}{\lambda}\beta_{R_m}(q-\tilde{q})d_{Rz}\right)}{1-\left(\frac{4\beta_{R_m}(q-\tilde{q})d_{Rz}}{\lambda}\right)^2} \tag{238}$$
$$\times \frac{\exp\{j2\pi(\nu - f_{T\max}\cos\gamma_T)A_{SBR} + j2\pi p_{x_{SBT}}\}}{\pi f_{R\max}\sqrt{1-[(\nu-f_{T\max}\cos\gamma_T)/f_{R\max}]^2}} \left[\frac{(3-2\gamma R_{r2}/D)R_{r2}^2}{3(R_{r2}^2 - R_{r1}^2)}\right.$$
$$\left.-\frac{(3-2\gamma R_{r1}/D)R_{r1}^2}{3(R_{r2}^2-R_{r1}^2)}\right] \cosh\Big[(k_R\sin(\mu_R-\gamma_R) + j2\pi p_{x_{SBR}}\sin\gamma_R - j2\pi p_{y_{SBR}}\cos\gamma_R)$$
$$\times \sqrt{1-[(\nu-f_{T\max}\cos\gamma_T)/f_{R\max}]^2}\Big]$$

$$S_{pq,\tilde{p}\tilde{q}}^{DB}(\nu) = \mathcal{F}_{\Delta t}\{R_{pq,\tilde{p}\tilde{q}}^{DB}(\Delta t, \Delta f = 0)\} = \frac{\eta_{TR} I_{DB}}{I_0(k_T)I_0(k_R)} \tag{239}$$
$$\times \frac{\cos\left(\frac{2\pi}{\lambda}\beta_{T_m}(p-\tilde{p})d_{Tz}\right)}{1-\left(\frac{4\beta_{T_m}(p-\tilde{p})d_{Tz}}{\lambda}\right)^2} \frac{\cos\left(\frac{2\pi}{\lambda}\beta_{R_m}(q-\tilde{q})d_{Rz}\right)}{1-\left(\frac{4\beta_{R_m}(q-\tilde{q})d_{Rz}}{\lambda}\right)^2}$$
$$\times \exp\{j(2\pi p_{x_{DB}}\cos\gamma_T + 2\pi p_{y_{DB}}\sin\gamma_T - jk_T\cos(\mu_T-\gamma_T))\nu/f_{T\max}\}$$
$$\times \frac{\cosh\Big[(k_T\sin(\mu_T-\gamma_T) + j2\pi p_{x_{DB}}\sin\gamma_T - j2\pi p_{y_{DB}}\cos\gamma_T)\sqrt{1-(\nu/f_{T\max})^2}\Big]}{\pi f_{T\max}\sqrt{1-(\nu/f_{T\max})^2}}$$
$$\odot \exp\{j(2\pi p_{z_{DB}}\cos\gamma_R + 2\pi p_{w_{DB}}\sin\gamma_R - jk_R\cos(\mu_R-\gamma_R))\nu/f_{R\max}\}$$
$$\times \frac{\cosh\Big[(k_R\sin(\mu_R-\gamma_R) + j2\pi p_{z_{DB}}\sin\gamma_R - j2\pi p_{w_{DB}}\cos\gamma_R)\sqrt{1-(\nu/f_{R\max})^2}\Big]}{\pi f_{R\max}\sqrt{1-(\nu/f_{R\max})^2}}$$

$$\begin{aligned} S_{pq,\tilde{p}\tilde{q}}^{LoS}(\nu) &= \mathcal{F}_{\Delta t}\{R_{pq,\tilde{p}\tilde{q}}^{LoS}(\Delta t, \Delta f = 0)\} \\ &= K e^{j\frac{2\pi}{\lambda}[(p-\tilde{p})d_{Tx}-(q-\tilde{q})d_{Rx}]}\delta(\nu + f_{T\max}\cos\gamma_T - f_{R\max}\cos\gamma_R), \end{aligned} \tag{240}$$

where $\mathcal{F}\{\,\cdot\,\}$ denotes the Fourier transform, $\cosh(\,\cdot\,)$ is the hyperbolic cosine, $\delta(\,\cdot\,)$ is the Dirac delta function, $|\nu + f_{R\max}\cos\gamma_R| \leq f_{T\max}$ and $|\nu - f_{T\max}\cos\gamma_T| \leq f_{R\max}$ for the single-bounced sD-psds, and $|\nu| \leq f_{T\max} + f_{R\max}$ for the double-bounced sD-psd. Finally, the parameters in (237) and (238) are defined in (422), the parameters in (239) are defined in (426), and $I_{DB} = (R_{t2}^2 - R_{t1}^2)(0.5R_{r2}^2 - \gamma R_{r2}^3/(3D) - 0.5R_{r1}^2 + \gamma R_{r1}^3/(3D)) + (R_{r2}^2 - R_{r1}^2)(0.5R_{t2}^2 - \gamma R_{t2}^3/(3D) - 0.5R_{t1}^2 + \gamma R_{t1}^3/(3D))$.

Fig. 48 plots several SISO and MIMO sD-psds, assuming 3-D non-isotropic scattering and the LoS conditions between the $\mathrm{T_x}$ and $\mathrm{R_x}$. These sD-psds are characteristic for the urban surface street environments. First, we compare our analytical SISO sD-psd with the measured SISO sD-psd in Fig. 8 (a) of [39]. The measurements in [39] were performed in the urban surface street area, at 5.2 GHz, and the maximum Doppler frequencies were $f_{T\max} = f_{R\max} = 75$ Hz. Both, the $\mathrm{T_x}$ and $\mathrm{R_x}$ were equipped with one omnidirectional antenna. The distance between the $\mathrm{T_x}$ and $\mathrm{R_x}$ was approximately $D = 300$ m. The moving directions were $\gamma_T = \gamma_R = 90°$, the antenna orientations were $\theta_T = \theta_R = \psi_T = \psi_R = 0°$, $\Delta_H = 0$. The same parameters are used to obtain all analytical results in Fig. 48. The rest of the parameters in the reference model, i.e., $K = 4$, $\mu_T = 70°$, $k_T = 5$, $\beta_{T_m} = 20°$, $R_{t1} = R_{r1} = 9$ m, $R_{t2} = R_{r2} = 90$ m, $\mu_R = 250°$, $k_R = 3.3$, $\beta_{R_m} = 20°$, $\eta_T = \eta_R = 0.1$, and $\eta_{TR} = 0.8$, are manually estimated from the measurements and summarized in the VI column of Table 9. The discussion on how to jointly estimate these parameters from measurements is presented in [52]. Fig. 48 shows the close agreement between the theoretical and empirical SISO sD-psds. Furthermore, note that the M-to-M sD-psd in an urban area differs from the U-shaped sD-psd of cellular channels. This is because the M-to-M sD-psd in an urban area has the DB rays more dominant than the SBT and SBR rays (i.e., $\eta_T = \eta_R = 0.1$, and $\eta_{TR} = 0.8$), whereas the sD-psd of cellular channels has only SBR and LoS rays (i.e, $\eta_T = 0$, $\eta_R = 1$, $\eta_{TR} = 0$). To illustrate the importance of combining the DB, SBT and SBR rays, Fig. 48 also plots the SISO sD-psd with only DB and LoS rays. The results show that for higher frequencies, the model with only DB and LoS rays overestimates the sD-psd. Furthermore, Fig. 48 shows that the

2-D model (i.e, $\beta_{T_m} = \beta_{R_m} = 0°$) underestimates the sD-psd. Finally, Fig. 48 plots the MIMO sD-psd, $S_{11,22}(\nu)$, with $d_T = d_R = 1\lambda$. The results show that the sD-psd decreases with the increase of the antenna elements separation. Fig. 49 plots several

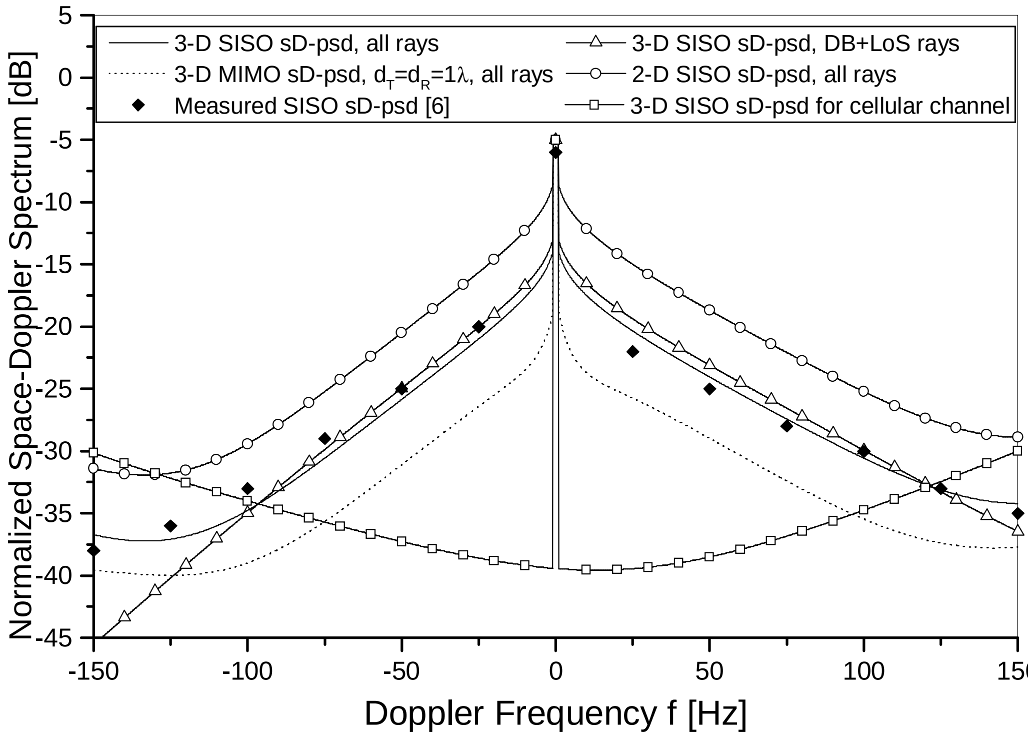

Figure 48: The normalized theoretical and measured space-Doppler power spectra in the urban environment.

SISO and MIMO sD-psds that can be found in the highway environments. First, we compare our analytical SISO sD-psd with the measured SISO sD-psd in Fig. 4(d) of [40]. The measurements in [40] were performed on the highway, at 2.4 GHz, and the maximum Doppler frequencies were $f_{T\max} = f_{R\max} = 200$ Hz. The vehicles were driven in the rightmost lane and very close to the sound blockers on the edge of the highway. Both, the T_x and R_x were equipped with one omnidirectional antenna. The distance between the T_x and R_x was approximately $D = 300$ m. The moving directions were $\gamma_T = \gamma_R = 0°$, the antenna orientations were $\theta_T = \theta_R = 90°$, $\psi_T = \psi_R = 0°$, $\Delta_H = 0$. The same parameters are used for all analytical results in Fig. 49. The rest of the parameters in the reference model, i.e, $K = 1.5$, $\mu_T = 0°$, $k_T = 4$, $\beta_{T_m} = 15°$,

$R_{t1} = R_{r1} = 9.6$ m, $R_{t2} = R_{r2} = 96$ m, $\mu_R = 180°$, $k_R = 4$, $\beta_{R_m} = 15°$, $\eta_T = \eta_R = 0.3$, and $\eta_{TR} = 0.4$, are manually estimated from the measurements and summarized in the VII column of Table 9. Fig. 49 shows the close agreement between the theoretical and empirical SISO sD-psds. Furthermore, we can observe that this spectrum is similar to the U-shaped spectrum of cellular channels. This is not surprising result because the single-bounced rays are prevalent (i.e., $\eta_T = \eta_R = 0.3$, and $\eta_{TR} = 0.4$) when the vehicles are driven very close to the sound blockers on the edge of the highway. To illustrate the importance of combining the DB, SBT and SBR rays, Fig. 49 also plots the SISO sD-psd with only DB and LoS rays. The results show that the model with only DB and LoS rays has significantly different shape of the sD-psd compared to the model with SBT, SBR, DB, and LoS rays. Furthermore, Fig. 48 shows that the 2-D model (i.e, $\beta_{T_m} = \beta_{R_m} = 0°$) underestimates the sD-psd. Finally, Fig. 49 plots the MIMO sD-psd, $S_{11,22}(\nu)$, for the antenna elements separation of $d_T = d = R = 1\lambda$ and shows that the sD-psd decreases with the increase of the antenna elements separation. Recently, we conducted the MIMO M-to-M channel-sounding experimental campaign along surface streets and on the Interstate highways in the Midtown Atlanta metropolitan area. The experimental campaign and the detailed verification of the reference model in terms of the cumulative distribution functions, stf-cfs, sD-psds, psds, and level crossing rates are presented in Chapter 9. These results and Figs. 48 and 49 confirm the utility of the proposed wideband model.

7.3.3 Power Space-delay Spectral Density (psds)

The psds of the time-variant transfer function is the inverse Fourier transform of the space-frequency correlation function $R_{pq,\tilde{p}\tilde{q}}(\Delta t = 0, \Delta f)$. From (215) follows that the psds is a summation of the psds functions of the single-bounced transmit, single-bounced receive, double-bounced, and LoS components. Appendix L shows that the

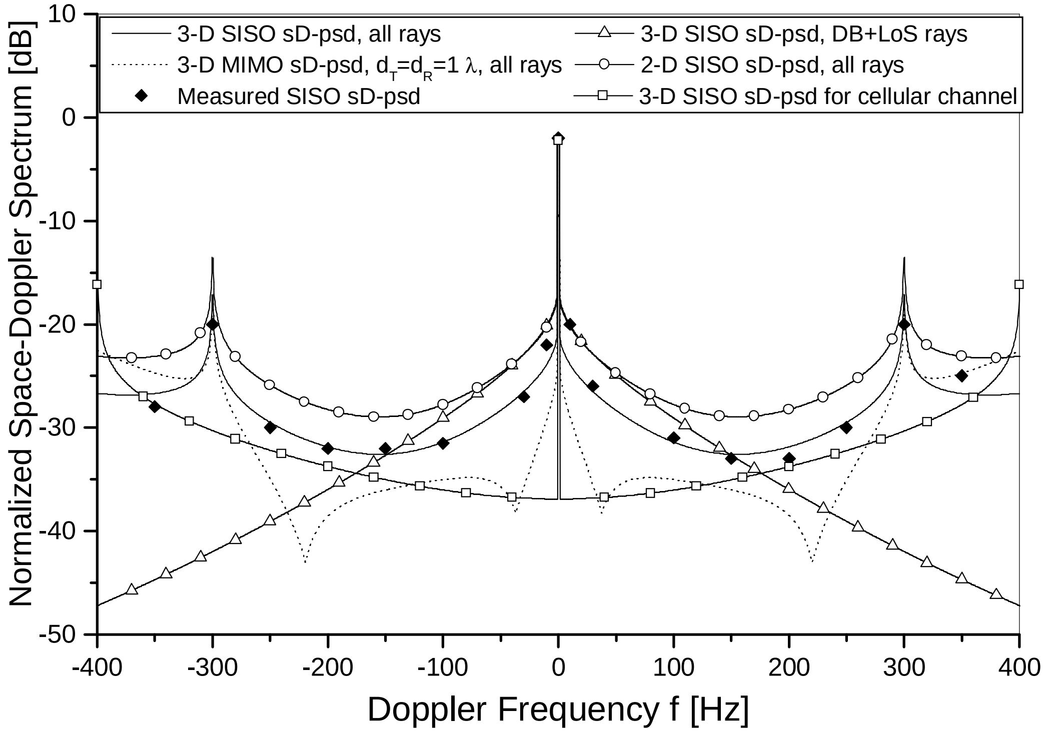

Figure 49: The normalized theoretical and measured space-Doppler power spectra in the highway environment.

psds of the SBT, SBR, DB, and LoS components are, respectively,

$$
\begin{aligned}
P_{pq,\tilde{p}\tilde{q}}^{SBT}(\tau_{\text{rel}}) &= \mathcal{F}_{\Delta f}^{-1}\{R_{pq,\tilde{p}\tilde{q}}^{SBT}(\Delta t = 0, \Delta f)\} = \frac{\eta_T}{I_0(k_T)} \frac{\cos\left(\frac{2\pi}{\lambda}\beta_{T_m}(p-\tilde{p})d_{Tz}\right)}{1-\left(\frac{4\beta_{T_m}(p-\tilde{p})d_{Tz}}{\lambda}\right)^2} \qquad (241)\\
&\times \; e^{-j\frac{2\pi}{\lambda}(q-\tilde{q})d_{Rx}} \frac{2}{R_{t2}^2 - R_{t1}^2} \int_{R_{ta}}^{R_{tb}} \left(1-\gamma\frac{R_t}{D}\right) R_t e^{j\frac{2\pi}{c_0}R_t B_{SBT}(c_0\tau_{\text{rel}}/R_t - 1)}\\
&\times \; \frac{\cosh\left(2jC_{SBT}\sqrt{\frac{c_0\tau_{\text{rel}}}{2R_t}\left(1-\frac{c_0\tau_{\text{rel}}}{2R_t}\right)}\right)}{\frac{2\pi}{c_0}R_t\sqrt{\frac{c_0\tau_{\text{rel}}}{2R_t}\left(1-\frac{c_0\tau_{\text{rel}}}{2R_t}\right)}} dR_t,
\end{aligned}
$$

$$
\begin{aligned}
P_{pq,\tilde{p}\tilde{q}}^{SBR}(\tau_{\text{rel}}) &= \mathcal{F}_{\Delta f}^{-1}\{R_{pq,\tilde{p}\tilde{q}}^{SBR}(\Delta t = 0, \Delta f)\} = \frac{\eta_R}{I_0(k_R)} \frac{\cos\left(\frac{2\pi}{\lambda}\beta_{R_m}(q-\tilde{q})d_{Rz}\right)}{1-\left(\frac{4\beta_{R_m}(q-\tilde{q})d_{Rz}}{\lambda}\right)^2} \qquad (242)\\
&\times \; e^{j\frac{2\pi}{\lambda}(p-\tilde{p})d_{Tx}} \frac{2}{R_{r2}^2 - R_{r1}^2} \int_{R_{ra}}^{R_{rb}} \left(1-\gamma\frac{R_r}{D}\right) R_r e^{j\frac{2\pi}{c_0}R_r B_{SBR}(c_0\tau_{\text{rel}}/R_r - 1)}\\
&\times \; \frac{\cosh\left(2jC_{SBR}\sqrt{\frac{c_0\tau_{\text{rel}}}{2R_r}\left(1-\frac{c_0\tau_{\text{rel}}}{2R_r}\right)}\right)}{\frac{2\pi}{c_0}R_r\sqrt{\frac{c_0\tau_{\text{rel}}}{2R_r}\left(1-\frac{c_0\tau_{\text{rel}}}{2R_r}\right)}} dR_r,
\end{aligned}
$$

$$
\begin{aligned}
&P^{DB}_{pq,\tilde{p}\tilde{q}}(\tau_{\text{rel}}) = \mathcal{F}^{-1}_{\Delta f}\{R^{DB}_{pq,\tilde{p}\tilde{q}}(\Delta t = 0, \Delta f)\} = \frac{\eta_{TR}}{I_0(k_T)I_0(k_R)} \\
&\times \frac{\cos\left(\frac{2\pi}{\lambda}\beta_{T_m}(p-\tilde{p})d_{Tz}\right)}{1-\left(\frac{4\beta_{T_m}(p-\tilde{p})d_{Tz}}{\lambda}\right)^2} \frac{\cos\left(\frac{2\pi}{\lambda}\beta_{R_m}(q-\tilde{q})d_{Rz}\right)}{1-\left(\frac{4\beta_{R_m}(q-\tilde{q})d_{Rz}}{\lambda}\right)^2} \frac{2}{(R_{t2}^2-R_{t1}^2)(R_{r2}^2-R_{r1}^2)} \\
&\times \Bigg[\int_{R_{ta}}^{R_{tb}} R_t e^{j\frac{2\pi}{c_0}R_t B_{DB}(c_0\tau_{\text{rel}}/R_t-1)} \frac{\cosh\left(2jC_{DB}\sqrt{\frac{c_0\tau_{\text{rel}}}{2R_t}\left(1-\frac{c_0\tau_{\text{rel}}}{2R_t}\right)}\right)}{\frac{2\pi}{c_0}R_t\sqrt{\frac{c_0\tau_{\text{rel}}}{2R_t}\left(1-\frac{c_0\tau_{\text{rel}}}{2R_t}\right)}} dR_t \qquad (243) \\
&\odot \int_{R_{ra}}^{R_{rb}} \left(1-\gamma\frac{R_r}{D}\right) R_r e^{j\frac{2\pi}{c_0}R_r D_{DB}(c_0\tau_{\text{rel}}/R_r-1)} \frac{\cosh\left(2jE_{DB}\sqrt{\frac{c_0\tau_{\text{rel}}}{2R_r}\left(1-\frac{c_0\tau_{\text{rel}}}{2R_r}\right)}\right)}{\frac{2\pi}{c_0}R_r\sqrt{\frac{c_0\tau_{\text{rel}}}{2R_r}\left(1-\frac{c_0\tau_{\text{rel}}}{2R_r}\right)}} dR_r \\
&+ \int_{R_{ta}}^{R_{tb}} \left(1-\gamma\frac{R_t}{D}\right) R_t e^{j\frac{2\pi}{c_0}R_t B_{DB}(c_0\tau_{\text{rel}}/R_t-1)} \frac{\cosh\left(2jC_{DB}\sqrt{\frac{c_0\tau_{\text{rel}}}{2R_t}\left(1-\frac{c_0\tau_{\text{rel}}}{2R_t}\right)}\right)}{\frac{2\pi}{c_0}R_t\sqrt{\frac{c_0\tau_{\text{rel}}}{2R_t}\left(1-\frac{c_0\tau_{\text{rel}}}{2R_t}\right)}} dR_t \\
&\odot \int_{R_{ra}}^{R_{rb}} R_r e^{j\frac{2\pi}{c_0}R_r D_{DB}(c_0\tau_{\text{rel}}/R_r-1)} \frac{\cosh\left(2jE_{DB}\sqrt{\frac{c_0\tau_{\text{rel}}}{2R_r}\left(1-\frac{c_0\tau_{\text{rel}}}{2R_r}\right)}\right)}{\frac{2\pi}{c_0}R_r\sqrt{\frac{c_0\tau_{\text{rel}}}{2R_r}\left(1-\frac{c_0\tau_{\text{rel}}}{2R_r}\right)}} dR_r\Bigg],
\end{aligned}
$$

$$
\begin{aligned}
P^{LoS}_{pq,\tilde{p}\tilde{q}}(\tau_{\text{rel}}) &= \mathcal{F}^{-1}_{\Delta f}\{R^{LoS}_{pq,\tilde{p}\tilde{q}}(\Delta t = 0, \Delta f)\} \\
&= K e^{j\frac{2\pi}{\lambda}[(p-\tilde{p})d_{Tx}-(q-\tilde{q})d_{Rx}]}\delta\left(\tau - \frac{\sqrt{D^2+\Delta_H^2}}{c_0}\right), \qquad (244)
\end{aligned}
$$

where $\cosh(\ \cdot\ )$ is the hyperbolic cosine, $\odot$ denotes convolution, $\delta(\ \cdot\ )$ denotes the Dirac delta function, and $\tau_{\text{rel}} = \tau - D/c_0$. The integrals in (241) - (243) need to be numerically evaluated over the range of possible radii R_t and R_r. For the range $0 \le \tau_{\text{rel}} \le 2R_{t1}/c_0$, the integration limits are $R_{ta} = R_{t1}$, $R_{tb} = R_{t2}$, $R_{ra} = R_{r1}$, and $R_{rb} = R_{r2}$. On the other hand, when $2R_{t1}/c_0 \le \tau_{\text{rel}} \le 2R_{t2}/c_0$, the integration limits are $R_{ta} = c_0\tau_{\text{rel}}/2$, $R_{tb} = R_{t2}$, $R_{ra} = c_0\tau_{\text{rel}}/2$, and $R_{rb} = R_{r2}$. Finally, the parameters in (241) and (242) are defined in (429), whereas the parameters in (243) are defined in (432). Note that existing power delay spectra derived assuming "one-circular-ring" model, are special cases of (242). For example, the 2-D non-isotropic power delay spectrum in [82] is obtained for $\beta_{R_m} = 0$, $\psi_R = 0$, and $d_T = d_R = 0$.

Figs. 50 and 51 show several SISO and MIMO psds that can be found in the highway environments and compare them with the measured SISO psds in [83]. The measurements in [83] were performed on the highway, at 2.4 GHz, and the maximum Doppler frequencies were $f_{T\max} = f_{R\max} = 200$ Hz. The vehicles were driven in the rightmost lane of the highway and the sound blockers on the edge of the highway were periodically present. Both, the $\mathrm{T_x}$ and $\mathrm{R_x}$ were equipped with one omnidirectional antenna. The distance between the $\mathrm{T_x}$ and $\mathrm{R_x}$ was approximately $D = 300$ m. The moving directions were $\gamma_T = \gamma_R = 90°$, the antenna orientations were $\theta_T = \theta_R = \psi_T = \psi_R = 0°$, and the antenna elevations were $\Delta_H = 0$. The same parameters are used to obtain all analytical results in Figs. 50 and 51. The measured SISO psds in Fig. 50 is obtained on the part of the highway without sound blockers. The estimated

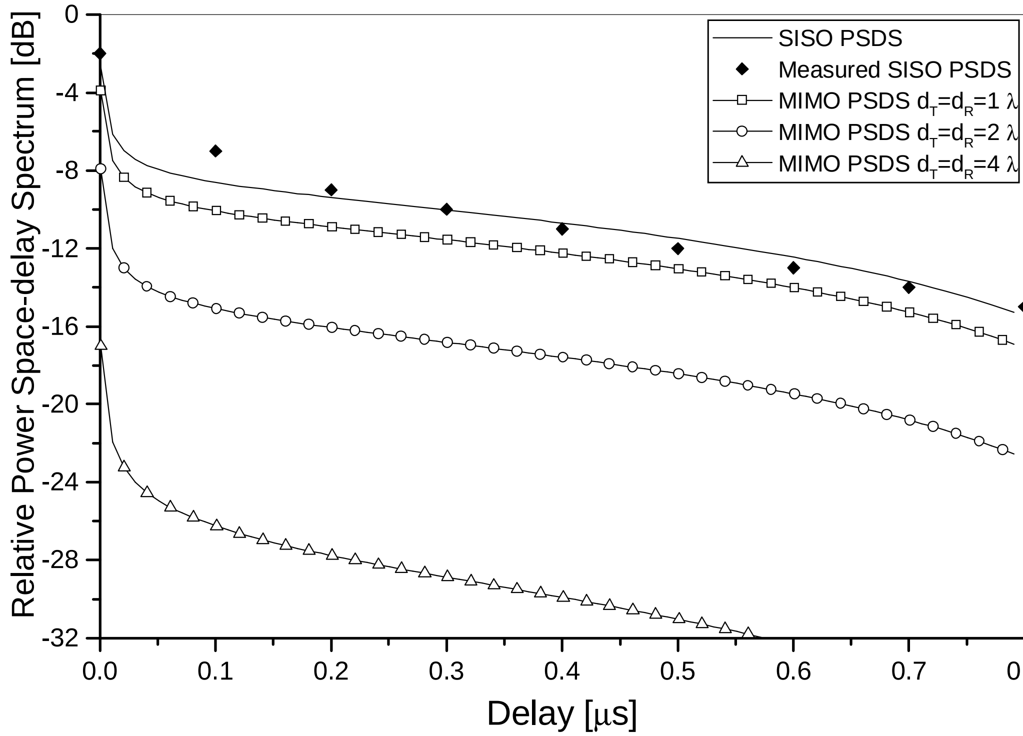

Figure 50: The theoretical and measured relative power space-delay spectra in the rightmost lane of the highway *without* the sound blockers.

parameters in Fig. 50 summarized in the VIII column of Table 9. Fig. 50 shows the close agreement between the theoretical and empirical SISO psds. The results show that the psds on the part of the highway without sound blockers has the DB rays more

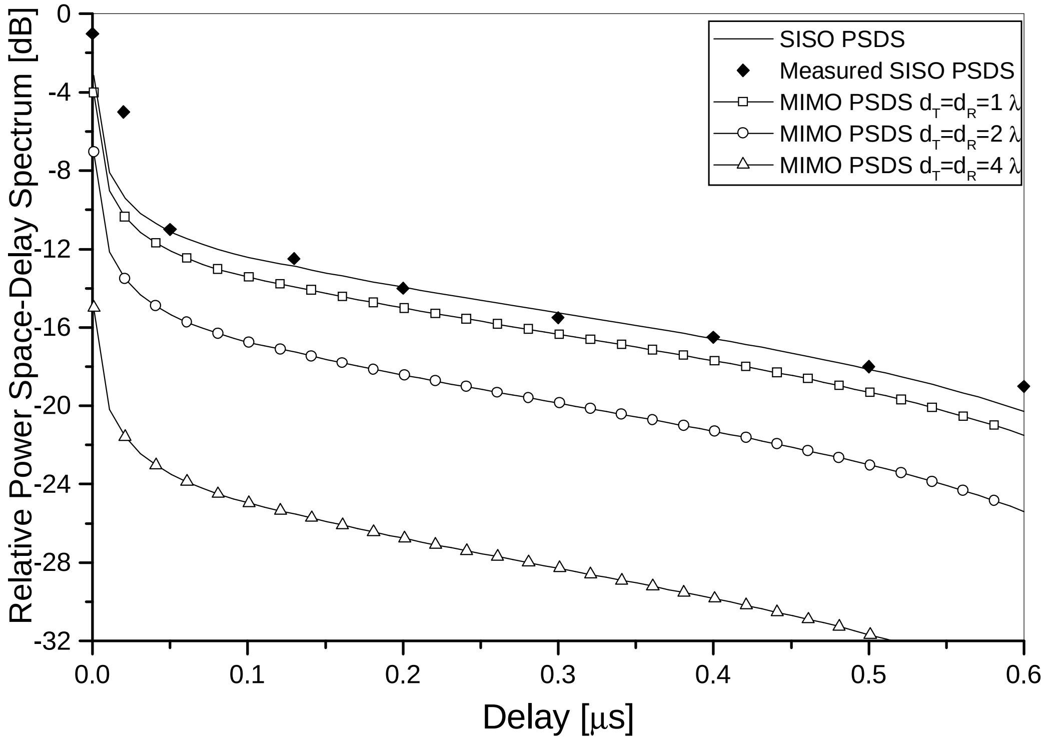

Figure 51: The theoretical and measured relative power space-delay spectra in the rightmost lane of the highway *with* the sound blockers.

dominant than the SBT and SBR rays (i.e., $\eta_T = \eta_R = 0.2$, and $\eta_{TR} = 0.6$). In this case, the psds closely follows the one-sided exponential function dies out after 0.8 μs. On the other hand, the measured SISO psds in Fig. 51 is obtained on the part of the highway with sound blockers. The estimated parameters in Fig. 51 summarized in the IX column of Table 9. Fig. 51 shows the close agreement between the theoretical and empirical SISO psds. The results show that the psds on the part of the highway with sound blockers has the SBT and SBR rays more dominant than the DB rays (i.e., $\eta_T = \eta_R = 0.45$, and $\eta_{TR} = 0.1$). We can observe that this psds does not follow the one-sided exponential function, which is characteristic for F-to-M cellular channels. The M-to-M micro-cell psds has two distinct slopes and dies out after 0.6 μs. Figs. 50 and 51 also show several MIMO psds, $P_{11,22}(\tau_{\text{rel}})$, with $d_T = d_R = \{1\lambda, 2\lambda, 4\lambda\}$. The results show that the psds decreases with the increase of the antenna elements separation.

7.4 Wideband MIMO M-to-M Simulation Models

The reference model for wideband MIMO M-to-M channel described in Section 7.2 assumes an infinite number of scatterers, which prevents practical implementation. It is desirable to design simulation models with a finite number of scatterers, while still matching the statistical properties of the reference model.

Assuming 3-D non-isotropic scattering and using the reference model described in Section 7.2, we propose the following function as a time-variant transfer function: $T_{pq}(t,f) = T_{pq}^{(I)}(t,f) + jT_{pq}^{(Q)}(t,f)$ where

$$
\begin{aligned}
&T_{pq}^{(I)}(t,f) = \qquad (245)\\
&\frac{\rho_{pq}^{SBT}}{\sqrt{M}} \sum_{l,m,i=1}^{L,M_A^{(l)},M_E^{(l)}} \left(1 - \frac{\gamma}{2}\frac{R_t^{(l)}}{D}\right) \cos\Big[K_p D_T^{SBT} + K_q D_R^{SBT} + 2\pi t f_{T\max} \cos\left(\alpha_T^{(m,l)} - \gamma_T\right)\\
&+ 2\pi t f_{R\max}\left(\Delta_T^{(l)} \sin\gamma_R \sin\alpha_T^{(m,l)} - \cos\gamma_R\right) - \frac{2\pi}{c_0} f\left(D + R_t^{(l)}\left(1 - \cos\alpha_T^{(m,l)}\right)\right) + \phi_{m,i,l}\Big]\\
&+ \frac{\rho_{pq}^{SBR}}{\sqrt{N}} \sum_{k,n,g=1}^{K,N_A^{(k)},N_E^{(k)}} \left(1 - \frac{\gamma}{2}\frac{R_r^{(k)}}{D}\right) \cos\Big[K_p D_T^{SBR} + K_q D_R^{SBR} + 2\pi t f_{R\max} \cos\left(\alpha_R^{(n,k)} - \gamma_R\right)\\
&+ 2\pi t f_{T\max}\left(\Delta_R^{(k)} \sin\gamma_T \sin\alpha_R^{(n,k)} + \cos\gamma_T\right) - \frac{2\pi}{c_0} f\left(D + R_r^{(k)}\left(1 + \cos\alpha_R^{(n,k)}\right)\right) + \phi_{n,g,k}\Big]\\
&+ \frac{\rho_{pq}^{DB}}{\sqrt{MN}} \sum_{l,m,i=1}^{L,M_A^{(l)},M_E^{(l)}} \sum_{k,n,g=1}^{K,N_A^{(k)},N_E^{(k)}} \left(1 - \frac{\gamma}{2}\frac{R_t^{(l)} + R_r^{(k)}}{2D}\right) \cos\Big[K_p D_T^{DB} + K_q D_R^{DB} + 2\pi t f_{T\max}\\
&\times \cos\left(\alpha_T^{(m,l)} - \gamma_T\right) + 2\pi t f_{R\max} \cos\left(\alpha_R^{(n,k)} - \gamma_R\right)\\
&- \frac{2\pi}{c_0} f\left(D + R_t^{(l)}\left(1 - \cos\alpha_T^{(m,l)}\right) + R_r^{(k)}\left(1 + \cos\alpha_R^{(n,k)}\right)\right) + \phi_{m,i,l,n,g,k}\Big]\\
&+ \rho_{pq}^{LoS} \cos\Big[2\pi t\left(f_T^{LoS} + f_R^{LoS}\right) - \frac{2\pi}{c_0} f\sqrt{D^2 + \Delta H^2} + K_p d_{Tx} + K_q d_R \cos\psi_R \cos(\alpha_{Rq}^{LoS} - \theta_R)\Big],
\end{aligned}
$$

$$T_{pq}^{(Q)}(t,f) = \tag{246}$$

$$\frac{\rho_{pq}^{SBT}}{\sqrt{M}} \sum_{l,m,i=1}^{L,M_A^{(l)},M_E^{(l)}} \left(1 - \frac{\gamma}{2}\frac{R_t^{(l)}}{D}\right) \sin\Big[K_p D_T^{SBT} + K_q D_R^{SBT} + 2\pi t f_{T\max} \cos\left(\alpha_T^{(m,l)} - \gamma_T\right)$$

$$+ 2\pi t f_{R\max}\left(\Delta_T^{(l)} \sin\gamma_R \sin\alpha_T^{(m,l)} - \cos\gamma_R\right) - \frac{2\pi}{c_0} f\left(D + R_t^{(l)}\left(1 - \cos\alpha_T^{(m,l)}\right)\right) + \phi_{m,i,l}\Big]$$

$$+ \frac{\rho_{pq}^{SBR}}{\sqrt{N}} \sum_{k,n,g=1}^{K,N_A^{(k)},N_E^{(k)}} \left(1 - \frac{\gamma}{2}\frac{R_r^{(k)}}{D}\right) \sin\Big[K_p D_T^{SBR} + K_q D_R^{SBR} + 2\pi t f_{R\max} \cos\left(\alpha_R^{(n,k)} - \gamma_R\right)$$

$$+ 2\pi t f_{T\max}\left(\Delta_R^{(k)} \sin\gamma_T \sin\alpha_R^{(n,k)} + \cos\gamma_T\right) - \frac{2\pi}{c_0} f\left(D + R_r^{(k)}\left(1 + \cos\alpha_R^{(n,k)}\right)\right) + \phi_{n,g,k}\Big]$$

$$+ \frac{\rho_{pq}^{DB}}{\sqrt{MN}} \sum_{l,m,i=1}^{L,M_A^{(l)},M_E^{(l)}} \sum_{k,n,g=1}^{K,N_A^{(k)},N_E^{(k)}} \left(1 - \frac{\gamma}{2}\frac{R_t^{(l)} + R_r^{(k)}}{2D}\right) \sin\Big[K_p D_T^{DB} + K_q D_R^{DB} + 2\pi t f_{T\max}$$

$$\times \left(\alpha_T^{(m,l)} - \gamma_T\right) + 2\pi t f_{R\max} \cos\left(\alpha_R^{(n,k)} - \gamma_R\right)$$

$$- \frac{2\pi}{c_0} f\left(D + R_t^{(l)}\left(1 - \cos\alpha_T^{(m,l)}\right) + R_r^{(k)}\left(1 + \cos\alpha_R^{(n,k)}\right)\right) + \phi_{m,i,l,n,g,k}\Big]$$

$$+ \rho_{pq}^{LoS} \sin\Big[2\pi t\left(f_T^{LoS} + f_R^{LoS}\right) - \frac{2\pi}{c_0} f\sqrt{D^2 + \Delta H^2} + K_p d_{Tx} + K_q d_R \cos\psi_R \cos(\alpha_{Rq}^{LoS} - \theta_R)\Big],$$

are the I and Q components of the time-variant transfer function, $M = \sum_{l=1}^{L} M^{(l)} = \sum_{l=1}^{L} M_A^{(l)} M_E^{(l)}$, $N = \sum_{k=1}^{F} N^{(k)} = \sum_{k=1}^{F} N_A^{(k)} N_E^{(k)}$, $\rho_{SBT} = \sqrt{\eta_T/(K+1)}$, $\rho_{SBR} = \sqrt{\eta_R/(K+1)}$, $\rho_{DB} = \sqrt{\eta_{TR}/(K+1)}$, $\rho_{LoS} = \sqrt{K/(1+K)}$, $K_p = \pi(L_t + 1 - 2p)/\lambda$, $K_q = \pi(L_r + 1 - 2q)/\lambda$, $D_T^{SBT} = d_{Tx}\cos\alpha_T^{(m,l)} + d_{Ty}\sin\alpha_T^{(m,l)} + d_{Tz}\sin\beta_T^{(i,l)}$, $D_R^{SBT} = d_{Ry}\Delta_T^{(l)}\sin\alpha_T^{(m,l)} - d_{Rx}$, $D_T^{SBR} = d_{Ty}\Delta_R^{(k)}\sin\alpha_R^{(n,k)} + d_{Tx}$, $D_R^{SBR} = d_{Rx}\cos\alpha_R^{(n,k)} + d_{Ry}\sin\alpha_R^{(n,k)} + d_{Rz}\sin\beta_R^{(g,k)}$, $D_T^{DB} = d_{Tx}\cos\alpha_T^{(m,l)} + d_{Ty}\sin\alpha_T^{(m,l)} + d_{Tz}\sin\beta_T^{(i,l)}$, $D_R^{DB} = d_{Rx}\cos\alpha_R^{(n,k)} + d_{Ry}\sin\alpha_R^{(n,k)} + d_{Rz}\sin\beta_R^{(g,k)}$, $f_T^{LoS} = f_{T\max}\cos(\pi - \alpha_{Rq}^{LoS} - \gamma_T)$, and $f_R^{LoS} = f_{R\max}\cos(\alpha_{Rq}^{LoS} - \gamma_R)$. Note that the input delay-spread function can be obtained as the inverse Fourier transformation of the time-variant transfer function, i.e. $h_{pq}(t,\tau) = \mathcal{F}_f^{-1}\{T_{pq}(t,f)\}$.

The AAoDs, $\alpha_T^{(m,l)}$, and the AAoAs, $\alpha_R^{(n,k)}$, are modeled using the von Mises pdf in (96) and are generated as follows:

$$\alpha_T^{(m,l)} = F^{-1}\left(\frac{m - 0.5}{M_A^{(l)}}\right), \tag{247}$$

$$\alpha_R^{(n,k)} = F^{-1}\left(\frac{n-0.5}{N_A^{(k)}}\right), \tag{248}$$

for $m = 1, \ldots, M_A^{(l)}$, $n = 1, \ldots, N_A^{(k)}$, where $F(\ \cdot\ )^{-1}$ denotes the inverse cumulative von Mises distribution function and is evaluated using method in [75]. The EAoDs, $\beta_T^{(m,l)}$, and the EAoAs, $\beta_R^{(n,k)}$, are modeled using the pdf in (152) and are generated as follows:

$$\beta_T^{(i,l)} = \frac{2\beta_{T_m}}{\pi}\arcsin\left(\frac{2i-1}{M_E^{(l)}}-1\right), \tag{249}$$

$$\beta_R^{(g,k)} = \frac{2\beta_{R_m}}{\pi}\arcsin\left(\frac{2g-1}{N_E^{(k)}}-1\right), \tag{250}$$

for $i = 1, \ldots, M_E^{(l)}$, $g = 1, \ldots, N_E^{(k)}$. The radii $R_t^{(l)}$ and $R_r^{(k)}$ are modeled using pdfs $f(R_t) = 2R_t/(R_{t2}^2 - R_{t1}^2)$ and $f(R_r) = 2R_r/(R_{r2}^2 - R_{r1}^2)$, respectively, and are generated as follows:

$$R_t^{(l)} = \sqrt{\frac{(l-0.5)(R_{t2}^2 - R_{t1}^2)}{L} + R_{t1}^2}, \tag{251}$$

$$R_r^{(k)} = \sqrt{\frac{(k-0.5)(R_{r2}^2 - R_{r1}^2)}{K} + R_{r1}^2}, \tag{252}$$

for $l = 1, \ldots, L$, $k = 1, \ldots, K$. The phases $\phi_{m,i,l}$, $\phi_{n,g,k}$, and $\phi_{m,i,l,n,g,k}$ are generated as independent random variables uniformly distributed on the interval $[-\pi, \pi)$.

For $M, N \to \infty$, our model can be shown to exhibit property (215) of the reference model. The derivations are omitted for brevity. Fig. 52 compares the simulated space-time-frequency correlation functions obtained using (245) and (246) and the theoretical space-time-frequency correlation functions in (215), assuming the 3-D non-isotropic radio propagation ($k_T = k_R = 2$, $\beta_{T_m} = \beta_{R_m} = 15°$) in the urban and highway environments. In the urban environment, the double-bounced rays bear more energy than the single-bounced rays ($\eta_T = \eta_R = 0.1$, $\eta_{TR} = 0.8$), whereas, on the highways, the single-bounced rays are prevalent ($\eta_T = \eta_R = 0.45$, $\eta_{TR} = 0.1$). In all simulations, we use a normalized sampling period $f_T T_s = 0.01$ ($f_{Tmax} = f_{Rmax}$), assume $L_t = L_r = 2$ antennas, use $M_A^{(l)} = 44$, $M_E^{(l)} = 9$, $N_A^{(k)} = 44$, and $N_E^{(k)} = 9$ scatterers and six tap-delays ($L = 3$ and $K = 3$). All parameters used to obtain the curves in Fig. 52 are summarized in the last column of Table 9. Results show that the space-time-frequency correlation function of the simulation model closely matches the theoretical one in the range of normalized time delays, $0 \leq f_{T\max} T_s \leq 6$. .

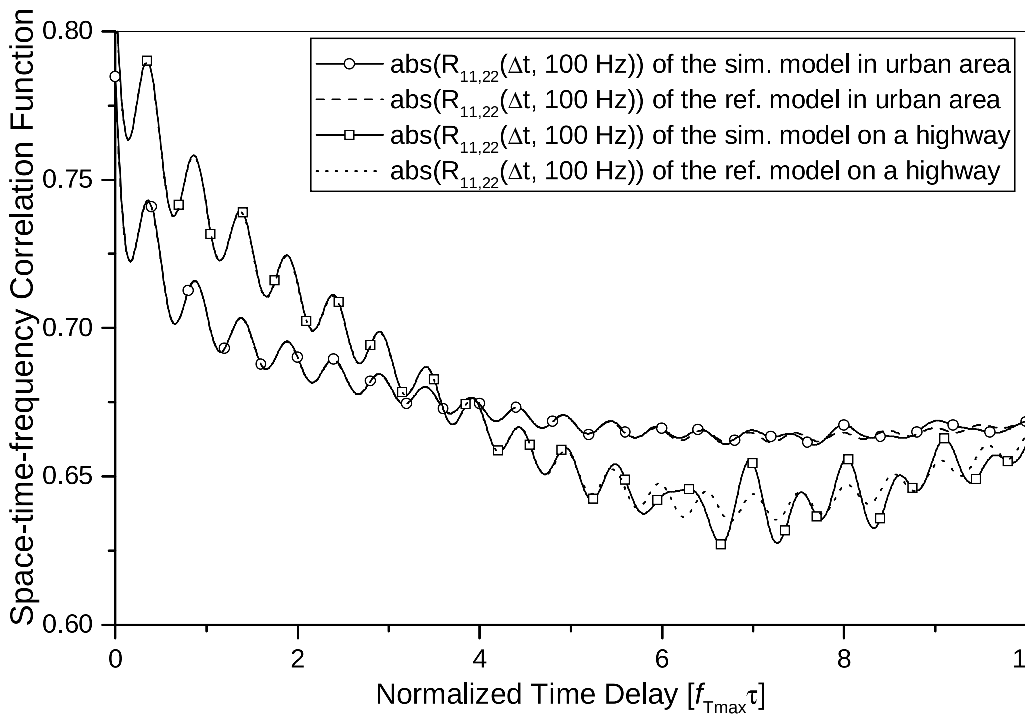

Figure 52: The simulated and theoretical space-time-frequency correlation functions in the urban and highway environments.

7.5 Summary

This chapter proposed the 3-D "concentric-cylinders" geometrical propagation model for wideband MIMO M-to-M multipath fading channels. Based in this model, the parametric reference model was proposed for MIMO M-to-M Ricean fading channels. From the reference model, the stf-cf was derived for a 3-D non-isotropic scattering environment. It was shown that the time dispersion and the frequency dispersion of a WSSUS channel cannot be treated independently, contrary to common practice.

Furthermore, the sD-psd and the psds were derived and compared with measured data. The close agreement between the theoretical and empirical curves confirms the utility of the proposed wideband model. Finally, two new SoS simulation models for wideband MIMO M-to-M Ricean fading channels were proposed. The statistics of the simulation models have been verified by simulation. The results show that the simulation models are a good approximation of the reference model.

Table 9: The parameters used in Figs. 45 - 52.

Parameters	Definition	Fig.3	Fig.4	Fig.5	Fig.6	Fig.7	Fig.8	Fig.9	Fig. 10
D [m]	The distance between the Tx and Rx.	500	500	500	300	300	300	300	200
d_T d_R	The spacing between two adjacent antenna elements at the Tx and Rx, respectively.	0.5λ 0.5λ	0 0	0.5λ 0.5λ	$0{,}1\lambda$ $0{,}1\lambda$	$0{,}1\lambda$ $0{,}1\lambda$	$0\text{-}4\lambda$ $0\text{-}4\lambda$	$0\text{-}4\lambda$ $0\text{-}4\lambda$	0.5λ 0.5λ
θ_T θ_R	The orientation of the Tx and Rx antenna array in the x-y plane (relative to the *x*-axis), respectively.	$\frac{\pi}{4}$ $\frac{\pi}{4}$	$\frac{\pi}{4}$ $\frac{\pi}{4}$	$\frac{\pi}{4}$ $\frac{\pi}{4}$	0° 0°	90° 90°	0° 0°	0° 0°	$\frac{\pi}{4}$ $\frac{\pi}{4}$
ψ_T ψ_R	The elevation of the Tx's and Rx's antenna array relative to the x-y plane, respectively.	$\frac{\pi}{6}$ $\frac{\pi}{6}$	$\frac{\pi}{6}$ $\frac{\pi}{6}$	$\frac{\pi}{6}$ $\frac{\pi}{6}$	0° 0°	0° 0°	0° 0°	0° 0°	$\frac{\pi}{3}$ $\frac{\pi}{3}$
γ_T γ_R	The moving directions of the Tx and Rx, in the x-y plane (relative to the *x*-axis), respectively.	40° 20°	40° 20°	40° 20°	90° 90°	0° 0°	90° 90°	90° 90°	20° 20°
Δ_H [m]	The difference between the Tx and Rx antenna heights.	0	0	0	0	0	0	0	0
λ [m]	The wavelength	0.3	0.3	0.3	0.058	0.123	0.123	0.123	0.3
$f_{T\max}$ [Hz] $f_{R\max}$ [Hz]	The maximum Doppler frequencies.	200 200	200 200	200 200	75 75	200 200	200 200	200 200	200 200
γ	The path loss exponent	4	4	4	4	4	4	4	4
K	The Rice factor	0	0	0	4	1.5	0	0	2
k_T k_R	The spread of scatterers around the mean; the parameter in the von Mises pdf.	2 2	2 2	2 2	5 3.3	4 4	9.1 9.1	9.4 9.4	1 1
μ_T μ_R	The mean angle at which the scatterers are distributed in the x-y plane; the parameter in the von Mises pdf.	$\frac{\pi}{2}$ $\frac{3\pi}{2}$	$\frac{\pi}{2}$ $\frac{3\pi}{2}$	$\frac{\pi}{2}$ $\frac{3\pi}{2}$	70° 250°	0° 180°	$\frac{\pi}{2}$ $\frac{3\pi}{2}$	$\frac{\pi}{2}$ $\frac{3\pi}{2}$	0 π
β_{Tm} β_{Rm}	The maximum elevation angles.	15° 15°	15° 15°	15° 15°	20° 20°	15° 15°	15° 15°	15° 15°	15° 15°
R_{t1} [m] R_{t2} [m] R_{r1} [m] R_{r2} [m]	The min and max radii of the cylinders around the Tx and Rx, respectively.	10 100 10 100	10 100 10 100	10 100 10 100	9 90 9 90	9.6 96 9.6 96	13 130 13 130	12 120 12 120	4 40 4 40
η_T η_R η_{TR}	Specify how much the single- and double-bounced rays contribute in the total averaged power, i.e., $\eta_T+\eta_R+\eta_{TR}=1$	$\frac{1}{3}$ $\frac{1}{3}$ $\frac{1}{3}$	$\frac{1}{3}$ $\frac{1}{3}$ $\frac{1}{3}$	$\frac{1}{3}$ $\frac{1}{3}$ $\frac{1}{3}$	0.1 0.1 0.8	0.3 0.3 0.4	0.2 0.2 0.6	0.45 0.45 0.1	Defi-ned in the text

CHAPTER VIII

ENVELOPE LEVEL CROSSING RATE AND AVERAGE FADE DURATION IN M-TO-M FADING CHANNELS

8.1 Overview

In Chapters 6 and 7, we have proposed 3-D models for *narrowband* and *wideband* MIMO M-to-M multipath fading channels and derived their first-order statistics. However, in some applications, accurate characterization of the second-order statistics, such as envelope level crossing rate (LCR) and average fade duration (AFD), is necessary. In this chapter, we derive the LCR and AFD for narrowband M-to-M channels. We first construct a 3-D SISO model that employs the "two-cylinder" model proposed in Section 6.2 and generates the complex faded envelope as a superposition of the LoS, single-bounced, and double-bounced rays (as proposed in Section 7.2). From the analytical model, we derive the LCR and AFD, assuming a 3-D non-isotropic scattering environment. Finally, we compare the analytical results for the LCR and AFD with the measured data in [39]. The close agreement between the analytical and empirical curves confirms the utility of the proposed model.

The remainder of the chapter is organized as follows. Section 8.2 presents a 3-D SISO model used to derive the LCR and AFD. Section 8.3 derives the LCR and AFD of the the complex faded envelope for 3-D non-isotropic scattering. Section 8.4 compares analytical and measurement results to verify theoretical derivations. Finally, Section 8.5 provides some concluding remarks.

8.2 *A 3-D SISO Model for M-to-M Channels*

Figure 53 shows a simplified (SISO) version of our 3-D MIMO "two-cylinder" geometrical model described in Section 6.2. The symbols $\alpha_T^{(m)}$ and $\alpha_T^{(n)}$ in Fig. 53 denote the azimuth angles of departure (AAoD), and $\beta_T^{(m)}$ and $\beta_T^{(n)}$ denote the elevation angles of departure (EAoD) of the waves that impinge on the scatterers $S_T^{(m)}$ and $S_R^{(n)}$, respectively. Likewise, $\alpha_R^{(m)}$ and $\alpha_R^{(n)}$ denote the azimuth angles of arrival (AAoA), and $\beta_R^{(m)}$ and $\beta_R^{(n)}$ denote the elevation angles of arrival (EAoA) of the waves scattered from $S_T^{(m)}$ and $S_R^{(n)}$, respectively. The symbols β_T^{LoS} and β_R^{LoS} denote the EDoA and EAoA of the LoS paths, respectively. Note that the ADoA and AAoA of the LoS paths, α_T^{LoS} and α_R^{LoS}, are equal to 0 and π, respectively, and they are omitted from Fig. 53. The symbols H_T and H_R denote the $\mathrm{T_x}$ and $\mathrm{R_x}$ antenna height, respectively. The rest of the parameters in Fig. 53 are defined as in Table 7.

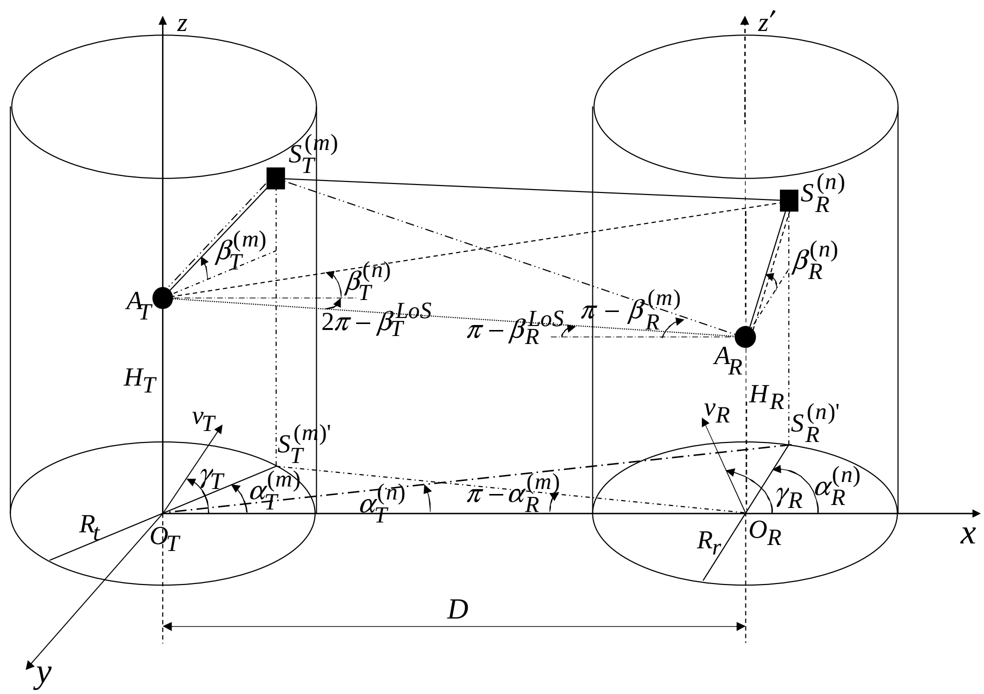

Figure 53: The 3-D geometrical model for SISO narrowband M-to-M channels.

The received complex faded envelope of the link A_T - A_R can be written as a superposition of LoS, single-bounced, and double-bounced rays, i.e.,

$$h(t) = h^{SBT}(t) + h^{SBR}(t) + h^{DB}(t) + h^{LoS}(t), \tag{253}$$

where the single-bounced components of the received complex faded envelope are, respectively,

$$\begin{aligned} h^{SBT}(t) &= \sqrt{\frac{\eta_T}{K+1}} \lim_{M\to\infty} \sum_{m=1}^{M} \frac{a_m}{\sqrt{M}} e^{j\phi_m} e^{j2\pi t f_{T\max} \cos(\alpha_T^{(m)} - \gamma_T)\cos\beta_T^{(m)}} \\ &\times \; e^{j2\pi t f_{R\max}(\cos\gamma_R - \Delta_T \sin\gamma_R \sin\alpha_T^{(m)})\cos(\Delta_T \beta_T^{(m)} + \frac{\Delta_H}{D})}, \end{aligned} \tag{254}$$

$$\begin{aligned} h^{SBR}(t) &= \sqrt{\frac{\eta_R}{K+1}} \lim_{N\to\infty} \sum_{n=1}^{N} \frac{a_n}{\sqrt{N}} e^{j\phi_n} e^{j2\pi t f_{T\max}(\Delta_R \sin\gamma_T \sin\alpha_R^{(n)} + \cos\gamma_T)\cos(\Delta_R \beta_R^{(n)} - \frac{\Delta_H}{D})} \\ &\times \; e^{j2\pi t f_{R\max} \cos(\alpha_R^{(n)} - \gamma_R)\cos\beta_R^{(n)}}, \end{aligned} \tag{255}$$

the double-bounced component of the received complex faded envelope is

$$\begin{aligned} h^{DB}(t) &= \sqrt{\frac{\eta_{TR}}{K+1}} \lim_{M,N\to\infty} \sum_{m,n=1}^{M,N} \frac{a_{mn} e^{j\phi_{mn}}}{\sqrt{MN}} \\ &\times \; e^{j2\pi t [f_{T\max} \cos(\alpha_T^{(m)} - \gamma_T)\cos\beta_T^{(m)} + f_{R\max}\cos(\alpha_R^{(n)} - \gamma_R)\cos\beta_R^{(n)}]}, \end{aligned} \tag{256}$$

and the LoS component of the received complex faded envelope is

$$h^{LoS}(t) = \sqrt{\frac{K}{K+1}} \, e^{j2\pi t f_{T\max}\cos(\gamma_T)\cos(\beta_T^{LoS}) + j2\pi t f_{R\max}\cos(\pi - \gamma_R)\cos(\beta_R^{LoS})}. \tag{257}$$

In (254) – (257), K denotes the Rice factor (ratio of LoS to scatter received power) while η_T, η_R, and η_{TR} specify the relative contribution of the single- and double-bounced rays, such that $\eta_T + \eta_R + \eta_{TR} = 1$. The random path gains a_m, a_n, and a_{mn} are chosen to satisfy $\lim_{M\to\infty} M^{-1} \sum_{m=1}^{M} a_m^2 = 1$, $\lim_{N\to\infty} N^{-1} \sum_{n=1}^{N} a_n^2 = 1$, and $\lim_{M,N\to\infty} (MN)^{-1} \sum_{m,n=1}^{M,N} a_{mn}^2 = 1$, respectively, so that $\mathrm{E}[|h(t)|^2]$ is normalized to unity. Frequencies $f_{T\max} = v_T/\lambda$ and $f_{R\max} = v_R/\lambda$ are the maximum Doppler frequencies associated with the $\mathrm{T_x}$ and $\mathrm{R_x}$, respectively. It is assumed that the angles of departure ($\alpha_T^{(m)}$, $\alpha_T^{(n)}$, $\beta_T^{(m)}$, and $\beta_T^{(n)}$) and the angles of arrival ($\alpha_R^{(m)}$, $\alpha_R^{(n)}$, $\beta_R^{(m)}$, and $\beta_R^{(n)}$) are random variables. To characterize the random azimuth angles α_T and

α_R, we use the von Mises pdf given in (96). To characterize the random elevation angles β_T and β_R, we use the pdf in (152). Finally, the phases ϕ_m, ϕ_n, and ϕ_{mn} are assumed to be independent uniform random variables on the interval $[-\pi, \pi)$, and are independent from the angles of departure and the angles of arrival.

The complex faded envelope in (253) also can be written as $h(t) = h_i(t) + jh_q(t)$ where

$$\begin{aligned} h_i(t) &= h_i^{SBT}(t) + h_i^{SBR}(t) + h_i^{DB}(t) + h_i^{LoS}(t) \\ &= \Re\{h^{SBT}(t)\} + \Re\{h^{SBR}(t)\} + \Re\{h^{DB}(t)\} + \Re\{h^{LoS}(t)\}, \end{aligned} \tag{258}$$

$$\begin{aligned} h_q(t) &= h_q^{SBT}(t) + h_q^{SBR}(t) + h_q^{DB}(t) + h_q^{LoS}(t) \\ &= \Im\{h^{SBT}(t)\} + \Im\{h^{SBR}(t)\} + \Im\{h^{DB}(t)\} + \Im\{h^{LoS}(t)\}, \end{aligned} \tag{259}$$

are the in-phase (I) and quadrature (Q) components of the complex faded envelope, and $\Re\{\,\cdot\,\}$ and $\Im\{\,\cdot\,\}$ denote the real and imaginary operation, respectively. Finally, we note that for 3-D non-isotropic scattering, the I and Q components of the complex faded envelope $h(t)$ are correlated.

8.3 LCR and AFD in M-to-M Narrowband Fading Channels

The LCR, $L(R)$, is defined as the rate at which the signal envelope crosses level R in the positive (or negative) going direction and can be written as [35]

$$L(R) = \int_0^\infty \dot{\alpha} f_{\alpha,\dot{\alpha}}(R, \dot{\alpha}) d\dot{\alpha}, \tag{260}$$

where $\alpha = |h(t)|$ is the envelope level, $\dot{\alpha} = |\dot{h}(t)|$ is the envelope slope, and $f_{\alpha,\dot{\alpha}}(R, \dot{\alpha})$ is the joint probability density function (pdf) of the envelope level and the envelope slope. To evaluate the LCR of the proposed analytical model, we need to derive the pdf of the fading envelope $\alpha = |h(t)|$ and consequently, the joint pdf $f_{\alpha,\dot{\alpha}}(\alpha, \dot{\alpha})$.

Theorem 1 *When the number of scatterers around the* $\mathrm{T_x}$ *and the number of scatterers around the* $\mathrm{R_x}$ *approach infinity (i.e.,* $M, N \to \infty$*), the envelope* $\alpha = |h(t)|$ *is Rician distributed with the pdf*

$$f_{|h(t)|}(\alpha) \;=\; 2(1+K)\alpha e^{-K-(1+K)\alpha^2} I_0\left(2\alpha\sqrt{K(K+1)}\right). \tag{261}$$

Proof: First, we note that the cosine and sine functions in the sums of $h_i^{SBT}(t)$ and $h_q^{SBT}(t)$ are statistically independent and identically distributed random variables with zero mean and a finite variance. According to the central limit theorem, for $M \to \infty$, $h_i^{SBT}(t)$ and $h_q^{SBT}(t)$ are stationary Gaussian processes with zero means and the identical variances $\mathrm{Var}\{h_i^{SBT}(t)\} = \mathrm{Var}\{h_q^{SBT}(t)\} = \eta_T/(2+2K)$. Similarly, for $N \to \infty$, $h_i^{SBR}(t)$ and $h_q^{SBR}(t)$ are stationary Gaussian processes with zero means and the identical variances $\mathrm{Var}\{h_i^{SBR}(t)\} = \mathrm{Var}\{h_q^{SBR}(t)\} = \eta_R/(2+2K)$. When channel does not experience keyhole behavior [i.e., the distance D is smaller than $4R_tR_rL_r/(\lambda(L_t-1)(L_r-1))$] and $M, N \to \infty$, $h_i^{DB}(t)$ and $h_q^{DB}(t)$ are also stationary Gaussian processes [58] with zero means and the identical variances $\mathrm{Var}\{h_i^{DB}(t)\} = \mathrm{Var}\{h_q^{DB}(t)\} = \eta_{TR}/(2+2K)$. Using the similar reasoning, we can conclude that the linear combinations of $h_{i/q}^{SBT}(t)$, $h_{i/q}^{SBR}(t)$, $h_{i/q}^{DB}(t)$, $h_{i/q}^{LoS}(t)$, i.e., $h_i(t)$ and $h_q(t)$, are also stationary Gaussian processes with the means $\mathrm{E}[h_i(t)] = h_i^{LoS}(t)$ and $\mathrm{E}[h_q(t)] = h_q^{LoS}(t)$, respectively, and the identical variances $\mathrm{Var}\{h_i(t)\} = \mathrm{Var}\{h_q(t)\} = 1/(2+2K)$. Following the derivations for the pdf of the envelope $\alpha = |h(t)| = \sqrt{h_i(t)^2 + h_q(t)^2}$ with the correlated $h_i(t)$ and $h_q(t)$ [84], we confirm that the envelope $\alpha = |h(t)| = \sqrt{h_i(t)^2 + h_q(t)^2}$ is Rician distributed with the pdf given in (261). The details are omitted for brevity. ⊡

It is worth noting that if $h_{i/q}(t)$ is a stationary Gaussian process with the mean $\mathrm{E}[h_{i/q}(t)] = h_{i/q}^{LoS}(t)$ and the variance $\mathrm{Var}\{h_{i/q}(t)\} = R_{h_i,h_i}(0)$, where $R_{h_i,h_i}(0) = \mathrm{E}[h_i(t)h_i(t)]$ and $\mathrm{E}[\;\cdot\;]$ denotes the statistical expectation operator, then its time derivative $\dot{h}_{i/q}(t)$ is also a stationary Gaussian process with mean $\mathrm{E}[\dot{h}_{i/q}(t)] = \dot{h}_{i/q}^{LoS}(t)$ and the variance $\mathrm{Var}\{\dot{h}_{i/q}(t)\} = R_{\dot{h}_i,\dot{h}_i}(0)$. Furthermore, note that the joint pdf

$f_{\alpha,\dot{\alpha}}(\alpha,\dot{\alpha})$ cannot be separated into product of of a Rice pdf $f_{|h(t)|}(\alpha)$ and a Gaussian pdf $f_{|\dot{h}(t)|}(\dot{\alpha})$ because the I and Q components of the complex faded envelope $h(t)$ are correlated.

The joint pdf $f_{\alpha,\dot{\alpha}}(\alpha,\dot{\alpha})$ for the complex faded envelope $h(t)$ with the correlated I and Q components can be written as [84]

$$\begin{aligned} f_{\alpha,\dot{\alpha}}(\alpha,\dot{\alpha}) &= \frac{\alpha}{\sqrt{(2\pi)^3(b_0b_2-b_1^2)b_0}} \exp\left\{-\left(\frac{\alpha^2}{2b_0}+K\right)\right\} \\ &\times \int_0^{2\pi} \exp\left\{2\sqrt{K(K+1)}\alpha\cos\theta - \frac{\left(b_0\dot{\alpha}+b_1\sqrt{\frac{K}{K+1}}\sin\theta\right)^2}{2b_0(b_0b_2-b_1^2)}\right\} d\alpha, \end{aligned} \tag{262}$$

where the parameters b_0, b_1, and b_2 are defined as [21]

$$b_0 \triangleq \mathrm{E}[h_i(t)^2] = \mathrm{E}[h_q(t)^2], \tag{263}$$

$$b_1 \triangleq \mathrm{E}[h_i(t)\dot{h}_q(t)] = \mathrm{E}[h_q(t)\dot{h}_i(t)], \tag{264}$$

$$b_2 \triangleq \mathrm{E}[\dot{h}_i(t)^2] = \mathrm{E}[\dot{h}_q(t)^2], \tag{265}$$

and $\dot{h}_i(t)$ and $\dot{h}_q(t)$ denote the first derivative of $h_i(t)$ and $h_q(t)$ with respect to time t. By substituting (262) into (260) and solving the integral, the LCR for LoS conditions (Rician fading, correlated I and Q components) becomes [84]

$$\begin{aligned} L(R) &= \frac{2R\sqrt{K+1}}{\pi^{3/2}}\sqrt{\frac{b_2}{b_0}-\frac{b_1^2}{b_0^2}}\, e^{-K-(K+1)R^2}\int_0^{\pi/2}\cosh\left(2\sqrt{K(K+1)}R\cos\theta\right) \\ &\times \left[e^{-(\chi\sin\theta)^2}+\sqrt{\pi}\chi\sin\theta\ \mathrm{erf}(\chi\sin\theta)\right] d\theta, \end{aligned} \tag{266}$$

where $\cosh(\ \cdot\ )$ is the hyperbolic cosine function, $\mathrm{erf}(\ \cdot\ )$ is the error function, and the parameter χ is equal to $\sqrt{Kb_1^2/(b_0b_2-b_1^2)}$. The LCR for NLoS conditions can be obtained from (266) by setting $K=0$, i.e.,

$$L(R) = \sqrt{\frac{b_2}{b_0}-\frac{b_1^2}{b_0^2}}\ \frac{R\ e^{-R^2}}{\sqrt{\pi}}. \tag{267}$$

Using the analytical model described in Section 8.2, we now derive closed-form expressions for the parameters b_0, b_1, and b_2. Since the number of local scatterers in the reference model described in Section 8.2 is infinite, the discrete AAoDs, $\alpha_T^{(m)}$, EAoDs, $\beta_T^{(m)}$, AAoAs, $\alpha_R^{(n)}$, and EAoAs, $\beta_R^{(n)}$ can be replaced with continuous random variables α_T, β_T, α_R, and β_R with joint probability density functions (pdfs) $f(\alpha_T, \beta_T)$ and $f(\alpha_R, \beta_R)$, respectively. We assume that the azimuth and elevation angles are independent of each other and, thus, the joint pdfs $f(\alpha_T, \beta_T)$ and $f(\alpha_R, \beta_R)$ can be decomposed to $f(\alpha_T)f(\beta_T)$ and $f(\alpha_R)f(\beta_R)$, respectively. This assumption is based on experimental data in [70]. By substituting (253) into (263), the parameter b_0 becomes

$$2b_0 \quad = \quad 2b_0^{SBT} + 2b_0^{SBR} + 2b_0^{DB} = \frac{1}{K+1}, \tag{268}$$

where b_0^{SBT}, b_0^{SBR}, and b_0^{DB} are, respectively,

$$2b_0^{SBT} \quad = \quad \frac{\eta_T}{K+1} \int_{-\beta_{T_m}}^{\beta_{T_m}} \int_{-\pi}^{\pi} f(\alpha_T) f(\beta_T) d\alpha_T d\beta_T = \frac{\eta_T}{K+1}, \tag{269}$$

$$2b_0^{SBR} \quad = \quad \frac{\eta_R}{K+1} \int_{-\beta_{R_m}}^{\beta_{R_m}} \int_{-\pi}^{\pi} f(\alpha_R) f(\beta_R) d\alpha_R d\beta_R = \frac{\eta_R}{K+1}, \tag{270}$$

$$\begin{aligned} 2b_0^{DB} \quad &= \quad \frac{\eta_{TR}}{K+1} \int_{-\beta_{T_m}}^{\beta_{T_m}} \int_{-\beta_{R_m}}^{\beta_{R_m}} \int_{-\pi}^{\pi} \int_{-\pi}^{\pi} f(\alpha_T) f(\beta_T) f(\alpha_R) f(\beta_R) d\alpha_T d\beta_T d\alpha_R d\beta_R \\ &= \quad \frac{\eta_{TR}}{K+1}, \end{aligned} \tag{271}$$

and β_{T_m} and β_{R_m} are the maximum elevation angles of the scatterers around the $\mathrm{T_x}$ and $\mathrm{R_x}$, respectively. Similarly, by substituting (253) into (264) and (265), the parameters b_1 and b_2 become

$$b_n \quad = \quad b_n^{SBT} + b_n^{SBR} + b_n^{DB}, \tag{272}$$

where $n \in \{1, 2\}$ and b_n^{SBT}, b_n^{SBR}, and b_n^{DB} are, respectively,

$$\begin{aligned} b_n^{SBT} \quad &= \quad (2\pi)^n \; b_0^{SBT} \int_{-\beta_{T_m}}^{\beta_{T_m}} \int_{-\pi}^{\pi} f(\alpha_T) f(\beta_T) \Big[f_{T\max} \cos(\alpha_T - \gamma_T) \cos\beta_T \\ &+ \quad f_{R\max} (\cos\gamma_R - \Delta_T \sin\gamma_R \sin\alpha_T) \cos\!\left(\Delta_T \beta_T + \frac{\Delta_H}{D} \right) - f_{LoS} \Big]^n d\alpha_T d\beta_T, \end{aligned} \tag{273}$$

$$
\begin{aligned}
b_n^{SBR} &= (2\pi)^n \ b_0^{SBR} \int_{-\beta_{R_m}}^{\beta_{R_m}} \int_{-\pi}^{\pi} f(\alpha_R) f(\beta_R) \Bigg[f_{R\max} \cos(\alpha_R - \gamma_R) \cos \beta_R \\
&+ f_{T\max} (\Delta_R \sin \gamma_T \sin \alpha_R + \cos \gamma_T) \cos\Bigg(\Delta_R \beta_R - \frac{\Delta_H}{D} \Bigg) - f_{LoS} \Bigg]^n d\alpha_R d\beta_R,
\end{aligned} \tag{274}
$$

$$
\begin{aligned}
b_n^{DB} &= (2\pi)^n \ b_0^{DB} \int_{-\beta_{R_m}}^{\beta_{R_m}} \int_{-\pi}^{\pi} \int_{-\beta_{T_m}}^{\beta_{T_m}} \int_{-\pi}^{\pi} f(\alpha_R) f(\beta_R) f(\alpha_T) f(\beta_T) \\
\times & \Bigg[f_{R\max} \cos(\alpha_R - \gamma_R) \cos \beta_R + f_{T\max} \cos(\alpha_T - \gamma_T) \cos \beta_T - f_{LoS} \Bigg]^n d\alpha_R d\beta_R d\alpha_T d\beta_T,
\end{aligned} \tag{275}
$$

and $f_{LoS} = f_{T\max} \cos(\gamma_T) \cos(\beta_T^{LoS}) + f_{R\max} \cos(\pi - \gamma_R) \cos(\beta_R^{LoS})$.

By denoting the pdfs for the $\mathrm{T_x}$ and $\mathrm{R_x}$ azimuth angles as $f(\alpha_T) = \exp[k_T \cos(\alpha_T - \mu_T)]/(2\pi I_0(k_T))$ and $f(\alpha_R) = \exp[k_R \cos(\alpha_R - \mu_R)]/(2\pi I_0(k_R))$, respectively, by denoting the pdfs for the $\mathrm{T_x}$ and $\mathrm{R_x}$ elevation angles as $f(\beta_T) = \pi \cos(\pi\beta_T/(2\beta_{T_m}))/(4\beta_{T_m})$ and $f(\beta_R) = \pi \cos(\pi\beta_R/(2\beta_{R_m}))/(4\beta_{R_m})$, respectively, and by using trigonometric identities, and the equality $\int_{-\pi}^{\pi} e^{-jm\theta + jz\sin\theta} d\theta = 2\pi J_m(z)$ [63, eq. 8.411], where $J_m(\ \cdot\ )$ is the m^{th}-order Bessel function of the first kind, Appendix M shows that the parameters b_1^{DB}, b_1^{SBT}, b_1^{SBR}, b_2^{DB}, b_2^{SBT}, and b_2^{SBR} become, respectively,

$$
\begin{aligned}
b_1^{DB} &= 2\pi b_0^{DB} \Bigg\{ f_{T\max} \cos(\mu_T - \gamma_T) \frac{I_1(k_T)}{I_0(k_T)} \frac{\pi^2 \cos \beta_{T_m}}{\pi^2 - 4\beta_{T_m}^2} + f_{R\max} \cos(\mu_R - \gamma_R) \frac{I_1(k_R)}{I_0(k_R)} \\
&\times \frac{\pi^2 \cos \beta_{R_m}}{\pi^2 - 4\beta_{R_m}^2} - f_{LoS} \Bigg\},
\end{aligned} \tag{276}
$$

$$
\begin{aligned}
b_1^{SBT} &= 2\pi b_0^{SBT} \Bigg\{ f_{T\max} \cos(\mu_T - \gamma_T) \frac{I_1(k_T)}{I_0(k_T)} \frac{\pi^2 \cos \beta_{T_m}}{\pi^2 - 4\beta_{T_m}^2} \\
&+ \Bigg[\Delta_T \sin \gamma_R \sin \mu_T \frac{I_1(k_T)}{I_0(k_T)} + \cos \gamma_R \Bigg] \\
&\times f_{R\max} \frac{\pi^2 [\cos(\Delta_T \beta_{T_m} + \frac{\Delta_H}{D}) + \cos(\Delta_T \beta_{T_m} - \frac{\Delta_H}{D})]}{2[\pi^2 - 4\Delta_T^2 \beta_{T_m}^2]} - f_{LoS} \Bigg\},
\end{aligned} \tag{277}
$$

$$
\begin{aligned}
b_1^{SBR} &= 2\pi b_0^{SBR} \Bigg\{ f_{R\max} \cos(\mu_R - \gamma_R) \frac{I_1(k_R)}{I_0(k_R)} \frac{\pi^2 \cos \beta_{R_m}}{\pi^2 - 4\beta_{R_m}^2} \\
&+ \Bigg[\cos \gamma_T - \Delta_R \sin \gamma_T \sin \mu_R \frac{I_1(k_R)}{I_0(k_R)} \Bigg] \\
&\times f_{T\max} \frac{\pi^2 [\cos(\Delta_R \beta_{R_m} + \frac{\Delta_H}{D}) + \cos(\Delta_R \beta_{R_m} - \frac{\Delta_H}{D})]}{2[\pi^2 - 4\Delta_R^2 \beta_{R_m}^2]} - f_{LoS} \Bigg\},
\end{aligned} \tag{278}
$$

$$
\begin{aligned}
b_2^{DB} &= (2\pi)^2 b_0^{DB}\Bigg\{ f_{T\max}^2\left[\frac{\pi^2\cos(2\beta_{T_m})}{2(\pi^2-16\beta_{T_m}^2)}+\frac{1}{2}\right]\frac{1+\cos(2(\mu_T-\gamma_T))I_2(k_T)}{2I_0(k_T)} \qquad (279)\\
&+ 2f_{T\max}f_{R\max}\frac{\pi^2\cos\beta_{T_m}}{\pi^2-4\beta_{T_m}^2}\frac{\pi^2\cos\beta_{R_m}}{\pi^2-4\beta_{R_m}^2}\cos(\mu_T-\gamma_T)\frac{I_1(k_T)}{I_0(k_T)}\cos(\mu_R-\gamma_R)\frac{I_1(k_R)}{I_0(k_R)}\\
&+ f_{R\max}^2\left[\frac{\pi^2\cos(2\beta_{R_m})}{2(\pi^2-16\beta_{R_m}^2)}+\frac{1}{2}\right]\frac{1+\cos(2(\mu_R-\gamma_R))I_2(k_R)}{2I_0(k_R)} - f_{LoS}\frac{b_1^{DB}}{\pi b_0^{DB}} - f_{LoS}^2\Bigg\},\\
b_2^{SBT} &= (2\pi)^2 b_0^{SBT}\Bigg\{ f_{T\max}^2\frac{\pi^2\cos(2\beta_{T_m})+\pi^2-16\beta_{T_m}^2}{2(\pi^2-16\beta_{T_m}^2)}\frac{1+\cos(2(\mu_T-\gamma_T))I_2(k_T)}{2I_0(k_T)}\\
&+ \frac{4\beta_{T_m}^2+8\Delta_T\beta_{T_m}^2-\pi^2+4\Delta_T^2\beta_{T_m}^2}{4\left[8\beta_{T_m}^2\pi^2-16\beta_{T_m}^4-\pi^4-16\Delta_T^4\beta_{T_m}^4+8\pi^2\Delta_T^2\beta_{T_m}^2+32\Delta_T^2\beta_{T_m}^4\right]}\\
&\times \Bigg[\cos\left((\Delta_T-1)\beta_{T_m}+\frac{\Delta_H}{D}\right)+\cos\left((\Delta_T+1)\beta_{T_m}+\frac{\Delta_H}{D}\right)\\
&+ \cos\left((\Delta_T-1)\beta_{T_m}-\frac{\Delta_H}{D}\right)+\cos\left((\Delta_T+1)\beta_{T_m}-\frac{\Delta_H}{D}\right)\Bigg]\\
&\times \Bigg[f_{T\max}f_{R\max}\Delta_T\sin\gamma_R\left(\frac{I_2(k_T)}{I_0(k_T)}\cos(2\mu_T-\gamma_T)-\cos\gamma_T\right)\\
&+ 2f_{T\max}f_{R\max}\cos\gamma_R\Bigg]+\Bigg[\frac{\cos\left[2\left(\Delta_T\beta_{T_m}+\frac{\Delta_H}{D}\right)\right]\pi^2+2\pi^2-32\Delta_T^2\beta_{T_m}^2}{4[\pi^2-16\Delta_T^2\beta_{T_m}]}\\
&+ \frac{\cos\left[2\left(\Delta_T\beta_{T_m}-\frac{\Delta_H}{D}\right)\right]\pi^2}{4[\pi^2-16\Delta_T^2\beta_{T_m}]}\Bigg]\Bigg[f_{R\max}^2\cos\gamma_R^2+f_{R\max}^2\Delta_T^2\sin\gamma_R^2\\
&\times \frac{1-\cos(2\mu_T)I_2(k_T)}{2I_0(k_T)}+f_{R\max}^2\Delta_T\sin(2\gamma_R)\sin\mu_T\frac{I_1(k_T)}{I_0(k_T)}\Bigg]\\
&- f_{LoS}\frac{b_1^{SBT}}{\pi b_0^{SBT}}-f_{LoS}^2\Bigg\}, \qquad (280)\\
b_2^{SBR} &= (2\pi)^2 b_0^{SBR}\Bigg\{ f_{R\max}^2\frac{\pi^2\cos(2\beta_{R_m})+\pi^2-16\beta_{R_m}^2}{2(\pi^2-16\beta_{R_m}^2)}\frac{1+\cos(2(\mu_R-\gamma_R))I_2(k_R)}{2I_0(k_R)}\\
&- f_{LoS}^2+\frac{4\beta_{R_m}^2+8\Delta_R\beta_{R_m}^2-\pi^2+4\Delta_R^2\beta_{R_m}^2}{4\left[8\beta_{R_m}^2\pi^2-16\beta_{R_m}^4-\pi^4-16\Delta_R^4\beta_{R_m}^4+8\pi^2\Delta_R^2\beta_{R_m}^2+32\Delta_R^2\beta_{R_m}^4\right]}\\
&\times \Bigg[\cos\left((\Delta_R-1)\beta_{R_m}+\frac{\Delta_H}{D}\right)+\cos\left((\Delta_R+1)\beta_{R_m}+\frac{\Delta_H}{D}\right)\\
&+ \cos\left((\Delta_R-1)\beta_{R_m}-\frac{\Delta_H}{D}\right)+\cos\left((\Delta_R+1)\beta_{R_m}-\frac{\Delta_H}{D}\right)\Bigg]\\
&\times \Bigg[f_{R\max}f_{T\max}\Delta_R\sin\gamma_T\left(\cos\gamma_R-\frac{I_2(k_R)}{I_0(k_R)}\cos(2\mu_R-\gamma_R)\right)\\
&+ 2f_{R\max}f_{T\max}\cos\gamma_T\Bigg]+\Bigg[\frac{\cos\left[2\left(\Delta_R\beta_{R_m}+\frac{\Delta_H}{D}\right)\right]\pi^2+2\pi^2-32\Delta_R^2\beta_{R_m}^2}{4[\pi^2-16\Delta_R^2\beta_{R_m}]}\\
&+ \frac{\cos\left[2\left(\Delta_R\beta_{R_m}-\frac{\Delta_H}{D}\right)\right]\pi^2}{4[\pi^2-16\Delta_R^2\beta_{R_m}]}\Bigg]\Bigg[f_{T\max}^2\cos\gamma_T^2+f_{T\max}^2\Delta_R^2\sin\gamma_T^2 \qquad (281)\\
&\times \frac{1-\cos(2\mu_R)I_2(k_R)}{2I_0(k_R)}-f_{T\max}^2\Delta_R\sin(2\gamma_T)\sin\mu_R\frac{I_1(k_R)}{I_0(k_R)}\Bigg]-f_{LoS}\frac{b_1^{SBR}}{\pi b_0^{SBR}}\Bigg\}.
\end{aligned}
$$

The average fade duration, $T(R)$, is defined as the average time that the signal envelope, $\alpha = |h(t)|$, remains below level R. The AFD can be written as [35]

$$T(R) \;=\; \frac{P(\alpha \leq R)}{L(R)}, \tag{282}$$

where $P(\alpha \leq R)$ denotes the probability of the received envelope level being less than R and $L(R)$ denotes the envelope level crossing rate. When a LoS component is present, the AFD in (282) becomes [35]

$$T(R) \;=\; \frac{1 - Q(\sqrt{2K}, \sqrt{2(K+1)R^2})}{L(R)}, \tag{283}$$

where $Q(a, b)$ is the Marcum Q function. For NLoS conditions, the AFD in (283) simplifies to

$$T(R) \;=\; \frac{1 - e^{-R^2}}{L(R)}. \tag{284}$$

8.4 Simulation Results

To validate our analytical results, we compare them with our own measured data collected in two different topological environments around the Georgia Tech campus in Atlanta, USA. One location was a LoS surface street environment and the other was a LoS highway environment. The wide-band channel measurements were performed at 2.435 GHz. Each collected data set contains the signal envelope (and phase) over a travelled distance of 61.36 m (5.49 s of time). Both, the $\mathrm{T_x}$ and $\mathrm{R_x}$ were equipped with two omnidirectional antenna elements. All antenna elements had the same height, i.e., $\Delta_H = 0$, and the moving directions were $\gamma_T = \gamma_R = 0°$. The maximum Doppler frequencies in the urban surface street area were $f_{T\max} = f_{R\max} = 90.86$ Hz, whereas the maximum Doppler frequencies on the highway were $f_{T\max} = f_{R\max} =$ 181.72 Hz. The distance between the $\mathrm{T_x}$ and $\mathrm{R_x}$ in the urban surface street area was approximately $D = 300$ m, whereas the distance between the $\mathrm{T_x}$ and $\mathrm{R_x}$ on the highway was approximately $D = 180$ m. The slow-fading component of the signal envelope is removed using the local sliding window technique [86].

Figs. 54 and 55 compare the 3-D and 2-D analytical LCR and AFD with the measured LCR and AFD obtained from our data collected in a surface street environment, respectively. In these figures, we use only the channel impulse response between the

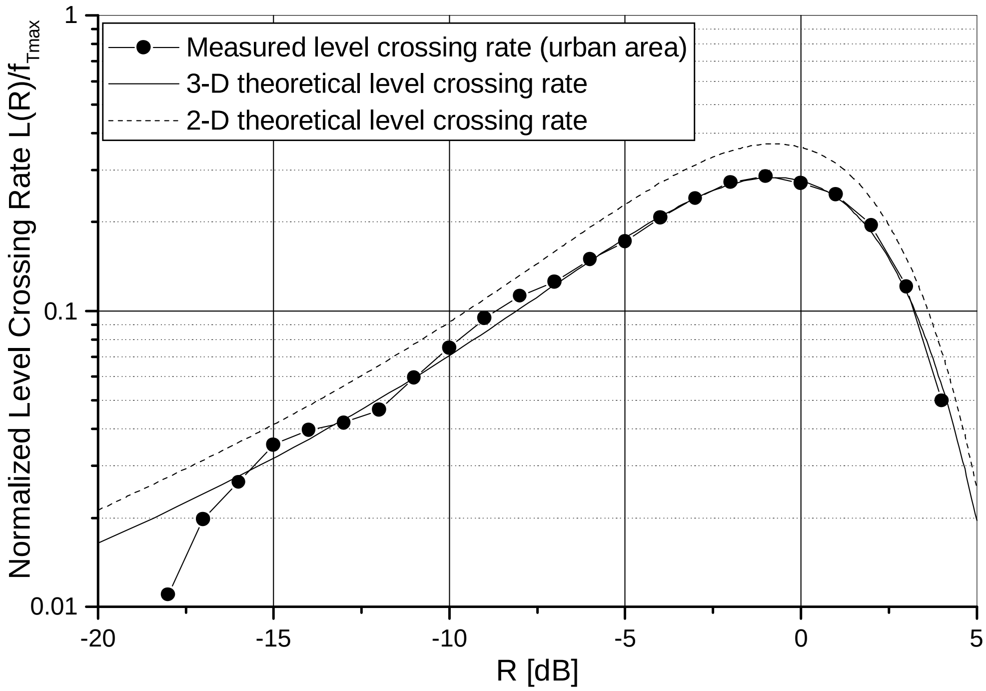

Figure 54: Comparison of the analytical LCR and measured LCR in an urban surface street environment.

first $\mathrm{T_x}$ and the first $\mathrm{R_x}$ antenna element, i.e., $h_{11}(t, \tau = 0)$. The 3-D analytical LCR and AFD are obtained using the parameters $K = 2.43$, $\mu_T = 12.5°$, $k_T = 20.2$, $\beta_{T_m} = 10.2°$, $\mu_R = 153.4°$, $k_R = 18.5$, $\beta_{R_m} = 12.2°$, $\eta_T = 0.043$, $\eta_R = 0.037$, and $\eta_{TR} = 0.92$. The Ricean parameter K is estimated from the measured data using the method in [88], and the other parameters are estimated from the measured data using the method in [52]. The parameters D, γ_T, γ_R, Δ_H, $f_{T\max}$, and $f_{R\max}$ are selected as in the measurement setup described above. The 2-D analytical LCR and AFD are obtained from the 3-D LCR and AFD by setting the maximum elevation angles β_{Tm} and β_{Rm} to zero. Note that the 2-D analytical curves underestimate actual LCR and AFD. These discrepancies will increase with larger maximal elevation angles.

Figs. 56 and 57 compare the 3-D analytical LCR and AFD with the measured LCR

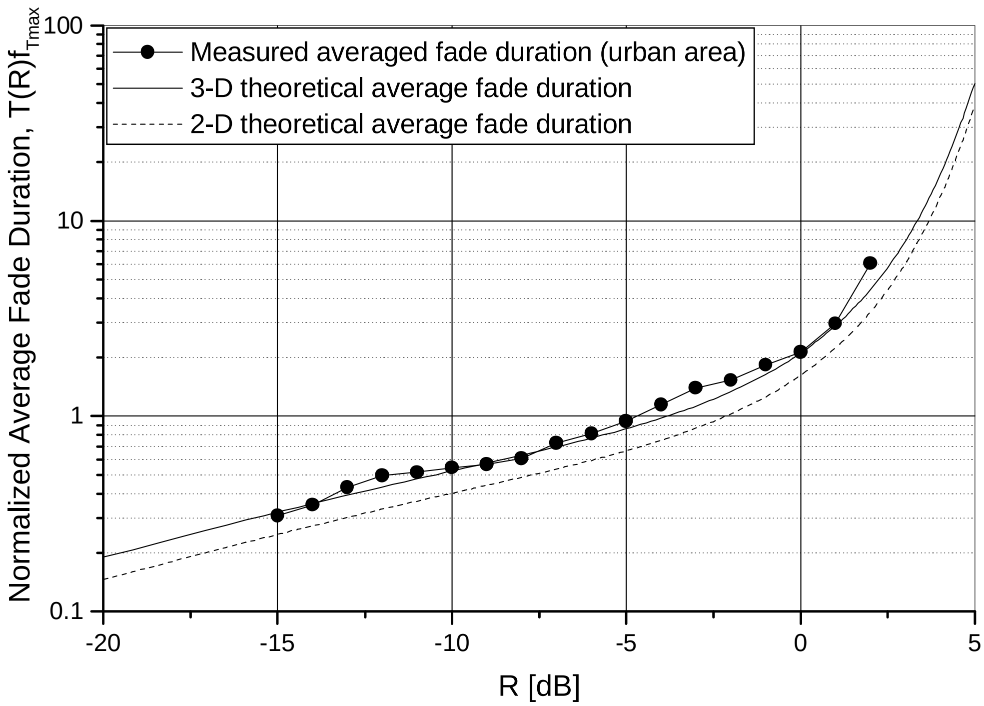

Figure 55: Comparison of the analytical AFD and measured AFD in an urban surface street environment.

and AFD obtained from our data collected in a highway environment, respectively. In these figures, we use only the channel impulse response between the second $\mathrm{T_x}$ and the second $\mathrm{R_x}$ antenna element, i.e., $h_{22}(t, \tau = 0)$. The analytical LCR and AFD are obtained using the parameters $K = 1.49$, $\mu_T = 93.4°$, $k_T = 10.5$, $\beta_{T_m} = 7.4°$, $\mu_R = 111.5°$, $k_R = 12.2$, $\beta_{R_m} = 8.3°$, $\eta_T = 0.424$, $\eta_R = 0.458$, and $\eta_{TR} = 0.118$. The parameters are estimated from the measured data using the methods in [88], [52].

Figs. 54 - 57 show close agreement between the theoretical and empirical LCR and AFD, confirming the utility of the proposed model. From the results we can also observe that the double-bounced rays bear more energy than the single-bounced rays in urban surface street areas, whereas the single-bounced rays are prevalent on the highway.

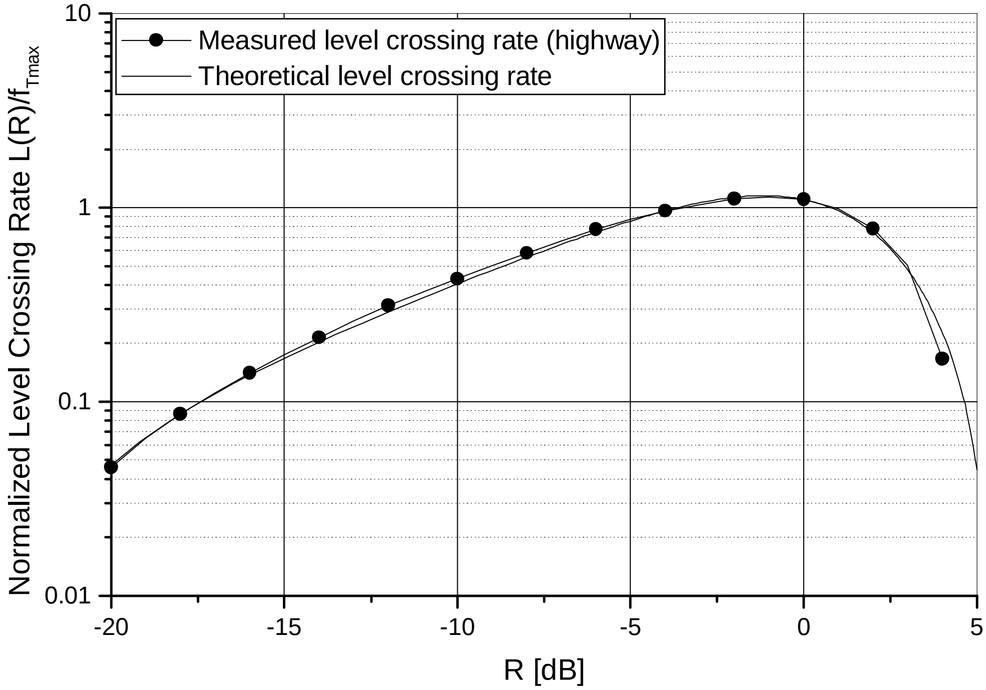

Figure 56: Comparison of the analytical LCR and measured LCR on a highway.

8.5 Summary

This chapter presented thr 3-D geometrical model for SISO M-to-M channels. From the geometrical model, the level crossing rate and average fade duration are derived, assuming a 3-D non-isotropic scattering environment. It is shown that the analytical results for the LCR and AFD compare very well with the measured data.

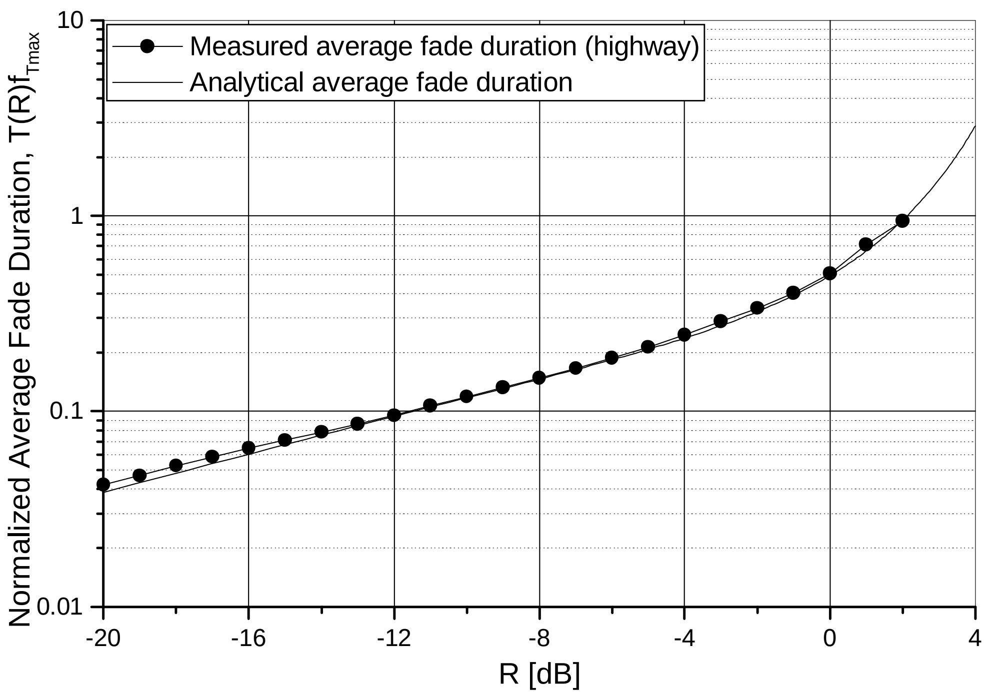

Figure 57: Comparison of the analytical AFD and measured AFD on a highway.

CHAPTER IX

EXPERIMENTAL VERIFICATION OF THE 3-D WIDEBAND MIMO M-TO-M CHANNEL MODEL

9.1 Overview

In Chapters 6 - 8, we have proposed the 3-D reference models and simulators for narrowband and wideband MIMO M-to-M channels. To validate these theoretical and simulation models, an experimental MIMO M-to-M channel-sounding campaign is conducted for M-to-M vehicular communication with vehicles travelling along surface streets near to Georgia Tech campus and along the Interstate highways near midtown in the Atlanta metropolitan area. Furthermore, to compare the first and second-order channel statistics obtained from our reference model described in Chapter 7 with those obtained from the empirical measurements, a new maximum likelihood based stochastic estimator is derived to extract the parameters needed for the reference model from the measured data. The new estimator jointly estimates the parameters of the distribution functions used to characterize the azimuth and elevation angles of departure, the azimuth and elevation angles of arrival, and the parameters that specify how much the single- and double-bounced rays contribute to the total averaged received power. This estimator is an extension of the stochastic estimator in [85], which only estimates the parameters of the distribution function used to characterize the azimuth angles of arrival. The performance of the new estimator is evaluated by deriving the Cramér-Rao lower bound (CRLB) and by comparing the mean square error of the parameter estimates to the CRLB. Simulation results show that the proposed estimator has an asymptotically optimal performance, since it reaches the CRLB for a small number of samples. Finally, the space-time-frequency correlation function (stf-cf), the space-Doppler power spectral density (sD-psd), the power space-delay spectral density (psds), and the envelope level crossing rate (LCR) obtained from the reference model with estimated parameters are compared with those obtained from the measured data. The close agreement between the analytical and empirical curves confirms the utility of the proposed 3-D model and the methodology used to extract the model parameters from the measured data.

The remainder of the chapter is organized as follows. Section 9.2 describes the measurement campaign and the data processing techniques used to process the measured data. Section 9.3 presents the new maximum likelihood based stochastic estimator. Section 9.4 compares the analytical and empirical results for the sD-psd, the psds, and the LCR. Finally, Section 9.5 provides some concluding remarks.

9.2 Measurement Campaign Description and Data Processing

This section describes our MIMO M-to-M channel-sounding experimental campaign as well as the signal processing techniques used to process the collected data.

9.2.1 Measurement Campaign Description

The MIMO M-to-M channel-sounding experimental campaign was conducted along surface streets around the Georgia Tech campus and on the Interstate highways in the midtown Atlanta metropolitan area. Major test assets associated with the campaign were two Econoline vans equipped with a power generator and rechargeable power supplies. Each van was equipped with a linear antenna array, consisting of four vertically-polarized, magnetic-mount, 2.435 GHz antenna elements. The antenna elements were placed across the roof of the van from the passenger side of the van to the driver side of the van and spaced 2.943 wavelengths apart from each other. The vans were usually driven in a convoy fashion (in the same lane and at the same speed), roughly 100 m to 300 m apart, and with speeds up to 60 mph.

Figure 58 depicts the block diagram for the MIMO transmitter system, located in the trailing vehicle. A rubidium clock provided a common 10 MHz reference for two Agilent E4438C signal generators. The third generator, an Agilent E4433B, synchronized the two E4438C signal generators. The arbitrary waveform feature of the E4438C signal generators was used to program orthogonal OFDM channel sounding waveforms to support 2×4 MIMO channel matrix estimation. One source transmitted on the odd subcarriers, while the other source transmitted on the even subcarriers. An FFT size of $N = 256$ was used for the OFDM signal with a sample rate of 18 million complex samples per second. The OFDM symbols were transmitted in a loop-back fashion with a pulse repetition interval of 300 μs, which corresponds to a maximum resolvable Doppler shift of 3.3 kHz. The signal generator output signals were passed through linear amplifiers and then coupled to two adjacent antenna elements in the

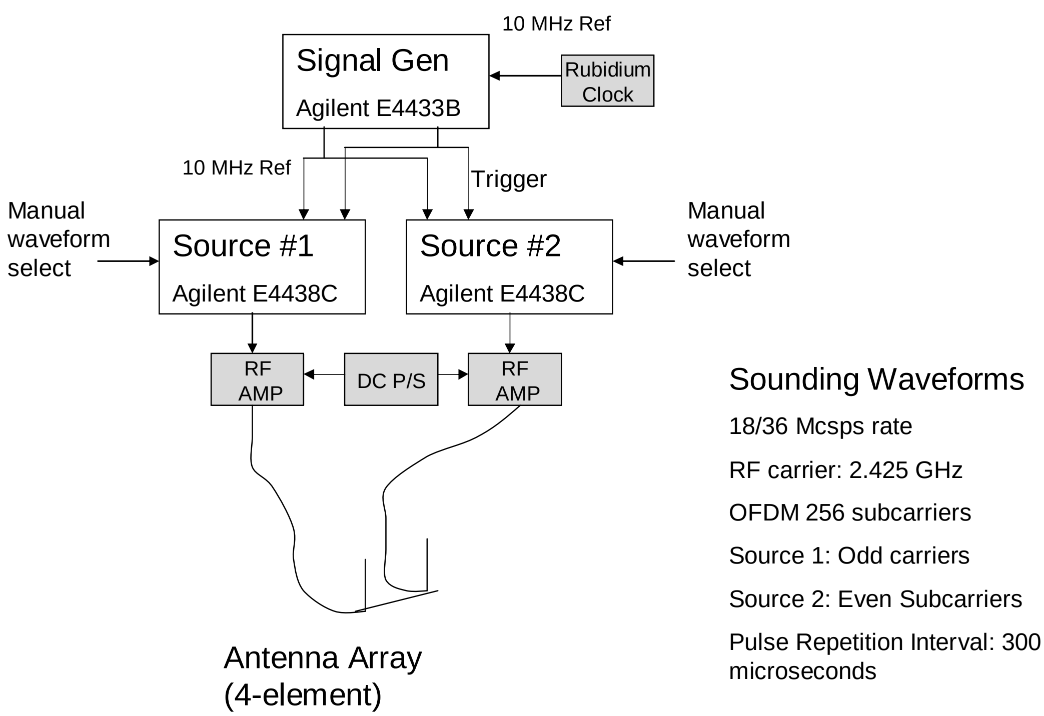

Figure 58: The block diagram of the MIMO transmitter system.

Figure 59 shows the block diagram for the MIMO receiver system, located in the leading vehicle. The signals were received by a four-element linear antenna array. Each of the received signals was coupled to a low-noise amplifier with 20 dB gain. The signals were then passed to VME-based radio frequency (RF)-to-intermediate frequency (IF) signal down-converters from Mercury Computer Systems, which converts the RF analog signal to an IF frequency of 20 MHz. The resulting analog signals were sent pairwise into Pentek model 6235 wideband receiver boards that performed anti-aliasing filtering, analog-to-digital conversion at a 72 MHz complex sample rate, digital down-conversion of the signals to complex baseband, and the 4:1 decimation and filtering. The wideband receiver was clocked with an Agilent E4433B source with a 10 MHz reference from a rubidium clock source. The channels were synchronized pairwise. The use of the rubidium sources in the both vans provided a mechanism to achieve frequency synchronization between the transmit and receive subsystems. The resulting baseband samples of each pairwise set from the digital down-converters were multiplexed and stored temporarily in a 2 GByte buffer, and were then streamed to a computer and stored on a hard disk. The buffer boards enabled 3 s contiguous snapshots to be collected from each of the 4 simultaneous channels at the sample rates of 18 million complex samples per channel per second. Due to processing memory constraints, the samples associated with any one snapshot were partitioned into eighteen time-contiguous segments. Snapshots were collected roughly 30 s apart.

Channel sounding waveforms were transmitted from the trailing vehicle and the signals were received and recorded by the leading vehicle. Video cameras were used in the vehicles to provide indications of time, velocity, and location, to support post-test processing of the collected data. The measurements typically included both LoS and NLoS conditions, as other vehicles and obstructions often masked the direct LoS. Details associated with the measurement campaign are summarized in Table 10. Finally, Figs. 60 and 61 show photographs of the locations where the data used in the paper were collected.

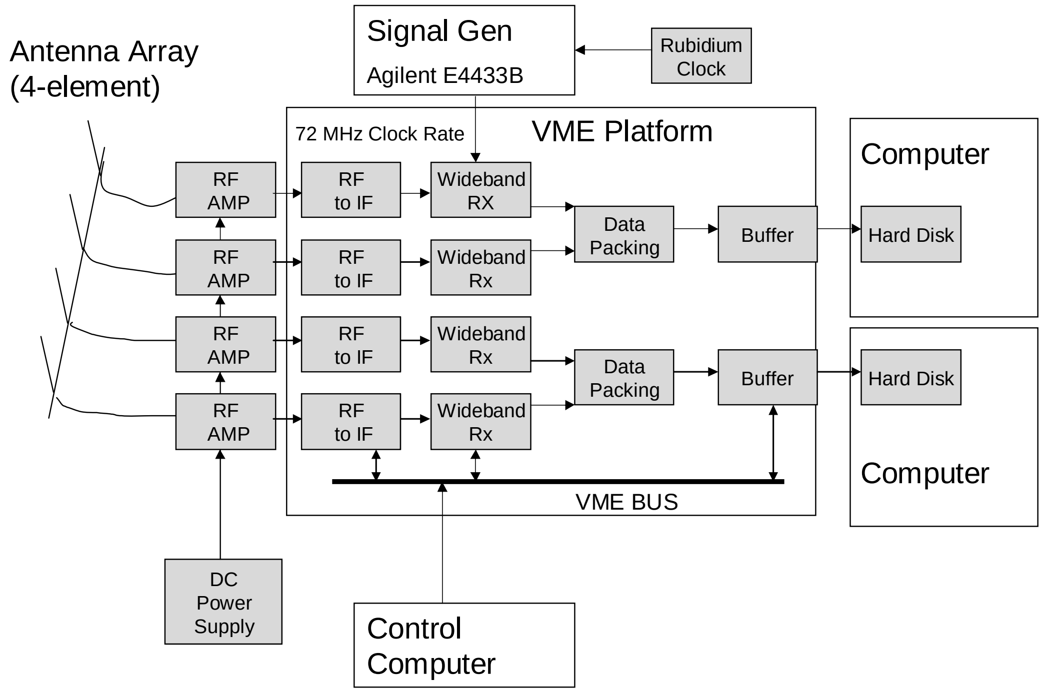

Figure 59: The block diagram of the MIMO receiver system.

9.2.2 Data Processing

Our wideband channel model described in Chapter 7 is focused on characterizing the fast-fading characteristics of the channel. To allow fair comparison between our wideband channel model and the measured data, the slow-fading component of the measured signal envelope is removed. This is achieved using the local sliding window technique [86], where the sliding window length is set to 20λ.

From the measured input delay-spread function $\hat{h}_{pq}(n\Delta t_s, k\Delta\tau_s)$, we have calculated the stf-cf, the sD-psd, the psds, and the LCR. The stf-cf is obtained as follows:

$$\tilde{R}_{pq,\tilde{p}\tilde{q}}(T\Delta t_s, F\Delta f_s) = \qquad (285)$$
$$(N_t N_\tau)^{-1} \sum_{n=0}^{N_t-1} \sum_{k=0}^{N_\tau-1} \hat{T}_{pq}(n\Delta t_s, k\Delta f_s)^* \hat{T}_{\tilde{p}\tilde{q}}((n+T)\Delta t_s, (k+F)\Delta f_s),$$

where Δt_s and N_t denote the sampling period and the number of samples with respect to the time variable t, $\Delta\tau_s$ and N_τ denote the sampling period and the number of samples with respect to the delay variable τ, $T \in \{0, \ldots, t_{\max} - 1\}$, $F \in \{0, \ldots, f_{\max} -$

Table 10: Description of the measurement campaign.

Carrier Frequency	2.435 GHz
Tx Antenna Configuration	2.435 GHz magnetic mount antennas mounted in a 1x4 linear array on the van rooftop; 2 adjacent elements from the array were used for transmission
Rx Antenna Configuration	2.435 GHz magnetic mount antennas mounted in a 1x4 linear array on the van rooftop
Signal Modulation	OFDM symbols with 256 subcarriers
Transmit Sample Rate (used to generate the OFDM signal)	18 MHz on a highway 36 MHz in an urban area
Transmit Waveform pulse repetition interval	The pulse repetition interval of the sounding waveform was approximately 300 microseconds
Frequency Synchronization	Rubidium clocks at the transmitter and the receiver
Data collection System	Pentek-based VME custom collection system with Mercury Computer Systems RF front ends; 4-channel receiver with pairwise sample synchronization
Data collection products at the receiver per snapshot (corresponding roughly to 3-second durations of contiguous data)	Approximately 55M contiguous complex baseband samples per antenna output
Collection Scenario with mobile vans	Vans traveling 25 to 60 mph in the same direction and within 100 m to 300 m apart on the I75 Expressway and in an urban area around Georgia Tech.

$1\}$, $t_{\max} = \lceil 1/(B_d \Delta t_s) \rceil$, $f_{\max} = \lceil 1/(\Delta f_s \tau_{\max}) \rceil$, B_d is the Doppler spread, and $\tau_{\max}$ is the maximum relative delay.[1] Note that the maximum relative delay denotes a difference $\tau_1 - \tau_2$, where τ_1 is a delay when the psds achieves its maximum value and τ_2 is a delay when the psds is 25 dB below its maximum value. The time-variant transfer function $\hat{T}_{pq}(n\Delta t_s, k\Delta f_s)$ is obtained from the input delay-spread function $\hat{h}_{pq}(n\Delta t_s, k\Delta \tau_s)$ using a fast Fourier transform. To allow fair comparison between the theoretical normalized stf-cf in (83) and the stf-cf obtained from the measured data, we need to normalize the power of each measured subchannel $A_T^{(p)}$ - $A_R^{(q)}$ to one. This

[1]Operation $\lceil \cdot \rceil$ denotes rounding up to the next integer, B_d is estimated from the measured sD-psd, and $\tau_{\max}$ is estimated from the measured psds.

Figure 60: Photograph of the street around Georgia Tech campus where the channel sounding experimental campaign was conducted.

normalization is performed as in (214), i.e.,

$$\hat{R}_{pq,\tilde{p}\tilde{q}}(T\Delta t_s, F\Delta f_s) = \frac{\tilde{R}_{pq,\tilde{p}\tilde{q}}(T\Delta t_s, F\Delta f_s)}{\sqrt{\mathrm{Var}[\hat{T}_{pq}(n\Delta t_s, k\Delta f_s)]\mathrm{Var}[\hat{T}_{\tilde{p}\tilde{q}}(n\Delta t_s, k\Delta f_s)]}}. \tag{286}$$

The space-Doppler power spectral density is obtained using the Welch algorithm [87]. The psds is obtained by averaging the squared magnitudes of the normalized input delay-spread function $\hat{h}_{pq}(n\Delta t_s, k\Delta\tau_s)$ over all times $n\Delta t_s$. Finally, the LCR, $L(R)$, is obtained by counting how many times per second the measured signal envelope crosses the level R in the positive going direction.

9.3 Parameter Estimation

The parametric nature of our wideband channel model makes it adaptable to a variety of propagation environments. To verify our reference model with measured data, we need to estimate the model parameters from the measurements. The distances

Figure 61: Photograph of the leading van, taken from the trailing van on the Interstate highway in the midtown Atlanta metropolitan area.

between antenna elements (d_T and d_R), the difference in antenna heights Δ_H, the directions and speeds of the $\mathrm{T_x}$ and $\mathrm{R_x}$ (γ_T, γ_R, v_T, and v_R), the azimuth angles of the $\mathrm{T_x}$'s and $\mathrm{R_x}$'s antenna arrays (θ_T and θ_R), and the elevation angles of the $\mathrm{T_x}$'s and $\mathrm{R_x}$'s antenna arrays (ψ_T and ψ_R) are estimated from the antenna array geometry and the video camera recordings. The remaining parameters, i.e., the parameters in the von Mises pdfs (k_T, μ_T, k_R, and μ_R), the parameters in the elevation angle pdfs (β_{T_m} and β_{R_m}), the parameters in the radii pdfs (R_{t1}, R_{t2}, R_{r1}, and R_{r2}), the parameters that specify how much the single- and double-bounced rays contribute to the total averaged power (η_T, η_R), and the Rice parameter K are estimated from the measured input delay-spread functions $\hat{h}_{pq}(n\Delta t_s, k\Delta\tau_s)$. Note that the parameter η_{TR} is equal to $1 - \eta_T - \eta_R$ and does not require estimation. First, the Rice factor is estimated using the moment-method in [88]. Then, the parameters R_{t2} and R_{r2}

are estimated from the measured psds by setting $R_{t2} = R_{r2} = c_0\tau_{\max}/2$, where $\tau_{\max}$ is the maximum relative delay and c_0 is the speed of light. The parameters R_{t1} and R_{r1} are chosen to be $R_{t1} = R_{r1} = 0.1R_{t2}$. Finally, to estimate the parameters $\mathbf{\Theta} = [\beta_{T_m}, k_T, \mu_T, \beta_{R_m}, k_R, \mu_R, \eta_T, \eta_R]$, we propose a new maximum likelihood based stochastic estimator. This estimator is an extension of the stochastic estimator in [85] which only estimates the parameters in the von Mises pdf. In contrast to the estimator in [85], which estimates its parameters from the spatial correlation function, our estimator uses the stf-cf to estimate the parameters.

By observing that the theoretical and normalized measured input delay-spread functions are both zero-mean and unit-variance complex Gaussian random processes, we estimate the parameters $\mathbf{\Theta} = [\beta_{T_m}, k_T, \mu_T, \beta_{R_m}, k_R, \mu_R, \eta_T, \eta_R]$ using a maximum-likelihood (ML) estimator with the log-likelihood function

$$\begin{aligned}\mathcal{L}\{\mathbf{\Theta}_{T,F}\} &= -N_s\Big\{ \ln \pi^{L_r L_t} + \ln |\mathbf{R}(\mathbf{\Theta}_{T,F}, T\Delta t_s, F\Delta f_s)| \\ &+ \operatorname{tr}\{\mathbf{R}(\mathbf{\Theta}_{T,F}, T\Delta t_s, F\Delta f_s)^{-1}\hat{\mathbf{R}}(T\Delta t_s, F\Delta f_s)\}\Big\}, \qquad (287)\end{aligned}$$

where $\ln(\ \cdot\ )$ denotes the natural logarithm operation, $\operatorname{tr}(\ \cdot\ )$ denotes the matrix trace, $N_s = N_t N_\tau$ is the total number of samples, L_t and L_r denote the number of transmit and receive antennas, and $\mathbf{\Theta}_{T,F}$ denotes the vector of estimated parameters in the time and frequency instances $T\Delta t_s$ and $F\Delta f_s$. The elements $[\hat{\mathbf{R}}(T\Delta t_s, F\Delta f_s)]_{q+L_r(p-1),\tilde{q}+L_r(\tilde{p}-1)} = \hat{R}_{pq,\tilde{p}\tilde{q}}(T\Delta t_s, F\Delta f_s)$ of the $L_tL_r \times L_tL_r$ matrix of the measured correlation functions, $\hat{\mathbf{R}}(T\Delta t_s, F\Delta f_s)$, are defined in (286), whereas the elements $[\mathbf{R}(\mathbf{\Theta}_{T,F}, T\Delta t_s, F\Delta f_s)]_{q+L_r(p-1),\tilde{q}+L_r(\tilde{p}-1)} = R_{pq,\tilde{p}\tilde{q}}(\mathbf{\Theta}_{T,F}, T\Delta t_s, F\Delta f_s)$ of the $L_tL_r \times L_tL_r$ matrix of the theoretical correlation functions, $\mathbf{R}(\mathbf{\Theta}_{T,F}, n\Delta t_s, k\Delta f_s)$, are defined in (214). After removing the constant terms that are not dependent on the channel, the ML estimates are obtained as

$$\begin{aligned}\hat{\mathbf{\Theta}}_{T,F} &= \text{argmax}_{\hat{\mathbf{\Theta}}_{T,F}}\Big\{ - \ln|\mathbf{R}(\mathbf{\Theta}_{T,F}, T\Delta t_s, F\Delta f_s)| \\ &- \text{tr}\{\mathbf{R}(\mathbf{\Theta}_{T,F}, T\Delta t_s, F\Delta f_s)^{-1}\hat{\mathbf{R}}(T\Delta t_s, F\Delta f_s)\Big\}, \end{aligned} \tag{288}$$

with the constraint $\eta_T + \eta_R + \eta_{TR} = 1$. The expression in (288) is optimized using the sequential quadratic programming algorithm [89]. The final vector of estimated parameters $\mathbf{\Theta}$ is obtained as $\mathbf{\Theta} = (t_{\max} f_{\max})^{-1} \sum_{T=0}^{t_{\max}-1} \sum_{F=0}^{f_{\max}-1} \mathbf{\Theta}_{T,F}$.

To study the performance of the proposed estimator, we derive the Cramér-Rao lower bounds (CRLB) for the estimated parameters $\mathbf{\Theta} = [\Theta_i]_{i=1}^{8} = [\beta_{T_m}, k_T, \mu_T, \beta_{R_m}, k_R, \mu_R, \eta_T, \eta_R]$. The CRLB bound of the estimated parameter Θ_i is the diagonal element of the inverse Fisher information matrix that corresponds to the parameter Θ_i. Appendix N shows that the $(i, j)^{th}$ element of the Fisher information matrix is

$$\begin{aligned}&[\mathbf{F}(\mathbf{\Theta})]_{i,j} = -\text{E}\left[\frac{\partial^2 \mathcal{L}(\mathbf{\Theta})}{\partial\Theta_i \partial\Theta_j}\right] = \frac{N_s}{t_{\max} f_{\max}} \sum_{T=0}^{t_{\max}-1} \sum_{F=0}^{f_{\max}-1} \text{tr}\Big\{\mathbf{R}(\mathbf{\Theta}_{T,F}, T\Delta t_s, F\Delta f_s)^{-1} \\ &\times \mathbf{D}_{\Theta_j}(\mathbf{\Theta}_{T,F}, T\Delta t_s, F\Delta f_s)\mathbf{R}(\mathbf{\Theta}_{T,F}, T\Delta t_s, F\Delta f_s)^{-1}\mathbf{D}_{\Theta_i}(\mathbf{\Theta}_{T,F}, T\Delta t_s, F\Delta f_s)\Big\}, \end{aligned} \tag{289}$$

where $\mathbf{D}_{\Theta_i}(\mathbf{\Theta}_{T,F}, T\Delta t_s, F\Delta f_s)$ denotes the derivative $\partial\mathbf{R}(\mathbf{\Theta}_{T,F}, T\Delta t_s, F\Delta f_s)/\partial\Theta_i$ for $i \in \{1, \ldots, 8\}$ and are derived in (439) - (446).

To illustrate the performance of the proposed estimator, we compare the derived CRLB with the mean square error MSE $= (\hat{\Theta}_i - \tilde{\Theta}_i)^2$ for the parameters $[\Theta_i]_{i=1}^{8} = [\beta_{T_m}, k_T, \mu_T, \beta_{R_m}, k_R, \mu_R, \eta_T, \eta_R]$, where $\hat{\Theta}_i$ denotes the exact value and $\tilde{\Theta}_i$ denotes the estimated value of the parameter Θ_i. Since the results obtained for the parameters $[\beta_{R_m}, k_R, \mu_R, \eta_R]$ are almost identical with those obtained for the parameters $[\beta_{T_m}, k_T, \mu_T, \eta_T]$, Fig. 62 plots the CRLB and the MSE only for the parameters $[\Theta_i]_{i=1}^{4} = [\beta_{T_m}, k_T, \mu_T, \eta_T]$. The curves in Fig. 62 are obtained with the estimated parameters $\beta_{Tm} = 5.1°$, $\beta_{Rm} = 10.2°$, $\mu_T = 31.3°$, $\mu_R = 141.7°$, $k_T = 12.5$, $k_R = 10.2$, $\eta_T = 0.213$, $\eta_R = 0.234$, $\eta_{TR} = 0.82$, $K = 2.41$, $R_{t1} = R_{r1} = 9.6$ m, $R_{t2} = R_{r2} = 96$ m and with the parameters $\theta_T = \theta_R = 0°$, $\psi_T = \psi_R = 0°$,

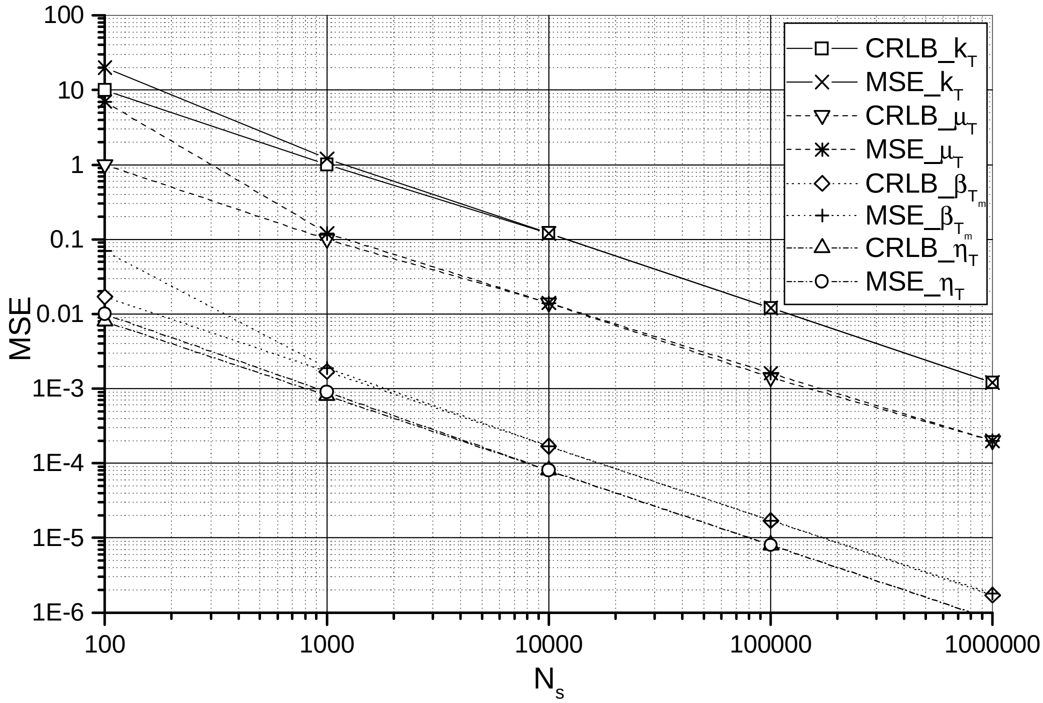

Figure 62: Comparison of the MSE and the CRLB for the parameters $[\Theta_i]_{i=1}^{4} = [\beta_{T_m}, k_T, \mu_T, \eta_T]$.

$\gamma_T = \gamma_R = 90°$, $\Delta_H = 0$, $L_t = L_r = 2$, $d_T = d_R = 2.943\ \lambda$, $D = 300$ m, $\lambda = 0.123$ m, $\gamma = 4$, $f_{T\max} = f_{R\max} = 90.86$ Hz, which are obtained from the antenna geometry and propagation conditions. The simulation results show that the proposed estimator has asymptotically optimal performance, since it reaches the CRLB for a small number of samples, i.e., $N_s = 10^3$. Finally, Figs. 63 - 66 compare the theoretical and measured correlation functions. The theoretical correlation functions are obtained with the parameters in Fig. 62, whereas the measured correlation functions are obtained from the data collected on the urban surface street area shown in Fig. 60. The close agreement between the theoretical and empirical curves confirms the utility of the proposed estimator.

9.4 Validation of the 3-D Wideband Reference Model

In this section, we compare the theoretical results in Chapters 7 and 8 with those obtained from the measurement campaign described in Section 9.2. The wideband

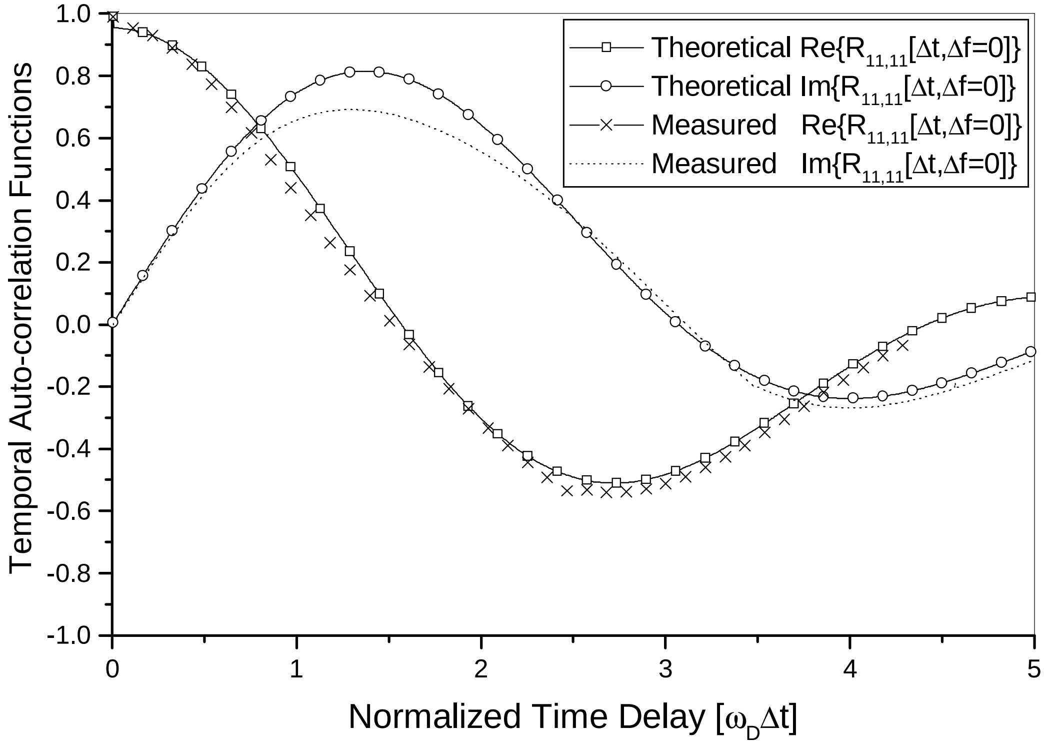

Figure 63: Comparison of the theoretical and the measured temporal auto-correlation functions $R_{11,11}(\Delta t, \Delta f = 0)$.

channel measurements collected in the urban surface street area (shown in Fig. 60) were performed at 2.435 GHz and the maximum Doppler frequencies were $f_{T\max} = f_{R\max} = 90.86$ Hz. The distance between the $\mathrm{T_x}$ and $\mathrm{R_x}$ was approximately $D = 300$ m and the moving directions were $\gamma_T = \gamma_R = 90°$. Both, the $\mathrm{T_x}$ and $\mathrm{R_x}$ were equipped with two omnidirectional antenna elements with the azimuth and elevation angles $\theta_T = \theta_R = 0°$ and $\psi_T = \psi_R = 0°$, respectively. All antenna elements have the same height, $\Delta_H = 0$, and the distance between the antenna elements is $d_T = d_R = 2.943\ \lambda$. It is assumed that the path loss exponent γ is 4, which is typical for radio propagation over a flat reflecting surface [35].

The reference model in (204) - (207) assumes an infinite number of scatterers around the $\mathrm{T_x}$ and $\mathrm{R_x}$, i.e, $M, N \to \infty$. Using the Central Limit Theorem [76], we can conclude that the theoretical time-variant transfer function $T_{pq}(t, f)$ is a complex Gaussian random process with the mean $\mathrm{E}[T_{pq}(t, f)] = T_{pq}^{LoS}(t, f)$ and the variance

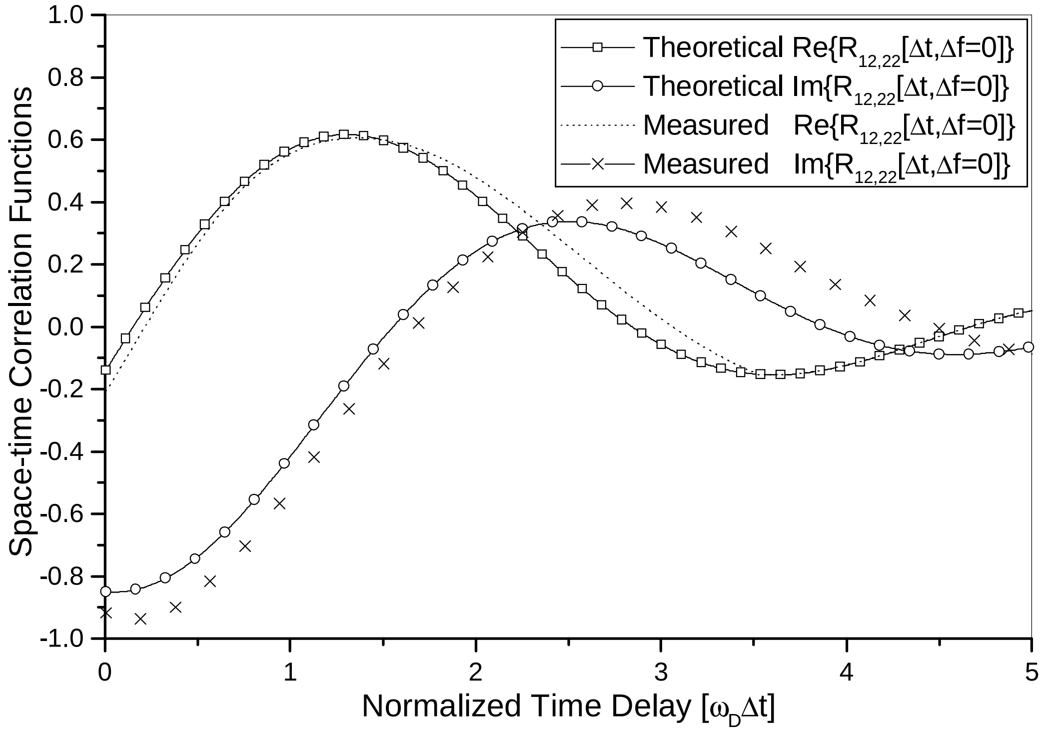

Figure 64: Comparison of the theoretical and the measured space-time correlation functions $R_{12,22}(\Delta t, \Delta f = 0)$.

$\mathrm{Var}[T_{pq}(t,f)] = \Omega_{pq}/(K+1)$. Before we compare the theoretical and measured sD-psd, psds, and LCR, we need to confirm that the measured time-variant transfer functions are also complex Gaussian random processes with the means and variances similar to those of the reference model. Fig. 67 compares the cumulative distribution functions (CDFs) of the real and imaginary components of the measured time-variant transfer function, $\hat{T}_{11}(t, 180\ \mathrm{MHz})$, with the CDFs of the real and imaginary components of the complex Gaussian process. The complex Gaussian process is obtained with the mean $\mathrm{E}[T_{11}^{\mathrm{RM}}(t, 180\ \mathrm{MHz})]$ and the variance $\mathrm{Var}[T_{11}^{\mathrm{RM}}(t, 180\ \mathrm{MHz})]$, respectively, where $T_{11}^{\mathrm{RM}}(t, 180\ \mathrm{MHz})$ is the time-variant transfer function of the reference model. The results show that CDFs of the real and imaginary components of the measured time-variant transfer function, $\hat{T}_{11}(t, 180\ \mathrm{MHz})$, can be closely approximated by the Gaussian distributions and that the reference model and measured data have the similar means and variances. Furthermore, the CDFs of the measured amplitude and

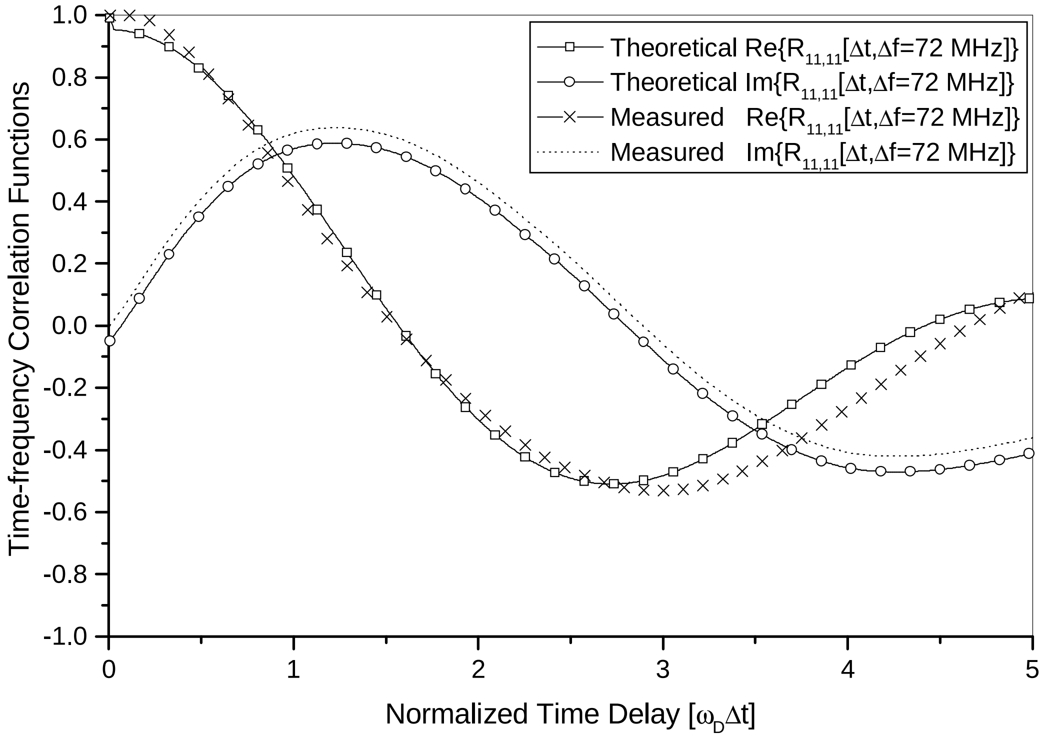

Figure 65: Comparison of the theoretical and the measured time-frequency correlation functions $R_{11,11}(\Delta t, \Delta f = 72 \text{ Hz})$.

phase can be closely approximated by a Rice and uniform distribution[2], respectively. We have performed similar analysis (i.e., comparison of CDF functions and quantile-quantile plots) for all measured time-variant transfer functions, and similar results were observed.

Figures 68 - 70 compare the theoretical and the measured sD-psd, psds, and LCR for the urban surface street environment, respectively. The analytical curves are obtained with the parameters $\beta_{Tm} = 5.1°$, $\beta_{Rm} = 10.2°$, $\mu_T = 73.3°$, $\mu_R = 264.7°$, $k_T = 5.7$, $k_R = 6.4$, $\eta_T = 0.043$, $\eta_R = 0.137$, $\eta_{TR} = 0.82$, $R_{t1} = R_{r1} = 9.6$ m, $R_{t2} = R_{r2} = 96$ m, and $K = 2.41$. These parameters are estimated from the measured data as described in Section 9.3. The parameters γ, D, γ_T, γ_R, θ_T, θ_R, ψ_T, ψ_R, d_T, d_R, Δ_H, $f_{T\max}$, and $f_{R\max}$ are selected to match the measurement conditions as described above. Figures 68 - 70 show close agreement between the theoretical and empirical

[2]With non-isotropic scattering, the phase may not be uniform distributed.

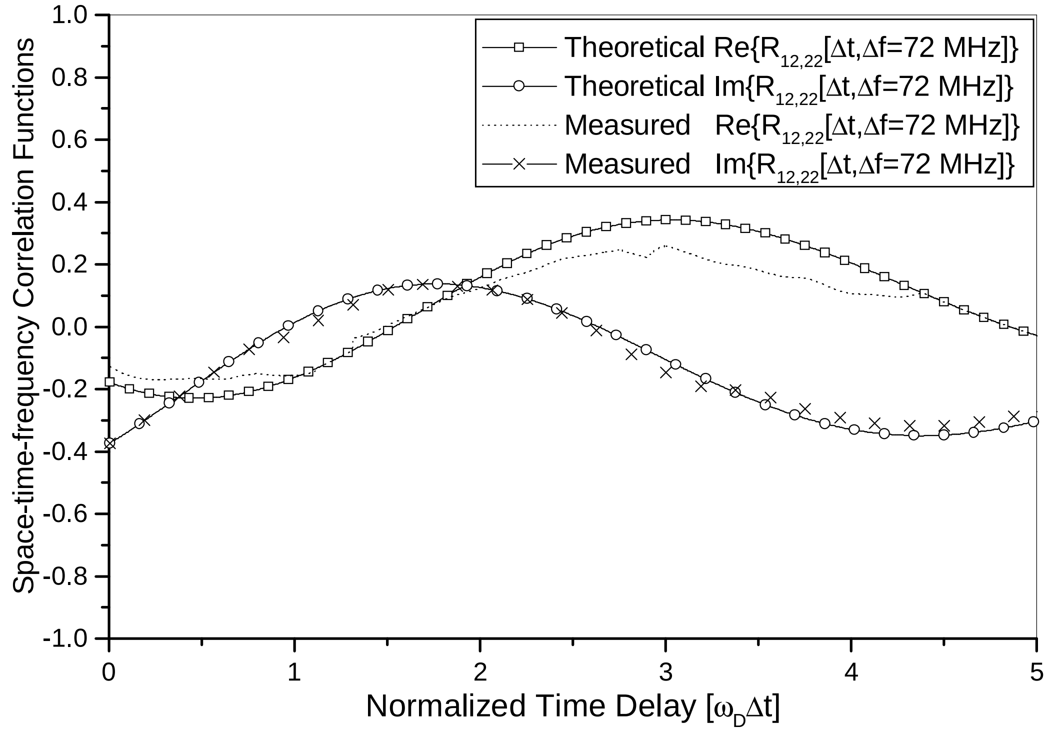

Figure 66: Comparison of the theoretical and the measured stf-cfs $R_{12,22}(\Delta t, \Delta f = 72\text{ Hz})$.

curves. Our results for urban surface street environments show that double-bounced rays bear more energy than the single-bounced rays. Note also that the estimated scattering radii $R_{t2} = R_{r2} = 96$ m are sufficiently small compared to the distance $D = 300$ m that the local scattering condition is satisfied.

Finally, we note that channel sounding measurements for narrowband and wideband SISO M-to-M channels in [39] and [83], similar to our theoretical results, show no oscillating pattern in the Doppler power spectrum. The oscillating pattern in our measurements for the case $d_T = d_R = 0$ may appear because it is not a true SISO scenario where only one transmit and one receive antenna are active. We have performed MIMO M-to-M channel measurements and calculated the SISO Doppler spectrum using the input delay-spread function $h_{11}(t, \tau)$. There may be a small degree of coupling with the other active antennas which is manifested as the oscillating pattern in the Doppler power spectrum for $d_T = d_R = 0$. Another explanation may be

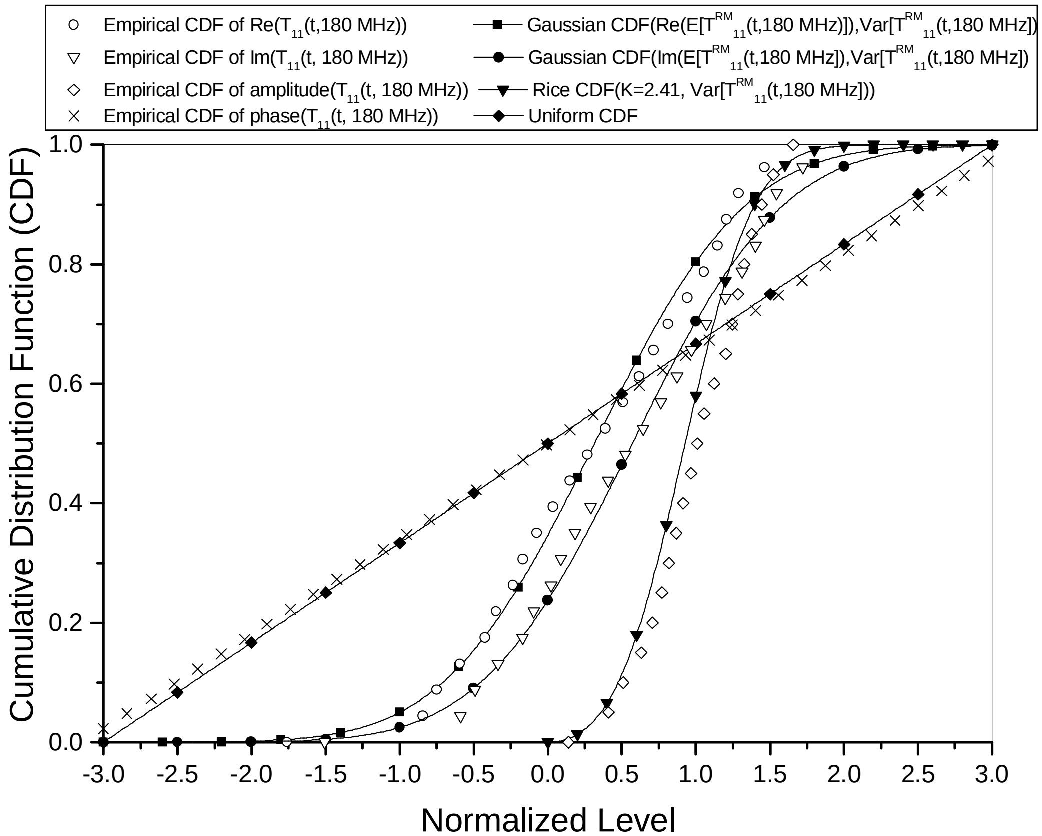

Figure 67: Theoretical and empirical distribution functions of $h_{11}(t,\tau)$ in an urban surface street area.

the presence of moving scatterers (vehicles), whereas our model assumes stationary scatterers. The measurements in [40] were conducted at nighttime with very little road traffic.

The wideband channel measurements, collected on the Interstate highway (shown in Fig. 61), were performed at 2.435 GHz and the maximum Doppler frequencies were $f_{T\max} = f_{R\max} = 181.72$ Hz. The distance between the $\mathrm{T_x}$ and $\mathrm{R_x}$ was approximately $D = 180$ m and the moving directions were $\gamma_T = \gamma_R = 90°$. The $\mathrm{T_x}$ was equipped with two, and the $\mathrm{R_x}$ was equipped with four omnidirectional antenna elements. The antenna array elements at both vehicles have the azimuth and elevation angles $\theta_T = \theta_R = 0°$ and $\psi_T = \psi_R = 0°$, respectively. All antenna elements have the same height, $\Delta_H = 0$, and the distance between the antenna elements is $d_T = d_R = 2.943\ \lambda$. The path loss exponent γ is set to 4.

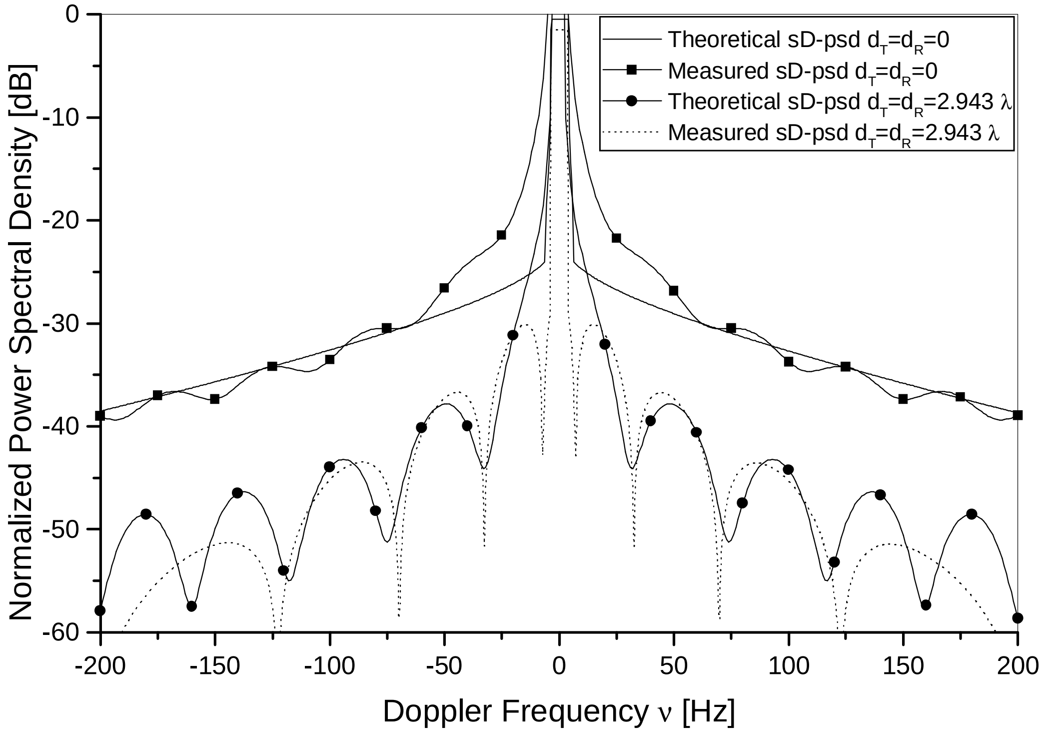

Figure 68: Theoretical and the measured sD-psd in an urban surface street area.

Figures 71 - 73 compare the theoretical and measured sD-psd, psds, and LCR, respectively, on the Interstate highway. The analytical curves are obtained with the parameters $\beta_{Tm} = 7.4°$, $\beta_{Rm} = 8.3°$, $\mu_T = 101.4°$, $\mu_R = 281.5°$, $k_T = 5.5$, $k_R = 5.2$, $\eta_T = 0.358$, $\eta_R = 0.288$, $\eta_{TR} = 0.354$, $R_{t1} = R_{r1} = 4.5$ m, $R_{t2} = R_{r2} = 45$ m, and $K = 1.29$. These parameters are estimated as described in Section 9.3. The remaining parameters D, γ, γ_T, γ_R, θ_T, θ_R, ψ_T, ψ_R, d_T, d_R, Δ_H, $f_{T\max}$, and $f_{R\max}$ are selected as in the highway measurement setup, described above. Figures 71 - 73 show close agreement between the theoretical and empirical curves. In this set of data, the single-bounced rays are more dominant than the double-bounced rays. This effect can be explained by the fact that both vans were in the rightmost lane and very close to the sound blockers on the edge of the highway (see Fig. 61). Finally, the estimated scattering radii $R_{t2} = R_{r2} = 45$ m are sufficiently small compared to the distance $D = 180$ m that the local scattering condition is satisfied.

By analyzing the data collected at four different locations along the highway, we

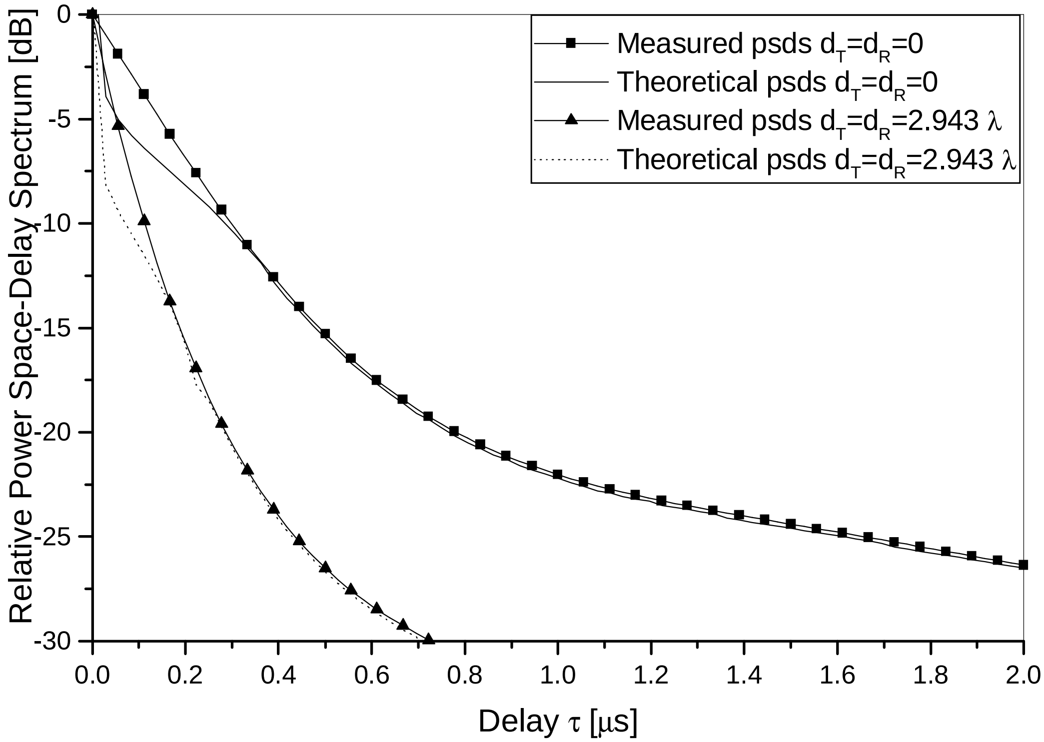

Figure 69: Theoretical and measured psds in an urban surface street area.

have observed that if the vehicles are driven in the rightmost or the leftmost lane and close to the large objects such as highway dividers or sound blockers on the edge of the highway, the single-bounced rays bear more energy than the double-bounced rays. However, if the vehicles are driven in the middle lanes of the highway, the double-bounced rays are prevalent.

Figures 67 - 73 show the close agreement between the theoretical and empirical curves. These results confirm the utility of the proposed model. From the results we can observe that, in the urban area, the double-bounced rays bear more energy than the single-bounced rays, whereas, on the highway, the single-bounced rays may be prevalent.

9.5 Summary

This chapter described the MIMO M-to-M channel-sounding experimental campaign that was conducted in the Atlanta metropolitan area. Furthermore, to compare the

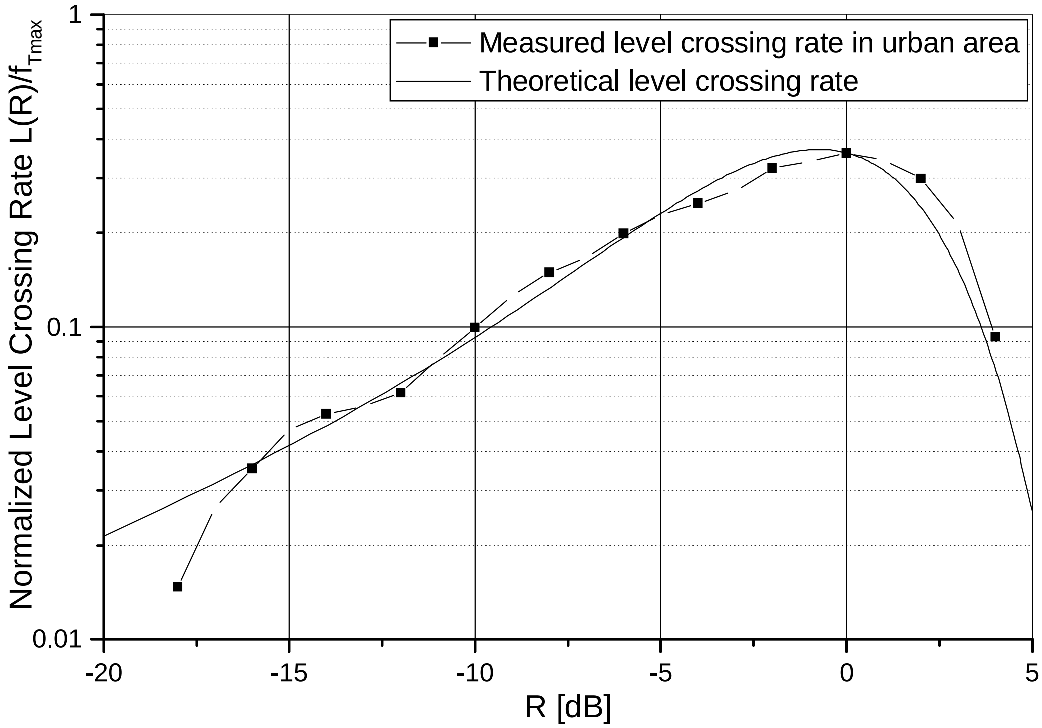

Figure 70: Theoretical and measured LCR in an urban surface street area.

analytical and empirical results, the new maximum likelihood based stochastic estimator was proposed in this chapter. The new estimator jointly estimates the parameters of the distribution functions used to characterize the azimuth and elevation angles of departure, the azimuth and elevation angles of arrival, and the parameters that specify how much the single- and double-bounced rays contribute in the total averaged received power. The performance of the new estimator was studied by deriving the CRLB and comparing the mean square error of the estimates to the CRLB. The simulations showed that the proposed estimator has asymptotically optimal performance since it reaches the CRLB for a small number of samples. Finally, the measured data was processed and compared with the analytical predictions. The close agreement between the analytical and empirical curves confirms the utility of the proposed reference model and methodology for extracting model parameters from the measured data.

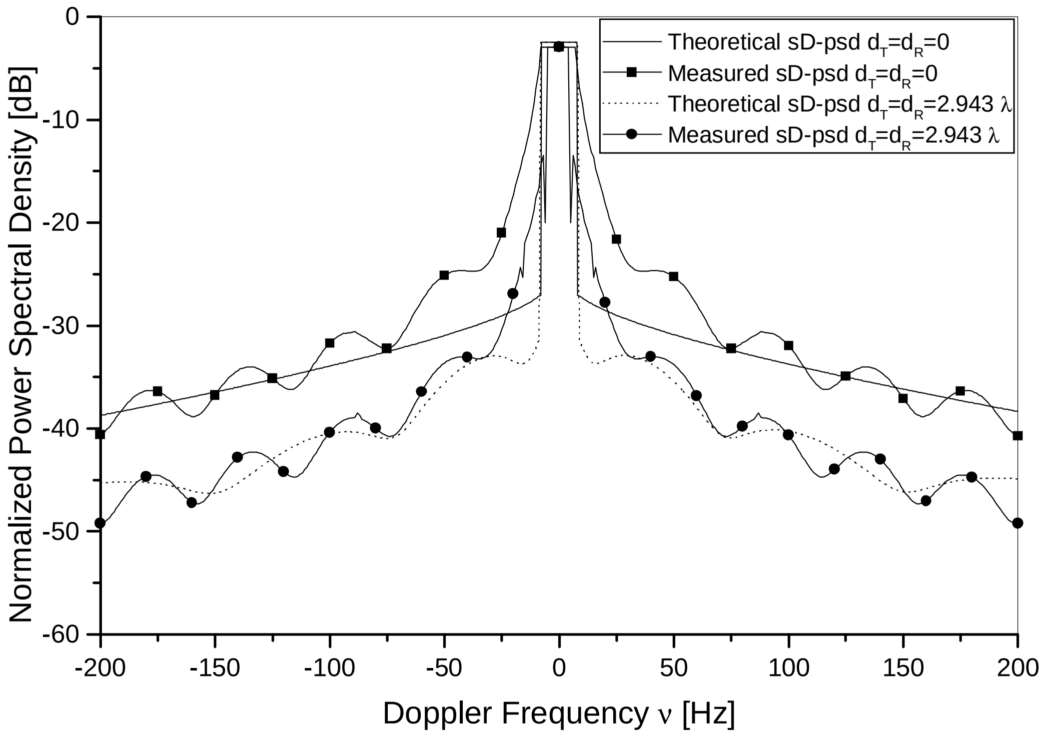

Figure 71: Theoretical and measured sD-psd on an Interstate highway.

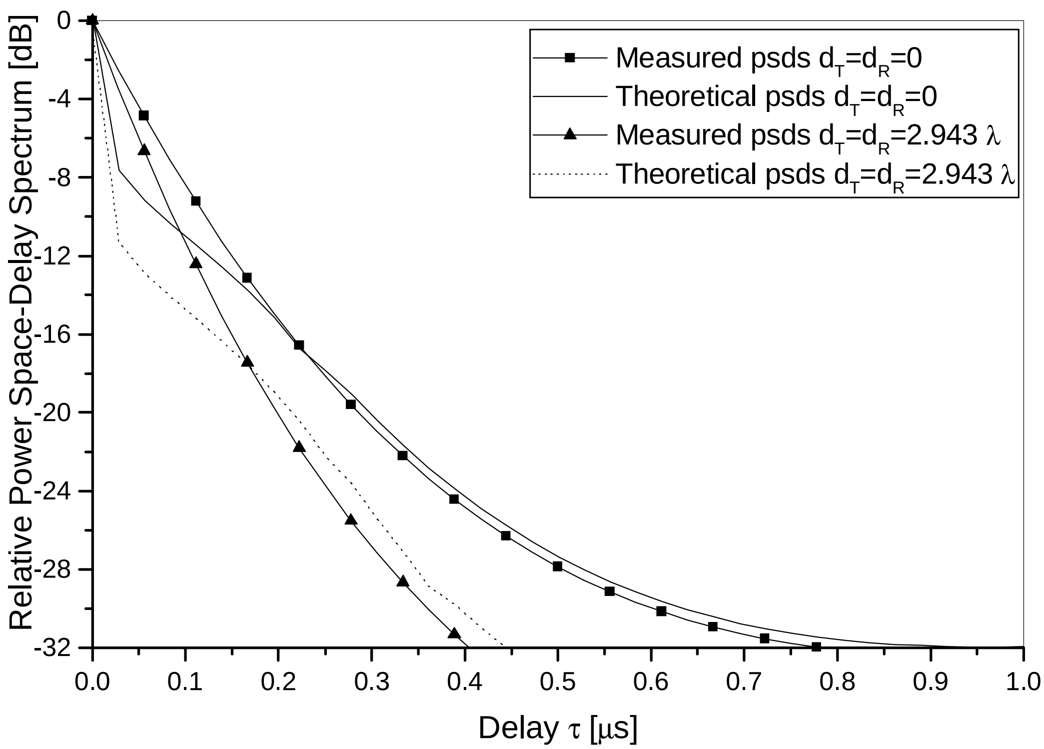

Figure 72: Theoretical and measured psds on an Interstate highway.

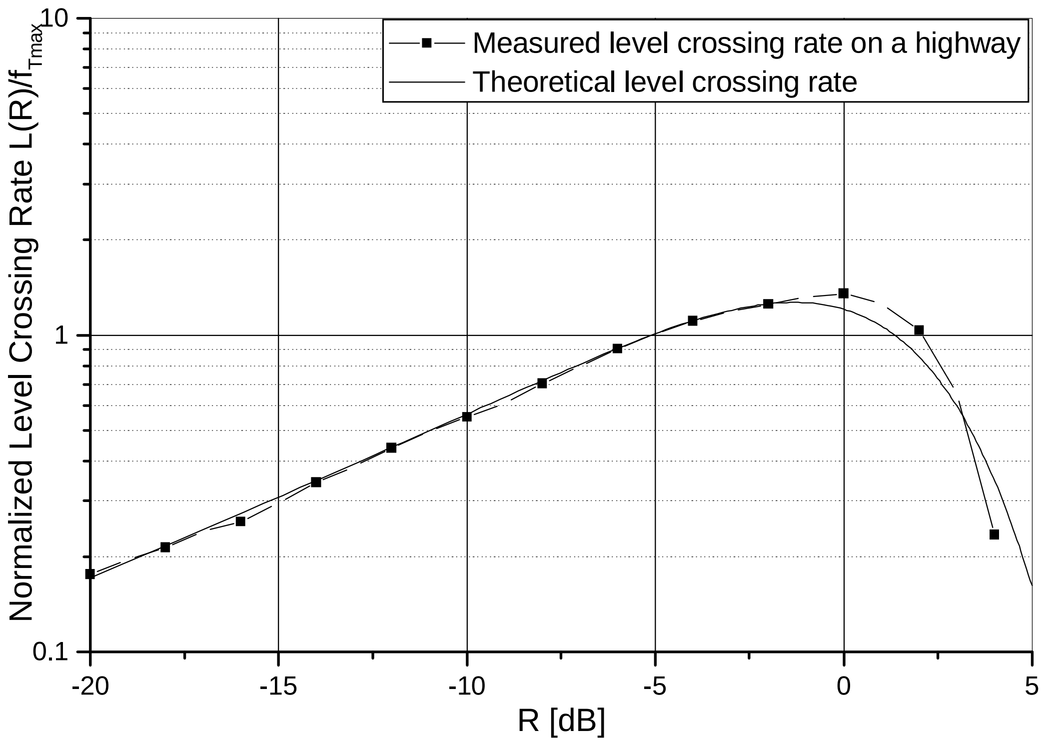

Figure 73: Theoretical and measured LCR on an Interstate highway.

CHAPTER X

A SPACE-TIME CODE DESIGN FOR CPM: DIVERSITY ORDER AND CODING GAIN

10.1 Overview

Space-time (ST) coding transmits coded waveforms from multiple antennas to maximize link performance. *Full spatial diversity* is one design objective for ST codes, being upper bounded by the product $L_t \times L_r$, where L_t and L_r are the number of transmit and receive antennas, respectively. *Coding gain* optimization is another design objective for space-time codes. Many different ST codes have been developed for quasi-static Rayleigh fading channels [4] - [14].

Space-time coding can be applied to continuous phase modulated signals. Zhang and Fitz [41], [42] derived design criteria for space-time coded CPM (ST-CPM) on quasi-static fading channels and identified a rank criterion, but only for particular CPM schemes: full-response 2^n-ary CPM with $h = 1/2$, full-response 4^n-ary CPM with $h = 1/4$ and $h = 3/4$, partial-response binary CPM with $h = 1/2$ and partial-response 4-ary CPM with $h = 1/4$ and $h = 3/4$. Some attempts to optimize coding gain of ST-CPM have been made in [43] - [45]. However, a general framework for ST-CPM is lacking both in terms of diversity order and coding gain.

This chapter derives sufficient conditions under which any M-ary partial- and full-response ST-CPM arrangement will attain full spatial diversity for any L_t. Design rules are specified for coding gain optimization. Paralleling the work of Mengali and Morelli [56], we first derive a linear decomposition of CPM signals with tilted-phase. The tilted-phase is time-invariant and simplifies receiver processing [90]. Based on our linear decomposition, we propose a rank criterion for M-ary partial- and full-response CPM that eventually defines a set of optimal modulation indices for any candidate CPM scheme (excluding multi-h CPM). We also propose a coding gain design criterion for ST-CPM. Maximization of the coding gain for ST-CPM depends not only on the codewords as in linear modulation, but also on the frequency/phase shaping function. Since the analytical or computer search for the codes and phase shaping functions that maximize the coding gain is a difficult problem, a coding gain optimization criterion that optimizes (improves or maximizes) the coding gain is developed. Finally, we discuss the optimization of ST-CPM and orthogonal ST-CPM as special cases.

The remainder of the chapter is as follows. Section 10.2 describes ST-CPM on a quasi-static fading channel. Section 10.3 derives the linear decomposition of CPM signals with tilted-phase. Section 10.4 presents our design criteria for M-ary partial- and full-response ST-CPM. Section 10.5 presents several examples and simulation results verifying the developed ST-CPM rank and coding gain design optimization criteria. Section 10.6 concludes the chapter.

10.2 ST-CPM with Tilted-Phase - System Model

This chapter considers a space-time coded tilted-phase CPM system with L_t transmit antennas and L_r receive antennas. As shown in Fig. 74, the ST encoder uses a block code $\mathcal{C}$ to encode blocks of K_b information symbols into length-$N = N_c L_t$ codeword vectors $\mathbf{u} \in \mathcal{C}$ that are mapped onto an $L_t \times N_c$ matrix $\mathbf{U}$ in the following manner: codeword

$$\mathbf{u} = \left(u_0^{(1)}, u_0^{(2)}, \ldots, u_0^{(L_t)}, u_1^{(1)}, u_1^{(2)}, \ldots, u_1^{(L_t)}, \ldots, u_{N_c-1}^{(1)}, u_{N_c-1}^{(2)}, \ldots, u_{N_c-1}^{(L_t)}\right) \quad (290)$$

is mapped to the $L_t \times N_c$ matrix

$$\mathbf{U} = \begin{bmatrix} u_0^{(1)} & u_1^{(1)} & \cdots & u_{N_c-1}^{(1)} \\ u_0^{(2)} & u_1^{(2)} & \cdots & u_{N_c-1}^{(2)} \\ \vdots & \vdots & \ddots & \vdots \\ u_0^{(L_t)} & u_1^{(L_t)} & \cdots & u_{N_c-1}^{(L_t)} \end{bmatrix}, \tag{291}$$

where $u_k^{(i)}$ is the code symbol assigned to i-th transmit antenna at time epoch k.

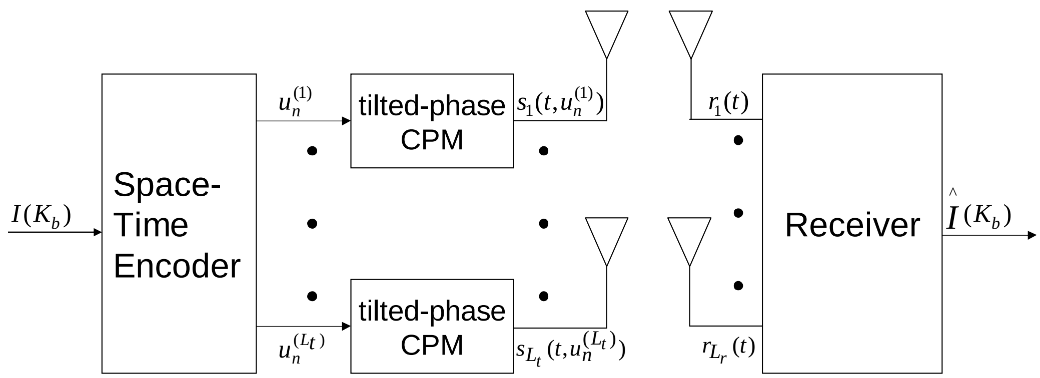

Figure 74: Block diagram for space-time coded tilted-phase CPM system.

The outputs of the space-time encoder are L_t streams of symbols, that are input to separate tilted-phase CPM modulators that drive the antennas. Due to the tilted-phase representation, the ST encoder outputs can be directly input to the CPM modulators without the need for additional modulation mapping as is the case if an excess-phase CPM modulator is used (see Fig. 4). The L_t modulated signals are simultaneously transmitted from L_t transmit antennas.

The signal at each receiver antenna is a noisy superposition of the L_t transmitted signals, each affected by quasi-static flat Rayleigh fading, and independent zero-mean complex additive white Gaussian noise (AWGN). The received signal can be represented in the convenient vector form

$$\mathbf{r}(t) = \mathbf{H}^\top \sqrt{E_s}\mathbf{s}(t, \mathbf{U}) + \mathbf{n}(t), \tag{292}$$

where $\mathbf{s}(t, \mathbf{U}) = \left[s_1\left(t, \mathbf{u}^{(1)}\right), \ldots, s_{L_t}\left(t, \mathbf{u}^{(L_t)}\right)\right]^\top$ is the vector of transmitted signals, $\mathbf{u}^{(i)} = \left[u_0^{(i)}, u_1^{(i)}, \ldots, u_{N_c-1}^{(i)}\right]$ is the vector of the code symbols assigned to i-th transmit antenna, $\mathbf{r}(t) = [r_1(t), \ldots, r_{L_r}(t)]^\top$ is the vector of received signals, $\mathbf{n}(t) = [n_1(t), \ldots, n_{L_r}(t)]^\top$ contains the noise samples that are independent zero-mean complex Gaussian random variables with variance $N_0/2$ per dimension, $\mathbf{H} = [h_{ij}]_{L_t \times L_r}$ is the matrix of complex channel fading gains, E_s is the symbol energy, and $(\ \cdot\ )^\top$ denotes the matrix transpose operation.

In some embodiments, the ST-CPM receiver employs maximum-likelihood sequence detection (MLSD) as implemented with the Viterbi algorithm. The bit error rate performance of MLSD is typically evaluated by upper bounding the pairwise error probability for any two space-time codewords $\mathbf{U}$, and $\hat{\mathbf{U}}$, defined as in (291). Let $\mathbf{s}(t, \mathbf{U})$ and $\hat{\mathbf{s}}(t, \hat{\mathbf{U}})$ denote the CPM vectors corresponding to matrices $\mathbf{U}$ and $\hat{\mathbf{U}}$, respectively. Finally, let $\mathbf{U_s}$ be the matrix of correlation functions of the differential CPM signals received at the different antennas [41]

$$\mathbf{U_s} = \tag{293}$$
$$\begin{bmatrix} \int_0^{N_cT_c} |\Delta s_1(t)|^2 dt & \int_0^{N_cT_c} \Delta s_1(t)\Delta s_2^*(t) dt & \cdots & \int_0^{N_cT_c} \Delta s_1(t)\Delta s_{L_t}^*(t) dt \\ \int_0^{N_cT_c} \Delta s_2(t)\Delta s_1^*(t) dt & \int_0^{N_cT_c} |\Delta s_2(t)|^2 dt & \cdots & \int_0^{N_cT_c} \Delta s_2(t)\Delta s_{L_t}^*(t) dt \\ \vdots & \vdots & \ddots & \vdots \\ \int_0^{N_cT_c} \Delta s_{L_t}(t)\Delta s_1^*(t) dt & \int_0^{N_cT_c} \Delta s_{L_t}(t)\Delta s_2^*(t) dt & \cdots & \int_0^{N_cT_c} |\Delta s_{L_t}(t)|^2 dt \end{bmatrix},$$

where differential CPM signals are defined as $\Delta s_i(t) \stackrel{\triangle}{=} s_i(t, \mathbf{u}^{(i)}) - \hat{s}_i(t, \hat{\mathbf{u}}^{(i)})$ for $1 \le i \le L_t$ and T_c denotes the symbol duration. As shown in Chapter 2, for a quasi-static flat Rayleigh fading channel, the pairwise error probability has the following, asymptotically tight, upper bound [4]:

$$P_e(\mathbf{U}, \hat{\mathbf{U}}|\mathbf{H}) \le \left(\frac{1}{\prod_{i=1}^{r}(1 + \lambda_i E_s/4N_0)}\right)^{L_r} \le \left(\frac{\eta E_s}{4N_0}\right)^{-rL_r}, \tag{294}$$

where r is the rank of matrix $\mathbf{U_s}$, $\{\lambda_1, \cdots, \lambda_r\}$ are the nonzero eigenvalues of $\mathbf{U_s}$, and $\eta = (\lambda_1\lambda_2\cdots\lambda_r)^{1/r}$ is their geometric mean.

10.3 Linear Decomposition of CPM with Tilted-Phase

Laurent [91] showed that a binary CPM signal can be decomposed into a linear combination of pulse amplitude modulated (PAM) waveforms. Mengali and Morelli [56] extended Laurent's CPM signal decomposition to M-ary CPM signals. These linear decomposition approaches [91], [56] use the CPM excess phase, but as mentioned previously, a decomposition based on the time-invariant CPM tilted-phase is desirable. Paralleling the work of Mengali and Morelli [56] (see Section 2.5), we derive a linear decomposition of CPM signals with tilted-phase.

The CPM tilted-phase baseband complex envelope is [90] $s(t, \mathbf{u}) = \sqrt{2/T_c} e^{j\psi(t,\mathbf{u})}$, $nT_c \leq t \leq (n+1)T_c$, where

$$\psi(t; \mathbf{u}) = 2\pi h \sum_{k=0}^{n-L} u_k + 4\pi h \sum_{i=0}^{L-1} u_{n-i}\beta(t - (n-i)T_c) + \pi h W(t - nT_c) \tag{295}$$

is the tilted-phase, h is the modulation index, $\mathbf{u} = (u_0, \ldots, u_{N_c-1})$ is the information sequence with elements chosen from the M-ary alphabet $\{0, 1, \ldots, M-1\}$, and T_c is the symbol duration. The term $W(t)$ in (295) is

$$W(t) = (M-1)\frac{t}{T_c} + (M-1)(L-1) - 2(M-1)\sum_{i=0}^{L-1} \beta(t + iT_c). \tag{296}$$

The phase shaping pulse $\beta(t)$ is defined as in Section 2.5.

To derive the CPM tilted-phase decomposition, first note that some integer F exists such that $2^{F-1} < M \leq 2^F$. Since u_k varies in the range $0 \leq u_k \leq (M-1) \leq 2^F - 1$, u_k has the radix-2 representation $u_k = \sum_{l=0}^{F-1} \gamma_{k,l} 2^l$, where $\gamma_{k,l} \in \{0, 1\}$. Hence, the tilted-phase in (295) can be rewritten as

$$\psi(t, \mathbf{u}) = \sum_{l=0}^{F-1} 2\pi h 2^l \left(\sum_{k=0}^{n-L} \gamma_{k,l} + 2\sum_{i=0}^{L-1} \gamma_{n-i,l}\beta(t - (n-i)T_c) \right) + \pi h W(t - nT_c). \tag{297}$$

Then, the CPM tilted-phase complex envelope has the form

$$s(t, \mathbf{u}) = \sqrt{\frac{2}{T_c}} e^{j\pi h W(t-nT_c)} \prod_{l=0}^{F-1} e^{j\left(2\pi h 2^l \sum_{k=0}^{n-L} \gamma_{k,l} + 4\pi h 2^l \sum_{i=0}^{L-1} \gamma_{n-i,l}\beta(t-(n-i)T_c)\right)}. \tag{298}$$

The next step replaces the partial-response term associated with the $(n-i)$-th bit in (298) by an equivalent sum of two terms, such that only the second term depends upon the $(n-i)$-th bit. The partial-response term in (298) associated with the l-th bit of symbol u_k satisfies

$$\begin{aligned} e^{j4\pi h 2^l \gamma_{k,l}\beta(t)} &= \\ &e^{j2\pi h 2^l \beta(t)}\left[\frac{\sin\left(\pi h 2^l - 2\pi h 2^l \beta(t)\right)}{\sin\left(\pi h 2^l\right)} + e^{j2\pi h 2^l \gamma_{k,l}}\frac{\sin\left(2\pi h 2^l \beta(t)\right)}{\sin\left(\pi h 2^l\right)} e^{-j\pi h 2^l}\right]. \end{aligned} \tag{299}$$

The equality in (299) can be shown by applying the Euler transformation on sine functions and by replacing $\gamma_{k,l}$ with 0 and 1, respectively.

Define

$$s^{(l)}(t) \triangleq \begin{cases} \exp\left(j2\pi h 2^l \beta(t) - j\pi h 2^l\right)\dfrac{\sin\left(2\pi h 2^l \beta(t)\right)}{\sin(\pi h 2^l)} & , \quad 0 \le t < LT_c \\ \exp\left(j2\pi h 2^l \beta(t-LT_c)\right)\dfrac{\sin\left(\pi h 2^l - 2\pi h 2^l \beta(t-LT_c)\right)}{\sin(\pi h 2^l)} & , \quad LT_c \le t \le 2LT_c \\ 0 & , \quad \text{otherwise} \end{cases}. \tag{300}$$

Therefore, when $0 \le t \le LT_c$,

$$e^{j4\pi h 2^l \gamma_{k,l}\beta(t)} = s^{(l)}(t+LT_c) + e^{j2\pi h 2^l \gamma_{k,l}} s^{(l)}(t). \tag{301}$$

From (298) and (301), the CPM tilted-phase complex envelope on the interval $nT_c \le t \le (n+1)T_c$ becomes

$$\begin{aligned} s(t,\mathbf{u}) &= \sqrt{\frac{2}{T_c}} e^{j\pi h W(t-nT_c)} \\ &\prod_{l=0}^{F-1}\left[e^{j2\pi h 2^l \sum_{k=0}^{n-L}\gamma_{k,l}} \prod_{i=0}^{L-1}\left(s^{(l)}(t-(n-i)T_c+LT_c) + e^{j2\pi h 2^l \gamma_{n-i,l}} s^{(l)}(t-(n-i)T_c)\right)\right]. \end{aligned} \tag{302}$$

Closely following the algorithm in [56], we obtain the complex envelope of M-ary partial-response CPM signals with tilted-phase as

$$s(t,\mathbf{u}) = \sum_{k=0}^{R-1}\sum_{n=0}^{N_c-1} B_{k,n} g_k(t-nT_c), \tag{303}$$

where $R = (2^F - 1)2^{F(L-1)}$ and the Laurent functions $g_k(t)$ and symbols $B_{k,n}$ are defined below. The Laurent functions $g_k(t)$ are

$$g_k(t) \triangleq e^{j\pi h W(t)} \prod_{l=0}^{F-1} \prod_{i=0}^{L-1} s^{(l)} \left[t + \left(i + La_{d_{j,l},i} + e_{j,l}^{(k-w_j)} \right) T_c \right], \tag{304}$$

where $a_{d_{j,l},i} \in \{0,1\}$ are coefficients in the binary representation of the index $d_{j,l} = \sum_{q=0}^{L-1} a_{d_{j,l},q} 2^{q-1}$, $0 \leq d_{j,l} \leq 2^{L-1} - 1$, and functions $s^{(l)}(t)$ are defined as in (300).

The symbols $B_{k,n}$ are

$$B_{k,n} \triangleq \prod_{l=0}^{F-1} \exp \left[j2\pi h 2^l \left(\sum_{r=0}^{n-e_{j,l}^{(k-w_j)}} \gamma_{r,l} - \sum_{r=1}^{L-1} \gamma_{n-r-e_{j,l}^{(k-w_j)},l} a_{d_{j,l},r} \right) \right], \tag{305}$$

where $\gamma_{r,l} \in \{0,1\}$ are coefficients in the binary representation of the information symbol u_r. The integer j, used in (303) - (305), is chosen from the set $j \in \{0, \ldots, 2^{F(L-1)} - 1\}$ and satisfies $j = \sum_{l=0}^{F-1} (2^{l(L-1)}) d_{j,l}$, where $0 \leq d_{j,l} \leq 2^{L-1} - 1$. Finally, integers $e_{j,l}^{(k-w_j)}$, used in (303) - (305), are chosen to satisfy $0 \leq e_{j,l}^{(k-w_j)} \leq T_{j,l} - 1$ and $\prod_{l=0}^{F-1} e_{j,l}^{(k-w_j)} = 0$, where $T_{j,l}$ are durations of the functions $\prod_{i=0}^{L-1} s^{(l)}[t + (i + La_{d_{j,l},i} + e_{j,l}^{(k-w_j)})T_c]$ and $w_j = \sum_{n=0}^{j-1} (\prod_{l=0}^{F-1} T_{n,l} - \prod_{l=0}^{F-1} (T_{n,l} - 1))$. The derivation of (303) - (305) is presented in Appendix O.

10.4 Design Criteria for ST-CPM

The CPM modulator inputs in Fig. 74 are elements from the $L_t \times N_c$ matrix $\mathbf{U}$ defined in (291), while the outputs are elements from the vector $\mathbf{s}(t, \mathbf{U}) = [s_1(t, \mathbf{u}^{(1)}), \ldots, s_{L_t}(t, \mathbf{u}^{(L_t)})]^\top$, where the signals $s_i(t, \mathbf{u}^{(i)})$ are defined in (303) and $1 \leq i \leq L_t$. Assume that $h = K/P$, where K and P are relatively prime integers. For M-ary, partial/full-response, ST-CPM codes, we define

$$v_{n,k}^{(i)} \triangleq \left[\sum_{r=0}^{n-e_{j,l}^{(k-w_j)}} u_r^{(i)} - X^{(i)} \right]_{\mathrm{mod\,P}}, \tag{306}$$

where $X^{(i)} = \sum_{l=0}^{F-1} 2^l \sum_{r=1}^{L-1} \gamma^{(i)}_{n-r-e_{j,l}^{(k-w_j)},l} a_{d_{j,l},r}$, $\gamma_{n,l}^{(i)} \in \{0,1\}$ are coefficients in the binary representation of the symbols $u_n^{(i)}$, and $a_{d_{j,l},i} \in \{0,1\}$ are coefficients in the binary representation of the index $d_{j,l}, 0 \leq d_{j,l} \leq 2^{L-1}-1$. Note that $v_{n,k}^{(i)}$ can only assume values from the set $\{0, 1, \cdots, P-1\}$.

From (303) - (306), the $L_t \times 1$ ST-CPM vector $\mathbf{s}(t, \mathbf{U})$ can be written as

$$\mathbf{s}(t, \mathbf{U}) = \sum_{k=0}^{R-1} \begin{bmatrix} e^{j2\pi h v_{k,0}^{(1)}} & e^{j2\pi h v_{k,1}^{(1)}} & \cdots & e^{j2\pi h v_{k,N_c-1}^{(1)}} \\ e^{j2\pi h v_{k,0}^{(2)}} & e^{j2\pi h v_{k,1}^{(2)}} & \cdots & e^{j2\pi h v_{k,N_c-1}^{(2)}} \\ \vdots & \ddots & \vdots & \\ e^{j2\pi h v_{k,0}^{(L_t)}} & e^{j2\pi h v_{k,0}^{(L_t)}} & \cdots & e^{j2\pi h v_{k,N_c-1}^{(L_t)}} \end{bmatrix}_{L_t \times N_c} \mathbf{g}_k(t), \tag{307}$$

where $\mathbf{g}_k(t) \triangleq [g_{0,k}(t), g_{1,k}(t), \ldots, g_{N_c-1,k}(t)]^T$ and $g_{n,k}(t) \triangleq g_k(t-nT_c)$. Then, the $L_t \times 1$ differential ST-CPM vector $\Delta\mathbf{s}(t) \triangleq \mathbf{s}(t, \mathbf{U}) - \hat{\mathbf{s}}(t, \hat{\mathbf{U}})$ for two space-time codewords, $\mathbf{U}$ and $\hat{\mathbf{U}}$ is equal to

$$\Delta\mathbf{s}(t) = \sum_{k=0}^{R-1} \begin{bmatrix} e^{j2\pi h v_{k,0}^{(1)}} - e^{j2\pi h \hat{v}_{k,0}^{(1)}} & \cdots & e^{j2\pi h v_{k,N_c-1}^{(1)}} - e^{j2\pi h \hat{v}_{k,N_c-1}^{(1)}} \\ e^{j2\pi h v_{k,0}^{(2)}} - e^{j2\pi h \hat{v}_{k,0}^{(2)}} & \cdots & e^{j2\pi h v_{k,N_c-1}^{(2)}} - e^{j2\pi h \hat{v}_{k,N_c-1}^{(2)}} \\ \vdots & \ddots & \vdots \\ e^{j2\pi h v_{k,0}^{(L_t)}} - e^{j2\pi h \hat{v}_{k,0}^{(L_t)}} & \cdots & e^{j2\pi h v_{k,N_c-1}^{(L_t)}} - e^{j2\pi h \hat{v}_{k,N_c-1}^{(L_t)}} \end{bmatrix}_{L_t \times N_c} \mathbf{g}_k(t). \tag{308}$$

To simplify further notations, we define the $L_t \times N_c$ matrix of accumulative values as $\mathbf{V}_k \triangleq [v_{n,k}^{(i)}]$, where $1 \leq i \leq L_t$, $0 \leq n \leq N_c - 1$, and $0 \leq k \leq R-1$. Furthermore, we denote the $L_t \times N_c$ matrices in (307) and (308) as $\mathbf{Z}_k \triangleq [e^{j2\pi h v_{n,k}^{(i)}}]$ and $\Delta\mathbf{Z}_k \triangleq \mathbf{Z}_k - \hat{\mathbf{Z}}_k$, respectively. Now, the ST-CPM vector $\mathbf{s}(t, \mathbf{U})$ can be rewritten as

$$\mathbf{s}(t, \mathbf{U}) = \sum_{k=0}^{R-1} \mathbf{Z}_k \ \mathbf{g}_k(t), \tag{309}$$

whereas the differential ST-CPM vector can be rewritten as

$$\Delta\mathbf{s}(t) = \sum_{k=0}^{R-1} \Delta\mathbf{Z}_k \ \mathbf{g}_k(t). \tag{310}$$

Using (293) and (310), the matrix of correlation functions of the differential ST-CPM signals, $\mathbf{U}_s$, can be written as

$$\mathbf{U}_s = \int_0^{N_c T_c} \Delta\mathbf{s}(t) \Delta\mathbf{s}^H(t) dt = \sum_{k=0}^{R-1} \sum_{m=0}^{R-1} \Delta\mathbf{Z}_k \mathbf{G}_{k,m} \ \Delta\mathbf{Z}_m{}^H, \tag{311}$$

where $\mathbf{G}_{k,m} = \int_0^{N_c T_c} \mathbf{g}_k(t) \mathbf{g}_m^H(t) \ dt$ and $(\cdot)^H$ denotes the Hermitian operation.

10.4.1 Full-Diversity Design Criterion

The ST-CPM signals achieve full diversity if the matrix $\mathbf{U}_s$ in (311) has full rank for any two space-time codewords. In [41] is shown that the matrix $\mathbf{U}_s$ has full rank iff the elements of the differential ST-CPM vector $\Delta\mathbf{s}(t)$ in (310) are linearly independent. Here, we show that a sufficient condition for achieving full diversity is that the matrices $\Delta\mathbf{Z}_k$ have full rank L_t for any two space-time codewords $\mathbf{U}$, and $\hat{\mathbf{U}}$. To show this result, we first introduce the following lemma.

Lemma 2 *Suppose that all the functions $g_{n,k}(t)$, for $0 \leq n \leq N_c - 1$ and $0 \leq k \leq R-1$, are collected to form the vector $\mathbf{g}(t) = [g_{0,0}(t), \ldots, g_{N_c-1,0}(t), \ldots, g_{0,R-1}(t), \ldots, g_{N_c-1,R-1}(t)]^T$. The components of the vector $\mathbf{g}(t)$ are linearly independent.*

The proof is shown in Appendix P.

Using the results from Lemma 2, we show the following.

Lemma 3 *If the complex matrices $\Delta\mathbf{Z}_k = (\mathbf{Z}_k - \hat{\mathbf{Z}}_k)$ have full rank, then the differential ST-CPM vector $\Delta\mathbf{s}(t)$ has linearly independent elements, i.e., the ST-CPM system achieves full spatial diversity L_t.*

The proof is shown in Appendix Q. Note that the Laurent functions $g_{n,k}(t)$ do not affect the full-diversity design criterion. However, they affect the coding gain, as discussed in the next subsection.

Next we determine conditions under which the matrices $\Delta\mathbf{Z}_k$ have full rank. Observe that each 2^F-ary codeword $\mathbf{U}$, defined in (291), has the form

$$\mathbf{U} = \sum_{l=0}^{F-1} 2^l \Phi_l(\mathbf{U}), \tag{312}$$

where $\Phi_l(\cdot)$ denotes the operation $(\mathbf{U}/2^l)_{\bmod 2}$.

Theorem 4 (Rank Design Criterion) *Denote $\mathcal{C}$ as a linear $L_t \times N_c$ space-time code over the commutative ring of nonnegative integers modulo-2^F, $\mathbb{Z}^*_{2^F}$, with $L_t \leq N_c$.*

Suppose that all nonzero codewords $\mathbf{U} \in \mathcal{C}$ have different nonzero modulo-2 projections $\Phi_0(\mathbf{U})$ and that matrices $\Phi_0(\mathbf{U})$ have full rank over the binary field $\mathbb{F}$. Then for any partial- or full-response 2^F-ary CPM scheme with $h = K/2^n$ (where $2^n \leq 2^F$, and 2^n and K are relatively prime integers), the space-time code $\mathcal{C}$ achieves full spatial diversity L_t.

Proof: Earlier we have defined the accumulative matrices $\mathbf{V}_k$ as

$$\mathbf{V}_k = \left[v_{n,k}^{(i)}\right] = \left[\left(\sum_{r=0}^{n-e_{j,l}^{(k-w_j)}} u_r^{(i)} - X^{(i)}\right)_{\bmod 2^n}\right], \tag{313}$$

where $1 \leq i \leq L_t$, $0 \leq n \leq N_c - 1$, $0 \leq k \leq R-1$, $X^{(i)} = \sum_{l=0}^{F-1} 2^l \sum_{r=1}^{L-1} \gamma^{(i)}_{n-r-e_{j,l}^{(k-w_j)},l}$ $a_{d_{j,l},r}$, $\gamma_{n,l}^{(i)} \in \{0,1\}$ are coefficients in the binary representation of the symbols $u_n^{(i)}$, and $a_{d_{j,l},i} \in \{0,1\}$ are coefficients in the binary representation of the index $0 \leq d_{j,l} \leq 2^{L-1} - 1$. The modulo-2 projection of the matrix $\mathbf{V}_k$ is

$$\Phi_0(\mathbf{V}_k) = \left[\left(\oplus_{r=0}^{n-e_{j,l}^{(k-w_j)}} \phi_0\left(u_r^{(i)}\right)\right) \oplus \phi_0\left(X^{(i)}\right)\right], \tag{314}$$

where $\oplus$ denotes modulo-2 summation. Since elements in the accumulative matrices $\Phi_0(\mathbf{V}_k)$ are obtained using linear nonsingular transformations of the binary inputs in $\mathbb{F}$, which do not change the rank property, the accumulative matrices $\Phi_0(\mathbf{V}_k)$ also have full rank. From the injection property of these linear transformations, if $\Phi_0(\mathbf{U}) \neq \Phi_0(\hat{\mathbf{U}})$ then $\Phi_0(\mathbf{V}_k) \neq \Phi_0(\hat{\mathbf{V}}_k)$.

Next we show that the matrices $\Delta\mathbf{Z}_k$ have full rank for any two different accumulative matrices $\mathbf{V}_k$ and $\hat{\mathbf{V}}_k$. We will prove this by contradiction. If the matrices $\Delta\mathbf{Z}_k$ do not have full rank, then there exists a nonzero vector $\mathbf{K} = [k_1, \ldots, k_{L_t}]^T$ such that

$$k_1\left(\beta^{v_{i,k}^{(1)}} - \beta^{\hat{v}_{i,k}^{(1)}}\right) + k_2\left(\beta^{v_{i,k}^{(2)}} - \beta^{\hat{v}_{i,k}^{(2)}}\right) + \cdots + k_{L_t}\left(\beta^{v_{i,k}^{(L_t)}} - \beta^{\hat{v}_{i,k}^{(L_t)}}\right) = 0 \tag{315}$$

for $i = \{0, \ldots, N_c - 1\}$, where $\beta = \exp(j2\pi K/2^n)$, $\left(\beta^{v_{i,k}^{(l)}} - \beta^{\hat{v}_{i,k}^{(l)}}\right)$ are elements of the matrix $\Delta\mathbf{Z}_k$, elements of the vector $\mathbf{K}$ are drawn from $\mathbb{Z}[\beta] = \left\{\sum_{i=0}^{2^n-1} z_i \beta^i, z_i \in \mathbb{Z}\right\}$, and not all of them are divisible by $(1-\beta)$. For two elements $a, b \in \mathbb{Z}_{2^n}$ following equality holds [13]:

$$\frac{\beta^a - \beta^b}{1-\beta} \equiv a + b \,(\mathrm{mod}\ 1-\beta) \equiv a + b \,(\mathrm{mod}\ 2)\,. \tag{316}$$

Dividing (315) by $(1-\beta)$ and using (316), the modulo-2 projection of (315) is

$$\phi_0(k_1)\left[\phi_0\left(v_{i,k}^{(1)}\right) \oplus \phi_0\left(\hat{v}_{i,k}^{(1)}\right)\right] + \cdots + \phi_0(k_{L_t})\left[\phi_0\left(v_{i,k}^{(L_t)}\right) \oplus \phi_0\left(\hat{v}_{i,k}^{(L_t)}\right)\right] = 0, \tag{317}$$

where $\phi_0(\cdot)$ denotes modulo-2 operation, i.e. $\phi_0\left(v_{i,k}^{(l)}\right) = \left(v_{i,k}^{(l)}\right)_{\mathrm{mod}\,2}$, and $\oplus$ denotes modulo-2 addition. Since not all components in $\mathbf{K}$ are divisible by $(1-\beta)$, i.e., 2, it follows that $\Phi_0(\mathbf{K})$ is a nonzero vector. Since $\Phi_0(\mathbf{V}_k) \neq \Phi_0(\hat{\mathbf{V}}_k)$, from the code linearity it follows that the accumulative matrices $\Phi_0(\mathbf{V}_k) \oplus \Phi_0(\hat{\mathbf{V}}_k)$ also have full rank. Hence, (317) can not be satisfied, which leads to contradiction. $\boxdot$

The previous theorem showed that if the space-time code $\mathcal{C}$ satisfies the CPM rank criterion, the matrices $\Delta\mathbf{Z}_k$ have full rank for any two different accumulative matrices $\mathbf{V}_k$ and $\hat{\mathbf{V}}_k$. Lemma 3 proved that the elements of the differential ST-CPM vector $\Delta\mathbf{s}(t)$ are linearly independent if matrices $\Delta\mathbf{Z}_k$ have full rank. In [41] is shown that the matrix $\mathbf{U}_s$ has full rank iff the elements of the differential ST-CPM vector $\Delta\mathbf{s}(t)$ are linearly independent. Consequently, the overall ST-CPM system achieves full diversity.

Remark 1: The CPM rank criterion requires that different codewords $\mathbf{U} \in \mathcal{C}$ have different modulo-2 projections $\Phi_0(\mathbf{U})$ because the linear transformation used in (313) to obtain the accumulative matrices $\mathbf{V}_k$ only preserves the rank of the lowest bit code matrix $\Phi_0(\mathbf{U})$. Hence, if $\Phi_0(\mathbf{U}) = \Phi_0(\hat{\mathbf{U}})$ there is no guarantee that matrices $\Delta\mathbf{Z}_k$ will have full rank even though codewords $\mathbf{U}$ and $\hat{\mathbf{U}}$ have full rank. The higher bit matrices $\Phi_{l=1,\ldots n}(\mathbf{U})$ can be used to optimize coding gain, as discussed in the sequel. Also note that if all modulo-2 projections are zero, the rank design criterion applies to modulo-4 projections, i.e., $\Phi_0(\mathbf{U}/2)$.

Remark 2: The proposed rank criterion for 2^F-ary CPM with modulation index

$h = 1/2$, is similar to the BPSK rank criterion [10] and, hence, it provides both necessary and sufficient conditions for full spatial diversity, whereas the proposed rank criterion for 2^F-ary CPM with modulation indices $h = \{1/4, \ldots, 1/2^F\}$ provides only sufficient conditions for full spatial diversity. Nonetheless, the CPM rank criterion is a useful design tool for ST-CPM.

Remark 3: To derive the CPM rank criterion we used the linear decomposition of CPM signals with tilted-phase. The CPM rank criterion applies to the original tilted-phase or excess-phase CPM waveform as well.

10.4.2 Optimization of Coding Gain

Once full diversity is guaranteed, the next objective is to maximize the coding gain, $\xi_{PEP}(\Delta\mathbf{s}(t))$, over all pairs of distinct codewords $\mathbf{U}$ and $\hat{\mathbf{U}}$, defined by geometric-mean of the nonzero eigenvalues of the matrix $\mathbf{U}_s$, i.e.,

$$\xi_{PEP}\left(\Delta\mathbf{s}(t)\right) = \left(\prod_{i=1}^{L_t} \lambda_i\right)^{1/L_t} = |\mathbf{U}_s|^{1/L_t}, \tag{318}$$

where $|\cdot|$ denotes the determinant operation. From (311), the determinant $|\mathbf{U}_s|$ can be written as

$$|\mathbf{U}_s| = \left|\sum_{k=0}^{R-1}\sum_{m=0}^{R-1} \Delta\mathbf{Z}_k \mathbf{G}_{k,m}\, \Delta\mathbf{Z}_m{}^H\right|. \tag{319}$$

Equation (319) shows that maximization of the coding gain for CPM modulated space-time codes is more difficult than that for linearly modulated space-time codes, because the coding gain is not only a function of codewords $\mathbf{U}$ and $\hat{\mathbf{U}}$, but also a function of the phase shaping pulses used in the vectors $\mathbf{g}_k(t)$. The following theorem introduces the coding gain design criterion.

Theorem 5 ***(Coding Gain Design Criterion)*** *The coding gain $\xi_{PEP}\left(\Delta\mathbf{s}(t)\right)$ is maximized if the positive-definite Hermitian matrix $\mathbf{U}_s = \sum_{k=0}^{R-1}\sum_{m=0}^{R-1}\Delta\mathbf{Z}_k\mathbf{G}_{k,m}\Delta\mathbf{Z}_m{}^H$ is a semi-identity matrix with maximized diagonal elements $\mathrm{tr}(\mathbf{U}_s)/L_t$ (i.e., constrained on the trace $\mathrm{tr}(\mathbf{U}_s)$).*

Proof: Using Hadamard's inequality [92], the coding gain $\xi_{PEP}(\Delta\mathbf{s}(t))$ becomes

$$\xi_{PEP}(\Delta\mathbf{s}(t)) = |\mathbf{U}_s| = \left|\sum_{k=0}^{R-1}\sum_{m=0}^{R-1}\mathbf{A}_{k,m}\right| \leq \prod_{i=1}^{L_t}\sum_{k=0}^{R-1}\sum_{m=0}^{R-1} a_{i,i,k,m}, \tag{320}$$

where $\mathbf{A}_{k,m} = \Delta\mathbf{Z}_k\mathbf{G}_{k,m}\Delta\mathbf{Z}_m{}^H$ and $a_{i,i,k,m}$ are diagonal elements in $\mathbf{A}_{k,m}$. The equality holds only if the matrix $\sum_{k=0}^{R-1}\sum_{m=0}^{R-1}\mathbf{A}_{k,m}$ is a diagonal matrix. Further maximization of the coding gain $\xi_{PEP}(\Delta\mathbf{s}(t))$ is possible by choosing the diagonal elements $a_{i,i,k,m}$ to maximize $\prod_{i=1}^{L_t}\sum_{k=0}^{R-1}\sum_{m=0}^{R-1} a_{i,i,k,m}$. From the arithmetic-geometric mean inequality follows that the necessary and sufficient condition for maximizing $\prod_{i=1}^{L_t}\sum_{k=0}^{R-1}\sum_{m=0}^{R-1} a_{i,i,k,m}$ is that all diagonal elements $a_{i,i,k,m}$ are equal to $\mathrm{tr}(\sum_{k=0}^{R-1}\sum_{m=0}^{R-1}\mathbf{A}_{k,m})/L_t$. Hence, the coding gain $\xi_{PEP}(\Delta\mathbf{s}(t))$ is maximized iff the matrix $\mathbf{U}_s$ is a semi-identity matrix (i.e., diagonal with all diagonal elements equal to $\mathrm{tr}(\sum_{k=0}^{R-1}\sum_{m=0}^{R-1}\Delta\mathbf{Z}_k\mathbf{G}_{k,m}\Delta\mathbf{Z}_m{}^H)/L_t$) and the trace $\mathrm{tr}(\mathbf{U}_s)=\mathrm{tr}(\sum_{k=0}^{R-1}\sum_{m=0}^{R-1}\Delta\mathbf{Z}_k\mathbf{G}_{k,m}$ $\Delta\mathbf{Z}_m{}^H)$ is maximized, what was our claim. ⊡

Analytical or computer search for the matrix $\sum_{k=0}^{R-1}\sum_{m=0}^{R-1}\Delta\mathbf{Z}_k\mathbf{G}_{k,m}\Delta\mathbf{Z}_m{}^H$ (i.e., the codes, phase shaping pulses, and modulation indices) that maximize the coding gain is a difficult problem. To simplify the problem, we introduce a proposition that offers a theoretical framework which leads to the coding gain optimization (improvement or maximization), as discussed below.

Proposition 6 ***(Coding Gain Optimization)*** *The coding gain $\xi_{PEP}(\Delta\mathbf{s}(t))$ can be optimized (maximized or improved) if the matrices $\mathbf{G}_{k,k}$ and $\Delta\mathbf{Z}_k\Delta\mathbf{Z}_k{}^H$ are designed to be semi-identity matrices, (i.e., $\mathbf{G}_{k,k} = \mathrm{tr}(\mathbf{G}_{k,k})\mathbf{I}_{N_c}/N_c$ and $\Delta\mathbf{Z}_k\Delta\mathbf{Z}_k{}^H = \mathrm{tr}(\Delta\mathbf{Z}_k\Delta\mathbf{Z}_k{}^H)\mathbf{I}_{L_t}/L_t$, where $\mathbf{I}_{N_c}$ and $\mathbf{I}_{L_t}$ are the $N_c\times N_c$ and $L_t\times L_t$ identity matrices) with maximized product of traces $\mathrm{tr}(\mathbf{G}_{k,k})$ and $\mathrm{tr}(\Delta\mathbf{Z}_k\Delta\mathbf{Z}_k{}^H)$.*

Reasoning behind the proposition: From Theorem 5 follows that the first step toward coding gain optimization is to design the matrix $\mathbf{U}_s = \sum_{k=0}^{R-1}\sum_{m=0}^{R-1}\Delta\mathbf{Z}_k\mathbf{G}_{k,m}\,\Delta\mathbf{Z}_m{}^H$ as a semi-identity matrix. Here we observe that the matrices $\mathbf{G}_{k,m}$ are different from zero only for coefficients $k = m$ (this will be proven in Subsection 10.4.3). Then, the matrix $\mathbf{U}_s$ simplifies to $\sum_{k=0}^{R-1} \Delta\mathbf{Z}_k\mathbf{G}_{k,k}\, \Delta\mathbf{Z}_k{}^H$. Note that the PAM pulse shaping functions $g_{n,k}(t)$ in $\mathbf{G}_{k,k}$ can be separated from the transmitted symbols $v_{n,k}^{(i)}$ and considered as part of the channel impulse response [93]. This allows us to separate the influence of the pulse shaping functions and codewords on the coding gain and optimize the matrices $\sum_{k=0}^{R-1} \Delta\mathbf{Z}_k\Delta\mathbf{Z}_k{}^H$ and $\mathbf{G}_{k,k}$ separately. The matrices $\mathbf{G}_{k,k}$ will be optimized if they are designed to be semi-identity matrices, $\mathbf{G}_{k,k} = Q_k\mathbf{I}_{N_c}$, where $\mathbf{I}_{N_c}$ is the $N_c \times N_c$ identity matrix and $Q_k = \mathrm{tr}(\mathbf{G}_{k,k})/N_c$. Then, the matrix $\mathbf{U}_s$ simplifies to $\sum_{k=0}^{R-1} Q_k\Delta\mathbf{Z}_k\Delta\mathbf{Z}_k{}^H$. The matrix $\mathbf{U}_s$ will be optimized if it is designed to be semi-identity matrix constrained on its trace. There is no unique solution for this problem. To simplify the problem, we choose a solution $\Delta\mathbf{Z}_k\Delta\mathbf{Z}_k{}^H = P_k\mathbf{I}_{L_t}$, where $\mathbf{I}_{L_t}$ is the $L_t \times L_t$ identity matrix and $P_k = \mathrm{tr}(\Delta\mathbf{Z}_k\Delta\mathbf{Z}_k{}^H)/L_t$. Then, it follows that the coding gain $\xi_{PEP}\,(\Delta\mathbf{s}(t))$ can be optimized if the matrices $\mathbf{G}_{k,k}$ and $\Delta\mathbf{Z}_k\Delta\mathbf{Z}_k{}^H$ are designed to be semi-identity matrices with maximized product of traces $\mathrm{tr}(\mathbf{G}_{k,k})\mathrm{tr}$ and $(\Delta\mathbf{Z}_k\Delta\mathbf{Z}_k{}^H)$, what was our claim. $\boxdot$

The following sections investigate conditions under which the matrices $\mathbf{G}_{k,k}$ and $\Delta\mathbf{Z}_k\Delta\mathbf{Z}_k{}^H$ can be constructed as semi-identity matrices.

10.4.3 Coding Gain Optimization Through Phase Shaping Pulses

As discussed in Proposition 6, the influence of the pulse shaping functions and codewords on the coding gain can be treated separately. In this section, we first show that the matrices $\mathbf{G}_{k,m\neq k}$ are equal to zero. Then, we investigate conditions under which the matrices $\mathbf{G}_{k,k}$ can be constructed as semi-identity matrices. A general analysis of the matrices $\mathbf{G}_{k,k}$ is difficult because functions $g_{i,k}(t)$ depend on the memory length L. Hence, we analyze matrices $\mathbf{G}_{k,k}$ for cases of practical importance ($L = 1, 2$). The results show that the matrices $\mathbf{G}_{k,k}$ are semi-identity matrices for the raised cosine frequency shaping function with memory length $L = 1, 2$ and the modulation indices $h = 1/2^n$ for $1 \leq n \leq F - 1$. Finally, the modulation indices h should be chosen to maximize the traces $\mathrm{tr}(\mathbf{G}_{k,k})$.

From (304), observe that functions $g_{n,k}(t)$ are non-zero in the time interval $nT_c \leq t \leq (n+L+1)T_c$. Then, the matrix $\mathbf{G}_{k,m}$ defined in (311) has the form

$$\mathbf{G}_{k,m} = \begin{bmatrix} \int_0^{(L+1)T_c} g_{0,k}(t)g_{0,m}^*(t)dt & \cdots & 0 \\ \vdots & \ddots & \vdots \\ 0 & \cdots & \int_{(N_c-1)T_c}^{(N_c+L)T_c} g_{N_c-1,k}(t)g_{N_c-1,m}^*(t)dt \end{bmatrix}, \quad (321)$$

where $(\cdot)^*$ denotes complex conjugate operation and the functions $g_{n,k}(t)$ are defined in (304). To show that the matrices $\mathbf{G}_{k,m\neq k}$ are equal to zero, we first evaluate the products

$$g_{n,k}(t)g_{n,m}^*(t) = \exp\left(j\pi hW\left(t-nT_c\right)\right)\exp\left(-j\pi hW\left(t-nT_c\right)\right) \quad (322)$$
$$\prod_{l=0}^{F-1}\prod_{i=0}^{L-1} s^{(l)}\left[t-\left(n-i-La_{d_{j,l},i}-e_{j,l}^{(k-w_j)}\right)T_c\right] s^{(l)}\left[t-\left(n-i-La_{d_{j,l},i}-e_{j,l}^{(m-w_j)}\right)T_c\right]^*,$$

where the functions $s^{(l)}(t)$ are defined in (300), $k,m \in \{0,\ldots,R-1\}$, and $k \neq m$. Note that the integers $e_{j,l}^{(k-w_j)}$ and $e_{j,l}^{(m-w_j)}$ are chosen to satisfy $0 \leq e_{j,l}^{(k(m)-w_j)} \leq T_{j,l}-1$ and $\prod_{l=0}^{F-1} e_{j,l}^{(k(m)-w_j)} = 0$, where $T_{j,l}$ are the durations of the functions $\prod_{i=0}^{L-1} s^{(l)}[t+(i+La_{d_{j,l},i}+e_{j,l}^{(k(m)-w_j)})T_c]$. Then, at least one integer $e_{j,l}^{(k-w_j)}=0$ and at least one integer $e_{j,l}^{(m-w_j)}=0$. Since k and m cannot be zero at the same time, we assume that $m \neq 0$. Hence, at least one integer $e_{j,x\neq l}^{(m-w_j)} \neq 0$ and least one pair of integers $e_{j,l}^{(k-w_j)}$ and $e_{j,l}^{(m-w_j)}$ satisfies $e_{j,l}^{(k-w_j)} \neq e_{j,l}^{(m-w_j)}$. Without loss of generality, we can assume that $e_{j,0}^{(k-w_j)} = a_{d_{j,0},0} = 0$ for $l=i=0$. Then, (322) can be modified to

$$g_{n,k}(t)g_{n,m}^*(t) = s^{(0)}(t-nT_c)s^{(0)}\left[t-\left(n-La_{d_{j,0},0}-e_{j,0}^{(k-w_j)}\right)T_c\right]^* \quad (323)$$
$$\prod_{l=1}^{F-1}\prod_{i=1}^{L-1} s^{(l)}\left[t-\left(n-i-La_{d_{j,l},i}-e_{j,l}^{(k-w_j)}\right)T_c\right] s^{(l)}\left[t-\left(n-i-La_{d_{j,l},i}-e_{j,l}^{(m-w_j)}\right)T_c\right]^*.$$

Note that the function $s^{(0)}(t-nT_c)$ and at least one of the functions $s^{(l)}(t-(n-i-La_{d_{j,l},i}-e_{j,l}^{(m-w_j)})T_c)$ are non-zero in the time intervals $nT_c \leq t \leq (n+L+1)T_c$ and $(n-i-La_{d_{j,l},i}-e_{j,l}^{(m-w_j)})T_c \leq t \leq (n+L+1-i-La_{d_{j,l},i}-e_{j,l}^{(m-w_j)})T_c$, respectively.

Since at least one $e_{j,l}^{(m-w_j)}, a_{d_{j,l},i} > 0$, these two functions cannot be non-zero at the same time. Hence, the product $g_{n,k}(t)g_{n,m}^*(t) = 0$ always. A similar argument can be used to show that $g_{n,k}^*(t)g_{n+x,k}(t) = 0$ for $x > 0$. Hence, for an arbitrary phase shaping function $\beta(t)$, matrices $\mathbf{G}_{k,l\neq k}$ are zero matrices. Then, the matrix $\mathbf{G}_{k,l}$ in (321) becomes

$$\mathbf{G}_{k,k} = \tag{324}$$
$$\begin{bmatrix} \int_0^{(L+1)T_c} |g_{0,k}(t)|^2 dt \cdots & \int_{LT_c}^{(L+1)T_c} g_{0,k}(t)g_{L,k}^*(t)dt \cdots & 0 \\ \vdots \quad \ddots & \vdots \quad \ddots & \vdots \\ 0 \quad \cdots & 0 \quad \cdots & \int_{(N_c-1)T_c}^{(N_c+L)T_c} |g_{N_c-1,k}(t)|^2 dt \end{bmatrix}.$$

In general, the matrix $\mathbf{G}_{k,k}$ has equal diagonal elements, i.e., $\int_0^{(L+1)T_c} |g_k(t)|^2 dt = \int_{T_c}^{(L+2)T_c} |g_k(t-T_c)|^2 dt = \cdots = \int_{(N_c-1)T_c}^{(N_c+L)T_c} |g_k(t-(N_c-1)T_c)|^2 dt$. Since all diagonal elements of the matrix $\mathbf{G}_{k,k}$ are equal, we just need to define conditions when $\mathbf{G}_{k,k}$ is a diagonal matrix. However, a general analysis of the matrices $\mathbf{G}_{k,k}$ is difficult because the Laurent functions $g_{n,k}(t)$ depend on the memory length L. Hence, we will analyze matrices $\mathbf{G}_{k,k}$ for cases of practical importance ($L = 1, 2$).

For full-response CPM ($L = 1$), the matrix $\mathbf{G}_{k,k}$ in (324) becomes

$$\mathbf{G}_{k,k} = \tag{325}$$
$$\begin{bmatrix} \int_0^{2T_c} |g_{0,k}(t)|^2 dt & \int_{T_c}^{2T_c} g_{0,k}(t)g_{1,k}^*(t)dt & \cdots & 0 \\ \int_{T_c}^{2T_c} g_{1,k}(t)g_{0,k}^*(t)dt & \int_{T_c}^{3T_c} |g_{1,k}(t)|^2 dt & \cdots & 0 \\ \vdots & \vdots & \ddots & \vdots \\ 0 & 0 & \cdots & \int_{(N_c-1)T_c}^{(N_c+1)T_c} |g_{k,N_c-1}(t)|^2 dt \end{bmatrix},$$

where the Laurent functions $g_{n,k}(t)$ can be written as

$$g_{n,k}(t) = e^{j\pi hW(t-nT_c)} \prod_{l=0}^{F-1} s^{(l)}\left(t - \left(n - e_{j,l}^{(k-w_j)}\right)T_c\right). \tag{326}$$

Since all diagonal elements are equal, the matrix $\mathbf{G}_{k,k}$ will be semi-identity if $I_{n,n+1} = \int_{(n+1)T_c}^{(n+2)T_c} g_{n,k}(t)g_{n+1,k}^*(t)dt = 0$ and $I_{n+1,n} = \int_{(n+1)T_c}^{(n+2)T_c} g_{n+1,k}(t)g_{n,k}^*(t)dt = 0$.

We start evaluation of these integrals, by evaluating the products

$$g_{n,k}(t)g^*_{n+1,k}(t) = \exp\left(j\pi hW\left(t-nT_c\right)\right)\exp\left(-j\pi hW\left(t-(n+1)T_c\right)\right) \quad (327)$$
$$\prod_{l=0}^{F-1} s^{(l)}\left(t-\left(n-e_{j,l}^{(k-w_j)}\right)T_c\right) s^{(l)}\left(t-\left(n+1-e_{j,l}^{(k-w_j)}\right)T_c\right)^*,$$

for $k \in \{1,\ldots,R-1\}$. Since integers $e_{j,l}^{(k-w_j)}$ are chosen to satisfy $0 \le e_{j,l}^{(k-w_j)} \le 1$ and $\prod_{l=0}^{F-1} e_{j,l}^{(k-w_j)} = 0$, for $1 \le k \le R-1$ at least one integer $e_{j,l}^{(k-w_j)} \ne 0$, and at least one integer $e_{j,x\neq l}^{(k-w_j)} = 0$. Without loss of generality, we can assume that $e_{j,0}^{(k-w_j)} = 0$ for $l = 0$. Then, (327) can be modified to

$$g_{n,k}(t)g^*_{n+1,k}(t) = e^{j\pi hW(t-nT_c)}e^{-j\pi hW(t-(n+1)T_c)}s^{(0)}(t-nT_c)s^{(0)}(t-(n+1)T_c)^* \quad (328)$$
$$\times \prod_{l=1}^{F-1} s^{(l)}\left(t-\left(n-e_{j,l}^{(k-w_j)}\right)T_c\right) s^{(l)}\left(t-\left(n+1-e_{j,l}^{(k-w_j)}\right)T_c\right)^*.$$

Note that the function $s^{(0)}(t-(n+1)T_c)$ and at least one of the functions $s^{(l)}(t-(n-e_{j,l\neq 0}^{(k-w_j)})T_c)$ are non-zero in the time intervals $(n+1)T_c \le t \le (n+3)T_c$ and $(n-e_{j,l}^{(k-w_j)})T_c \le t \le (n+2-e_{j,l}^{(k-w_j)})T_c$, respectively. Since at least one $e_{j,l\neq 0}^{(k-w_j)} > 0$, these two functions cannot be non-zero at the same time. Hence, the product $g_{n,k}(t)g^*_{n+1,k}(t) = 0$ always. A similar argument can be used to show that $g^*_{n,k}(t)g_{n+1,k}(t) = 0$. Hence, for an arbitrary phase shaping function $\beta(t)$, matrices $\mathbf{G}_{k,k}$, $k \in \{1,\ldots,R-1\}$, are semi-identity matrices.

Previous reasoning cannot be applied to matrix $\mathbf{G}_{0,0}$, because all integers $e_{j,l}^{(k-w_j)} = 0$ for $k = 0$. Hence, we need to evaluate the integrals $I_{n,n+1} = \int_{(n+1)T_c}^{(n+2)T_c} g_{n,0}(t)g^*_{n+1,0}(t)dt$ for particular phase shaping functions. Using (326) and $M = 2^F$, the integral $I_{n,n+1}$ can be written as

$$I_{n,n+1} = \exp\left(j2\pi h(2^F-1)\right) \quad (329)$$
$$\int_{(n+1)T_c}^{(n+2)T_c} \prod_{l=0}^{F-1} \frac{\sin\left(\pi h2^l - 2\pi h2^l\beta(t-(n+1)T_c)\right)\sin\left(2\pi h2^l\beta(t-(n+1)T_c)\right)}{\sin(\pi h2^l)\sin(\pi h2^l)}dt$$

as derived in Appendix R. In general, $I_{n,n+1} \ne 0$. We have observed that these integrals have solutions in the form AT_c, where A is a constant that depends on the modulation index h and phase shaping function $\beta(t)$. Hence, the integrals $I_{n,n+1}$ will be minimized if the constant A is made as small as possible. Furthermore, the following proposition shows that for commonly used phase shaping functions, $I_{n,n+1} = 0$ and $I_{n+1,n} = 0$.

Proposition 7 *For the phase shaping functions [15]*

$$\beta(t) = \begin{cases} \frac{bt}{2aT_c} & , \quad 0 \leq t < aT_c \\ \frac{ta(1-2b)}{2T_c(1-2a)} + \frac{b}{2} & , \quad aT_c \leq t \leq (1-a)T_c \\ \frac{b}{2a}\left(\frac{t}{T_c} - 1\right) + \frac{1}{2} & , \quad (1-a)T_c \leq t \leq T_c \\ \frac{1}{2} & , \quad T_c \leq t \end{cases}, \tag{330}$$

with adequate selection of parameters a and b, $I_{n,n+1} = I_{n+1,n} = 0$. For the raised cosine (1RC) frequency shaping function, $q(t)$, with the modulation indices $h = 1/2^x$, where $1 \leq x \leq F-1$, the integrals $I_{n,n+1}$ and $I_{n+1,n}$ are approximately zero.

The proof is shown in Appendix S.

Remark 4: If the rectangular pulse (1REC) is selected as the frequency shaping function $q(t)$ (i.e., $\beta(t)$ has $a = 1$ and $b = 1$) the integrals $I_{i,i+1}$ and $I_{i+1,i}$ are not always zero. However, for minimum-shift keying (MSK) modulation (1REC with $h = 1/2$), $I_{i,i+1} = I_{i+1,i} = 0$, because MSK has orthogonal carriers with minimum frequency separation.

For $L = 2$ partial-response CPM, the Laurent functions $g_{n,k}(t)$ become

$$\begin{aligned} g_{n,k}(t) &= \exp\left(j\pi hW\left(t - nT_c\right)\right) \\ & \prod_{l=0}^{F-1} s^{(l)}\left(t - \left(n - e_{j,l}^{(k-w_j)}\right)T_c\right) s^{(l)}\left(t - \left(n - 1 - 2a_{d_{j,l},1} - e_{j,l}^{(k-w_j)}\right)T_c\right), \end{aligned} \tag{331}$$

where $a_{d_{j,l},1} \in \{0, 1\}$.

For indexes k having at least one coefficient $a_{d_{j,l},1} = 1$, $g_{n,k}(t) \neq 0$ only on the time interval $nT_c \leq t \leq (n+1)T_c$. Since there is no overlap among functions $g_{n,k}(t)$ and $g_{n+y,k}(t)$ for $y > 0$, matrices $\mathbf{G}_{k,k}$ are semi-identity for arbitrary phase shaping functions. For indexes k for which $\mathbf{G}_{k,k}$ are not semi-identity for an arbitrary phase shaping function, the integrals $I_{n,n+1} = \int_{(n+1)T_c}^{(n+3)T_c} g_{n,k}(t) g_{n+1,k}^*(t) dt$ and $I_{n+1,n} = \int_{(n+1)T_c}^{(n+3)T_c} g_{n+1,k}(t) g_{n,k}^*(t) dt$ for integers $e_{j,l}^{(k-w_j)} \in \{0,1\}$, and $I_{n,n+2} = \int_{(n+2)T_c}^{(n+3)T_c} g_{n,k}(t) g_{n+2,k}^*(t) dt$ and $I_{n+2,n} = \int_{(n+2)T_c}^{(n+3)T_c} g_{n+2,k}(t) g_{n,k}^*(t) dt$ for $e_{j,l}^{(k-w_j)} = 0$ should be minimized. Furthermore, the following proposition shows when the integrals $I_{n,n+1}$, $I_{n+1,n}$, $I_{n,n+2}$, and $I_{n,n+2}$ are approximately zero.

Proposition 8 *For the raised cosine (2RC) frequency shaping function, $q(t)$, with the modulation indices $h = 1/2^x$, where $1 \leq x \leq F-1$, the integrals $I_{n,n+1}$, $I_{n+1,n}$, $I_{n,n+2}$, and $I_{n,n+2}$ are approximately zero.*

The proof is shown in Appendix T.

10.4.4 Optimization of Coding Gain Through Codewords

Theorem 5 implies that if the $\mathbf{G}_{k,k}$ have semi-identity form, then the ST-CPM coding gain simplifies to

$$\xi_{PEP}\left(\Delta\mathbf{s}(t)\right) = \left|\mathbf{U}_s\right|^{1/L_t} = \left|\sum_{k=0}^{R-1} Q_k \Delta\mathbf{Z}_k \Delta\mathbf{Z}_k{}^H\right|^{1/L_t}, \tag{332}$$

where $Q_k = \int_0^{2T_c} |g_k(t)|^2 dt$. While it is difficult in general to optimize the exact coding gain $\xi_{PEP}\left(\Delta\mathbf{s}(t)\right)$, it is possible to optimize the trace upper bound $|\mathbf{U}_s|^{1/L_t} \leq \mathrm{tr}(\mathbf{U}_s)/L_t$ on the coding gain. Furthermore, in [9] is shown that for systems with $L_t L_r \geq 4$, maximization of trace $\mathrm{tr}(\mathbf{U}_s)$ is a sufficient condition for coding gain optimization. The trace $\mathrm{tr}(\mathbf{U}_s)$ is equal to

$$\begin{aligned}
\mathrm{tr}(\mathbf{U}_s) &= \sum_{k=0}^{R-1} Q_k \mathrm{tr}\left(\Delta\mathbf{Z}_k \Delta\mathbf{Z}_k{}^H\right) = \sum_{k=0}^{R-1} Q_k d_{E_k}^2\left(\mathbf{Z}_k, \hat{\mathbf{Z}}_k\right) \qquad (333)\\
&= \sum_{k=0}^{R-1} Q_k \sum_{i=1}^{L_t} \sum_{n=0}^{N_c-1} \left| e^{j2\pi h v_{n,k}^{(i)}} - e^{j2\pi h \hat{v}_{n,k}^{(i)}} \right|^2 \\
&= \sum_{k=0}^{R-1} Q_k \sum_{i=1}^{L_t} \sum_{n=0}^{N_c-1} 4\sin^2\left(\pi h \left(v_{n,k}^{(i)} - \hat{v}_{n,k}^{(i)}\right)\right),
\end{aligned}$$

where elements $v_{n,k}^{(i)}$ are defined in (306) and $d^2_{E_k}(\mathbf{Z}_k, \hat{\mathbf{Z}}_k)$ is the squared Euclidean distance between the code matrices $\mathbf{Z}_k = [e^{j2\pi h v_{n,k}^{(i)}}]$ and $\hat{\mathbf{Z}}_k = [e^{j2\pi h \hat{v}_{n,k}^{(i)}}]$. The optimization of $\mathrm{tr}(\mathbf{U}_s)$ is not straight forward because elements in matrices $\mathbf{V}_k$ and $\hat{\mathbf{V}}_k$ are obtained as linear combinations of elements in the codewords $\mathbf{U}$ and $\hat{\mathbf{U}}$. Using (313), the trace of the matrix $\mathbf{U}_s$ becomes

$$\mathrm{tr}(\mathbf{U}_s) = \sum_{k=0}^{R-1} Q_k \sum_{i=1}^{L_t} \sum_{n=0}^{N_c-1} 4\sin^2\left(\pi h \left(f_{k,P}\left(u_n^{(i)}\right) - f_{k,P}\left(\hat{u}_{n,}^{(i)}\right)\right)\right), \tag{334}$$

where functions $f_{k,P}(\ \cdot\ )$ are

$$f_{k,P}(\mathbf{U}) = \mathbf{V}_k = \left[f_{k,P}\left(u_n^{(i)}\right)\right] = \left[\left(\sum_{r=0}^{n-e_{j,l}^{(k-w_j)}} u_r^{(i)} - X^{(i)}\right)_{\mathrm{mod\,P}}\right], \tag{335}$$

$X^{(i)} = \sum_{l=0}^{F-1} 2^l \sum_{r=1}^{L-1} \gamma^{(i)}_{n-r-e_{j,l}^{(k-w_j)},l} a_{d_{j,l},r}$, $\gamma_{n,l}^{(i)} \in \{0,1\}$ are coefficients in the binary representation of the symbols $u_n^{(i)}$, $a_{d_{j,l},i} \in \{0,1\}$ are coefficients in the binary representation of the index $0 \leq d_{j,l} \leq 2^{L-1}-1$, $h = K/P$, and $P = 2^H$ for $1 \leq H \leq F-1$. From (334) follows that the trace of the matrix $\mathbf{U}_s$ over all pairs of codewords $\mathbf{U} \neq \hat{\mathbf{U}} \in \mathcal{C}$ will be optimized if the squared minimum Euclidean distances $d^2_{E_k\min} = \min\{d^2_{E_k}(e^{j2\pi h f_{k,P}(\mathbf{U})}, e^{j2\pi h f_{k,P}(\hat{\mathbf{U}})}) : \mathbf{U} \neq \hat{\mathbf{U}} \in \mathcal{C}\}$ for $k \in \{0, \ldots, R-1\}$ are maximized.

In [94] is shown that the squared minimum Euclidean distance $d^2_{E\min}(\exp(j2\pi h\mathcal{C}))$ of a linear 2^H-ary block code $\mathcal{C}$ with codewords $c = \sum_{i=0}^{H-1} 2^i b_i$ is

$$d^2_{E\min}(e^{j2\pi h\mathcal{C}}) = \min_{i=0,\ldots,H-1} \left\{4\sin^2\left(\pi h 2^i\right) d_{H_i\min}\right\}, \tag{336}$$

where $\mathcal{B}_0$, $\mathcal{B}_1$, …, $\mathcal{B}_{H-1}$ are binary block codes with the same block length, $b_i \in \mathcal{B}_i$, and $d_{H_i\min} = \min\{d_H(x_i, y_i) : x_i, y_i \in \mathcal{B}_i\}$ is the minimum Hamming distance for the code $\mathcal{B}_i$.

By observing that each matrix of accumulative values $\mathbf{V}_k$ has the form

$$\mathbf{V}_k = f_{k,P}(\mathbf{U}) = \sum_{l=0}^{H-1} 2^l \Phi_l(f_{k,P}(\mathbf{U})), \tag{337}$$

where $\Phi_l(\cdot)$ denotes operation $(f_{k,P}(\mathbf{U})/2^l)_{\mathrm{mod}\,2}$ and using (336), the minimum trace of the matrix $\mathbf{U}_s$ over all pairs of codewords $\mathbf{U} \neq \hat{\mathbf{U}} \in \mathcal{C}$ can be written as

$$\min_{\mathbf{U}\neq\hat{\mathbf{U}}\in\mathcal{C}} \mathrm{tr}(\mathbf{U}_s) = \sum_{k=0}^{R-1} Q_k \min_{l=0,\ldots,H-1} \left\{4\sin^2\left(\pi h 2^l\right) d_{H_{l,k}\mathrm{min}}\right\}, \tag{338}$$

where $d_{H_{l,k}\mathrm{min}} = \min\left\{d_H\left(\Phi_l\left(f_{k,P}(\mathbf{U})\right), \Phi_l(f_{k,P}(\hat{\mathbf{U}}))\right)\right\}$ is the minimum Hamming distance over all code matrices $\Phi_l(f_{k,P}(\mathbf{U}))$ and $\Phi_l(f_{k,P}(\hat{\mathbf{U}}))$. From (338) follows that the trace of the matrix $\mathbf{U}_s$ over all pairs of codewords $\mathbf{U} \neq \hat{\mathbf{U}} \in \mathcal{C}$ will be optimized if all minimum Hamming distances $d_{H_{l,k}\mathrm{min}}$ are maximized. When the codewords $\mathbf{U}$ cannot be designed to maximize all minimum Hamming distances $d_{H_{l,k}\mathrm{min}}$, then they should be designed to maximize the minimum Hamming distances associated with the matrices $\mathbf{G}_{k,k}$ that contain most of the signal energy.

As shown in Proposition 6, the coding gain is optimized when matrices $\Delta\mathbf{Z}_k$ are orthogonal with maximized trace $\mathrm{tr}\left(\Delta\mathbf{Z}_k\Delta\mathbf{Z}_k^H\right)$. Since orthogonal space-time block codes can satisfy these conditions, matrices $\mathbf{Z}_k$ can be designed as orthogonal space-time (OST) codewords. We will start with the orthogonal code for two transmit antennas proposed by Alamouti [95]. The elements in the matrix $\mathbf{Z}_k$ should be equal to elements in the Alamouti's codeword, i.e.,

$$\mathbf{Z}_k = \begin{bmatrix} e^{j2\pi h v_{1,k}^{(1)}} & e^{j2\pi h v_{2,k}^{(1)}} \\ e^{j2\pi h v_{1,k}^{(2)}} & e^{j2\pi h v_{2,k}^{(2)}} \end{bmatrix} = \begin{bmatrix} x_1 & x_2 \\ -x_2^* & x_1^* \end{bmatrix}, \tag{339}$$

where x_1 and x_2 are complex numbers from the modulation alphabet. Code elements $v_{1,k}^{(1)}$ and $v_{2,k}^{(1)}$ should be selected to maximize $\left|v_{1,k}^{(1)}\right|^2 + \left|v_{2,k}^{(1)}\right|^2$. The other two code elements $v_{1,k}^{(2)}$ and $v_{2,k}^{(2)}$ should be chosen to satisfy

$$v_{1,k}^{(2)} = \left(1/(2h) - v_{2,k}^{(1)}\right)_{\mathrm{mod\,P}} \tag{340}$$

and

$$v_{2,k}^{(2)} = \left(1/h - v_{1,k}^{(1)}\right)_{\mathrm{mod\,P}}, \tag{341}$$

where the modulation index is $h = 1/P$ and $P = 2^H$ for $1 \le H \le F - 1$.

For more than two transmit antennas orthogonal space-time codes are unsuitable for CPM modulation, because orthogonal space-time codes have some zero elements in the code matrices whereas symbols $e^{j2\pi h v_{n,k}^{(i)}}$ are non-zero. Quasi-orthogonal space-time codes may be used instead. The code matrices $\mathbf{V}_k$ can be designed using a similar algorithm as for orthogonal space-time codes.

10.5 Examples and Numerical Results

Several ST-CPM codewords are constructed using our rank and coding gain design criteria. Simulation results are presented to verify proposed design criteria. Each spatial channel is modelled as being independently Rayleigh faded. All simulations use a frame length of 130. The receiver is designed as in [90] with $L_r = 1$. As pointed out earlier, we used the linear decomposition of CPM signals with tilted-phase to derive the rank and coding gain criteria, but these criteria also apply to the original tilted-phase or excess-phase CPM waveforms. Depending on the CPM waveform that is transmitted, reduced-complexity receivers can be used, but they are beyond the scope of this paper.

The first example uses a full-response raised cosine (1RC) frequency shaping function. Two space-time codewords are constructed from a (4×4) 8-ary CPM space-time code $\mathcal{C}$ that satisfies the rank design criterion. We construct codewords $\mathbf{U} \in \mathcal{C}$ as $\mathbf{U} = f_{0,8}^{-1}(\sum_{l=0}^{2} 2^l \mathbf{U}_l)$, where $f_{0,8}^{-1}(\ \cdot\ )$ denotes the inverse of the function $f_{0,8}(\ \cdot\ )$ defined in (335), $\mathbf{U}_l$ are binary codewords from linear (4×4) space-time codes, $\mathcal{C}_l$, all codewords $\mathbf{U}_0 \in \mathcal{C}_0$ have full rank over $\mathbb{F}$ and all codewords $\mathbf{U}_0$ satisfy $\mathbf{U}_0 \neq \hat{\mathbf{U}}_0$. Note that any method for constructing CPM space-time codes that satisfies the rank design criterion can be used. Some of the methods for constructing binary space-time codes with full rank are described in [10] and [12]. According to the rank design criterion, the binary codewords $\mathbf{U}_1$, $\hat{\mathbf{U}}_1$, $\mathbf{U}_2$, and $\hat{\mathbf{U}}_2$ can be arbitrary selected. We first construct binary codewords $\mathbf{U}_1$, $\hat{\mathbf{U}}_1$, $\mathbf{U}_2$, and $\hat{\mathbf{U}}_2$ the same way as codewords $\mathbf{U}_0$ and $\hat{\mathbf{U}}_0$ and use them as a benchmark to measure further coding gain improvement. Following the method described in [12], we use α as a zero of the primitive polynomial $f(x) = x^4 + x + 1$ over $\mathbb{F}$ and we use the generator matrix $G = [1 \quad \alpha \quad \alpha^2 \quad \alpha^3]$ to construct benchmark codewords:

$$\mathbf{U}_{bm} = \tag{342}$$
$$= \begin{bmatrix} 4 & 6 & 7 & 7 \\ 6 & 3 & 3 & 0 \\ 3 & 1 & 2 & 4 \\ 5 & 1 & 5 & 6 \end{bmatrix} = f_{0,8}^{-1} \left\{ \begin{bmatrix} 0 & 0 & 1 & 0 \\ 0 & 1 & 0 & 0 \\ 1 & 0 & 0 & 0 \\ 1 & 0 & 1 & 1 \end{bmatrix} + 2 \begin{bmatrix} 0 & 1 & 0 & 0 \\ 1 & 0 & 0 & 0 \\ 1 & 0 & 1 & 1 \\ 0 & 1 & 1 & 0 \end{bmatrix} + 4 \begin{bmatrix} 1 & 0 & 0 & 0 \\ 1 & 0 & 1 & 1 \\ 0 & 1 & 1 & 0 \\ 1 & 1 & 0 & 0 \end{bmatrix} \right\}$$

and

$$\hat{\mathbf{U}}_{bm} = \tag{343}$$
$$= \begin{bmatrix} 5 & 1 & 5 & 6 \\ 2 & 1 & 2 & 7 \\ 5 & 0 & 5 & 4 \\ 6 & 4 & 3 & 6 \end{bmatrix} = f_{0,8}^{-1} \left\{ \begin{bmatrix} 1 & 0 & 1 & 1 \\ 0 & 1 & 1 & 0 \\ 1 & 1 & 0 & 0 \\ 0 & 0 & 1 & 1 \end{bmatrix} + 2 \begin{bmatrix} 0 & 1 & 1 & 0 \\ 1 & 1 & 0 & 0 \\ 0 & 0 & 1 & 1 \\ 1 & 1 & 0 & 1 \end{bmatrix} + 4 \begin{bmatrix} 1 & 1 & 0 & 0 \\ 0 & 0 & 1 & 1 \\ 1 & 1 & 0 & 1 \\ 1 & 0 & 1 & 0 \end{bmatrix} \right\}.$$

According to the CPM rank criterion, these two codewords will achieve full spatial diversity, if modulation index h takes values from the set $\{1/2, 1/4, 1/8\}$. We now verify this statement for each h in the set.

First, let $h = 1/4$. To verify that codewords (342) and (343) achieve full diversity, we need to check if all functions in the differential matrix $\Delta\mathbf{s}(t)$, defined in (310), are linearly independent. This will be satisfied if components of the vector $\mathbf{g}_k(t)$ are linearly independent and the matrices $\Delta\mathbf{Z}_k$ have full rank. From (326) we calculate functions $g_k(t)$. Results are presented in the first column of Table 11 from which we conclude that they are linearly independent. The first column in Table 12 shows the matrices $\Delta\mathbf{Z}_k = (\mathbf{Z}_k - \hat{\mathbf{Z}}_k)$, where $\mathbf{Z}_k = e^{j2\pi h f_{k,4}(\mathbf{U}_{bm})}$. Observe that all matrices have full rank, implying that this pair of codewords achieves full spatial diversity.

Table 11: Modulation functions for 1RC, M=8, L=1, and h=1/4.

k	$g_k(t)$	$\mathbf{G}_{k,k}$	$\lvert\mathbf{G}_{k,k}\rvert$
0	$e^{j\pi h W(t)} s^{(0)}(t) s^{(1)}(t) s^{(2)}(t)$	$\begin{bmatrix} 0.6165 & (2+4j)\cdot 10^{-4} & 0 & 0 \\ (2-4j)\cdot 10^{-4} & 0.6165 & (2+4j)\cdot 10^{-4} & 0 \\ 0 & (2-4j)\cdot 10^{-4} & 0.6165 & (2+4j)\cdot 10^{-4} \\ 0 & 0 & (2-4j)\cdot 10^{-4} & 0.6165 \end{bmatrix}$	$1.444 \cdot 10^{-1}$
1	$e^{j\pi h W(t)} s^{(0)}(t+T_c) s^{(1)}(t) s^{(2)}(t)$	$\begin{bmatrix} 0.1489 & 0 & 0 & 0 \\ 0 & 0.1489 & 0 & 0 \\ 0 & 0 & 0.1489 & 0 \\ 0 & 0 & 0 & 0.1489 \end{bmatrix}$	$4.92 \cdot 10^{-4}$
2	$e^{j\pi h W(t)} s^{(0)}(t) s^{(1)}(t+T_c) s^{(2)}(t)$	$\begin{bmatrix} 0.1489 & 0 & 0 & 0 \\ 0 & 0.1489 & 0 & 0 \\ 0 & 0 & 0.1489 & 0 \\ 0 & 0 & 0 & 0.1489 \end{bmatrix}$	$4.92 \cdot 10^{-4}$
3	$e^{j\pi h W(t)} s^{(0)}(t+T_c) s^{(1)}(t+T_c) s^{(2)}(t)$	$\begin{bmatrix} 0.3082 & 0 & 0 & 0 \\ 0 & 0.3082 & 0 & 0 \\ 0 & 0 & 0.3082 & 0 \\ 0 & 0 & 0 & 0.3082 \end{bmatrix}$	$9.02 \cdot 10^{-3}$
4	$e^{j\pi h W(t)} s^{(0)}(t) s^{(1)}(t) s^{(2)}(t+T_c)$	$\begin{bmatrix} 0.3082 & 0 & 0 & 0 \\ 0 & 0.3082 & 0 & 0 \\ 0 & 0 & 0.3082 & 0 \\ 0 & 0 & 0 & 0.3082 \end{bmatrix}$	$9.02 \cdot 10^{-3}$
5	$e^{j\pi h W(t)} s^{(0)}(t+T_c) s^{(1)}(t) s^{(2)}(t+T_c)$	$\begin{bmatrix} 0.1489 & 0 & 0 & 0 \\ 0 & 0.1489 & 0 & 0 \\ 0 & 0 & 0.1489 & 0 \\ 0 & 0 & 0 & 0.1489 \end{bmatrix}$	$4.92 \cdot 10^{-4}$
6	$e^{j\pi h W(t)} s^{(0)}(t) s^{(1)}(t+T_c) s^{(2)}(t+T_c)$	$\begin{bmatrix} 0.1489 & 0 & 0 & 0 \\ 0 & 0.1489 & 0 & 0 \\ 0 & 0 & 0.1489 & 0 \\ 0 & 0 & 0 & 0.1489 \end{bmatrix}$	$4.92 \cdot 10^{-4}$

Second, let $h = 1/2$. Functions $g_k(t)$ remain the same as in Table 11. The second column in Table 12 shows the recalculated matrices $\Delta\mathbf{Z}_k$. Since all matrices have full rank, this pair of codewords achieves full diversity and also satisfies rank criterion proposed by Zhang and Fitz [41].

Finally, for $h = 1/8$ it can be similarly verified that full diversity is achieved.

Since this pair of codewords achieves full spatial diversity, the next objective is to maximize their coding gain. According to the coding gain design criterion and Proposition 6, the coding gain will be optimized if all the $\mathbf{G}_{k,k}$ are designed as semi-identity matrices and the determinant $|\sum_{k=0}^{6} Q_k \Delta\mathbf{Z}_k \Delta\mathbf{Z}_k{}^H|$ is maximized, where $Q_k = \int_0^{2T_c} |g_k(t)|^2 dt$. From (325), we calculate matrices $\mathbf{G}_{k,k}$, and determinants $|\mathbf{G}_{k,k}|$ for modulation index $h = 1/4$. The results are presented in the second and third columns of Table 11. Obtained results confirm theoretical results derived in

Table 12: Coding gain optimization for full-response CPM space-time codes with M=8.

k	$\Delta\mathbf{Z}_k$ – *benchmark* $h=1/4$	$\Delta\mathbf{Z}_k$ – *benchmark* $h=1/2$	$\Delta\mathbf{Z}_k$ – *improved* $h=1/4$	$\Delta\mathbf{Z}_k$ – *optimized* $h=1/4$
0	$\begin{bmatrix} 1-j & 0 & 2j & 1-j \\ 0 & 2j & 1-j & 0 \\ -2j & 1-j & 0 & 0 \\ 1+j & 0 & -2j & 2j \end{bmatrix}$	$\begin{bmatrix} 2 & 0 & 0 & 2 \\ 0 & 0 & 2 & 0 \\ 0 & 2 & 0 & 0 \\ -2 & 0 & 0 & 0 \end{bmatrix}$	$\begin{bmatrix} 1-j & 2 & -2j & 1-j \\ 2 & 0 & -1+j & -2 \\ 0 & -1-j & -2 & 0 \\ 1+j & 0 & 0 & 2j \end{bmatrix}$	$\begin{bmatrix} -2 & 1+j & -2j & -1-j \\ 2 & 2j & 1+j & -1-j \\ 2j & 1-j & -2j & 0 \\ 1+j & 2j & -1-j & 2 \end{bmatrix}$
1	$\begin{bmatrix} 1-j & -1-j & 1+j & 0 \\ 0 & 2j & 1-j & 0 \\ -2j & -1-j & 0 & 0 \\ 1+j & 1+j & -1-j & 1+j \end{bmatrix}$	$\begin{bmatrix} 2 & 2 & -2 & 0 \\ 0 & 0 & 2 & 0 \\ 0 & -2 & 0 & 0 \\ -2 & -2 & 2 & 2 \end{bmatrix}$	$\begin{bmatrix} 1-j & 1-j & -1-j & 0 \\ 2 & 0 & -1+j & -2 \\ 0 & -1+j & 2j & 0 \\ 1+j & 1+j & 1-j & 1+j \end{bmatrix}$	$\begin{bmatrix} -2 & 1+j & -2j & -1-j \\ 2 & 2j & 1+j & -1-j \\ 2j & -1-j & -2 & 0 \\ 1+j & 1+j & -2 & 1-j \end{bmatrix}$
2	$\begin{bmatrix} 1-j & 0 & 2j & 1-j \\ 0 & -2j & -1+j & 0 \\ -2j & -1-j & 2 & 2 \\ 1+j & -2 & 0 & 0 \end{bmatrix}$	$\begin{bmatrix} 2 & 0 & 0 & 2 \\ 0 & 0 & 2 & 0 \\ 0 & 2 & 0 & 0 \\ -2 & 0 & 0 & 0 \end{bmatrix}$	$\begin{bmatrix} 1-j & 2 & -2j & 1-j \\ 2 & -2j & -1-j & 0 \\ 0 & 1+j & 2 & 0 \\ 1+j & -2 & 2j & 0 \end{bmatrix}$	$\begin{bmatrix} -2 & 1-j & 0 & -1+j \\ 2 & 0 & 1-j & -1+j \\ 2j & 1+j & 0 & 2 \\ 1+j & 0 & 1-j & 0 \end{bmatrix}$
3	$\begin{bmatrix} 1-j & -1-j & 1+j & 0 \\ 0 & -2j & -1+j & 0 \\ -2j & -1+j & -2j & -2j \\ 1+j & -1+j & -1+j & 1-j \end{bmatrix}$	$\begin{bmatrix} 2 & 2 & -2 & 0 \\ 0 & 0 & 2 & 0 \\ 0 & -2 & 0 & 0 \\ -2 & -2 & 2 & 2 \end{bmatrix}$	$\begin{bmatrix} 1-j & 1-j & -1-j & 0 \\ 2 & -2j & -1-j & 0 \\ 0 & 1-j & -2j & 0 \\ 1+j & -1+j & 1+j & 1-j \end{bmatrix}$	$\begin{bmatrix} -2 & 1-j & 0 & -1+j \\ 2 & 0 & 1-j & -1+j \\ 2j & 1-j & 0 & -2j \\ 1+j & 1-j & 0 & -1-j \end{bmatrix}$
4	$\begin{bmatrix} 1-j & 0 & 2j & 1-j \\ 0 & 2j & 1-j & 0 \\ -2j & 1-j & 0 & 0 \\ 1+j & 0 & -2j & 2j \end{bmatrix}$	$\begin{bmatrix} 2 & 0 & 0 & 2 \\ 0 & 0 & 2 & 0 \\ 0 & 2 & 0 & 0 \\ -2 & 0 & 0 & 0 \end{bmatrix}$	$\begin{bmatrix} 1-j & 2 & -2j & 1-j \\ 2 & 0 & -1+j & -2 \\ 0 & -1-j & -2 & 0 \\ 1+j & 0 & 0 & 2j \end{bmatrix}$	$\begin{bmatrix} -2 & 1+j & -2j & -1-j \\ 2 & 2j & 1+j & -1-j \\ 2j & 1-j & -2j & 0 \\ 1+j & 2j & -1-j & 2 \end{bmatrix}$
5	$\begin{bmatrix} 1-j & -1-j & 1+j & 0 \\ 0 & 2j & 1-j & 0 \\ -2j & -1-j & 0 & 0 \\ 1+j & 1+j & -1-j & 1+j \end{bmatrix}$	$\begin{bmatrix} 2 & 2 & -2 & 0 \\ 0 & 0 & 2 & 0 \\ 0 & -2 & 0 & 0 \\ -2 & -2 & 2 & 2 \end{bmatrix}$	$\begin{bmatrix} 1-j & 1-j & -1-j & 0 \\ 2 & 0 & -1+j & -2 \\ 0 & -1+j & 2j & 0 \\ 1+j & 1+j & 1-j & 1+j \end{bmatrix}$	$\begin{bmatrix} -2 & 1+j & -2j & -1-j \\ 2 & 2j & 1+j & -1-j \\ 2j & -1-j & -2 & 0 \\ 1+j & 1+j & -2 & 1-j \end{bmatrix}$
6	$\begin{bmatrix} 1-j & 0 & 2j & 1-j \\ 0 & -2j & -1+j & 0 \\ -2j & -1-j & 2 & 2 \\ 1+j & -2 & 0 & 0 \end{bmatrix}$	$\begin{bmatrix} 2 & 0 & 0 & 2 \\ 0 & 0 & 2 & 0 \\ 0 & 2 & 0 & 0 \\ -2 & 0 & 0 & 0 \end{bmatrix}$	$\begin{bmatrix} 1-j & 2 & -2j & 1-j \\ 2 & -2j & -1-j & 0 \\ 0 & 1+j & 2 & 0 \\ 1+j & -2 & 2j & 0 \end{bmatrix}$	$\begin{bmatrix} -2 & 1-j & 0 & -1+j \\ 2 & 0 & 1-j & -1+j \\ 2j & 1+j & 0 & 2 \\ 1+j & 0 & 1-j & 0 \end{bmatrix}$

Subsection 10.4.3. The $\mathbf{G}_{k,k}$, $k \in \{1, \ldots, 6\}$, are semi-identity matrices as expected. For the 1RC frequency shaping function and modulation index $h = 1/4$, $\mathbf{G}_{0,0}$ is approximately a semi-identity matrix, as shown in Proposition 7. Obtained results also show that the asymptotic expansion used in the proof of Proposition 7 is justified because non-diagonal elements of the matrix $\mathbf{G}_{0,0}$ are either exactly equal to zero or much smaller than diagonal elements. For practical purposes, the matrix $\mathbf{G}_{0,0}$ can be considered as a semi-identity matrix because the difference between determinants $|\mathbf{G}_{0,0}|$ and $|0.6165{\cdot}\mathbf{I}_4|$, where $\mathbf{I}_4$ is the $4{\times}4$ identity matrix, is negligible (i.e. $3.46{\cdot}10^{-5}$). Finally, the trace upper bound on the coding gain, obtained using codewords $\mathbf{U}_{bm}$ and $\hat{\mathbf{U}}_{bm}$, is equal to $\mathrm{tr}(\mathbf{U}_s)/4 = \sum_{k=0}^{6}(Q_k/4)d_{E_k}^2(\mathbf{Z}_k, \hat{\mathbf{Z}}_k) = 14.02$. The minimum trace upper bound of this ST-CPM code is $\sum_{k=0}^{6}(Q_k/4)d_{E\min}^2(\mathbf{Z}_k, \hat{\mathbf{Z}}_k) \approx 3.66$. This

result is obtained from (338), using the fact that the code proposed in [12] has the minimum Hamming distance $d_{Hmin} = 4$.

Since the rank design criterion only requires distinct matrices $\mathbf{U}_0$ and $\hat{\mathbf{U}}_0$ to have full rank, the higher bit matrices $\mathbf{U}_1$, $\hat{\mathbf{U}}_1$, $\mathbf{U}_2$, and $\hat{\mathbf{U}}_2$ can be used for coding gain improvement. In this example, optimization of binary matrices $\mathbf{U}_2$ and $\hat{\mathbf{U}}_2$ is ineffective because the modulation index is $h = 1/4$ and, hence, these matrices do not have impact on obtained values in matrices $\Delta\mathbf{Z}_k$. Also, we keep matrices $\mathbf{U}_0$ and $\hat{\mathbf{U}}_0$ unchanged, since they satisfy the rank criterion. Using the binary space-time code proposed in [96] with elementary polynomial $f(x) = 1 + 32x + 288x^2 + 512x^3 + 256x^4$ and minimum Hamming distance $d_{Hmin} = 8$ for codewords $\mathbf{U}_1$ and $\hat{\mathbf{U}}_1$, we construct the improved codewords:

$$\mathbf{U}_{imp} = \tag{344}$$
$$= \begin{bmatrix} 6 & 3 & 2 & 0 \\ 4 & 5 & 3 & 2 \\ 1 & 3 & 3 & 1 \\ 5 & 0 & 6 & 5 \end{bmatrix} = f_{0,8}^{-1}\left\{ \begin{bmatrix} 0 & 1 & 1 & 1 \\ 0 & 1 & 0 & 0 \\ 1 & 1 & 0 & 1 \\ 1 & 1 & 1 & 0 \end{bmatrix} + 2 \begin{bmatrix} 1 & 0 & 1 & 1 \\ 0 & 0 & 0 & 1 \\ 0 & 0 & 1 & 0 \\ 0 & 0 & 1 & 0 \end{bmatrix} + 4 \begin{bmatrix} 1 & 0 & 0 & 0 \\ 1 & 0 & 1 & 1 \\ 0 & 1 & 1 & 0 \\ 1 & 1 & 0 & 0 \end{bmatrix} \right\}$$

and

$$\hat{\mathbf{U}}_{imp} = \tag{345}$$
$$= \begin{bmatrix} 4 & 2 & 3 & 7 \\ 2 & 1 & 4 & 6 \\ 7 & 6 & 4 & 3 \\ 6 & 5 & 1 & 6 \end{bmatrix} = f_{0,8}^{-1}\left\{ \begin{bmatrix} 0 & 0 & 1 & 0 \\ 0 & 1 & 1 & 1 \\ 1 & 1 & 1 & 0 \\ 0 & 1 & 0 & 0 \end{bmatrix} + 2 \begin{bmatrix} 0 & 1 & 0 & 0 \\ 1 & 1 & 1 & 0 \\ 1 & 0 & 0 & 0 \\ 1 & 1 & 0 & 1 \end{bmatrix} + 4 \begin{bmatrix} 1 & 1 & 0 & 0 \\ 0 & 0 & 1 & 1 \\ 1 & 1 & 0 & 1 \\ 1 & 0 & 1 & 0 \end{bmatrix} \right\}.$$

The fourth column of Table 12 shows the matrices $\Delta\mathbf{Z}_{k,imp}$ obtained using codewords $\mathbf{U}_{imp}$ and $\hat{\mathbf{U}}_{imp}$. Observe that all matrices still have a full rank. The trace upper bound on the coding gain, obtained using codewords $\mathbf{U}_{imp}$ and $\hat{\mathbf{U}}_{imp}$, is equal to $\mathrm{tr}(\mathbf{U}_s)/4 = \sum_{k=0}^{6}(Q_k/4)d_{E_k}^2(\mathbf{Z}_k, \hat{\mathbf{Z}}_k) = 15.24$. However, the minimum trace upper bound of this ST-CPM code is still $\sum_{k=0}^{6}(Q_k/4)d_{E\min}^2(\mathbf{Z}_k, \hat{\mathbf{Z}}_k) \approx 3.66$.

Further enhancement of the coding gain can be obtained if matrices $\mathbf{U}_0$ and $\hat{\mathbf{U}}_0$ are constructed not only to have full rank, but also to optimize coding gain. Using the binary space-time code proposed in [96] for codewords $\mathbf{U}_0$, $\mathbf{U}_1$, $\hat{\mathbf{U}}_0$, and $\hat{\mathbf{U}}_1$, we obtain the optimized codewords:

$$\mathbf{U}_{opt} = \tag{346}$$
$$= \begin{bmatrix} 4 & 4 & 3 & 5 \\ 4 & 7 & 3 & 0 \\ 3 & 3 & 0 & 2 \\ 5 & 1 & 3 & 0 \end{bmatrix} = f_{0,8}^{-1}\left\{\begin{bmatrix} 0 & 0 & 1 & 0 \\ 0 & 1 & 0 & 0 \\ 1 & 0 & 0 & 0 \\ 1 & 0 & 1 & 1 \end{bmatrix} + 2\begin{bmatrix} 0 & 0 & 1 & 0 \\ 0 & 1 & 1 & 1 \\ 1 & 1 & 1 & 0 \\ 0 & 1 & 0 & 0 \end{bmatrix} + 4\begin{bmatrix} 1 & 0 & 0 & 0 \\ 1 & 0 & 1 & 1 \\ 0 & 1 & 1 & 0 \\ 1 & 1 & 0 & 0 \end{bmatrix}\right\}$$

and

$$\hat{\mathbf{U}}_{opt} = \tag{347}$$
$$= \begin{bmatrix} 5 & 1 & 3 & 0 \\ 2 & 1 & 4 & 5 \\ 7 & 6 & 3 & 4 \\ 6 & 4 & 3 & 6 \end{bmatrix} = f_{0,8}^{-1}\left\{\begin{bmatrix} 1 & 0 & 1 & 1 \\ 0 & 1 & 1 & 0 \\ 1 & 1 & 0 & 0 \\ 0 & 0 & 1 & 1 \end{bmatrix} + 2\begin{bmatrix} 0 & 1 & 0 & 0 \\ 1 & 1 & 1 & 0 \\ 1 & 0 & 0 & 0 \\ 1 & 1 & 0 & 1 \end{bmatrix} + 4\begin{bmatrix} 1 & 1 & 0 & 0 \\ 0 & 0 & 1 & 1 \\ 1 & 1 & 0 & 1 \\ 1 & 0 & 1 & 0 \end{bmatrix}\right\}.$$

The fifth column of Table 12 shows the matrices $\Delta\mathbf{Z}_{k,opt}$ obtained using codewords $\mathbf{U}_{opt}$ and $\hat{\mathbf{U}}_{opt}$. The trace upper bound on the coding gain, obtained using codewords $\mathbf{U}_{opt}$ and $\hat{\mathbf{U}}_{opt}$, is equal to $\mathrm{tr}(\mathbf{U}_s)/4 = \sum_{k=0}^{6}(Q_k/4)d_{E_k}^2(\mathbf{Z}_k, \hat{\mathbf{Z}}_k) = 18.61$. The minimum trace upper bound of this ST-CPM code is increased to $\sum_{k=0}^{6}(Q_k/4)d_{E\min}^2(\mathbf{Z}_k, \hat{\mathbf{Z}}_k) \approx 7.31$.

Figure 75 compares the performance curves obtained for full-response 8-ary, $h = 1/4$, 1RC, CPM with $L_t = \{1, 2, 3, 4\}$ transmit antennas. The codewords used to obtain the second, third, and fourth curve are constructed to satisfy only the rank design criterion. The fifth curve is obtained using the optimized codewords. Figure 75 plots the frame error rate versus the signal to noise ratio (E_b/N_0, where E_b denotes the received energy per bit) and shows that full diversity and coding gain improvement are achieved when the space-time codes meet both the rank and coding gain optimization criteria.

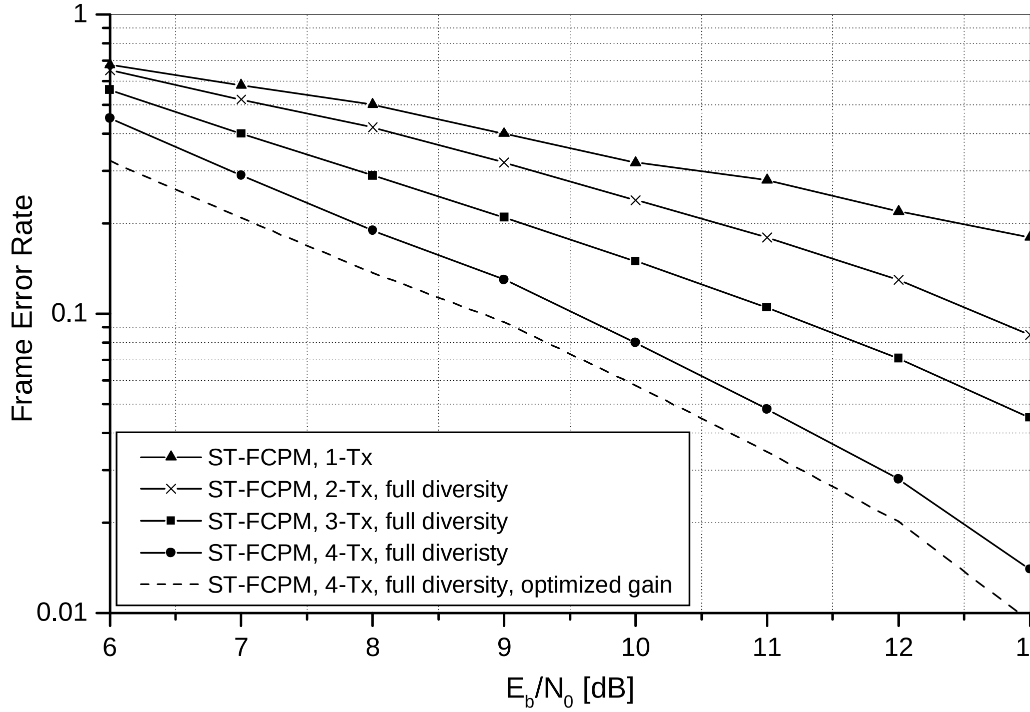

Figure 75: Frame-error rate of 8-ary ST-CPM with 1RC and $h = 1/4$ in quasi-static fading.

The second example uses a partial-response raised cosine (2RC) frequency shaping function. The space-time codewords are chosen from a (4×4) 16-ary CPM space-time code $\mathcal{C}$, where codewords $\mathbf{U} \in \mathcal{C}$ are constructed as $\mathbf{U} = f_{0,16}^{-1}(\sum_{l=0}^{3} 2^l \mathbf{U}_l)$, where $f_{0,16}^{-1}(\ \cdot\ )$ denotes the inverse of the function $f_{0,16}(\ \cdot\ )$ defined in (335), $\mathbf{U}_l$ are binary codewords from linear (4×4) space-time codes, $\mathcal{C}_l$, all codewords $\mathbf{U}_0 \in \mathcal{C}_0$ have full rank over $\mathbb{F}$ and all codewords $\mathbf{U}_0$ satisfy $\mathbf{U}_0 \neq \hat{\mathbf{U}}_0$.

Figure 76 compares the performance curve obtained for partial-response 16-ary CPM signals with 2RC frequency shaping function, $h = 1/4$, and $L_t = \{1, 2, 3, 4\}$ transmit antennas. As in the first example, the codewords used to obtain the second, third, and fourth curve are obtained using the binary space-time code described in [12]. The codewords used to obtain the fifth curve are obtained using the binary space-time code proposed in [96]. Figure 76 shows that full diversity and coding gain improvement are achieved when the space-time codes are constructed to satisfy the rank and coding gain optimization criteria.

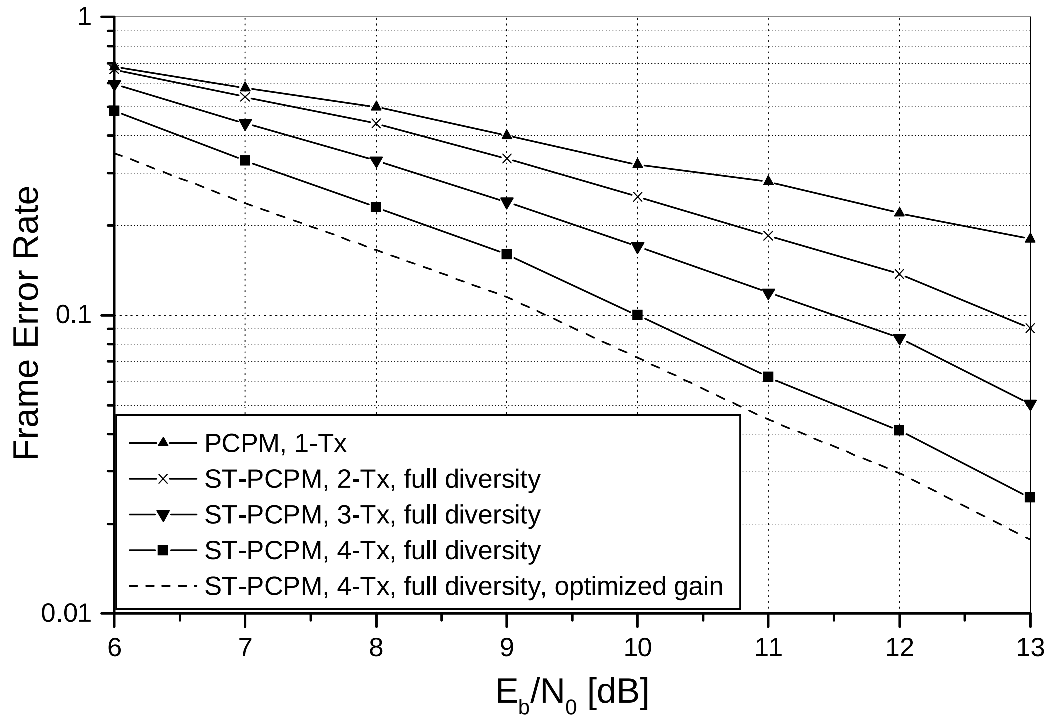

Figure 76: Frame-error rate of 16-ary ST-CPM with 2RC and $h = 1/4$ in quasi-static fading.

The last example uses a full-response 1RC frequency shaping function. The space-time codewords are chosen from a (2×2) 8-ary CPM space-time code $\mathcal{C}$, where codewords $\mathbf{U} \in \mathcal{C}$ are constructed as $\mathbf{U} = f_{0,8}^{-1}(\sum_{l=0}^{2} 2^l \mathbf{U}_l)$, where $f_{0,8}^{-1}(\ \cdot\ )$ denotes the inverse of the function $f_{0,8}(\ \cdot\ )$ defined in (335), $\mathbf{U}_l$ are binary codewords from linear (2×2) space-time codes $\mathcal{C}_l$ described in [12] with the generator matrix $G = [1 \quad \alpha]$, where α is a zero of the primitive polynomial $f(x) = x^2 + x + 1$ over $\mathbb{F}$. All codewords $\mathbf{U}_0 \in \mathcal{C}_0$ have full rank over $\mathbb{F}$ and all codewords $\mathbf{U}_0$ satisfy $\mathbf{U}_0 \neq \hat{\mathbf{U}}_0$. The performance curves for this 8-ary, 1RC, $h = 1/4$, CPM space-time code with $L_t = \{1, 2\}$ transmit antennas are plotted in Fig. 77. Results shows that full diversity is obtained using this space-time code. The minimum trace upper bound of this ST-CPM code is

$\sum_{k=0}^{6}(Q_k/2)d^2_{E\min}(\mathbf{Z}_k, \hat{\mathbf{Z}}_k) \approx 3.66$. The coding gain can be improved if the codewords are constructed as in (339), using the orthogonal code for two transmit antennas [95]. The minimum trace upper bound of this ST-CPM code is $\sum_{k=0}^{6}(Q_k/2)d^2_{E\min}(\mathbf{Z}_k, \hat{\mathbf{Z}}_k) \approx 7.31$. We refer to this design as orthogonal space-time full-response CPM (OST-FCPM) design. Further enhancement of the coding gain can be obtained if the codewords are constructed using the super-orthogonal 2-state trellis space-time code for two transmit antennas proposed in [97]. The minimum trace upper bound of this ST-CPM code is $\sum_{k=0}^{6}(Q_k/2)d^2_{E\min}(\mathbf{Z}_k, \hat{\mathbf{Z}}_k) \approx 9.78$. We refer to this design as super-orthogonal space-time full-response CPM (SOST-FCPM) design. Figure 77 compares our OST-FCPM and SOST-FCPM designs with OST-FCPM design [44] and ST-FCPM design with mapping scheme [45], respectively. Results show that our SOST-FCPM design has similar performance as ST-FCPM with mapping scheme [45] and performs better than the OST-FCPM design [44] and our OST-FCPM design.

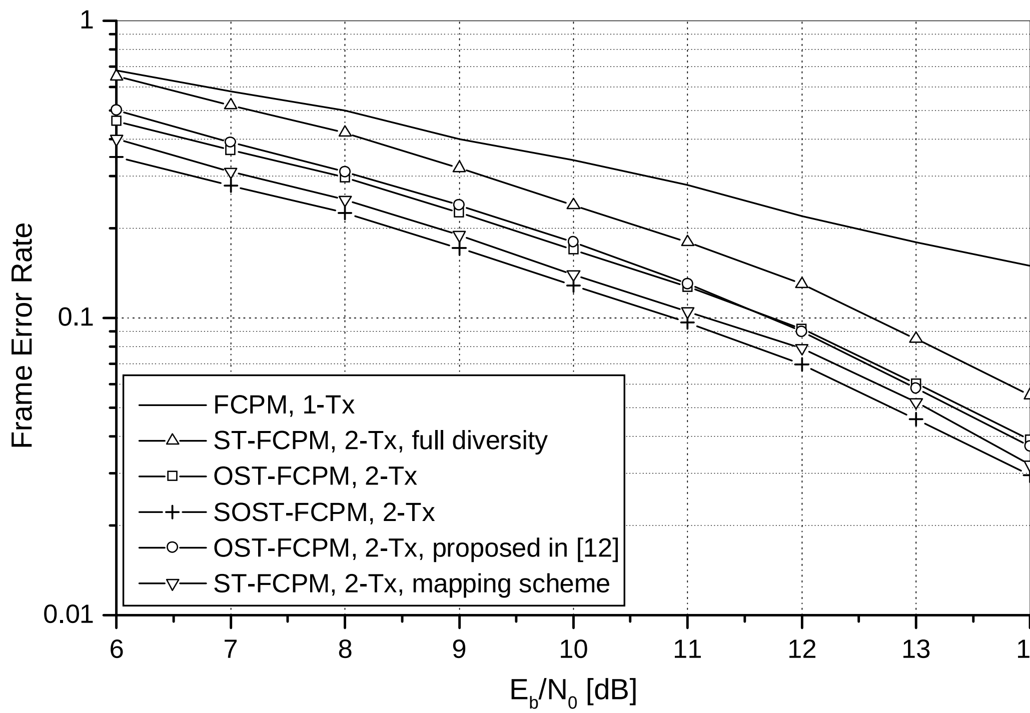

Figure 77: Frame-error rate of (2×2) 8-ary ST-CPM with 1RC and $h = 1/4$ in quasi-static fading.

In Subsection 10.4.3 is shown that the raised cosine frequency shaping function satisfies the coding gain design criterion. Figures 78 and 79 illustrate how much the coding gain is sacrificed if other frequency shaping functions are used instead of the raised cosine frequency shaping function. The results are obtained using the (2×2) 8-ary orthogonal space-time code and modulation index $h = 1/4$. In Fig. 78, the second curve is obtained using the Gaussian frequency shaping function (GSP, frequency shaping function used in GMSK) with normalized filter bandwidth $BT = 0.25$, the third curve is obtained using the full-response rectangular frequency shaping function (1REC), and the fourth curve is obtained using the full-response raised cosine shaping function (1RC). Results show that the full-response raised cosine shaping function improves the coding gain for approximately 0.89 dB compared to the Gaussian frequency shaping function and approximately 0.57 dB compared to the full-response rectangular frequency shaping function. In Fig. 79, the second and the third curve are obtained using the rectangular frequency shaping function with $L = 3$ (3REC) and $L = 2$ (2REC), respectively. The fourth curve is obtained using the Gaussian frequency shaping function (GSP) with normalized filter bandwidth $BT = 0.25$. Finally, the fifth and the sixth curve are obtained using the raised cosine shaping function with $L = 3$ (3RC) and $L = 2$ (2RC), respectively. Results show that the Gaussian frequency shaping function with $BT = 0.25$ performs similar to the raised cosine shaping function with $L = 3$. The raised cosine shaping function with $L = 2$ improves the coding gain for approximately 0.47 dB compared to the Gaussian frequency shaping function and approximately 0.86 dB compared to the rectangular frequency shaping function with $L = 2$. Finally, note that the full-response raised cosine shaping function outperforms the partial-response raised cosine shaping function with $L = 2$ for approximately 0.34 dB. This is expected result because all matrices $\mathbf{G}_{k,k}$, $k \in \{1, \ldots, R-1\}$, defined in (311), are exactly diagonal matrices for full-response frequency shaping pulses, where as for partial-response frequency shaping pulses, these matrices are semi-diagonal (non-diagonal elements are much smaller than diagonal ones), which decreases the coding gain.

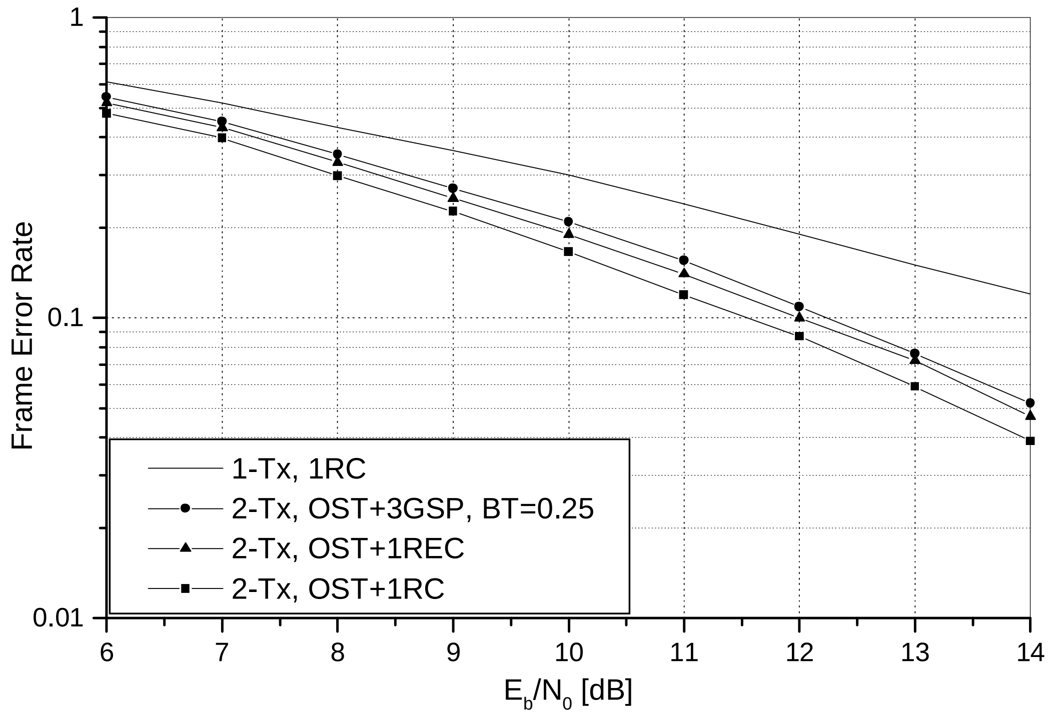

Figure 78: Frame-error rate of 8-ary OST-CPM with Gaussian frequency shaping function ($BT = 0.25$), full-response rectangular, and full-response raised cosine frequency shaping function and $h = 1/4$ in quasi-static fading.

10.6 Summary

In this chapter, we have derived sufficient conditions under which M-ary partial- and full-response CPM space-time codes will attain both full spatial diversity and optimized coding gain. Using a linear decomposition of CPM signals in a tilted-phase representation, we have identified the rank criterion for the M-ary partial- and full-response CPM that specifies the set of allowable modulation indices. We have also proposed a coding gain design criterion. It is shown that the optimization of the coding gain for ST-CPM depends on selection of phase shaping pulses, modulation indices, and codewords. We have specified the set of allowable modulation indices and phase shaping functions which can be used toward ST-CPM coding gain optimization

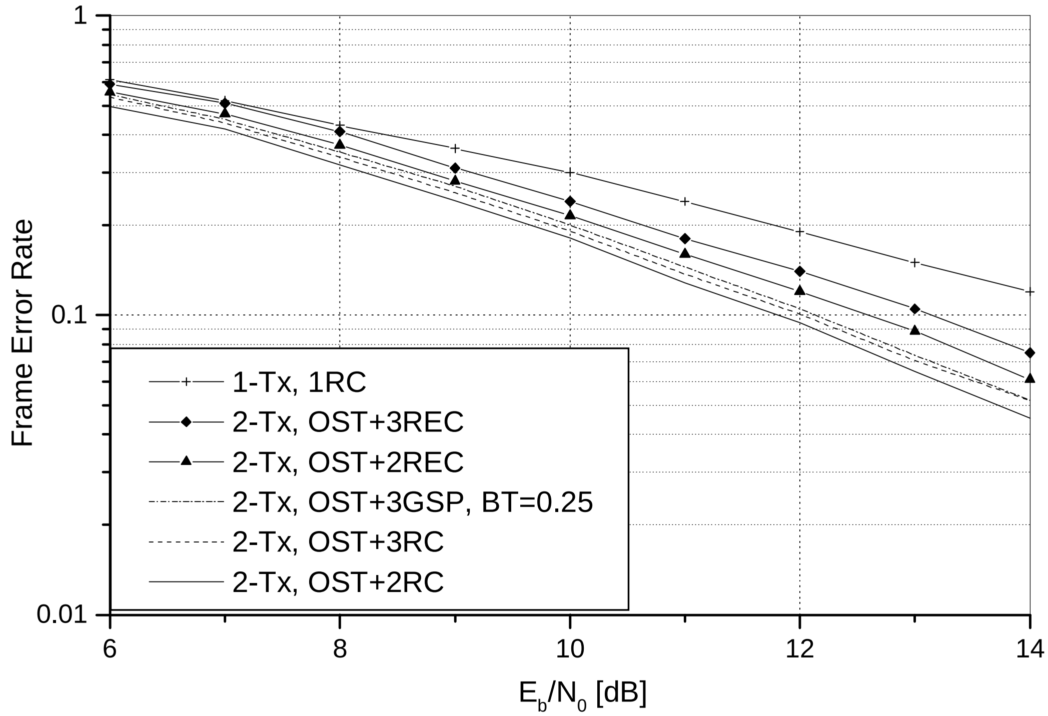

Figure 79: Frame-error rate of 8-ary OST-CPM with Gaussian frequency shaping function ($BT = 0.25$), partial-response rectangular, and partial-response raised cosine frequency shaping function and $h = 1/4$ in quasi-static fading.

(improvement or maximization) and we have established rules for ST-CPM and OST-CPM codeword optimization. Several examples and simulation results show that full spatial diversity and optimal coding gain are achieved for ST-CPM systems that meet the proposed CPM rank criterion and the coding gain design criterion.

CHAPTER XI

RESEARCH CONTRIBUTIONS AND FUTURE RESEARCH DIRECTIONS

11.1 Research Contributions

The demand for high-speed wireless services makes MIMO M-to-M systems the leading candidates for future communication systems. To enable the successful design of MIMO M-to-M systems, our research was focused on modeling of SISO and MIMO M-to-M multipath fading channels and on diversity techniques for MIMO systems. The contributions of our research are summarized below.

- New SoS simulation models are proposed for SISO F-to-M Rayleigh fading channels and compared with existing simulation models. First, a deterministic model is proposed. The statistical properties of the deterministic model are derived and verified by simulation. Compared to existing models, the deterministic model yields a lower cross-correlation between different faded envelopes and between the in-phase and quadrature components of each complex faded envelope. However, the auto-correlation functions of the in-phase and quadrature components still do not exactly match the theoretical functions. To overcome this disadvantage, a new non-ergodic statistical model is proposed. The proposed statistical model has correct statistical properties, converges faster than existing statistical models, and has lower cross-correlations between different complex envelopes and between the quadrature components of each complex envelope. This new statistical model yields adequate statistics with only 30 simulation runs.

- A new statistical SoS simulation model is proposed for SISO M-to-M Rayleigh fading channels. The new model employs the double ring model, where orthogonal functions are chosen as the in-phase and quadrature components of the complex faded envelope. The statistical properties of the proposed model are derived and verified by simulation. Compared to existing models, the new statistical model converges faster, has a lower variance of the auto-correlation functions and has a lower correlation between the in-phase and quadrature components of the complex faded envelope. Finally, unlike existing M-to-M models, the new model generates multiple uncorrelated faded envelopes as well.

- A single- and double-bounced two-ring parametric reference model is proposed for MIMO M-to-M Ricean fading channels. From the new reference model, a closed-form joint space-time correlation function and a space-Doppler power spectrum are derived for a 2-D non-isotropic scattering environment. Also, space-time correlation functions of the in-phase and quadrature components of the complex faded envelope are derived, assuming 2-D isotropic scattering environment. Finally, two new SoS simulation models for MIMO M-to-M Ricean fading channels are proposed. The statistics of the simulation models are verified by simulation. The results show that the simulation models are a good approximation of the reference model and that they outperform existing simulation models.

- A 3-D "two-cylinder" geometrical propagation model for narrowband MIMO M-to-M communications is proposed. Based on this geometrical model, a 3-D reference model for narrowband MIMO M-to-M multipath fading channels is developed. From the reference model, a closed-form joint space-time correlation function for a 3-D non-isotropic scattering environment is derived. Furthermore, the SoS simulation models for 3-D non-isotropic scattering environment are proposed. The statistical properties of the simulation models are derived and verified by simulations. These simulation models are used to evaluate the effect of space-time correlation on the outage capacity of uniform linear antenna arrays. The effect of antenna spacing and antenna orientations on the outage capacity are studied. Finally, the capacities of linear, circular, and spherical antenna arrays are compared. The results show that if volume available for antenna array realization is a constraint, circular antenna arrays placed in the x-y plane will provide the highest capacity.

- A 3-D "concentric-cylinders" geometrical propagation model for wideband MIMO M-to-M communications is proposed. Based on the geometrical model, a 3-D parametric reference model for wideband MIMO M-to-M multipath fading channels is developed. From the reference model, a space-time-frequency correlation function is derived for a 3-D non-isotropic scattering environment. It is shown that the time and frequency dispersion of a wide sense stationary uncorrelated scattering channel cannot be treated independently, contrary to common practice. From the space-time-frequency correlation function, a space-Doppler power spectral density and a power space-delay spectrum are derived and compared with SISO measured data. Finally, two SoS simulation models for wideband MIMO M-to-M Ricean fading channels are proposed. The statistics of the simulation models are verified by simulation. The results show that the simulation models are a good approximation of the reference model.

- The first-order statistics of the channel impulse response are not sufficient to assess system characteristics such as handoff, velocities of the transmitter and receiver, and fading rate. To assess the aforementioned system characteristics, accurate characterization of the second-order statistics, such as envelope level crossing rate and average envelope fade duration, is necessary. Using our 3-D reference models for narrowband and wideband MIMO M-to-M channel models, we derive the envelope level crossing rate and average envelope fade duration for M-to-M multipath fading channels.

- We proposed the 3-D channel models and simulators for narrowband and wideband MIMO M-to-M channels. To validate these theoretical and simulation models, an experimental MIMO M-to-M channel-sounding campaign was conducted for M-to-M vehicular communication with vehicles travelling along surface streets and expressways in a metropolitan area. To compare the first and second-order channel statistics obtained from the models with those obtained from the empirical measurements, a new maximum likelihood based stochastic estimator is derived to extract the relevant model parameters from the measured data. Finally, the measured data is processed and compared with the analytical results. The close agreement between the analytically and empirically obtained channel statistics confirms the utility of the proposed reference model and the method used to estimate the model parameters.

- Sufficient conditions are derived under which M-ary partial- and full-response CPM-ST codes will attain both full spatial diversity and optimal coding gain. General code construction rules are desirable because of the nonlinearity and inherent memory of the CPM signals which makes manual design or computer search difficult. Using a linear decomposition of CPM signals with tilted-phase, a rank criterion for M-ary partial- and full-response CPM that specifies the set of allowable modulation indices is identified. A coding gain design criterion is proposed. Optimization of the coding gain for CPM-ST codes is shown to depend on the CPM frequency/phase shaping pulse, modulation index, and codewords. The modulation indices and phase shaping functions that optimize the coding gain are specified. Finally, optimization of coding gain for CPM-ST and orthogonal CPM-ST codewords is discussed.

11.2 Future Research Directions

In this thesis, we have addressed the problem of 3-D narrowband and wideband channel modeling and simulation of MIMO M-to-M multipath fading channels. Furthermore, we have verified the accuracy of our models by comparing them with measured data. Although the close agreement between the analytical and empirical curves is obtained, there is still room for improvements. For example, our models assume that all scattering objects are stationary, which is an unrealistic assumption. Therefore, our models can be extended to include non-stationary scattering objects, such as cars and people. Another possible enhancement is to develop new MIMO M-to-M channel models that account for antenna coupling effects. Since capacity of MIMO systems is strongly dependent on the number of antennas in the transmitter and receiver, it is highly desirable to use as many antennas as possible. On the other hand, transmitter/receiver usually has limited space/volume to distribute antenna elements. The general belief is that mutual coupling between antenna elements will deteriorate the channel, increase the correlation, and reduce achievable capacity. However, recently is found that mutual coupling has a de-correlating effect on the channel coefficients, and thereby improve capacity. Hence, the future research efforts may be devoted to developing MIMO M-to-M channel models that will allow us to study spatial correlation and coupling effects separately and jointly.

A possible extension of our work is the development of 3-D wideband models for relay channels. Relay channels are encountered in systems that utilize co-operative diversity or virtual antenna arrays. It is found that the overall channel from the source to the destination via the relay in amplify and forward systems is “double” Gaussian with properties quite different from typical F-to-M or M-to-M channels. Hence, there is the need for 3-D wideband relay channel models.

This thesis has also proposed the design criteria for space-time coded CPM systems. In particular, we have proposed the rank and coding gain optimization criteria for M-ary partial- and full-response CPM. However, we did not find the design criteria for space-time coded multi-h CPM system. The future research efforts may be directed toward finding the design criteria for such system. Another possible extension of our work is the development of optimal space-time codes that satisfy our design criteria for ST-CPM.

APPENDIX A

DERIVATIONS OF THE STATISTICAL PROPERTIES OF THE F-TO-M DETERMINISTIC MODEL

Derivation of the auto-correlation function of the in-phase component is presented below

$$\begin{aligned} R_{g_{ik}g_{ik}}(\tau) &= \mathrm{E}\left[g_{ik}(t)g_{ik}(t+\tau)\right] \qquad (348) \\ &= \frac{8}{N}\sum_{n=0}^{M}\sum_{i=0}^{M}\frac{a_n a_i}{2}\mathrm{E}\left[\cos(\omega_d(t+\tau)\cos\alpha_{ik}+\omega_d t\cos\alpha_{nk}+\phi_{ik}+\phi_{nk})\right] \\ &+ \frac{8}{N}\sum_{n=0}^{M}\sum_{i=0}^{M}\frac{a_n a_i}{2}\mathrm{E}\left[\cos(\omega_d(t+\tau)\cos\alpha_{ik}-\omega_d t\cos\alpha_{nk}+\phi_{ik}-\phi_{nk})\right]. \end{aligned}$$

Since ϕ_{nk} and ϕ_{ik} are independent when $n \neq i$, and all other terms in the sums are deterministic, we obtain

$$R_{g_{ik}g_{ik}}(\tau) = \frac{4}{N}\sum_{n=0}^{M}\frac{a_n^2}{2}\cos(\omega_d\tau\cos\alpha_{nk}). \qquad (349)$$

Furthermore, Riemann integral theory can be used to show that as $N \to \infty$ the auto-correlation of the in-phase component has the limiting value

$$\lim_{N\to\infty} R_{g_{ik}g_{ik}}(\tau) = J_0(\omega_d\tau) + J_4(\omega_d\tau). \qquad (350)$$

Likewise, the auto-correlation function of the quadrature component is

$$\begin{aligned} \lim_{N\to\infty} R_{g_{qk}g_{qk}}(\tau) &= \lim_{N\to\infty}\mathrm{E}\left[g_{qk}(t)g_{qk}(t+\tau)\right] \qquad (351) \\ &= \lim_{N\to\infty}\frac{4}{N}\sum_{n=0}^{M}\sum_{i=0}^{M}\frac{b_n b_i}{2}\mathrm{E}\left[\cos(\omega_d(t+\tau)\sin\alpha_{ik}-\omega_d t\sin\alpha_{nk}+\phi_{ik}-\phi_{nk})\right] \\ &- \lim_{N\to\infty}\frac{4}{N}\sum_{n=0}^{M}\sum_{i=0}^{M}\frac{b_n b_i}{2}\mathrm{E}\left[\cos(\omega_d(t+\tau)\sin\alpha_{ik}+\omega_d t\sin\alpha_{nk}+\phi_{ik}+\phi_{nk})\right] \\ &= \lim_{N\to\infty}\frac{4}{N}\sum_{n=0}^{M}\frac{b_n^2}{2}\cos(\omega_d\tau\sin\alpha_{nk}) = J_0(\omega_d\tau) - J_4(\omega_d\tau). \end{aligned}$$

The cross-correlation function of the in-phase and quadrature components is

$$
\begin{aligned}
R_{g_{ik}g_{qk}}(\tau) &= R_{g_{qk}g_{ik}}(\tau) = \mathrm{E}\left[g_{ik}(t)g_{qk}(t+\tau)\right] = \mathrm{E}\left[g_{qk}(t)g_{ik}(t+\tau)\right] \\
&= \frac{4}{N}\sum_{n=0}^{M}\sum_{i=0}^{M}\frac{a_n b_i}{2}\mathrm{E}\left[\sin(\omega_d(t+\tau)\sin\alpha_{ik} + \omega_d t\cos\alpha_{nk} + \phi_{ik} + \phi_{nk})\right] \\
&+ \frac{4}{N}\sum_{n=0}^{M}\sum_{i=0}^{M}\frac{a_n b_i}{2}\mathrm{E}\left[\sin(\omega_d(t+\tau)\sin\alpha_{ik} - \omega_d t\cos\alpha_{nk} + \phi_{ik} - \phi_{nk})\right] \\
&= 0.
\end{aligned} \tag{352}
$$

The auto-correlation function of the multiple complex envelopes is

$$
\begin{aligned}
R_{g_k g_k}(\tau) &= \frac{2}{N}\sum_{n=0}^{M}\frac{b_n^2}{2}\cos(\omega_d\tau\sin\alpha_{nk}) + \frac{2}{N}\sum_{n=0}^{M}\frac{a_n^2}{2}\cos(\omega_d\tau\cos\alpha_{nk}) \\
&= J_0(\omega_d\tau)
\end{aligned} \tag{353}
$$

Finally, the auto-correlation of the squared envelope is

$$
\begin{aligned}
R_{|g_k|^2|g_k|^2}(\tau) &= \frac{8}{N^2}\sum_{n=0}^{M}a_n^4 + \frac{8}{N^2}\sum_{n=0}^{M}b_n^4 + 2R^2_{g_{i_k}g_{i_k}}(\tau) \\
&+ 2R^2_{g_{q_k}g_{q_k}}(\tau) + 4R^2_{g_{i_k}g_{q_k}}(\tau).
\end{aligned} \tag{354}
$$

APPENDIX B

DERIVATIONS OF THE STATISTICAL PROPERTIES OF THE F-TO-M STATISTICAL MODEL

Derivation of the auto-correlation function of the in-phase component is presented below

$$\begin{aligned} R_{g_{ik}g_{ik}}(\tau) &= \frac{4}{M}\sum_{n=1}^{M}\sum_{i=1}^{M}\mathrm{E}\left[\cos\beta_{nk}\cos\beta_{ik}\right] \\ &\times \mathrm{E}\left[\cos(\omega_d t\cos\alpha_{nk}+\phi_{nk})\cos(\omega_d(t+\tau)\cos\alpha_{ik}+\phi_{ik})\right] \\ &= \frac{1}{M}\sum_{n=1}^{M}\mathrm{E}\left[\cos(\omega_d\cos\alpha_{nk}\tau)\right] \\ &= \frac{1}{M}\frac{1}{2\pi}\sum_{n=1}^{M}\int_{-\pi}^{\pi}\cos\left(\omega_d\tau\cos\left(\frac{2\pi n}{N}+\frac{2\pi k}{PN}+\frac{\theta-\pi}{N}\right)\right)d\theta. \end{aligned} \tag{355}$$

As in [14], the proof can be completed by replacing the variable of integration θ with $\gamma_{nk} = 2\pi n/N + (2\pi k)/(PN) + (\theta - \pi)/N$ and integrating

$$\lim_{M\to\infty} R_{g_{ik}g_{ik}}(\tau) = \lim_{M\to\infty}\frac{1}{M}\frac{1}{2\pi}\sum_{n=1}^{M}\int_{\frac{2\pi n-2\pi}{N}+\frac{2\pi k}{PN}}^{\frac{2\pi n}{N}+\frac{2\pi k}{PN}}\cos(\omega_d\tau\cos\gamma_{nk})4M\,d\gamma_{nk} = J_0(\omega_d\tau). \tag{356}$$

The auto-correlation function of the quadrature component is

$$\begin{aligned} \lim_{N\to\infty} R_{g_{qk}g_{qk}}(\tau) &= \lim_{N\to\infty}\frac{4}{M}\sum_{n=1}^{M}\sum_{i=1}^{M}\mathrm{E}\left[\sin\beta_{nk}\sin\beta_{ik}\right] \\ &\times \mathrm{E}\left[\sin(\omega_d t\sin\alpha_{nk}+\phi_{nk})\sin(\omega_d(t+\tau)\sin\alpha_{ik}+\phi_{ik})\right] \\ &= \lim_{N\to\infty}\frac{1}{M}\sum_{n=1}^{M}\mathrm{E}\left[\cos(\omega_d\sin\alpha_{nk}\tau)\right] \\ &= \lim_{N\to\infty}\frac{1}{M}\frac{1}{2\pi}\sum_{n=1}^{M}\int_{-\pi}^{\pi}\cos\left(\omega_d\tau\sin\left(\frac{2\pi n}{N}+\frac{2\pi k}{PN}+\frac{\theta-\pi}{N}\right)\right)d\theta \\ &= J_0(\omega_d\tau). \end{aligned} \tag{357}$$

The cross-correlation function of the in-phase and quadrature components is

$$\begin{aligned} R_{g_{ik}g_{qk}}(\tau) &= \mathrm{E}\left[g_{ik}(t)g_{qk}(t+\tau)\right] = \frac{4}{M}\sum_{n=1}^{M}\sum_{i=1}^{M}\mathrm{E}\left[\cos\beta_{nk}\sin\beta_{ik}\right] \\ &\times \mathrm{E}\left[\cos(\omega_d t\cos\alpha_{nk}+\phi_{nk})\sin(\omega_d(t+\tau)\sin\alpha_{ik}+\phi_{ik})\right] = 0. \quad (358)\end{aligned}$$

Similarly, the auto-correlation function of the multiple complex envelopes is

$$R_{g_k g_k}(\tau) = \frac{1}{2}\left(\mathrm{E}\left[g_{ik}(t)g_{ik}(t+\tau)\right] + \mathrm{E}\left[g_{qk}(t)g_{qk}(t+\tau)\right]\right) = J_0(\omega_d\tau). \quad (359)$$

Finally, derivation of the auto-correlation function of the squared envelope is given below. We follow a procedure similar to the one outlined in [30].

$$\begin{aligned} R_{|g_k|^2|g_k|^2}(\tau) &= \mathrm{E}\left[g_{ik}^2(t)g_{ik}^2(t+\tau)\right] + \mathrm{E}\left[g_{qk}^2(t)g_{qk}^2(t+\tau)\right] \\ &+ \mathrm{E}\left[g_{ik}^2(t)g_{qk}^2(t+\tau)\right] + \mathrm{E}\left[g_{qk}^2(t)g_{ik}^2(t+\tau)\right]. \quad (360)\end{aligned}$$

The computation of the first term in the right-hand side of (360) is shown below

$$R_{|g_{ik}|^2|g_{ik}|^2}(\tau) = \frac{16}{M^2}\mathrm{E}\left[\sum_{p=1}^{M}a_p\sum_{j=1}^{M}b_j\sum_{q=1}^{M}c_q\sum_{n=1}^{M}d_n\right], \quad (361)$$

where $a_p = \cos(\beta_{pk})\cos(\omega_d(t+\tau)\cos\alpha_{pk}+\phi_{pk})$, $b_j = \cos(\beta_{jk})\cos(\omega_d t\cos\alpha_{jk}+\phi_{jk})$, $c_q = \cos(\beta_{qk})\cos(\omega_d(t+\tau)\cos\alpha_{qk}+\phi_{qk})$, and $d_n = \cos(\beta_{nk})\cos(\omega_d t\cos\alpha_{nk}+\phi_{nk})$. The mutual independence of the ϕ_{ik}'s ensures that all terms in the above equation are zero, except the four terms with: 1) $n=j=p=q$; 2) $n=j,\ p=q,\ j\neq p$; 3) $n=p,\ j=q,\ n\neq j$; 4) $n=q,\ j=p,\ n\neq j$. We compute each of these terms individually to derive overall expression.

Term 1: $n=j=p=q$

$$= \tfrac{16}{M^2}\sum_{n=1}^{M}\tfrac{3}{8}\mathrm{E}\left[\tfrac{1}{4}w_n y_n\right] = \tfrac{3}{2M} + \tfrac{3}{4M}J_0\left(2\omega_d\tau\right), \quad (362)$$

where $w_n = (1+\cos(2\omega_d t\cos\alpha_{nk}+2\phi_{nk}))$ and $y_n = (1+\cos(2\omega_d(t+\tau)\cos\alpha_{nk}+2\phi_{nk}))$.

Term 2: $n = j,\ p = q,\ j \neq p$

$$\begin{aligned} &= \frac{16}{M^2} \sum_{j=1}^{M} \mathrm{E}\left[\cos^2(\beta_{jk}) \cos^2(\omega_d t \cos\alpha_{jk} + \phi_{jk})\right] \\ &\times \sum_{p=1, p\neq j}^{M} \mathrm{E}\left[\cos^2(\beta_{pk}) \cos^2(\omega_d (t+\tau) \cos\alpha_{pk} + \phi_{pk})\right] \\ &= \frac{16}{M^2} \sum_{j=1}^{M} \frac{1}{2} \cdot \frac{1}{2} \sum_{p=1, p\neq j}^{M} \frac{1}{2} \cdot \frac{1}{2} = \frac{M-1}{M}, \end{aligned} \tag{363}$$

Term 3: $n = p,\ j = q,\ n \neq j$

$$= \frac{1}{M^2} \sum_{n=1}^{M} \mathrm{E}\left[\cos(\omega_d \tau \cos\alpha_{nk})\right] \sum_{j=1, j\neq n}^{M} \mathrm{E}\left[\cos(\omega_d \tau \cos\alpha_{jk})\right] = \frac{M-1}{M} J_0^2(\omega_d \tau)\,. \tag{364}$$

It can be shown that Term 4 is equal to Term 3. Adding all four terms gives

$$\mathrm{E}\left[g_{ik}^2(t) g_{ik}^2(t+\tau)\right] = \frac{M-1}{M} + 2\frac{M-1}{M} J_0^2(\omega_d \tau) + \frac{3}{2M} + \frac{3}{4M} J_0(2\omega_d \tau)\,. \tag{365}$$

Similarly can be shown that

$$\mathrm{E}\left[g_{qk}^2(t) g_{qk}^2(t+\tau)\right] = \mathrm{E}\left[g_{ik}^2(t) g_{ik}^2(t+\tau)\right], \tag{366}$$

$$\mathrm{E}\left[g_{ik}^2(t) g_{qk}^2(t+\tau)\right] = \mathrm{E}\left[g_{qk}^2(t) g_{ik}^2(t+\tau)\right] = \frac{M-1}{M} + \frac{1}{2M} + \frac{1}{4M} J_0(2\omega_d \tau)\,. \tag{367}$$

Substituting the above terms in (360) and letting $M \to \infty$, gives the desired expression (8).

APPENDIX C

DERIVATIONS OF THE STATISTICAL PROPERTIES OF THE SISO M-TO-M STATISTICAL MODEL

Derivation of the auto-correlation function of the in-phase component of the k^{th} complex faded envelope is presented below

$$\begin{aligned}
R_{g_{ik}g_{ik}}(\tau) &= \mathrm{E}[g_{ik}(t+\tau)g_{ik}(t)] = \frac{4}{N_0 M}\sum_{n,m=1}^{N_0,M}\sum_{p,r=1}^{N_0,M}\mathrm{E}\bigg[\cos\left(\omega_2(t+\tau)\cos\beta_{mk}\right) \\
&\times \cos\left(\omega_2 t\cos\beta_{pk}\right)\cos\left(\omega_1(t+\tau)\cos\alpha_{nk}+\phi_{nmk}\right)\cos\left(\omega_1 t\cos\alpha_{rk}+\phi_{prk}\right)\bigg] \\
&= \frac{1}{N_0 M}\sum_{n=1}^{N_0}\sum_{m=1}^{M}\mathrm{E}\left[\cos\left(\omega_2\tau\cos\beta_{mk}\right)\cos\left(\omega_1\tau\cos\alpha_{nk}\right)\right] \\
&= \frac{1}{M}\sum_{m=1}^{M}\frac{1}{2\pi}\int_{-\pi}^{\pi}\cos\left(\omega_2\tau\cos\left(\frac{2\pi m}{2M}+\frac{2\pi k}{2PM}+\frac{\psi-\pi}{2M}\right)\right)d\psi \\
&\times \frac{1}{N_0}\sum_{n=1}^{N_0}\frac{1}{2\pi}\int_{-\pi}^{\pi}\cos\left(\omega_1\tau\cos\left(\frac{2\pi n}{4N_0}+\frac{2\pi k}{4PN_0}+\frac{\theta-\pi}{4N_0}\right)\right)d\theta. \qquad (368)
\end{aligned}$$

As in [27], the derivation can be completed by replacing the variables of integration, θ and ψ, with $\gamma_{nk} = (2\pi n)/(4N_0) + (2\pi k)/(4PN_0) + (\theta-\pi)/(4N_0)$ and $\delta_{mk} = (2\pi m)/(2M) + (2\pi k)/(2PM) + (\psi-\pi)/(2M)$, respectively.

$$\begin{aligned}
\lim_{N_0,M\to\infty} R_{g_{ik}g_{ik}}(\tau) &= \lim_{N_0,M\to\infty}\frac{1}{N_0}\frac{2}{\pi}\int_{2\pi k/4PN_0}^{\pi/2+2\pi k/4PN_0}\cos\left(\omega_1\tau\cos\gamma_{nk}\right)d\gamma_{nk} \qquad (369) \\
&\times \frac{1}{M}\frac{1}{\pi}\int_{2\pi k/2PM}^{\pi+2\pi k/2PM}\cos\left(\omega_2\tau\cos\delta_{mk}\right)d\delta_{mk} = J_0\left(\omega_1\tau\right)J_0\left(\omega_2\tau\right).
\end{aligned}$$

Likewise, the auto-correlation function of the quadrature component of the k^{th}

complex faded envelope is

$$\begin{aligned}
\lim_{N_0,M\to\infty} R_{g_{qk}g_{qk}}(\tau) &= \lim_{N_0,M\to\infty} \mathrm{E}[g_{qk}(t+\tau)g_{qk}(t)] = \lim_{N_0,M\to\infty} \frac{4}{N_0 M} \\
&\times \sum_{n,m=1}^{N_0,M} \sum_{p,r=1}^{N_0,M} \mathrm{E}\Big[\sin\left(\omega_2(t+\tau)\cos\beta_{mk}\right) \sin\left(\omega_2 t \cos\beta_{pk}\right) \\
&\times \sin\left(\omega_1(t+\tau)\sin\alpha_{nk} + \phi_{nmk}\right) \sin\left(\omega_1 t \sin\alpha_{rk} + \phi_{prk}\right) \Big] \\
&= \lim_{N_0,M\to\infty} \frac{1}{N_0 M} \sum_{n=1}^{N_0} \sum_{m=1}^{M} \mathrm{E}\left[\cos\left(\omega_2 \tau \cos\beta_{mk}\right) \cos\left(\omega_1 \tau \sin\alpha_{nk}\right)\right] \\
&= \lim_{N_0,M\to\infty} \frac{1}{N_0} \frac{2}{\pi} \int_{2\pi k/4PN_0}^{\pi/2+2\pi k/4PN_0} \cos\left(\omega_1 \tau \sin\gamma_{nk}\right) d\gamma_{nk} \\
&\times \frac{1}{M} \frac{1}{\pi} \int_{2\pi k/2PM}^{\pi+2\pi k/2PM} \cos\left(\omega_2 \tau \cos\delta_{mk}\right) d\delta_{mk} = J_0\left(\omega_1 \tau\right) J_0\left(\omega_2 \tau\right).
\end{aligned} \tag{370}$$

The cross-correlation function of the in-phase and quadrature components is

$$\begin{aligned}
R_{g_{ik}g_{qk}}(\tau) &= \mathrm{E}[g_{qk}(t+\tau)g_{ik}(t)] = \frac{4}{N_0 M} \sum_{n,m=1}^{N_0,M} \sum_{p,r=1}^{N_0,M} \mathrm{E}\Big[\sin\left(\omega_2(t+\tau)\cos\beta_{mk}\right) \\
&\times \cos\left(\omega_2 t \cos\beta_{pk}\right) \sin\left(\omega_1(t+\tau)\sin\alpha_{nk} + \phi_{nmk}\right) \cos\left(\omega_1 t \cos\alpha_{rk} + \phi_{prk}\right) \Big] \\
&= 0.
\end{aligned} \tag{371}$$

Finally, the auto-correlation function of the multiple complex envelopes is

$$R_{g_k g_k}(\tau) = \frac{1}{2}\left(\mathrm{E}\left[g_{ik}(t)g_{ik}(t+\tau)\right] + \mathrm{E}\left[g_{qk}(t)g_{qk}(t+\tau)\right]\right) = J_0(\omega_1\tau)J_0(\omega_2\tau). \tag{372}$$

APPENDIX D

DERIVATIONS OF EQUATIONS (77) - (82)

From Fig. 18, using the cosine law, the distances ϵ_{pm}, ϵ_{mq}, ϵ_{pn}, and ϵ_{nq} can be written as

$$\begin{aligned}
\epsilon_{pm}^2 &= [(0.5L_t + 0.5 - p)\delta_T]^2 + R_t^2 - 2(0.5L_t + 0.5 - p)\delta_T R_t \cos\left(\theta_T - \alpha_T^{(m)}\right), && (373)\\
\epsilon_{mq}^2 &= [(0.5L_r + 0.5 - q)\delta_R]^2 + \epsilon_m^2 - 2(0.5L_r + 0.5 - q)\delta_R \epsilon_m \cos\left(\alpha_R^{(m)} - \theta_R\right), && (374)\\
\epsilon_{pn}^2 &= [(0.5L_t + 0.5 - p)\delta_T]^2 + \epsilon_n^2 - 2(0.5L_t + 0.5 - p)\delta_T \epsilon_n \cos\left(\theta_T - \alpha_T^{(n)}\right), && (375)\\
\epsilon_{nq}^2 &= [(0.5L_r + 0.5 - q)\delta_R]^2 + R_r^2 - 2(0.5L_r + 0.5 - q)\delta_R R_r \cos\left(\alpha_R^{(n)} - \theta_R\right). && (376)
\end{aligned}$$

By applying the sine law to the triangles $\triangle O_T S_T^{(m)} O_R$ and $\triangle O_T S_R^{(n)} O_R$, respectively, we obtain following identities

$$\frac{\epsilon_m}{\sin\alpha_T^{(m)}} = \frac{R_t}{\sin\left(\pi - \alpha_R^{(m)}\right)} = \frac{D}{\sin\left(\pi - \alpha_T^{(m)} - \left(\pi - \alpha_R^{(m)}\right)\right)}, \quad (377)$$

$$\frac{R_r}{\sin\alpha_T^{(n)}} = \frac{\epsilon_n}{\sin\left(\pi - \alpha_R^{(n)}\right)} = \frac{D}{\sin\left(\pi - \alpha_T^{(n)} - \left(\pi - \alpha_R^{(n)}\right)\right)}. \quad (378)$$

From Fig. 18, we observe that $\pi - \alpha_R^{(m)} \leq \arcsin(R_t/D)$ and $\alpha_T^{(n)} \leq \arcsin(R_r/D)$. Based on the assumption $\min\{R_t, R_r\} \ll D$, we can conclude that $\arcsin(R_t/D) \approx R_t/D = \Delta_T$ and $\arcsin(R_r/D) \approx R_r/D = \Delta_R$, and consequently $\pi - \alpha_R^{(m)}$ and $\alpha_T^{(n)}$ are small angles. From (377) and (378), using approximations $\sin x \approx x$, $\cos x \approx 1$, and $\sqrt{1+x} \approx 1 + x/2$, for small x, the distances ϵ_{pm}, ϵ_{mq}, ϵ_{pn}, and ϵ_{nq} become

$$\epsilon_{pm} \approx R_t - \frac{(L_t + 1 - 2p)\delta_T}{2}\cos(\theta_T - \alpha_T^{(m)}), \quad (379)$$

$$\epsilon_{mq} \approx D - \frac{(L_r + 1 - 2q)\delta_R}{2}[\Delta_T \sin\theta_R \sin\alpha_T^{(m)} - \cos\theta_R], \quad (380)$$

$$\epsilon_{pn} \approx D - \frac{(L_t + 1 - 2p)\delta_T}{2}[\Delta_R \sin\theta_T \sin\alpha_R^{(n)} + \cos\theta_T], \quad (381)$$

$$\epsilon_{nq} \approx R_r - \frac{(L_r + 1 - 2q)\delta_R}{2}\cos(\alpha_R^{(n)} - \theta_R). \quad (382)$$

From Fig. 18, by applying the sine law to the triangle $\triangle S_T^{(m)} S_R^{(n)} O_R$, we obtain the following identity

$$\frac{R_r}{\sin\chi} = \frac{\epsilon_{mn}}{\sin\left(\alpha_R^{(m)} - \alpha_R^{(n)}\right)} = \frac{\epsilon_m}{\sin\left(\pi - \chi - \left(\alpha_R^{(m)} - \alpha_R^{(n)}\right)\right)}. \tag{383}$$

From (383), using approximation $\sin x \approx x$ for small x, the distance ϵ_{mn} can be written as

$$\epsilon_{mn} = \epsilon_m \frac{\sin\left(\alpha_R^{(m)} - \alpha_R^{(n)}\right)}{\sin\left(\chi + \left(\alpha_R^{(m)} - \alpha_R^{(n)}\right)\right)} \approx D. \tag{384}$$

From Fig. 19, using the cosine low, the distance ϵ_{pq} can be written as

$$\epsilon_{pq}^2 = \left[(0.5L_r + 0.5 - q)\delta_R\right]^2 + \epsilon^2 - 2(0.5L_r + 0.5 - q)\delta_R \epsilon \cos\left(\alpha_{Rq}^{LoS} - \theta_R\right), \tag{385}$$

where $\epsilon^2 = \left[(0.5L_t + 0.5 - p)\delta_T\right]^2 + D^2 - 2(0.5L_t + 0.5 - p)\delta_T D \cos\theta_T$. Using the approximation $\sqrt{1+x} \approx 1 + x/2$, the distance ϵ_{pq} becomes

$$\epsilon_{pq} \approx D - (0.5L_t + 0.5 - p)\,\delta_T \cos\theta_T - (0.5L_r + 0.5 - q)\,\delta_R \cos\left(\alpha_{Rq}^{LoS} - \theta_R\right). \tag{386}$$

APPENDIX E

DERIVATIONS OF THE SPACE-TIME CORRELATION FUNCTIONS FOR THE I AND Q COMPONENTS OF THE 2-D REFERENCE MODEL

Derivation of the space-time correlation function of the in-phase component is presented below

$$
\begin{aligned}
&R^{(I,I)}_{pq,\tilde{p}\tilde{q}}(\delta_T, \delta_R, \tau) = \mathrm{E}\left[h^{(I)}_{pq}(t) h^{(I)}_{\tilde{p}\tilde{q}}(t+\tau)\right] / \sqrt{\mathrm{E}[|h^{(I)}_{pq}(t)|^2]\mathrm{E}[|h^{(I)}_{\tilde{p}\tilde{q}}(t)|^2]} = \qquad (387)\\
&\frac{\eta_T}{2\pi}\int_{-\pi}^{\pi} \cos\left[\frac{2\pi}{\lambda}(\tilde{p}-p)\delta_T \cos(\theta_T - \alpha_T) + \frac{2\pi}{\lambda}(\tilde{q}-q)\delta_R\left(\Delta_T \sin\theta_R \sin\alpha_T - \cos\theta_R\right)\right.\\
&\left. - 2\pi\tau f_{T\max}\cos(\alpha_T - \gamma_T) - 2\pi\tau f_{R\max}\left(\Delta_T \sin\gamma_R \sin\alpha_T - \cos\gamma_R\right)\right] d\alpha_T\\
&+ \frac{\eta_R}{2\pi}\int_{-\pi}^{\pi} \cos\left[\frac{2\pi}{\lambda}(\tilde{q}-q)\delta_R \cos(\alpha_R - \theta_R) + \frac{2\pi}{\lambda}(\tilde{p}-p)\delta_T\left(\Delta_R \sin\theta_T \sin\alpha_R + \cos\theta_T\right)\right.\\
&\left. - j2\pi\tau f_{T\max}\left(\Delta_R \sin\gamma_T \sin\alpha_R + \cos\gamma_T\right) - 2\pi\tau f_{R\max}\cos(\alpha_R - \gamma_R)\right] d\alpha_R\\
&+ \frac{\eta_{TR}}{2\pi}\int_{-\pi}^{\pi} \cos\left\{\frac{2\pi}{\lambda}(\tilde{p}-p)\delta_T \cos(\alpha_T - \theta_T) - 2\pi\tau f_{T\max}\cos(\alpha_T - \gamma_T)\right\} d\alpha_T\\
&\times \frac{1}{2\pi}\int_{-\pi}^{\pi} \cos\left\{\frac{2\pi}{\lambda}(\tilde{q}-q)\delta_R \cos(\alpha_R - \theta_R) - 2\pi\tau f_{R\max}\cos(\alpha_R - \gamma_R)\right\} d\alpha_R\\
&+ \sqrt{K_{pq}K_{\tilde{p}\tilde{q}}}\cos\left[\frac{2\pi}{\lambda}\delta_T \cos\theta_T - \frac{2\pi}{\lambda}\delta_R \cos\theta_R - 2\pi\tau f_{T\max}\cos\gamma_T + 2\pi\tau f_{R\max}\cos\gamma_R\right].
\end{aligned}
$$

Using the trigonometric equality $\cos(x-y)=\cos(x)\cos(y)+\sin(x)\sin(y)$, equation (387) can be rewritten as

$$
\begin{aligned}
&R^{(I,I)}_{pq,\tilde{p}\tilde{q}}(\delta_T,\delta_R,\tau)= \\
&\int_{-\pi}^{\pi}\frac{\eta_T\cos\{x_{iSBT}\cos\alpha_T+y_{iSBT}\sin\alpha_T\}d\alpha_T}{2\pi}+\int_{-\pi}^{\pi}\frac{\eta_R\cos\{x_{iSBR}\cos\alpha_R+y_{iSBR}\sin\alpha_R\}d\alpha_R}{2\pi} \\
&+\eta_{TR}\int_{-\pi}^{\pi}\frac{\cos\{x_{iDB}\cos\alpha_T+y_{iDB}\sin\alpha_T\}d\alpha_T}{2\pi}\int_{-\pi}^{\pi}\frac{\cos\{z_{iDB}\cos\alpha_R+w_{iDB}\sin\alpha_R\}d\alpha_R}{2\pi} \\
&+\sqrt{K_{pq}K_{p'q'}}\cos\left[\frac{2\pi}{\lambda}\delta_T\cos\theta_T-\frac{2\pi}{\lambda}\delta_R\cos\theta_R-2\pi\tau f_{T\max}\cos\gamma_T+2\pi\tau f_{R\max}\cos\gamma_R\right],
\end{aligned}
$$

where parameters x_{iSBT}, y_{iSBT}, x_{iSBR}, y_{iSBR}, x_{iDB}, y_{iDB}, z_{iDB}, and w_{iDB} are defined below (108). Finally, using the equality [63, eq. 3.032-2]

$$\int_{-\pi}^{\pi}\cos\left(a\cos x+b\sin x\right)dx=2\int_{0}^{\pi}\cos\left(\sqrt{a^2+b^2}\cos x\right)dx, \tag{388}$$

the space-time correlation function of the in-phase component becomes expression in (107). Similarly can be shown that the space-time correlation function of the quadrature component is as in (107).

The space-time correlation function of the I and Q component can be obtained by substituting (87) and (88) into (89), assuming 2-D isotropic scattering, integrating, and using the equality [63, eq. 3.032-2]

$$\int_{-\pi}^{\pi}\sin\left(a\cos x+b\sin x\right)dx=2\int_{0}^{\pi}\sin\left(\sqrt{a^2+b^2}\cos x\right)dx. \tag{389}$$

The final result is

$$
\begin{aligned}
&R^{(Q,I)}_{pq,p'q'}(\delta_T,\delta_R,\tau)= \\
&\sqrt{K_{pq}K_{\tilde{p}\tilde{q}}}\sin\left[\frac{2\pi}{\lambda}\delta_T\cos\theta_T-\frac{2\pi}{\lambda}\delta_R\cos\theta_R-2\pi\tau f_{T\max}\cos\gamma_T+2\pi\tau f_{R\max}\cos\gamma_R\right].
\end{aligned}
\tag{390}
$$

APPENDIX F

DERIVATIONS OF EQUATIONS (125) - (129)

To derive expressions for the distances $\epsilon_{p,m}$, $\epsilon_{\tilde{p},m}$, $\epsilon_{n,q}$, $\epsilon_{\tilde{n},q}$, and $\epsilon_{m,n}$, we use the law of cosines, assume that $\max\{d_T(p,\tilde{p}), d_R(q,\tilde{q})\} \ll \min\{R_t, R_r\} \ll D$, and denote the distance between two points a and b as $d(a,b)$. From Fig. 29, the distance $\epsilon_{p,m}$ can be written as

$$\epsilon_{p,m}^2 \;=\; d\left(A_T^{(p)'}, S_T^{(m)'}\right)^2 + \left[d\left(S_T^{(m)}, S_T^{(m)'}\right) - d\left(A_T^{(p)}, A_T^{(p)'}\right)\right]^2. \tag{391}$$

By observing the triangle $\triangle A_T^{(p)'} O_T S_T^{(m)'}$, the distance $d(A_T^{(p)'}, S_T^{(m)'})$ can be approximated as

$$\left(A_T^{(p)'}, S_T^{(m)'}\right) \approx d\left(S_T^{(m)}, O_T\right) \cos\beta_T^{(m)} - d\left(A_T^{(p)}, O_T\right) \cos\psi_T^{(p)} \cos\left(\alpha_T^{(m)} - \theta_T^{(p)}\right). \tag{392}$$

Similarly, the distances $d(S_T^{(m)}, S_T^{(m)'})$ and $d(A_T^{(p)}, A_T^{(p)'})$ are equal to $d(S_T^{(m)}, O_T)\sin\beta_T^{(m)}$ and $d(A_T^{(p)}, O_T)\sin\psi_T^{(p)}$, respectively. Using approximations $\sqrt{1+x} \approx 1 + x/2$, $R_t \approx d(S_T^{(m)}, O_T)$ for $|\beta_T^{(m)}| \leq 20°$, and the inequality $2d(A_T^{(p)}, O_T) \ll d(S_T^{(m)}, O_T)\cos\beta_T^{(m)}$, the distance $\epsilon_{p,m}$ can be approximated by

$$\begin{aligned} \epsilon_{p,m} \;&\approx\; \frac{R_t}{\cos\beta_T^{(m)}} - d(A_T^{(p)}, O_T)\sin\psi_T^{(p)}\sin\beta_T^{(m)} - d(A_T^{(p)}, O_T)\cos\theta_T^{(p)}\cos\psi_T^{(p)} \\ &\times\; \cos\alpha_T^{(m)}\cos\beta_T^{(m)} - d(A_T^{(p)}, O_T)\sin\theta_T^{(p)}\cos\psi_T^{(p)}\sin\alpha_T^{(m)}\cos\beta_T^{(m)}, \end{aligned} \tag{393}$$

Using similar reasoning, the distances $\epsilon_{\tilde{p},m}$, $\epsilon_{n,q}$, $\epsilon_{\tilde{n},q}$, and $\epsilon_{m,n}$ can be approximated by

$$\begin{aligned} \epsilon_{\tilde{p},m} \;&\approx\; \frac{R_t}{\cos\beta_T^{(m)}} - d(A_T^{(\tilde{p})}, O_T)\sin\psi_T^{(\tilde{p})}\sin\beta_T^{(m)} - d(A_T^{(\tilde{p})}, O_T)\cos\theta_T^{(\tilde{p})}\cos\psi_T^{(\tilde{p})} \\ &\times\; \cos\alpha_T^{(m)}\cos\beta_T^{(m)} - d(A_T^{(\tilde{p})}, O_T)\sin\theta_T^{(\tilde{p})}\cos\psi_T^{(\tilde{p})}\sin\alpha_T^{(m)}\cos\beta_T^{(m)}, \end{aligned} \tag{394}$$

$$\begin{aligned}\epsilon_{n,q} &\approx \frac{R_r}{\cos\beta_R^{(n)}} - d(A_R^{(q)}, O_R)\sin\psi_R^{(q)}\sin\beta_R^{(n)} - d(A_R^{(q)}, O_R)\cos\theta_R^{(q)}\cos\psi_R^{(q)} \\ &\times \cos\alpha_R^{(n)}\cos\beta_R^{(n)} - d(A_R^{(q)}, O_R)\sin\theta_R^{(q)}\cos\psi_R^{(q)}\sin\alpha_R^{(n)}\cos\beta_R^{(n)}, \end{aligned} \tag{395}$$

$$\begin{aligned}\epsilon_{n,\tilde{q}} &\approx \frac{R_r}{\cos\beta_R^{(n)}} - d(A_R^{(\tilde{q})}, O_R)\sin\psi_R^{(\tilde{q})}\sin\beta_R^{(n)} - d(A_R^{(\tilde{q})}, O_R)\cos\theta_R^{(\tilde{q})}\cos\psi_R^{(\tilde{q})} \\ &\times \cos\alpha_R^{(n)}\cos\beta_R^{(n)} - d(A_R^{(\tilde{q})}, O_R)\sin\theta_R^{(\tilde{q})}\cos\psi_R^{(\tilde{q})}\sin\alpha_R^{(n)}\cos\beta_R^{(n)}, \end{aligned} \tag{396}$$

From Fig. 29, the distance $\epsilon_{m,n}$ can be written as

$$\epsilon_{m,n}^2 = d\left(S_T^{(m)'}, S_R^{(n)'}\right)^2 + \left[d\left(S_T^{(m)}, S_T^{(m)'}\right) - d\left(S_R^{(n)}, S_R^{(n)'}\right)\right]^2. \tag{397}$$

Observing triangles $\triangle A_T^{(p)'} A_T^{(\tilde{p})'} S_T^{(m)'}$ and $\triangle A_R^{(q)'} A_R^{(\tilde{q})'} S_R^{(n)'}$, the distance $d(S_T^{(m)'}, S_R^{(n)'})$ is equal to $d(S_T^{(m)'}, S_R^{(n)'}) = D - R_t\cos\alpha_T^{(m)} + R_r\cos\alpha_R^{(n)} \approx D$. Similarly, observing triangles $\triangle S_T^{(m)} S_T^{(m)'} O_T$ and $\triangle S_R^{(n)} S_R^{(n)'} O_R$, the distances $d(S_T^{(m)}, S_T^{(m)'})$ and $d(S_R^{(n)}, S_R^{(n)'})$ can be written, respectively, as

$$d\left(S_T^{(m)}, S_T^{(m)'}\right) = h_T + R_t\tan\beta_T^{(m)}, \tag{398}$$

$$d\left(S_R^{(n)}, S_R^{(n)'}\right) = h_R + R_r\tan\beta_R^{(n)}. \tag{399}$$

Since $\max\{d_T(p,\tilde{p}), d_R(q,\tilde{q})\} \ll \min\{R_t, R_r\} \ll D$, the distance $\epsilon_{m,n}$ can be approximated by

$$\epsilon_{m,n} \approx \sqrt{D^2 + (h_T - h_R)^2}. \qquad \square \tag{400}$$

APPENDIX G

DERIVATIONS OF THE SPACE-TIME CORRELATION FUNCTIONS OF THE 3-D MIMO M-TO-M SIMULATION MODELS

The outline for derivation of the space-time correlation function of the deterministic simulation model is presented below

$$\begin{aligned}
R_{pq,\tilde{p}\tilde{q}}[\tau] \approx & \qquad\qquad\qquad\qquad\qquad\qquad\qquad\qquad\qquad\qquad\qquad\qquad\qquad\qquad\qquad\qquad\qquad\qquad (401) \\
& \lim_{M_A \to \infty} \frac{1}{M_A} \sum_{m=1}^{M_A} e^{j\frac{2\pi}{\lambda}(d_{T_x}^{(p,\tilde{p})} \cos\alpha_T^{(m)} + d_{T_y}^{(p,\tilde{p})} \sin\alpha_T^{(m)}) - j2\pi\tau f_{T\max}\cos(\alpha_T^{(m)} - \gamma_T)} \\
\times & \lim_{N_A \to \infty} \frac{1}{N_A} \sum_{n=1}^{N_A} e^{j\frac{2\pi}{\lambda}(d_{R_x}^{(q,\tilde{q})} \cos\alpha_R^{(n)} + d_{R_y}^{(q,\tilde{q})} \sin\alpha_R^{(n)}) - j2\pi\tau f_{R\max}\cos(\alpha_R^{(n)} - \gamma_R)} \\
\times & \lim_{M_E \to \infty} \frac{1}{M_E} \sum_{i=1}^{M_E} e^{j\frac{2\pi}{\lambda} d_{T_z}^{(p,\tilde{p})} \sin\beta_T^{(i)}} \lim_{N_E \to \infty} \frac{1}{N_E} \sum_{k=1}^{N_E} e^{j\frac{2\pi}{\lambda} d_{R_z}^{(q,\tilde{q})} \sin\beta_R^{(k)}} \\
= & \int_{-\pi}^{\pi} e^{-j2\pi\tau f_{R\max}\cos(\alpha_R - \gamma_R) + j\frac{2\pi}{\lambda}(d_{R_x}^{(q,\tilde{q})}\cos\alpha_R + d_{R_y}^{(q,\tilde{q})}\sin\alpha_R)} f(\alpha_R) d\alpha_R \\
\times & \int_{-\pi}^{\pi} e^{-j2\pi\tau f_{T\max}\cos(\alpha_T - \gamma_T) + j\frac{2\pi}{\lambda}(d_{T_x}^{(p,\tilde{p})}\cos\alpha_T + d_{T_y}^{(p,\tilde{p})}\sin\alpha_T)} f(\alpha_T) d\alpha_T \\
\times & \int_{-\beta_{T_m}}^{\beta_{T_m}} e^{j\frac{2\pi}{\lambda} d_{T_z}^{(p,\tilde{p})} \sin\beta_T} f(\beta_T) d\beta_T \int_{-\beta_{R_m}}^{\beta_{R_m}} e^{j\frac{2\pi}{\lambda} d_{R_z}^{(q,\tilde{q})} \sin\beta_R} f(\beta_R) d\beta_R,
\end{aligned}$$

where pdfs $f(\alpha_T)$, $f(\alpha_R)$, $f(\beta_T)$, and $f(\beta_R)$ are defined in (96) and (152), respectively. Using trigonometric transformations and the equality [63, eq. 3.338-4], the space-time correlation function becomes

$$\begin{aligned}
R_{pq,\tilde{p}\tilde{q}}[\tau] = & \; R_{p,\tilde{p}}^{T}[\tau]\, R_{q,\tilde{q}}^{R}[\tau] \qquad\qquad\qquad\qquad\qquad\qquad\qquad\qquad\qquad\qquad\qquad\qquad (402) \\
\approx & \; \frac{I_0\!\left(\sqrt{x_1^2 + y_1^2}\right) \cos\left(\frac{2\pi}{\lambda}\beta_{T_m} d_{T_z}^{(p,\tilde{p})}\right)}{I_0(k_T)\left[1 - \left(\frac{4\beta_{T_m} d_{T_z}^{(p,\tilde{p})}}{\lambda}\right)^2\right]} \frac{I_0\!\left(\sqrt{w_1^2 + z_1^2}\right) \cos\left(\frac{2\pi}{\lambda}\beta_{R_m} d_{R_z}^{(q,\tilde{q})}\right)}{I_0(k_R)\left[1 - \left(\frac{4\beta_{R_m} d_{R_z}^{(q,\tilde{q})}}{\lambda}\right)^2\right]},
\end{aligned}$$

where parameters x_1, y_1, z_1, and w_1 are defined in (155) - (158). Similarly, the space-time correlation function of the statistical simulation model has the form in (402).

APPENDIX H

ANGLES OF ARRIVAL AND ANGLES OF DEPARTURE FOR SINGLE-BOUNCED RAYS

Applying the sine law to the triangles $\triangle O'_T S_T^{(m,l)''} O'_R$ and $\triangle O'_T S_R^{(n,k)''} O'_R$ in Fig. 43, respectively, we obtain following identities

$$\frac{D}{\sin\left(\pi - \alpha_T^{(m,l)} - \left(\pi - \alpha_R^{(m,l)}\right)\right)} = \frac{R_t^{(l)}}{\sin\left(\pi - \alpha_R^{(m,l)}\right)}, \tag{403}$$

$$\frac{D}{\sin\left(\pi - \alpha_T^{(n,k)} - \left(\pi - \alpha_R^{(n,k)}\right)\right)} = \frac{R_r^{(k)}}{\sin \alpha_T^{(n,k)}}. \tag{404}$$

From Fig. 43, we observe that $\pi - \alpha_R^{(m,l)} \leq \arcsin(R_t^{(l)}/D)$ and $\alpha_T^{(n,k)} \leq \arcsin(R_r^{(k)}/D)$. Based on the assumption $\min\{R_{t2}, R_{r2}\} \ll D$, we conclude that $\arcsin(R_t^{(l)}/D) \approx R_t^{(l)}/D = \Delta_T^{(l)}$ and $\arcsin(R_r^{(k)}/D) \approx R_r^{(k)}/D = \Delta_R^{(k)}$, and consequently $\pi - \alpha_R^{(m,l)}$ and $\alpha_T^{(n,k)}$ are small angles. Using (403) and (404), and the approximations $\sin x \approx x$ and $\cos x \approx 1$ for small x, we derive the following approximations for the azimuth angles of arrival and departure, respectively,

$$\alpha_R^{(m,l)} \approx \pi - \Delta_T^{(l)} \sin \alpha_T^{(m,l)}, \tag{405}$$

$$\alpha_T^{(n,k)} \approx \Delta_R^{(k)} \sin \alpha_R^{(n,k)}. \tag{406}$$

Furthermore, using (405) and (406), we obtain the following approximations

$$\cos\left(\alpha_R^{(m,l)} - \gamma_R\right) \approx -\cos\gamma_R + \Delta_T^{(l)} \sin\gamma_R \sin\alpha_T^{(m,l)}, \tag{407}$$

$$\cos\left(\alpha_T^{(n,k)} - \gamma_T\right) \approx \cos\gamma_T + \Delta_R \sin\gamma_T \sin\alpha_R^{(n,k)}. \tag{408}$$

Finally, observing Fig. 43, we obtain the following identities

$$R_r^{(k)} \tan\beta_R^{(n,k)} - \Delta_H = (D + R_r^{(k)}) \tan\beta_T^{(n,k)}, \tag{409}$$

$$R_t^{(l)} \tan\beta_T^{(m,l)} + \Delta_H = (D - R_t^{(l)}) \tan\left(\pi - \beta_R^{(m,l)}\right), \tag{410}$$

where $\Delta_H = h_p - h_q$. Using (409) and (410), the assumption $\min\{R_{t2}, R_{r2}\} \ll D$, and approximations $\sin x \approx x$ and $\cos x \approx 1$ for small x, we derive the following approximations for the elevation angles of arrival and departure, respectively,

$$\beta_R^{(m,l)} \approx \pi - \left(\Delta_T^{(l)} \beta_T^{(m,l)} + \Delta_H / D\right), \tag{411}$$

$$\beta_T^{(n,k)} \approx \Delta_R^{(k)} \beta_R^{(n,k)} - \Delta_H / D. \tag{412}$$

APPENDIX I

DERIVATIONS OF EQUATIONS (197) - (202)

To derive expressions for the distances $\epsilon_{p,m,l}$, $\epsilon_{m,l,q}$, $\epsilon_{p,n,k}$, $\epsilon_{n,k,q}$, $\epsilon_{m,l,n,k}$, and $\epsilon_{p,q}$, we use the cosine law, assume that $\max\{d_T, d_R\} \ll \min\{R_{t1}, R_{r1}\} < \min\{R_{t2}, R_{r2}\} \ll D$, and denote the distance between two points a and b as $d(a,b)$. From Fig. 43, the distance $\epsilon_{p,m,l}$ can be written as

$$\epsilon_{p,m,l}^2 = d\left(A_T^{(p)'}, S_T^{(m,l)'}\right)^2 + \left[d\left(S_T^{(m,l)}, S_T^{(m,l)'}\right) - d\left(A_T^{(p)}, A_T^{(p)'}\right)\right]^2. \quad (413)$$

By using the inequality $d_T \ll R_t^{(l)}$, the distance $\epsilon_{p,m,l}$ can be approximated as

$$\begin{aligned} \epsilon_{p,m,l}^2 \approx\ & \frac{R_t^{(l)}}{\cos^2 \beta_T^{(m,l)}} \\ & - R_t^{(l)} \left(L_t + 1 - 2p\right) \left[d_{Tx} \cos \alpha_T^{(m,l)} + d_{Ty} \sin \alpha_T^{(m,l)} + d_{Tz} \tan \beta_T^{(m,l)}\right], \end{aligned} \quad (414)$$

where $d_{Tx} = d_T \cos \psi_T \cos \theta_T$, $d_{Ty} = d_T \cos \psi_T \sin \theta_T$, and $d_{Tz} = d_T \sin \psi_T$. Using approximations $\sqrt{1+x} \approx 1 + x/2$ and $R_t^{(l)} \approx d(S_T^{(m)}, O_T')$ for $|\beta_T^{(m)}| \leq 20°$, the distance $\epsilon_{p,m,l}$ becomes

$$\begin{aligned} \epsilon_{p,m,l} \approx\ & R_t^{(l)} - \frac{L_t + 1 - 2p}{2} \\ & \times \left[d_{Tx} \cos \alpha_T^{(m,l)} \cos \beta_T^{(m,l)} + d_{Ty} \sin \alpha_T^{(m,l)} \cos \beta_T^{(m,l)} + d_{Tz} \sin \beta_T^{(m,l)}\right]. \end{aligned} \quad (415)$$

Using similar reasoning, the distances $\epsilon_{m,l,q}$, $\epsilon_{p,n,k}$, $\epsilon_{n,k,q}$, $\epsilon_{m,l,n,k}$, and $\epsilon_{p,q}$ can be approximated as in (198) - (202).

APPENDIX J

THE CLOSED-FORM STF-CFS OF THE SBT, SBR AND DB COMPONENTS

After replacing (186), (187), and (191) with (233) - (235), respectively, calculating the new single-bounced transmit, single-bounced receive and double-bounced components of the time-variant transfer function, using trigonometric transformations, the equality $\int_{-\pi}^{\pi} \exp\{a\sin(c) + b\cos(c)\}dc = 2\pi I_0\left(\sqrt{a^2+b^2}\right)$ [63, eq. 3.338-4], and the results in Chapter 6, the closed-form STF-CFs of the single-bounced transmit, single-bounced receive, and double-bounced components can be written as

$$\begin{aligned}
R_{pq,\tilde{p}\tilde{q}}^{SBT}(\Delta t)R_{pq,\tilde{p}\tilde{q}}^{SBT}(\Delta f) &= \frac{\eta_T}{I_0(k_T)}\frac{\cos\left(\frac{2\pi}{\lambda}\beta_{Tm}(p-\tilde{p})d_{Tz}\right)}{1-\left(\frac{4\beta_{Tm}(p-\tilde{p})d_{Tz}}{\lambda}\right)^2} I_{SBT}e^{-j\frac{2\pi}{\lambda}(q-\tilde{q})d_{Rx}} \qquad (416)\\
&\times \; e^{-j2\pi\Delta t f_{R\max}\cos\gamma_R}\frac{e^{-j\frac{2\pi}{c_0}\Delta f D}}{R_{t2}^2-R_{t1}^2} I_0\left(\sqrt{x_{SBT1}^2+y_{SBT1}^2}\right),\\
R_{pq,\tilde{p}\tilde{q}}^{SBR}(\Delta t)R_{pq,\tilde{p}\tilde{q}}^{SBR}(\Delta f) &= \frac{\eta_R}{I_0(k_R)}\frac{\cos\left(\frac{2\pi}{\lambda}\beta_{Rm}(q-\tilde{q})d_{Rz}\right)}{1-\left(\frac{4\beta_{Rm}(q-\tilde{q})d_{Rz}}{\lambda}\right)^2} I_{SBR}e^{j\frac{2\pi}{\lambda}(p-\tilde{p})d_{Tx}} \qquad (417)\\
&\times \; e^{j2\pi\Delta t f_{T\max}\cos\gamma_T}\frac{e^{-j\frac{2\pi}{c_0}\Delta f D}}{R_{r2}^2-R_{r1}^2} I_0\left(\sqrt{x_{SBR1}^2+y_{SBR1}^2}\right),\\
R_{pq,\tilde{p}\tilde{q}}^{DB}(\Delta t)R_{pq,\tilde{p}\tilde{q}}^{DB}(\Delta f) &= \frac{\eta_{TR}}{I_0(k_T)I_0(k_R)}\frac{\cos\left(\frac{2\pi}{\lambda}\beta_{Tm}(p-\tilde{p})d_{Tz}\right)}{1-\left(\frac{4\beta_{Tm}(p-\tilde{p})d_{Tz}}{\lambda}\right)^2}\frac{\cos\left(\frac{2\pi}{\lambda}\beta_{Rm}(q-\tilde{q})d_{Rz}\right)}{1-\left(\frac{4\beta_{Rm}(q-\tilde{q})d_{Rz}}{\lambda}\right)^2}\\
&\times \; \frac{e^{-j2\pi\Delta f D/c_0}}{(R_{t2}^2-R_{t1}^2)(R_{r2}^2-R_{r1}^2)} I_0\left(\sqrt{x_{DB1}^2+y_{DB}^2}\right)\\
&\times \; I_0\left(\sqrt{z_{DB1}^2+w_{DB}^2}\right)\left(I_{T1}I_{R2}+I_{T2}I_{R1}\right), \qquad (418)
\end{aligned}$$

where $a = 2\pi\Delta f/c_0$, $c = \gamma/D$, and

$$\begin{aligned}
x_{SBT1} &= j(2\pi/\lambda)(p-\tilde{p})d_{Tx} + j2\pi\Delta t f_{T\max}\cos\gamma_T + k_T\cos\mu_T, \qquad (419)\\
y_{SBT1} &= j2\pi(p-\tilde{p})d_{Ty}/\lambda + j2\pi(q-\tilde{q})d_{Ry}(R_{t1}+0.5(R_{t2}-R_{t1}))/(D\lambda)\\
&+ j2\pi\Delta t f_{T\max}\sin\gamma_T + j2\pi\Delta t f_{R\max}\sin\gamma_R(R_{t1}+0.5(R_{t2}-R_{t1}))/D\\
&+ k_T\sin\mu_T,\\
x_{SBR1} &= j(2\pi/\lambda)(q-\tilde{q})d_{Rx} + j2\pi\Delta t f_{R\max}\cos\gamma_R + k_R\cos\mu_R,\\
y_{SBR1} &= j2\pi(q-\tilde{q})d_{Ry}/\lambda + j2\pi(p-\tilde{p})d_{Ty}(R_{r1}+0.5(R_{r2}-R_{r1}))/(D\lambda)\\
&+ j2\pi\Delta t f_{R\max}\sin\gamma_R + j2\pi\Delta t f_{T\max}\sin\gamma_T(R_{r1}+0.5(R_{r2}-R_{r1}))/D\\
&+ k_R\sin\mu_R,\\
x_{DB1} &= j(2\pi/\lambda)(p-\tilde{p})d_{Tx} + j2\pi\Delta t f_{T\max}\cos\gamma_T + k_T\cos\mu_T,\\
z_{DB1} &= j(2\pi/\lambda)(q-\tilde{q})d_{Rx} + j2\pi\Delta t f_{R\max}\cos\gamma_R + k_R\cos\mu_R,\\
I_{T1} &= \frac{2}{a^2}\left(e^{-jaR_{t2}}(1+jaR_{t2}) - e^{-jaR_{t1}}(1+jaR_{t1})\right),\\
I_{R1} &= \frac{2}{a^2}\left(e^{-jaR_{r2}}(1+jaR_{r2}) - e^{-jaR_{r1}}(1+jaR_{r1})\right),\\
I_{SBT} &= \frac{1}{2a^3}\Bigg[e^{-2jaR_{t2}}\Bigg(jc+2ja^2R_{t2}+a-2caR_{t2}-2jca^2R_{t2}^2\Bigg)\\
&- e^{-2jaR_{t1}}\Bigg(jc+2ja^2R_{t1}+a-2caR_{t1}-2jca^2R_{t1}^2\Bigg)\Bigg],\\
I_{SBR} &= \frac{1}{2a^3}\Bigg[e^{-2jaR_{r2}}\Bigg(jc+2ja^2R_{r2}+a-2caR_{r2}-2jca^2R_{r2}^2\Bigg)\\
&- e^{-2jaR_{r1}}\Bigg(jc+2ja^2R_{r1}+a-2caR_{r1}-2jca^2R_{r1}^2\Bigg)\Bigg],\\
I_{T2} &= \frac{1}{a^3}\Bigg[e^{-jaR_{t2}}\Bigg(2jc+ja^2R_{t2}+a-2caR_{t2}-jca^2R_{t2}^2\Bigg)\\
&- e^{-jaR_{t1}}\Bigg(2jc+ja^2R_{t1}+a-2caR_{t1}-jca^2R_{t1}^2\Bigg)\Bigg],\\
I_{R2} &= \frac{1}{a^3}\Bigg[e^{-jaR_{r2}}\Bigg(2jc+ja^2R_{r2}+a-2caR_{r2}-jca^2R_{r2}^2\Bigg)\\
&- e^{-jaR_{r1}}\Bigg(2jc+ja^2R_{r1}+a-2caR_{r1}-jca^2R_{r1}^2\Bigg)\Bigg].
\end{aligned}$$

APPENDIX K

THE SD-PSDS OF THE SBT, SBR, DB, AND LOS COMPONENTS

The sD-psds of the single-bounced components can be obtained by noting that the functions $I_0\left(\sqrt{x_{SBT}^2+y_{SBT}^2}\right)$ and $I_0\left(\sqrt{x_{SBR}^2+y_{SBR}^2}\right)$ can be written as

$$I_0\left[j2\pi f_{T\max}\sqrt{(\Delta t+A_{SBT})^2+\left(\frac{p_{x_{SBT}}\sin\gamma_T}{f_{T\max}}-\frac{p_{y_{SBT}}\cos\gamma_T}{f_{T\max}}-\frac{w_{y_{SBT}}}{2\pi f_{T\max}}\right)^2}\right], \quad (420)$$

$$I_0\left[j2\pi f_{R\max}\sqrt{(\Delta t+A_{SBR})^2+\left(\frac{p_{x_{SBR}}\sin\gamma_R}{f_{R\max}}-\frac{p_{y_{SBR}}\cos\gamma_R}{f_{R\max}}+\frac{w_{y_{SBR}}}{2\pi f_{R\max}}\right)^2}\right], \quad (421)$$

and by using equality $\int_0^\infty J_0(\alpha\sqrt{t^2+u^2})\cos(\beta t)dt = \cos(u\sqrt{\alpha^2-\beta^2})/\sqrt{\alpha^2-\beta^2}$ [63, eq. 6.677-3]. Parameters in equations (420) and (421) are defined as follows:

$$\begin{aligned}
A_{SBT} &= (2\pi p_{x_{SBT}}\cos\gamma_T+2\pi p_{y_{SBT}}\sin\gamma_T-w_{x_{SBT}})/2\pi f_{T\max}, \quad (422)\\
p_{x_{SBT}} &= (p-\tilde{p})d_{Tx}/\lambda,\\
w_{x_{SBT}} &= jk_T\cos(\gamma_T-\mu_T),\\
p_{y_{SBT}} &= [(p-\tilde{p})d_{Ty}+(q-\tilde{q})d_{Ry}(R_{t1}+0.5(R_{t2}-R_{t1}))/D]/\lambda,\\
w_{y_{SBT}} &= jk_T\sin(\gamma_T-\mu_T),\\
A_{SBR} &= (2\pi p_{x_{SBR}}\cos\gamma_R+2\pi p_{y_{SBR}}\sin\gamma_R+w_{x_{SBR}})/2\pi f_{R\max},\\
p_{x_{SBR}} &= (q-\tilde{q})d_{Rx}/\lambda,\\
w_{x_{SBR}} &= -jk_R\cos(\gamma_R-\mu_R),\\
p_{y_{SBR}} &= [(q-\tilde{q})d_{Ry}+(p-\tilde{p})d_{Ty}(R_{r1}+0.5(R_{r2}-R_{r1}))/D]/\lambda,\\
w_{y_{SBR}} &= -jk_R\sin(\gamma_R-\mu_R).
\end{aligned}$$

After extensive calculations, the sD-psds of the single-bounced transmit and the single-bounced receive components can be written as in (237), (238), respectively.

The first step to calculate the sD-psd of the double-bounced component is to note that

$$\begin{aligned}&\mathcal{F}\Big\{I_0\Big(\sqrt{x_{DB}^2+y_{DB}^2}\Big)I_0\Big(\sqrt{z_{DB}^2+w_{DB}^2}\Big)\Big\} = \\ &\qquad \mathcal{F}\Big\{I_0\Big(\sqrt{x_{DB}^2+y_{DB}^2}\Big)\Big\}\odot\mathcal{F}\Big\{I_0\Big(\sqrt{z_{DB}^2+w_{DB}^2}\Big)\Big\}\end{aligned} \tag{423}$$

where $\odot$ denotes convolution. Then,noting that the functions $I_0\left(\sqrt{x_{DB}^2+y_{DB}^2}\right)$ and $I_0\left(\sqrt{z_{DB}^2+w_{DB}^2}\right)$ can be written as

$$I_0\left[j2\pi f_{T\max}\sqrt{(\Delta t+A_{DB1})^2+\left(\frac{p_{x_{DB}}\sin\gamma_T}{f_{T\max}}-\frac{p_{y_{DB}}\cos\gamma_T}{f_{T\max}}+\frac{v_{y_{DB}}}{2\pi f_{T\max}}\right)^2}\,\right], \tag{424}$$

$$I_0\left[j2\pi f_{R\max}\sqrt{(\Delta t+A_{DB2})^2+\left(\frac{p_{z_{DB}}\sin\gamma_R}{f_{R\max}}-\frac{p_{w_{DB}}\cos\gamma_R}{f_{R\max}}+\frac{v_{w_{DB}}}{2\pi f_{R\max}}\right)^2}\,\right], \tag{425}$$

where

$$\begin{aligned}
A_{DB1} &= (2\pi p_{x_{DB}}\cos\gamma_T+2\pi p_{y_{DB}}\sin\gamma_T+v_{x_{DB}})/2\pi f_{T\max}, \qquad (426)\\
p_{x_{DB}} &= (p-\tilde{p})d_{Tx}/\lambda,\\
v_{x_{DB}} &= -jk_T\cos(\gamma_T-\mu_T),\\
p_{y_{DB}} &= (p-\tilde{p})d_{Ty}/\lambda,\\
v_{y_{DB}} &= -jk_T\sin(\gamma_T-\mu_T),\\
A_{DB2} &= (2\pi p_{z_{DB}}\cos\gamma_R+2\pi p_{w_{DB}}\sin\gamma_R+v_{z_{DB}})/2\pi f_{R\max},\\
p_{z_{DB}} &= (q-\tilde{q})d_{Rx}/\lambda,\\
v_{z_{DB}} &= -jk_R\cos(\gamma_R-\mu_R),\\
p_{w_{DB}} &= (q-\tilde{q})d_{Ry}/\lambda,\\
v_{w_{DB}} &= -jk_R\sin(\gamma_R-\mu_R),
\end{aligned}$$

and using the equality [63, eq. 6.677-3], we obtain the sD-psds of the double-bounced component in (239).

Finally, calculating the Fourier transform of the space-time correlation function in (232), we obtain the sD-psd of the LoS component in (240).

APPENDIX L

THE PSDS OF THE SBT, SBR, DB, AND LOS COMPONENTS

We start the derivation for the psds of the single-bounced components by noting that the functions $I_0\left(\sqrt{x_{SBT}^2 + y_{SBT}^2}\right)$ and $I_0\left(\sqrt{x_{SBR}^2 + y_{SBR}^2}\right)$ can be written as

$$I_0\left(j\pi\frac{2R_t}{c_0}\sqrt{\left(\Delta f - B_{SBT}\right)^2 + \left(\frac{C_{SBT}c_0}{2R_t\pi}\right)^2}\right), \tag{427}$$

$$I_0\left(j\pi\frac{2R_r}{c_0}\sqrt{\left(\Delta f - B_{SBR}\right)^2 + \left(\frac{C_{SBR}c_0}{2R_r\pi}\right)^2}\right), \tag{428}$$

respectively, where

$$B_{SBT} = (2\pi(p-\tilde{p})d_{Tx}/\lambda - jk_T\cos\mu_T)c_0/(2R_t\pi), \tag{429}$$

$$C_{SBT} = 2\pi(p-\tilde{p})d_{Ty}/\lambda + 2\pi(q-\tilde{q})d_{Ry}(R_{t1} + 0.5(R_{t2} - R_{t1}))/(D\lambda) - jk_T\sin\mu_T,$$

$$B_{SBR} = (2\pi(q-\tilde{q})d_{Rx}/\lambda - jk_R\cos\mu_R)c_0/(2R_r\pi),$$

$$C_{SBR} = 2\pi(q-\tilde{q})d_{Ry}/\lambda + 2\pi(q-\tilde{q})d_{Ty}(R_{r1} + 0.5(R_{r2} - R_{r1}))/(D\lambda) - jk_R\sin\mu_R.$$

Using the equality [63, eq. 6.677-3] and after extensive calculations, the psds of the single-bounced components can be written as in (241), (242), respectively.

Using (423), noting that the functions $I_0\left(\sqrt{x_{DB}^2 + y_{DB}^2}\right)$ and $I_0\left(\sqrt{z_{DB}^2 + w_{DB}^2}\right)$ can be written as

$$I_0\left(j\pi\frac{2R_t}{c_0}\sqrt{\left(\Delta f - B_{DB}\right)^2 + \left(\frac{C_{DB}c_0}{2R_t\pi}\right)^2}\right), \tag{430}$$

$$I_0\left(j\pi\frac{2R_r}{c_0}\sqrt{\left(\Delta f - D_{DB}\right)^2 + \left(\frac{E_{DB}c_0}{2R_r\pi}\right)^2}\right), \tag{431}$$

respectively, where

$$\begin{aligned} B_{DB} &= (2\pi(p-\tilde{p})d_{Tx}/\lambda - jk_T\cos\mu_T)c_0/(2R_t\pi), \qquad (432)\\ C_{DB} &= 2\pi(p-\tilde{p})d_{Ty}/\lambda - jk_T\sin\mu_T,\\ D_{DB} &= (2\pi(q-\tilde{q})d_{Rx}/\lambda - jk_R\cos\mu_R)c_0/(2R_r\pi),\\ E_{DB} &= 2\pi(q-\tilde{q})d_{Ry}/\lambda - jk_R\sin\mu_R, \end{aligned}$$

and using the equality [63, eq. 6.677-3], we obtain the psds of the double-bounced component in (243).

Finally, calculating the inverse Fourier transform of the space-frequency correlation function in (232), we obtain the psds of the LoS component in (244).

APPENDIX M

DERIVATIONS OF EQUATIONS (277) - (279)

The derivation of parameter b_1^{SBT} is as follows:

$$\begin{aligned}
b_1^{SBT} &= 2\pi\ b_0^{SBT} \int_{-\beta_{T_m}}^{\beta_{T_m}} \int_{-\pi}^{\pi} f(\alpha_T) f(\beta_T) \Big[f_{T\max} \cos(\alpha_T - \gamma_T) \cos\beta_T \qquad (433)\\
&+ f_{R\max} \cos\left(\Delta_T \beta_T + \frac{\Delta_H}{D}\right) (\cos\gamma_R - \Delta_T \sin\gamma_R \sin\alpha_T) - f_{LoS} \Big] d\alpha_T d\beta_T \\
&= \frac{b_0^{SBT}}{I_0(k_T)} \frac{\pi}{4\beta_{T_m}} \Bigg[\int_{-\beta_{T_m}}^{\beta_{T_m}} \cos\left(\frac{\pi}{2}\frac{\beta_T}{\beta_{T_m}}\right) \cos\beta_T d\beta_T \int_{-\pi}^{\pi} f_{T\max} \cos(\alpha_T - \gamma_T) \\
&\times\ e^{k_T \cos(\alpha_T - \mu_T)} d\alpha_T + \int_{-\beta_{T_m}}^{\beta_{T_m}} \cos\left(\frac{\pi}{2}\frac{\beta_T}{\beta_{T_m}}\right) \cos\left(\Delta_T\beta_T + \frac{\Delta_H}{D}\right) d\beta_T \\
&\times \int_{-\pi}^{\pi} f_{R\max} \left[\cos\gamma_R - \Delta_T \sin\gamma_R \sin\alpha_T\right] e^{k_T \cos(\alpha_T - \mu_T)} d\alpha_T \Bigg] - 2\pi b_0^{SBT} f_{LoS} \\
&= \frac{b_0^{SBT}\pi^2}{I_0(k_T)} \Bigg[\frac{\cos\beta_{T_m}}{\pi^2 - 4\beta_{T_m}^2} \int_{-\pi}^{\pi} f_{T\max} \cos(\alpha_T - \gamma_T) e^{k_T\cos(\alpha_T - \mu_T)} d\alpha_T \\
&+ \left(\frac{\cos(\Delta_T \beta_{T_m} + \Delta_H/D)}{2(\pi^2 - 4\Delta_T^2\beta_{T_m}^2)} + \frac{\cos(\Delta_T \beta_{T_m} - \Delta_H/D)}{2(\pi^2 - 4\Delta_T^2\beta_{T_m}^2)} \right) \\
&\times \int_{-\pi}^{\pi} f_{R\max} \left[\cos\gamma_R - \Delta_T \sin\gamma_R \sin\alpha_T\right] e^{k_T \cos(\alpha_T - \mu_T)} d\alpha_T \Bigg] - 2\pi b_0^{SBT} f_{LoS}.
\end{aligned}$$

The integral $\int_{-\pi}^{\pi} f_{T\max} \cos(\alpha_T - \gamma_T) e^{k_T \cos(\alpha_T - \mu_T)} d\alpha_T$ can be solved by applying the Euler transformation on the cosine function and by using the equality $\int_{-\pi}^{\pi} e^{-jm\theta + jz\sin\theta} d\theta$ $= 2\pi J_m(z)$ [63, eq. 8.411], where $J_m(\ \cdot\ )$ is the m^{th}-order Bessel function of the first kind, i.e.,

$$\begin{aligned}
&\int_{-\pi}^{\pi} f_{T\max} \cos(\alpha_T - \gamma_T) e^{k_T \cos(\alpha_T - \mu_T)} d\alpha_T = \int_{-\pi}^{\pi} \frac{f_{T\max}}{2} e^{j\gamma_T} \left\{ e^{-j\alpha_T + j\frac{-k_T}{j}\sin(\alpha_T - \mu_T + \pi/2)} \right\} d\alpha_T \\
&+ \int_{-\pi}^{\pi} \frac{f_{T\max}}{2} e^{-j\gamma_T} \left\{ e^{-j(-\alpha_T) + j\frac{-k_T}{j}\sin(\alpha_T - \mu_T + \pi/2)} \right\} d\alpha_T = 2\pi \cos(\mu_T - \gamma_T) I_1(k_T). \qquad (434)
\end{aligned}$$

Using the similar reasoning as above, we obtain the following result

$$\begin{aligned}
&\int_{-\pi}^{\pi} f_{R\max} [\cos\gamma_R - \Delta_T \sin\gamma_R \sin\alpha_T] e^{k_T \cos(\alpha_T - \mu_T)} d\alpha_T = \\
&\qquad = 2\pi f_{R\max} [\cos\gamma_R + \Delta_T \sin\gamma_R \sin\mu_T I_1(k_T)]. \qquad (435)
\end{aligned}$$

Finally, substituting (434) and (435) into (433), we obtain the result in (277).

The parameters b_1^{SBR}, b_1^{DB}, b_2^{SBT}, b_2^{SBR}, and b_2^{DB} in (278) - (279) are similarly obtained.

APPENDIX N

CRAMÉR-RAO LOWER BOUND

This Appendix derives the Cramér-Rao lower bound for the estimator proposed in Section 9.3. The CRLB for each element of the vector $\mathbf{\Theta} = [\Theta_i]_{i=1}^{8} = [\beta_{T_m}, k_T, \mu_T, \beta_{R_m}, k_R, \mu_R, \eta_T, \eta_R]$ can be obtained from the inverse Fisher information matrix. The $(i,j)^{th}$ element of the Fisher information matrix can be written as $[\mathbf{F}(\mathbf{\Theta})]_{i,j} = -\mathrm{E}[\partial^2 \mathcal{L}(\mathbf{\Theta})/\partial\Theta_i\partial\Theta_j]$, where $i, j \in \{1, \ldots, 8\}$. To obtain the elements of the Fisher information matrix, we calculate the first and the second derivative of the log-likelihood function in (287) as follows:

$$\begin{aligned}
\frac{\partial \mathcal{L}(\mathbf{\Theta}_{T,F})}{\partial \Theta_i} &= -N_s \frac{\partial(\mathrm{tr}\{\mathbf{R}(\mathbf{\Theta}_{T,F}, T\Delta t_s, F\Delta f_s)^{-1}\hat{\mathbf{R}}(T\Delta t_s, F\Delta f_s)\})}{\partial\Theta_i} \\
&\quad -N_s \frac{\partial(\ln|\mathbf{R}(\mathbf{\Theta}_{T,F}, T\Delta t_s, F\Delta f_s)|)}{\partial\Theta_i} \\
&= -N_s \mathrm{tr}\Big[\Big[\mathbf{I}_{L_t L_R} - \mathbf{R}(\mathbf{\Theta}_{T,F}, T\Delta t_s, F\Delta f_s)^{-1}\hat{\mathbf{R}}(T\Delta t_s, F\Delta f_s)\Big] \\
&\quad \times \mathbf{R}(\mathbf{\Theta}_{T,F}, T\Delta t_s, F\Delta f_s)^{-1}\mathbf{D}_{\Theta_i}(\mathbf{\Theta}_{T,F}, T\Delta t_s, F\Delta f_s)\Big], \qquad (436)
\end{aligned}$$

$$
\begin{aligned}
\frac{\partial^2 \mathcal{L}(\boldsymbol{\Theta}_{T,F})}{\partial \Theta_i \partial \Theta_j} &= -N_s \mathrm{tr}\Bigg\{ \frac{\partial}{\partial \Theta_j} \Bigg[\Big(\mathbf{I}_{L_t L_R} - \mathbf{R}(\boldsymbol{\Theta}_{T,F}, T\Delta t_s, F\Delta f_s)^{-1} \hat{\mathbf{R}}(T\Delta t_s, F\Delta f_s) \Big) \\
&\times \mathbf{R}(\boldsymbol{\Theta}_{T,F}, T\Delta t_s, F\Delta f_s)^{-1} \mathbf{D}_{\Theta_i}(\boldsymbol{\Theta}_{T,F}, T\Delta t_s, F\Delta f_s) \Bigg] \\
&+ \Big(\mathbf{I}_{L_t L_R} - \mathbf{R}(\boldsymbol{\Theta}_{T,F}, T\Delta t_s, F\Delta f_s)^{-1} \hat{\mathbf{R}}(T\Delta t_s, F\Delta f_s) \Big) \\
&\times \frac{\partial}{\partial \Theta_j} \Big[\mathbf{R}(\boldsymbol{\Theta}_{T,F}, T\Delta t_s, F\Delta f_s)^{-1} \mathbf{D}_{\Theta_i}(\boldsymbol{\Theta}_{T,F}, T\Delta t_s, F\Delta f_s) \Big] \Bigg\} \\
&= -N_s \mathrm{tr}\Big\{ \mathbf{R}(\boldsymbol{\Theta}_{T,F}, T\Delta t_s, F\Delta f_s)^{-1} \mathbf{D}_{\Theta_j}(\boldsymbol{\Theta}_{T,F}, T\Delta t_s, F\Delta f_s) \\
&\times \mathbf{R}(\boldsymbol{\Theta}_{T,F}, T\Delta t_s, F\Delta f_s)^{-1} \hat{\mathbf{R}}(T\Delta t_s, F\Delta f_s) \mathbf{R}(\boldsymbol{\Theta}_{T,F}, T\Delta t_s, F\Delta f_s)^{-1} \\
&\times \mathbf{D}_{\Theta_i}(\boldsymbol{\Theta}_{T,F}, T\Delta t_s, F\Delta f_s) + \Big(\mathbf{I}_{L_t L_R} - \mathbf{R}(\boldsymbol{\Theta}_{T,F}, T\Delta t_s, F\Delta f_s)^{-1} \\
&\times \hat{\mathbf{R}}(T\Delta t_s, F\Delta f_s) \Big) \frac{\partial}{\partial \Theta_j} \Big[\mathbf{R}(\boldsymbol{\Theta}_{T,F}, T\Delta t_s, F\Delta f_s)^{-1} \\
&\times \mathbf{D}_{\Theta_i}(\boldsymbol{\Theta}_{T,F}, T\Delta t_s, F\Delta f_s) \Big] \Big\},
\end{aligned} \tag{437}
$$

where $\mathbf{D}_{\Theta_i}(\boldsymbol{\Theta}_{T,F}, T\Delta t_s, F\Delta f_s) = \partial \mathbf{R}(\boldsymbol{\Theta}_{T,F}, T\Delta t_s, F\Delta f_s)/\partial \Theta_i$, $\mathbf{I}_{L_t L_r}$ is the $L_t L_r \times L_t L_r$ identity matrix, and $\mathbf{D}_{\Theta_j}(\boldsymbol{\Theta}_{T,F}, T\Delta t_s, F\Delta f_s) = \partial \mathbf{R}(\boldsymbol{\Theta}_{T,F}, T\Delta t_s, F\Delta f_s)/\partial \Theta_j$.

By observing that $\mathrm{E}[\hat{\mathbf{R}}(T\Delta t_s, F\Delta f_s)] = \mathbf{R}(\boldsymbol{\Theta}_{T,F}, T\Delta t_s, F\Delta f_s)$, the $(i,j)^{th}$ element of the Fisher information matrix becomes

$$
\begin{aligned}
[\mathbf{F}(\boldsymbol{\Theta})]_{i,j} &= -\mathrm{E}\left[\frac{\partial^2 \mathcal{L}(\boldsymbol{\Theta})}{\partial \Theta_i \partial \Theta_j} \right] = \frac{N_s}{t_{\max} f_{\max}} \sum_{T=0}^{t_{\max}-1} \sum_{F=0}^{f_{\max}-1} \\
&\quad \mathrm{tr}\Big\{ \mathbf{R}(\boldsymbol{\Theta}_{T,F}, T\Delta t_s, F\Delta f_s)^{-1} \mathbf{D}_{\Theta_j}(\boldsymbol{\Theta}_{T,F}, T\Delta t_s, F\Delta f_s) \\
&\quad \times \mathbf{R}(\boldsymbol{\Theta}_{T,F}, T\Delta t_s, F\Delta f_s)^{-1} \mathbf{D}_{\Theta_i}(\boldsymbol{\Theta}_{T,F}, T\Delta t_s, F\Delta f_s) \Big\},
\end{aligned} \tag{438}
$$

where the derivatives $\mathbf{D}_{\Theta_i}(\boldsymbol{\Theta}_{T,F}, T\Delta t_s, F\Delta f_s)$ for $i \in \{1, \ldots, 8\}$ are given by

$$
\begin{aligned}
&[\mathbf{D}_{\Theta_1}(\boldsymbol{\Theta}_{T,F}, T\Delta t_s, F\Delta f_s)]_{q+L_r(p-1),\tilde{q}+L_r(\tilde{p}-1)} \qquad (439)\\
&= \left[\frac{\partial \mathbf{R}(\boldsymbol{\Theta}_{T,F}, T\Delta t_s, F\Delta f_s)}{\partial \beta_{T_m}}\right]_{q+L_r(p-1),\tilde{q}+L_r(\tilde{p}-1)} =\\
&= \frac{\partial R^{SBT}_{pq,\tilde{p}\tilde{q}}(T\Delta t_s, F\Delta f_s)}{\partial \beta_{T_m}} + \frac{\partial R^{DB}_{pq,\tilde{p}\tilde{q}}(T\Delta t_s, F\Delta f_s)}{\partial \beta_{T_m}} = \Bigg\{ \frac{\eta_T}{I_0(k_T)} e^{-j\frac{2\pi}{\lambda}(q-\tilde{q})d_{Rx}}\\
&\times e^{-j2\pi T\Delta t_s f_{R\max}\cos\gamma_R} \int_{R_{t1}}^{R_{t2}} \left(1-\gamma\frac{R_t}{D}\right) e^{-j\frac{2\pi}{c_0}F\Delta f_s(D+R_t)} I_0\left(\sqrt{x^2_{SBT}+y^2_{SBT}}\right)\\
&\times \frac{2R_t}{R^2_{t2}-R^2_{t1}} dR_t + \Bigg[\int_{R_{t1}}^{R_{t2}} 2e^{-j\frac{2\pi}{c_0}F\Delta f_s R_t} R_t I_0\left(\sqrt{x^2_{DB}+y^2_{DB}}\right) dR_t \int_{R_{r1}}^{R_{r2}} e^{-j\frac{2\pi}{c_0}F\Delta f_s R_r} R_r\\
&\times I_0\left(\sqrt{w^2_{DB}+z^2_{DB}}\right)\left(1-\gamma\frac{R_r}{D}\right) dR_r + \int_{R_{r1}}^{R_{r2}} 2e^{-j\frac{2\pi}{c_0}F\Delta f_s R_r} R_r I_0\left(\sqrt{w^2_{DB}+z^2_{DB}}\right) dR_r\\
&\times \int_{R_{t1}}^{R_{t2}} e^{-j\frac{2\pi}{c_0}F\Delta f_s R_t} R_t I_0\left(\sqrt{x^2_{DB}+y^2_{DB}}\right)\left(1-\gamma\frac{R_t}{D}\right) dR_t\Bigg]\\
&\times \frac{\eta_{TR}}{I_0(k_T)I_0(k_R)} \frac{\cos\left(\frac{2\pi}{\lambda}\beta_{Rm}d_{Rz}\right)}{1-\left(\frac{4\beta_{Rm}d_{Rz}}{\lambda}\right)^2} \frac{e^{-j2\pi F\Delta f_s D/c_0}}{(R^2_{t2}-R^2_{t1})(R^2_{r2}-R^2_{r1})}\Bigg\} \left(\frac{2\pi}{\lambda}d_{Tz}\right)\\
&\times \frac{8\cos\left(\frac{2\pi}{\lambda}\beta_{Tm}d_{Tz}\right)\left(\frac{2\pi}{\lambda}\beta_{Tm}d_{Tz}\right) + 4\left(\frac{2\pi}{\lambda}\beta_{Tm}d_{Tz}\right)^2 \sin\left(\frac{2\pi}{\lambda}\beta_{Tm}d_{Tz}\right) - \sin\left(\frac{2\pi}{\lambda}\beta_{Tm}d_{Tz}\right)}{1-8\left(\frac{2\pi}{\lambda}\beta_{Tm}d_{Tz}\right)^2 + 16\left(\frac{2\pi}{\lambda}\beta_{Tm}d_{Tz}\right)^4},
\end{aligned}
$$

$$
\begin{aligned}
&[\mathbf{D}_{\Theta_2}(\boldsymbol{\Theta}_{T,F}, T\Delta t_s, F\Delta f_s)]_{q+L_r(p-1),\tilde{q}+L_r(\tilde{p}-1)} \qquad (440)\\
&= \frac{\partial R^{SBT}_{pq,\tilde{p}\tilde{q}}(T\Delta t_s, F\Delta f_s)}{\partial k_T} + \frac{\partial R^{DB}_{pq,\tilde{p}\tilde{q}}(T\Delta t_s, F\Delta f_s)}{\partial k_T}\\
&= \frac{\eta_T}{I_0(k_T)} \frac{\cos\left(\frac{2\pi}{\lambda}\beta_{Tm} d_{Tz}\right)}{1-\left(\frac{4\beta_{Tm} d_{Tz}}{\lambda}\right)^2} e^{-j\frac{2\pi}{\lambda}(q-\tilde{q})d_{Rx}} e^{-j2\pi T\Delta t_s f_{R\max}\cos\gamma_R} \Bigg\{ -\frac{I_1(k_T)}{I_0(k_T)} \int_{R_{t1}}^{R_{t2}} \left(1-\gamma\frac{R_t}{D}\right)\\
&\times e^{-j\frac{2\pi}{c_0}F\Delta f_s(D+R_t)} I_0\left(\sqrt{x_{SBT}^2+y_{SBT}^2}\right) \frac{2R_t}{R_{t2}^2-R_{t1}^2} dR_t + \int_{R_{t1}}^{R_{t2}} \left(1-\gamma\frac{R_t}{D}\right) e^{-j\frac{2\pi}{c_0}\Delta f(D+R_t)}\\
&\times I_1\left(\sqrt{x_{SBT}^2+y_{SBT}^2}\right) \frac{x_{SBT}\cos\mu_T + y_{SBT}\sin\mu_T}{\sqrt{x_{SBT}^2+y_{SBT}^2}} \frac{2R_t}{R_{t2}^2-R_{t1}^2} dR_t \Bigg\} + \frac{\eta_{TR}}{I_0(k_T) I_0(k_R)}\\
&\times \frac{\cos\left(\frac{2\pi}{\lambda}\beta_{Tm} d_{Tz}\right)}{1-\left(\frac{4\beta_{Tm} d_{Tz}}{\lambda}\right)^2} \frac{\cos\left(\frac{2\pi}{\lambda}\beta_{Rm} d_{Rz}\right)}{1-\left(\frac{4\beta_{Rm} d_{Rz}}{\lambda}\right)^2} \frac{e^{-j2\pi F\Delta f_s D/c_0}}{(R_{t2}^2-R_{t1}^2)(R_{r2}^2-R_{r1}^2)} \Bigg\{ -\frac{I_1(k_T)}{I_0(k_T)} \Bigg[\int_{R_{t1}}^{R_{t2}} 2e^{-j\frac{2\pi}{c_0}F\Delta f_s R_t}\\
&\times R_t I_0\left(\sqrt{x_{DB}^2+y_{DB}^2}\right) dR_t \int_{R_{r1}}^{R_{r2}} e^{-j\frac{2\pi}{c_0}F\Delta f_s R_r} R_r I_0\left(\sqrt{w_{DB}^2+z_{DB}^2}\right)\left(1-\gamma\frac{R_r}{D}\right) dR_r +\\
&\int_{R_{r1}}^{R_{r2}} 2e^{-j\frac{2\pi}{c_0}F\Delta f_s R_r} R_r I_0\left(\sqrt{w_{DB}^2+z_{DB}^2}\right) dR_r \int_{R_{t1}}^{R_{t2}} e^{-j\frac{2\pi}{c_0}F\Delta f_s R_t} R_t I_0\left(\sqrt{x_{DB}^2+y_{DB}^2}\right)\left(1-\gamma\frac{R_t}{D}\right)\\
&dR_t \Bigg] + \int_{R_{t1}}^{R_{t2}} 2e^{-j\frac{2\pi}{c_0}F\Delta f_s R_t} R_t I_1\left(\sqrt{x_{DB}^2+y_{DB}^2}\right) \frac{x_{DB}\cos\mu_T + y_{DB}\sin\mu_T}{\sqrt{x_{DB}^2+y_{DB}^2}} dR_t \int_{R_{r1}}^{R_{r2}} e^{-j\frac{2\pi}{c_0}F\Delta f_s R_r}\\
&\times R_r I_0\left(\sqrt{w_{DB}^2+z_{DB}^2}\right)\left(1-\gamma\frac{R_r}{D}\right) dR_r + \int_{R_{r1}}^{R_{r2}} 2e^{-j\frac{2\pi}{c_0}F\Delta f_s R_r} R_r I_0\left(\sqrt{w_{DB}^2+z_{DB}^2}\right) dR_r\\
&\times \int_{R_{t1}}^{R_{t2}} e^{-j\frac{2\pi}{c_0}F\Delta f_s R_t} R_t I_1\left(\sqrt{x_{DB}^2+y_{DB}^2}\right) \frac{x_{DB}\cos\mu_T + y_{DB}\sin\mu_T}{\sqrt{x_{DB}^2+y_{DB}^2}} \left(1-\gamma\frac{R_t}{D}\right) dR_t,
\end{aligned}
$$

$$
\begin{aligned}
&[\mathbf{D}_{\Theta_3}(\boldsymbol{\Theta}_{T,F}, T\Delta t_s, F\Delta f_s)]_{q+L_r(p-1),\tilde{q}+L_r(\tilde{p}-1)} \qquad (441)\\
&= \frac{\partial R^{SBT}_{pq,\tilde{p}\tilde{q}}(T\Delta t_s, F\Delta f_s)}{\partial \mu_T} + \frac{\partial R^{DB}_{pq,\tilde{p}\tilde{q}}(T\Delta t_s, F\Delta f_s)}{\partial \mu_T}\\
&= \frac{\eta_T}{I_0(k_T)} \frac{\cos\left(\frac{2\pi}{\lambda}\beta_{Tm} d_{Tz}\right)}{1-\left(\frac{4\beta_{Tm}d_{Tz}}{\lambda}\right)^2} e^{-j\frac{2\pi}{\lambda}(q-\tilde{q})d_{Rx}} e^{-j2\pi T\Delta t_s f_{R\max}\cos\gamma_R} \Bigg\{ \int_{R_{t1}}^{R_{t2}} \left(1-\gamma\frac{R_t}{D}\right)\\
&\times\ e^{-j\frac{2\pi}{c_0}F\Delta f_s(D+R_t)} I_1\left(\sqrt{x^2_{SBT}+y^2_{SBT}}\right) \frac{y_{SBT}k_T\cos\mu_T - x_{SBT}k_T\sin\mu_T}{\sqrt{x^2_{SBT}+y^2_{SBT}}} \frac{2R_t}{R^2_{t2}-R^2_{t1}} dR_t \Bigg\}\\
&+\ \frac{\eta_{TR}}{I_0(k_T)I_0(k_R)} \frac{\cos\left(\frac{2\pi}{\lambda}\beta_{Tm}d_{Tz}\right)}{1-\left(\frac{4\beta_{Tm}d_{Tz}}{\lambda}\right)^2} \frac{\cos\left(\frac{2\pi}{\lambda}\beta_{Rm}d_{Rz}\right)}{1-\left(\frac{4\beta_{Rm}d_{Rz}}{\lambda}\right)^2} \frac{e^{-j2\pi F\Delta f_s D/c_0}}{(R^2_{t2}-R^2_{t1})(R^2_{r2}-R^2_{r1})}\\
&\times\ \Bigg\{ \int_{R_{t1}}^{R_{t2}} 2e^{-j\frac{2\pi}{c_0}F\Delta f_s R_t} R_t I_1\left(\sqrt{x^2_{DB}+y^2_{DB}}\right) \frac{y_{DB}k_T\cos\mu_T - x_{DB}k_T\sin\mu_T}{\sqrt{x^2_{DB}+y^2_{DB}}} dR_t\\
&\times\ \int_{R_{r1}}^{R_{r2}} e^{-j\frac{2\pi}{c_0}F\Delta f_s R_r} R_r I_0\left(\sqrt{w^2_{DB}+z^2_{DB}}\right) \left(1-\gamma\frac{R_r}{D}\right) dR_r + \int_{R_{r1}}^{R_{r2}} 2e^{-j\frac{2\pi}{c_0}F\Delta f_s R_r} R_r\\
&\times\ I_0\left(\sqrt{w^2_{DB}+z^2_{DB}}\right) dR_r \int_{R_{t1}}^{R_{t2}} e^{-j\frac{2\pi}{c_0}F\Delta f_s R_t} R_t I_1\left(\sqrt{x^2_{DB}+y^2_{DB}}\right)\\
&\times\ \frac{y_{DB}k_T\cos\mu_T - x_{DB}k_T\sin\mu_T}{\sqrt{x^2_{DB}+y^2_{DB}}} \left(1-\gamma\frac{R_t}{D}\right) dR_t,
\end{aligned}
$$

$$
\begin{aligned}
&[\mathbf{D}_{\Theta_4}(\boldsymbol{\Theta}_{T,F}, T\Delta t_s, F\Delta f_s)]_{q+L_r(p-1),\tilde{q}+L_r(\tilde{p}-1)} \qquad (442)\\
&= \frac{\partial R^{SBR}_{pq,\tilde{p}\tilde{q}}(T\Delta t_s, F\Delta f_s)}{\partial \beta_{R_m}} + \frac{\partial R^{DB}_{pq,\tilde{p}\tilde{q}}(T\Delta t_s, F\Delta f_s)}{\partial \beta_{R_m}}\\
&= \Bigg\{ \frac{\eta_R}{I_0(k_R)} \frac{\cos\left(\frac{2\pi}{\lambda}\beta_{Rm}d_{Rz}\right)}{1-\left(\frac{4\beta_{Rm}d_{Rz}}{\lambda}\right)^2} e^{j\frac{2\pi}{\lambda}(p-\tilde{p})d_{Tx}} e^{j2\pi T\Delta t_s f_{T\max}\cos\gamma_T} \int_{R_{r1}}^{R_{r2}} \left(1-\gamma\frac{R_r}{D}\right)\\
&\times\ e^{-j\frac{2\pi}{c_0}F\Delta f_s(D+R_r)} I_0\left(\sqrt{x^2_{SBR}+y^2_{SBR}}\right) \frac{2R_r}{R^2_{r2}-R^2_{r1}} dR_r + \frac{\eta_{TR}}{I_0(k_T)I_0(k_R)} \frac{\cos\left(\frac{2\pi}{\lambda}\beta_{Rm}d_{Rz}\right)}{1-\left(\frac{4\beta_{Rm}d_{Rz}}{\lambda}\right)^2}\\
&\times\ \frac{e^{-j2\pi F\Delta f_s D/c_0}}{(R^2_{t2}-R^2_{t1})(R^2_{r2}-R^2_{r1})} \Bigg[\int_{R_{t1}}^{R_{t2}} 2e^{-j\frac{2\pi}{c_0}F\Delta f_s R_t} R_t I_0\left(\sqrt{x^2_{DB}+y^2_{DB}}\right) dR_t \int_{R_{r1}}^{R_{r2}} e^{-j\frac{2\pi}{c_0}F\Delta f_s R_r} R_r\\
&\times\ I_0\left(\sqrt{w^2_{DB}+z^2_{DB}}\right)\left(1-\gamma\frac{R_r}{D}\right) dR_r + \int_{R_{r1}}^{R_{r2}} 2e^{-j\frac{2\pi}{c_0}F\Delta f_s R_r} R_r I_0\left(\sqrt{w^2_{DB}+z^2_{DB}}\right) dR_r\\
&\times\ \int_{R_{t1}}^{R_{t2}} e^{-j\frac{2\pi}{c_0}F\Delta f_s R_t} R_t I_0\left(\sqrt{x^2_{DB}+y^2_{DB}}\right)\left(1-\gamma\frac{R_t}{D}\right) dR_t \Bigg]\Bigg\} \frac{2\pi}{\lambda} d_{Rz}\\
&\times\ \frac{8\cos\left(\frac{2\pi}{\lambda}\beta_{Rm}d_{Rz}\right)\left(\frac{2\pi}{\lambda}\beta_{Rm}d_{Rz}\right) + 4\left(\frac{2\pi}{\lambda}\beta_{Rm}d_{Rz}\right)^2 \sin\left(\frac{2\pi}{\lambda}\beta_{Rm}d_{Rz}\right) - \sin\left(\frac{2\pi}{\lambda}\beta_{Rm}d_{Rz}\right)}{1-8\left(\frac{2\pi}{\lambda}\beta_{Rm}d_{Rz}\right)^2 + 16\left(\frac{2\pi}{\lambda}\beta_{Rm}d_{Rz}\right)^4},
\end{aligned}
$$

$$
\begin{aligned}
&[\mathbf{D}_{\Theta_5}(\mathbf{\Theta}_{T,F}, T\Delta t_s, F\Delta f_s)]_{q+L_r(p-1),\tilde{q}+L_r(\tilde{p}-1)} \qquad (443)\\
&= \frac{\partial R^{SBR}_{pq,\tilde{p}\tilde{q}}(T\Delta t_s, F\Delta f_s)}{\partial k_R} + \frac{\partial R^{DB}_{pq,\tilde{p}\tilde{q}}(T\Delta t_s, F\Delta f_s)}{\partial k_R}\\
&= \frac{\eta_R}{I_0(k_R)} \frac{\cos\left(\frac{2\pi}{\lambda}\beta_{Rm} d_{Rz}\right)}{1-\left(\frac{4\beta_{Rm} d_{Rz}}{\lambda}\right)^2} e^{j\frac{2\pi}{\lambda}(p-\tilde{p})d_{Tx}} e^{j2\pi T\Delta t_s f_{T\max}\cos\gamma_T} \Bigg\{ -\frac{I_1(k_R)}{I_0(k_R)} \int_{R_{r1}}^{R_{r2}} \left(1-\gamma\frac{R_r}{D}\right)\\
&\times e^{-j\frac{2\pi}{c_0}F\Delta f_s(D+R_r)} I_0\left(\sqrt{x^2_{SBR}+y^2_{SBR}}\right) \frac{2R_r}{R^2_{r2}-R^2_{r1}} dR_r + \int_{R_{r1}}^{R_{r2}} \left(1-\gamma\frac{R_r}{D}\right)\\
&\times e^{-j\frac{2\pi}{c_0}F\Delta f_s(D+R_r)} I_1\left(\sqrt{x^2_{SBR}+y^2_{SBR}}\right) \frac{x_{SBR}\cos\mu_R + y_{SBR}\sin\mu_R}{\sqrt{x^2_{SBR}+y^2_{SBR}}} \frac{2R_r}{R^2_{r2}-R^2_{r1}} dR_r \Bigg\}\\
&+ \frac{\eta_{TR}}{I_0(k_T)I_0(k_R)} \frac{\cos\left(\frac{2\pi}{\lambda}\beta_{Tm} d_{Tz}\right)}{1-\left(\frac{4\beta_{Tm} d_{Tz}}{\lambda}\right)^2} \frac{\cos\left(\frac{2\pi}{\lambda}\beta_{Rm} d_{Rz}\right)}{1-\left(\frac{4\beta_{Rm} d_{Rz}}{\lambda}\right)^2} \frac{e^{-j2\pi F\Delta f_s D/c_0}}{(R^2_{t2}-R^2_{t1})(R^2_{r2}-R^2_{r1})} \Bigg\{ -\frac{I_1(k_R)}{I_0(k_R)}\\
&\times \Bigg[\int_{R_{t1}}^{R_{t2}} 2e^{-j\frac{2\pi}{c_0}F\Delta f_s R_t} R_t I_0\left(\sqrt{x^2_{DB}+y^2_{DB}}\right) dR_t \int_{R_{r1}}^{R_{r2}} e^{-j\frac{2\pi}{c_0}F\Delta f_s R_r} R_r I_0\left(\sqrt{w^2_{DB}+z^2_{DB}}\right)\\
&\times \left(1-\gamma\frac{R_r}{D}\right) dR_r + \int_{R_{r1}}^{R_{r2}} 2e^{-j\frac{2\pi}{c_0}F\Delta f_s R_r} R_r I_0\left(\sqrt{w^2_{DB}+z^2_{DB}}\right) dR_r \int_{R_{t1}}^{R_{t2}} e^{-j\frac{2\pi}{c_0}F\Delta f_s R_t} R_t\\
&\times I_0\left(\sqrt{x^2_{DB}+y^2_{DB}}\right)\left(1-\gamma\frac{R_t}{D}\right) dR_t\Bigg] + \int_{R_{t1}}^{R_{t2}} 2e^{-j\frac{2\pi}{c_0}F\Delta f_s R_t} R_t I_0\left(\sqrt{x^2_{DB}+y^2_{DB}}\right) dR_t\\
&\times \int_{R_{r1}}^{R_{r2}} e^{-j\frac{2\pi}{c_0}F\Delta f_s R_r} R_r \frac{z_{DB}\cos\mu_R + w_{DB}\sin\mu_R}{\sqrt{z^2_{DB}+w^2_{DB}}} I_1\left(\sqrt{w^2_{DB}+z^2_{DB}}\right)\left(1-\gamma\frac{R_r}{D}\right) dR_r\\
&+ \int_{R_{r1}}^{R_{r2}} 2e^{-j\frac{2\pi}{c_0}F\Delta f_s R_r} R_r I_1\left(\sqrt{w^2_{DB}+z^2_{DB}}\right) \frac{z_{DB}\cos\mu_R + w_{DB}\sin\mu_R}{\sqrt{z^2_{DB}+w^2_{DB}}} dR_r\\
&\times \int_{R_{t1}}^{R_{t2}} e^{-j\frac{2\pi}{c_0}F\Delta f_s R_t} R_t I_0\left(\sqrt{x^2_{DB}+y^2_{DB}}\right)\left(1-\gamma\frac{R_t}{D}\right) dR_t,
\end{aligned}
$$

$$
\begin{aligned}
&[\mathbf{D}_{\Theta_6}(\boldsymbol{\Theta}_{T,F}, T\Delta t_s, F\Delta f_s)]_{q+L_r(p-1),\tilde{q}+L_r(\tilde{p}-1)} \qquad (444)\\
&= \frac{\partial R^{SBR}_{pq,\tilde{p}\tilde{q}}(T\Delta t_s, F\Delta f_s)}{\partial \mu_R} + \frac{\partial R^{DB}_{pq,\tilde{p}\tilde{q}}(T\Delta t_s, F\Delta f_s)}{\partial \mu_R}\\
&= \frac{\eta_R}{I_0(k_R)} \frac{\cos\left(\frac{2\pi}{\lambda}\beta_{Rm}d_{Rz}\right)}{1-\left(\frac{4\beta_{Rm}d_{Rz}}{\lambda}\right)^2} e^{j\frac{2\pi}{\lambda}(p-\tilde{p})d_{Tx}} e^{j2\pi T\Delta t_s f_{T\max}\cos\gamma_T} \left\{ \int_{R_{r1}}^{R_{r2}} \left(1-\gamma\frac{R_r}{D}\right)\right.\\
&\times e^{-j\frac{2\pi}{c_0}F\Delta f_s(D+R_r)} I_1\left(\sqrt{x^2_{SBR}+y^2_{SBR}}\right) \frac{y_{SBR}k_R\cos\mu_R - x_{SBR}k_R\sin\mu_R}{\sqrt{x^2_{SBR}+y^2_{SBR}}} \frac{2R_r}{R^2_{r2}-R^2_{r1}} dR_r \Bigg\}\\
&+ \frac{\eta_{TR}}{I_0(k_T)I_0(k_R)} \frac{\cos\left(\frac{2\pi}{\lambda}\beta_{Tm}d_{Tz}\right)}{1-\left(\frac{4\beta_{Tm}d_{Tz}}{\lambda}\right)^2} \frac{\cos\left(\frac{2\pi}{\lambda}\beta_{Rm}d_{Rz}\right)}{1-\left(\frac{4\beta_{Rm}d_{Rz}}{\lambda}\right)^2} \frac{e^{-j2\pi F\Delta f_s D/c_0}}{(R^2_{t2}-R^2_{t1})(R^2_{r2}-R^2_{r1})} \left\{ \int_{R_{t1}}^{R_{t2}} 2\right.\\
&\times e^{-j\frac{2\pi}{c_0}F\Delta f_s R_t} R_t I_0\left(\sqrt{x^2_{DB}+y^2_{DB}}\right) dR_t \int_{R_{r1}}^{R_{r2}} e^{-j\frac{2\pi}{c_0}F\Delta f_s R_r} R_r I_1\left(\sqrt{w^2_{DB}+z^2_{DB}}\right)\left(1-\gamma\frac{R_r}{D}\right)\\
&\times \frac{w_{DB}k_R\cos\mu_R - z_{DB}k_R\sin\mu_R}{\sqrt{w^2_{DB}+z^2_{DB}}} dR_r + \int_{R_{r1}}^{R_{r2}} 2e^{-j\frac{2\pi}{c_0}F\Delta f_s R_r} R_r I_1\left(\sqrt{w^2_{DB}+z^2_{DB}}\right)\\
&\times \frac{w_{DB}k_R\cos\mu_R - z_{DB}k_R\sin\mu_R}{\sqrt{z^2_{DB}+w^2_{DB}}} dR_r \int_{R_{t1}}^{R_{t2}} e^{-j\frac{2\pi}{c_0}F\Delta f_s R_t} R_t I_0\left(\sqrt{x^2_{DB}+y^2_{DB}}\right)\left(1-\gamma\frac{R_t}{D}\right) dR_t,
\end{aligned}
$$

$$
\begin{aligned}
&[\mathbf{D}_{\Theta_7}(\boldsymbol{\Theta}_{T,F}, T\Delta t_s, F\Delta f_s)]_{q+L_r(p-1),\tilde{q}+L_r(\tilde{p}-1)} \qquad (445)\\
&= \frac{\partial R^{SBT}_{pq,\tilde{p}\tilde{q}}(T\Delta t_s, F\Delta f_s)}{\partial \eta_T} + \frac{\partial R^{DB}_{pq,\tilde{p}\tilde{q}}(T\Delta t_s, F\Delta f_s)}{\partial \eta_T} = \frac{1}{I_0(k_T)}\\
&\times \frac{\cos\left(\frac{2\pi}{\lambda}\beta_{Tm}d_{Tz}\right)}{1-\left(\frac{4\beta_{Tm}d_{Tz}}{\lambda}\right)^2} e^{-j\frac{2\pi}{\lambda}(q-\tilde{q})d_{Rx}} e^{-j2\pi T\Delta t_s f_{R\max}\cos\gamma_R} \int_{R_{t1}}^{R_{t2}} \left(1-\gamma\frac{R_t}{D}\right) e^{-j\frac{2\pi}{c_0}F\Delta f_s(D+R_t)}\\
&\times I_0\left(\sqrt{x^2_{SBT}+y^2_{SBT}}\right) \frac{2R_t}{R^2_{t2}-R^2_{t1}} dR_t - \frac{1}{I_0(k_T)I_0(k_R)} \frac{\cos\left(\frac{2\pi}{\lambda}\beta_{Tm}d_{Tz}\right)}{1-\left(\frac{4\beta_{Tm}d_{Tz}}{\lambda}\right)^2} \frac{\cos\left(\frac{2\pi}{\lambda}\beta_{Rm}d_{Rz}\right)}{1-\left(\frac{4\beta_{Rm}d_{Rz}}{\lambda}\right)^2}\\
&\times \frac{e^{-j2\pi F\Delta f_s D/c_0}}{(R^2_{t2}-R^2_{t1})(R^2_{r2}-R^2_{r1})} \left\{ \int_{R_{t1}}^{R_{t2}} 2e^{-j\frac{2\pi}{c_0}F\Delta f_s R_t} R_t I_0\left(\sqrt{x^2_{DB}+y^2_{DB}}\right) dR_t \int_{R_{r1}}^{R_{r2}} e^{-j\frac{2\pi}{c_0}F\Delta f_s R_r} R_r \right.\\
&\times I_0\left(\sqrt{w^2_{DB}+z^2_{DB}}\right)\left(1-\gamma\frac{R_r}{D}\right) dR_r + \int_{R_{r1}}^{R_{r2}} 2e^{-j\frac{2\pi}{c_0}F\Delta f_s R_r} R_r I_0\left(\sqrt{w^2_{DB}+z^2_{DB}}\right) dR_r\\
&\times \left.\int_{R_{t1}}^{R_{t2}} e^{-j\frac{2\pi}{c_0}F\Delta f_s R_t} R_t I_0\left(\sqrt{x^2_{DB}+y^2_{DB}}\right)\left(1-\gamma\frac{R_t}{D}\right) dR_t \right\},
\end{aligned}
$$

$$
\begin{aligned}
&[\mathbf{D}_{\Theta_8}(\mathbf{\Theta}_{T,F}, T\Delta t_s, F\Delta f_s)]_{q+L_r(p-1),\tilde{q}+L_r(\tilde{p}-1)} \\
&= \frac{\partial R^{SBR}_{pq,\tilde{p}\tilde{q}}(T\Delta t_s, F\Delta f_s)}{\partial \eta_R} + \frac{\partial R^{DB}_{pq,\tilde{p}\tilde{q}}(T\Delta t_s, F\Delta f_s)}{\partial \eta_R} = \frac{1}{I_0(k_R)} \\
&\times \frac{\cos\left(\frac{2\pi}{\lambda}\beta_{Rm} d_{Rz}\right)}{1-\left(\frac{4\beta_{Rm} d_{Rz}}{\lambda}\right)^2} e^{j\frac{2\pi}{\lambda}(p-\tilde{p})d_{Tx}} e^{j2\pi T\Delta t_s f_{T\max}\cos\gamma_T} \int_{R_{r1}}^{R_{r2}} \left(1-\gamma\frac{R_r}{D}\right) e^{-j\frac{2\pi}{c_0}F\Delta f_s(D+R_r)} \\
&\times I_0\left(\sqrt{x^2_{SBR}+y^2_{SBR}}\right)\frac{2R_r}{R^2_{r2}-R^2_{r1}} dR_r - \frac{1}{I_0(k_T)I_0(k_R)} \frac{\cos\left(\frac{2\pi}{\lambda}\beta_{Tm} d_{Tz}\right)}{1-\left(\frac{4\beta_{Tm} d_{Tz}}{\lambda}\right)^2} \frac{\cos\left(\frac{2\pi}{\lambda}\beta_{Rm} d_{Rz}\right)}{1-\left(\frac{4\beta_{Rm} d_{Rz}}{\lambda}\right)^2} \\
&\times \frac{e^{-j2\pi F\Delta f_s D/c_0}}{(R^2_{t2}-R^2_{t1})(R^2_{r2}-R^2_{r1})} \left\{ \int_{R_{t1}}^{R_{t2}} 2e^{-j\frac{2\pi}{c_0}F\Delta f_s R_t} R_t I_0\left(\sqrt{x^2_{DB}+y^2_{DB}}\right) dR_t \int_{R_{r1}}^{R_{r2}} e^{-j\frac{2\pi}{c_0}F\Delta f_s R_r} R_r \right. \\
&\times I_0\left(\sqrt{w^2_{DB}+z^2_{DB}}\right)\left(1-\gamma\frac{R_r}{D}\right) dR_r + \int_{R_{r1}}^{R_{r2}} 2e^{-j\frac{2\pi}{c_0}F\Delta f_s R_r} R_r I_0\left(\sqrt{w^2_{DB}+z^2_{DB}}\right) dR_r \\
&\times \left. \int_{R_{t1}}^{R_{t2}} e^{-j\frac{2\pi}{c_0}F\Delta f_s R_t} R_t I_0\left(\sqrt{x^2_{DB}+y^2_{DB}}\right)\left(1-\gamma\frac{R_t}{D}\right) dR_t \right\}.
\end{aligned} \tag{446}
$$

Finally, the Cramér-Rao bound of the estimated parameter Θ_i is the diagonal element of the inverse Fisher information matrix that corresponds to the parameter Θ_i.

APPENDIX O

DERIVATIONS OF EQUATIONS (303) - (305)

Similar to Laurent's decomposition [91], M-ary partial-response CPM signals with tilted-phase can be presented as

$$s(t, \mathbf{u}) = \prod_{l=0}^{F-1} \sum_{i=0}^{2^{L-1}-1} \sum_{n=0}^{N_c-1} e^{j2\pi h 2^l A_{i,n}^{(l)}} c_i^{(l)}(t - nT_c), \tag{447}$$

where functions $c_i^{(l)}(t)$ and symbols $A_{i,n}^{(l)}$ are defined below. Functions $c_i^{(l)}(t)$ are

$$c_i^{(l)}(t) = e^{j\pi h W(t)} \prod_{n=0}^{L-1} s^{(l)}\left[t + (n + La_{i,n})T_c\right], \tag{448}$$

where $W(t)$ is defined in (296), functions $s^{(l)}(t)$ are defined as in (300), $0 \leq i \leq 2^{L-1} - 1$, $0 \leq t \leq T_c \cdot \min_n[L(2 - a_{i,n}) - n]$, and $l = 0, \ldots, F-1$. Symbols $A_{i,n}^{(l)}$ are

$$A_{i,n}^{(l)} = \sum_{m=0}^{n} \gamma_{m,l} - \sum_{m=0}^{L-1} \gamma_{n-m,l} a_{i,m}, \tag{449}$$

where $a_{i,m} \in \{0, 1\}$ are coefficients in the radix-2 representation of $i = \sum_{m=0}^{L-1} 2^{m-1} a_{i,m}$.

The output signal $s(t, \mathbf{u})$ in (447) is presented as a product of two sums, what makes our further analysis difficult. To simplify equations, we modify the output signal $s(t, \mathbf{u})$ following the algorithm proposed by Mengali and Morelli [56]. We start from radix-2^{L-1} representation of an integer j from the interval $0 \leq j \leq (2^{(L-1)^F} - 1)$

$$j = \sum_{l=0}^{F-1} 2^{l(L-1)} d_{j,l}, \tag{450}$$

where $d_{j,l} \in \{0, \ldots, 2^{L-1} - 1\}$. Then, for each pair (j, l), we choose the corresponding $d_{j,l}$ and use it as a subscript for functions $c_{d_{j,l}}^{(l)}(t)$ defined in (448). As the next step, we form the vector $\mathbf{T}_j = \{T_{j,F-1}, T_{j,F-2}, \ldots, T_{j,0}\}$, where elements of the vector, $T_{j,l}$, are durations of the functions $c_{d_{j,l}}^{(l)}(t)$. Then, for a given $\mathbf{T}_j$, we choose the F-tuples $\mathbf{e}_j^{(m)} = \{e_{j,F-1}^{(m)}, e_{j,F-2}^{(m)}, \ldots, e_{j,0}^{(m)}\}$ that have integer components which satisfy

$0 \leq e_{j,l}^{(m)} \leq T_{j,l} - 1$, $\prod_{l=0}^{F-1} e_{j,l}^{(m)} = 0$, and $m = 0, 1, 2, \ldots$. It can be shown that there are $\mathcal{M}_j$ such F-tuples [56], where $\mathcal{M}_j$ is equal to $\prod_{l=0}^{F-1} T_{j,l} - \prod_{l=0}^{F-1}(T_{j,l} - 1)$. This result implies that index m can take only values in the interval $0 \leq m \leq \mathcal{M}_j - 1$.

Now, the signal $s(t, \mathbf{u})$ in (447) can be modified to

$$s(t, \mathbf{u}) = \sum_{k=0}^{R-1} \sum_{n=0}^{N_c-1} B_{k,n} g_k(t - nT_c), \tag{451}$$

where $R = (2^F - 1)2^{F(L-1)}$ and the Laurent functions $g_k(t)$ and symbols $B_{k,n}$ are defined as

$$g_k(t) = \prod_{l=0}^{F-1} c_{d_{j,l}}^{(l)} \left[t + e_{j,l}^{(m)} T_c \right], \tag{452}$$

$$B_{k,n} = \exp\left(j2\pi h \sum_{l=0}^{F-1} 2^l A_{d_{j,l}, n - e_{j,l}^{(m)}}^{(l)} \right), \tag{453}$$

respectively, where $c_{d_{j,l}}^{(l)}$ are defined in (448), $A_{d_{j,l}, n - e_{j,l}^{(m)}}^{(l)}$ are defined in (449), and $k = m + \sum_{n=0}^{j-1} \mathcal{M}_n$. Finally, by substituting (448) in (452) and using the equality $k = m + \sum_{n=0}^{j-1} \mathcal{M}_n$, we obtain the expression in (304). Similarly, by substituting (449) into (453), we obtain the expression in (305).

APPENDIX P

PROOF OF LEMMA 2

We will prove this lemma by contradiction. Assume that not all functions in the vector $\mathbf{g}(t)$ are linearly independent. Then, there exists some nonzero complex vector $[K_{0,0}, \ldots, K_{N_c-1,R-1}]^T$ that satisfies

$$\textstyle\sum_{k=0}^{R-1} \{K_{0,k} g_{0,k}(t) + \cdots + K_{N_c-1,k} g_{N_c-1,k}(t)\} = 0 \ . \tag{454}$$

Note that every function $g_{n,k}(t)$ has nonzero value only over the interval $nT_c \leq t \leq (n+L+1)T_c$, where $0 \leq n \leq N_c - 1$. Hence, for an arbitrary time interval $lT_c \leq t \leq (l+1)T_c$, (454) can be modified to

$$\textstyle\sum_{k=0}^{R-1} \{K_{l-L,k} g_{l-L,k}(t) + \cdots + K_{l+L,k} g_{l+L,0}(t)\} = 0 \ . \tag{455}$$

From (304), observe that functions $g_k(t)$ and $g_{p \neq k}(t)$ have different combinations of functions $s^{(l)}(t)$, defined in (300). Then, (455) can be rewritten as

$$K_{l-L,k} g_{l-L,k}(t) + \cdots + K_{l,k} g_{l,k}(t) \cdots + K_{l+L,k} g_{l+L,k}(t) = 0, \tag{456}$$

for $0 \leq k \leq R-1$. For $L = 1$, (456) reduces to

$$K_{l-1,k} g_{l-1,k}(t) + K_{l+1,k} g_{l+1,k}(t) = K_{l,k} g_{l,k}(t), \tag{457}$$

for non-zero coefficients $K_{l-1,k}$, $K_{l+1,k}$. When $(l-1)T_c \leq t \leq lT_c$, the right term in (457) is equal to zero, because $g_{l,k}(t) = 0$. The left term in (457) is equal to $K_{l-1,k} g_{l-1,k}(t) = 0$. This equality is satisfied only if $K_{l-1,k} = 0$. Similarly, when $(l+2)T_c \leq t \leq (l+3)T_c$, the right term in (457) is equal to zero, because $g_{l,k}(t) = 0$. Following the similar argument as above, it follows that $K_{l+1,k} = 0$. The fact that

$K_{l-1,k} = 0$ and $K_{l+1,k} = 0$ causes a contradiction. Therefore, for $L = 1$ all functions $g_{n,k}(t)$ are linearly independent.

Using the similar reasoning as above, we now show that all functions in $\mathbf{g}(t)$ are linearly independent for an arbitrary L. For $(l - L)T_c \leq t \leq (l - L + 1)T_c$, (456) simplifies to $K_{l-L,k}g_{l-L,k}(t) = 0$. This equality is satisfied only if $K_{l-L,k} = 0$. Similarly, for $(l + 3L - 1)T_c \leq t \leq (l + 3L)T_c$, (456) simplifies to $K_{l+L,k}g_{l+L,k}(t) = 0$. Following the similar argument as above, it follows that $K_{l+L,k} = 0$. For $(l-L+1)T_c \leq t \leq (l - L + 2)T_c$, (456) simplifies to $K_{l-L,k}g_{l-L,k}(t) + K_{l-L+1,k}g_{l-L+1,k}(t) = 0$. Since $K_{l-L,k} = 0$, the equality is satisfied only if $K_{l-L+1,k} = 0$. Similarly, for $(l+3L-2)T_c \leq t \leq (l + 3L - 1)T_c$, (456) simplifies to $K_{l+L-1,k}g_{l+L-1,k}(t) + K_{l+L,k}g_{l+L,k}(t) = 0$ and it follows that $K_{l+L-1,k} = 0$. Using the similar reasoning (or induction) for other time intervals, it follows that coefficients $K_{l-L,k}, \ldots, K_{l-1,k}, K_{l+1,k}, \ldots, K_{l+L,k}$ are zero which causes a contradiction. Therefore, all functions $g_{n,k}(t)$ are linearly independent for an arbitrary L. $\boxdot$

APPENDIX Q

PROOF OF LEMMA 3

We will prove this lemma by contradiction. Assume that the elements of the differential ST-CPM vector $\Delta\mathbf{s}(t)$ are not linearly independent. Then there exists some nonzero complex vector $[k_1, k_2, \ldots, k_{L_t}]^T$ that satisfies

$$\begin{aligned} & k_1 \Delta s_1(t) + \cdots + k_{L_t} \Delta s_{L_t}(t) = \\ = \; & \sum_{n=0}^{N_c-1} \left[k_1 \Delta z_{n,0}^{(1)} + \cdots + k_{L_t} \Delta z_{n,0}^{(L_t)} \right] g_{n,0}(t) + \\ & \vdots \\ + \; & \sum_{n=0}^{N_c-1} \left[k_1 \Delta z_{n,R-1}^{(1)} + \cdots + k_{L_t} \Delta z_{n,R-1}^{(L_t)} \right] g_{n,R-1}(t) = 0, \end{aligned} \tag{458}$$

where $\Delta z_{n,k}^{(i)}$ are elements of the matrices $\Delta\mathbf{Z}_k$ for $0 \leq k \leq R-1$, $1 \leq i \leq L_t$. Since all functions $g_{n,k}(t)$ are linearly independent (as shown in Lemma 2), it follows that

$$k_1 \Delta z_{n,k}^{(1)} + \cdots + k_{L_t} \Delta z_{n,k}^{(L_t)} = 0, \tag{459}$$

for each $k \in \{0, \ldots, R-1\}$ and $n \in \{0, \ldots, N_c - 1\}$. Equation (459) implies that the matrices $\Delta\mathbf{Z}_k$ do not have full rank, which contradicts our assumption. $\boxdot$

APPENDIX R

DERIVATION OF EQUATION (329)

Using (326) and $M = 2^F$, the integral $I_{n,n+1}$ can be written as

$$
\begin{aligned}
I_{n,n+1} &= \qquad (460)\\
&= \int_{(n+1)T_c}^{(n+2)T_c} \prod_{l=0}^{F-1} e^{j\pi h W(t-nT_c)} e^{-j\pi h W(t-(n+1)T_c)} s^{(l)}(t-nT_c) s^{(l)}(t-(n+1)T_c)^* dt \\
&= \int_{(n+1)T_c}^{(n+2)T_c} \prod_{l=0}^{F-1} \exp\left(j\pi h(2^F-1)\frac{t-nT_c}{T_c}\right) \frac{\sin\left(\pi h 2^l - 2\pi h 2^l \beta(t-(n+1)T_c)\right)}{\sin(\pi h 2^l)} \\
&\times \exp\left(-j\pi h(2^F-1)\frac{t-(n+1)T_c}{T_c} + j\pi h 2^l\right) \left\{\frac{\sin\left(2\pi h 2^l \beta(t-(n+1)T_c)\right)}{\sin(\pi h 2^l)}\right\}^* dt \\
&= \exp\left(j2\pi h(2^F-1)\right) \\
&\times \int_{(n+1)T_c}^{(n+2)T_c} \prod_{l=0}^{F-1} \frac{\sin\left(\pi h 2^l - 2\pi h 2^l \beta(t-(n+1)T_c)\right)\sin\left(2\pi h 2^l \beta(t-(n+1)T_c)\right)}{\sin(\pi h 2^l)\sin(\pi h 2^l)} dt. \boxdot
\end{aligned}
$$

APPENDIX S

PROOF OF PROPOSITION 7

Proof: The proof of this proposition starts by evaluating the integral $I_{n,n+1}$ with the phase shaping function defined in (330). Choosing parameters $a = 0.5$ and $b = 0$, the integral $I_{n,n+1}$ is equal to

$$I_{n,n+1} = e^{j2\pi h(2^F-1)} \int_{(n+1.5)T_c}^{(n+2)T_c} \prod_{l=0}^{F-1} \frac{\sin\left(\pi h 2^l - \pi h 2^l\right)\right) \sin\left(\pi h 2^l\right)}{\sin(\pi h 2^l)\sin(\pi h 2^l)} dt = 0. \quad (461)$$

Also, if we choose parameters $a = 1$, $b = 2$, and the modulation index $h = 1/2$, the integral $I_{n,n+1}$ is equal to

$$\begin{aligned} I_{n,n+1} &= \qquad (462) \\ &= \frac{e^{j2\pi h(2^F-1)}}{\prod_{l=0}^{F-1}\sin(\pi 2^{l-1})\sin(\pi 2^{l-1})} \int_0^{T_c} \prod_{l=0}^{F-1} \sin\left(\pi 2^{l-1} - \frac{\pi 2^l \tau}{T_c}\right) \sin\left(\frac{\pi 2^l \tau}{T_c}\right) d\tau = 0. \end{aligned}$$

Note that the same result can be obtained for other values of parameters a and b.

If the raised cosine function (1RC) is selected as the phase shaping function $\beta(t)$ and modulation index is $h = 1/2^x$, where $1 \le x \le F-1$, the integrals $I_{n,n+1}$ are equal to

$$\begin{aligned} I_{n,n+1} &= e^{j2\pi h(2^F-1)} \qquad (463) \\ &\int_0^{T_c} \prod_{l=0}^{F-1} \frac{\sin\left(\pi 2^{l-x} - 2^{l-x-1}\left(\frac{2\pi\tau}{T_c} - \sin\left(\frac{2\pi\tau}{T_c}\right)\right)\right) \sin\left(2^{l-x-1}\left(\frac{2\pi\tau}{T_c} - \sin\left(\frac{2\pi\tau}{T_c}\right)\right)\right)}{\sin(\pi 2^{l-x})\sin(\pi 2^{l-x})} d\tau. \end{aligned}$$

Using the asymptotic expansion of integrals [98], (463) can be simplified to yield

$$\begin{aligned} I_{n,n+1} &\approx e^{j2\pi h(2^F-1)} \frac{1}{\prod_{l=0}^{F-1}\sin(\pi 2^{l-x})^2} \qquad (464) \\ &\times \int_0^{T_c} \prod_{l=0}^{F-1} \left(\frac{4}{3}\sin(\pi 2^{l-x}) 2^{l-1-x}\left(\frac{\pi\tau}{T_c}\right)^3 - \frac{4}{15}\sin(\pi 2^{l-x}) 2^{l-1-x}\left(\frac{\pi\tau}{T_c}\right)^5\right) d\tau = 0. \end{aligned}$$

By noting that $I_{n+1,n} = (I_{n,n+1})^*$ and that all functions inside the integrals $I_{n+1,n}$ are real functions, we can conclude that integrals $I_{n+1,n}$ are also equal to zero. $\boxdot$

APPENDIX T

PROOF OF PROPOSITION 8

Proof: Proof of this proposition begins by evaluating the integral $I_{n,n+1}$ for all integers $e_{j,l}^{(k-w_j)}$ equal to zero. The integral $I_{n,n+1}$ can be written as

$$
\begin{aligned}
I_{n,n+1} &= e^{j2\pi h(2^F-1)} \int_{(n+1)T_c}^{(n+2)T_c} \prod_{l=0}^{F-1} \frac{\sin\left(2\pi h 2^l \beta(t-nT_c)\right)^2}{\sin(\pi h 2^l)^2} \\
&\times \frac{\sin\left(2\pi h 2^l \beta(t-(n+1)T_c)\right)}{\sin(\pi h 2^l)} \frac{\sin\left(\pi h 2^l - 2\pi h 2^l \beta(t-(n+1)T_c)\right)}{\sin(\pi h 2^l)} dt \\
&+ e^{j2\pi h(2^F-1)} \int_{(n+2)T_c}^{(n+3)T_c} \prod_{l=0}^{F-1} \frac{\sin\left(\pi h 2^l - 2\pi h 2^l \beta(t-(n+2)T_c)\right)^2}{\sin(\pi h 2^l)^2} \\
&\times \frac{\sin\left(2\pi h 2^l \beta(t-(n+1)T_c)\right)}{\sin(\pi h 2^l)} \frac{\sin\left(\pi h 2^l - 2\pi h 2^l \beta(t-(n+1)T_c)\right)}{\sin(\pi h 2^l)} dt.
\end{aligned} \tag{465}
$$

For the raised cosine function (2RC) and modulation index $h = 1/2^x$, where $1 \le x \le F-1$, the integral $I_{n,n+1}$ is equal to

$$
\begin{aligned}
&I_{n,n+1} = e^{j2\pi h(2^F-1)} \int_0^{T_c} \prod_{l=0}^{F-1} \frac{\sin\left(\pi 2^{l-x}\left(\frac{\tau+T_c}{2T_c} - \frac{1}{4\pi}\sin\left(\frac{2\pi(\tau+T_c)}{T_c}\right)\right)\right)^2}{\sin(\pi 2^{l-x})^2} \\
&\times \frac{\sin\left(\pi 2^{l-x}\left(\frac{\tau}{2T_c} - \frac{1}{4\pi}\sin\left(\frac{2\pi\tau}{T_c}\right)\right)\right)}{\sin(\pi 2^{l-x})} \frac{\sin\left(\pi 2^{l-x}\left(1 - \frac{\tau}{2T_c} + \frac{1}{4\pi}\sin\left(\frac{2\pi\tau}{T_c}\right)\right)\right)}{\sin(\pi 2^{l-x})} \\
&+ \prod_{l=0}^{F-1} \frac{\sin\left(\pi 2^{l-x}\left(1 - \frac{\tau}{2T_c} + \frac{1}{4\pi}\sin\left(\frac{2\pi\tau}{T_c}\right)\right)\right)^2}{\sin(\pi 2^{l-x})^2} \frac{\sin\left(\pi 2^{l-x}\left(\frac{\tau+T_c}{2T_c} + \frac{1}{4\pi}\sin\left(\frac{2\pi(\tau+T_c)}{T_c}\right)\right)\right)}{\sin(\pi 2^{l-x})} \\
&\times \frac{\sin\left(\pi 2^{l-x}\left(1 - \frac{\tau+T_c}{2T_c} + \frac{1}{4\pi}\sin\left(\frac{2\pi(\tau+T_c)}{T_c}\right)\right)\right)}{\sin(\pi 2^{l-x})} d\tau.
\end{aligned} \tag{466}
$$

Using the asymptotic expansion of integrals, (466) can be rewritten as

$$
\begin{aligned}
I_{n,n+1} \quad \approx \quad & e^{j2\pi h(2^F-1)} \frac{1}{\prod_{l=0}^{F-1} \sin(\pi 2^{l-x})^4} \\
\times \quad & \int_0^{T_c} \prod_{l=0}^{F-1} \frac{1}{3} \sin(\pi 2^{l-x}) 2^{l-x} \left(1 - \cos(\pi 2^{l-x-1})^2\right) \left(\frac{\pi\tau}{T_c}\right)^3 \\
+ \quad & \prod_{l=0}^{F-1} \left(\sin(\pi 2^{l-x})^2 \sin(\pi 2^{l-x-1})^2 + \frac{1}{2} \sin(\pi 2^{l-x})^3 2^{l-x} \frac{\pi\tau}{T_c} \right) d\tau = 0.
\end{aligned}
\tag{467}
$$

By noting that the value of the integral $I_{n+1,n}$ is equal to a complex conjugate value of the integral $I_{n,n+1}$ and that all functions inside the integral are real functions, we can conclude that integrals $I_{n+1,n}$ are also equal to zero. Similarly can be shown that integrals $I_{n,n+1}$ and $I_{n+1,n}$ for other combinations of integers $e_{j,l}^{(k-w_j)} \in \{0,1\}$ and integrals $I_{n,n+2}$ and $I_{n,n+2}$ for all $e_{j,l}^{(k-w_j)} = 0$ are equal to zero. $\boxdot$

REFERENCES

[1] R. Wang and D. Cox, "Channel modeling for ad hoc mobile wireless networks," *Proc. IEEE VTC'02*, vol. 1, pp. 21–25, Birmingham, AL, May 2002.

[2] R. Pabst *at al.*, "Relay-based deployment concepts for wireless and mobile broadband radio," *IEEE Commun. Magazine*, vol. 42, pp. 80–89, September 2004.

[3] Í. E. Telatar, "Capacity of multi-antenna Gaussian channels," *Eur. Trans. on Telecommun.*, vol. 10, no. 6, pp. 585–595, November 1999.

[4] V. Tarokh *at al.*, "Space-time codes for high data rate wireless communication: performance criterion and code construction," *IEEE Trans. on Information Theory*, vol. 44, pp. 744–765, March 1998.

[5] J. Grimm *et al.*, "Further results in space-time coding for Rayleigh fading," *Proc. Annual Allerton Conf. Commun., Control, and Computing*, Monticello, USA, September 1998.

[6] S. Baro *at al.*, "Improved codes for spacetime trellis coded modulation," *IEEE Commun. Letters*, vol. 4, pp. 20–22, January 2000.

[7] Q. Yan and R. S. Blum, "Optimum spacetime convolutional codes," *Proc. IEEE WCNC'00*, vol. 3, pp. 1351–1355, September 2000.

[8] D. M. Ionescu, "On space-time code design," *IEEE Trans. on Wireless Commun.*, vol. 2, pp. 20–28, January 2003.

[9] J. Yuan *at al.*, "Performance and design of space-time coding in fading channels," *IEEE Trans. on Commun.*, vol. 51, pp. 1991–1996, December 2003.

[10] A. R. Hammons and H. E. Gamal, "On the theory of space-time codes for PSK modulation," *IEEE Trans. on Information Theory*, vol. 46, pp. 524–542, March 2000.

[11] Y. Liu *at al.*, "A rank criterion for QAM space-time codes," *IEEE Trans. on Information Theory*, vol. 48, pp. 3062–3079, December 2002.

[12] Hsiao-feng Lu and P. V. Kumar, "Rate-diversity tradeoff of space-time codes with fixed alphabet and optimal constructuins for (PSK) modulation," *IEEE Trans. on Information Theory*, vol. 49, pp. 2747–2751, October 2003.

[13] Hsiao-feng Lu and P. V. Kumar, "A unified construction of space-time codes with optimal rate-diversity tradeoff," *IEEE Trans. on Information Theory*, vol. 51, pp. 1709–1730, May 2005.

[14] V. Tarokh *at al.*, "Space-time block codes from orthogonal designs," *IEEE Trans. on Information Theory*, vol. 45, pp. 1456–1467, July 1999.

[15] T. Aulin *at al.*, "Continuous phase modulation - part I and part II," *IEEE Trans. on Commun.*, vol.COM 29, pp. 196–225, March 1981.

[16] D. J. Young and N. C. Beaulieu, "A quantitative evaluation of generation methods for correlated Rayleigh random variates," *Proc. GLOBECOM '98*, Sydney, Australia, November, 1998, pp. 3332–3337.

[17] D. J. Young and N. C. Beaulieu, "The generation of correlated Rayleigh random variates by inverse discrete Fourier transform," *IEEE Trans. on Communications*, vol. 48, July 2000, pp. 1114–1127.

[18] D. Verdin and T. C. Tozer, "Generating a fading process for the simulation of land-mobile radio communications," *Electronics Letters*, vol. 29, no.23, November 1993, pp. 2011–2012.

[19] S. A. Fechtel, "A novel approach to modeling and efficient simulation of frequency-selecive fading radio channels," *IEEE Journal on Selected Areas in Commun.*, vol. 11, no. 3, April 1993, pp. 422–431.

[20] R. H. Clarke, "A statistical theory of mobile-radio reception," *Bell Syst. Tech. J.*, pp. 957–1000, July 1968.

[21] W. C. Jakes, *Microwave Mobile Communications*, 2nd ed. Piscataway, NJ: Wiley-IEEE Press, 1994.

[22] M. Pätzold and F. Laue,"Statistical properties of Jakes' fading channel simulator," *Proc. IEEE VTC'98*, pp. 712–718, Ottawa, Canada, May 1998.

[23] M. F. Pop and N. C. Beaulieu, "Limitations of sum-of-sinusoids fading channel simulators," *IEEE Trans. on Commun.*, vol. 49, pp. 699–708, April 2001.

[24] P. Dent *et al.*, "Jakes fading model revisited," *Electronics Letters*, vol. 29, no. 13, pp. 1162–1163, June 1993.

[25] Y. X. Li and X. Huang, "The simulation of independent Rayleigh faders," *IEEE Trans. on Commun.*, vol. 50, pp. 1503–1514, September 2002.

[26] M. Pätzold *et al.*, "On the statistical properties of deterministic simulation models for mobile fading channels," *IEEE Trans. on Veh. Technology*, vol. 47, pp. 254–269, February 1998.

[27] Y. R. Zheng and C. Xiao, "Simulation models with correct statistical properties for Rayleigh fading channels," *IEEE Trans. on Commun.*, vol. 51, pp. 920–928, June 2003.

[28] Y. R. Zheng and C. Xiao, "Improved models for the generation of multiple uncorrelated Rayleigh fading waveforms," *IEEE Commun. Letters*, vol. 6, no. 6, pp. 256–258, June 2002.

[29] Y. R. Zheng and C. Xiao, "A statistical simulation model for mobile radio fading channels," *Proc. IEEE WCNC'03*, pp. 144–149, New Orleans, USA, March 2003.

[30] C. S. Patel *et al.*, "Comparative analysis of statistical models for the simulation of Rayleigh faded cellular channels," *IEEE Trans. on Commun.*, vol. 53, pp. 1017–1026, June 2005.

[31] A. S. Akki and F. Haber, "A statistical model for mobile-to-mobile land communication channel," *IEEE Trans. on Veh. Technology*, vol. 35, no. 1, pp. 2–10, February 1986.

[32] A. S. Akki, "Statistical properties of mobile-to-mobile land communication channels," *IEEE Trans. on Veh. Technology*, vol. 43, no. 4, pp. 826–831, November 1994.

[33] F. Vatalaro and A. Forcella, "Doppler spectrum in mobile-to-mobile communications in the resence of three-dimensional multipath scattering," in *IEEE Trans. on Veh. Technology*, vol. 46, no. 1, pp. 213–219, Feb. 1997.

[34] C. S. Patel *et al.*, "Simulation of Rayleigh-faded mobile-to-mobile communication channels," *IEEE Trans. on Commun.*, vol. 53, pp. 1876–1884, November 2005.

[35] G. L. Stuber, *Principles of mobile communication*, 2nd ed. Norwell, MA: Kluwer, 2001.

[36] M. Pätzold, *Mobile Fading Channels*, West Sussex, England: John Wiley and Sons, 2002.

[37] M. Pätzold *et al.*, "A MIMO mobile-to-mobile channel model: part I-the reference model," *Proc. IEEE PIMRC'05*, vol. 1, pp. 573–578, Berlin, Germany, September 2005.

[38] B. O. Hogstad *et al.*, "A MIMO mobile-to-mobile channel model: part II-the simulation model," *Proc. IEEE PIMRC'05*, vol. 1, pp. 562–567, Berlin, Germany, September 2005.

[39] J. Maurer, T. Fügen, and W. Wiesbeck, "Narrow-band measurement and analysis of the inter-vehicle transmission channel at 5.2 GHz," *Proc. IEEE VTC 02*, vol. 3, pp. 1274–1278, Birmingham, AL, USA, May 2002.

[40] G. Acosta, K. Tokuda, and M. A. Ingram, "Measured joint Doppler-delay power profiles for vehicle-to-vehicle communications at 2.4 GHz," *Proc. IEEE GLOBECOM 04*, vol. 6, pp. 3813–3817, Dallas, TX, USA, Nov. 2004.

[41] X. Zhang and M. P. Fitz, "Space-time code design with continuous phase modulation," *IEEE Journal on Selected Areas in Commun.*, vol. 21, pp. 783–792, June 2003.

[42] X. Zhang and M. P. Fitz, "Space-time code design with CPM transmission," *IEEE Int. Symp. on Information Theory*, (Washington, DC), p. 327, June 2001.

[43] D. Wang *et al.*, "An orthogonal space-time coded partial response CPM system with fast decoding for two transmit antennas," *IEEE Trans. on Wireless Commun.*, vol. 4, no. 5, pp. 2410–2422, September 2005.

[44] G. Wang and X.-G. Xia, "Orthogonal spacetime coding for CPM system with fast decoding," *IEEE Trans. on Information Theory*, vol. 50, no. 3, pp. 486–493, March 2004.

[45] X. Zhang and M. P. Fitz, "Space-time coding for Rayleigh fading channels in CPM system," *Proc. Annual Allerton Conf. Commun., Control, and Computing*, Monticello, IL, October 2000.

[46] A. G. Zajić and G. L. Stüber, "A efficient simulation of Rayleigh fading with enhanced de-correlation properties," *IEEE Trans. on Wireless Commun.*, vol. 5, pp. 1866–1875, July, 2006.

[47] A. G. Zajić and G. L. Stüber, "A new simulation model for mobile-to-mobile Rayleigh fading channels," *Proc. IEEE WCNC'06*, vol. 3, pp. 1266–1270, Las Vegas, NE, USA, April 2006.

[48] A. G. Zajić and G. L. Stüber, "Space-time correlated mobile-to-mobile channels: modeling and simulation," vol. 57, pp. 715–726, *IEEE Trans. on Vehicular Tech.*, March, 2008.

[49] A. G. Zajić and G. L. Stüber, "Three-dimensional modeling, simulation, and capacity analysis of space-time correlated mobile-to-mobile channels," to appear in *IEEE Trans. on Vehicular Tech.*, June, 2008.

[50] A. G. Zajić and G. L. Stüber, "Three-dimensional modeling and simulation of wideband MIMO mobile-to-mobile channels," revised, submitted to *IEEE Trans. on Wireless Commun.*, June, 2008.

[51] A. G. Zajić and G. L. Stüber, "Envelope level crossing rate and average fade duration in mobile-to-mobile fading channels," submitted to *IEEE Trans. on Vehicular Tech.*, April, 2008.

[52] A. G. Zajić, G. L. Stüber, Thomas G. Pratt, and Son Nguyen, "Wideband MIMO mobile-to-mobile channels: geometry-based statistical modeling with experimental verification," to appear in *IEEE Trans. on Vehicular Tech.*, March, 2009.

[53] A. G. Zajić and G. L. Stüber, "A space-time code design for CPM: diversity order and coding gain," revised, submitted to *IEEE Trans. on Information Theory*, July, 2008.

[54] G. Durgin, *Space-time wireless channels*, Upper Saddle, NJ: Prentice Hall, 2002.

[55] G. J. Byers and F. Takawira, "Spatially and temporally correlated MIMO channels: modeling and capacity analysis," *IEEE Trans. on Veh. Technology*, vol. 53, pp. 634–643, May 2004.

[56] U. Mengali and M. Morelli, "Decomposition of M-ary CPM signals into PAM waveforms," *IEEE Trans. on Information Theory*, vol. 41, pp. 1265–1275, September 1995.

[57] C. Xiao, Y. R. Zheng and N. Beaulieu, "Statistical simulation models for Rayleigh and Ricean fading," *Proc. IEEE Int. Commun. Conf.*, Anchorage, AK, vol. 65, pp. 3524–3529, May 2003.

[58] D. Gesbert, H. Bölcskei, D.A. Gore, and A.J. Paulraj, "Outdoor MIMO wireless channels: models and performance prediction," *IEEE Trans. on Commun.*, vol. 50, pp. 1926–1934, Dec. 2002.

[59] J. Salz and J. H. Winters, "Effect of fading correlation on adaptive arrays in digital mobile radio," *IEEE Trans. on Veh. Tech.*, vol. 43, pp. 1049–1057, Nov. 1994.

[60] A. Abdi, J. A. Barger, and M. Kaveh, "A parametric model for the distribution of the angle of arrival and the associated correlation function and power spectrum at the mobile station," *IEEE Trans. on Veh. Tech.*, vol. 51, pp. 425–434, May 2002.

[61] K. I. Pedersen, P. E. Mogensen, and B. H. Fleury, "Power azimuth spectrum in outdoor environments," *IEEE Electronics Letters*, vol. 33, pp. 1583–1584, Aug. 1997.

[62] K. I. Pedersen, P. E. Mogensen, and B. H. Fleury, "A stochastic model of the temporal and azimuthal dispersion seen at the base station in outdoor propagation environments," *IEEE Trans. on Veh. Tech.*, vol. 49, pp. 437–447, Mar. 2000.

[63] I. S. Gradshteyn and I. M. Ryzhik, *Table of Integrals, Series, and Products* 5^{th} *ed.*. A. Jeffrey, Ed. San Diego CA: Academic, 1994. submitted.

[64] D. Shiu, G. J. Foschini, M. J. Gans, and J. M. Khan, "Fading correlation and its effect on the capacity of multielement antenna systems," *IEEE Trans. on Commun.*, vol. 48, pp. 502–513, Mar. 2000.

[65] A. Abdi and M. Kaveh, "A space-time correlation model for multielement antenna systems in mobile fading channels," *IEEE J. on Select. Areas in Commun.*, vol. 20, pp. 550–560, Apr. 2002.

[66] H. Kang, G. L. Stüber, T. G. Pratt, and M. A. Ingram, "Studies on the capacity of MIMO systems in mobile-to-mobile environment," *Proc. IEEE WCNC 04*, vol. 1, pp. 363–368, Atlanta, GA, USA, Mar. 2004.

[67] T. Aulin, "A modified model for the fading at a mobile radio channel," *IEEE Trans. on Veh. Tech.*, vol. VT–28, pp. 182–203, 1979.

[68] J. D. Parsons and A. M. D. Turkmani, "Characterisation of mobile radio signals: model description," *IEE Proc. I, Commun., Speach, and Vision*, vol. 138, pp. 549–556, December 1991.

[69] P. Almers, F. Tufvesson, P. Karlsson, and A. F. Molisch, "The effect of horizontal array orientation on MIMO channel capacity," *Proc. IEEE VTC'03*, vol. 1, pp. 34–38, April 2003.

[70] K. Kalliola, K. Sulonen, H. Laitinen, O. Kivekäs, J. Krogerus, and P. Vainikainen "Angular power distribution and mean effective gain of mobile antenna in different propagation environments," *IEEE Trans. on Veh. Tech.*, vol. 51, pp. 823–838, September 2002.

[71] Y. Yamada, Y. Ebine, and N. Nakajima, "Base station/vehicular antenna design techniques employed in high capacity land mobile communications system," *Rev. Elec. Commun. Lab.*, NTT, pp. 115–121, 1987.

[72] R. H. Clarke, and W. L. Khoo, "3-D mobile radio channel statistics," *IEEE Trans. on Veh. Tech.*, vol. 46, pp. 798–799, August 1997.

[73] T. Taga, "Analysis for mean effective gain of mobile antennas in land mobile radio environments," *IEEE Trans. on Veh. Tech.*, vol. 39, pp. 117–131, May 1990.

[74] A. Kuchar, J. P. Rossi, and E. Bonek, "Directional macro-cell channel characterization from urban measurements," *IEEE Trans. on Antennas and Prop.*, vol. 48, pp. 137–146, February 2000.

[75] K. V. Mardia and P. E. Jupp, *Directional Statistics.* New York. Wiley 1999.

[76] J. G. Proakis, *Digital Communications 4e.* New York:McGraw Hill, 2001.

[77] P. Hoeher, "A statistical discrete-time model for the WSSUS multipath channel," *IEEE Trans. on Veh. Tech.*, vol. 41, pp. 461–468, Nov. 1992.

[78] E. Chiavaccini and G.M. Vitetta, "GQR models for multipath Rayleigh fading channels," *IEEE Journal on Select. Areas in Commun.*, vol. 19, pp. 1009–1018, June 2001.

[79] R. S. Kennedy, *Fading dispersive communication channels.* New York: Wiley-Interscience, 1969.

[80] P. Bello, " Characterization of randomly time-variant linear channels," *IEEE Trans. on Commun.*, vol. 11, pp. 360–393, Dec. 1963.

[81] Z. Latinovic, A. Abdi, and Y. Bar-Ness, "A wideband space-time model for MIMO mobile fading channels," *Proc. IEEE WCNC'03*,vol. 1, pp. 338–342, New Orleans, LA, USA, March 2003.

[82] Z. Latinovic, A. Abdi, and Y. Bar-Ness, "On the utility of the circular ring model for wideband MIMO channels," *Proc. IEEE VTC'04*,vol. 1, pp. 96–100, Los Angeles, CA, USA, Sept. 2004.

[83] G. Acosta and M. A. Ingram, "Model development for the wideband expressway vehicle-to-vehicle 2.4 GHz channel," *Proc. IEEE WCNC'06*,vol. 3, pp. 1283–1288, Las Vegas, NE, USA, April 2006.

[84] M. Pätzold, U. Killat, and F. Laue, "An extended Suzuki model for land mobile satellite channels and its statistical properties,"*IEEE Trans. on Veh. Tech.*, vol. 47, pp. 617–630, May 1998.

[85] C. B. Ribeiro, E. Ollila, and V. Koivunen, "Stochastic maximum likelihood method for propagation parameter estimation," *Proc. IEEE PIMRC*, Sept. 2004.

[86] W. C. Y. Lee,"Estimate of local average power of mobile radio signal," *IEEE Trans. on Veh. Tech.*, vol. 34, pp. 22–27, February 1985.

[87] P. D. Welch, "The use of fast fourier transform for the estimation of power spectra: a method based on time averaging over short, modified periodograms," *IEEE Trans. Audio Electroacoustics*, vol. AU-15, pp. 70–73, June 1967.

[88] L. J. Greenstein, D. G. Michelson, and V. Erceg, "Moment-method estimation of the Ricean K-factor," *IEEE Commun. Letters*, vol. 3, pp. 175–176, June 1999.

[89] R. Fletcher, *Practical Methods of Optimization - Constrained Optimization 2e.*. John Wiley and Sons, 1981.

[90] B. E. Rimoldi, "A decomposition approach to CPM," *IEEE Trans. on Information Theory*, vol. 34, pp. 260–270, March 1988.

[91] P. A. Laurent, "Exact and approximate construction of digital phase modulations by superposition of amplitude modulated pulses," *IEEE Trans. on Communications*, vol. 34, pp. 150–160, Febrary 1986.

[92] R. A. Horn and C. R. Johnson, *Matrix analysis.* Cambridge University Press, 1985.

[93] J. R. Barry, E. A. Lee, D. G. Messerschmitt, *Digital communication 3e.* Kluwer Academic Publishers, 2004.

[94] G. Caire and E. Biglieri, "Linear block codes over cyclic groups," *IEEE Trans. on Information Theory*, vol. 41, pp. 1246–1256, September 1995.

[95] S. M. Alamouti, "A simple transmit diversity technique for wireless communications," *IEEE Journal on Selected Areas in Communications*, vol. 16, pp 1451–1458, October 1998.

[96] H. Lu, Y. Wang, P. V. Kumar, and K. M. Chugg, "Remarks on space-time codes including a new lower bound and an improved code," *IEEE Trans. on Information Theory*, vol. 49, pp. 2752–2757, October 2003.

[97] H. Jafarkhani and N. Seshadri, "Super-orthogonal space-time trellis codes," *IEEE Trans. on Information Theory*, vol. 49, pp. 937–950, April 2003.

[98] C. M. Bender and S. A. Orszag, *Advanced mathematical methods for scientists and engineers 2e.* Springer, 1999.

VITA

Alenka G. Zajić was born in Belgrade, Serbia, on April 28, 1977. She received the B.Sc. and M.Sc. degrees form the School of Electrical Engineering, University of Belgrade, in 2001 and 2003, respectively. From 2001 to 2003, she was a design engineer for Skyworks Solutions Inc., Fremont, CA.

Since 2004, she has been a Graduate Research Assistant with the Wireless Systems Laboratory, and pursuing the Ph.D. degree in the School of Electrical and Computer Engineering, Georgia Institute of Technology. Her research interests are in wireless communications and applied electromagnetics.

She received the Best Student Paper Award at WCNC 2007, the Best Paper Award at ICT 2008, and was also the recipient of the Dan Noble Fellowship in 2004, awarded by Motorola Inc. and IEEE Vehicular Technology Society for quality impact in the area of vehicular technology.